Assessing Groundwater Sustainability in Gardnerville Ranchos, Nevada, from 2024 to 2043 through Scenario-Based Groundwater Modeling

Daniel Saftner

Rishi Parashar

PREPARED BY
Division of Hydrologic Sciences, DRI

PREPARED FOR
Gardnerville Ranchos General Improvement District

July 2025
Publication No. 41309

THIS PAGE LEFT INTENTIONALLY BLANK

Assessing Groundwater Sustainability in Gardnerville Ranchos, Nevada, from 2024 to 2043 through Scenario-Based Groundwater Modeling

Daniel Saftner
Rishi Parashar

July 2025

Publication No. 41309

Prepared by
Division of Hydrologic Sciences, DRI

Prepared for
Gardnerville Ranchos General Improvement District

THIS PAGE LEFT INTENTIONALLY BLANK

EXECUTIVE SUMMARY

In Carson Valley in northwestern Nevada, groundwater is an important water source that supports homes, businesses, and agriculture. However, increased groundwater use over recent decades has led to lower groundwater levels across the valley, especially in the Gardnerville Ranchos area. These lower groundwater levels raise concerns about the long-term availability of groundwater and highlight the need for careful water resource planning.

This study developed a groundwater flow model to assess the future availability of groundwater resources in the Gardnerville Ranchos area of Carson Valley. The purpose of this model is to help the Gardnerville Ranchos General Improvement District (GRGID) evaluate the groundwater system response to population and temperature changes to inform water management decisions.

Using historical groundwater level and pumping data, and data from aquifer tests conducted during this study, the model was designed to:

- Explain how groundwater moves within the Gardnerville Ranchos area and the broader southern Carson Valley.
- Estimate future changes in groundwater levels under different climate and water demand scenarios.
- Evaluate if the Gardnerville Ranchos supply well network can meet future water demands.

The model examined monthly groundwater conditions from 1965 to 2023 and projected future conditions from 2024 to 2043. The projections included scenarios with different rates of increased groundwater pumping (0.2% and 1.5% per year) and temperature (0.1°F and 0.2°F per year). These scenarios provide a range of potential future outcomes related to population growth and warmer temperatures.

The results show declining groundwater levels under all scenarios, even if pumping rates and temperatures stay the same. Despite these declines, groundwater levels will remain above operational thresholds at all wells. Therefore, the existing well network in Gardnerville Ranchos is expected to meet future water demands through 2043. The model reflects average monthly conditions and not short-term spikes in water use that could temporarily lower groundwater levels. The strength of this model is its ability to compare different scenario outcomes rather than predicting exact water levels.

Under the base-case scenario (i.e., no increase in pumping or temperature), groundwater levels could decrease by up to 10 feet (3 meters) in western Gardnerville Ranchos due to pumping from domestic wells and reduced infiltration from irrigation canals. Warmer temperatures and earlier streamflow in the East and West Forks of the Carson River initially cause slight groundwater level increases in spring, but reduced annual streamflow eventually leads to overall declines in groundwater levels.

The greatest declines are predicted in southern and eastern Gardnerville Ranchos because of higher pumping rates (1.5% per year) and higher temperatures (0.2°F per year). In this case, groundwater levels could drop another 3 to 10 feet (1 to 3 meters) compared to the base-case scenario by summer 2043. Groundwater level declines are less severe with a moderate increase in groundwater pumping (0.2% per year), typically less than 1.6 feet

(0.5 meters) lower than the base-case scenario. The groundwater level declines in eastern and southern Gardnerville Ranchos are related to pumping from high-demand wells, such as Wells 1 and 2, and geologic faults that inhibit groundwater flow.

To ensure sustainable groundwater use, this study recommends that GRGID continue investing in water conservation programs, adjust pumping patterns seasonally to address climate and demand variations, and regularly update the model with new data. The model developed in this study can be used to choose the location of future supply wells, evaluate the impacts of land use changes on groundwater resources, and simulate pumping scenarios. This model is intended to be a practical tool to guide planning efforts and preserve a reliable water supply for Gardnerville Ranchos residents.

CONTENTS

LIST OF FIGURES

LIST OF TABLES

LIST OF ACRONYMS

AC_x	Upgradient contributing inflow area
af	acre-feet
amsl	above mean sea level
AR	irrigation application rate
AT_x	Total subsurface inflow area for the east or west side of the Carson River
CWC	cell-to-well conductance
d_{ext}	evapotranspiration extinction depth
DRI	Desert Research Institute
ET	evapotranspiration
ET_{actual}	actual evapotranspiration
ET_{ag}	agricultural evapotranspiration
ET_{gw}	groundwater evapotranspiration
ET_{max}	maximum evapotranspiration
EVT or EVT1	MODFLOW Evapotranspiration Package
FWM	Federal Water Master
ft	feet
GHB	General Head Boundary
GHB1	General Head Boundary MODFLOW Package
GMS	Groundwater Modeling System software
GRGID	Gardnerville Ranchos General Improvement District
GW_{in}	Groundwater flux into the study area
GW_{out}	Groundwater flux out of the study area
GW_{pump}	Groundwater discharge through pumping
HFB6	Horizontal Flow Barrier Package for MODFLOW
HSU	hydrostratigraphic unit
in	inch
k	thousand
LS	land surface
MGA	millions of gallons
MNW2	Multi-Node Well Package for MODFLOW
MODFLOW	Modular Three-Dimensional Finite-Difference Groundwater Flow Model
MSE	mid-screen elevation
MW	monitoring well
NDWR	Nevada Division of Water Resources
NLCD	National Land Cover Dataset
NOAA	National Oceanic and Atmospheric Administration
NV	Nevada
NW	northwest
NWIS	National Water Information System

NWT	Newton formulation for MODFLOW
PEST	parameter estimation package
$PPT_{effective}$	effective precipitation
Q_{des}	the maximum desired flow rate
Q_{EF}	East Fork Carson River discharge into the model domain
Q_{IC}	Indian Creek discharge into the model domain
Q_{INtot}	total groundwater flow into the model domain
Q_{INx}	groundwater flow into the model domain from area x
Q_{ret}	irrigation water that becomes runoff and flows into the canal network
Q_{sim}	simulated flow rate
Q_{stream}	groundwater seepage from the aquifer to surface water
RCH or RCH1	Recharge Package for MODFLOW
RMSE	root mean square error
$RMSE_{rel}$	relative root mean square error
STR or STR1	Stream Package for MODFLOW
UPW	Upstream Weighting Package for MODFLOW
USGS	United States Geological Survey
WEL or WEL1	Well Package for MODFLOW
yr	year

LIST OF HYDROGEOLOGIC AND MODELING TERMS

Aquifer: A body of permeable rock or sediment that stores and transmits groundwater.

Basin-fill Aquifer: An aquifer formed by sediments that have filled a basin, typically consisting of gravel, sand, silt, and clay.

Bedrock: Solid rock underlying soil or unconsolidated material, often considered the lower boundary in groundwater models.

Confined Aquifer: An aquifer that is bounded above and below by layers of impermeable material and is under pressure.

Drawdown: The lowering of the water level in a well due to groundwater extraction.

Evapotranspiration (ET): The combined process of water evaporation from the land and transpiration from plants.

Fault (in hydrogeology): A fracture or zone of fractures in rock that may impede or facilitate groundwater flow.

General Head Boundary (GHB): A model boundary where water can enter or leave the model domain depending on the difference between model head and specified head outside the model.

Horizontal Flow Barrier (HFB): A model feature used to simulate a fault or geologic feature that impedes horizontal groundwater flow.

Hydraulic Conductivity (K): A property of soil or rock that describes how easily water can move through pore spaces or fractures.

Hydraulic Gradient: The slope of the water table or potentiometric surface, which drives groundwater flow.

Hydrostratigraphic Unit (HSU): A layer or set of layers in the subsurface that have similar hydraulic properties and behave similarly with respect to groundwater flow.

Infiltration: The process by which water on the ground surface enters the soil, contributing to soil moisture or recharge of aquifers.

Manning's Roughness Coefficient (n): A parameter representing surface resistance to flow in open channel hydraulics, used in flow and flood modeling.

Model Residuals: The differences between observed and simulated values in a model, used to assess model accuracy.

Model Calibration: The iterative process of adjusting model parameters to minimize residuals and improve agreement between observed and simulated data.

MODFLOW: A modular finite-difference groundwater flow model developed by the USGS for simulating groundwater conditions.

Numerical Model: A computer simulation that uses mathematical equations to approximate physical processes such as groundwater flow.

Permeability: A measure of how easily fluids can flow through a porous medium, directly affecting groundwater movement.

Phreatophytes: Deep-rooted plants that extract water directly from the saturated zone, potentially influencing local groundwater levels.

Potentiometric Surface: an imaginary or hypothetical surface that represents the total hydraulic head of groundwater in an aquifer, providing a visualization of the pressure of groundwater within an aquifer.

Recharge: The process by which water enters an aquifer, typically from precipitation, rivers, or irrigation.

Riparian Zones: Vegetated areas adjacent to rivers and streams that interact with surface and groundwater, playing key roles in water quality and ecosystem function.

Runoff: Water that flows over the land surface toward streams or other bodies, typically after rainfall, due to limited infiltration.

Specific Capacity: The rate at which water is produced from a well per unit of drawdown, often used as an indirect estimate of aquifer transmissivity.

Stable Isotope Analysis: A method of using naturally occurring isotopes in water to determine the source or history of water movement.

Storativity (Specific Storage/Storage Coefficient): The amount of water a portion of an aquifer releases or stores per unit area per unit change in head (pressure).

Steady-State Model: A model where the groundwater system is assumed to be in balance, with no change in water levels or storage over time.

Transmissivity: A measure of how much water can be transmitted horizontally, such as through an aquifer. It is the product of hydraulic conductivity and the aquifer thickness.

Transient Model: A model that simulates changes in groundwater levels and storage over time due to varying conditions.

Uncertainty: A measure of the lack of certainty in model predictions, often arising from simplifications in model design, imprecise or unknown parameter values, or limitations in observed data. In groundwater models, uncertainty reflects how closely the simulated results can be trusted to represent real-world conditions.

Unconfined Aquifer: An aquifer where the water table is open to the atmosphere through porous material.

Upstream Weighting (UPW): A method used in groundwater models to improve numerical stability in calculating water flow between cells.

Vadose Zone: The area between the land surface and the water table where soil pores may contain both air and water.

THIS PAGE LEFT INTENTIONALLY BLANK

1.0 INTRODUCTION

1.1 Description of the Gardnerville Ranchos Study Area

The unincorporated community of Gardnerville Ranchos is in the Carson Valley Hydrographic Basin ("Carson Valley") of northern Nevada (Figure 1). The study area extends beyond the Gardnerville Ranchos boundary to account for the effects of groundwater pumping in adjacent areas, including agricultural land and the communities of Gardnerville and Ruhenstroth (Figure 2).

The Gardnerville Ranchos water system, which is managed by the Gardnerville Ranchos General Improvement District (GRGID), is reliant solely on groundwater from the basin-fill aquifer of the Carson Valley. The basin-fill aquifer is the primary groundwater source of the Carson Valley. Groundwater level trends in Carson Valley have raised concerns among residents regarding the long-term sustainability of the groundwater supply and the aquifer's ability to support future water demands under a warming climate.

Development of the Gardnerville Ranchos subdivision began in the mid-1960s. The Gardnerville Ranchos General Improvement District (GRGID) was established on April 9, 1965, to provide services that include maintenance of the water system, sewer system, and storm drain system. Groundwater is extracted from seven supply wells, conveyed via 58 miles of distribution piping, stored in two storage tanks, including one 3.0 million-gallon (MGA) (11,356 m^3) and one 1.5 MGA (5,678 m^3) tank, disinfected, and is then distributed for use.

The water system serves approximately 4,500 connections, 98% of which are residential dwellings. Other water uses include commercial/industrial and community/public spaces. In 2020, the Gardnerville Ranchos had a population of 11,432, which accounts for more than one-third of the population of Carson Valley. GRGID's water rights are all groundwater rights and currently total approximately 5,308 acre-feet per year (af/yr) (6.5 million m^3/yr). The land use of Gardnerville Ranchos is primarily residential with some land used for commercial purposes, public use (e.g., parks), and schools. Land outside of Gardnerville Ranchos is primarily irrigated land used for agriculture, ranching, and business (e.g., Carson Valley Golf Course).

The reliance on groundwater as the sole water source for Gardnerville Ranchos underscores the importance of careful resource management, particularly as the region faces increasing water demand and potential climate-related stressors. Seasonal fluctuations in groundwater levels, coupled with prolonged drought conditions, have the potential to impact both water availability and quality. Additionally, increased pumping demands for residential, agricultural, and industrial uses necessitate careful monitoring and management strategies to ensure the long-term reliability of the water supply in Gardnerville Ranchos.

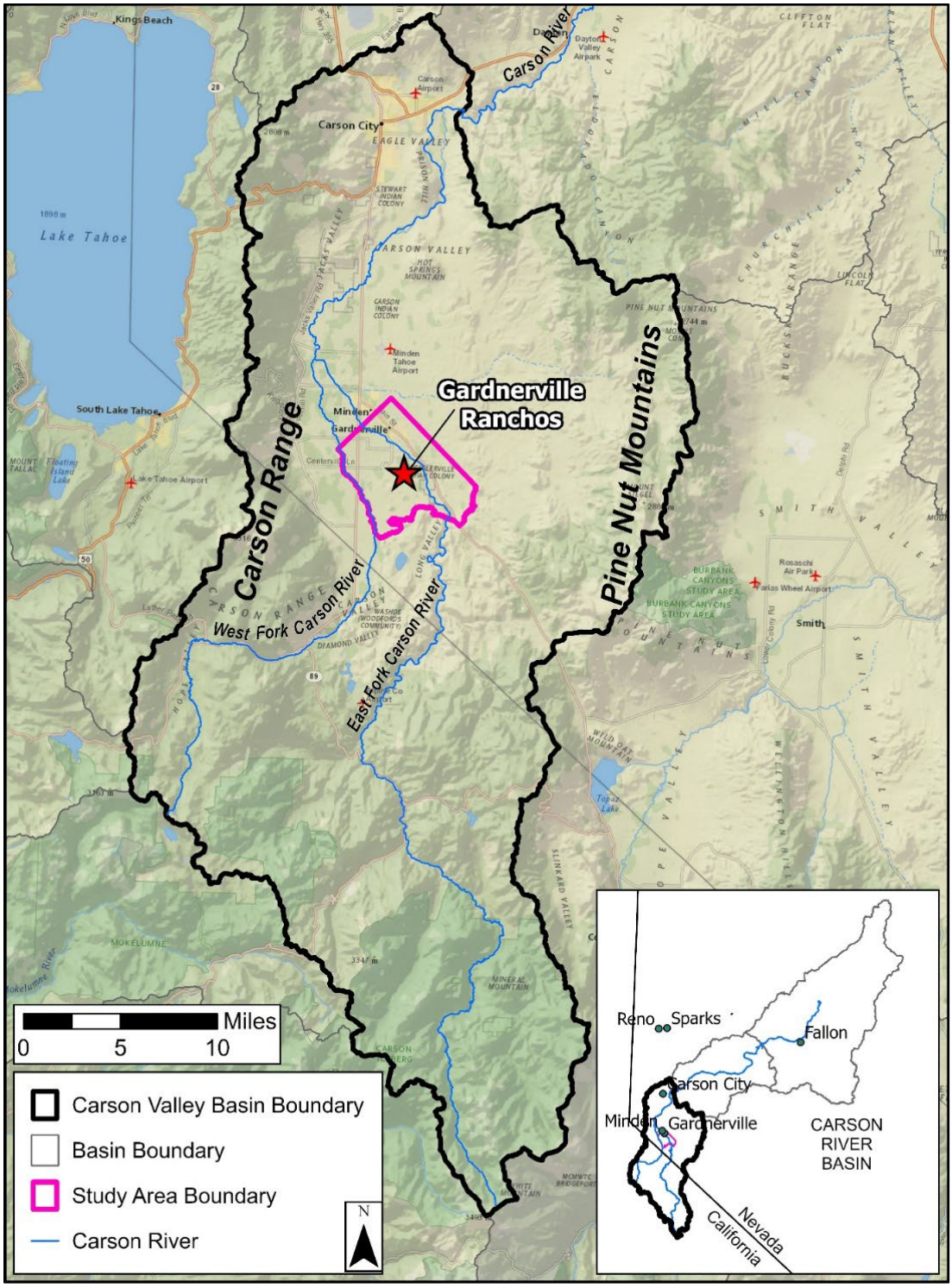

Figure 1. The boundaries of the study area within the Carson Valley Hydrographic Basin. The major hydrologic features of the Carson Valley are included, showing that Gardnerville Ranchos is between the West Fork Carson River and East Fork Carson River. The inset map shows the extent of the Carson River Basin. The Carson River terminates in the most downstream basin and past the city of Fallon. The study area is in the most upstream basin of the Carson River Basin.

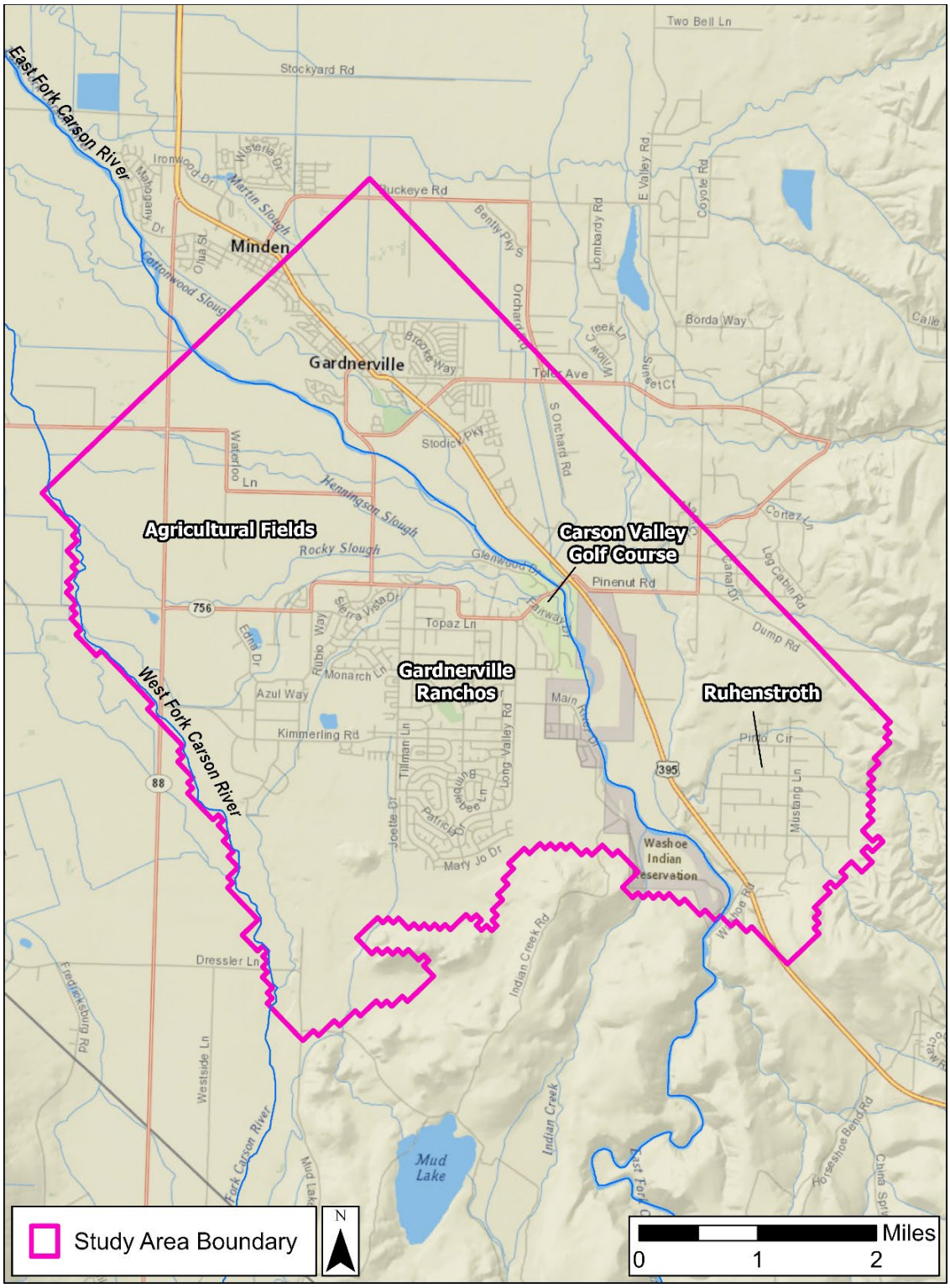

Figure 2. The study area boundary extends beyond Gardnerville Ranchos to account for groundwater pumping in adjacent areas, including the communities of Gardnerville and Ruhenstroth, the Carson Valley Golf Course, and agricultural fields.

1.2 Study Objectives and Scope

In 2021, GRGID approached the Desert Research Institute (DRI) with concerns regarding the current and future groundwater availability in the Gardnerville Ranchos area. GRGID entered a contract with DRI to conduct a hydrogeologic characterization and develop a predictive numerical groundwater flow model ("model") to simulate future changes to groundwater in response to changes in climate and water demand.

To address concerns related to groundwater availability in the Gardnerville Ranchos area, specific objectives of the modeling study include:

1. Estimating the range of potential future changes to average monthly groundwater levels under various climate and water-demand scenarios from 2024 through 2043; and
2. Assessing whether the existing supply well network of Gardnerville Ranchos is expected to meet future monthly water demands over this time frame under various climate and water-usage scenarios.

This report summarizes activities performed by DRI to meet these objectives, including field data collection and groundwater flow modeling. All field data were collected from fall 2021 through fall 2023. The purpose of these investigations was to characterize local aquifer and hydrologic conditions. The field data collection activities included borehole drilling, monitoring well installation, water level monitoring, aquifer testing, and water sampling for stable isotope analysis. Field data collection activities and results are described in detail in Appendix A. The estimated aquifer properties, including hydraulic conductivity and storativity, and aquifer boundary conditions, were used to inform the development of the model. Additionally, the model was calibrated for the study area using the most up-to-date data available, including water levels during seven aquifer tests and five new monitoring wells. The calibrated model was used to run predictive simulations to identify and assess groundwater level changes under projected future climate and water demand scenarios.

Along with the primary data collected during the field campaign, secondary data synthesized include:

- Surface water level and discharge data from the United States Geological Survey's (USGS) National Water Information System (NWIS) and the Federal Water Master (FWM) for local stream gaging stations; and
- Relevant geological, hydrological, geophysical, meteorological, and climate data from existing reports, publications, and databases.

This report does not address water quality concerns beyond stable isotope analysis, nor does it evaluate potential contamination sources or their impact on groundwater resources. Additionally, while the study includes predictive simulations for future groundwater conditions, it does not incorporate socio-economic factors, policy implications, or specific water management strategies for mitigating potential shortages. Furthermore, the modeling efforts focus on groundwater flow dynamics rather than surface water, ecological impacts, or broader watershed management considerations.

1.3 Previous Investigations

Previous studies contribute much to the understanding of the groundwater conditions of the Carson Valley and the broader Carson River Basin, providing foundational data for the development of the model presented in this report. However, there have been only a few previous investigations that focus specifically on the groundwater and hydrogeology of the Gardnerville Ranchos area. From 1970 to 2005, the USGS conducted about 37 aquifer tests to estimate hydraulic properties of the basin-fill aquifer throughout Carson Valley. Of these tests, approximately nine were conducted in GRGID supply wells, providing point estimates of transmissivity in Gardnerville Ranchos. These were single-well tests, so bulk aquifer transmissivity and storage parameters were not estimated. Using the results of these previous tests, Yager et al. (2012) established a relationship between specific capacity (ratio of discharge rate to drawdown) and transmissivity to estimate the spatial distribution of transmissivity of sediments throughout Carson Valley. The spatial distribution of aquifer properties estimated by Yager et al. (2012) has since been used for other hydrology models in Carson Valley (e.g., Kitlasten et al. [2021]).

One of the first groundwater models of the Carson Valley was developed by Maurer (1986) to enhance the understanding of groundwater flow of the Carson Valley basin-fill aquifer system and to simulate the effect of various development scenarios on Carson River outflow and groundwater levels. Simulations reported in Yager et al. (2012), a groundwater model for the Carson Valley basin-fill aquifer to evaluate effects of expected increasing demand on the water budget from 2006 to 2060, indicated that projected increases in groundwater withdrawals would result in 5 to 20 ft (1.5 to 6 m) of water table decline in the Gardnerville Ranchos area by 2060, 40 ft (12 m) declines on the west and east sides of the valley, and minimal changes in the central part of the valley. A regional model developed by Kitlasten et al. (2021) integrated hydrology and operations modeling to evaluate climate impacts on water availability for agriculture in Carson Valley. Their study assessed the effects of projected changes in precipitation and temperature on streamflow timing and magnitude, and groundwater recharge. The model by Kitlasten et al. (2021) highlights that earlier snowmelt results in less surface water availability during the growing season and, ultimately, greater groundwater reliance for agriculture.

Several other studies have led to supporting information and an improved understanding of the water budget for Carson Valley. Reconnaissance-level water budgeting was performed by Glancy and Katzer (1975) for the Carson River Basin, which includes Carson Valley (Figure 1). A study by Maurer and Halford (2004) improved estimates of the distribution of precipitation in Carson Valley. Maurer et al. (2006) estimated groundwater recharge rates of various sedimentary deposits in Carson Valley, including Quaternary gravel deposits (0.04 ft/yr [0.01 m/yr]), Quaternary eolian sand deposits (0.03 ft/yr [0.01 m/yr]), and between 600-700 af/yr (740k-863k m^3/yr) for alluvial fans in southwestern Carson Valley (or 4-5% of annual precipitation). Maurer et al. (2004) led a study on perennial streamflow in tributaries of the Carson Valley. Watershed models by Jeton and Maurer (2007) estimate ephemeral streamflow and groundwater recharge from the Carson Range and Pine Nut Mountains. A study by Maurer et al. (2006) provides estimates of evapotranspiration (ET) from various vegetation types and land uses in Carson Valley, recharge from precipitation, and rates of streamflow losses/gains from streams and irrigation ditches on the valley floor. The study by Maurer et al. (2006) found that the Carson River and irrigation ditches in

southern and eastern Carson Valley, including the area of Gardnerville Ranchos, lose flow to groundwater. A report by Maurer and Berger (2007) presented updated estimates of all water-budget components for Carson Valley. Huntington et al. (2012) explored the interactions between groundwater and surface water in the Carson Valley, providing data on streamflow and groundwater recharge. The study by Huntington et al. (2012) emphasized the importance of surface water bodies, such as the Carson River, in sustaining groundwater levels, especially during periods of low precipitation. Berger (1987, 1990) analyzed groundwater levels and estimated groundwater pumping in the Carson Valley for water years 1984-1987. As part of the Washoe Project, Dillingham (1980) focused on groundwater conditions of the Carson River Basin, with some specifics on the hydrogeology of the Gardnerville Ranchos area.

Geologic studies in the region have focused on the area's tectonic evolution and aquifer characteristics. Maurer (1984) conducted a gravity survey that provided essential data on the depth to bedrock and its relationship with groundwater flow in Carson Valley. The study by Maurer (1984) was particularly important for understanding lateral aquifer boundaries based on faults and vertical boundaries based on sediment thickness. Cashman (2009) offered insights into the Neogene tectonic evolution of the Sierra Nevada, examining how the region's geological history influences groundwater movement.

These studies, along with others referenced throughout this document, provide a critical foundation for understanding the hydrogeologic conditions of the Gardnerville Ranchos area. By synthesizing historical data with recent field measurements, the conceptual model captures spatial variations in aquifer properties, and the spatial and temporal distribution of groundwater recharge, ET, and extraction patterns. Incorporating updated datasets and refined projections enhances the reliability of groundwater simulations, allowing for a more precise assessment of potential changes in water availability. This report not only builds upon past research but also advances predictive capabilities to better inform water resource management strategies under evolving climate conditions and increasing demand pressures.

2.0 HYDROGEOLOGIC SETTING AND CONCEPTUAL MODEL

A field-based hydrogeologic investigation was conducted by the Desert Research Institute (DRI) from fall 2021 through fall 2023 to characterize the hydrogeology of the Gardnerville Ranchos and surrounding areas. Details of the field data collection methodologies, data analysis, and results of the hydrogeologic characterization are provided in Appendix A. This section summarizes the key takeaways from the field investigations, as well as other studies and datasets that are relevant to the study area and the broader Carson Valley and were used to develop the hydrogeologic conceptual model. A hydrogeologic conceptual model is a simplified, qualitative representation of the aquifer system, including hydrogeological features, boundaries, and processes that govern groundwater flow. A conceptual model provides a water budget of inflows and outflows and serves as a foundation for building a numerical model. The water budget of the numerical model is compared to the conceptual model water balance to check for any inconsistencies.

2.1 Climate and Physiography

Gardnerville Ranchos is in the western Great Basin section of the Basin and Range physiographic province. The community is situated in the Carson Valley (Nevada Division of Water Resources Basin No. 105), at the southern edge of the valley floor (unconsolidated, undifferentiated unit in Figure 3). Carson Valley is an intermontane basin situated between the Carson Range of the Sierra Nevada to the west and the Pine Nut Mountains to the East (Figure 3). The basin is oval-shaped, approximately 20 miles (32 km) wide and 60 miles (97 km) long. The valley floor slopes to the northwest from an altitude of about 5,000 feet above mean sea level (amsl) (1,524 m amsl) in the south to 4,600 ft amsl (1,402 m amsl) in the north. The Carson Range rises abruptly from the valley floor to a maximum altitude of about 10,900 ft (3,320 m), whereas the Pine Nut Mountains rise more gradually to about 9,500 ft (2,900 m).

The area's climate is strongly influenced by the rain-shadow effect of the Sierra Nevada, resulting in low annual precipitation on the valley floor. The nearest meteorological station to Gardnerville Ranchos is in Minden, NV. Daily meteorological data was compiled for the Minden station from 1965 to 2023 (the transient model calibration period; see Section 3.0) and was used to calculate monthly and annual precipitation totals. A time series of annual precipitation (by calendar year) for the Minden station from the National Oceanic and Atmospheric Administration's (NOAA) Global Historical Climatological Network is included as Figure 4 (Menne et al., 2012). The average annual precipitation from 1965 to 2023 was 8.7 inches (220 mm).

Figure 4 shows the inter-annual variability of precipitation for the Minden station, which fluctuated between approximately 2.5 inches and 20 inches. A ten-year period of below average precipitation occurred from 1984 to 1994, which was followed by four years of above-average precipitation. Another period of above-average precipitation occurred from 2015 to 2019. The second highest annual precipitation total since 1965 was recorded during the field campaign of this study in 2022.

Daily precipitation totals from 2020 through 2023 are shown in Figure 5 to illustrate precipitation leading up to, during, and after the field campaign of this study. With few exceptions, daily precipitation was less than 0.5 inches. The summer of 2022 was one of the wettest since 1965, with 2.5 inches (63.5 mm) of rain recorded in a single day in August. Daily precipitation totals were also high during the 2022-2023 winter, which is when most aquifer tests were conducted during this study.

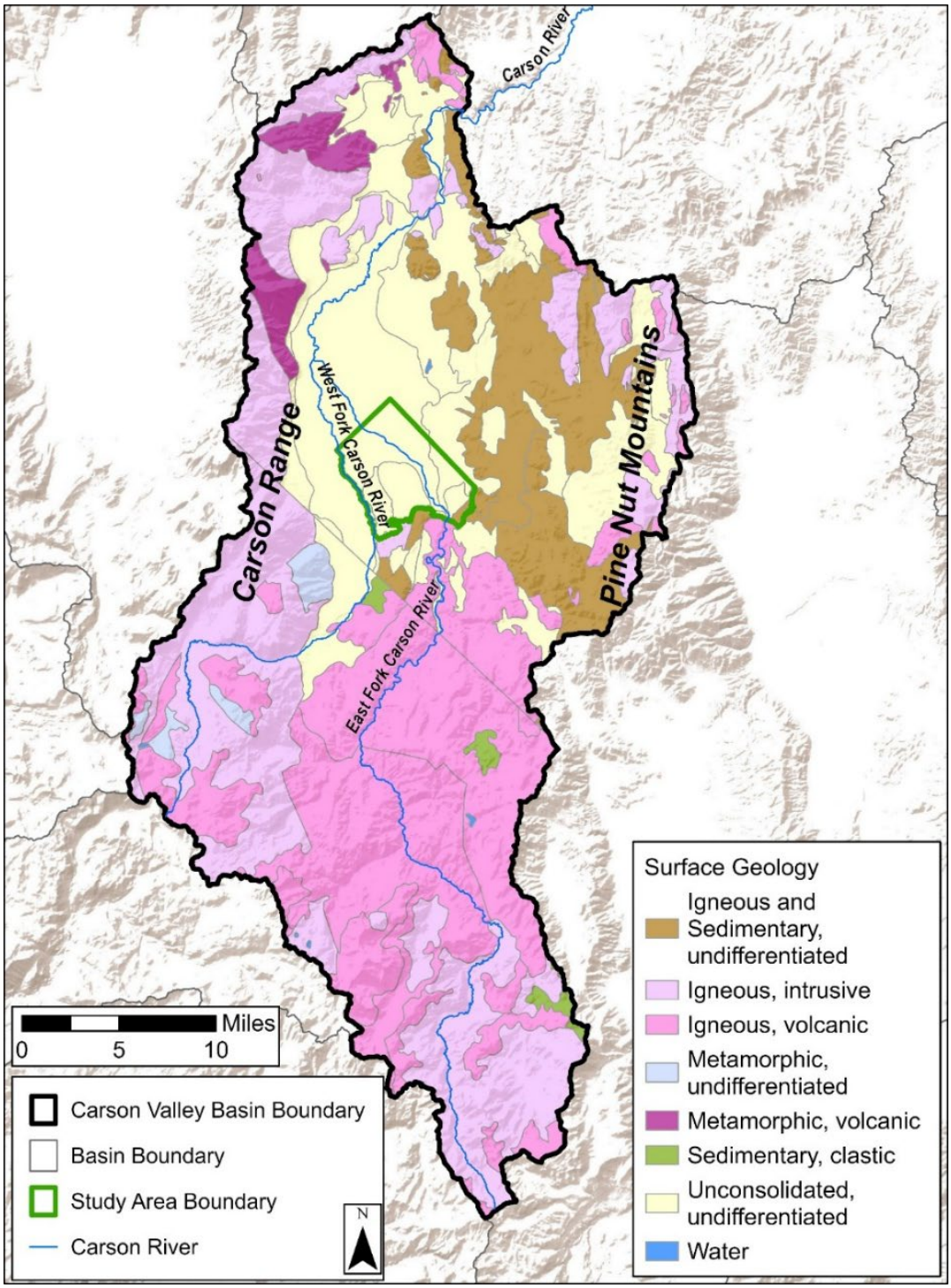

Figure 3. Surface geology from the USGS State Geologic Map Compilation (Horton et al., 2017) for the Carson Valley hydrographic basin. The study area is located at the southern edge of the unconsolidated sediment of the valley floor.

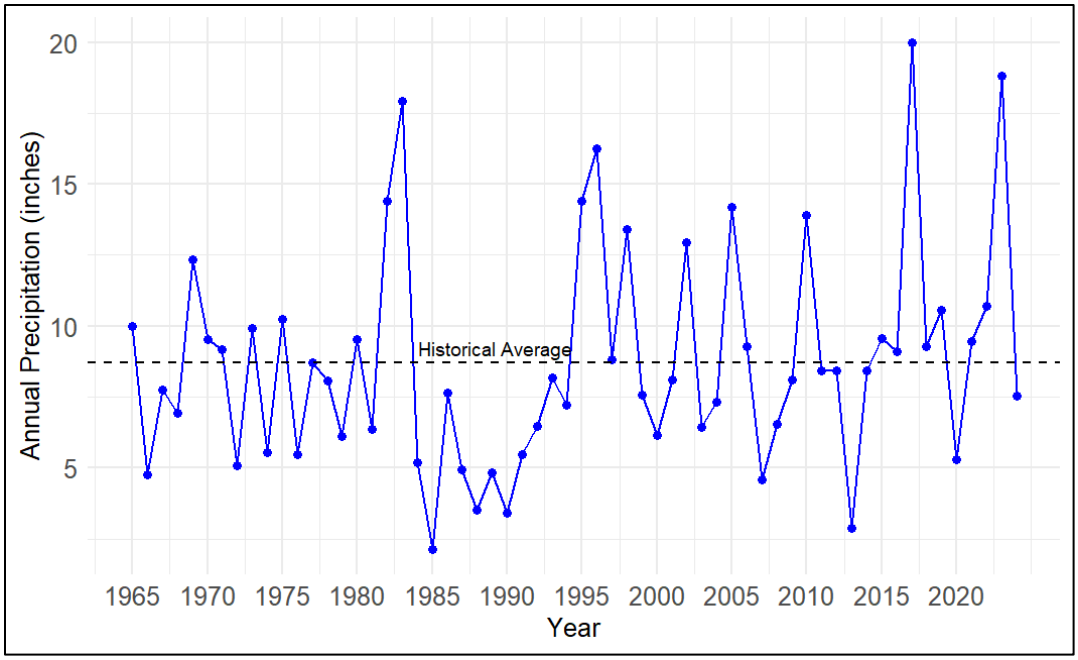

Figure 4. Historical total annual precipitation (inches) by calendar year in Minden, Nevada, using data from the NOAA Global Historical Climatological Network (Menne et al., 2012). The black dotted line shows the average annual precipitation calculated between 1965 to 2023).

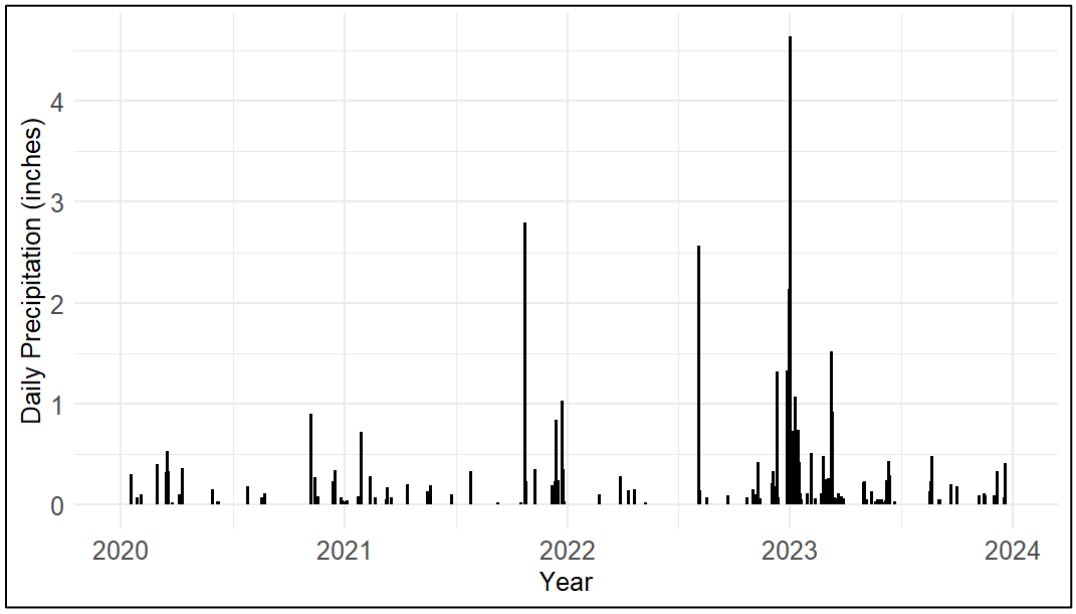

Figure 5. Daily precipitation totals (inches) measured at a NOAA station from 2020 to 2023 for Minden, Nevada, illustrating precipitation leading up to and during the field campaign, which extended from fall 2021 to fall 2023. Data retrieved from the NOAA Global Historical Climatological Network (Menne et al., 2012).

The seasonality of precipitation, as well as the precipitation-elevation relation and the precipitation phase (rain versus snow), play a role in the timing and magnitude of water availability in Carson Valley. The range of monthly precipitation totals for Minden from 1965 through 2023 are shown by the box plots in Figure 6. On average, about 58% of the annual precipitation occurs during winter months (December through March). Annual precipitation increases with elevation, reaching 40 in/yr (1,016 mm/yr) in the Carson Range and 18 in/yr (457 mm/yr) near the crest of Pine Nut Mountain (Maurer and Halford, 2004). Most of the precipitation in the upper elevations falls as snow.

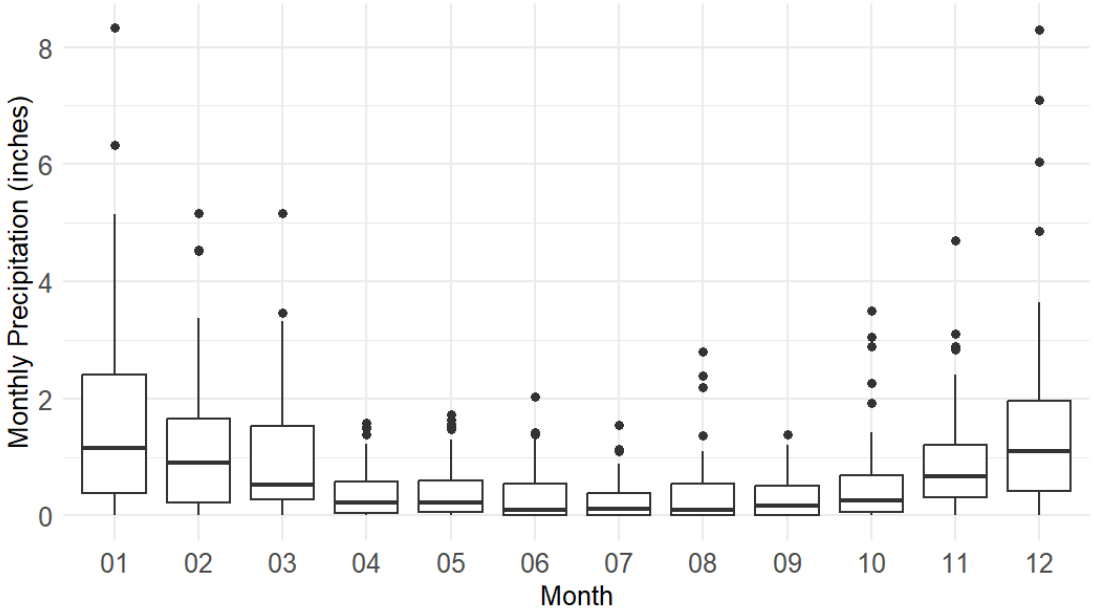

Figure 6. Box plots showing the range of monthly precipitation totals from 1965 through 2023 for Minden, Nevada. Each box plot shows how the precipitation data are distributed. Months are numbered as in the calendar year (e.g., 01 = January). For each month, the bottom of the lower vertical line is the minimum precipitation total for that month, the bottom of the box is the first quartile (25% of the data points are below this value), the horizontal line in the middle of the box is the median, the top of the box is the third quartile, and the top of the upper vertical line is the maximum. The black dots are outlier data points, defined as values exceeding 1.5 times the interquartile range above the third quartile.

The precipitation trends observed in the Gardnerville Ranchos area provide necessary inputs for groundwater model development, as they directly influence recharge dynamics and water availability. Seasonality of precipitation, with the majority occurring in winter, plays a key role in groundwater recharge processes. Incorporating these spatial and temporal precipitation patterns into the groundwater model improves its ability to simulate aquifer response under different climate and water demand scenarios.

2.2 Surface Water Hydrology and Irrigation

The dominant surface water feature of Carson Valley is the Carson River, which is a snowmelt-dominated river with perennial flow. The main stem of the Carson River forms at the confluence of the East Fork Carson River and West Fork Carson River near the community of Genoa in the Upper Carson River Basin (Figure 1). The combined flow of the Carson River continues to the northeast, exits Carson Valley, and continues through the Middle and Lower Carson River Basins (Figure 1), before reaching the Lahontan Reservoir (Figure 1). Flows out of the Lahontan Reservoir are controlled and the majority is used for agriculture before it can reach the Carson Sink. Prior to the construction of the reservoir, the Carson River terminated in the Carson Sink. The entire Carson River Basin covers approximately 2.6 million acres (10.4k square km).

Headwaters of the East and West Forks are in the Carson Range. Flows of the East and West Forks are controlled by the timing and magnitude of snowmelt, with peak flows typically occurring in May or June. Warming temperatures in the region result in earlier snowmelt, which impacts the timing of surface water availability and groundwater recharge (Kitlasten et al., 2021). The upper watersheds of the East Fork and West Fork Carson River have a combined drainage area of 270,600 acres (1,095 square km) and consist mainly of low permeability bedrock (Figure 3), so water drains quickly to the rivers during rain or snowmelt events (Kitlasten et al., 2021).

The East and West Forks enter the valley from the south, and the community of Gardnerville Ranchos is located between them (Figure 7). The Carson Water Subconservancy District calculated average flows from 1965 to 2023 and determined 272,883 af/yr (337 million m^3/yr) for the East Fork and 75,698 af/yr (93.4 million m^3/yr) for the West Fork (L Marsh and E. James, personal communication, July 1, 2025). Maurer and Berger (2007) compared the flows of the Carson River for two periods, including 1941-1970 and 1990-2005 (Table 1). The decreased flows during 1990-2005 in both the East and West Forks are the result of dry conditions from 1987 to 1992 and 1999 to 2005.

Table 1. Average annual inflows to the Carson Valley from the East Fork Carson River and West Fork Carson River from Maurer and Berger (2007).

River	Average annual inflow to Carson Valley from 1941 to 1970 (af/yr)	Average annual inflow to Carson Valley from 1990 to 2005 (af/yr)
East Fork	265,950	256,240
West Fork	75,430	73,350

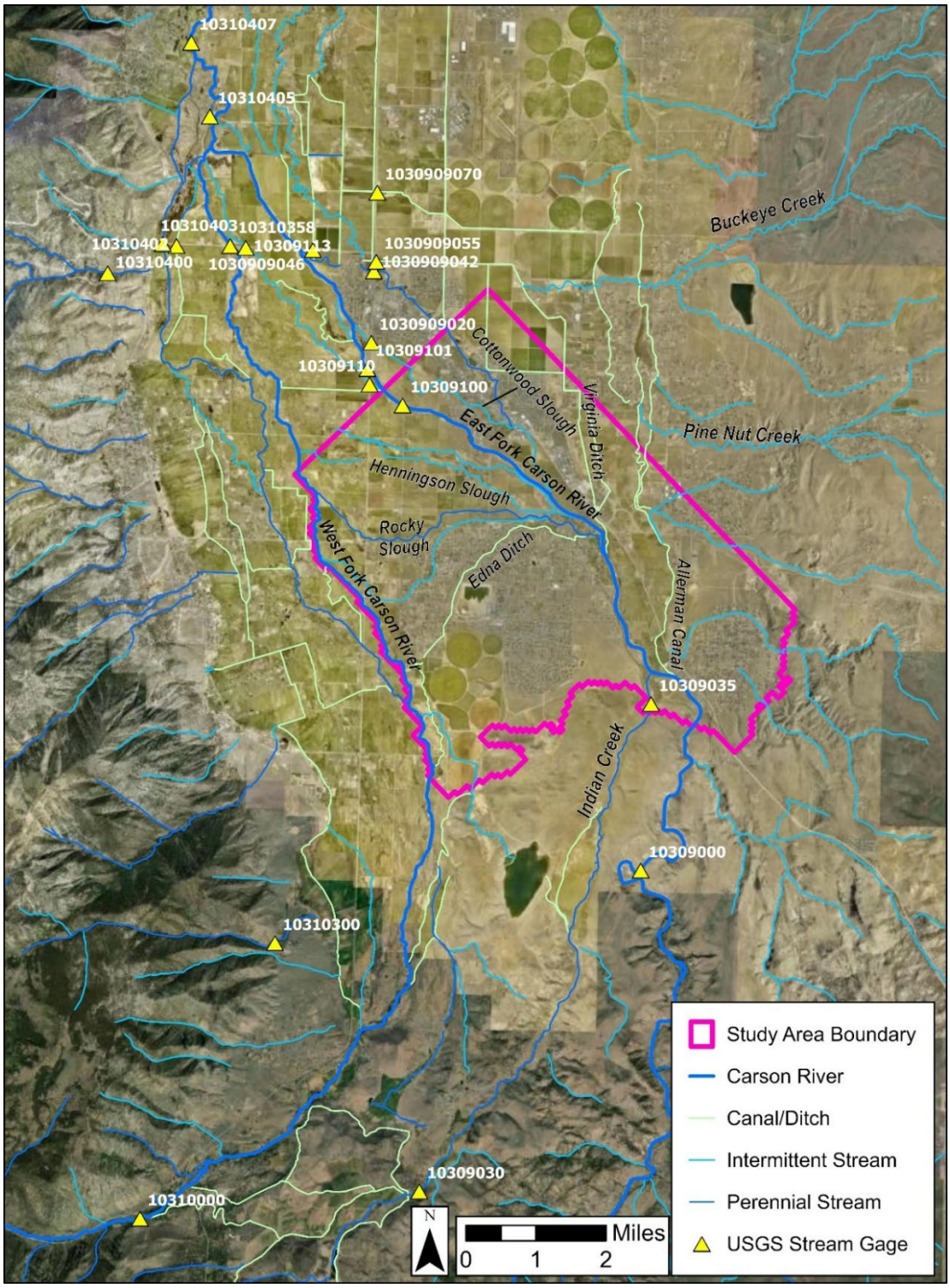

Figure 7. Map of hydrologic features of southern Carson Valley, including the Carson River, intermittent and perennial drainages of Carson Range on the west and Pine Nut Mountains on the east (Pine Nut and Indian Creeks), and canals, ditches, and sloughs on the valley floor. Major surface water diversions in the study area are labeled by name. Locations and IDs of USGS stream gages are shown as triangles.

Upstream of the valley floor, streamflow is diverted from the West Fork to the Snowshoe Thompson Ditches for irrigation water in Diamond Valley. Return flows from the ditches drain to Indian Creek, which is tributary to the East Fork on the valley floor. Total diversions to the ditches averaged about 5,900 af/yr (7.3 million m^3/yr) for water years 1993-2003 (with 61% going to Ditch 1) (Maurer et al., 2007). Sporadic field measurements of streamflow for Indian Creek near the model boundary (site number 10309035) date back to 1981. Daily streamflow measurements were made at the Indian Creek gage from 1995 through 1998, a period of above average streamflow (8,480 af/yr [10.5 million m^3/yr]) (Preissler et al., 1999). The average flow entering Carson Valley from Indian Creek for water years 1940-2005 is about 5,100 af/yr (6.3 million m3/yr) (Maurer et al., 2007).

The Carson Valley also receives inflows of surface water from thirteen perennial streams that drain the Carson Range (Maurer et al., 2004). Average annual surface water inflows from tributaries along the west side of the valley are 30,000 af (37 million m^3/yr). From the east, two perennial streams, Buckeye and Pine Nut Creeks, drain the Pine Nut Mountains. The combined average annual flow of Buckeye and Pine Nut Creeks was about 1,400 af/yr (1.7 million m^3/yr) from 1990 to 2002 (Maurer et al., 2004). However, streamflow only reaches the valley floor and Carson River during spring runoff of very wet years or storm events (Yager et al., 2012).

Surface waters from the East and West Forks are diverted to a complex network of unlined canals, ditches, and sloughs for flood irrigation of alfalfa and native pasture grasses that cover most of the southern and western parts of the Carson Valley floor (Figure 7). Several points of diversion to canals and ditches reroute surface water through and around the Gardnerville Ranchos area. Water allocation for irrigation is controlled under the Alpine Decree (United States v. Alpine Land and Reservoir Co., 1980), a legally binding framework of water allocation for over 900 individual water rights within the Carson River Basin. The FWM oversees irrigation water distribution and operates stream gaging stations to monitor flow at major diversions during the irrigation season, generally from April through September. Flow from the East Fork is regulated when flow at the East Fork Gardnerville gage falls below 200 ft^3/sec (5.66 m^3/s), at which point the FWM adjusts irrigation deliveries based on water availability. Major diversions included in the model and mean annual streamflow calculated by Maurer et al. (2009) using streamflow data from the FWM are presented in Table 2.

Table 2. Mean annual streamflow at major irrigation diversions in the study area from 1984 to 2006 (Maurer et al., 2009) and the ratio of mean annual flow of each ditch/slough to the mean annual flow of the Allerman Canal over this time frame. These ratios are used to estimate flows during model calibration and for predictive simulations.

Gaging Station Name	Mean Annual Streamflow, 1984-2006 (af/yr)	Mean Annual Streamflow, 1984-2006, as Percent of Allerman Canal Mean Annual Streamflow (%)
Allerman Canal	25,300	-
Virginia Ditch	11,800	47
Rocky Slough	17,200	68
Edna Slough	5,400	21
Cottonwood Slough	6,100	24
Henningson Slough	5,100	20

Three canals distribute water northeast of the East Fork, including the Allerman Canal, Virginia Ditch, and Cottonwood Slough. The Allerman Canal is the first diversion of the East Fork on the Carson Valley floor. Once the flow at the Gardnerville gage reduces to 200 ft^3/s, one-third of the flow is diverted to the Allerman Canal and the remaining two-thirds stay in the East Fork for downstream use. Irrigation water that becomes runoff and returns to the irrigation system is termed “return flows.” Return flows from these diversions generally return to the irrigation system at ditches and sloughs west of U.S. 395 northwest of Minden, eventually flowing out of the study area.

The other principal canals, including Henningson Slough, Rocky Slough, and Edna Ditch, divert flows to the west of the East Fork for irrigation between the East and West Forks. Rocky Slough connects the East and West Forks and provides water for approximately 17 ditches and additional flow to the West Fork. Return flows from the Rocky Slough diversions ultimately reach the West Fork.

Monthly flow data are available from the FWM for the Allerman Canal and Virginia Ditch from 2015 to 2023 (Figures 8 and 9). Diversion rates are higher during the irrigation season (April-September) and lower during the non-irrigation season (October-March), with no flow in some instances. Peak diversion flow typically occurs between May and July. In some cases, diversion rates are not measured during the non-irrigation season, which may explain some of the zero flow periods of Virginia Ditch.

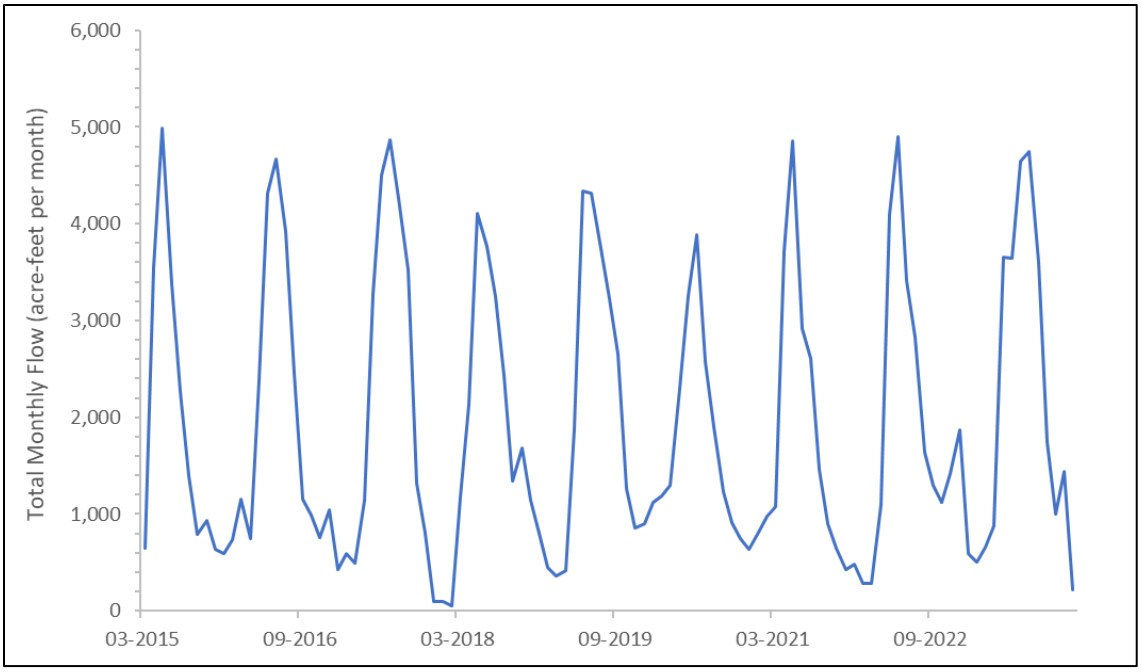

Figure 8. Allerman Canal monthly flow totals from 2015 to 2023 in acre-feet per month (FWM, 2024).

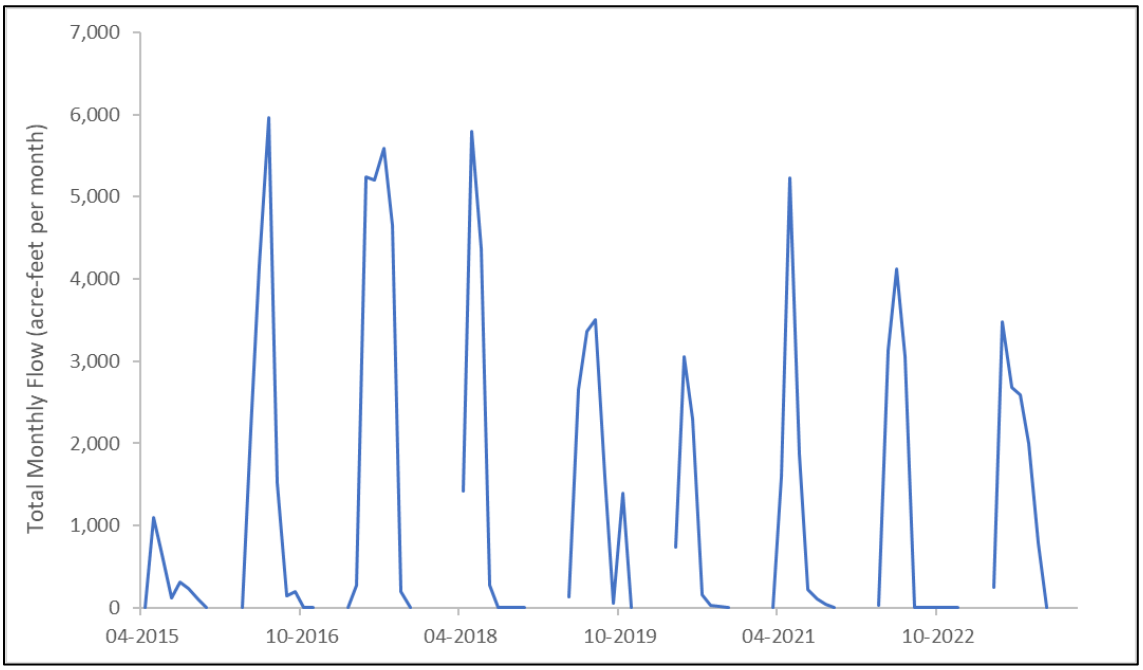

Figure 9. Virginia Ditch monthly flow totals from 2015 to 2023 in acre-feet per month (FWM, 2024).

Water applied for irrigation either becomes return flow, is consumed by ET, or infiltrates the subsurface to the water table (Yager et al., 2012). Infiltration of surface water through streambeds, ditches, and canals and beneath flood-irrigated fields ("agricultural recharge") contributes significant groundwater recharge, maintaining a shallow water table of less than 5 feet beneath much of the valley floor (Maurer, 2007). Return flow to the irrigation system from irrigated fields in Carson Valley was estimated to be 30 to 50% of applied water in the 1970s (Guitjens et al., 1978) and decreased to 20 to 30% since the 1980s because of fields being laser-leveled for improved irrigation efficiency (Yager et al., 2012).

Supplemental groundwater is generally pumped from the deeper leaky-to-confined aquifer for irrigation and is applied through flood irrigation, sprinklers, or pivots. During years of average or less than average precipitation, groundwater pumpage for irrigation usually accounts for the greatest groundwater use in the valley. In some cases, pumped groundwater is discharged to the canals and ditches and applied as flood irrigation. Sprinkler irrigation systems have also been used along the eastern side of the valley since the 1990s (Yager et al., 2012). Sprinkler systems to the southwest of Gardnerville Ranchos have been in use since the mid-1980s (Yager et al., 2012).

Effluent from several entities is discharged into Carson Valley, including the South Tahoe Public Utility District, Douglas County Lake Tahoe Sewer Authority, Incline Village General Improvement District, and Minden Gardnerville Sanitation District. Maurer and Berger (2007) estimated that imported effluent applied for irrigation averaged about 9,500 af/yr (12 million m^3/yr) from 1990 to 1995. Areas of effluent application are downgradient and outside of the study area and therefore are not considered in this study.

2.3 Geology and Hydrogeology

2.3.1 Regional Geology and Hydrogeology

Granitic, metamorphic, and volcanic rocks of Jurassic to Tertiary age make up the bedrock that surrounds and underlies the valley floor (Figure 3). The bedrock, which is relatively impermeable to groundwater flow, is overlain by Tertiary sediments and Quaternary alluvial and fluvial sediments. The semi-consolidated Tertiary sediments consist of fine-grained and tuffaceous siltstone with lenses of sandstone and gravel (Muntean, 2001). The thickness of the Tertiary deposits is estimated to exceed 3,000 ft (914 m) (Muntean, 2001).

Basin-fill deposits consist of Quaternary sediments that have been deposited by the Carson River and tributary streams from the Carson Range and Pine Nut Mountains. Alluvial fans surround the valley and underlie much of the floodplain of the Carson River. The alluvial deposits are the primary aquifer of Carson Valley and consist of a fine- to coarse-grained, poorly sorted mixture of sand, gravel, silt, and clay (Yager et al., 2012). Floodplain deposits consist of well-sorted sand and gravel interbedded with over-bank flood deposits of fine-grained silt and clay. Fluvial deposits cover most of the valley floor and interfinger with alluvial-fan deposits beneath the valley margins.

Hydraulic conductivity values for basin-fill sediments in Nevada generally range from 0.001 feet per day (ft/d) to 590 ft/d (0.0003 to 180 m/d) depending on composition, association with geomorphic features, and geographic position with the basin (Maurer et al., 2004). In that study, Maurer et al. evaluated aquifer hydraulic properties from various

geographic positions and geomorphic features in basins in Nevada, many of which are present in the study area (Tables 3 and 4). Geomorphic features are landforms created by geological processes, while geomorphic position refers to a specific location of a feature within a landscape. As described by Maurer et al. (2004), hydraulic conductivity typically decreases with grain size from the upper alluvial slope to the valley center, with the greatest hydraulic conductivity typically observed in fluvial deposits.

Table 3. Range in hydraulic conductivity for unconsolidated sediment in Nevada by geomorphic position (modified from Maurer et al. [2004]).

Geomorphic Position	Range in Hydraulic Conductivity (ft/day)
Fluvial deposits	4 to 2,200
Basin fill, undifferentiated	0.001 to 590
Upper alluvial slope	0.5 to 140
Lower alluvial slope	0.02 to 140
Undifferentiated	0.0002 to >150
Valley floor	2 to 90

Table 4. Range of hydraulic conductivity values for unconsolidated sediments by geomorphic feature (modified from Maurer et al. [2004])

Geomorphic Feature	Range in Hydraulic Conductivity (ft/day)
Alluvial slope/dune sand	20 to 30
Alluvial slope/stream channel	10 to 20
Valley floor alluvium	5 to 10
Flood plain/lake deposits	1 to 5

Using single-well aquifer testing data, Yager et al. (2012) estimated that transmissivity of Tertiary and Quaternary sediments of Carson Valley ranges from 20 to 31,000 feet squared per day (ft^2/d) (1.9 to 2,800 m^2/d). Quaternary basin-fill sediments within 0.5 miles of the Carson River were estimated to have the greatest transmissivity, exceeding 15,000 ft^2/d (1,390 m^2/d). Low transmissivity values of 160 and 800 ft^2/d (15 to 75 m^2/d) were estimated from two wells in Tertiary sediments.

Yager et al. (2012) also established a relationship between specific capacity (ratio of discharge rate to drawdown) and transmissivity and estimated the median transmissivity for Quaternary alluvial fan deposits (316 ft^2/d [29 m^2/d]), Quaternary fluvial deposits (3,120 ft^2/d [290 m^2/d]), and Tertiary sediments (110 ft^2/d [10 m^2/d]).

2.3.2 Local Geology and Hydrogeology

Gardnerville Ranchos sits atop a flat river terrace of late to middle Pleistocene age (Dillingham, 1980) (Figure 10). The river terrace is a former floodplain where the surrounding sediment has been cut into by the East and West Forks and flushed downstream, leaving behind a “bench-like” feature that is approximately 30 ft (10 m) higher than the valley floor. The terrace consists of alternating layers of alluvial and floodplain deposits. The

southern edge of the terrace is covered by alluvial fan deposits derived from adjacent volcanic outcrops (Ramelli et al., 2014). The alluvial fan deposits interfinger with floodplain deposits with depth.

At the local scale of the study area, layers of fine sediments (clays and silts) associated with floodplain deposits create leaky-to-confined aquifer conditions beneath Gardnerville Ranchos. Aquifer testing results (described in Appendix A, "Aquifer Testing Results") also suggest the presence of a two-aquifer system throughout the study area that includes a deeper leaky-to-confined aquifer and a shallow unconfined aquifer with leakage through the aquitard that separates the two aquifers. There were several instances during aquifer testing of increasing drawdown with distance from the test well (i.e., tests at Wells 1, 2, 6, and 9; locations shown on Figure 10). For example, in the eastern segment of the river terrace, during the Well 1 test, the drawdown at MW5 (only 850 ft [260 m] from the pumping well) was approximately 3.4 ft (1 m), while the maximum drawdown at Well 2 (1,640 ft [500 m] away from the pumping well) was greater, at approximately 18 ft (5 m). This distance-drawdown relationship is explained by Well 2 being screened in the pumped aquifer (Well 2 screened interval = 270 to 650 ft [82 to 200 m] bgs; Test Well 1 screened interval = 140 to 420 ft [43 to 128 m] bgs) and MW5 being screened in the shallow unpumped aquifer (MW5 screened interval = 105 to 125 ft [32 to 38 m] bgs).

Based on aquifer test results and lithology data from three boreholes drilled during this study, overlapping clay layers at depths of about 100-200 feet create the leaky-to-confined aquifer conditions and separate the shallow unconfined aquifer from the deeper aquifer. The shallow deposits (<100 ft [30 m]) that make up the unconfined aquifer in the eastern section of the river terrace consist primarily of sandy gravels with alternating zones of clayey gravels. Gravels and boulders supported by a matrix of stiff-to-hard clays are abundant at depths greater than 100 ft (30 m) with silt and clay lenses of thicknesses up to 20 ft (6 m).

Shallow deposits (<115 ft [<35 m]) of the unconfined aquifer in the western segment of the river terrace consist predominantly of poorly sorted sands, gravels, and boulders. Clay lenses in the western portion of the terrace occur at depths as shallow as 115 ft (35 m) below ground surface and range in thickness from 5 ft to >12 ft (1.2 to >3.7 m) in the northwest (near Well 6 and Well 9) to 15 ft (4.6 m) in the southwest (near Well 5). These clay lenses become more abundant with depth, with clays being most prevalent at depths exceeding 400 ft (122 m). Lithology logs of previous and new boreholes are included in Appendix A.

This conceptualization of a two-aquifer system is consistent with Dillingham (1980), who stated that there is no laterally continuous clay bed, but rather, leaky-to-confined conditions result from discontinuous clay beds scattered beneath the valley floor. Maurer (1985) stated that the Carson Valley groundwater basin contains a deeper confined basin-fill aquifer system and a shallow unconfined aquifer where the top of the aquifer is defined by the shallow water table (Maurer, 1985).

Throughout the report, the leaky-to-confined aquifer may be referred to more simply as the "confined aquifer" or "deep aquifer," while the unconfined aquifer is commonly referred to as the "shallow aquifer." For the purposes of this report, 200 ft (61 m) is used as the general cutoff between "shallow" and "deep" wells, aquifers, and deposits. Monitoring wells MW1-6, MW1_Bing, MW2_Bing, and Sweetwater are considered shallow monitoring

wells (average depth = 137 ft [42 m] bgs, max depth = 198 ft [60 m] bgs) and are completed in the unconfined aquifer. Well 7 is a deep monitoring well (depth = 480 ft [146 m]). Supply wells in Gardnerville Ranchos range in depth from 372 ft (113 m) at Well 4 to 650 ft (198 m) at Well 2. The leaky-to-confined aquifer is the primary aquifer pumped by the supply wells. However, some of the pumping wells are partially screened in both aquifers (i.e., Well 1 and Well 4). Well details including coordinates, depth, screened intervals, and pump depths are provided in Table A-1.

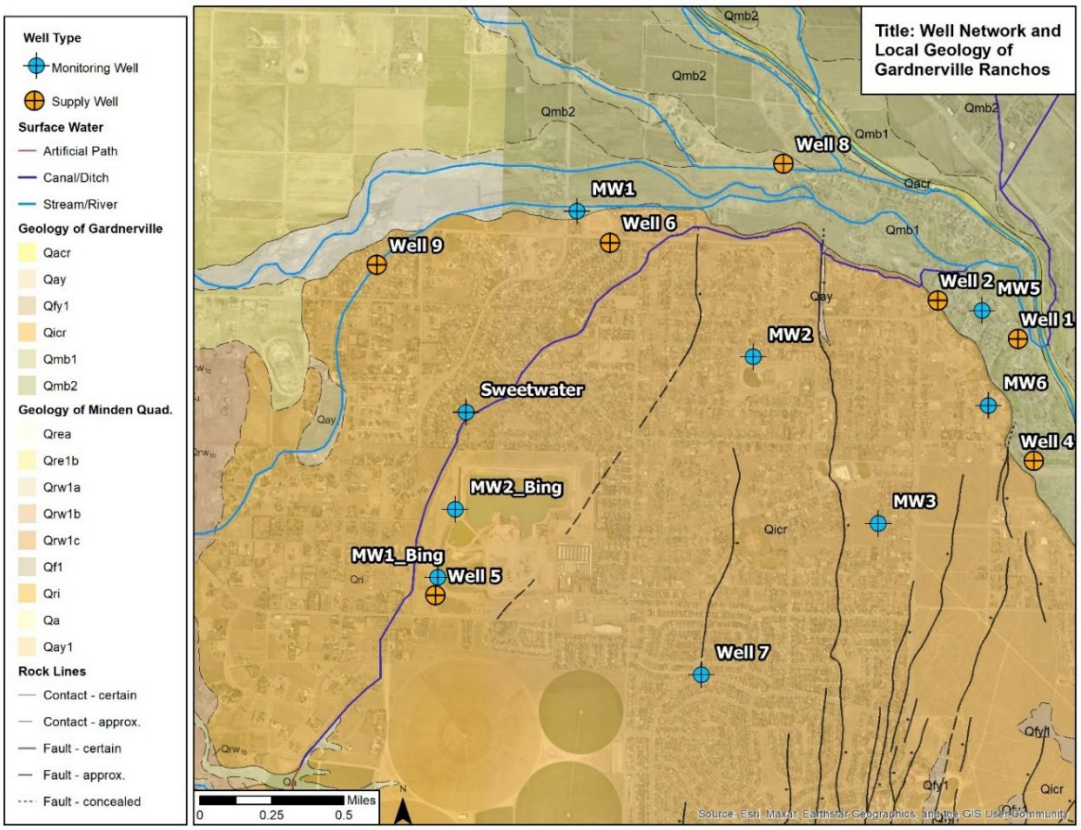

Figure 10. Well network and surface geology of the Gardnerville Ranchos area. Surface geology from Ramelli et al. (2014) and dePolo et al. (2000). Geologic units are described in more detail in Table 4. The term "artificial paths" refer to modified watercourses, such as diversion structures, canal extensions and/or feeder paths for irrigation etc.

2.3.2.1 Hydrostratigraphic Units

Based on a review of geologic maps, previous and new lithology data, and previous groundwater flow models, the aquifer materials in the Gardnerville Ranchos area are divided into several hydrostratigraphic units (HSUs), as listed in Table 5, representing groups of rock types and unconsolidated material that have similar hydraulic properties. The range in hydraulic conductivities for these HSUs is summarized in Table 6.

Table 5. Summary of hydrostratigraphic units in the study area.

Geology Type	Geologic Units	Geologic Unit Description	Geology Source
Fluvial, Meander Belt, and Floodplain	Qacr - active channel of the East Fork	Sand and gravel deposits within the active channel of the East Fork that are generally subaqueous and rearranged by high river flows.	dePolo et al. (2000)
	Qmb1,2 (Qre1,2) - later and earlier meander belt deposits of the East Fork	Lateral accretion of cobbles, gravels, and sands; vertical accretion of fine-grained sands and silts	Ramelli et al. (2014); dePolo et al. (2000)
	Qrw1,2 - young and intermediate meander belt deposits of the West Fork	Sandy gravels with interbeds of clay and cobble to boulder gravels	Ramelli et al. (2014)
	Qfp - Carson River floodplain deposits	Fine-grained sands and silts	dePolo et al. (2000)
	Qf1,2 - young and intermediate floodplain deposits	Clay and sands	Ramelli et al. (2014)
Pine Nut Quaternary-Tertiary Alluvium/Colluvium	QTa - alluvium of the western Pine Nut Mountains	Bouldery, sandy, cobble and pebble gravels and interspersed sands	dePolo et al. (2000)
	QTc - colluvial deposits	Matrix-supported sands and cobbly sands	dePolo et al. (2000)
	Tsc - Tertiary sediments	Siltstone, sandstone, and conglomerate, locally with tephras	dePolo et al. (2000)
Older Alluvium	Qai - intermediate age alluvial fan deposits	Sand and gravel with abundant boulders (reworked granite)	Ramelli et al. (2014); dePolo et al. (2000)
	Qao - older alluvial fan deposits	Sand and gravel with abundant boulders (surface boulders are weathered)	Ramelli et al. (2014); dePolo et al. (2000)
Young Alluvium	Qa - active alluvium	Cobble, pebble, and sand deposits	dePolo et al. (2000)
	Qay - stream terrace and flood plain deposits	Cobbly, pebble gravels and medium-to-fine grained sands.	dePolo et al. (2000)
Alluvium - West Dressler Bench	Qri - undivided Carson River deposits	Cobble gravel and gravelly sand	Ramelli et al. (2014)
Alluvium - Central Dressler Bench	Qicr - East Fork Carson River alluvium	Bouldery, cobbly, sandy pebble gravel in moderately stratified to massive, clast-supported deposits.	dePolo et al. (2000)
Alluvium - East Dressler Bench			
Young Alluvial Fan	Qfy	Similar to Qay, but commonly coarser grained	dePolo et al. (2000)
Bedrock	Ta - Tertiary andesite	Jurassic to Tertiary age granitic, metamorphic, and volcanic rock	dePolo et al. (2000)

Table 6. The range of hydraulic conductivity values for hydrostratigraphic units in the study area from various sources: Range in hydraulic conductivity values for basin-fill sediments and association with geomorphic features in Nevada (Maurer et al., 2004).

Geology Type	Geologic Units	K (ft/d)[a]	K (ft/d)[b]	K (ft/d)[c]	K (ft/d)[d]
Fluvial, Meander Belt, and Floodplain	Qacr - active channel of the East Fork	4 to 2,200	0.75 to 185	Deep: 0.17 to 150 Shallow: 0.20 to 57.1	5.7 to 31.5
	Qmb1,2 (Qre1,2) - later and earlier meander belt deposits of the East Fork				
	Qrw1,2 - young and intermediate meander belt deposits of the West Fork				
	Qfp - Carson River floodplain deposits				
	Qf1,2 - young and intermediate floodplain deposits				
Pine Nut Quaternary-Tertiary Alluvium/Colluvium	QTa - alluvium of the western Pine Nut Mountains	0.05 to 140	0.11 to 8.26	-	0.20 to 1.11
	QTc - colluvial deposits				
	Tsc - Tertiary sediments				
Older Alluvium	Qai - intermediate age alluvial fan deposits	0.02 to 140	0.24 to 55.7	-	-
	Qao - older alluvial fan deposits				
Young Alluvium	Qa - active alluvium	0.02 to 140	0.08 to 36.3	-	-
	Qay - stream terrace and flood plain deposits				
Alluvium - West Dressler Bench	Qri - undivided Carson River deposits	0.02 to 140	1.38 to 52.5	Deep: 6.05 to 560 Shallow: 664 to 4215	0.59 to 3.2
Alluvium - Central Dressler Bench	Qicr - East Fork Carson River alluvium	0.02 to 140	0.85 to 15.6	Deep: 22.2 to 83.3 Shallow: 8.4 to 8.4	
Alluvium - East Dressler Bench				Deep: 4.18 to 90.8 Shallow: 5.7E-05 to 14.4	
Young Alluvial Fan	Qfy	0.02 to 140	0.14 to 1.6	-	0.59 to 3.2
Bedrock	Ta - Tertiary andesite	-	0.002 to 23.7	-	-

a - Average range in hydraulic conductivity for basin-fill sediments and association with geomorphic features in Nevada (Maurer et al., 2004); b - Range in hydraulic conductivity based on wells with specific capacity data in southern Carson Valley, Nevada (NDWR, 2024); c - Range in hydraulic conductivity based on aquifer tests in this study; d - Median transmissivity estimated by Yager et al. (2012) converted to a range of hydraulic conductivity values assuming screened intervals between 99 to 540 ft (the minimum and maximum screen length of wells used in calculations by Yager et al. [2012]); "Deep" is used to describe the aquifer >200 ft bgs and "shallow" describes the aquifer <200 ft bgs.

To estimate aquifer hydraulic properties and boundary conditions in the Gardnerville Ranchos area, a series of aquifer tests were conducted. Details of the aquifer testing program and results are included as Appendix A.

In summary, results of aquifer testing suggest that hydraulic properties of the basin-fill deposits vary spatially by several orders of magnitude. This variability is largely attributed to spatial distribution of sediment of varying grain size (clays to boulders), as well as the degree and interconnectedness of geologic faults and fractures (Figure 10). Overall, field-measured transmissivity values are greatest in the west due to the abundance of coarser sediments (i.e., sands and gravels). Aquifer transmissivity decreases overall to the east as the fine sediment (i.e., silts and clays) increases and aquifer thickness decreases because of shallower bedrock. However, results of some aquifer tests do show zones of higher transmissivity in the eastern segment of the study area as well. While faults in the area are mapped as singular planar features based on the lineaments that are visible at the land surface, faults and fractures can intersect in the subsurface. The distribution of sediment of varying grain size within the alluvial fan and fluvial deposits, coupled with the north-south orientation of faults, have resulted in corridors of high transmissivity in the north-south direction, as discovered during the aquifer tests. Results of the aquifer tests suggest that these zones of high transmissivity are bounded by low permeability fault zones that impede groundwater flow in the east-west direction (perpendicular to fault planes), especially during pumping.

2.3.3 Local Groundwater Levels

Groundwater elevation data near and adjacent to the Gardnerville Ranchos were compiled and analyzed to characterize the occurrence and movement of groundwater in the study area. The potentiometric surface of the basin-fill aquifer of the study area is provided in Figure 11. Static groundwater elevations in the Gardnerville Ranchos area range from 4,827 ft above mean sea level (amsl) (1,471 m amsl) at Well 4 near the East Fork Carson River to 4,730 ft amsl (1,442 m amsl) at Well 9 toward the valley center. The general groundwater flow direction in the study area is to the west-northwest. Aquifer heterogeneities result in localized flow directions that vary due to variations in hydraulic conductivity. Understanding these variations is essential for accurately characterizing groundwater availability and potential vulnerabilities in the system.

Horizontal hydraulic gradients were calculated as the difference in hydraulic head between two wells divided by the horizontal distance between the wells. Horizontal hydraulic gradients in the confined aquifer in the Gardnerville Ranchos area range from 0.002 ft/ft to 0.046 ft/ft (0.0006 m/m to 0.014 m/m). The area with the steepest horizontal gradient is between Well 4 and Well 1, which is driven by topography, low aquifer transmissivity, and a fault zone that extends between these wells and impedes horizontal flow. Hydraulic gradients reduce to the northwest, indicating a flattening of the water table that is likely explained by increasing aquifer transmissivity.

Vertical hydraulic gradients were estimated where groundwater levels are monitored at varying depths from adjacent wells over a small area. There are no multi-level piezometers in the study area to measure vertical gradients in any well/borehole. Vertical hydraulic gradients were estimated by using the following equation:

$$\frac{difference\ in\ hydraulic\ head}{vertical\ distance\ between\ midpoint\ of\ well\ screen} = \frac{h_a - h_b}{MSE_b - MSE_a} \quad (1)$$

where h_a is the hydraulic head at the well with the lowest mid-screen elevation (Well A), h_b is the hydraulic head at the well with the highest mid-screen elevation (Well B), MSE_a is the mid-screen elevation of Well A, MSE_b is the mid-screen elevation of Well B. Negative values indicate a downward vertical gradient and positive values indicate an upward vertical gradient.

An upward vertical gradient may exist in northeastern Gardnerville Ranchos, ranging from 0.003 ft/ft to 0.02 ft/ft (0.0009 to 0.006 m/m). MW-5 is screened in the shallow unconfined aquifer, where the groundwater elevation is marked by the water table. Well 1 and Well 2 are supply wells screened in the deeper leaky-to-confined aquifer. This section of the leaky-to-confined aquifer is under pressure and the potentiometric surface rises above the water table of the unconfined aquifer. An upward vertical gradient of approximately 0.003 ft/ft (0.0009 m/m) exists in northern Gardnerville Ranchos between Well 6 and MW1.

A downward vertical gradient of approximately -0.01 ft/ft (0.003 m/m) exists in southwest Gardnerville Ranchos near Well 5 and MW1_Bing. MW1_Bing is a shallow monitoring well (depth = 108 ft) completed in the unconfined aquifer, while Well 5 is a deeper well (depth = 450) completed in the leaky-to-confined aquifer. The groundwater elevation at MW1_Bing is consistently greater than the levels at Well 5, suggesting that groundwater from the unconfined aquifer has a downward vertical gradient toward the deeper aquifer in this area.

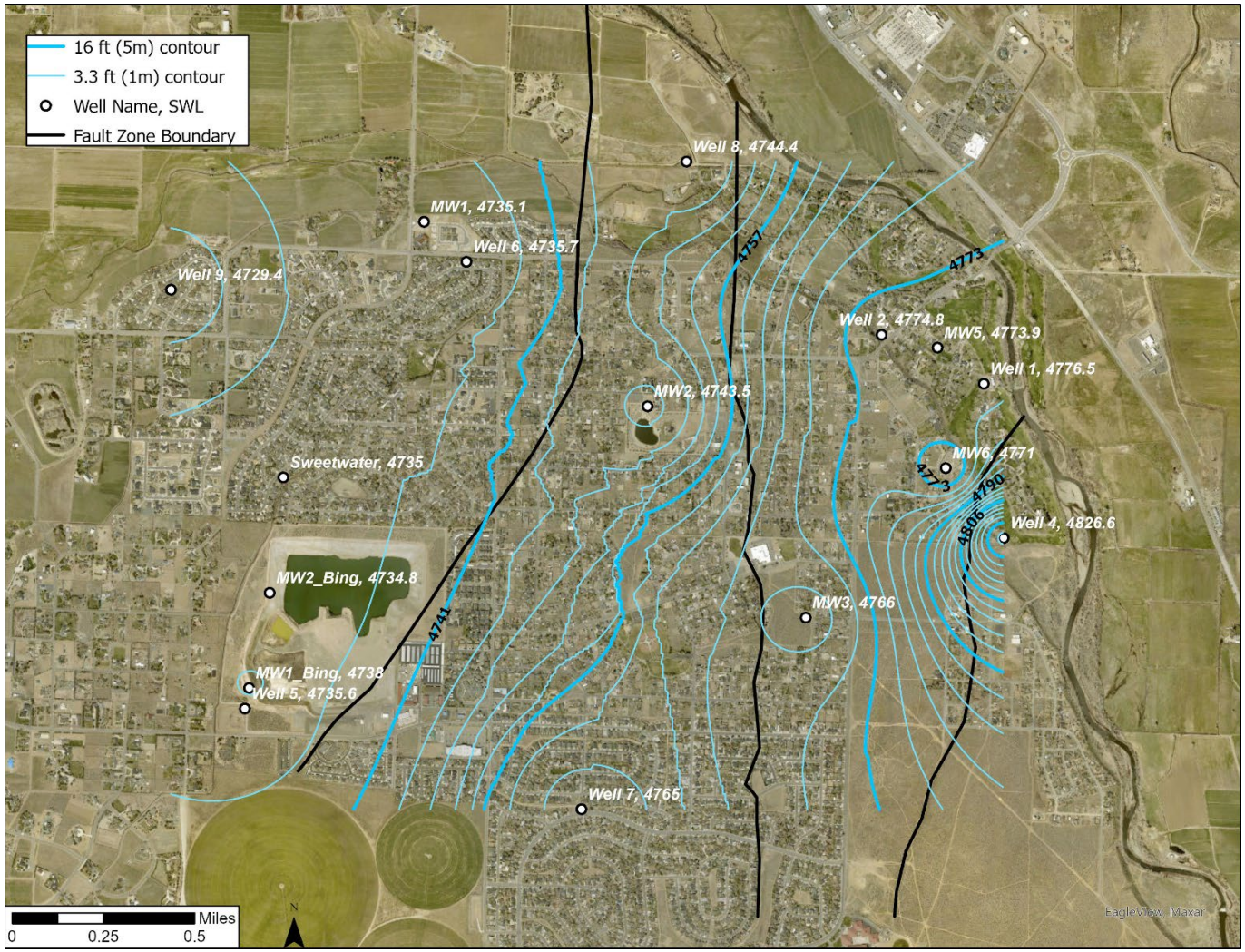

Figure 11. Potentiometric surface (feet above mean sea level) estimated for the Gardnerville Ranchos based on groundwater elevation data for supply and monitoring wells. A potentiometric surface is an imaginary or hypothetical surface that represents the total hydraulic head of groundwater in an aquifer, providing a visualization of the pressure of groundwater within an aquifer. Key fault zone boundaries are also shown (the fault zone boundaries are described in detail in Section 2.3.4).

2.3.4 Local Groundwater Compartments

Crustal extension in the Basin and Range Physiographic Province is reflected by topography with fault-bounded mountain ranges and intervening alluvial basins. Fault and fracture zones impact groundwater levels, flow directions, and gradients to varying degrees throughout the study area. A review of the USGS Quaternary Fault and Fold Database of the United States (USGS, 2023) and 7.5-minute geologic quadrangles (dePolo et al., 2000; Ramelli et al., 2014) show significant faulting in the eastern portion of the study area (Figures 10 and 12). Several faults in the study area propagate through the basin-fill deposits to the land surface, producing topographic linear features at the location of the fault.

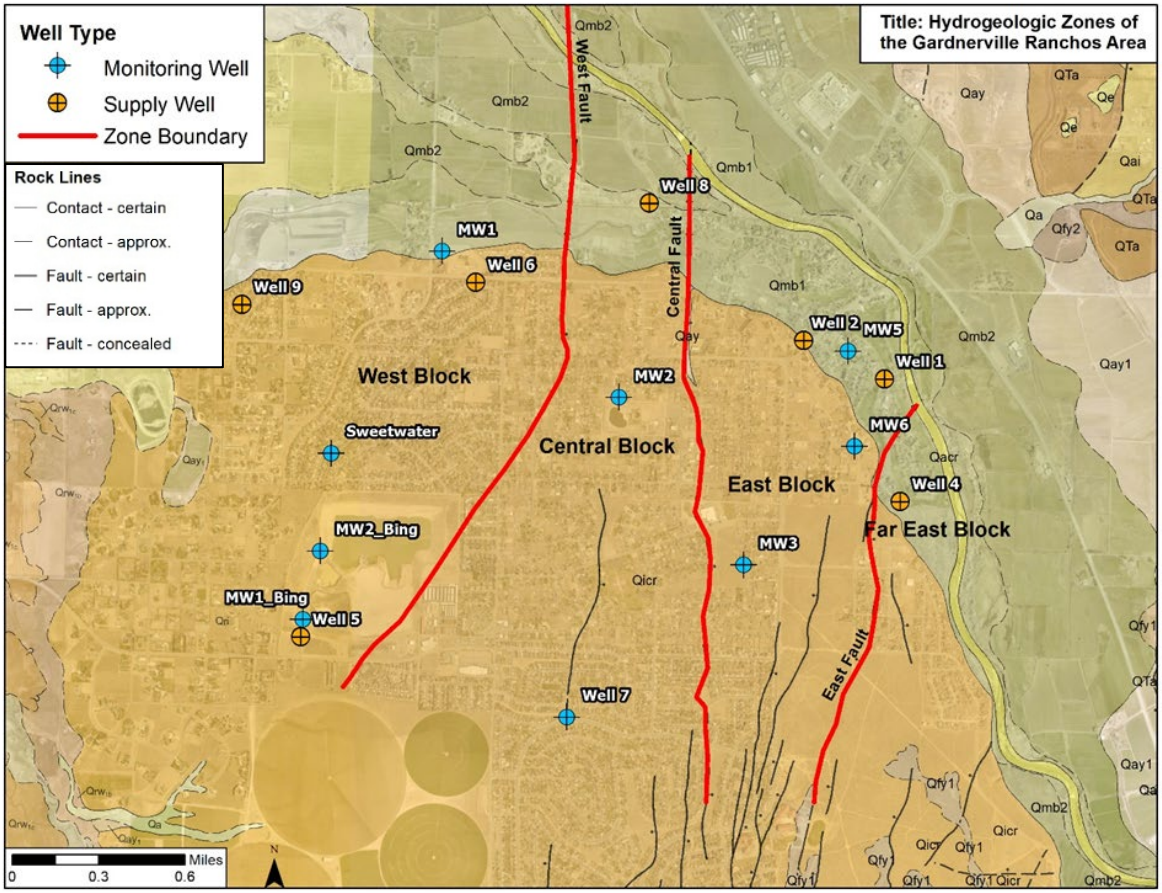

Figure 12. Locations of hydrogeologic blocks delineated by faults that affect groundwater flow in Gardnerville Ranchos. For spatial reference, the footprint of Gardnerville Ranchos can be seen through the geology basemap. The basemap includes surface geology and mapped faults from dePolo et al. (2000) and Ramelli et al. (2014). Geologic units and fault types (black lines) are listed in Figure 10.

Faults in the study area generally extend in the north-south direction, nearly perpendicular to the west-northwest groundwater flow direction. A vertical offset (approximately 50-55 ft; 15-17 m) in static groundwater elevations occurs between Well 4 (4,826.6 ft amsl; 1,471.1 m amsl) and MW-6 (4,771.0 ft amsl; 1,454.2 m amsl) and Well 1 (4,776.5 ft amsl; 1,455.9 m amsl). Well 4 is 1,300 ft (396 m) and 2,300 ft (701 m) away from MW-6 and Well 1, respectively. Steep horizontal hydraulic gradients in this area illustrate that the fault that extends between them ("East Fault") is a barrier that restricts groundwater inflow from the east into the Gardnerville Ranchos area. As discussed in Appendix A, results of aquifer tests at Wells 1, 2, and 4 corroborate that the East Fault is a low-permeability barrier and suggest that it extends to the north beneath the fluvial deposits.

A north-south trending fault that extends almost the entire length of the river terrace is referred to as the "Central Fault." Results of the Well 8 and Well 2 aquifer tests show minimal hydraulic connection between these two wells, which highlights the barrier effect of the Central Fault. Additionally, the lack of drawdown responses suggest the Central Fault extends north beyond the river terrace deposits into the fluvial deposits (Figure 12).

The "Hot Spring Fault" described by Yager et al. (2012) and Kitlasten et al. (2021) generally aligns with the most westerly mapped fault in the study area. For consistency with other fault nomenclature, this fault is referred to as the "West Fault" (Figure 12). Consistent with Yager et al. (2012) and Kitlasten et al. (2021), the West Fault extends north through the model domain.

Results of the aquifer tests suggest that the West and Central Faults impede groundwater flow across the faults during transient (i.e., pumping) conditions. As such, groundwater pumping on either side of the three faults described here result in four distinct groundwater compartments or hydrogeologic "blocks," namely the West, Central, East, and Far East Blocks (Figure 12). Pumping within a given block results in pronounced drawdown within that block and minimal drawdown in adjacent blocks. Groundwater flow to the pumping wells is primarily from the north and south within the pumped block.

2.3.5 Local Groundwater Level Trends

Hydrographs showing historical water levels prior to and during the study period for all monitoring wells are included as Figure 13 and are included in Appendix A. The hydrogeologic characterization considers groundwater levels up to November 1, 2023. The period of record start date varies by well, depending on when the monitoring well was constructed and equipped with a datalogger for continuous water level monitoring:

- March 2022 for MW-1_Bing, MW-2_Bing, Sweetwater, Well 5, and Well 7
- May 2022 for MW-1, MW-2, MW-3
- October 2022 for MW-5 and MW-6

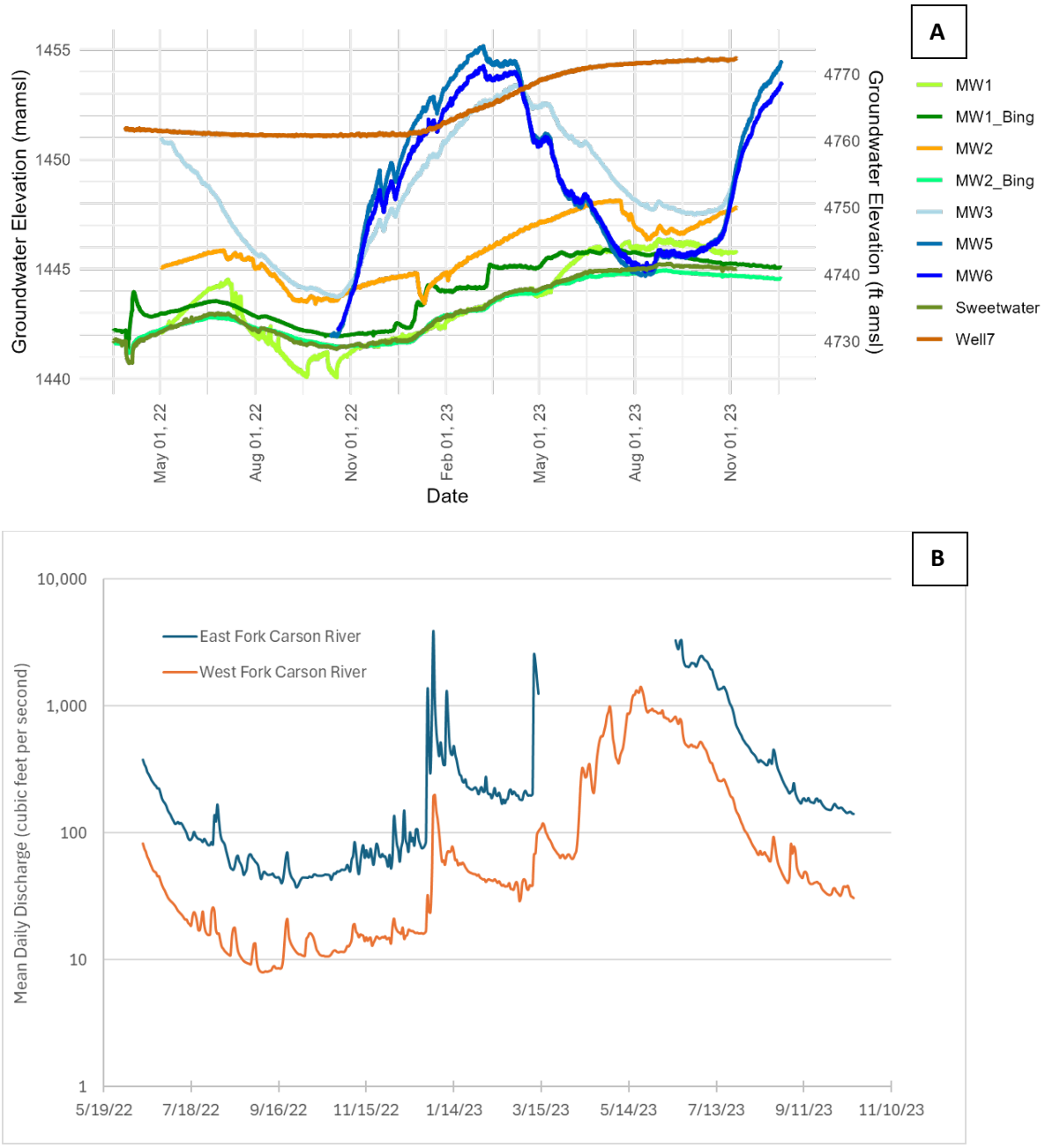

Figure 13. A) Hydrographs of groundwater elevation over time at monitoring wells in Gardnerville Ranchos. Wells are colored by hydrogeologic block: West Block wells (green): MW1, MW1_Bing, MW2_Bing, Sweetwater; Central Block wells (orange): MW2, Well 7; East Block wells (blue): MW3, MW5, MW6. B) Hydrographs of mean daily discharge of the East Fork (USGS site no. 10309000) and West Fork (USGS site no. 10310000) of the Carson River. Note that the *y*-axis is log scale. Mean daily flow data for the East Fork were not available from March to July 2023. Comparison of plots A and B show that surface water flows and groundwater levels begin to increase in fall 2022.

Groundwater levels show seasonal variability in all monitoring wells, with increasing water levels from late fall to spring, and decreasing water levels through summer and into fall. High precipitation totals in the Carson Pass during the winter 2023 led to a visually discernible sitewide increase in groundwater levels during spring 2023. Groundwater levels also vary spatially in Gardnerville Ranchos. Spatial trends by hydrogeologic block are described below.

2.3.5.1 West Block

The magnitude and timing of seasonal water level variability is consistent in all monitoring wells in the West Block (MW1, Sweetwater, MW1_Bing, MW2_Bing). At these wells, water levels declined from spring 2022 to fall 2022 by 4 ft (1.2 m) followed by an increase of >10 ft (3 m) from fall 2022 to spring 2023. The relative change in spring 2023 is the result of increased recharge from the wet winter of 2023. Over this same time frame at MW-1, in the northern section of the West Block, water levels declined by approximately 14 ft (4.3 m) from spring to fall 2022 and increased by >15 ft (4.6 m) by spring 2023. MW-1 may have more pronounced recharge because it is completed in fluvial deposits that are more readily recharged by stream infiltration (e.g., the Rocky Slough).

2.3.5.2 Central Block

Water levels at in the Central Block (MW2) show a similar seasonal trend to wells in the West Block. Water levels at Well 7 gradually decreased from March 2022 through October 2022, with a total decrease of approximately 1 ft (0.3 m). Water levels then stabilized through December before increasing rapidly through June 2023 by a total of >10 ft (3 m). Well 7 is situated near a mapped fault, which may explain why seasonal trends are different from most other monitoring wells in the study area (Figure 13). The fault, and higher land surface elevation at Well 7, may also explain why the groundwater elevation at Well 7 is higher than many other wells.

2.3.5.3 East Block

The difference in magnitude and timing of seasonal water level changes in the Gardnerville Ranchos area is controlled, in part, by distance from the East Fork, which is a major recharge source. As a result, groundwater levels in the East Block (MW3, MW5, MW6) show the greatest magnitude of seasonal variability in the Gardnerville Ranchos area. Water levels at MW-5 and MW-6 track similarly. At these wells, water levels increased by approximately 43 ft (13 m) from fall 2022 to spring 2023. To the south, at MW-3, water levels increased by 33 ft (10 m) over this time frame. The timing of seasonal changes in the East Block is also distinct from the West and Central Blocks; water levels at MW-3, MW-5, and MW-6 begin to decrease during the spring (April 2023), while wells in the West and Central Blocks do not start to decline until the summer (June/July 2023). A recharge “pulse,” likely from infiltrating streamflow from the East Fork, causes the steep and rapid water level peaks in the East Block. This pulse dissipates to the west, resulting in broader water level peaks in the Central and West Blocks. This is supported by the hydrographs in Figure 13, which show similar seasonal trends between surface water discharge and groundwater elevations at monitoring wells in the East Block. Stream discharge starts to increase in mid-September 2022 and groundwater levels start increasing in October 2022. There is a greater lag between stream discharge and groundwater elevation increases in the Central and West Blocks because of the greater distance from the East Fork.

2.4 Groundwater/Surface-Water Interaction

2.4.1 Water Level Assessment

As stated previously, the Carson Valley contains a confined aquifer that is beneath an unconfined aquifer. Water moves between the river and the unconfined aquifer in either direction, depending mostly on the stage of the river and groundwater levels near the river. Maurer et al. (2006) estimated streamflow gains and losses at 37 sites throughout Carson Valley through measurements of streamflow and streambed temperature. Key findings of that study were that the Carson River and irrigation ditches generally gained flow from groundwater at sites in northern and western Carson Valley, whereas the East and West Forks and irrigation canals in the southern and eastern sides of the valley generally lost flow to groundwater. This distribution of flow is consistent with increasing depth to groundwater to the southeast as land surface gains elevation.

An assessment of groundwater elevations in wells shows groundwater levels ranging from 40 to 70 ft (12.2 to 21.3 m) below the land surface in wells near the East Fork within the model domain, which suggests that streamflow infiltrates from the river into the aquifer. The offset between river stage and groundwater levels suggests the presence of a thick vadose zone and little to no hydraulic connection between the East Fork and the underlying unconfined aquifer in much of the study area. This is consistent with previous studies (Spane, 1977; Maurer, 1986; Maurer, 2007) which showed that infiltration from the East Fork is a source of recharge to the local unconfined aquifer. Spane (1977) concluded that the streamflow of the East Fork is lost to infiltration in areas upstream of Gardnerville.

Overall, a shallow depth to groundwater near the West Fork Carson River suggests a hydraulic connection between the river and the shallow aquifer. The relative direction and rate of flow between the river and aquifer likely varies seasonally as water levels change (Maurer, 2009). Generally, groundwater elevations recently reported along the West Fork Carson River are lower than the river stage, suggesting that the West Fork loses water overall to the shallow unconfined aquifer. Conversely, Spane (1977) stated that the shallow groundwater altitudes along the West Fork and main-stem Carson River suggest the river is gaining flow from groundwater. Welch et al. (1997) stated that the shallow unconfined aquifer is hydraulically connected to the river throughout most, if not all, of Carson Valley. The model presented in this report incorporates these seasonal variations in river stage and groundwater levels, providing boundary conditions based on observed stream data and allowing for a dynamic representation of flow direction and rate.

2.4.2 Stable Isotope Assessment

The hydrogeologic conceptual model was also informed by a stable isotope analysis to estimate the degree of mixing of surface water, groundwater, and precipitation in the aquifer of the study area. Details of the stable isotope methodology, analysis, results, and figures are provided in Appendix A. In summary, the mixture of water sources varies in the study area as a function of depth, hydrostratigraphy, and position relative to surface water. Groundwater in the unconfined aquifer in proximity to surface water sources, such as the East Fork Carson River, are primarily recharged from the infiltration of surface water, as indicated by stable isotope analyses showing a high proportion of surface water in shallow

monitoring wells. In contrast, the confined aquifer is more influenced by groundwater from deeper HSUs, with decreasing surface water contribution over time as drawdown increases during pumping.

3.0 GROUNDWATER MODEL

3.1 Description

Movement of water through an aquifer can be expressed by mathematical equations that form the basis for computer models used in the field of hydrogeology. Models can be divided into two broad categories, including analytical or numerical models. Analytical models are exact solutions and are used for ideal aquifer conditions that are homogeneous with simple boundaries. Ideal aquifer conditions rarely occur in nature. Therefore, solving these equations analytically is not possible. Numerical models are used to approximate solutions for aquifers that have heterogeneous and anisotropic aquifer materials and complex hydrologic boundaries. The model approximates the aquifer system and includes several assumptions and simplifications that are described in this section. The model projects aquifer responses to assumed future pumping and changes in near-surface temperatures.

3.2 Modeling Code and Packages

MODFLOW-NWT (Niswonger et al., 2011) was used to simulate groundwater flow within the model domain. MODFLOW-NWT is an update of the USGS three-dimensional, finite difference groundwater flow code MODFLOW (McDonald and Harbaugh, 1988). MODFLOW-NWT has solvers and time-stepping options that facilitate numerical solutions encountered during pumping and re-saturation of model cells. The Upstream Weighting (UPW) flow package was used. MODFLOW-NWT also accommodates MODFLOW packages that are needed to represent the flow system. Packages used in the development and operation of the model are described in Section 3.7 and include:

- General head boundary (GHB1)
- Recharge (RCH1)
- Evapotranspiration (EVT1)
- Stream (STR1)
- Well (WEL1)
- Multi-node well (MNW2)
- Specified flow boundary (integrates the WEL1 package)
- Horizontal flow barrier (HFB6)

Groundwater Modeling System (GMS) is the graphical user interface used for model development calibration, pre- and post-processing for the model, and as a visualization tool for model construction and review of output (GMS version 10.7; Aquaveo, LLC, 2007).

3.3 Objectives

The objectives of the calibrated model are to:

- Provide an understanding of the groundwater flow system at Gardnerville Ranchos and how it integrates into the larger Carson Valley aquifer system.

- Provide an assessment of the range of potential changes in groundwater levels under projected climate and water demand scenarios.
- Assess the magnitude of groundwater drawdown under future pumping scenarios.
- Assess whether the future water demand can be met under future groundwater conditions using the existing supply well network.

3.4 Approach

A steady state model represents a groundwater system where flow conditions remain constant over time, meaning hydraulic heads, inflows, and outflows from the model domain don't change. This type of model is useful for understanding long-term average conditions when hydrologic conditions are relatively stable. For this model, the year 1965 represents "pre-development" when groundwater conditions were relatively stable because Gardnerville Ranchos was not pumping groundwater. There was some pumping in the area for agriculture prior to 1965, so it is assumed that the aquifer system was in a state of dynamic equilibrium in 1965.

The calibrated steady-state model was used in the development of two transient models that match simulated and observed heads over time, validating that the model captures time-varying groundwater conditions to the degree possible with the available information. The transient models include: 1) a "historical transient" model that represents the history of groundwater development in the model domain from 1965 to 2023 and 2) an "aquifer testing transient" model which simulates water levels during the aquifer testing program during this study. The calibrated historical transient model was used to run predictive simulations from 2024 to 2043 to assess the range of changes in groundwater levels under several climate and water-demand scenarios.

3.5 Model Domain

The model domain is a portion of the southern segment of the Carson Valley hydrographic basin. To examine the effects of future climate and water demand scenarios on groundwater levels, and to consider cumulative effects with the nearby pumping for other uses, the model domain includes Gardnerville Ranchos and neighboring areas. The model domain includes pumping at the agricultural center southwest of Gardnerville Ranchos, domestic wells in Gardnerville Ranchos and neighboring communities (i.e., Ruhenstroth), municipal water systems for the towns of Minden and Gardnerville, and the Carson Valley Golf Course.

3.6 Spatial Discretization

The groundwater flow model covers an area of 28 square miles (73 square km) in the southeastern portion of the valley floor of Carson Valley (Figure 14). The horizontal dimensions of the model domain are determined by perimeter boundaries, which include both physical and hydraulic boundaries. The model area is smaller in extent than that of the groundwater basin and, as such, the perimeter boundaries are different from the basin boundaries. Physical boundaries include the southeastern model boundary, which is defined by the exposed bedrock of the Sierra Nevada, and the southwestern model boundary, marked by the West Fork Carson River. The northeast and northwest boundaries are hydraulic boundaries (general head boundaries) approximately 2.0 miles (3.2 km) and 1.3 miles (2.1 km) away from Gardnerville Ranchos, respectively. Hydraulic boundaries are used

because extending the model domain to physical boundaries would be computationally expensive in terms of time to run the models and data storage, dropping to the point of diminishing returns. The northeast and northwest boundaries are set to minimize pumping effects on water levels at the boundaries. However, given the abundance of pumping wells throughout the Carson Valley, it is difficult to establish hydraulic boundaries on the valley floor that are not impacted by pumping to some degree. The model grid is oriented at 316° NW, which is approximately parallel to the principal groundwater flow direction in the model domain. This orientation also minimizes the number of inactive cells.

The model simulates flow in the basin-fill aquifer. Therefore, the lower model boundary is set at the elevation of the interface of basin-fill and bedrock. The spatial distribution of the bedrock elevation is based on well logs and approximations by Maurer (1984) and Shah and Boyd (2018). A profile of the depth to bedrock along the northwest perimeter of the model domain is shown in Figure 15, which shows that the thickness of the basin-fill aquifer is greater in the western portion of the model domain.

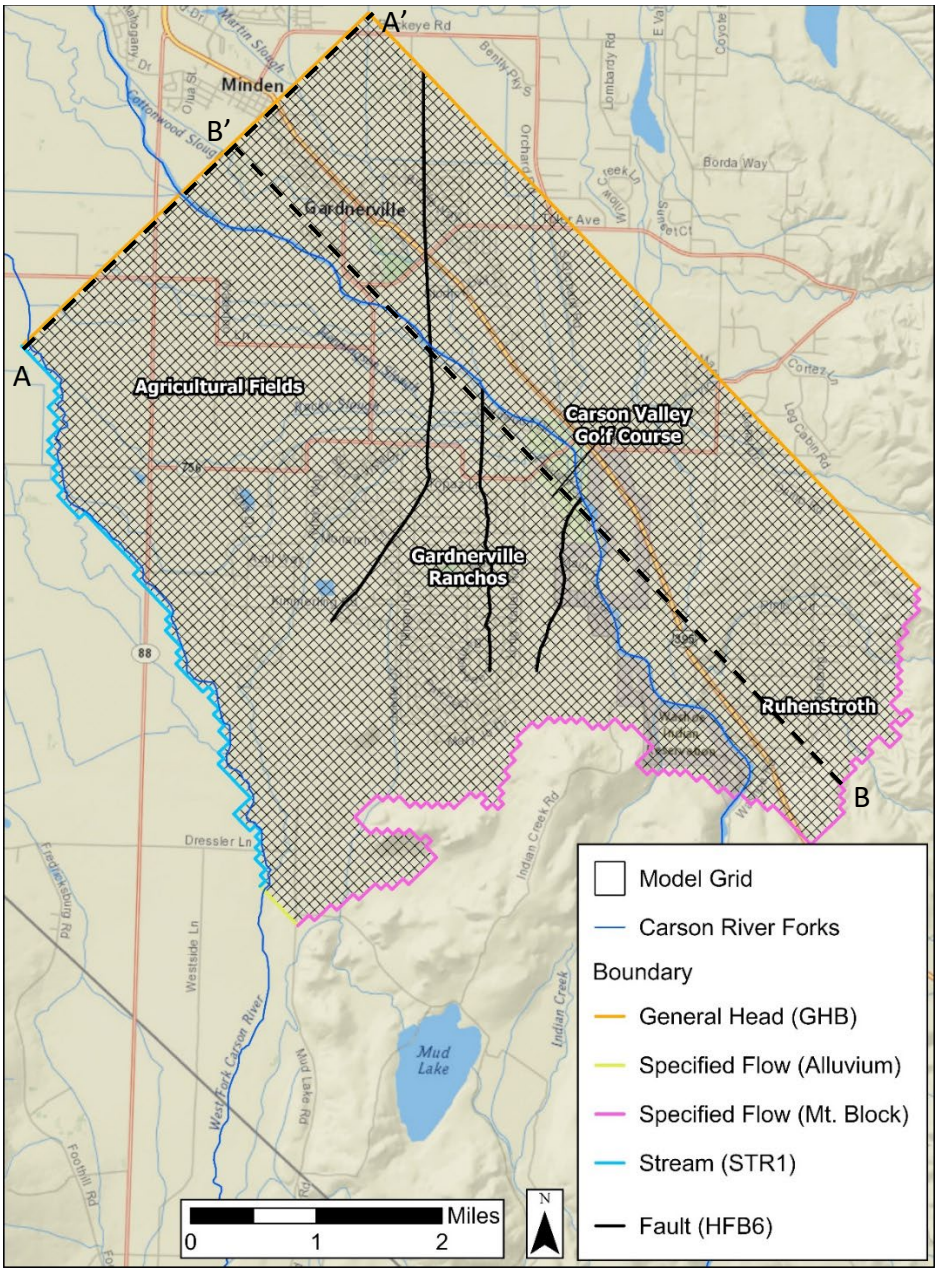

Figure 14. Map of the active model grid cells (black squares) in model domain and perimeter boundary types. All model grid cells are uniform in the horizontal direction (328 ft × 328 ft; 100 m × 100 m). The depth profile along the northwest boundary (dashed line labeled A-A') is shown in Figure 15. Model layers and boundaries along cross section B-B' are shown in Figure 16. General head boundary (GHB) types allow groundwater to flow into or out of the northeast and northwest model boundaries based on a specified head and conductance at each boundary. A specified flow boundary specifies the rate of flow into the southern model boundary from the mountain block and alluvium. The stream boundary along the western perimeter of the model domain simulates the interaction between the West Fork Carson River and groundwater. Select faults are included in the model to impede horizontal groundwater flow based on field tests.

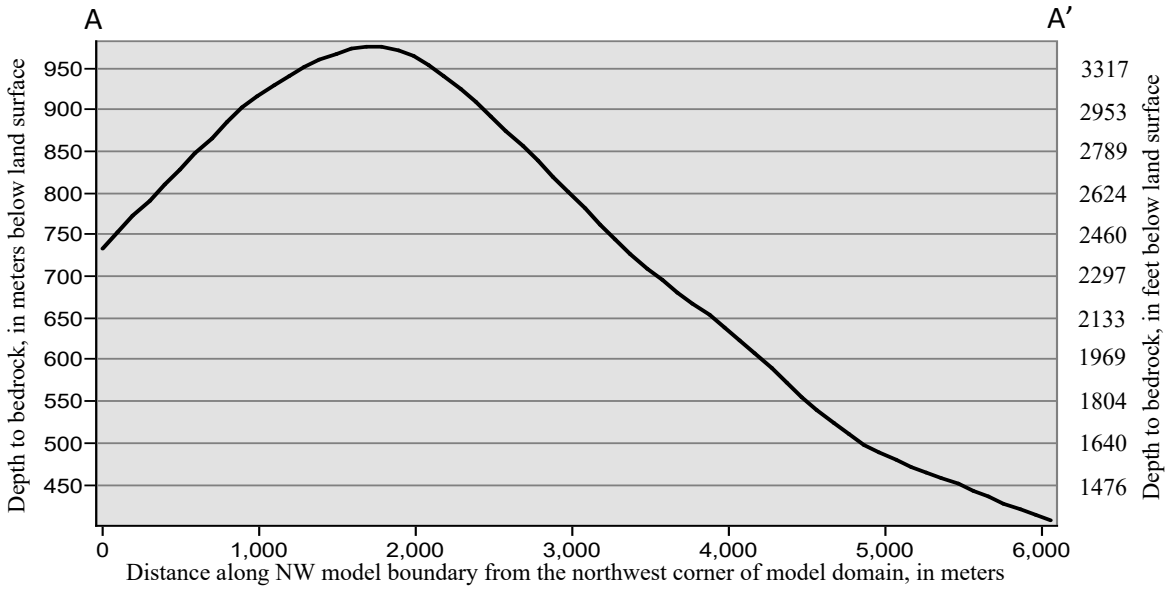

Figure 15. Depth to bedrock along the northwestern model boundary shows that the thickness of the basin-fill aquifer is greater in the western portion of the model domain. The extent of A-A' is shown as the red line on Figure 14.

The three-dimensional model domain was discretized using cells that form the computational framework. A block-centered grid is used in which grid lines form the edges of the cell and nodes are centered in the cell. The grid consists of 41,536 cells, including 28,054 active cells where hydraulic heads are computed. All cells are uniform in the horizontal direction (328 ft × 328 ft; 100 m × 100 m). The grid consists of 118 rows, 88 columns, and 5 layers. Horizontal nodal spacing is selected to increase solution accuracy (agreement between modeled and observed heads), capture boundary irregularities (i.e., the bedrock boundary on the southeast side), and to reflect the level of heterogeneity in aquifer hydraulic properties.

The model consists of five horizontal layers, with layer 1 representing the top model layer and layer 5 as the bottom. A cross section showing the model layers of column 64 of the model is shown as Figure 16. The number of model layers and the vertical nodal spacing (layer thickness) were assigned based on depth to bedrock, the magnitude of vertical head gradients, and vertical variability in hydraulic conductivity. The hydrostratigraphy of each layer was defined based on lithology data from boreholes drilled during this study and well driller reports. The top layer (Layer 1) has a constant thickness, while Layers 2-5 have variable thickness depending on the depth to bedrock. Layer 1 spans the entire model domain, while Layers 2-5 are not included along some portions the southern model boundary where the basin-fill aquifer becomes thin ("pinched out"). The model domain is dominated by horizontal flow, with relatively limited vertical head gradients and vertical changes in hydraulic conductivity.

All layers were simulated as being confined. Whether the top model layer is simulated as confined versus unconfined can impact groundwater flow and levels as well as surface water-groundwater exchanges and the interpretations of storage properties for Layer 1. See additional discussion in Section 3.8.5.

Below is a description of each model layer, including the layer thickness, number of active cells, and hydrostratigraphy:

- Layer 1: Younger fluvial and alluvial deposits; constant thickness of 65 ft (20 m); 7,246 active cells of 10,384 total cells in layer.
- Layer 2: Younger and older fluvial and alluvial deposits combined. Thickness up to 410 ft (125 m) (where depth to bedrock >1,310 ft [>400 m]); 6,936 active cells of 10,384 total cells in layer.
- Layer 3: Older fluvial and alluvial deposits; thickness up to 410 ft (125 m) (where depth to bedrock >1,310 ft [> 400 m]); 6,936 active cells of 10,384 total cells in layer.
- Layer 4: Older fluvial deposits (where depth to bedrock >1,310 ft [> 400 m]) or Tertiary sediments (where depth to bedrock <1,310 ft [<400 m]); thickness up to 425 ft (130 m); 6,936 active cells of 10,384 total cells in layer.
- Layer 5: Tertiary sediments; thickness up to 1,900 ft (580 m) (where depth to bedrock reaches 3,150 ft [960 m]); 6,936 active cells of 10,384 total cells in layer.

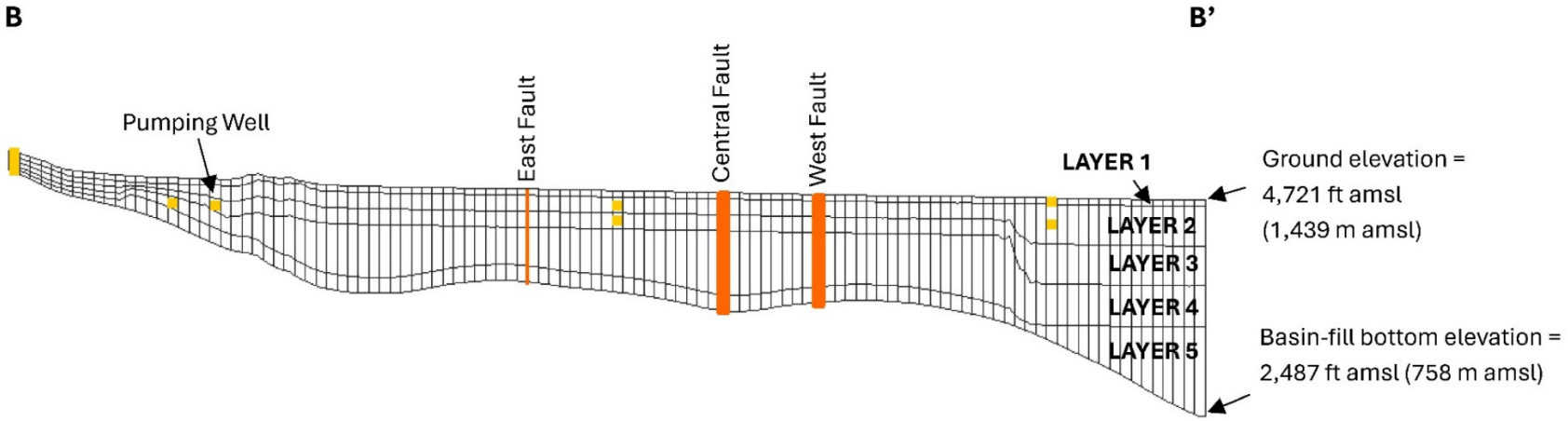

Figure 16. Cross section B-B' shows the vertical model layers along a 7 mile transect from northwest to southeast. The extent of cross section B-B' is shown in Figure 14. The cross section has a 3X vertical exaggeration to show the detail of the model layers. Model layers are numbered from top to bottom, with the top of Layer 1 set at the land surface and bottom of Layer 5 at the bottom of the basin-fill aquifer. Layer 1 has a constant thickness, while Layers 2-5 have variable thickness depending on depth to bedrock. The thickness of Layers 2-5 increase from B to B' as the depth to bedrock increases. Orange lines are faults simulated using the Horizontal Flow Barrier (HFB6) package and yellow squares show the location and layer of the screened intervals of pumping wells simulated using the Well (WEL1) Package.

3.7 Simulation of Hydrologic Boundaries

3.7.1 Groundwater Budget

The groundwater budget is the summation of the inflows and outflows to groundwater in the model domain. The groundwater system is assumed to be in a state of dynamic equilibrium, with changes in groundwater storage due only to short-term variabilities in climate. The addition of new pumping wells, for example, introduces transient conditions and a change in aquifer storage, changing the water budget. Components of the groundwater budget for the model domain were either specified in or computed by the model. Assuming steady-state (equilibrium) conditions within the model domain, total inflows equal total outflows, and the steady state groundwater budget is expressed as:

$$\sum Inflows - \sum Outflows = \Delta S \quad (2)$$

with the following components:

$$[R_{val} + R_{ag} + R_{mb} + I_{stream} + GW_{in}] - [ET_{gw} + ET_{ag} + Q_{stream} + GW_{pump} + GW_{out}] = 0 \quad (3)$$

where:

- R_{val} is valley recharge from precipitation on the valley floor;
- R_{ag} is agricultural recharge from irrigated fields;
- R_{mb} is mountain-block recharge from the mountain block on the southern edge of the model domain;
- I_{stream} is infiltration of streamflow from rivers, creeks, and the irrigation network to groundwater;
- GW_{in} is subsurface inflow of groundwater to the model domain through upgradient basin-fill;
- ET_{gw} is evapotranspiration from the water table by vegetation on the valley floor;
- ET_{ag} is evapotranspiration of water applied to fields for irrigation;
- Q_{stream} is groundwater seepage from the aquifer to rivers, creeks, and the irrigation canals;
- GW_{pump} is total pumping of groundwater; and
- GW_{out} is subsurface outflow of groundwater through basin-fill.

3.7.2 Valley Recharge and Agricultural Recharge

Groundwater recharge derived from precipitation directly to the valley floor (R_{val}) and recharge from irrigation water (R_{ag}) are represented as specified flow in the top model layer using the Recharge Package (RCH1). R_{val} and R_{ag} are summed for each time step of the transient models and represent total surface recharge. The estimated steady state total surface recharge is 1,634 af/yr (5,522 m^3/d).

3.7.2.1 Valley Recharge

Recharge from precipitation that falls directly on the basin-fill sediment deposits on the valley floor are accounted for in estimates of groundwater recharge. The relation between precipitation and elevation established by Maurer and Halford (2004) was applied, which uses daily precipitation records from the Minden, Nevada climate station and linear regression using seven weather stations on the southern and eastern side of Carson Valley where elevations range from 4,709 to 7,201 ft amsl (1,435 to 2,195 m amsl). The linear model representing the average annual precipitation as a function of elevation is:

$$y = 2.2 \times 10^{-4} x - 0.14 \quad (4)$$

where y is the average annual precipitation in meters and x is the elevation in meters above sea level.

A gridded precipitation dataset for the model domain was created by applying this equation to a one-meter digital elevation model for the model domain. Of the total precipitation, 4% is estimated to become groundwater recharge based on recharge estimated by Maurer et al. (2006) for alluvial fan deposits of southern Carson Valley. The spatial distribution of valley recharge for the steady state model is shown in Figure 17. For the historical transient model, annual recharge rates were adjusted proportionally to the annual precipitation measured in Minden relative to the mean annual precipitation and then partitioned monthly based on measured precipitation in Minden. For example, if measured annual precipitation for a given year was 5% higher than average, then valley recharge also increased by 5%.

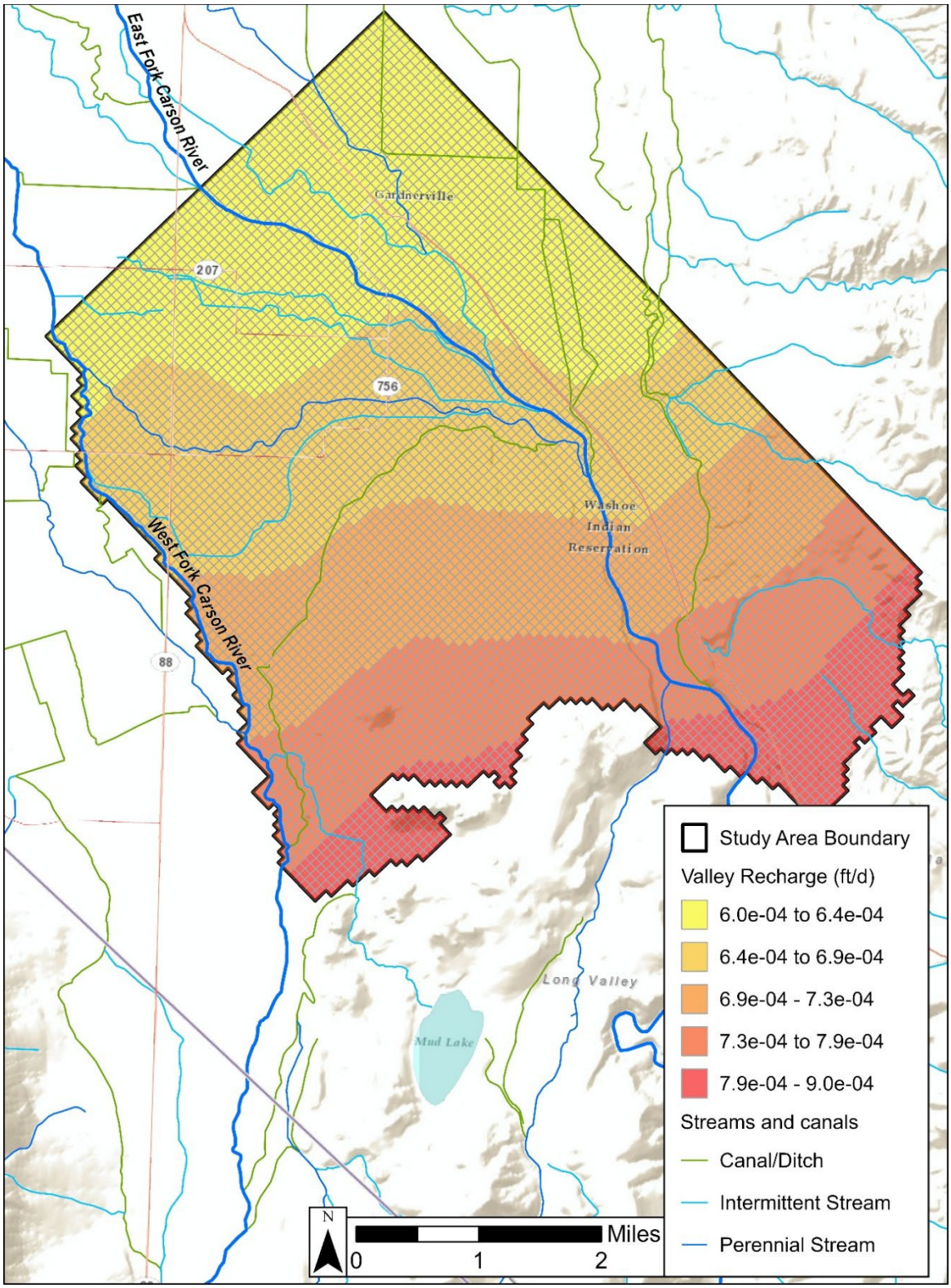

Figure 17. Valley recharge from precipitation applied to Layer 1 (0-65 ft [0-20 m] below land surface) of the steady state model.

3.7.2.2 Agricultural Recharge

Infiltration of irrigation water to the water table is also accounted for in estimates of groundwater recharge. The volume of water diverted from the irrigation system is referred to as the irrigation application rate (AR). The water applied for irrigation is either consumed by crop ET (ET_{ag}), becomes runoff and returns to the canal system (Q_{ret}), or infiltrates to the water table (R_{ag}). A schematic of this process is provided as Figure 18.

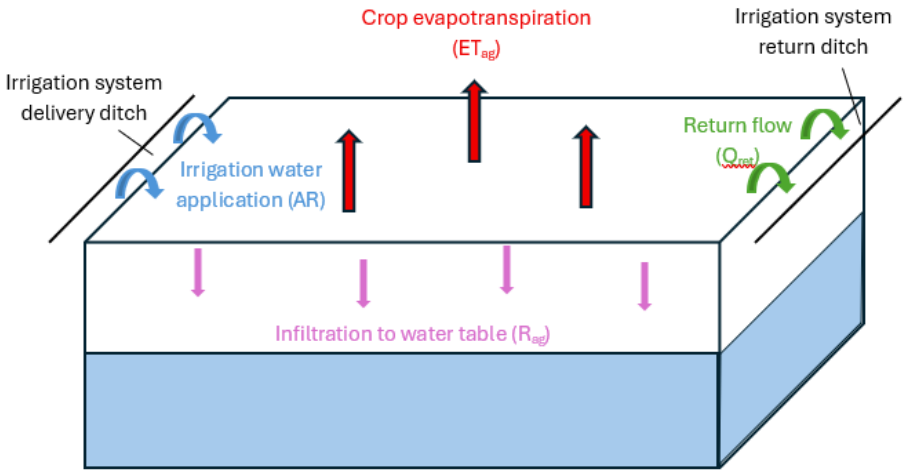

Figure 18. Schematic showing the application and fate of irrigation water. Irrigation water is removed from the delivery ditch and applied as irrigation. Irrigation water is either consumed by crop evapotranspiration, infiltrates to the water table, or becomes return flow to the irrigation system.

The R_{ag} rates are calculated based on measurements of ET from the OpenET Ensemble Monthly Evapotranspiration v2.0 dataset (Melton et al., 2021), as described here. The AR is defined as:

$$AR = \frac{ET_{ag}}{Irr_{eff}} \tag{5}$$

where:

$$ET_{ag} = ET_{actual} - PPT_{Effective} \tag{6}$$

ET_{actual} is a measured value that accounts for the actual ET of effective precipitation (the portion of precipitation that is stored in the soil, $PPT_{effective}$) and applied irrigation water. Irrigation efficiency (Irr_{eff}) is the percentage of applied irrigation water that is used by the crops, which is assumed to remain constant for each crop type for the duration of the model. The irrigation efficiency ranges from 50-90% depending on land surface slope, soil texture and moisture content, depth to groundwater, and conveyance efficiencies. ET_{ag} can also be estimated by:

$$ET_{ag} = AR \times Irr.Eff. \quad (7)$$

The remaining volume that is not consumed by ET_{ag} is partitioned between Q_{ret} (75% of remaining flow) and R_{ag} (25% of remaining flow). These percentages were selected knowing that a relatively small fraction infiltrates to the water table beneath the irrigated fields (Yager et al., 2012). Additionally, these percentages were used so that the average percentage of AR that becomes Q_{ret} here is 25% (median = 26%), which is close to the value of 30% applied by Yager et al. (2012) and Kitlasten et al. (2021. Irrigation efficiencies from Melton et al. (2021) were used to partition irrigation water. As an example, the distribution of R_{ag} for July 2023 is shown in Figure 19.

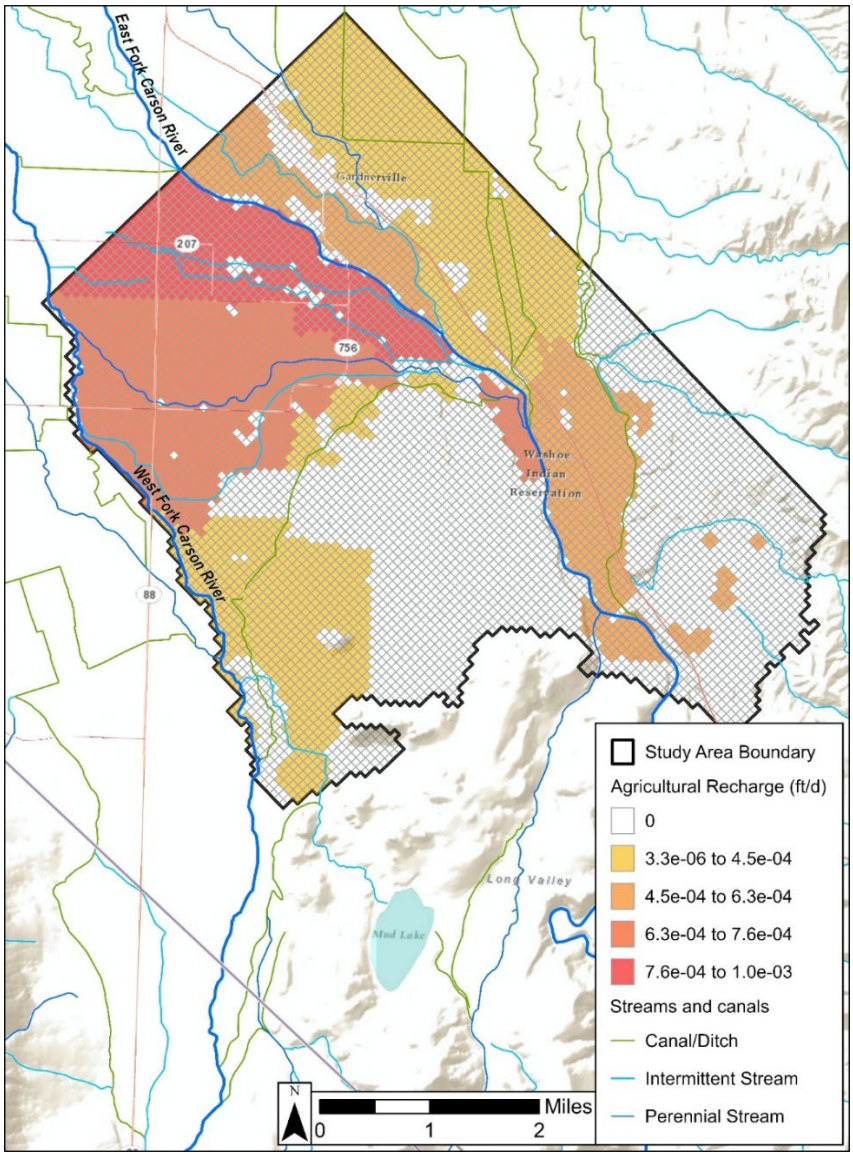

Figure 19. Agricultural recharge applied to Layer 1 (0-65 ft [0-20 m] below land surface) for July 2023 during the historical transient model.

3.7.3 Streamflow Routing and Infiltration

Rivers, creeks, and canals are assigned as head dependent boundaries using the Stream (STR) Package (Prudic, 1989). The STR package calculates time-varying stream stage and enables flow between surface water and groundwater. The West Fork Carson River defines the western boundary of the model domain as it is generally understood to be in hydraulic connection with the local aquifer and therefore exerts control over groundwater as a perennial source/sink. The eastern model boundary extends beyond the East Fork because it is not hydraulically connected to groundwater through most of the eastern segment of the model domain.

Using the STR package, groundwater discharges to the stream when the water table is higher than stream stage, and streamflow infiltrates to groundwater when the stream stage is higher than the water table. The STR package uses Manning's roughness coefficient to calculate the head in the stream. The flux into or out of a stream is calculated for each cell of a stream reach as the difference in head between stage and water table multiplied by the streambed conductance (hydraulic conductivity of the streambed material). Initial stream bed conductance values are based on values reported by Yager et al. (2012) and were adjusted during model calibration. The conductance term C is calculated by:

$$C = \frac{kLW}{t} \tag{8}$$

where k is the hydraulic conductivity of the sediment of the stream bed material, L is the length of the cell containing the stream, W is the width of the cell containing the stream, and t = the vertical thickness of the streambed sediment. Figure 20 is a schematic of river channel with these terms labeled for context.

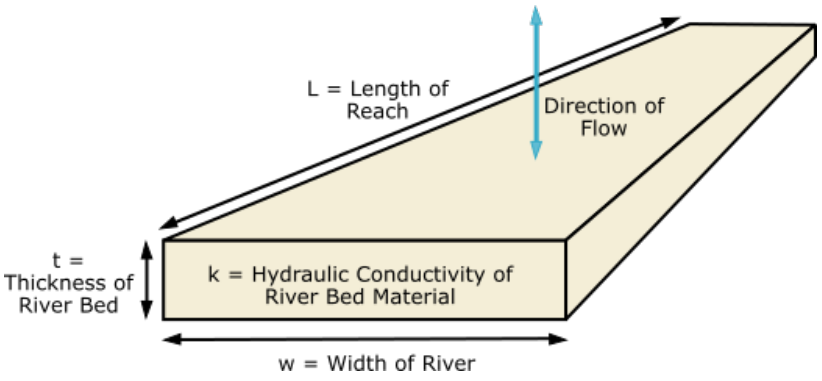

Figure 20. Schematic of a river channel with the terms labeled that are relevant to calculating riverbed conductance (from xmswiki.com).

The widths of the channels were determined using satellite imagery. Streambed thickness was assigned uniformly as 1 ft (0.3 m) based on the Yager et al. (2012). Stream sinuosity was calculated as the ratio of curvilinear stream length to straight line distance between stream end points. Estimated rates of streamflow loss by Maurer et al. (2006) near Gardnerville Ranchos were used to estimate the infiltration flux for each reach in the model

domain (Table 7). The total estimated streamflow infiltration in the model domain is 48,565 af/yr (164,120 m^3/d). Yager et al. (2012) estimated an average annual streamflow infiltration 120k af/yr (405k m^3/d) for all of Carson Valley, with the greatest rates in the southeast part of Carson Valley (where the Gardnerville Ranchos model domain is located).

Table 7. Estimates of streamflow infiltration in the model domain for the MODFLOW streamflow package (STR).

Reach	Channel Length in Model Domain (ft)	Channel Width (ft)	Infiltration (ft/d)	Infiltration (ft^3/d)	Infiltration (af/yr)
East Fork Carson River	38,737	49.2	1.8*	3,439,922.23	28,752.75
Indian Creek	3,425	6.6	1.8*	40,555.36	338.98
West Fork Carson River	33,547	19.7	2.5+	1,646,581.65	13,833.45
Allerman Canal	21,634	16.4	1.8*	640,378.51	2,676.32
Rocky Slough	28,114	3.3	1.8*	166,436.26	695.58
Cottonwood Slough	19,042	4.9	1.8*	169,097.22	706.70
Upper New Virginia Ditch	16,814	3.0	1.8+	89,588.90	374.42
Henningson Slough	21,457	3.3	2.4+	168,599.28	707.84
Edna Ditch	19,354	3.3	1.8*	114,576.67	478.85
TOTAL				164,119.94	48,564.90

+Infiltration rates from Maurer et al. (2006).

*Infiltration rate assumed to be equal to Upper New Virginia Ditch from Maurer et al. (2006).

Monthly flow volumes into the model domain via the West and East Forks are assigned to the historical transient model using measured streamflow from NWIS and the FWM. Streamflow of the East and West Forks of the Carson River is gaged upstream of the valley floor (and upstream of the model domain). Along the East Fork Carson River, daily streamflow measurements have been collected at an upstream gage called “East Fork near Gardnerville” (USGS site number 10309000 on Figure 7) since 1890 until present. Changes in flow are likely minimal between the gage and the valley floor because there are no streamflow diversions and losses/gains are small (Maurer et al., 2007). As such, streamflow measurements at the upstream East Fork gage are specified as inflows for each stress period in the historical transient simulation.

In the West Fork, daily streamflow data are available at an upstream gage called "West Fork at Woodfords" (USGS site number 10310000 on Figure 7) for the historical transient model. Streamflow is diverted between the Woodfords gage and the valley floor to the Snowshoe Thompson Ditches 1 and 2 for irrigation water in Diamond Valley. Diversion rates are likely offset by inflows from unmeasured springs downstream, and therefore, the decrease in inflow to Carson Valley from the West Fork diversion is assumed to be negligible relative to the total inflow volume (Maurer et al., 2007). As such, streamflow measurements at Woodfords gage are specified as inflows to the model domain via the West Fork.

Monthly inflow volumes from Indian Creek into the model domain are calculated for the historical transient model using daily streamflow measurements (1994-1998) and sporadic field measurements of instantaneous streamflow (1981, 1999-2014) (USGS, 2016). For periods with no flow data, streamflow is estimated using linear regression to relate measured streamflow data at Indian Creek and the East Fork near Gardnerville gage:

$$Q_{IC} = 0.2615 \times Q_{EF} + 122745 \quad (9)$$

where Q_{IC} is the estimated monthly surface water discharge into the model domain via Indian Creek and Q_{EF} is the monthly surface water discharge into the model domain via the East Fork. The estimated inflows are greater than that of Yager et al. (2012), who specified inflow via Indian Creek as 2% of the East Fork inflow.

Surface water in the East Fork is diverted to canals and ditches on the valley floor for irrigation water. The monthly flow volumes measured for the Allerman Canal and Virginia Ditch (Figures 8 and 9) are used to fill historical data gaps to fulfill the monthly stress periods for the transient model. For canals and ditches that have limited or no available streamflow data, streamflow is estimated based on the ratio of streamflow in the canal of interest to streamflow in the Allerman Canal using mean annual streamflow data (annual streamflow data and ratios presented in Table 2).

Streamflow in the canals was adjusted to account for water removed for irrigation. As described in Section 3.7.2, the monthly streamflow volume removed from the canals for irrigation, or AR, is calculated based on ET measurements from 1985 to 2023 in agricultural field in southern Carson Valley by Melton et al. (2021). In the simulations, the AR required to irrigate all downstream fields in the model domain is removed at the point where the canal begins. Q_{ret} is simulated to remain in the canal, consistent with the approach of Yager et al. (2012). Streamflow is adjusted by deducting fluxes of ET_{ag} and R_{ag}. ET_{ag} is removed from the simulation. The monthly ET_{ag} and R_{ag} removed from streamflow are shown in Figure 21. The flux of R_{ag} is added to the RCH package. Therefore, the simulated total recharge equals the sum of valley recharge and agricultural recharge. AR is estimated for the 1965-1985 (the portion of the study period with no ET data from Melton et al. [2021] to deduce AR) by linear regression using the relationship between unadjusted and adjusted canal flow rates from 1985 to 2023. If the point of use of water from irrigation wells overlaps agricultural land with surface water rights, then the AR is reduced by half, assuming half of the irrigation water is from supplemental groundwater.

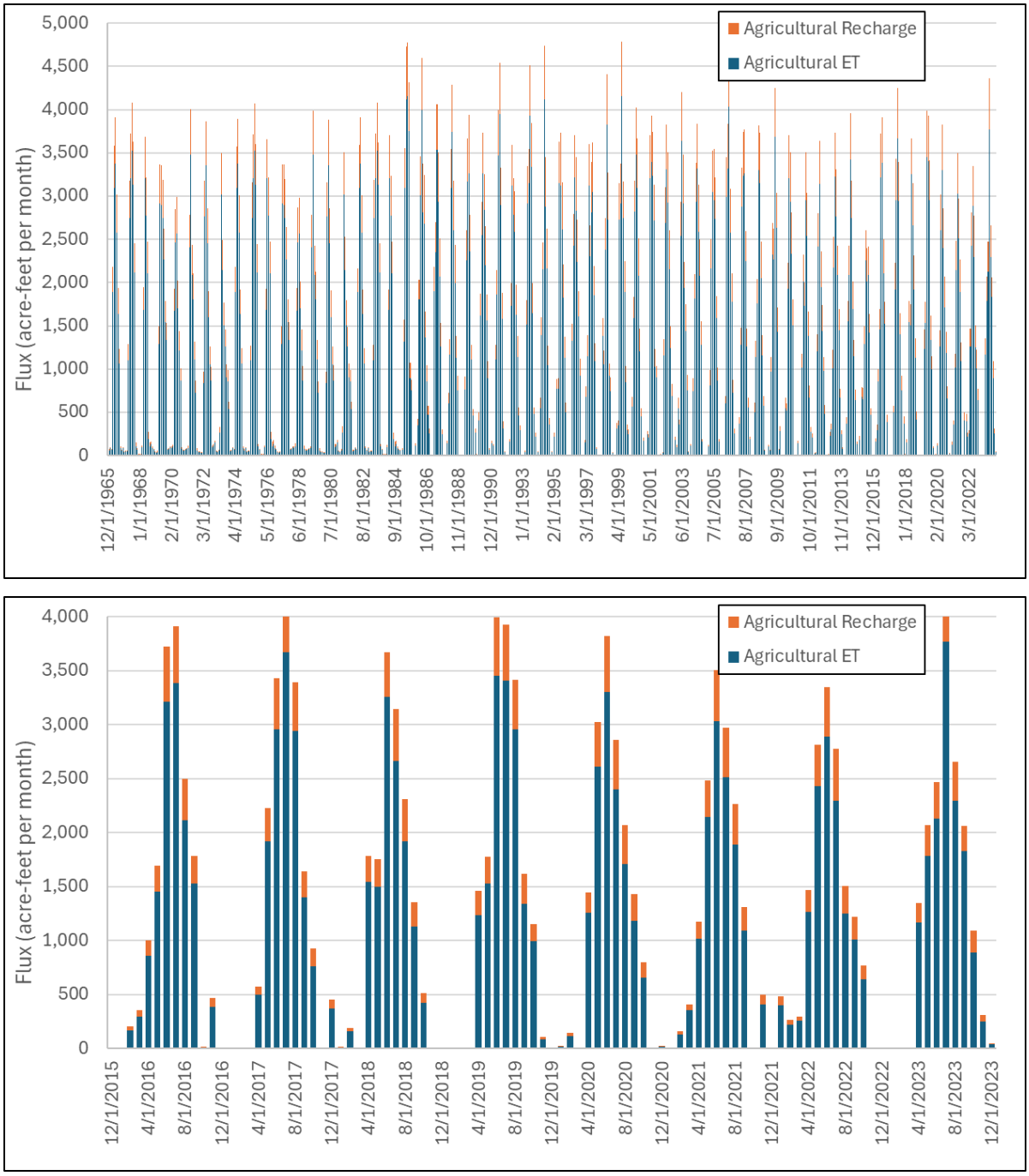

Figure 21. Total agricultural ET and agricultural recharge rates, in acre feet per month, in the model domain from 1965 to 2023 (top) and 2015 to 2023 (bottom). The top and bottom plots show the same data, but for different time periods, to provide additional context.

3.7.4 Subsurface Groundwater Inflows and Outflows

Groundwater flows into the model domain along the southeast boundary as mountain block recharge (R_{mb}), through alluvium underneath the West Fork Carson River at the southwestern corner, and through upgradient alluvium along the northeastern boundary. The bottom model boundary is represented as a no-flow boundary condition because the bedrock hydraulic conductivity is expected to be several orders of magnitude lower than the basin-fill aquifer.

R_{mb} is simulated as a specified flow boundary condition. For the estimated groundwater budget, mountain-block recharge includes inflows along the mountain-front and through alluvium beneath the West Fork. Flow is added to each cell using injection wells through the Well Package (WEL1). R_{mb} is defined separately for three distinct subbasins of the Carson Valley (Figure 22). The subbasin boundaries are defined using hydrologic unit code 10 (HUC10) boundaries (USGS, 2024). R_{mb} rates were assumed for initial model runs and adjusted during model calibration. Initial inflow rates for each segment are calculated as a fraction of the total R_{mb} estimates for the east or west sides of Carson River by Glancy and Katzer (1975):

$$Q_{INx} = \frac{A_{Cx}}{A_{Tx}} \times Q_{INtot} \tag{10}$$

where Q_{INx} is the subsurface inflow for segment x, A_{Cx} is the upgradient contributing inflow area to segment x, A_{Tx} is the total subsurface inflow area for the east or west side of the Carson River, and Q_{INtot} is the total subsurface inflow contribution for either the east or west side of the Carson River.

The estimated steady state R_{mb} in the model domain is 1,892 af/yr (2.3 million m³/yr), with approximately 704 af/yr (0.9 million m³/yr) in the West Fork subbasin, 573 af/yr (0.7 million m³/yr) in the Middle East Fork subbasin, 218 af/yr (0.3 million m³/yr) in the Lower East Fork subbasin, and 397 af/yr (0.5 million m³/yr) beneath the West Fork. Subsurface inflow through alluvium under the West Fork is calculated using Darcy's Law:

$$Q = (K \times d) \times \frac{\Delta h}{\Delta l} \times W \tag{11}$$

where K is the hydraulic conductivity, d is the average alluvium thickness, $\Delta h/\Delta l$ is the horizontal hydraulic gradient in southwest corner of model domain, and W is the width of the inflow area. Like valley floor recharge, for the historical transient simulation, rates of subsurface inflows from mountain block recharge and West Fork alluvium were adjusted proportionally to yearly precipitation measured in Minden relative to the mean yearly precipitation.

For context, estimates of R_{mb} to the larger Carson Valley range from 37,000 to 57,000 af/yr (46 million to 70 million m³/yr) (Maurer, 1986; Prudic and Wood, 1995; Glancy and Katzer, 1975). Glancy and Katzer (1975) estimated 7,000 af/yr (8.6 million m³/yr) of subsurface inflow transmitted via alluvial deposits under the West Fork at the Nevada-California state line, upgradient of the study area.

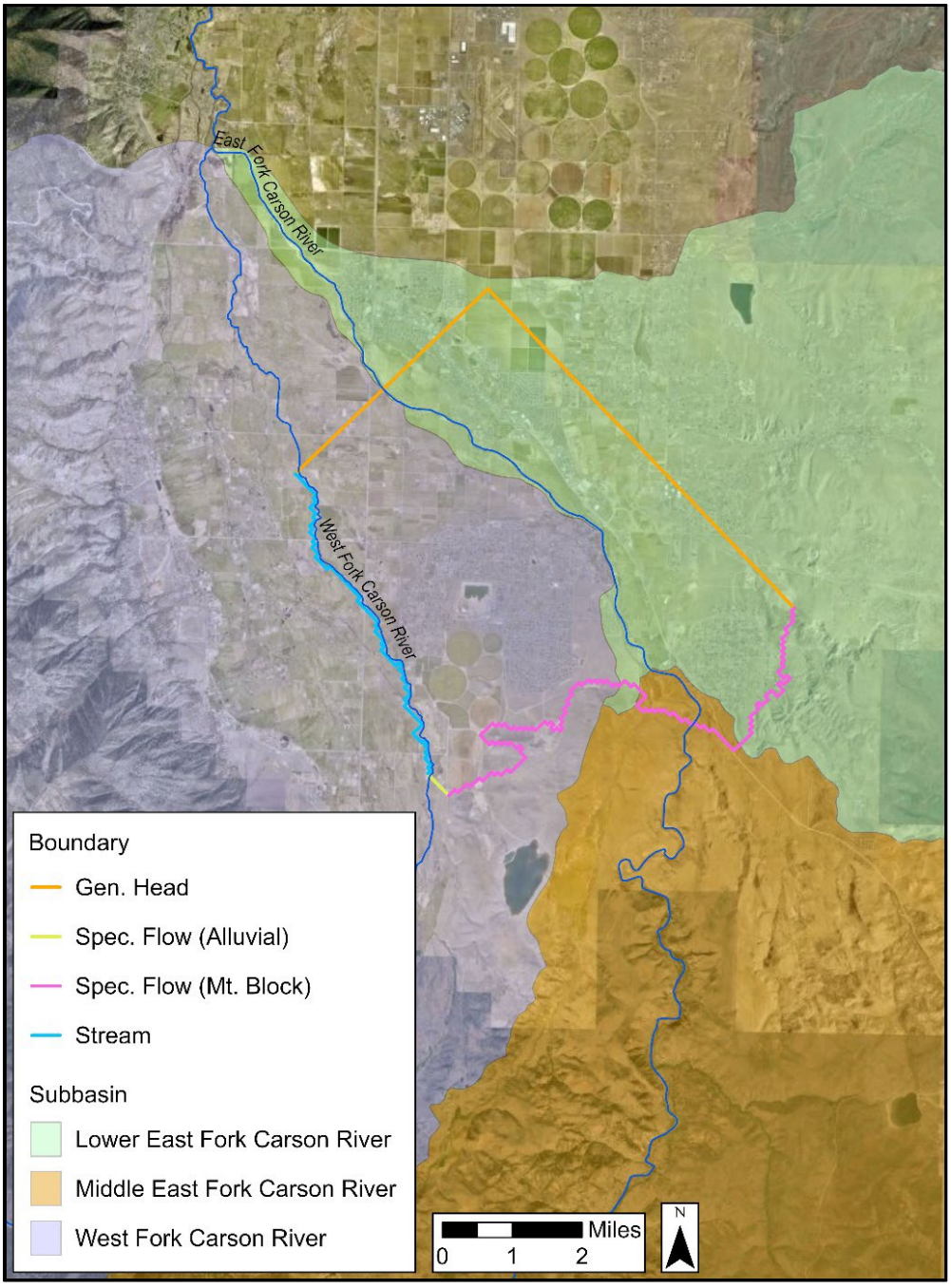

Figure 22. Map of subbasins and model boundary conditions. General head boundary types allow groundwater to flow into or out of the northeast and northwest model boundaries based on a specified head and conductance at each boundary. A specified flow boundary specifies the rate of flow into the southern model boundary from the mountain block and alluvium. Mountain block recharge (R_{mb}) is defined separately for each subbasin. Subbasins are defined using HUC10 boundaries (USGS, 2024). The stream boundary simulates the interaction between the West Fork Carson River and groundwater along the western boundary.

The northeast model boundary was set to be as close to parallel to the overall groundwater flow direction as possible. However, the westerly flow from the Pine Nut Mountains controls the general flow direction at the northeast boundary. The northeast boundary is assigned as a general head boundary (GHB) to allow groundwater to flow into and out of the model domain depending on transient groundwater conditions. Starting heads along the northeast boundary were estimated based on the horizontal hydraulic gradient from Kitlasten (2021), which also suggest some inflow to the model domain along this boundary during steady state conditions. Using Darcy's Law, the subsurface inflow to the model domain through the northeast model boundary via upgradient alluvium is estimated to be approximately 3,007 af/yr (3.7 million m^3/yr) during steady state conditions.

The northwestern boundary is oriented perpendicular to groundwater flow and the steady state subsurface outflow through the basin-fill is estimated as 31,215 af/yr (38.5 million m^3/yr), which is calculated as the sum of inflows to the model domain less ET_{gw} and discharge from pumping. The rate of groundwater outflow varies with transient conditions.

3.7.5 Pumping Wells

The NDWR well log database contains records for pumping wells in the model domain dating back to 1947 that include information on well construction, construction date, location, manner of use, and screen interval. Pumping wells in the model domain included in the historical transient model (1965-2023) are shown in Figure 23.

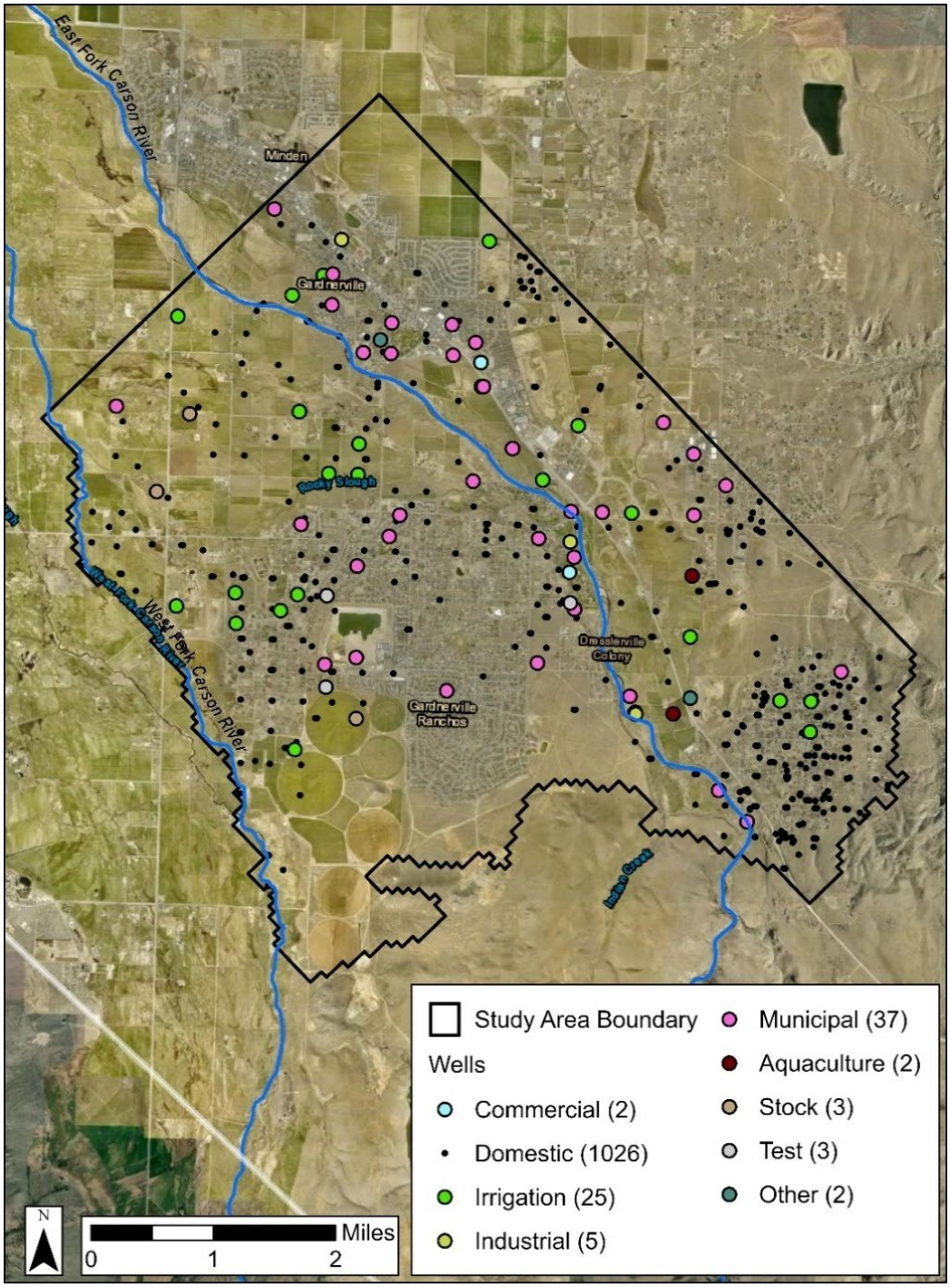

Figure 23. Locations of wells pumped in the transient simulation.

The manner of use that each well was registered for is assumed to be the manner of use for its duration of simulated pumping. Well logs commonly do not contain spatial coordinates for the well location and may instead be provided as Township, Range, Section, and Quarter-Quarter. To prevent having two or more domestic wells within the same model cell, the cumulative discharge of all wells in a single model cell is applied to a single well.

For all other well types, the location of one well is slightly modified so that wells are located in separate cells. Well screen altitudes were used to assign the wells to model layers. When well screen data were not available, well depths were set equal to typical depths in the model domain for domestic wells (150 ft [45 m]) and all other well types (300 ft [91 m]).

When available, reported pumpage data were applied in the model. For periods with no available pumpage data, pumpage rates were estimated by manner of use (methods are described in the following paragraphs). Available groundwater pumpage records for the model domain were compiled from NDWR, municipal water purveyors (G. Reed, personal communication, April 1, 2023), and published reports (Harrill and Worts, 1968; Walters et al., 1970; Glancy and Katzer, 1976; Maurer, 1986; Berger, 1987; Berger, 1990; Maurer et al., 2009). Monthly pumpage totals for municipal supply wells for years 2001-2020 and annual pumpage totals by permit number (for all manners of use) for years 1994-2000 were provided by NDWR. Annual pumpage totals by permit number are reported in NDWR's pumpage inventories for Carson Valley for years 2001-2020. Pumping wells drilled in 1965 or earlier are included in the steady state model. In the steady state model, the number of pumping locations (n=50) and pumping rates are constant. The cumulative discharge from pumping wells in the steady model is estimated at 800 af/yr (1.0 million m^3/yr).

The reported and estimated total annual pumping rates by well type/manner of use in the model domain for the historical transient simulation are shown in Figure 24. The historical average annual pumping rate is 3,160 af/yr (3.9 million m^3/yr). Total annual pumpage has increased steadily since 1965 primarily due to increased municipal and agricultural pumping. Interannual variability is explained, in part, by annual precipitation totals and surface water availability. For example, 2017 was the wettest year for the periods of record in this study (Figure 4), with an annual precipitation total of 20 inches (508 mm) in Minden, and during that year, groundwater pumping was notably low. Historically there has been relatively little pumping from aquaculture, stock, commercial, industrial, mining, dewatering, and domestic wells. Domestic wells are the greatest in number in the model domain (n =1,026), but account for a low proportion of annual pumping totals. The historical transient model has monthly stress periods to capture monthly and seasonal variability of pumping rates.

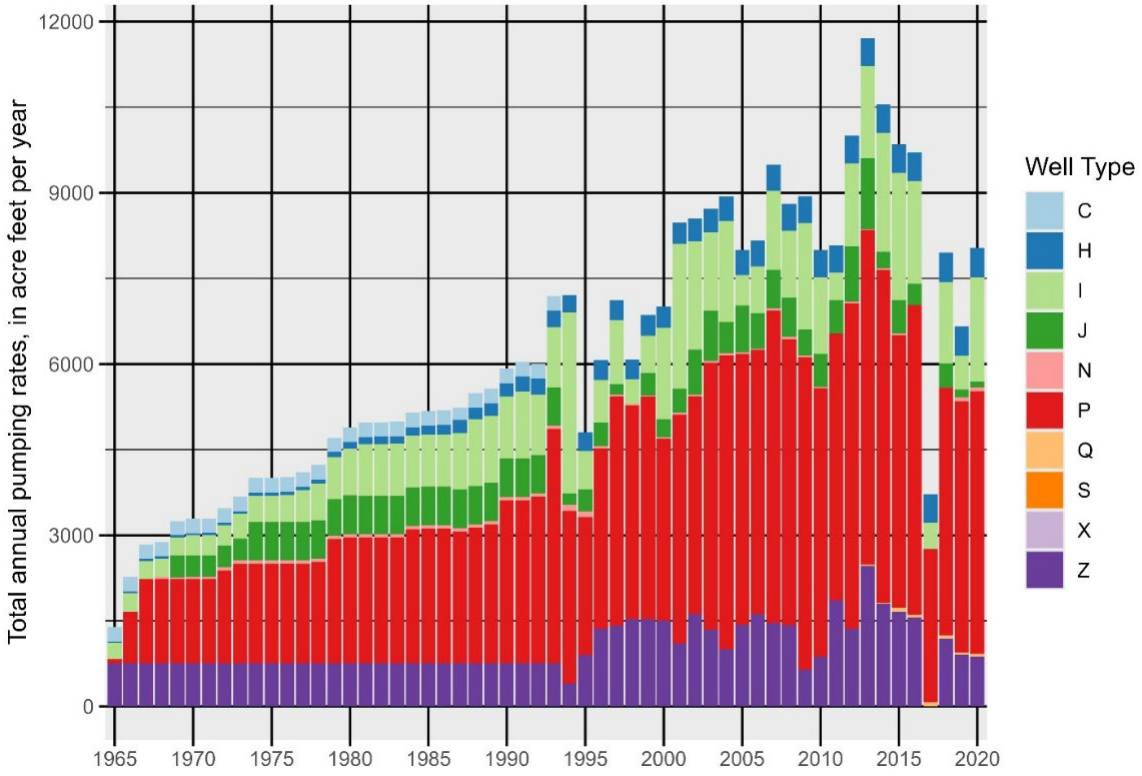

Figure 24. Estimated total annual pumping rates by manner of use in the model domain. C = Commercial, H = Domestic, I = Irrigation, J = Industrial-Cooling, N = Industrial, P = Municipal, Q = Aquaculture, S = Stock, X = Test Well, Z = Other.

Municipal wells were pumped at reported rates from 1994 to 2020 (NDWR, 2024b; N. Goehring, written communication, 2024). Total pumpage from GRGID wells reported by Glancy and Katzer (1975) for the years 1971 (160 acre-feet) and 1993 (2,847 acre-feet) were also applied. For years with no or incomplete pumpage records (1965-1993), municipal pumping was extrapolated according to population records and was distributed between wells in operation for each year. Figure 25 shows the percentage of total annual pumpage by GRGID supply wells. Well 1 was the only GRGID well in use from 1965 to 1967. From 1967 to 1974, pumpage was split evenly between Wells 1 and 2. From 1975 to 1993, annual pumpage was distributed between Wells 1, 2, 3, 4, 5, and 6 based on relative pumping amounts between these wells using records from 1993 to 1997. Well 5 was pulled from primary pumping following the 2001 EPA ruling for arsenic, which reduced the drinking water standard from 50 parts per billion (ppb) to 10 ppb. Similarly, Well 8 is subject to a water blending plan due to elevated arsenic. Annual pumpage was apportioned monthly based on average ratios of monthly-to-annual totals from 2002 to 2023 (from January to December: 2.9%, 2.9%, 2.8%, 3.3%, 6.6%, 10.4%, 13.8%, 16.5%, 16.3%, 13.4%, 7.8%, and 3.3%).

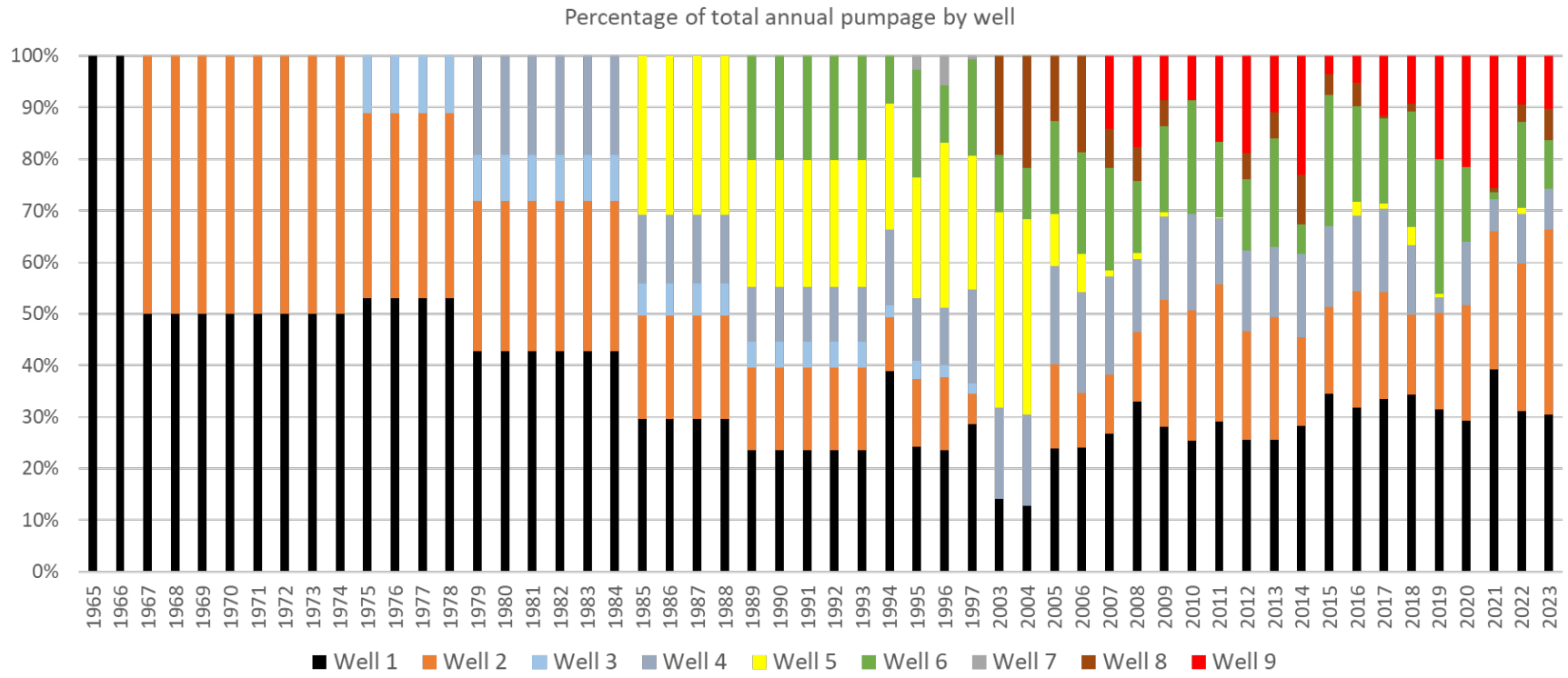

Figure 25. Percentage of total annual pumping by Gardnerville Ranchos supply well.

For municipal, industrial, and commercial wells outside of Gardnerville Ranchos, pumpage totals prior to 1994 were set equal to the duty or the maximum reported annual pumpage (NDWR, 2024b), whichever value was lower. Annual pumpage was distributed into monthly volumes following the same distribution as Gardnerville Ranchos wells.

Records of annual pumpage for irrigation wells are available from 1994 to 2020 (NDWR, 2024b). Glancy and Katzer (1975) estimated the basin-wide pumpage for irrigation during years of average precipitation (5,000 af/yr [(6.2 million m^3/yr]), dry years (10,000 af/yr [12.3 million m^3/yr]), and wet years (3,000 af/yr [3.7 million m^3/yr]). The average annual pumpage per irrigation well for Carson Valley was calculated (87.17 af/yr [0.1 million m^3/yr]) using yearly pumpage totals and the number of irrigation wells each year in Carson Valley (1971, 1981, 1987-2020). The average pumpage rate was applied to irrigation wells when no pumpage data were available, except for the Ruhenstroth area where the average measured pumpage for a respective well was applied for years with no available pumpage data. Yearly pumpage was divided into monthly pumpage using the seasonal percentages applied to irrigation wells by Yager et al., (2012) and dividing them equally between the three months in that season: 28% of annual total for each summer month (June, July, August), 2.3% for each fall month (September, October, November), 0% during winter months (December, January, February), and 3% for each spring month (March, April, May).

Domestic wells in the model domain were assumed to pump at 0.545 af/yr (0.7 million m^3/yr) (Berger, 1987), beginning in the year they were completed and continuing through the end of the simulated period. Other annual estimates of domestic well pumping range from 0.20 to 0.23 af/capita (247 to 284 m^3/yr) (NV Division of Water Planning, 1999) and 1.12 af/yr per well (1.4 thousand m^3/yr) (Maurer, 2007; Yager et al., 2012). Maurer et al. (2007) estimated that 0.15 to 0.28 af/yr (185 to 345 m^3/yr) of water pumped from domestic wells returns to the aquifer as secondary recharge from the percolation of water used for lawn watering and from septic tanks. Because percolation of water from lawns and septic tanks are not directly represented in the model, the rate of 0.545 af/yr (0.7 million m^3/yr) was used because it is understood to more accurately reflect the net annual consumption per domestic well. Annual pumpage from domestic wells is apportioned monthly following the same pattern as municipal wells.

For the steady state model, pumping wells are represented using the Well (WEL1) package. For the transient models, the Multi-Node Well Package (MNW2) is used to apply pumping constraints to the Gardnerville Ranchos supply wells. Pumping from all other wells in the transient models was simulated using the WEL1 package. The MNW2 package is useful for models used for water management and water supply operations because pumping is constrained by the water level in the well (h_{well}) and flow from the aquifer into the well. The specified flow rate for an MNW2 well is the maximum desired flow rate (Q_{des}). If h_{well} drops to an elevation within 16 to 23 ft (5 to 7 m) of the pump intake elevation (Z_{pump}) or if flow from the aquifer to well is limited (see "well losses" discussion below), then the simulated flow rate (Q_{sim}) is reduced to a rate $<Q_{des}$ to maintain a water level above the specified elevation threshold (h_{lim}).

Water levels in a pumping well are typically lower than water levels in the surrounding aquifer due to well losses (Figure 26). Well losses can result from turbulent flow near the well or from the hydraulic effects of the wellbore skin, which is the zone around the wellbore where formation permeability is altered due to drilling. MNW2 accounts for well

losses to estimate the head in a well, in addition to head in the nearest node. The cell-to-well conductance (CWC) value represents the rate of water flow between a single model cell and a well. The CWC value for each GRGID supply well was adjusted during transient model calibration to reduce the residuals between measured and simulated head inside of a pumping well. It is important to represent well losses in the predictive simulations to assess whether Q_{des} can be met under various predictive scenarios.

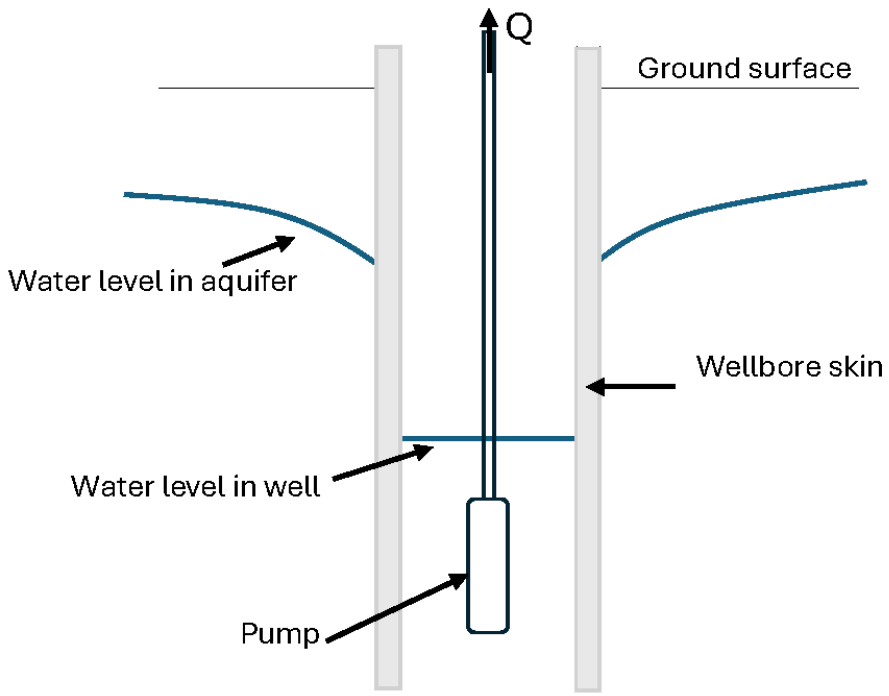

Figure 26. The MNW2 package calculates the hydraulic head in a pumping well based on the water level in the pumped cell, the pump intake elevation, and hydraulic conductance of the wellbore skin.

Table 8 includes the rated pumping capacities of GRGID supply wells and input parameters for the MNW2 package, including the calibrated CWC. The Q_{des} and minimum h_{lim} thresholds are assigned based on recorded discharge rates and minimum heads for each well. The Q_{des} exceeds the manufacturer rated pumping capacity for Wells 1 and 4, while Wells 2, 6, and 9 are lower. At the time of this study, because of elevated arsenic levels, Well 5 was not in use and Well 8 was not contributing at its full capacity. Well 5 is not included in predictive scenarios and therefore was excluded from MNW2 calibration. In the predictive model, Well 8 is assumed to continue contributing at a reduced capacity into the future.

Table 8. Input parameters to the MODFLOW's Multi-Node Well (MNW2) package for Gardnerville Ranchos supply wells

Supply Well Information		MNW2 Input Parameters			
Name	**Rated Pumping Capacity (gpm)**	**Qdes (gpm)**	**Zpump (ft asl)**	**hlim (ft asl)**	**Calibrated CWC (ft2/d)/ft**
Well 1	1,181	1,436	4,590	4,610	295
Well 2	1,765	1,660	4,554	4,577	377
Well 4	236	298	4,544	4,560	164
Well 5	1,745	**Not simulated with MNW2 package**			
Well 6	600	569	4,577	4,596	121
Well 8	1,200	202	4,551	4,570	328
Well 9	855	734	4,560	4,580	492

3.7.6 Evapotranspiration

In the simulations, ET estimates were made separately for irrigated fields ("agricultural ET") and non-agricultural ET (phreatophytes and wetland/riparian). ET from groundwater (ET_{gw}) is represented as a head-dependent boundary for three vegetation classes (i.e., native phreatophytes, irrigated fields, and wetland/riparian) using the Evapotranspiration Package (EVT). The distribution of ET zones in the model domain for the steady state model is shown in Figure 27. The areas of each vegetation type were estimated using the National Land Cover Dataset (NLCD, 2021). To estimate the area of each vegetation type during pre-development conditions (1965), the NLCD dataset was modified by applying changes in land use between 1979 and 2005 reported by Maurer (2007). Prior to development of Gardnerville Ranchos, land use was for agriculture/ranching, so the land cover was reverted to irrigated fields (Figure 27). The vegetation distribution of 2023 was applied and remained static throughout the duration of the historical transient model, as land development over this time was minimal and is not expected to have had a significant impact on ET and recharge in the model domain (J. Huntington, personal communication, July 29, 2024).

The three input parameters for the EVT package are maximum ET rate, ET surface (set equal to land surface elevation), and extinction depth (maximum rooting depth). The EVT module removes groundwater on a cell-by-cell basis, based on the depth of the water table below land surface at a linear rate, until the defined extinction depth is reached, at which point no groundwater is removed.

The rate of ET loss per unit surface area is computed in transient simulation using a depth-dependent function:

$$Q_{ET} = \frac{ET_{max}}{d_{ET}}(h - (LS - d_{ET})) \quad (12)$$

where ET_{max} is the maximum ET rate, d_{ET} is the extinction depth below which no ET occurs, h is the hydraulic head, and LS is the land surface elevation.

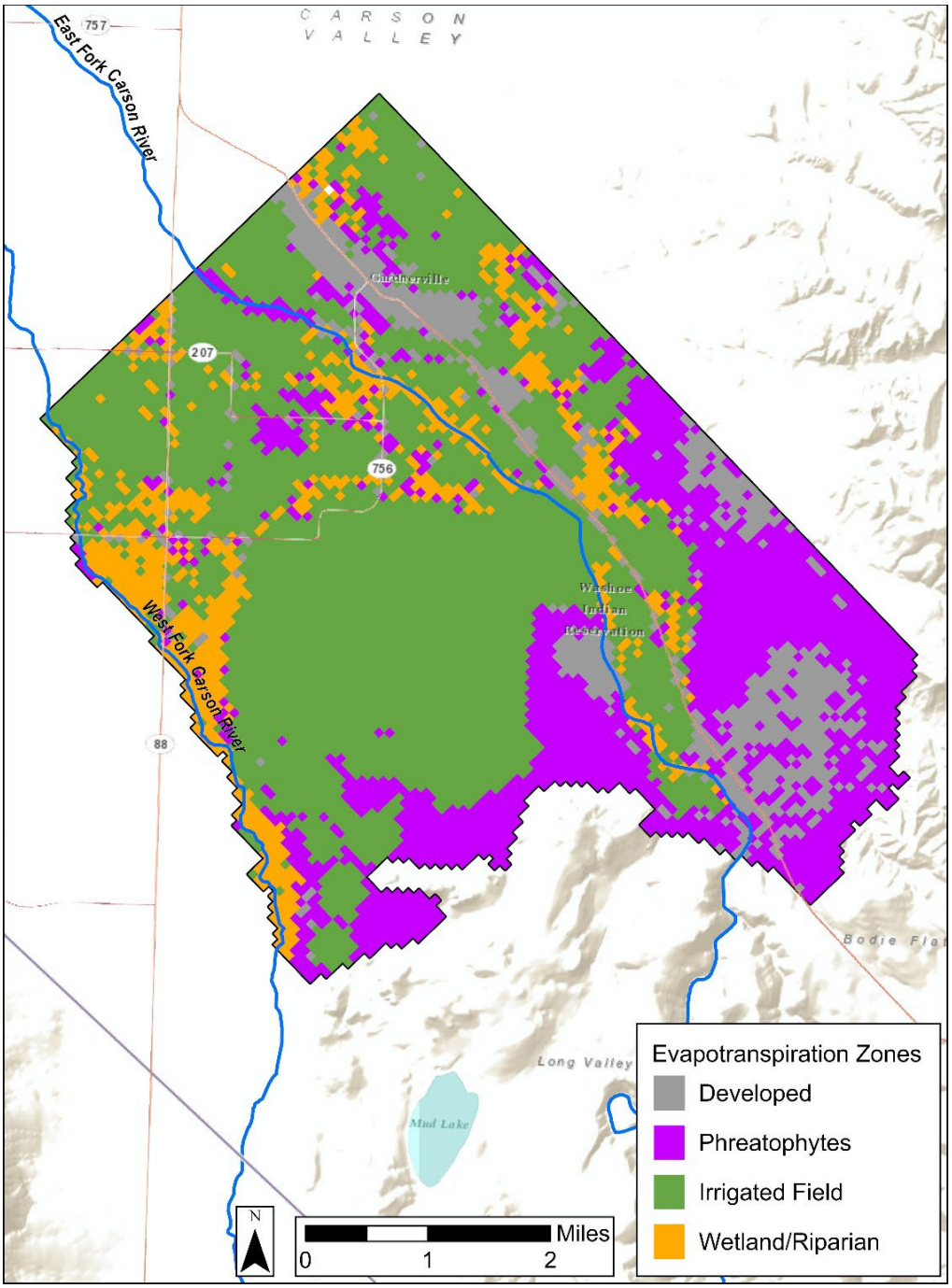

Figure 27. Evapotranspiration zones over the model domain. Zone definitions: Developed – areas dominated by constructed materials, such as asphalt, concrete, and buildings, where evapotranspiration is virtually zero; Phreatophytes – zones dominated by plants with a deep root system that draws its water supply from near the water table; Irrigated fields – zones of land where water is artificially applied to the soil for crop growth; Wetland – areas where the soil is saturated with water and support vegetation adapted to these conditions; Riparian – areas along rivers, streams, and other water bodies where the land meets the water.

The ET_{max} and d_{ET} for each vegetation type were adjusted during steady state calibration. The ET_{max} establishes the upper limit for groundwater withdrawal, applied when the depth to groundwater is zero, or above land surface. Initial values for ET are based on published values by Maurer (2006, 2007) and Huntington (2003) in Carson Valley, including 3.0 ft/yr (0.91 m/yr) for irrigated fields, 1.9 ft/yr (0.58 m/yr) for phreatophytes, and 4.4 ft/yr (1.4 m/yr) for wetlands/riparian. The initial d_{ET} are consistent with Yager et al. (2012) and include 30 ft (9 m) for phreatophytes and wetland/riparian zones and 10 ft (3 m) for irrigated fields. The non-agricultural ET within the model domain was estimated to be 23,082 af/yr (28.5 million m^3/yr), including 12,231 af/yr (15.1 million m^3/yr) for irrigated fields, 2,482 af/yr (3.1 million m^3/yr) for phreatophytes, and 8,368 af/yr (10.3 million m^3/yr) for wetlands/riparian. In estimating ET, areas of higher elevation in the southern segment of the model domain are excluded where the depth to water exceeds the d_{ET}, and ET is expected to be zero. For transient simulations, the ET_{max} is specified based on monthly rates from Maurer et al. (2006).

As described in Section 3.7.2, a portion of the water removed from the canal network for irrigation is consumed by ET_{ag}. The monthly ET_{ag} volumes in the transient model are based on ET_{ag} estimates for southern Carson Valley (Melton et al., 2021). The estimated monthly ET_{ag} flux for the transient simulation is shown in Figure 21.

3.7.7 Faults

The Horizontal-Flow Barrier (HFB6) package was used to simulate faults as thin and vertical low-permeability geologic features that impede flow. Faults are conceptually situated on the boundaries between pairs of adjacent cells. A fault is assigned a hydraulic characteristic value, which is equal to the barrier hydraulic conductivity divided by barrier width. Faults within the model domain were identified from geologic maps of the Gardnerville quadrangle (dePolo et al., 2000) and the Minden quadrangle (Ramelli et al., 2014) and the USGS Quaternary Faults and Folds Database (USGS, 2023) Three faults are represented in the model that affect groundwater flow based on water levels during aquifer testing and non-pumping conditions (Figure 12; described in Section 2.3.4). Appendix A includes details and results of aquifer testing and fault characterization. A unique hydraulic characteristic value was estimated for each fault during transient model calibration using water levels measured during aquifer testing.

3.8 Model Development and Calibration

3.8.1 Calibration Description

Model calibration is performed so that the model can be used to answer questions about the groundwater system and forecast groundwater conditions. Calibration is an iterative process of adjusting model parameters (i.e., hydraulic conductivity and storage parameters), which are not known with certainty, to obtain a reasonable match between field measurements (or "observations") and model-computed (or "simulated") values that are consistent with the local geology and hydrogeology. For the model developed here, the calibration process begins with steady state calibration to observed hydraulic heads any time prior to 1965, which is before development and groundwater pumping in Gardnerville Ranchos. Calibration then advances to the transient model calibration to historical pumping and temporally varying hydraulic heads in the model domain from 1965 to 2023. A separate transient calibration is performed to controlled pumping conditions and high frequency

drawdown measurements during the aquifer tests conducted as part of this study. The transient models focus on adjusting aquifer storage parameters and conductance of faults. The terms hydraulic heads, heads, groundwater elevations, and water levels are used interchangeably herein.

3.8.2 Calibration Objective

The goal of model calibration is to minimize the objective function, which is the metric that quantifies the deviation between simulated and observed hydraulic heads. Calibration results are documented by reporting summary statistics for the steady state model (i.e., mean error, mean absolute error, root mean square error, and relative root mean square error). To minimize the effect of model size and hydraulic head range on calibration results, the relative root mean square error ($RMSE_{rel}$) is used to quantify the error of the model on a relative basis and is the primary metric used to assess model fit:

$$RMSE_{rel} = \frac{RMSE}{h_{max} - h_{min}} \tag{13}$$

where h_{max} is the maximum observed head, h_{min} is the minimum observed head, and $RMSE$ is the root mean square error calculated using the following equation:

$$RMSE = [\frac{\sum(h_{obs} - h_{sim})_i^2}{n}]^{0.5} \tag{14}$$

where h_{obs} is the measured hydraulic head of the i_{th} observation, h_{sim} is the simulated head of the i_{th} observation, and n is the total number of observations.

$RMSE$ is defined as the standard deviation of the residuals (modeled minus observed values). In other words, $RMSE$ is a measure of how spread out the residuals are around the line of best fit (statisticshowto.com). $RMSE_{rel}$ normalizes the $RMSE$ by dividing it by the range of observed water levels to allow for more meaningful model comparison for the study area.

A lower objective function indicates a closer match between simulated and observed heads and better model performance. Generally, an acceptable model has an $RMSE_{rel} < 10\%$. Additional evaluation of model performance is achieved through the assessment of scatter plots of observed versus simulated values, spatial maps of residuals, and the simulated water budget. Ultimately, the calibration is adequate if the fit between simulated and observed values is acceptable and the hydrogeologic parameters and assumptions used to obtain the fit are reasonable. This means that calibration also relies on knowledge about the system that is not directly comparable to quantitative model outputs and draws on locally relevant geological and hydrologic information.

3.8.3 Steady State Calibration

The steady state model is calibrated to groundwater elevations, or calibration "targets," measured prior to 1965 or during "pre-development" conditions. Steady state targets were developed using location and depth to water information from well drillers' reports filed in the Well Log Database (NDWR, 2024a) for wells drilled in or prior to 1965. In total, there were 19 steady state targets. Groundwater elevation targets were estimated by

subtracting the depth to water from land surface elevation (from a 1-meter digital elevation model). While these targets provide valuable constraints for model calibration, the accuracy of the estimated groundwater elevations depends heavily on the precision of the depth to water measurements and land surface elevations. Therefore, it is important to note the uncertainty associated with the depth to water measurements, such as the unknown accuracy of the water level measuring device, unknown measuring point (e.g., top of well casing versus land surface), or operator error.

The steady state calibration focuses on adjusting hydraulic conductivity, conductance of head-dependent boundaries (i.e., GHBs and streams), and ET rates to minimize the difference ("residual" or "error") between the steady state head targets and the simulated heads. The model is calibrated using a combination of manual (trial-and-error) and automated calibration techniques. The trial-and-error methodology includes the manual adjustment of parameter values and running the model to observe the effects. Streambed conductance, GHB conductance, ET, and vertical hydraulic conductivity were adjusted entirely by trial and error. Hydraulic conductivity was calibrated through a combination of trial and error and the PEST parameter estimation package (Doherty and Hunt, 2010), which is commonly used for calibrating MODFLOW models. PEST is an automatic inverse calibration model where multiple iterations of parameter variations are constrained within a defined range of parameter values. In this study, PEST was constrained using parameter ranges informed by results from field testing as well as values reported in the literature, ensuring that the calibration remained physically realistic and consistent with site-specific data . Initial values and the range of values applied to calibration parameters are summarized in Table 9. Initial values were assigned to all parameters, and then PEST was run allowing the hydraulic conductivity values to vary within prescribed ranges (described below). The final hydraulic conductivity of each K zone was estimated iteratively between the steady state and transient model. Between iterations, the trial-and-error calibration parameters were adjusted manually (within the range of values shown in Table 9), targeting estimated fluxes in the conceptual model, including streamflow infiltration, subsurface inflows and outflow through GHBs, and ET fluxes. The estimated fluxes are described in Section 3.7. Table 10 compares the flow budgets of the conceptual and steady state models. Table 10 compares the flow budgets of the conceptual and steady state models.

Table 9. Parameters adjusted during steady state model calibration, initial value, range allowed, and calibrated value.

Parameter Group (unit)	Parameter	Description	Aquifer	Position	Initial Value	Min Value During Calibration	Max Value During Calibration	Source of Initial, Min, Max Values	Calibrated Value
Evapotranspiration (ft/d)	EVT_1	open water	-	-	0.016	0.010	0.020	Maurer (2006, 2007) and Huntington (2003)	0.020
	EVT_3	phreatophytes	-	-	0.005	0.004	0.005	Maurer (2006, 2007) and Huntington(2003)	0.004
	EVT_4	irrigated fields	-	-	0.008	0.008	0.013	Maurer (2006, 2007) and Huntington (2003)	0.013
	EVT_5	wetland/riparian	-	-	0.013	0.003	0.016	Maurer (2006, 2007) and Huntington (2003)	0.010
General Head Boundary Conductance (ft/d)	GHB_40	northeast boundary (upper)	-	-	68.787	0.033	32.808	-	2.717
	GHB_60	northwest boundary	-	-	792.651	0.033	32.808	-	17.323
	GHB_70	northeast boundary (lower)	-	-	250.574	0.033	32.808	-	2.717
Horizontal Hydraulic Conductivity (ft/d)	HK_11	fluvial deposits	shallow	western valley margin	1.502	0.839	1.542	Specific capacity from NDWR driller logs, this study	1.542
	HK_111	fluvial deposits	deep	western valley margin	0.820	0.820	1.502	Specific capacity from NDWR driller logs, this study	0.820
	HK_12	fluvial deposits	shallow	valley center	3.281	3.281	328.084		196.850

Table 9. Parameters adjusted during steady state model calibration, initial value, range allowed, and calibrated value (continued).

Parameter Group (unit)	Parameter	Description	Aquifer	Position	Initial Value	Min Value During Calibration	Max Value During Calibration	Source of Initial, Min, Max Values	Calibrated Value
Horizontal Hydraulic Conductivity (ft/d)	HK_112	fluvial deposits	deep	valley center	32.808	1.529	185.206	Specific capacity from NDWR driller logs, this study	185.203
	HK_13	fluvial deposits	shallow	between west and central fault	65.617	7.874	98.425	Specific capacity from NDWR driller logs, this study	86.503
	HK_113	fluvial deposits	deep	between west and central fault	65.617	8.136	41.010	Specific capacity from NDWR driller logs, this study	9.660
	HK_14	fluvial deposits	shallow	between central and east fault	22.966	0.197	23.787	This study	19.086
	HK_114	fluvial deposits	deep	between central and east fault	17.370	1.312	33.000	Specific capacity from NDWR driller logs, this study	32.808
	HK_15	fluvial deposits	shallow	East Fork enters Carson Valley	1.115	0.820	5.085	Specific capacity from NDWR driller logs, this study	5.081
	HK_115	fluvial deposits	deep	East Fork enters Carson Valley	1.394	0.839	1.502	Specific capacity from NDWR driller logs, this study	1.083
	HK_21	river terrace deposits	shallow	western terrace; west of West Fault	541.339	57.087	4215.333	This study	7.980

Table 9. Parameters adjusted during steady state model calibration, initial value, range allowed, and calibrated value (continued).

Parameter Group (unit)	Parameter	Description	Aquifer	Position	Initial Value	Min Value During Calibration	Max Value During Calibration	Source of Initial, Min, Max Values	Calibrated Value
Horizontal Hydraulic Conductivity (ft/d)	HK_221	river terrace deposits	deep	western terrace	6.070	6.055	560.467	This study	12.056
	HK_22	river terrace deposits	shallow	central terrace; between West and Central Faults	65.617	0.328	328.084	This study	8.432
	HK_222	river terrace deposits	deep	central terrace; between West and Central Faults	24.606	0.328	83.333	This study	3.568
	HK_23	river terrace deposits	shallow	eastern terrace, between Central and East Fault	49.213	0.000	328.084	This study	328.084
	HK_223	river terrace deposits	deep	eastern terrace, between Central and East Fault	8.858	0.167	90.791	Specific capacity from NDWR driller logs, this study	90.791
	HK_24	river terrace deposits	shallow	far east terrace, east of East Fault	1.575	0.033	3.281	this study	0.033
	HK_224	river terrace deposits	deep	far east terrace, east of East Fault	1.785	0.328	32.808	this study	25.158
	HK_31	alluvial deposits	shallow	eastern valley margin	0.328	0.111	11.155	Specific capacity from NDWR driller logs	2.718
	HK_331	alluvial deposits	deep	eastern valley margin	0.946	0.111	11.230	Specific capacity from NDWR driller logs	0.484

Table 9. Parameters adjusted during steady state model calibration, initial value, range allowed, and calibrated value (continued).

Parameter Group (unit)	Parameter	Description	Aquifer	Position	Initial Value	Min Value During Calibration	Max Value During Calibration	Source of Initial, Min, Max Values	Calibrated Value
Riverbed Conductance (ft/d)	STR_66	West Fork			2.531	0.032	32.808	Yager et al. (2012)	98.425
	STR_77	East Fork Lower			0.347	0.032	32.808		328.084
	STR_88	East Fork Upper			1.684	0.032	32.808		3.281
	STR_99	Indian Creek			28.563	0.032	32.808		32.808
	STR_109	Allerman Canal			0.033	0.032	32.808		0.328
	STR_119	Rocky Slough			6.299	0.032	98.425		98.425
	STR_129	Cottonwood Slough			0.328	0.032	98.425		98.425
	STR_139	Henningson Slough			6.299	0.032	32.808		32.808
	STR_149	Edna Ditch			6.299	0.032	328.084		39.370
	STR_159	Virginia Ditch			0.328	0.032	328.084		32.808
Vertical Hydraulic Conductivity (Kh/Kv)	VK_50	fluvial deposits		all fluvial deposits	1000.00	1000.00	9700.00	Yager et al. (2012), this study	1000.00
	VK_51	river terrace deposits		entire terrace	10.00	1.00	100.00		13.18
	VK_53	alluvial deposits		eastern valley margin	10.00	1.00	100.00		12.40
	VK_54	Tertiary deposits		buried Tertiary unit	1000.00	500.00	1000.00		1000.00

The conceptual model includes a heterogeneous hydraulic conductivity field that varies spatially in the model domain. Heterogeneity is incorporated in the model using a zonation approach, in which the model domain is divided into 21 zones of equal hydraulic conductivity ("K zones"). The K zones were defined based on the surface geology described by dePolo et al. (2000) and Ramelli et al. (2014), borehole lithology data, and interpretations of time-drawdown data during aquifer testing. During calibration, the hydraulic conductivity for each K zone in Gardnerville Ranchos is allowed to vary within the range of hydraulic conductivity values estimated during aquifer testing and using specific capacity data from well driller reports (Table 9). Layers 1 and 2 have the same K zones, so hydraulic conductivity varies uniformly in these layers. The same is true for layers 3 and 4. Layer 5 hydraulic conductivity varies separately from all other layers.

The distribution of calibrated hydraulic conductivities for each model layer are shown in Figures 28 and 29. Layers 2-5 are not included along the southern model boundary where the basin-fill thickness reaches zero. Simulated hydraulic conductivities ranged from 0.03 ft/d (0.01 m/d) in the young alluvial deposits of the Far East Block in Layers 1 and 2 to 328 ft/d (100 m/d) in the young fluvial and alluvial deposits of the East Block in Layers 1 and 2. The East Block has the highest fault density in the study area, which contributes to the high hydraulic conductivity. The fault zone acts as a conduit to flow in the direction of groundwater flow and as barrier when perpendicular to groundwater flow. In Layers 1-4, the distribution of calibrated hydraulic conductivity indicates larger values toward the valley center (northern portion of the study area) in the young fluvial deposits between the East and West Forks and lower values in alluvial and fluvial deposits toward the valley margins. This distribution is consistent with the pattern of transmissivity estimated in Carson Valley by Yager et al. (2012). Generally, calibrated hydraulic conductivity decreases with depth. An exception is the Far East Block, where hydraulic conductivity increases with depth from Layer 2 to 3. This increase in hydraulic conductivity could be the result of faults intersecting with depth. Layer 5 has a uniform calibrated hydraulic conductivity of 0.13 ft/d (0.04 m/d). The low hydraulic conductivity of Layer 5 is consistent with increased compaction and cementation of Tertiary sediments.

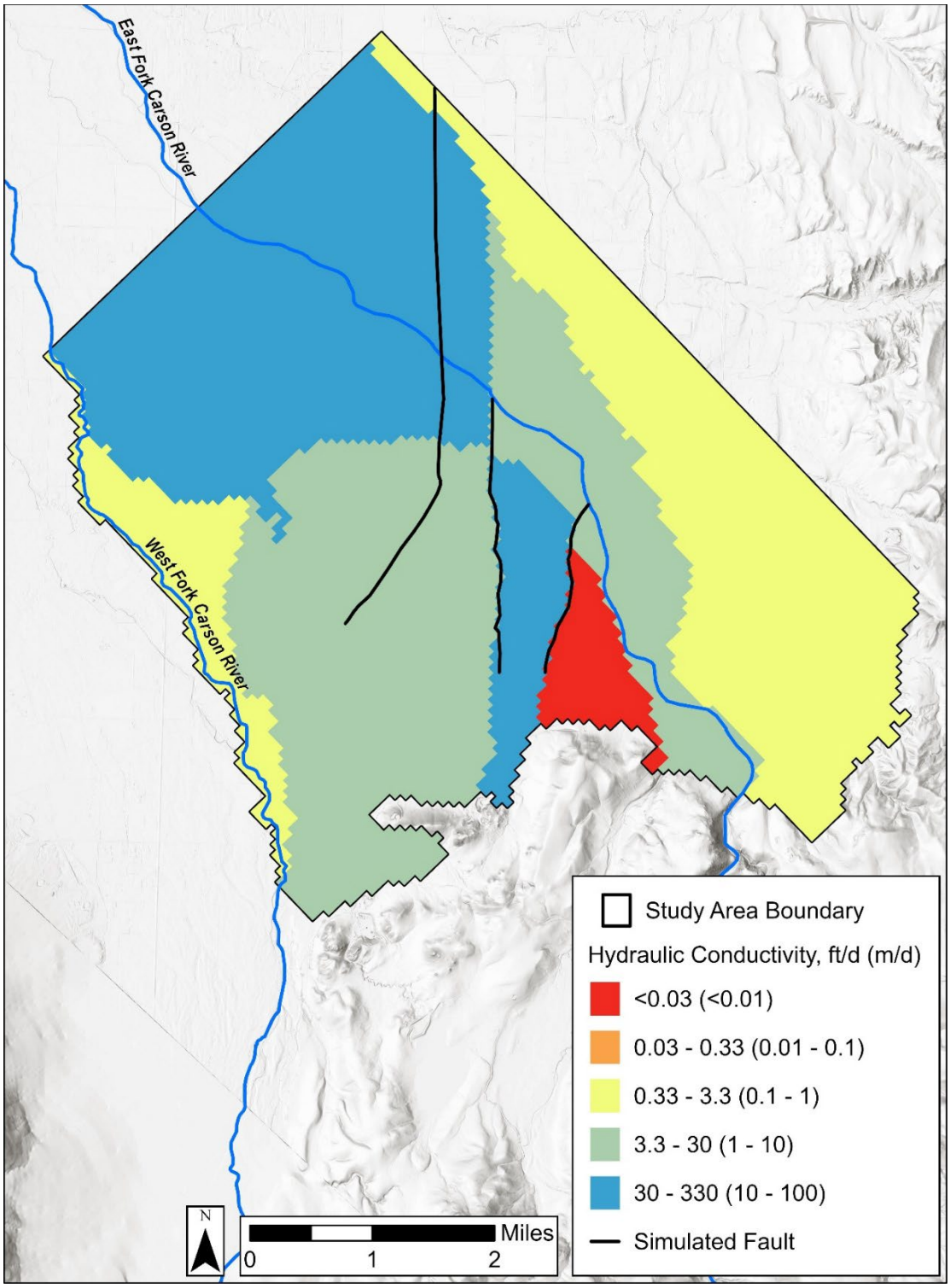

Figure 28. Simulated hydraulic conductivity field for model layers 1 and 2.

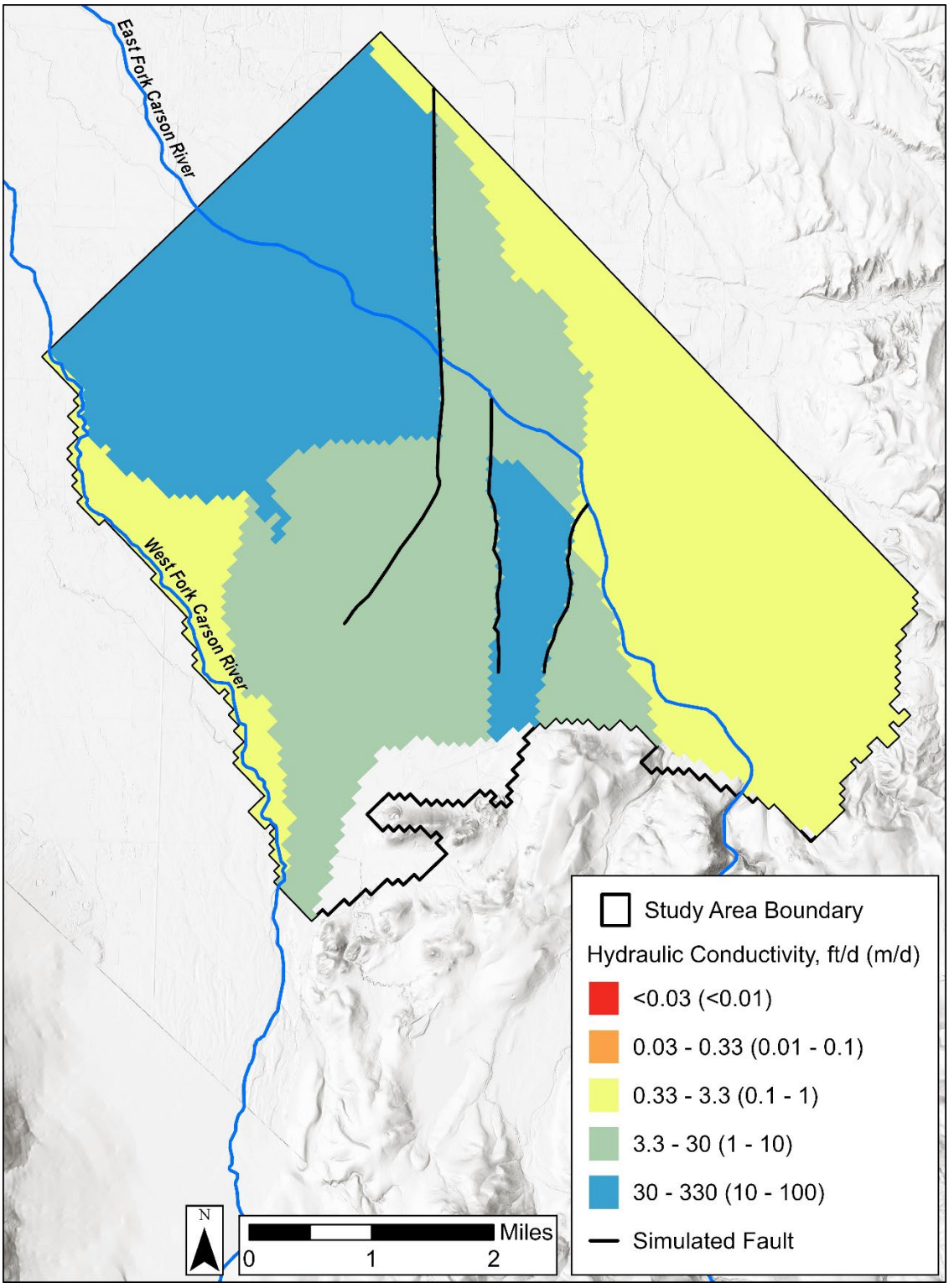

Figure 29. Simulated hydraulic conductivity field for model layers 3 and 4.

Table 10 is a comparison of the groundwater flow budgets of the calibrated steady state model and the estimated steady state budget of the conceptual model. Overall, the flow budget components have similar fluxes. Streambed conductance was calibrated targeting the total estimated steady-state streamflow infiltration into the aquifer (river loss) of 48,565 af/yr (59.9 million m^3/yr). The calibrated conductance values per unit length range from 0.3 (ft^2/d)/ft [0.1 (m^2/d)/m] in the Allerman Canal to 328 (ft^2/d)/ft [100 (m^2/d)/m] in the East Fork. Generally, the irrigation canals are simulated to have lower conductance values compared to the East and West Forks. The greatest inflow to the model domain is from I_{stream}, with a total of 49,796 af/yr (61.4 million m^3/yr). The total simulated outflow from the aquifer to streamflow was 5,999 af/yr (7.4 million m^3/yr) because simulated groundwater elevations exceed surface water elevations in some areas of the calibrated model. The conceptual model assumes groundwater elevations are below surface water elevations throughout the model domain and that there is no groundwater discharge to streamflow. The difference between the conceptual model and calibrated model outflows to streamflow is considered negligible with respect to the overall groundwater budget.

Maximum ET rates and d_{ET} were calibrated for each ET type, including irrigated fields, riparian/wetland, and phreatophytes, targeting the estimated total steady state rate of 23,082 af/yr (28.5 million m^3/yr). The simulated total ET was 24,787 af/yr (30.6 million m^3/yr). For irrigated fields, the ET_{max} rate was 4.8 ft/yr (0.004 m/d) with a d_{ET} of 9.8 ft (3.0 m). Riparian/wetland vegetation had a ET_{max} rate of 3.59 ft/yr (0.003 m/d) and a d_{ET} of 49 ft (15 m). For phreatophytes, the ET_{max} was 1.56 ft/yr (0.0013 m/d) and the d_{ET} was 49 ft (15 m).

Total simulated subsurface inflow to the model domain is 6,832 af/yr (8.4 million m^3/yr), including 1,769 af/yr (2.2 million m^3/yr) of R_{mf} and 5,062 af/yr (6.2 million m^3/yr) of GW_{in}. The flux of R_{mb} is assigned in the model; this value was adjusted during model calibration. The calibrated flux of GW_{in} is 1.7 times the estimated flux in the conceptual model, which is likely a result of the conductance assigned to the GHB along the northeast model boundary. The flux of GW_{out} in the calibrated model is approximately 4,000 af/yr (4.9 million m^3/yr) less than the estimated flux; the outflow of Q_{stream} makes up this difference. Consistent with the conceptual model, the calibrated model suggests that subsurface outflow out of the northwest model boundary is the greatest flux out of the model domain.

Table 10. Comparison of groundwater budgets for the steady state model and conceptual model. R_{val} is valley recharge from precipitation on the valley floor; R_{ag} is agricultural recharge from irrigated fields; R_{mb} is mountain-block recharge from the mountain block on the southern edge of the model domain; I_{stream} is infiltration of streamflow from rivers, creeks, and the irrigation network to groundwater; GW_{in} is subsurface inflow of groundwater to the model domain through upgradient basin-fill; ET_{gw} is evapotranspiration from the water table by vegetation on the valley floor; ET_{ag} is evapotranspiration of water applied to fields for irrigation; Q_{stream} is groundwater seepage from the aquifer to rivers, creeks, and the irrigation canals; GW_{pump} is total pumping of groundwater; and GW_{out} is subsurface outflow of groundwater through basin-fill

Inflow Components	**Calibrated Steady State Flows**		**Conceptual Model Flows**	
	af/yr	**Percent of total**	**af/yr**	**Percent of total**
$R_{val} + R_{ag}$	1,634	3%	1,634	3%
R_{mb*}	1,769	3%	1,892	3%
I_{stream}	49,796	85%	48,564	88%
GW_{in}	5,062	9%	3,007	5%
Total inflows	58,261	100%	55,097	100%
Outflow Components	**af/yr**	**Percent of total**	**af/yr**	**Percent of total**
ET_{gw}	24,787	43%	23,082	42%
Q_{stream}	5,999	10%	0	0%
GW_{pump}	801	1%	801	1%
GW_{out}	26,669	46%	31,215	57%
Total outflows	58,256	100%	55,098	100%

Calibration statistics for the calibrated steady state and transient models are summarized in Table 11. The final calibrated steady state model, on average, slightly underestimates groundwater levels compared to observed data (mean head residual of -2.49 ft [-0.76 m]). The model's simulated groundwater levels differ from observed levels by about 9.06 ft (2.76 m) on average, regardless of whether they are too high or too low (this is the mean absolute head residual). The model's RMSE is 10.7 ft (3.3 m). The $RMSE_{rel}$ is 6.9%, which means that the average error is 6.9% of the total range in observed groundwater levels (155 ft [47.3 m]). The $RMSE_{rel}$ is less than 10%, which is an acceptable difference given the difficulties in capturing the complexities of a natural system in a numerical model. A comparison of simulated and observed heads (Figure 30) also indicates that the model accurately simulates the groundwater system.

Table 11. Calibration statistics for the steady state, historical transient, and aquifer test transient models

Calibration Statistic	Steady State	Historical Transient	Aquifer Test Transient
Mean Head Residual, ft (m)	-2.49 (-0.76)	-22.2 (-6.78)	-2.6 (-0.80)
Mean Absolute Head Residual, ft (m)	9.06 (2.76)	27.4 (8.36)	5.1 (1.55)
Root Mean Square Head Residual, ft (m)	10.7 (3.3)	43.9 (13.4)	7.1 (2.16)

On Figure 30, points above the 1:1 line overestimate head, whereas points below the line underestimate head. The spatial distribution of head residuals is shown on Figure 31. The highest residuals occur in the southern and eastern section of the model domain, where heads are generally over-predicted (blue circles).

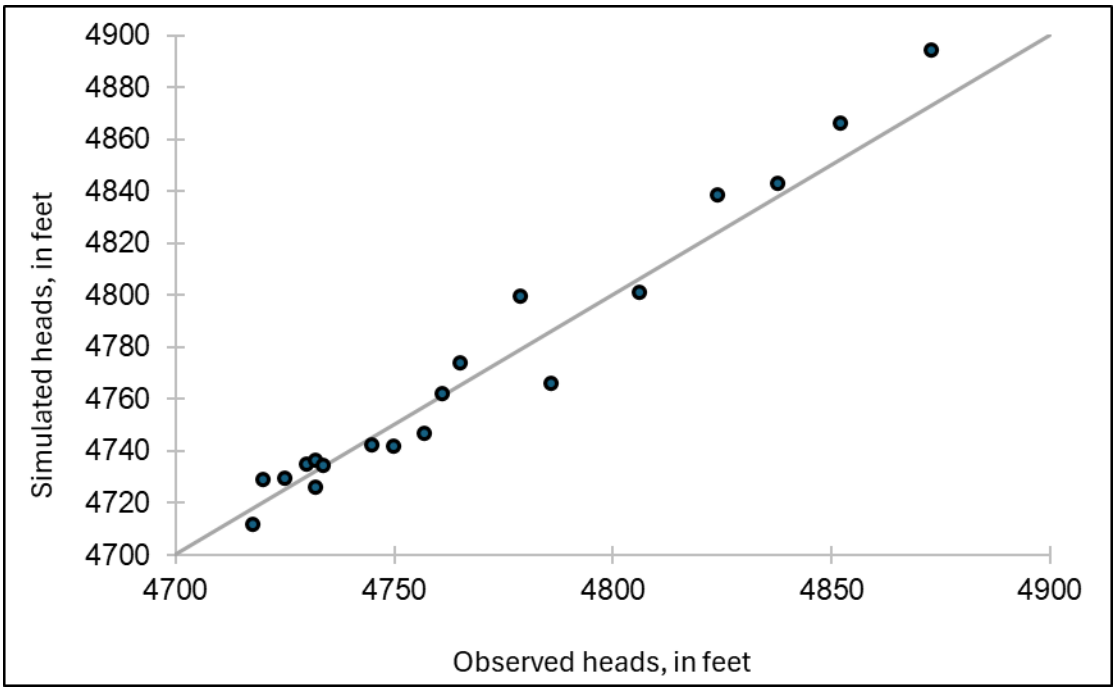

Figure 30. Comparison of simulated and observed heads from the calibrated steady state model, plotted along a one-to-one line. Points that plot above the line overestimate head and points below the line underestimate head.

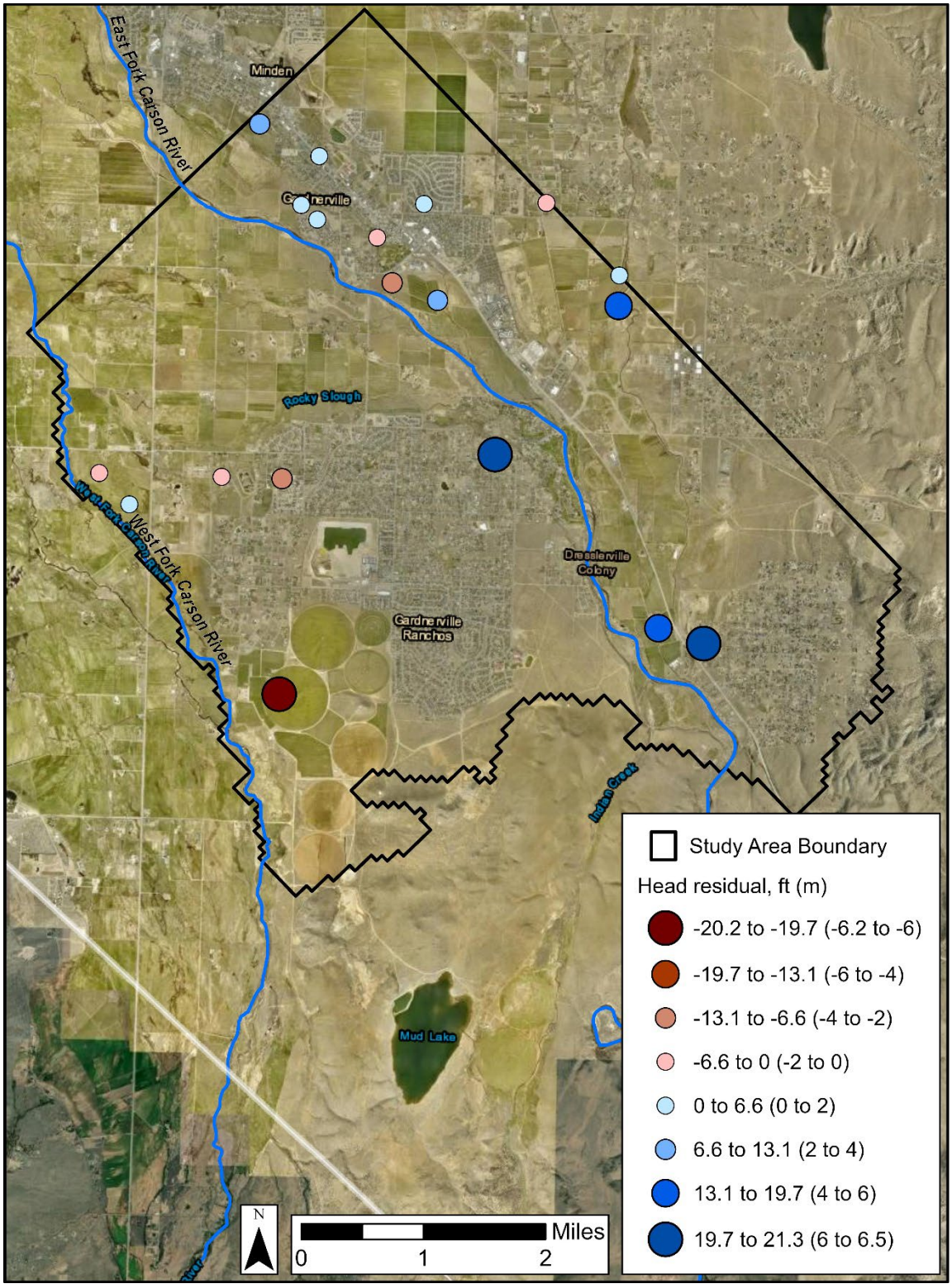

Figure 31. Head residuals for the calibrated steady state model. Negative values (red circles) indicate points where simulated heads are less than observed heads. Positive values (blue circles) indicate points where simulated heads are greater than observed heads.

3.8.4 Transient Calibration

Two separate transient calibrations are performed, including a "historical" transient model (calendar years 1965-2023) and "aquifer testing" transient model (November 1, 2022, to March 1, 2023). The transient models are developed to show that the natural system is captured by the numerical model through calibration of aquifer storage parameters, fault hydraulic characteristics, and cell-to-well conductance (CWC) values for GRGID supply wells for use in the predictive models. Zones of equal storage are assigned to the same zones used for hydraulic conductivity. Storage parameters and fault hydraulic characteristics were calibrated to trends in observed heads using manual (trial and error) and automated approaches (PEST). Storage parameters and fault hydraulic characteristics were adjusted iteratively between the historical and aquifer test transient models; the historical transient model calibration aims to capture long-term changes to the groundwater system, while the aquifer transient aims to capture local and short-term changes specific to the area of the aquifer that is pumped by Gardnerville Ranchos supply wells. CWC values were manually calibrated to observed heads (Table 8). Initially, faults were not included in the model to assess whether spatial heterogeneity in aquifer storage and hydraulic conductivity sufficiently captured temporal changes in groundwater levels. Ultimately, three faults (West, Central, East Faults) were physically represented in the model to capture spatial drawdown distributions during both transient models. Table 12 summarizes the initial values, allowable range during calibration, and the final calibrated value for each parameter. CWC values were manually calibrated to observed heads.

Table 12. Parameters adjusted during calibration of transient models, initial value, range allowed, and calibrated value.

Parameter Group (unit)	Parameter	Description	Initial Value	Min Value During Calibration	Max Value During Calibration	Source of Initial, Min, Max Values	Calibrated Value
Specific Storage (1/ft)	511	western valley margin	3.2E-05	2.0E-06	6.2E-05	Yager et al. (2012), Domenico and Mifflin (1965), this study	3.6E-05
	5111	western valley margin	3.2E-05	2.0E-06	6.2E-05	Yager et al. (2012), Domenico and Mifflin (1965), this study	6.2E-05
	512	valley center	1.8E-06	1.8E-06	6.2E-05	Yager et al. (2012), Domenico and Mifflin (1965), this study	6.0E-04
	5112	valley center	3.2E-05	2.0E-06	6.2E-05	Yager et al. (2012), Domenico and Mifflin (1965), this study	6.2E-05
	513	between west and central fault	3.2E-05	2.0E-06	6.2E-05	Yager et al. (2012), Domenico and Mifflin (1965), this study	3.9E-05
	5113	between west and central fault	3.9E-04	2.0E-06	3.9E-04	Yager et al. (2012), Domenico and Mifflin (1965), this study	1.3E-03
	514	between central and east fault	4.5E-11	4.5E-11	6.2E-05	Yager et al. (2012), Domenico and Mifflin (1965), this study	2.0E-05
	5114	between central and east fault	1.2E-06	1.2E-06	6.2E-05	Yager et al. (2012), Domenico and Mifflin (1965), this study	4.0E-06
	515	East Fork enters Carson Valley	6.0E-09	6.0E-09	6.2E-05	Yager et al. (2012), Domenico and Mifflin (1965), this study	6.2E-05
	5115	East Fork enters Carson Valley	3.2E-05	2.0E-06	6.2E-05	Yager et al. (2012), Domenico and Mifflin (1965), this study	2.0E-07
	521	western terrace; west of West Fault	1.1E-06	1.1E-06	6.2E-05	Yager et al. (2012), Domenico and Mifflin (1965), this study	6.7E-04
	5221	western terrace	4.3E-07	4.3E-07	6.2E-05	Yager et al. (2012), Domenico and Mifflin (1965), this study	6.2E-05
	522	central terrace; between West and Central Faults	2.3E-06	2.0E-06	6.2E-05	Yager et al. (2012), Domenico and Mifflin (1965), this study	2.8E-04

Table 12. Parameters adjusted during calibration of transient models, initial value, range allowed, and calibrated value (continued).

Parameter Group (unit)	Parameter	Description	Initial Value	Min Value During Calibration	Max Value During Calibration	Source of Initial, Min, Max Values	Calibrated Value
Specific Storage (1/ft)	5222	central terrace; between West and Central Faults	3.2E-05	2.0E-06	6.2E-05	Yager et al. (2012), Domenico and Mifflin (1965), this study	4.1E-05
	523	eastern terrace, between Central and East Fault	3.3E-11	3.3E-11	6.2E-05	Yager et al. (2012), Domenico and Mifflin (1965), this study	2.2E-04
	5223	eastern terrace, between Central and East Fault	3.2E-05	2.0E-06	6.2E-05	Yager et al. (2012), Domenico and Mifflin (1965), this study	2.0E-06
	524	far east terrace, east of East Fault	3.2E-05	2.0E-06	6.2E-05	Yager et al. (2012), Domenico and Mifflin (1965), this study	2.0E-06
	5224	far east terrace, east of East Fault	3.2E-05	2.0E-06	6.2E-05	Yager et al. (2012), Domenico and Mifflin (1965), this study	2.0E-06
	531	eastern valley margin	3.2E-05	2.0E-06	6.2E-05	Yager et al. (2012), Domenico and Mifflin (1965), this study	1.7E-05
	5331	eastern valley margin	3.2E-05	2.0E-06	6.2E-05	Yager et al. (2012), Domenico and Mifflin (1965), this study	6.0E-05
Fault Hydraulic Characteristic (ft/d)	HFB_8	West Fault	1.0E-05	1.0E-08	1.0E-01		1.3E-02
	HFB_7	Central Fault	1.0E-05	1.0E-08	1.0E-01		1.1E-04
	HFB_6	East Fault	1.0E-05	1.0E-08	1.0E-01		1.3E-07

Final values of specific storage range from 2.0×10^{-7} ft^{-1} (6.1×10^{-8} m^{-1}) to 1.3×10^{-3} ft^{-1} (3.9×10^{-4} m^{-1}). Specific storage is greatest in young fluvial deposits of the East and West Forks in layers 1 and 2. Specific storage of the river terrace deposits in layers 1 and 2 beneath Gardnerville Ranchos increases from east to west, ranging from 2.2×10^{-4} ft^{-1} (6.6×10^{-5} m^{-1}) in the Far East Block to 6.6×10^{-4} ft^{-1} (2.0×10^{-4} m^{-1}) in the West Block. Generally, calibrated specific storage decreases throughout the model domain from layers 1 and 2 to Layers 3 and 4. Specific storage of the Tertiary sediments in Layer 5 were calibrated at 6.6×10^{-5} ft^{-1} (2.0×10^{-5} m^{-1}).

Three faults that impede groundwater flow are represented in the model, including the East, Central, and West Faults. The calibrated hydraulic characteristic values are 0.013 (ft/d)/ft) [3.9×10^{-3} (m/d)/m] for the West Fault, 1.1×10^{-4} (ft/d)/ft [3.2×10^{-5} (m/d)/m] for the Central Fault, and 1.2×10^{-7} (ft/d)/ft [3.8×10^{-8} (m/d)/m] for the East Fault. The low hydraulic characteristic value of the East Fault is consistent with observed water levels that suggest the East Fault is a barrier to flow during both pumping and static conditions. The calibrated hydraulic characteristic values suggest that the Central and West Faults impede flow but are not complete barriers. This is consistent with observed heads during aquifer testing, which showed some drawdown across these faults.

The calibrated CWC values for each supply well are provided in Table 8. Calibrated CWC values range from 164 (ft^2/d)/ft [50 (m^2/d)/m] for Well 4 to 492 (ft^2/d)/ft [150 (m^2/d)/m] for Well 9.

The locations of transient head observations discussed below are shown in Figure 32. The discussion below begins with a comparison of observed and simulated seasonal, interannual, and long-term trends in the historical transient model (1965-2023) and then moves into comparison of observed and simulated water levels in GRGID supply wells and monitoring wells during the aquifer testing model (November 2022 to March 2023). Wells owned by GRGID are referred to in the text by their well name (e.g., Well 1, MW-2, etc.), while other wells are referred to by the letter shown in Figure 32.

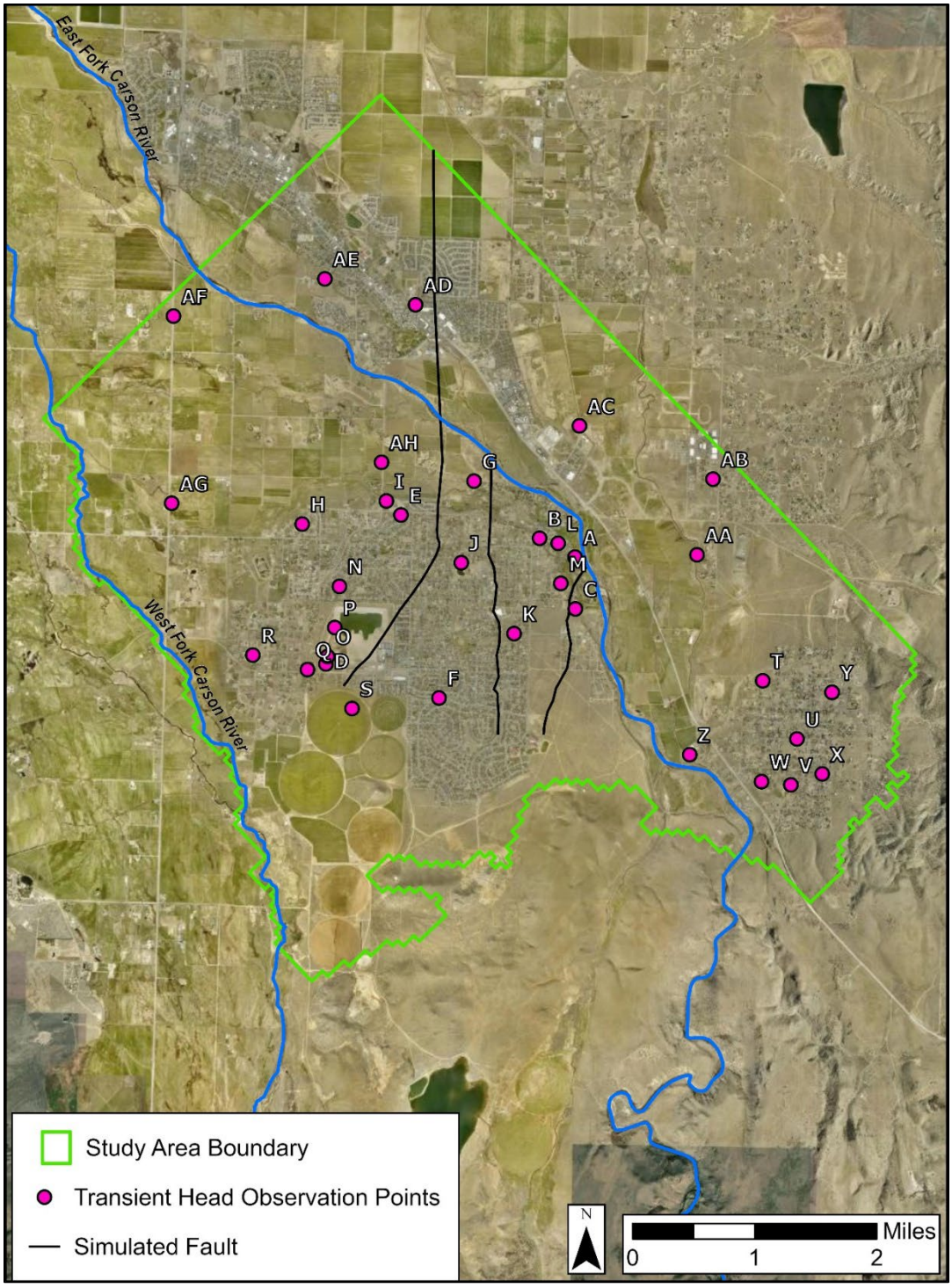

Figure 32. Locations of transient head observations in the model domain. Plots of the observed and simulated heads for these locations are shown in Figure 33A-AH. Key for Gardnerville Ranchos wells – A: Well 1, B: Well 2, C: Well 4, D: Well 5, E: Well 6, F: Well 7, G: Well 8, H: Well 9, I: MW1, J: MW2, K: MW3, L: MW5, M: MW6, N: Sweetwater, O: MW1_Bing, P: MW2_Bing

3.8.4.1 Historical Transient Model

The historical transient model is calibrated to time-varying hydraulic heads in response to pumping in the model domain from 1965 to 2023. In total, there are 5,641 transient head targets at 134 calibration points. The starting head distribution for the historical transient is set using the head distribution from the calibrated steady-state model. Monthly stress periods are applied during the historical model. Stresses and boundary conditions can change at the start of each stress period and remain constant during each stress period. Stress periods are subdivided into ten time steps to simulate head changes within the stress period. A time-step multiplier of 1.1 is applied to the historical transient, with shorter time steps at the beginning of each stress period to capture rapid changes in hydraulic head and longer time steps after the initial stress responses have been absorbed by the system and head changes are smaller. In other words, the time-step multiplier helps the model run more efficiently by using smaller time steps when water levels change rapidly and larger time steps when water levels are more stable. With a time step multiplier of 1.1, each time step is 10% longer than the one before it.

Calibration statistics for the historical transient model are summarized in Table 11. Final calibration of the historical transient model resulted in a mean head residual of -22.2 ft (-6.78 m), a mean absolute head residual of 27.4 ft (8.36 m), and a root mean square head residual of 43.9 ft (13.4 m), equating to an $RMSE_{rel}$ of 8.7% over an observed head range of 502 ft (153 m). Relatively high errors between observed and simulated heads exist for pumping wells because MODFLOW estimates head in the cell (aquifer) and does not account for well losses. Rather than removing head targets from pumping wells (which would reduce model errors), pumping water levels are kept in the model to calibrate the CWC value in GRGID pumping wells in both the historical and aquifer testing transient models (see "Simulation of Hydrologic Boundaries – Pumping Wells" for discussion on CWC). Because model results will inform supply well operations at Gardnerville Ranchos, it is important to estimate heads both inside the GRGID supply well and in the surrounding aquifer. Heads in the GRGID supply wells are estimated separately using the MNW2 package. Plots of simulated and observed heads for the locations in Figure 32 are shown in Figure 33A-AH. The plots for GRGID supply wells show simulated heads inside the supply wells from the MNW2 package, while all other plots show the simulated heads in the aquifer at the well.

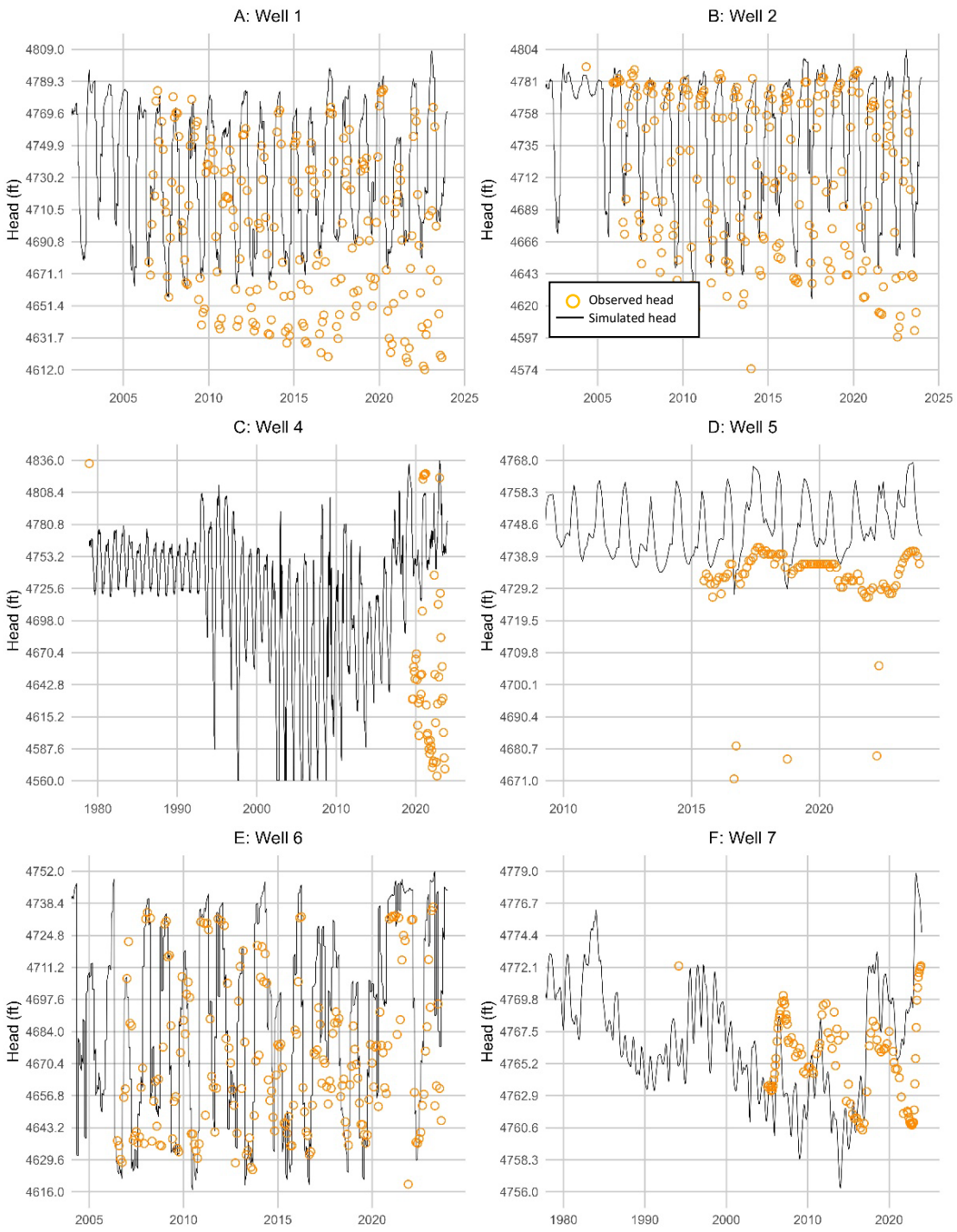

Figure 33A-F. Observed heads (orange circles) and simulated heads (black lines) at wells A-F for the historical transient model (1965-2023). The title for each plot includes the well letter and ID. Plots for GRGID supply wells A, B, C, E show simulated heads inside the supply wells, while plots for D and F show simulated heads in the aquifer. Locations of the wells are shown in Figure 32. The *x*-axis varies between plots to show temporal variability during the period of observed heads for each well.

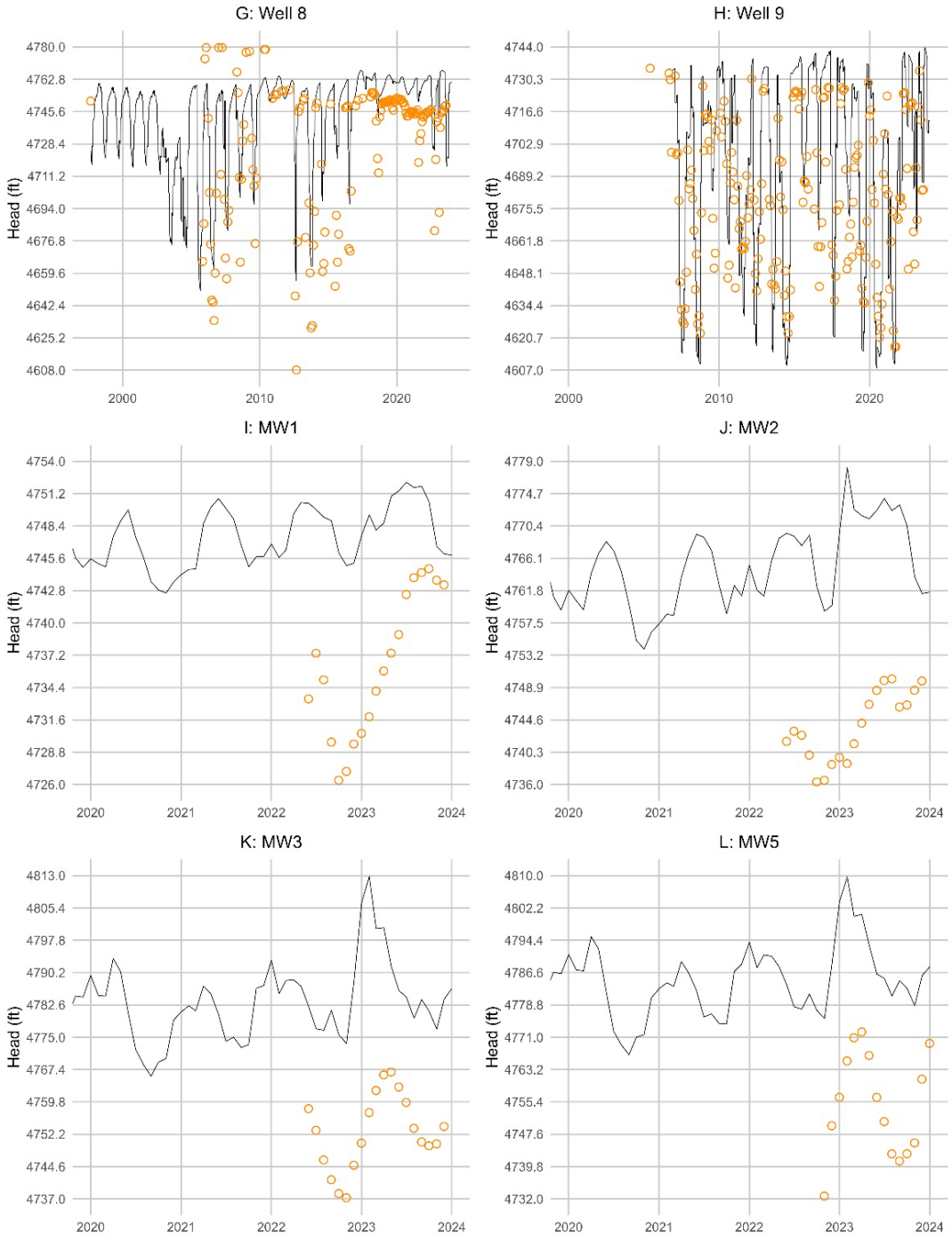

Figure 33G-L. Observed heads (orange circles) and simulated heads (black lines) at wells G-L for the historical transient model (1965-2023). The title for each plot includes the well letter and ID. Plots for GRGID supply wells G and H show simulated heads inside the supply wells, while plots for I-L show simulated heads in the aquifer. Locations of the wells are shown in Figure 28. The *x*-axis varies between plots to show temporal variability during the period of observed heads for each well.

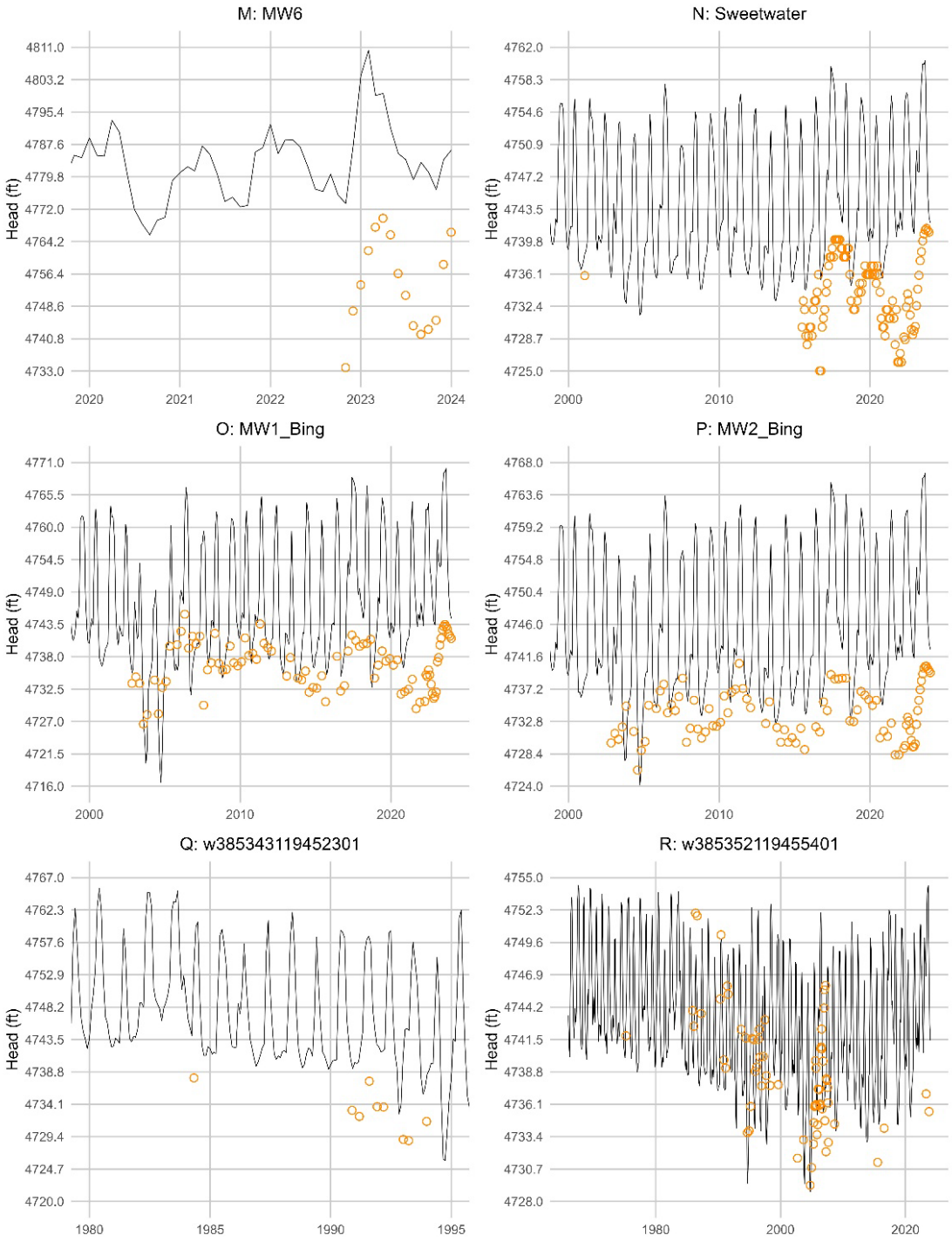

Figure 33M-R. Observed heads (orange circles) and simulated heads (black lines) at wells M-R for the historical transient model (1965-2023). The title for each plot includes the well letter and ID. Locations of the wells are shown in Figure 28. The *x*-axis varies between plots to show temporal variability during the period of observed heads for each well.

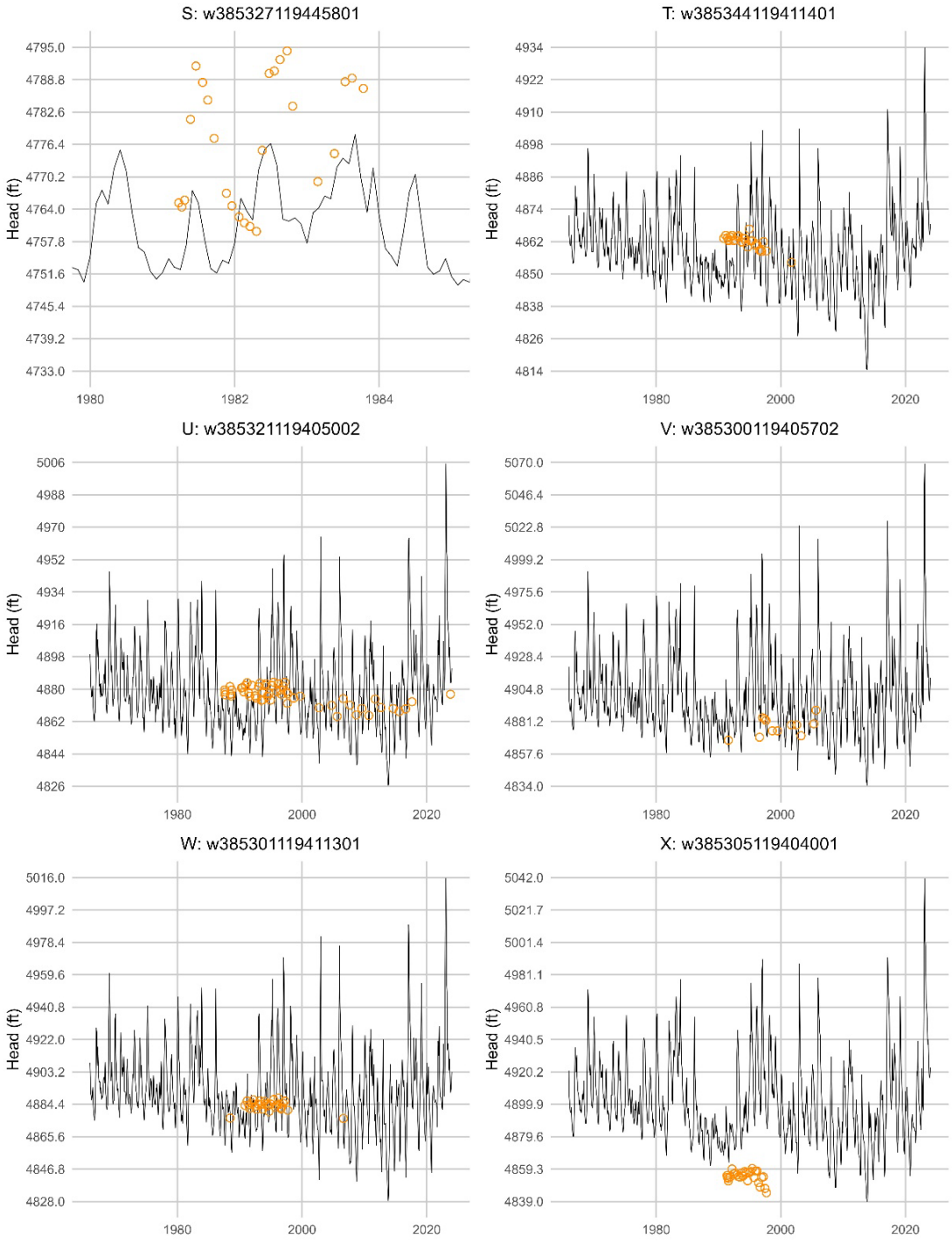

Figure 33S-X. Observed heads (orange circles) and simulated heads (black lines) at wells S-X for the historical transient model (1965-2023). The title for each plot includes the well letter and ID. Locations of the wells are shown in Figure 28. The *x*-axis varies between plots to show temporal variability during the period of observed heads for each well.

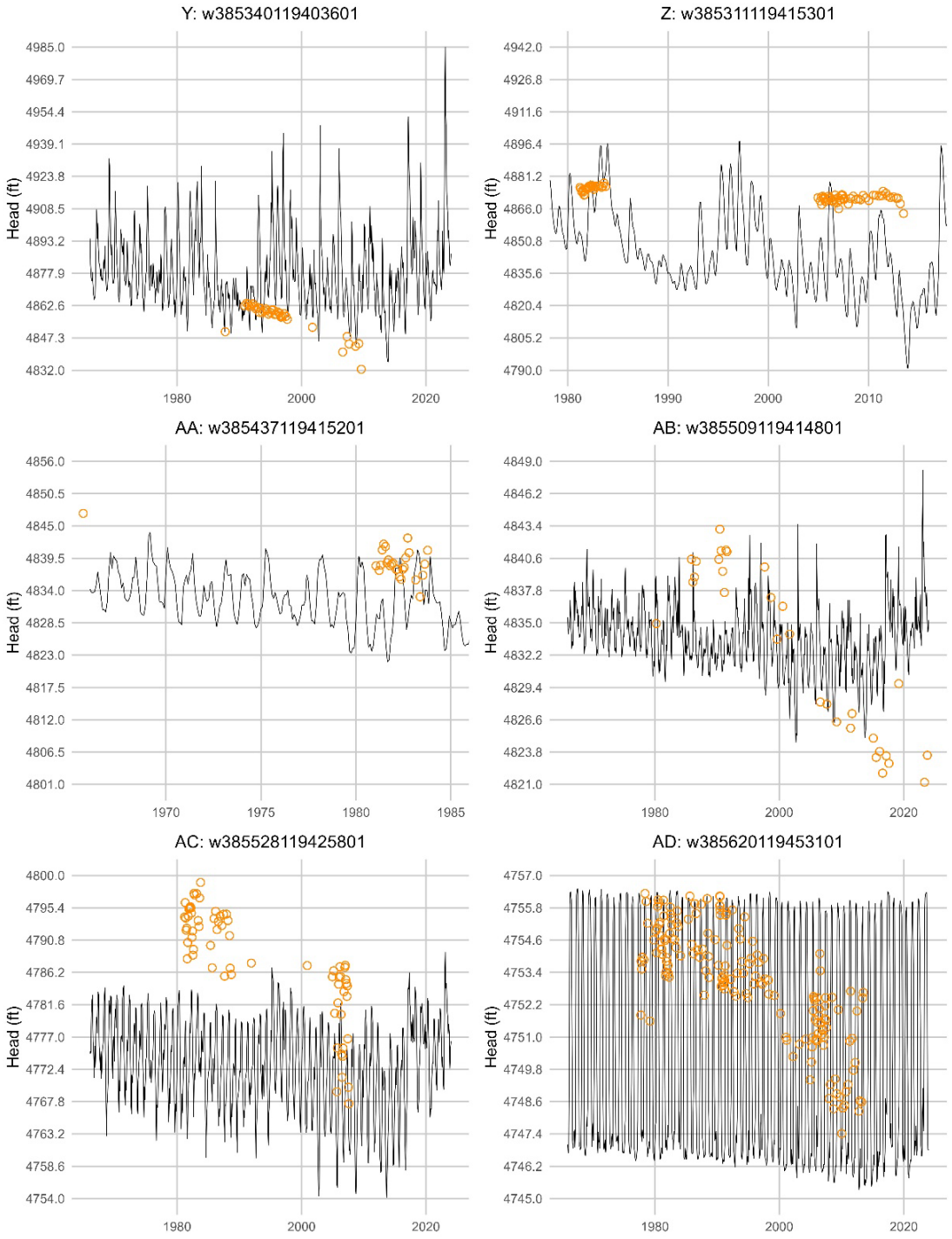

Figure 33Y-AD. Observed heads (orange circles) and simulated heads (black lines) at wells Y-AD for the historical transient model (1965-2023). The title for each plot includes the well letter and ID. Locations of the wells are shown in Figure 28. The *x*-axis varies between plots to show temporal variability during the period of observed heads for each well.

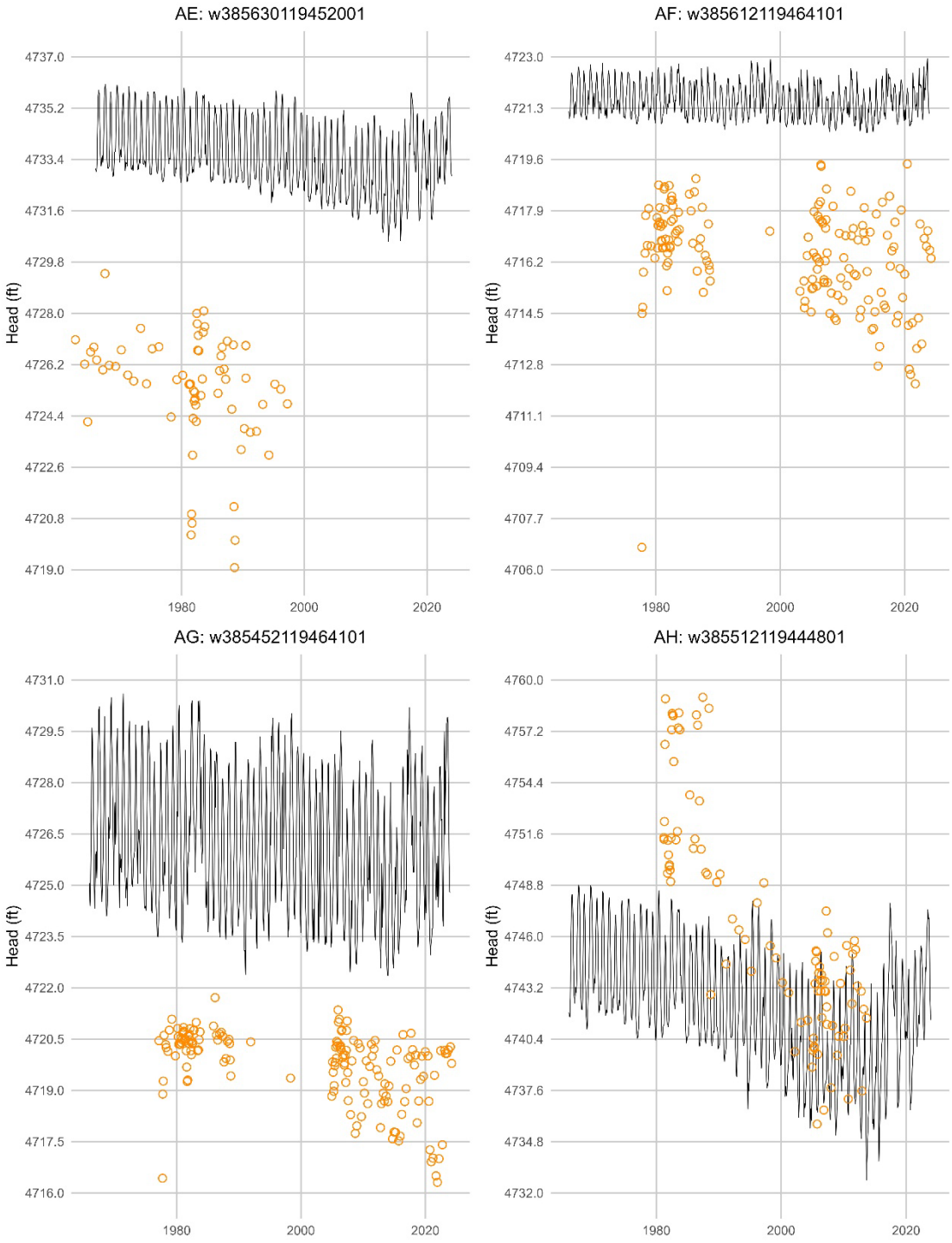

Figure 33AE-AH. Observed heads (orange circles) and simulated heads (black lines) at wells AE-AH for the historical transient model (1965-2023). The title for each plot includes the well letter and ID. Locations of the wells are shown in Figure 28. The *x*-axis varies between plots to show temporal variability during the period of observed heads for each well.

Within Gardnerville Ranchos, observed heads indicate that water levels in the fluvial deposits and river terrace deposits have remained stable or decreased at varying rates over the past several decades. Since 2010 in the West Block, static water levels have shown little to no change in the deep supply wells 5 (D) and 6 (E) and shallow monitoring wells Sweetwater (N), MW1 Bing (O), and MW2 Bing (P). Static water levels at Well 9 (H) show a decreasing trend since 2005. Overall, the simulated heads in the West Block remain stable over the long term. The timing and magnitude of seasonal and interannual changes in water levels in supply wells 6 (E) and 9 (H), and shallow monitoring wells, are captured by the model. Drawdown is greatest in the supply wells during the summer months, when the wells have the greatest monthly pumpage. The magnitude of seasonal fluctuations is generally over-estimated for the Bing wells. However, the timing of seasonal fluctuations is captured overall.

Farther to the west, observed water levels have declined at points Q and R. The simulated head elevations at point Q are greater than the observed heads, but the long-term declining trend of about 1.0 ft/yr (0.3 m/yr) since 1984 is captured by the model. The low frequency of observed heads at point Q may not capture the actual magnitude of seasonal variability. The simulated heads at point R accurately represent the decreasing trend of about 0.3 ft/yr (0.1 m/yr) since 1975. The magnitude of seasonal variability at point R is well represented by the simulated heads. Seasonal variability is associated with increased pumping from domestic wells in warmer months and recharge from the West Fork during the spring. The model also captures the recent increase in water levels after 2020 at point R.

In the Central Block, the static water levels observed show declining trends in deep wells 7 (F) and 8 (G). At Well 7 (F), simulated heads represent long-term and interannual trends. Observed heads show that long-term water levels declined at a rate of approximately 0.03 ft/yr (0.01 m/yr) from 2006 to 2019. The declining trend may have started prior to 2006, as suggested by the observed water level in 1994. In 2023, simulated water levels capture the increased water levels at Well 7 (F) in response to the high annual precipitation. Well 8 (G) shows a decreasing trend of about 0.3 ft/yr (0.1 m/yr) since 2010, during which time simulated heads remain relatively stable. Observed water levels in Well 8 were lower during dry years when the pumping demand was higher for this well and others GRGID supply wells; the simulation captures these interannual changes. A systematic shift in observed static water levels from 2010 to 2011 at Well 8 (G) is likely the result of human interference. Annual pumpage from Well 8 (G) shows a visually discernible decrease since 2015 (due to elevated arsenic levels), resulting in less drawdown. The observed changes over time in pumping water levels at Well 8 are represented by the simulated heads. The simulation captures the timing and magnitude of seasonal variability in the shallow aquifer at MW2 (J) from 2022 to 2023, although the absolute head elevation is overestimated. Water levels at MW2 vary seasonally in response to increased recharge from stream infiltration from the East Fork during the spring and increased pumping from Gardnerville Ranchos wells in the summer/fall.

In the East Block, observed heads in supply wells 1 and 2 show that static and pumping water levels in the leaky-to-confined aquifer have declined steadily since 2004 at a rate of about 2.3 ft/yr (0.7 m/yr). The simulated water levels are relatively stable over this period. The model represents the timing and magnitude of drawdown in supply wells 1 (A) and 2 (B), with the greatest drawdown during summer months when discharge rates are

highest. The seasonal variability since 2022 in shallow monitoring wells MW3 (K), MW5 (L), and MW6 (M) is also well represented, capturing increases from spring recharge (infiltration from East Fork) and declines during the summer when ET is high and pumping from Gardnerville Ranchos is also high. Simulated head elevations are higher than observed elevations in these monitoring wells and in most other shallow monitoring wells in Gardnerville Ranchos. In the Far East Block, the simulated heads do not closely match the magnitude of observed drawdown in Well 4 (C). However, the timing of seasonal fluctuations is accurately characterized.

The model shows that irrigation water infiltrates to the water table in the agricultural field southwest of Gardnerville Ranchos (point S). Three years of observed water levels at point S in the early 1980s show that water levels rose by 26 to 33 ft (8 to 10 m) during the irrigation season in response to agricultural recharge. Three wells are in agricultural fields downgradient of Gardnerville Ranchos (points AF, AG, and AH). Observed heads at points AF and AG show similar temporal trends, with seasonal fluctuations in head of about 3.3 to 4.9 ft (1 to 1.5 m) (controlled primarily by agricultural recharge) and a long-term decreasing trend of 0.03 ft/yr (0.01 m/yr). These trends are well represented at point AG along the Rocky Slough near the confluence with the West Fork Carson River. The simulated heads at point AF, toward the northwest model boundary, remain relatively stable over the long term compared to observed heads. Simulated heads are consistently 3.3 to 4.9 ft (1 to 1.5 m) greater in elevation than observed heads at points AF and AG. At point AH, located on an agricultural land downgradient of GRGID's Well 8 (G) and MW-1 (I), observed heads have declined at about 0.46 ft/yr (0.14 m/yr) since 1981. During the irrigation season, water levels typically rise by 10 to 13 ft (3 to 4 m) at point AH. Simulated heads match the timing and magnitude of head changes from agricultural recharge. The simulated heads show a long-term decreasing trend, but at a lower rate than observed.

Points AA-AE, all located on the east side of the East Fork, show long-term declining trends. While at a low rate (0.1 ft/yr; 0.03 m/yr), water levels in the well in the deep confined aquifer in Minden-Gardnerville (point AE) decreased steadily from 1951 to 1997. The shallow well (point AD) had stable water levels from 1978 to 1991 before declining (0.3 ft/yr; 0.09 m/yr) until 2013. In the shallow well (point AD), observed water levels fluctuate seasonally by about 3.3 ft (1.0 m). Simulated heads at point AD show greater seasonal variability than observed, which likely indicates that the simulated effect of streamflow infiltration from the East Fork is greater than actual streamflow infiltration in this area. The deeper well (point AE) shows seasonal variability of about 6.6 ft (2 m). The simulated heads at point AE capture the seasonal and long-term trends, while overestimating the absolute head elevation. At points AB and AC, simulated heads decline overall, but at a lower rate than observed heads. Seasonal variability is represented in the model at points AB and AC.

Points of observed heads in the community of Ruhenstroth (in the southeast corner of the model domain) have varying long-term trends. In the northern segment of Ruhenstroth, the observed heads at points T, U and Y decreased at rates ranging from 0.3 to 1.7 ft/yr (0.1 to 0.5 m/yr) from the 1980s to the early 2000s. Observed heads in the southern segment of Ruhenstroth at points V, W, and X show periods of stable or increasing trends. Observed heads at point V showed an increasing trend of approximately 0.7 ft/yr (0.2 m/yr) from 1991 to 2005. This is one of the few locations in the model domain that showed a long-term increasing trend over the calibration period. Points W and X are completed at a similar depth

to Point V and showed stable trends from about 1990 to 1996, followed by decreasing trends until at least 1997. Overall, the simulated heads in the southern Ruhenstroth area show long-term decreasing trends at a rate similar to those observed in the north, followed by an increasing trend after 2020. Simulated heads show seasonal fluctuations that are greater in magnitude than observed; the available water level data at several locations in Ruhenstroth are not frequent enough to capture seasonal variability.

3.8.4.2 Aquifer Testing Transient

The aquifer testing transient model is calibrated to high-frequency hydraulic head measurements made during aquifer testing. A description of the aquifer tests conducted during this study are described in detail in Appendix A. In short, six constant-rate aquifer tests were conducted from November 2022 through February 2023. During the tests, one supply well at a time was pumped at a predetermined discharge rate and duration, during which high frequency water level measurements were made in all supply and monitoring wells to monitor for drawdown caused by pumping. In total, there were >215k transient head targets at 16 calibration points. The goal of the aquifer test transient model is to simulate the temporal trends in water levels by refining storage properties in the aquifer extent influenced by pumping from GRGID supply wells. Additionally, fault hydraulic characteristics and CWC values for supply wells were refined. The aquifer test model period is from November 1, 2022, to March 1, 2023, with daily stress periods that are divided into ten time steps with a multiplier of 1.5 to capture rapid water level changes at the start and end of each test. With a multiplier of 1.5, each time step is 50% longer than the previous one.

Calibration statistics for the aquifer test transient are summarized in Table 11. Final calibration of the aquifer test transient model resulted in a mean head residual of -2.6 ft (-0.80 m), a mean absolute head residual of 5.1 ft (1.55 m), and a root mean square head residual of 7.1 ft (2.16 m), equating to an $RMSE_{rel}$ of 2.7% over an observed head range of 263 ft (80 m). Plots of simulated and observed heads for the 16 calibration points are shown in Figure 34. The locations of the calibration points are shown in Figure 32. Like the historical transient model, the plots for GRGID supply wells show simulated heads inside the supply well, while all other plots show the simulated heads in the aquifer at each well. Overall, the timing and magnitude of simulated changes in water levels are close to the observed changes. Simulated water levels in monitoring wells in the unconfined aquifer (MW1-6, Sweetwater, MW1_Bing, MW2_Bing) consistently overestimate. This may be a result of Layer 1 being simulated as confined.

Calibration statistics show that the simulated groundwater levels approximate observed groundwater levels. The model represents background trends during non-pumping conditions, as well as the timing and magnitude of drawdown responses to pumping. The winter of 2022-2023 experienced high precipitation, resulting in increasing trends in observed background water levels at all wells for the duration of the model period. Wells near the East Fork Carson River show the greatest head increase, resulting from streamflow infiltration. Over the model period, observed heads increased by a total of about 33 ft (10 m) in MW-5 (L) and MW-6 (M). These are shallow monitoring wells of the unconfined aquifer that receive recharge primarily from streamflow infiltration. Static water levels increase by about 16.4 ft (5 m) in supply wells 1 (A) and 2 (B), suggesting recharge to the confined aquifer. Well 8 (G) is a deep supply well near the East Fork where static water levels

increased at a lower rate. This may be because Well 8 (G) is farther downstream and because the Central Fault impedes flow and reduces the flux of streamflow infiltration that reaches the well. Simulated background trends match the observed trends in each of these wells.

Moving farther west of the East Fork, recharge from streamflow decreases, so the change in observed heads reduces. The heads in shallow monitoring wells MW2 (J), Sweetwater (N), and MW2 Bing (P) increased by a total of about 5.3 ft (1.6 m). A slope change is observed in early January in all shallow monitoring well hydrographs in the West Block due to increased valley recharge from storms in late December and early January. Wells 5 (D) and 7 (F) are deep wells of the confined aquifer that show the same slope change. In deep supply wells 5 (D), 6 (E), and 9 (H), water levels increased by a total of about 7 to 10 ft (2 to 3 m). The simulated background trends closely match the observed trends described here.

With respect to pumping water levels in GRGID supply wells, simulated heads generally match observed heads. The CWC value was adjusted iteratively between the aquifer testing and historical transient models to reduce residuals in supply wells for short-term changes in pumping (hourly to daily) and seasonal/long-term changes in pumping. Simulated pumping water levels in Wells 1 (A) and 2 (B) represent observed pumping water levels, generally overestimating drawdown by about 10 to 16 ft (3 to 5 m). Simulated pumping water levels in Well 4 (C) underestimate drawdown by >130 ft (>40 m). The extreme drawdown at Well 4 (C) results from low specific capacity (Well 4 produces little water relative to the amount of drawdown; see Table A-2 and discussion of the Well 4 test in the Appendix), which is difficult to simulate with the MNW2 package. At Well 6 (E), simulated pumping water levels over- or underestimate drawdown within about 16 ft (5 m). At Well 8 (G), simulated pumping water levels over- and underestimate drawdown by low magnitudes, whereas Well 9 (H) overestimates drawdown by about 16 ft (5 m).

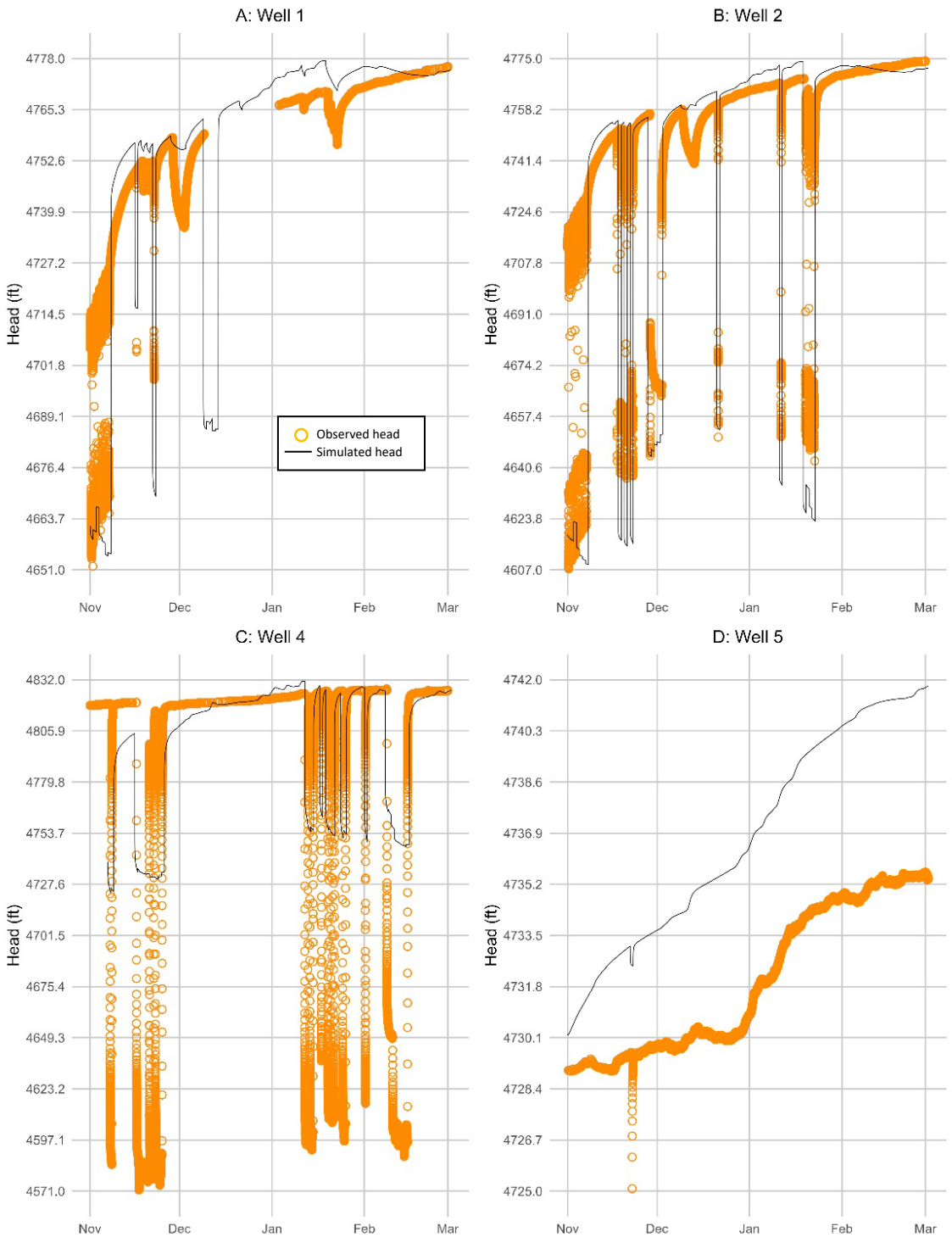

Figure 34A-C. Observed (orange circles) and simulated (black lines) heads at test wells A, B, and C and monitoring well D in Gardnerville Ranchos for the aquifer testing transient model (November 1, 2022, through March 1, 2023). The plots for GRGID test wells A, B, and C show simulated heads in the supply wells, while D shows the simulated heads in the aquifer.

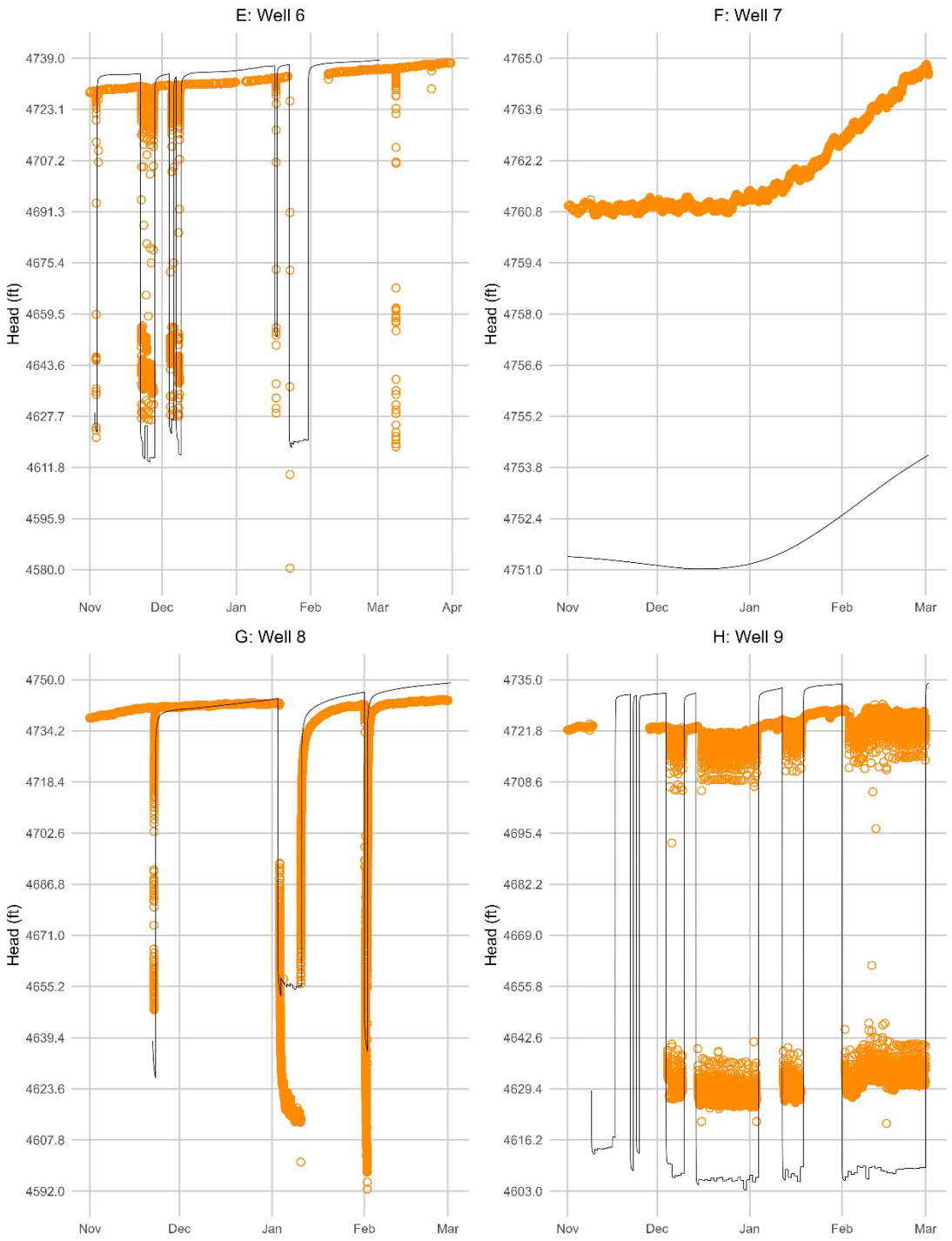

Figure 34E-H. Observed (orange circles) and simulated (black lines) heads at test wells E, G, and H and monitoring well F in Gardnerville Ranchos for the aquifer testing transient model (November 1, 2022, through March 1, 2023). The plots for GRGID test wells E, G, and H show simulated heads in the supply wells, while F shows the simulated heads in the aquifer.

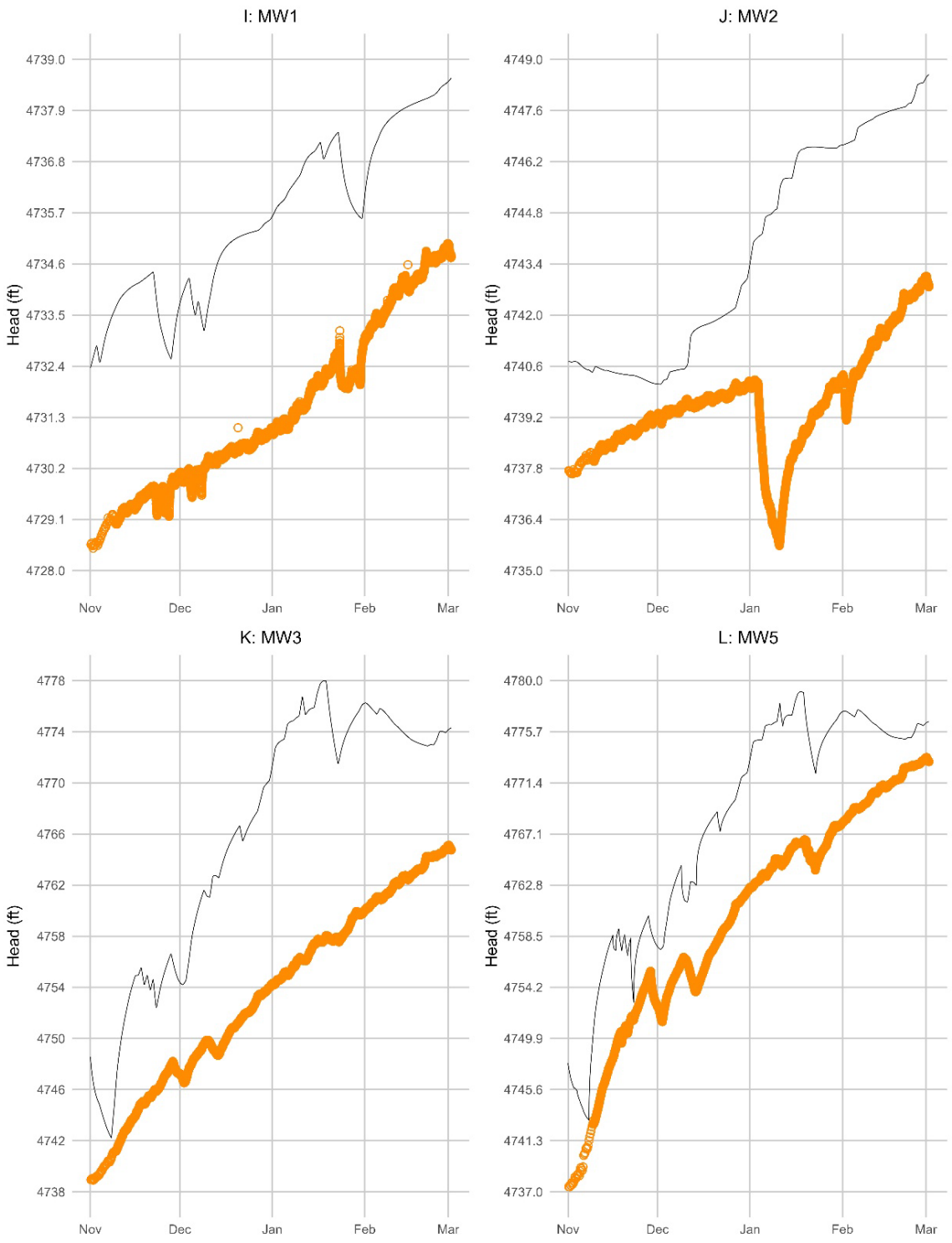

Figure 34I-L. Observed (orange circles) and simulated (black lines) heads at monitoring wells I-L in Gardnerville Ranchos for the aquifer testing transient model (November 1, 2022, through March 1, 2023).

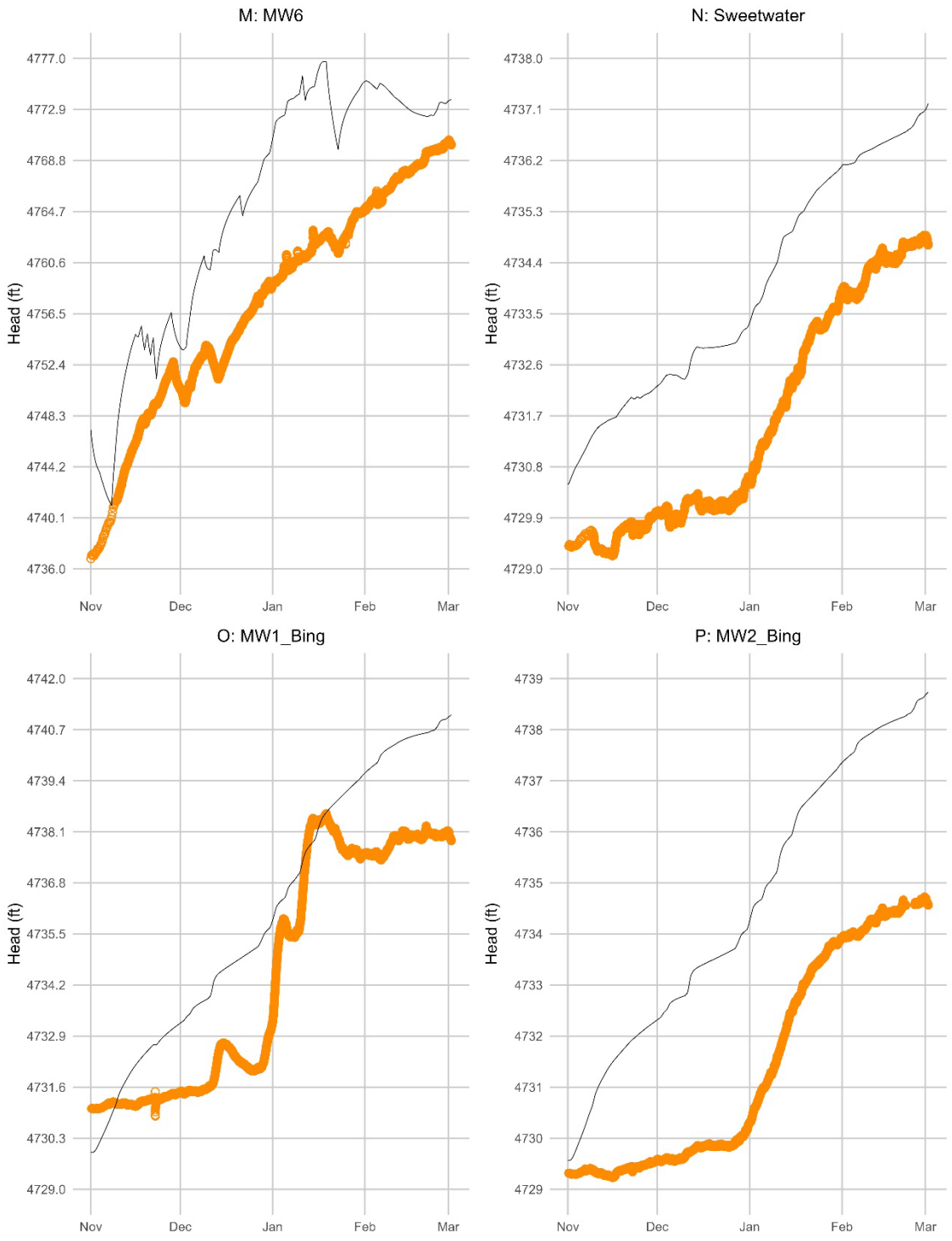

Figure 34M-P. Observed (orange circles) and simulated (black lines) heads at monitoring wells M-P in Gardnerville Ranchos for the aquifer testing transient model (November 1, 2022, through March 1, 2023).

3.8.5 Model Limitations, Assumptions, and Uncertainty

As with all numerical groundwater flow models, the model described here has several limitations, many of which are related to underlying assumptions made during model development. There are also several types of error and sources of uncertainty in the model. For the discussion on model uncertainty, the focus is on three general sources of error that cause simulated heads to be different from observed heads, including: 1) model design error, 2) parameter error, and 3) predictive scenario error. A fourth source of error results from measurement of the observations (water levels). Manual water level measurements made using steel tape or electric tape typically show precision within 0.05 ft. The pressure transducers used to measure hydraulic head during the field campaign of this study have an accuracy of ±0.05%. This source of error is likely less than the others and therefore is not discussed in detail here.

Error associated with model design is rooted in the assumptions of the hydrogeologic system, which entails representing a complex physical system using theoretical mathematical equations. Design error includes the oversimplification of geological layering, distribution of hydrostratigraphic units, and fault structures. The geometry of the aquifer system in this study is based on limited geologic data from boreholes, surface geology maps, and geophysical surveys from past studies.

The spatial discretization of the model grid that represents the hydrogeologic system can result in smooth hydraulic gradients if too coarse or increased computational error if too fine. The model has monthly time steps, which is a higher temporal resolution than some of the available data used to define model boundary conditions. The assumptions made to estimate monthly fluxes may not accurately capture seasonal variations in transient simulations. For example, when monthly pumpage data were not available, annual pumpage at municipal, domestic industrial, and commercial wells was apportioned monthly based on average ratios of monthly-to-annual totals from 2002 to 2023 of Gardnerville Ranchos wells. This approach may overestimate or underestimate pumping during certain months of the year, especially at commercial and industrial wells where there may be less seasonality to pumpage.

The model is limited by sparse information on the timing and location of irrigation pumping prior to 1994. Irrigation wells were assumed to pump at the basin average for an irrigation well based on available historical pumpage data and well logs. The average is likely an overestimate of pumping during wet years, when there is available surface water, and an underestimate during dry years, when there is a heightened need for supplemental pumping. If the point of use of water from an irrigation well overlaps agricultural land with surface water rights, the water removed from the associated irrigation canal (“application rate”) is reduced by half, assuming the remaining irrigation water is from supplemental groundwater.

The model has other limitations related to flow in the irrigation canals. The model does not aim to capture the complex and irregular timing of controlled flows in the canal network, nor the relationship between surface water availability and supplemental pumping for irrigation. There is limited historical data on diversion rates for canals in the model

domain, so the model assumes that canal flows are directly proportional to East Fork flows. Because of these assumptions and associated uncertainty, the model should not be used to simulate or estimate potential changes to irrigation practices.

Agricultural recharge (R_{ag}) and Q_{ret} are difficult to measure directly, so both are estimated using a relationship between measured ET_{ag}, Q_{ret}, and R_{ag}. The ET_{ag} dataset used here only goes back as far as 1985, so there is additional uncertainty associated with the partitioning of applied irrigation water (AR) between ET_{ag}, Q_{ret}, and R_{ag} from 1965 to 1985. Textbook values of ET for phreatophytes and wetland/riparian vegetation were used, adding additional uncertainty to ET applied in the model.

Another source of uncertainty in the model design is the assumption of confined conditions for the unconfined portion of the top layer of the model. The MODFLOW-NWT solver was used; it is designed to handle nonlinearities associated with unconfined aquifers and the drying and rewetting of cells (Niswonger et al., 2011). In an attempt to facilitate numerical convergence, the vertical grid resolution was adjusted to capture sharp vertical gradients near the water table and rewetting parameters were modified. However, the model failed to converge until the top layer was switched to confined. Specific storage is generally several orders of magnitude smaller than specific yield, so the calibrated specific storage values for Layer 1 are high to mimic the volume of water released during drawdown in an unconfined system. The calibrated specific storage values for Layer 1 are therefore only used to approximate the volumetric response that is typically governed by specific yield in unconfined aquifers.

The model is limited by the lack of information on the timing and location of mountain block recharge. The largest errors in absolute head in the model are along the southern model boundary, which may be a result of the distribution and rates of mountain block recharge. The initial rates were assigned by rescaling values from Glancy and Katzer (1975) for three distinct contributing areas. The calibrated rates were less than the initial estimates. This discrepancy reflects the uncertainty in mountain block recharge values. Quantifying the error associated with model design can be difficult and time-intensive. One approach to quantifying model design uncertainty is through running models of alternative design. However, this approach was beyond the scope of the current study due to limitations of time and computational capacity.

The second source of error is related to the values of hydraulic properties (parameters) of the aquifer system. The parameter error reflects uncertainty in the estimated parameter values and in their distribution in the model domain. To reduce uncertainty, hydraulic conductivity (transmissivity) and storage parameters were estimated independently through aquifer testing. However, there is uncertainty associated with the assumptions made during the analysis of aquifer testing data. Additionally, results of aquifer tests conducted during this study and past single-well tests were used to make inferences of hydraulic properties in segments of the aquifer outside of tested areas. The model results, therefore, are most reliable in the aquifer beneath Gardnerville Ranchos.

Parameter error in the Gardnerville Ranchos model is assessed and reduced through model calibration. Through the automated calibration PEST algorithm, parameter sensitivities are calculated to identify parameters that exert the greatest control on the calibration to head observations. Parameter sensitivity analysis suggests that there are two

major components that exert high control on calibration: 1) hydraulic properties of fluvial and alluvial deposits at the base of the Pine Nut Mountains along the northeastern model boundary and 2) the hydraulic characteristic of the West Fault. The uncertainty of parameter values associated with these hydrogeologic features are likely to affect model results. There is little information available concerning the hydraulic conductivity and specific storage of the alluvial and fluvial deposits along the eastern portion of the model domain. This information is critical because the hydraulic properties of these units control the hydraulic gradients that drive flow through these sediments. The GHB along the northeast model boundary also controls inflows to the model domain through the alluvial deposits, but the conductance parameter for the GHB had a low sensitivity during model calibration. The conductance term for the northeast GHB was calibrated automatically through PEST to match observed heads and adjusted manually to match horizontal hydraulic gradients from the regional groundwater flow model by Kitlasten et al. (2021).

The hydraulic characteristic of the West Fault is another highly sensitive parameter and is well informed by the head observations. The West Fault plays an important role in controlling groundwater flow patterns because it extends through much of the model domain and is perpendicular to the groundwater flow paths. The West Fault controls east-to-west flow in the river terrace deposits beneath Gardnerville Ranchos and in the fluvial deposits north of Gardnerville Ranchos.

The model is also limited by the lack of streamflow data within the model domain for calibration purposes regarding where the rivers and canals in the model are gaining or losing flow. Streambed conductance was calibrated to fluxes based on infiltration rates estimated in previous studies specific to the study area (see “Streamflow Routing and Infiltration”). This means that the model has limitations in its use in making future predictions in fluxes to and from the rivers and irrigation canals.

In addition to the uncertainty associated with model design and parameter error, there is uncertainty associated with the specification of future conditions used in the predictive model. To account for uncertainty associated with future climate and pumping conditions, a “scenario modeling” approach is used in which a range of future boundary conditions that might occur are estimated and represented as various predictive scenarios. A goal of scenario modeling is to produce an ensemble of results that define a representative envelope of uncertainty around the forecast (Anderson et al., 2015). See Section 3.9 for additional discussion on the pumping and climate considerations, predictive scenario parameters, and predictive results. It is difficult to assess whether one scenario is more likely to occur than another, so results for several predictive scenarios are reported to show a range of potential changes to groundwater levels.

The predictive model has monthly periods, during which simulated pumping rates, and all other aquifer stresses, are constant. Therefore, the model assumes that, to meet the monthly demand of each well, each well’s pumping rate is equal to the monthly average for that well. This is a model limitation because during real-world operations, a single supply well does not operate continuously for an entire month; rather, the pump is turned on for a period (with a discharge rate that often exceeds the monthly average) and is then turned off for a period. The predictive model also does not account for potential future declines in well efficiencies that may result from the physical and/or chemical buildup of materials in the well screens.

3.9 Predictive Simulations

The calibrated model is applied in 20-year predictive simulations from 2024 to 2043. The goals of the predictive simulations are to 1) predict a range of potential changes in groundwater levels from projected future changes in atmospheric temperature and groundwater pumping and 2) assess whether the existing GRGID supply well network is expected to meet future demands under these changes. The 20-year predictive simulation is based on the calibrated historical transient model and is divided into monthly stress periods to simulate monthly changes in stresses to the aquifer.

The predictive simulations consider climate scenarios and streamflow consistent with Kitlasten et al. (2021) and water demand scenarios from the Gardnerville Ranchos Water Master Plan (Lumos, 2024). Recall that Kitlasten et al. (2021) evaluated the effects of projected changes in precipitation and temperature on streamflow timing, magnitude, and groundwater recharge, showing that earlier snowmelt results in less surface water availability during the growing season and greater groundwater reliance for agriculture.

A range of potential changes to the groundwater system is estimated by varying future monthly pumping rates and stream inflows. Future pumping rates are estimated based on projected population growth for Gardnerville Ranchos (Lumos, 2024). Past studies show that the timing and flux of streamflow in the East and West Forks are expected to change with temperature. Streamflow infiltration is the largest inflow to the model domain and, therefore, the predictive model accounts for a range of potential streamflow changes (Kitlasten et al., 2021).

3.9.1 Pumping Considerations and Inputs

To account for the uncertainty associated with the future increases in pumping, three groundwater pumping scenarios are considered:

1. **Base Case Pumping Scenario ("0% increase" scenario):** The base-case model assumes that annual and monthly pumping totals for the duration of the predictive period are equal to the measured annual and monthly averages for the years 2018 to 2023. Data from 2018 to 2023 were used to establish the base-case pumping scenario because 2018 was the first year that the GRGID service area was fully metered, marking the start of a "new normal" for groundwater pumping in Gardnerville Ranchos. Throughout the simulated period, monthly pumping rates are held constant at the normalized average monthly rates from 2018 to 2023. The base-case model represents the "best-case" future pumping scenario because it assumes a 0% annual increase in pumping relative to the 2018-2023 average.
2. **1.5% Annual Pumping Increase ("1.5% increase" scenario):** This scenario is considered the upper bound, or "worst-case scenario," of potential future groundwater pumping. The timing of future development in Gardnerville Ranchos is unknown, but a 1.5% annual growth rate is assumed to be a conservative (high) estimate (Lumos, 2024). This scenario assumes a 1:1 relation between population growth and groundwater pumping increase. In other words, a 1.5% annual increase in population equates to a 1.5% annual increase in pumping. As such,

this scenario does not consider water conservation measures (i.e., additional water meter installations, rate structure changes, zeroscaping and/or xeriscaping, turf-buy-back programs, etc.) that would reduce the future per capita water demand.

3. **0.2% Annual Pumping Increase ("0.2% increase" scenario):** This scenario represents a more likely projection of future groundwater pumping. An annual pumping increase of 0.2% is expected to be a reasonable estimate based on expected population growth (Lumos, 2024) and planned conservation measures that would reduce the per capita water demand (G. Reed and J. Lesperance, personal communication, January 30, 2024).

Annual pumping totals from 2018 to 2023 are shown in Figure 35. Annual pumping totals vary depending on several natural and anthropogenic factors. For example, the annual pumping was high in 2020 when demand increased during the COVID-19 pandemic (G. Reed, personal communication, April 1, 2023). Annual pumping was low in 2023 following a season of historically great snow accumulation during the winter of 2022-2023.

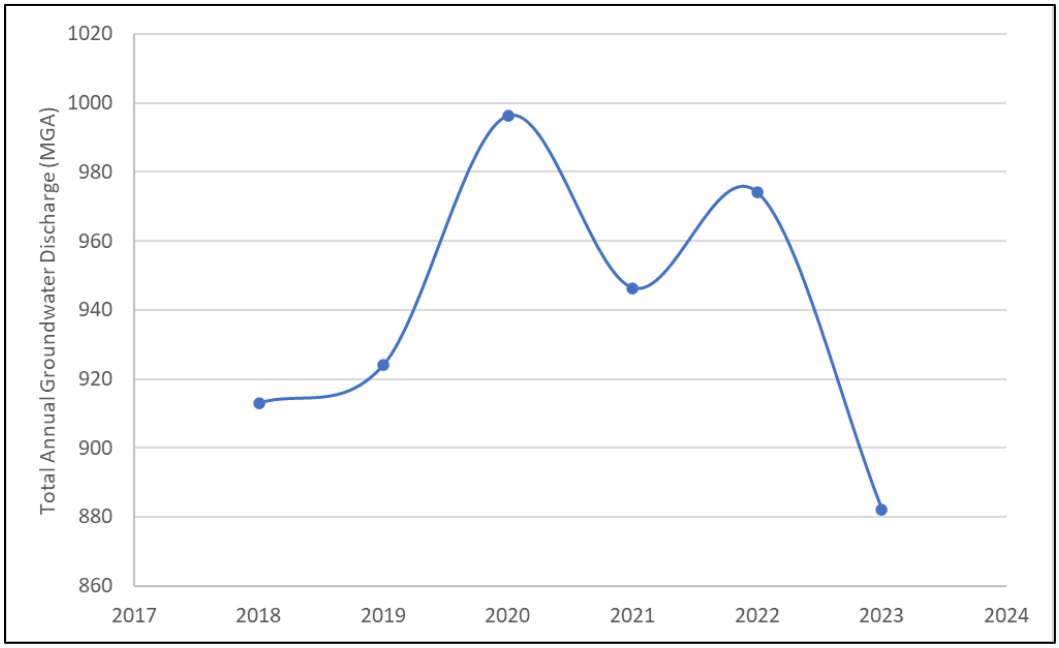

Figure 35. Annual groundwater pumping totals from Gardnerville Ranchos supply wells between 2018 and 2023.

Simulated annual pumping totals for the period 2024-2043 under the three different pumping scenarios are shown in Figure 36. Each scenario assumes that the total annual pumping at the start of the predictive period (2024) is 939 million gallons (MGA) (2,880 af/yr [3.6 million m^3/yr]), which is the average annual total from 2018 to 2023. By the end of the predictive period, total annual pumping equals 939 MGA (2,880 af/yr [3.6 million m^3/yr]) under the base-case scenario, 978 MGA (3,000 af/yr [3.7 million m^3/yr]) under the 0.2% increase scenario, and 1,265 MGA (3,880 af/yr [4.8 million m^3/yr]) under the 1.5% increase scenario.

Targeted monthly pumping rates (Q_{des}) are calculated for the monthly stress periods. As described previously, the specified flow rate for an MNW2 well is the maximum desired, or "target", flow rate (Q_{des}). During the predictive simulations, the Q_{des} may not be reached during a given stress period if the simulated water level in a supply well drops below the specified elevation threshold (h_{lim}) or if flow from the aquifer to the well becomes limited by the cell-to-well conductance. If either of these conditions occurs, then the simulated flow rate (Q_{sim}) is automatically reduced to a rate less than Q_{des}. These pumping constraints are applied on a well-by-well basis for the predictive model to assess whether each GRGID supply well can meet its monthly Q_{des} throughout the predictive period. The input parameters for MNW2 wells for the predictive model are the same as for the historical transient model (Table 8).

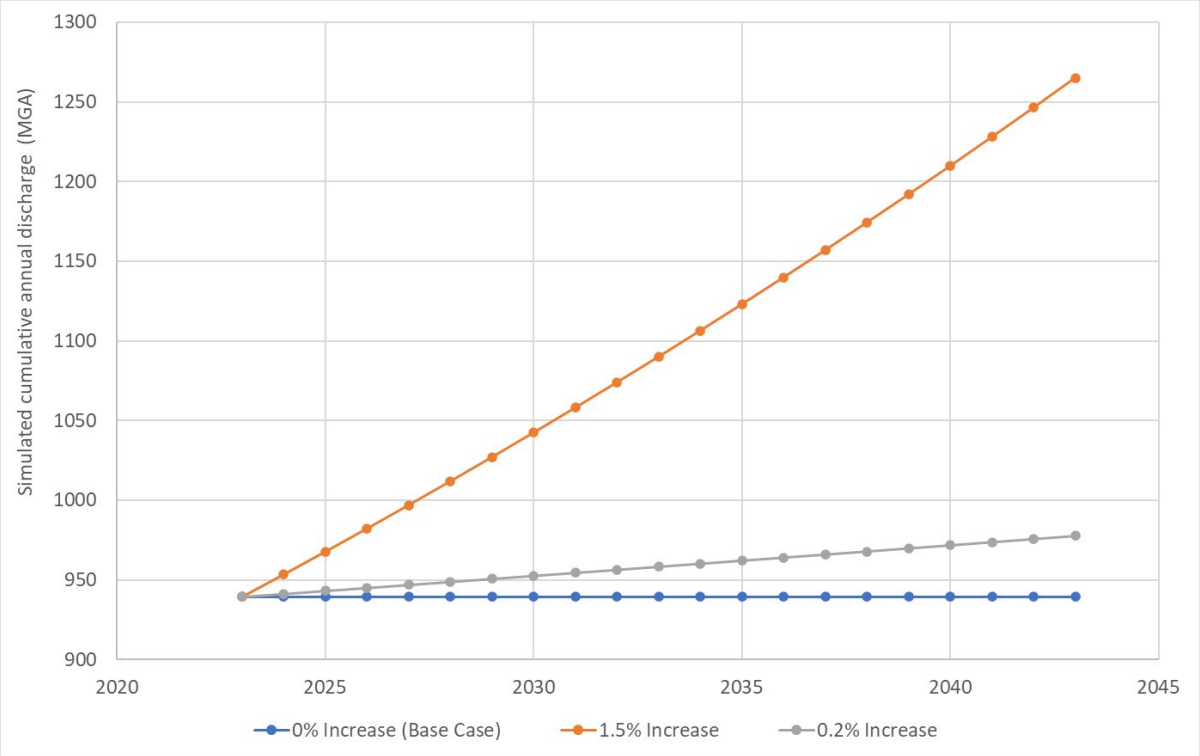

Figure 36. Simulated cumulative annual pumping for Gardnerville Ranchos supply wells for the years 2023-2043 under three predictive model scenarios, including 0% (base-case), 0.2%, and 1.5%.

Annual pumping totals are partitioned into monthly Q_{des} inputs using measured monthly pumping totals from 2018 to 2023. For each month of the year, the average monthly pumping total from 2018 to 2023 was normalized by the average total annual pumping (939 MGA [2,880 af/yr (3.6 million m^3/yr)]) over this time frame. The Q_{des} is the same for the first year (2024) of each predictive simulation. For the base-case model, the monthly Q_{des} is held constant for the duration of the predictive period. Monthly Q_{des} increases linearly for the 0.2% and 1.5% increase scenarios.

Monthly Q_{des} is partitioned between GRGID wells based on the average observed pumping distribution between wells from 2018 to 2023. The Q_{des} inputs by well for the 0.2% and 1.5% scenarios are shown in Figures 37 and 38. As illustrated, monthly Q_{des} is greatest for each well during the high-demand summer months. Wells 1 and 2 contribute the greatest volume during the summer months. During the low demand months of fall and winter, pumping is mostly split between Wells 1, 4, 6, and 9. As shown in Figures 37 and 38, Well 5 is not used in any of the predictive scenarios and Well 8 continues to be used at a reduced capacity (as it was from 2018 to 2023).

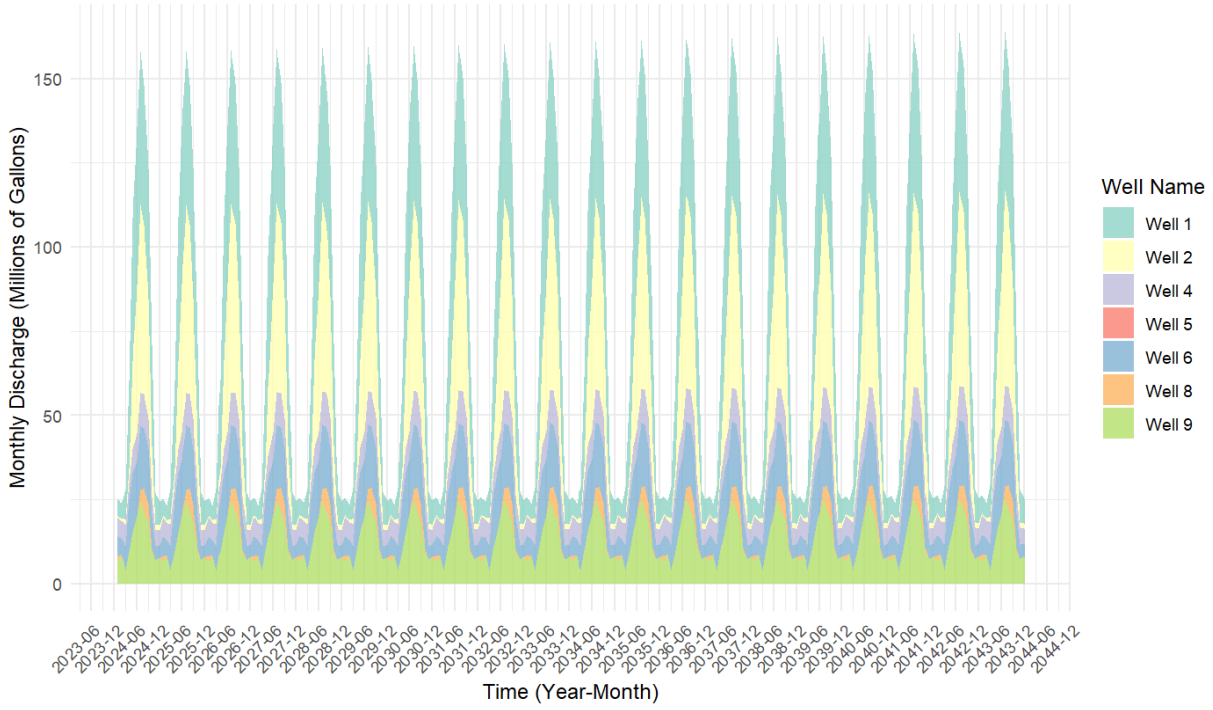

Figure 37. Targeted total monthly discharge (Q_{des}) by well for the 0.2% annual pumping increase predictive model scenario.

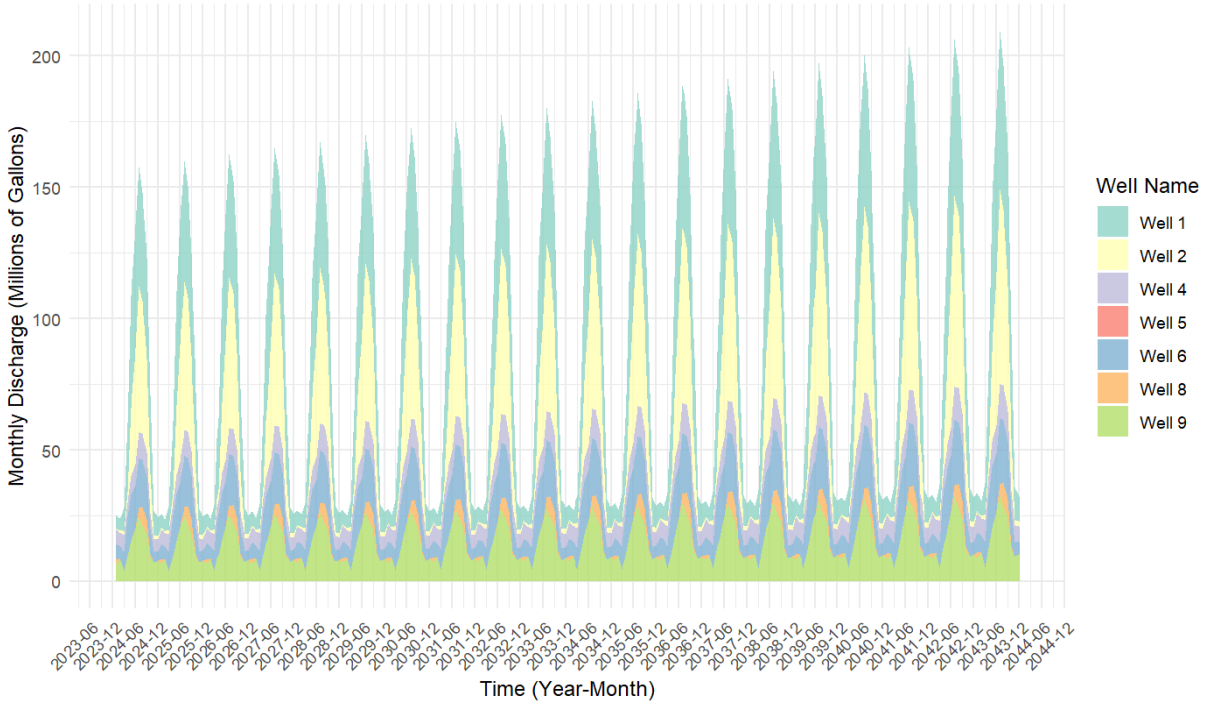

Figure 38. Targeted total monthly discharge (Q_{des}) by well for the 1.5% annual pumping increase predictive model scenario.

3.9.2 Climate Considerations and Streamflow Inputs

To account for uncertainty associated with future changes in atmospheric temperatures, future monthly streamflows are estimated for a range of projected temperature increases, including total increases of 0°F, 2°F, and 4°F (about 0°C, 1°C, and 2°C, respectively) above average by 2043. Temperatures are increased linearly over the 20-year period at rates of 0°F/yr (0°C/yr), 0.1°F/yr (0.05°C/yr), and 0.2°F/yr (0.1°C/yr), respectively. Understanding the monthly variations in streamflow trends is critical for managing water resources, particularly in snowmelt-fed systems like the East Fork and West Fork Carson River. These streams are heavily influenced by seasonal snow accumulation and melting, making them particularly sensitive to shifts in climate and temperature patterns. Estimating future streamflow based on historical trends provides insight into long-term hydrological shifts, helping resource managers make informed decisions regarding water allocation and ecosystem sustainability.

There is consensus between climate models that temperatures are expected to increase in the Sierra Nevada, particularly toward the end of the 21st century. Climate models by He et al. (2018) predict annual near-surface (measured approximately two meters above the ground) temperatures in the northern Sierra Nevada Region (or "North Lahontan Region") to increase by as much as 9°F (5°C) by the end of the 21st century. With projected increases in temperature due to climate change, snowmelt dynamics are expected to change, influencing not only the timing of peak flows but also the overall magnitude of runoff throughout the year. Earlier snowmelt could result in reduced water availability during the late summer and fall, increasing the risk of drought and placing additional strain on groundwater resources.

Projections by He et al. (2018) suggest that, when compared to historical precipitation amounts, annual average precipitation is expected to increase slightly for the Sierra Nevada region, by up to 6.6% by the mid-21st century and 10.3% by the late century. With respect to the regional water balance, the projected increase in precipitation is offset by the impact of heightened evaporation (He et al., 2018). Kirtman et al. (2013), on the other hand, projected decreases in future precipitation with warming. Because of a lack of concensus regarding changes in precipitation totals with future warming, and because changes in precipitation and ET may offset, precipitation and ET rates are not adjusted for the predictive scenarios.

Streamflow inputs for the predictive model are established through integration of trend analysis with climate projections. By accounting for changes in streamflow with temperature, the predictive model can be better equipped to incorporate seasonal flow variations, improving its ability to simulate surface water-groundwater interactions under future climate conditions. Additionally, understanding how historical trends translate into future streamflow projections allows for the development of proactive adaptation strategies for GRGID and other water managers in the Carson River Basin.

To evaluate streamflow trends in the East Fork and West Fork, historical daily flow data from 1995 to 2023 (focusing on this period to extract recent climatic trends) were analyzed for both streams. The analysis focused on capturing seasonal variations and long-term changes by computing the median daily flow values for each of the twelve months across multiple water years. This approach provided a clearer representation of typical monthly flow patterns while reducing the influence of short-term fluctuations and extreme events.

To assess trends over different periods, a moving window technique was applied, allowing for a dynamic evaluation of changes over time. Each moving window covered a time span of N years, where N ranged between 10 and 20 years, ensuring a balance between capturing long-term patterns and maintaining statistical reliability. The first window, spanning 20 years, covered 1995-2014, followed by subsequent windows shifting forward by one year each (e.g., 1996-2015, 1997-2016, etc.). The tenth window (2004-2023) marked the last complete 20-year window, after which the available data limited subsequent windows to progressively shorter durations. The final, twentieth window, covering 2014-2023, spanned only 10 years.

By employing this method, the analysis accounted for interannual variability while revealing underlying trends in seasonal streamflow behavior. The gradual shift in window length ensured that observed trends were not overly influenced by short-term anomalies, providing a more reliable assessment of hydrological changes in both streams. This moving-window approach helps reveal how trends evolve over time, rather than relying on just one fixed time period. By sliding the window forward year by year, it captures shifts or emerging patterns that might otherwise be missed.

For each of the twelve months for both streams, linear trend lines were fitted through the moving-window median flow values over time, allowing for a systematic evaluation of increasing or decreasing streamflow trends. The analysis was conducted separately for the East Fork and the West Fork. To quantify the uncertainty in trend estimates, 95% confidence bounds were also plotted alongside the trend lines (Figure 39 gives an example of April and June trendlines).

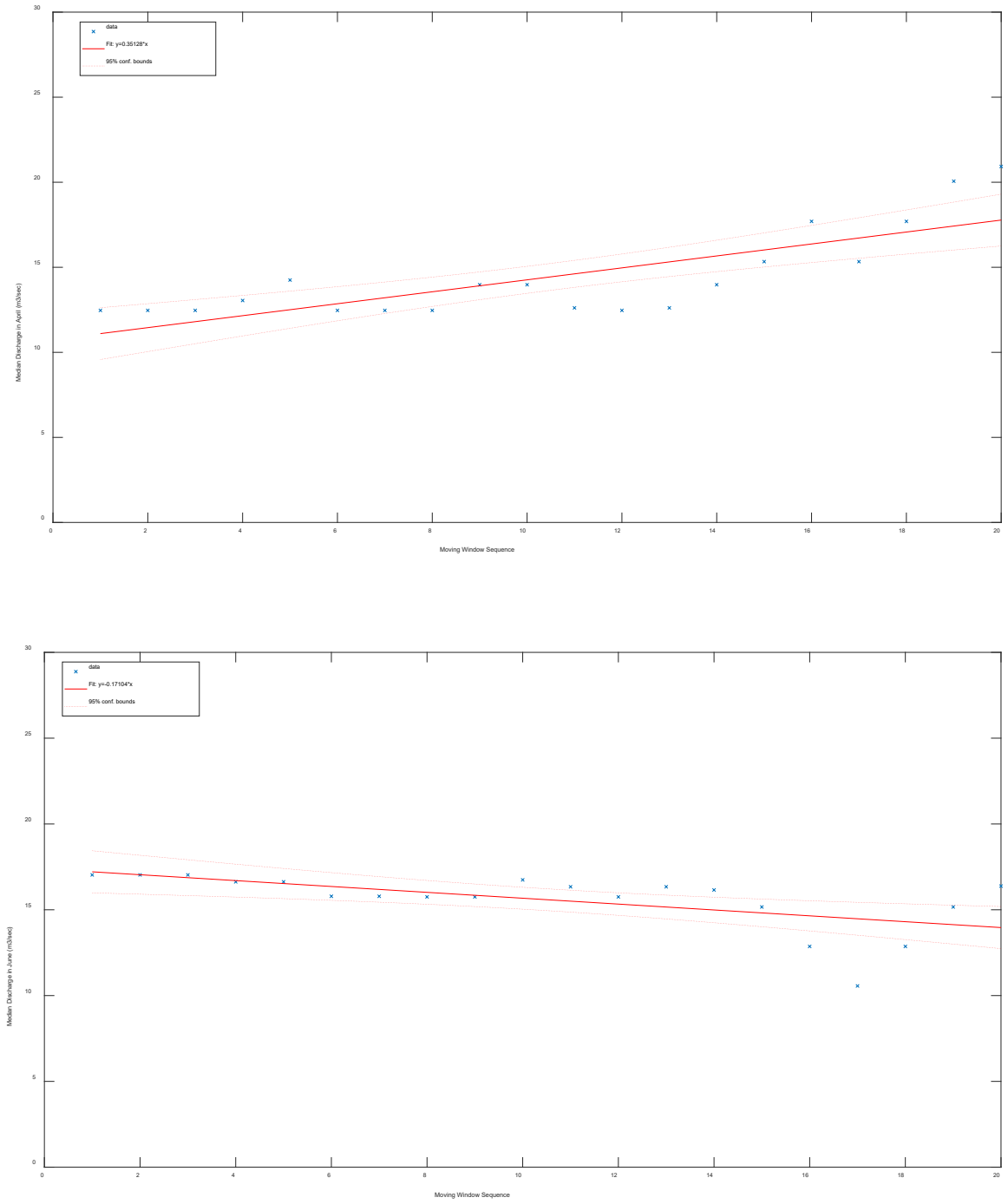

Figure 39. Trend of median streamflow discharge for the East Fork for the months of April (top) and June (bottom) as a function of the sequence of moving windows (window is at least 10 years and no more than 20 years). The first window covers a 20-year period of 1995-2014; the last window covers a 10-year period of 2014-2023.

The results indicated dramatic positive slopes in early spring (April), suggesting an increasing trend in stream-flows during this period. Conversely, significant negative slopes were observed in late spring and early summer (May and June), indicating decreasing stream-flow trends, potentially due to earlier snowmelt and higher ET rates driven by rising temperatures. Winter months (December through March) exhibited smaller yet consistent positive trends, implying a potential increase in winter base flows, possibly due to shifts in precipitation patterns favoring more rainfall over snowfall and mid-winter snowmelt events.

Using the slopes obtained from the trend analysis (summarized in Table 13), future streamflow projections for the period 2024-2043 were generated. The projections were based on simulated daily flow values by Kitlasten et al. (2021) for both the East Fork and the West Fork. Three different scenarios were considered:

1. Base Case: The observed historical trends were directly applied to Kitlasten's simulated historical streamflow values to project future streamflow values.
2. +2°F Temperature Scenario: The trendline slopes were applied to Kitlasten's simulated streamflow values under a temperature increase of +2°F (1°C) by the end of the 20-year predictive period (+0.1°F/yr [+0.06°C/yr]) to assess how moderate warming might impact streamflow values.
3. +4°F Temperature Scenario: The trendline slopes were applied to Kitlasten's simulated streamflow values under a temperature increase +4°F (2°C) by the end of the 20-year predictive period (+0.2°F/yr [+0.11°C/yr]) to assess how greater warming conditions might impact streamflow values.

Table 13. Trendline slopes (percentage change over a period of 20 years) for all twelve months for the East Fork and West Fork.

Month	East Fork, percent change in flow	West Fork, percent change in flow
Jan	1.553	0.185
Feb	5.269	0.811
Mar	0.290	0.387
Apr	35.128	12.592
May	-15.718	-9.352
Jun	-17.104	-4.361
Jul	-2.885	-0.457
Aug	-2.697	-0.166
Sep	-0.575	-0.082
Oct	-1.901	-0.794
Nov	-2.855	-0.615
Dec	4.125	-0.238

One challenge in projecting future streamflows was ensuring that zero or negative streamflow values did not arise due to downward trends in some months. To address this, a lower threshold was applied to the projections. Specifically, if the projected daily flow for a given month fell below zero, it was adjusted to match the minimum historical daily flow observed in that month. This adjustment ensured that the streams retained positive net flow, preserving ecological integrity, maintaining downstream water availability, and avoiding numerical instabilities in the model. Figure 40 shows side-by-side plots of historical flow and projected flow for a few representative cases.

The analysis of historical streamflow trends in the East Fork and West Fork highlights the seasonal shifts occurring in response to climate variability. The increasing trends in early spring and winter suggest that snowmelt timing is shifting to occur earlier, while decreasing trends in late spring and early summer indicate potential reductions in magnitude of peak flows. Future projections based on historical trends and temperature scenarios reinforce the importance of adaptive water management strategies. By leveraging historical data, trend analysis, and climate-informed projections, this analysis provides insights into the evolving hydrology of the East Fork and West Fork streams and underscores the need for seasonal and climate-aware adjustments to groundwater models to improve predictive capabilities for adaptive management.

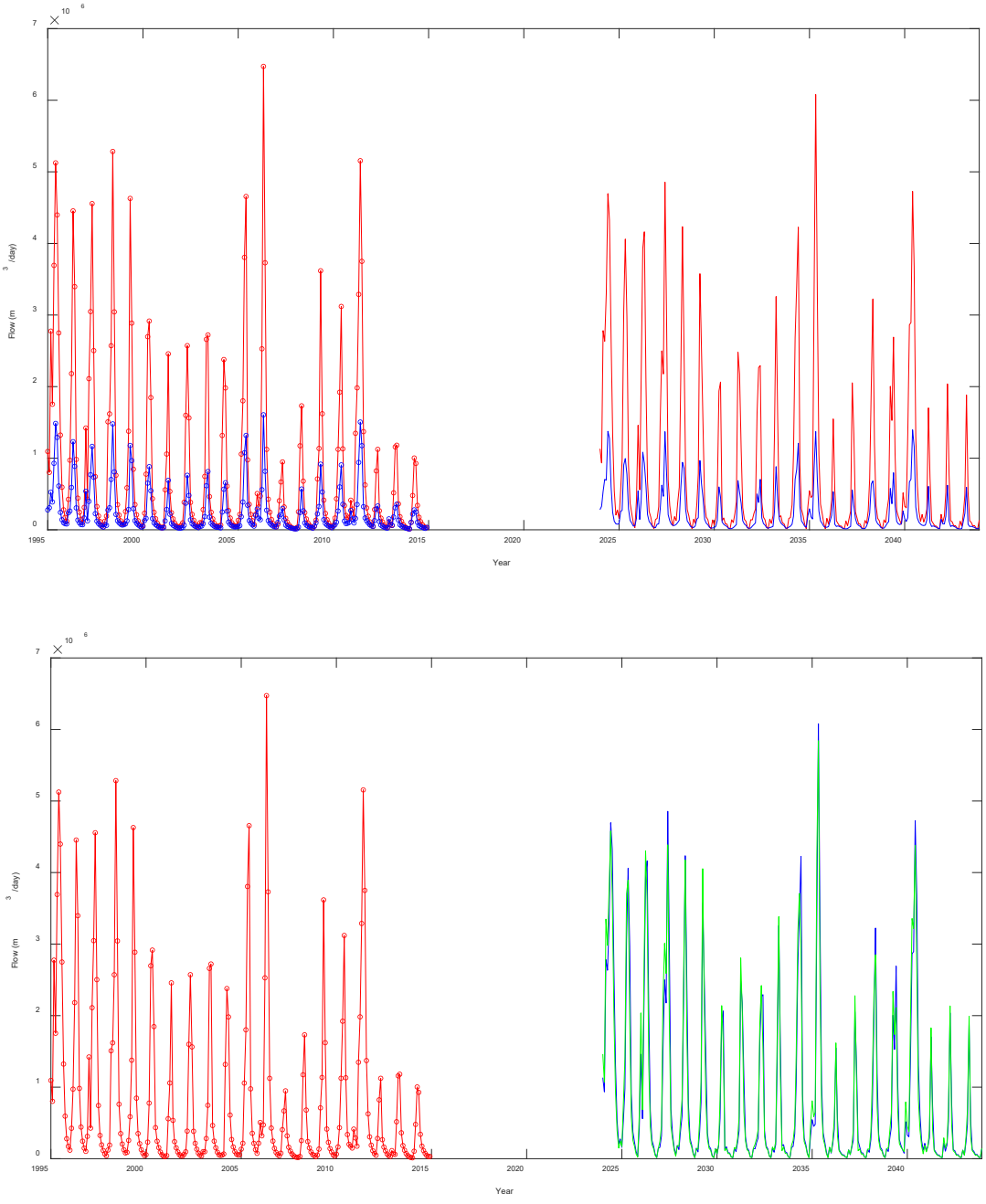

Figure 40. Historical (Kitlasten et al., 2021; 1995-2014) and projected flow (2024-2043) for some representative cases. Top: Historical and base case projected flows for the East Fork (red) and West Fork (blue). Bottom: East Fork historical flows (red), East Fork base-case projected flows (blue), and projected flows in the East Fork under a +4°F (2°C) by the end of the 20-year predictive period (+0.2°F/yr [+0.11°C/yr]) (green). Of note is the difference in the values of the peaks between the base case (blue) and +4°F (+2.2°C) (green) flows.

3.9.3 Predictive Scenarios

The predictive models are developed using a "scenario modeling" approach, in which a base-case model and several hypothetical models are run to predict a range of potential future changes to the groundwater system. A goal of scenario modeling is to produce an ensemble of results that define a representative envelope of uncertainty around the forecast (Anderson et al., 2015). In other words, scenario modeling creates a range of possible outcomes. Each predictive scenario has distinct pumping rates and/or streamflows. The hypothetical model runs are identical to the base-case run, except for projected changes in streamflow (associated with temperature change) and/or pumping from existing GRGID supply wells. A summary of each predictive scenario is provided as Table 14.

Table 14. Summary of predictive scenarios.

Simulation No.	Scenario	Simulation Name	Annual Temperature Increase from Average (°F/yr)	Annual Increase in Total Pumping from GRGID Wells (%/yr)
1	Base Case	BC	0	0
2	Climate	C2F	0.1	0
3		C4F	0.2	0
4	Pumping 1	P1a	0	1.5
5		P1b	0.1	1.5
6		P1c	0.2	1.5
7	Pumping 2	P2a	0	0.2
8		P2b	0.1	0.2
9		P2c	0.2	0.2

The goal of the base-case model is to determine the effects to groundwater levels under "base-case" pumping and climate scenarios, as presented in the preceding sections. The base-case model assumes that monthly pumping rates from GRGID supply wells are equal to the monthly averages from 2018 to 2023 throughout the predictive period and that streamflows are equal to the observed monthly values from 1995 to 2015. For non-GRGID wells, monthly pumping rates are equal to historical averages as defined in the 1965-2023 historical transient pumping record. Historical pumping varied widely in most non-GRGID wells, so average historical pumping values were considered a more representative estimate of future pumping than any single year or set of years. For example, pumping rates from irrigation wells vary between wet and dry years. All other water budget components are set equal to the historical averages.

The hypothetical models include "climate scenarios" that aim to isolate the effect of increasing atmospheric temperatures on future groundwater levels and "pumping scenarios" that aim to 1) isolate the effects of increased pumping on groundwater levels and 2) assess the combined effects of increased pumping and temperature on groundwater levels (Table 14). To account for uncertainty associated with the magnitude of future temperature and pumping increases, predictive models consider temperature increases of +0.1 and +0.2°F/yr (+0.06 and 0.11°C/yr) above average and annual pumping increases of +0.2% and +1.5% for GRGID supply wells. The difference in groundwater levels between the base case and each hypothetical model is the predictive change to groundwater levels that can be attributed to the changes in pumping and/or streamflow in the model domain for the respective scenario.

Climate scenarios C2F and C4F include projected stream inflows to the model domain under temperature increases of +0.1 and +0.2°F/yr (+0.06 and 0.11°C/yr) from average, respectively (equates to +2 and +4°F [+1.1 and 2.2°C] above average, respectively, by the end of the predictive period). During both climate scenarios, monthly pumping rates for GRGID supply wells are equal to the monthly averages from 2018 to 2023 for the duration of the predictive period (annual increase = 0%) and non-GRGID well pumping rates are held at historical averages.

Pumping scenario 1 (P1) includes a projected pumping increase of 1.5% annually for the duration of the predictive period for GRGID wells. For pumping scenario 1, simulations P1a, P1b, and P1c incorporate sequential increases in temperature above average, including +0, +0.1, and +0.2°F/yr (+0, +0.06, and 0.11°C/yr), respectively. Pumping scenario 2 (P2) includes a projected pumping increase of 0.2% annually, with +0, +0.1, and +0.2°F/yr (+0, +0.06, and 0.11°C/yr) temperature increases above average for simulations P2a, P2b, and P2c, respectively. All non-GRGID wells were pumped at their historical mean rates during each simulation in pumping scenarios P1 and P2.

The pumping wells included in the predictive models are the same as the pumping wells in 2023 at the end of the historical transient simulation. For GRGID pumping wells, Q_{sim} is reduced automatically in the model if the h_{well} drops below h_{lim} to maintain water levels that are above h_{lim}. Aside from changes to streamflow, all other water budget components (Table 10) are held constant at historical averages.

3.9.4 Predictive Results – Spatial Distribution of Head Changes

This section focuses on results related to predictive simulation goal 1 (to predict the range of potential changes in groundwater levels from projected future changes in atmospheric temperature and groundwater pumping). The results of the base-case model are presented first (Figure 41). Results of all other predictive simulations are then presented in terms of the head difference between the base-case scenario and each simulation for the specified month. The spatial distribution of predicted head decline for the months of May and September after 1, 10, and 20 years for each predictive simulation are shown in Figures 42-49. In the predictive maps, shades of orange (positive values) indicate areas where the simulated head is lower (dryer conditions) than the base case and shades of blue (negative values) represent areas where the head is higher (wetter conditions) than the base case. The discussion focuses on the months of May and September because these months typically have the highest and lowest annual water levels, respectively. The discussion refers to the

months of May and September by name, or more generally as “spring” and “summer” months, respectively. Head decline maps are provided for model layer 2 because most of the pumping takes place in layer 2. Layer 2 is not included along the southern model boundary where the basin-fill aquifer thickness reduces. Of the 1,105 pumping wells in the model domain, 906 are screened in layer 2 (81%). Most of these are domestic wells. Layers 1, 3, 4, and 5 account for 26%, 41%, 30%, and 22% of wells, respectively. Many wells are screened across multiple layers, and therefore, are counted separately in each layer.

3.9.4.1 Base Case Changes to Groundwater Levels

Figure 41 is a map of the predicted water level decline over the 20-year predictive period for the model domain. This map shows the predicted head decline between spring 2023 (the last year of the historical transient model) and spring 2043 (the last year of the predictive period) in model layer 2. Water levels during spring best represent natural conditions because pumping rates in the model domain are generally lower before the start of the irrigation season and runoff is higher. As illustrated in Figure 41, water levels are expected to decline throughout the model domain over the 20-year predictive period. In Gardnerville Ranchos, groundwater levels decline by 0.8 to 1.6 ft (0.25-0.5 m) in the east side, reaching up to 10 ft (3 m) in the west. The area of greatest water level declines (3 to 10 ft; 1 to 3 m) is in the southwestern section of the model domain, where there is a high density of domestic wells. There is also pumping in this area for irrigation water, stock water, and industrial water. Another area of pronounced water table decline is in the southeast corner of the model domain, where there is a high density of domestic wells in the community of Ruhenstroth, in addition to pumping for irrigation, aquaculture, and public water supply. To the north of Ruhenstroth, and on the eastern side of the East Fork, water levels are expected to decline by <0.8 ft (<0.25 m). In the irrigated fields north of Gardnerville Ranchos, water levels are expected to decline by <0.8 ft (<0.25 m).

The distribution of water table decline is also associated with the irrigation canal network. This suggests that, even under base-case streamflow conditions, recharge from infiltration from the base of the canals is reduced. Less recharge from infiltration may contribute to the pronounced water table declines beneath canals that run east to west in the western portion of the study area, in addition to the narrow area of decline beneath the Upper New Virginia Ditch in the northeastern model area.

The spatial distribution of predicted water table declines over the 20-year predictive period is similar to that of the base-case scenario by Yager et al. (2012) for the Gardnerville Ranchos area. The base-case predictive model in the study by Yager et al. (Figure 40) projects a water table decline of 5 to 10 ft (1.5 to 3 m) in the Gardnerville Ranchos area from 2010 to 2060. In comparison, the base-case model in this study shows 3 to 10 ft (1 to 3 m) of water table decline from 2024 to 2043. Predicted temporal variability of water levels during the base-case scenario, and all predictive scenarios, at GRGID wells is described in Section 3.9.5.

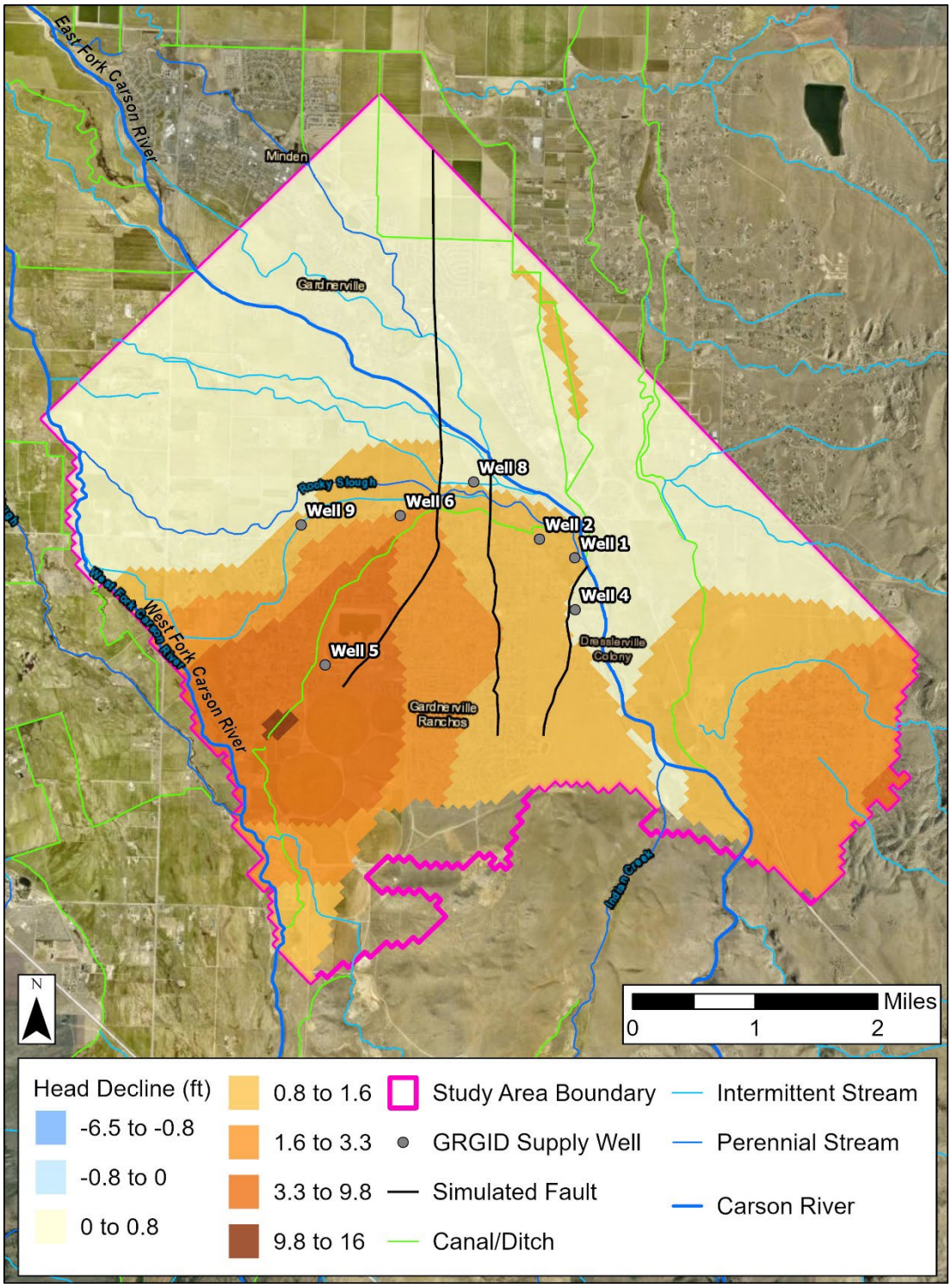

Figure 41. Map of predicted water level (head) declines for the base-case model from spring 2023 to spring 2043 in model layer 2. Negative declines (shades of blue) indicate increased water levels (wetter conditions) and positive declines (shades of orange) indicate decreased water levels (dryer conditions).

3.9.4.2 Climate-Driven Changes to Groundwater Levels

When compared to base-case heads, both climate simulations (C2F and C4F) show that increased temperatures would result in increased heads throughout the study area in the spring and summer through 2034. Maps of predicted head declines for simulations C2F and C4F are provided as Figures 42 and 43, respectively. By 2043, heads are lower compared to the base-case scenario throughout most of the model domain for both scenarios (Figure 42E-F, Figure 43E-F). This temporal trend suggests that changes in streamflow timing and discharge both contribute to future head changes. Streamflow timing controls heads for the first ten years of the predictive period, with earlier streamflow leading to increased heads overall during both the spring and summer (Figure 43C-D). However, by year 20, the overall reduction in annual stream discharge results in heads that are 0.8 to 1.6 ft (0.25 to 0.5 m) lower than the base case throughout most of the model domain for both simulations. Simulation C4F shows greater extremes than C2F, including greater head increases in the first ten years, and greater head reductions in year 20.

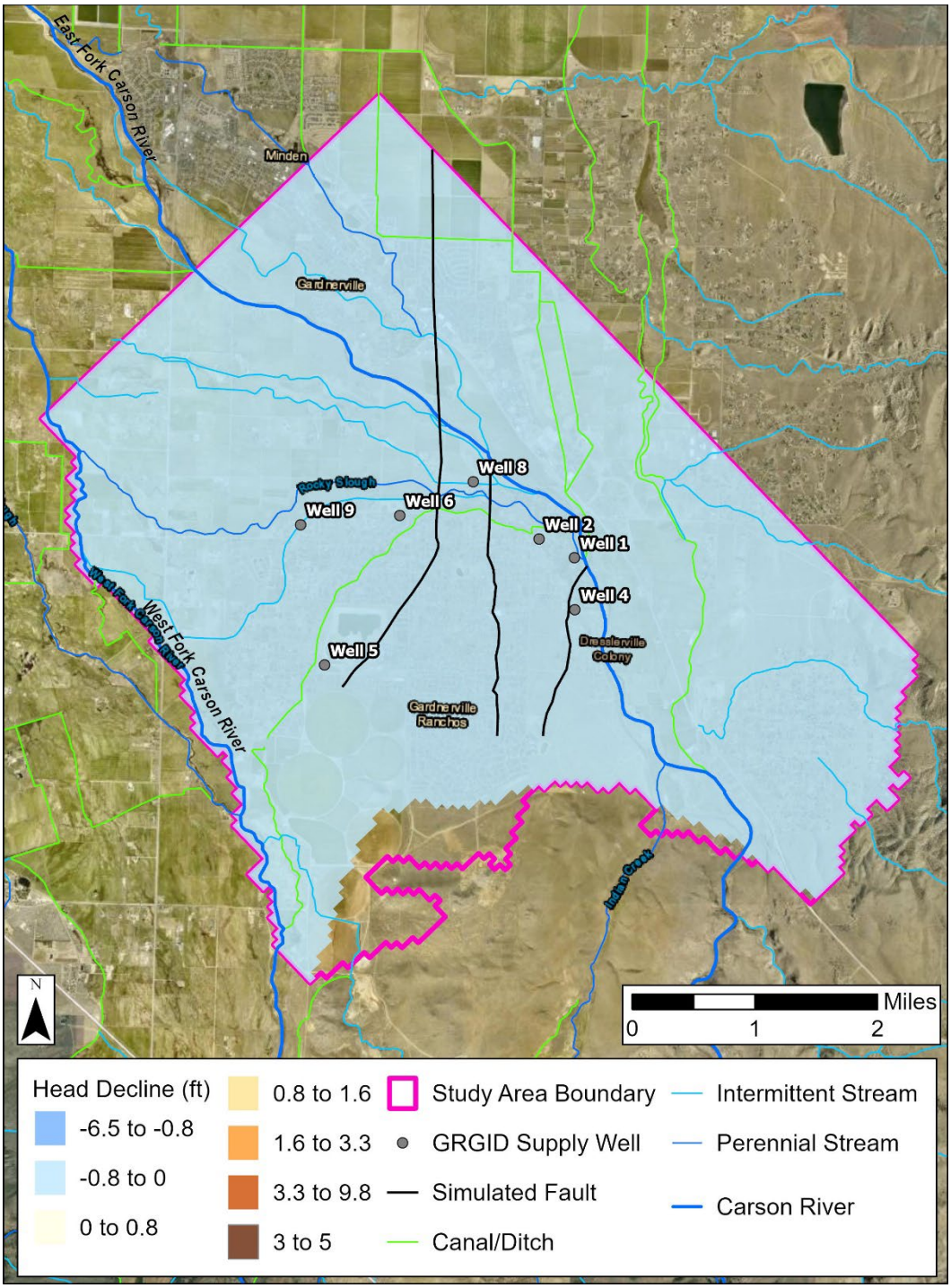

Figure 42A. Map of predictive declines in groundwater levels for simulation C2F in model layer 2 relative to the base-case model for May 2025 under a temperature increase of 0.1°F/yr (+0.05°C/yr) from average and pumping rates equal to the 2018-2023 average for Gardnerville Ranchos supply wells. Areas in blue (negative values) have higher groundwater levels compared to the base-case model and areas in orange (positive values) have lower groundwater levels compared to the base-case model.

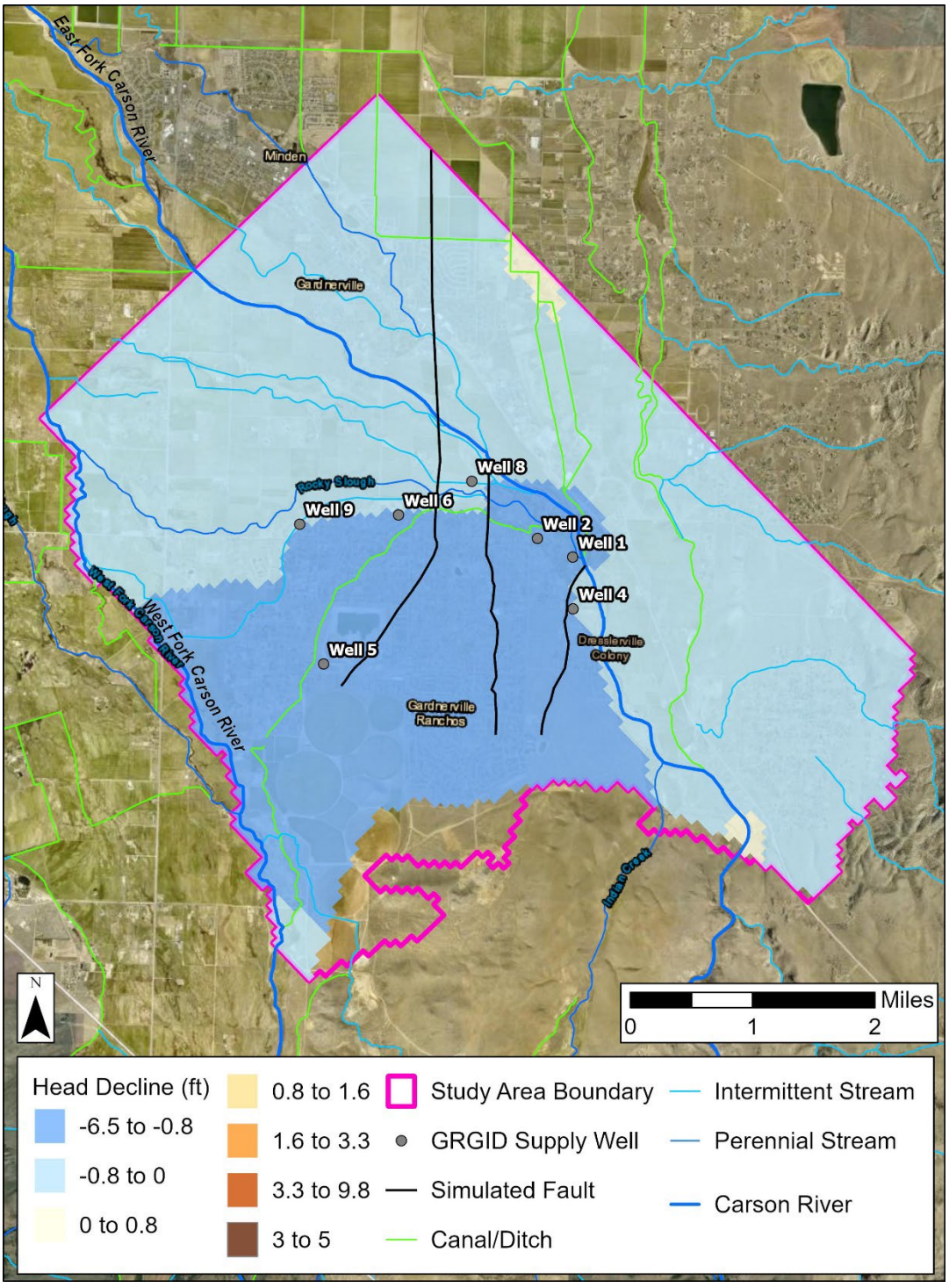

Figure 42B. Map of predictive declines in groundwater levels for simulation C2F in model layer 2 relative to the base-case model for September 2025 under a temperature increase of 0.1°F/yr (0.05°C/yr) from average and pumping rates equal to the 2018-2023 average for Gardnerville Ranchos supply wells. Areas in blue (negative values) have higher groundwater levels compared to the base-case model and areas in orange (positive values) have lower groundwater levels.

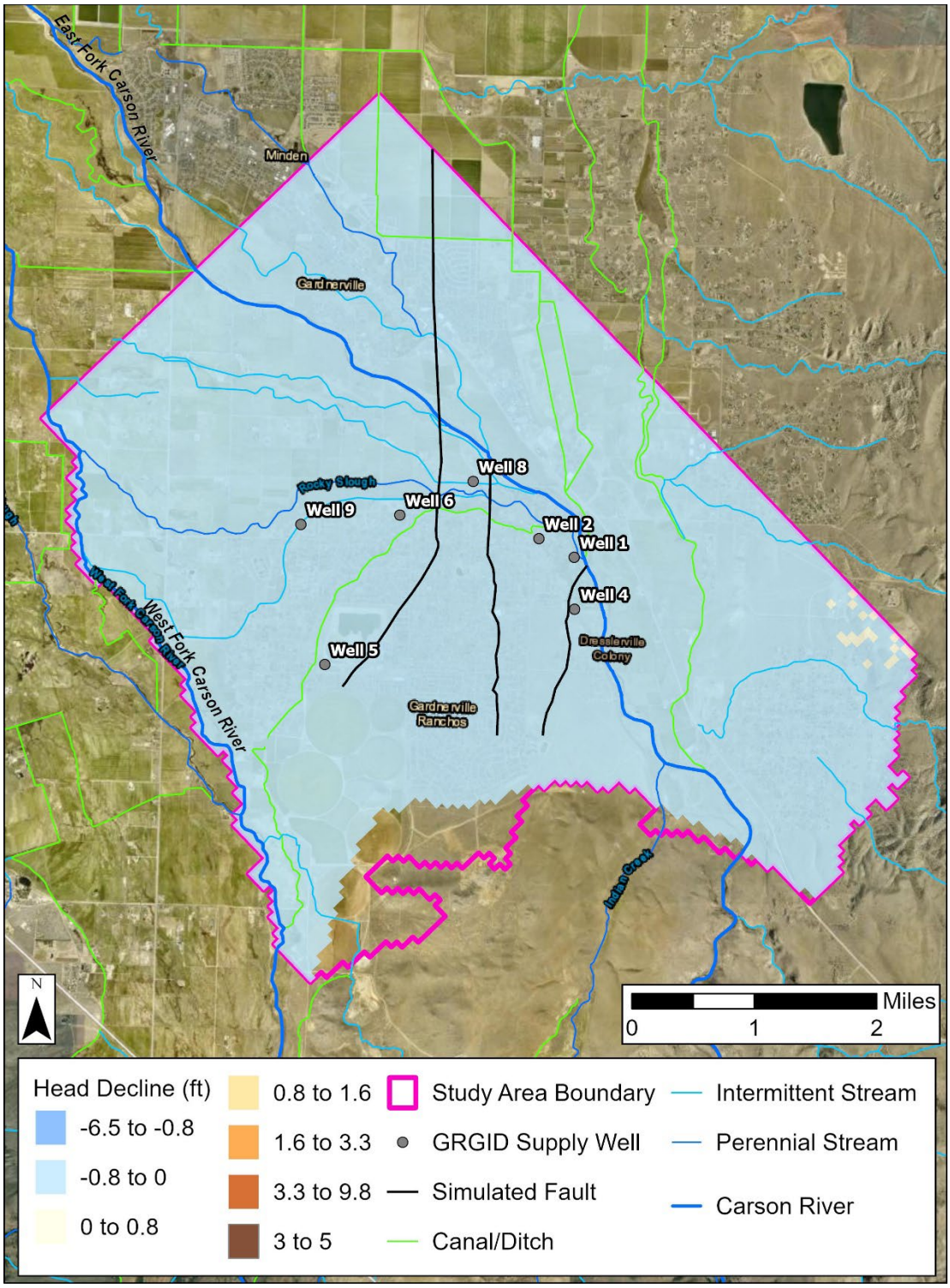

Figure 42C. Map of predictive declines in groundwater levels for simulation C2F in model layer 2 relative to the base-case model for May 2034 under a temperature increase of 0.1°F/yr (0.05°C/yr) from average and pumping rates equal to the 2018-2023 average for Gardnerville Ranchos supply wells. Areas in blue (negative values) have higher groundwater levels compared to the base-case model and areas in orange (positive values) have lower groundwater levels.

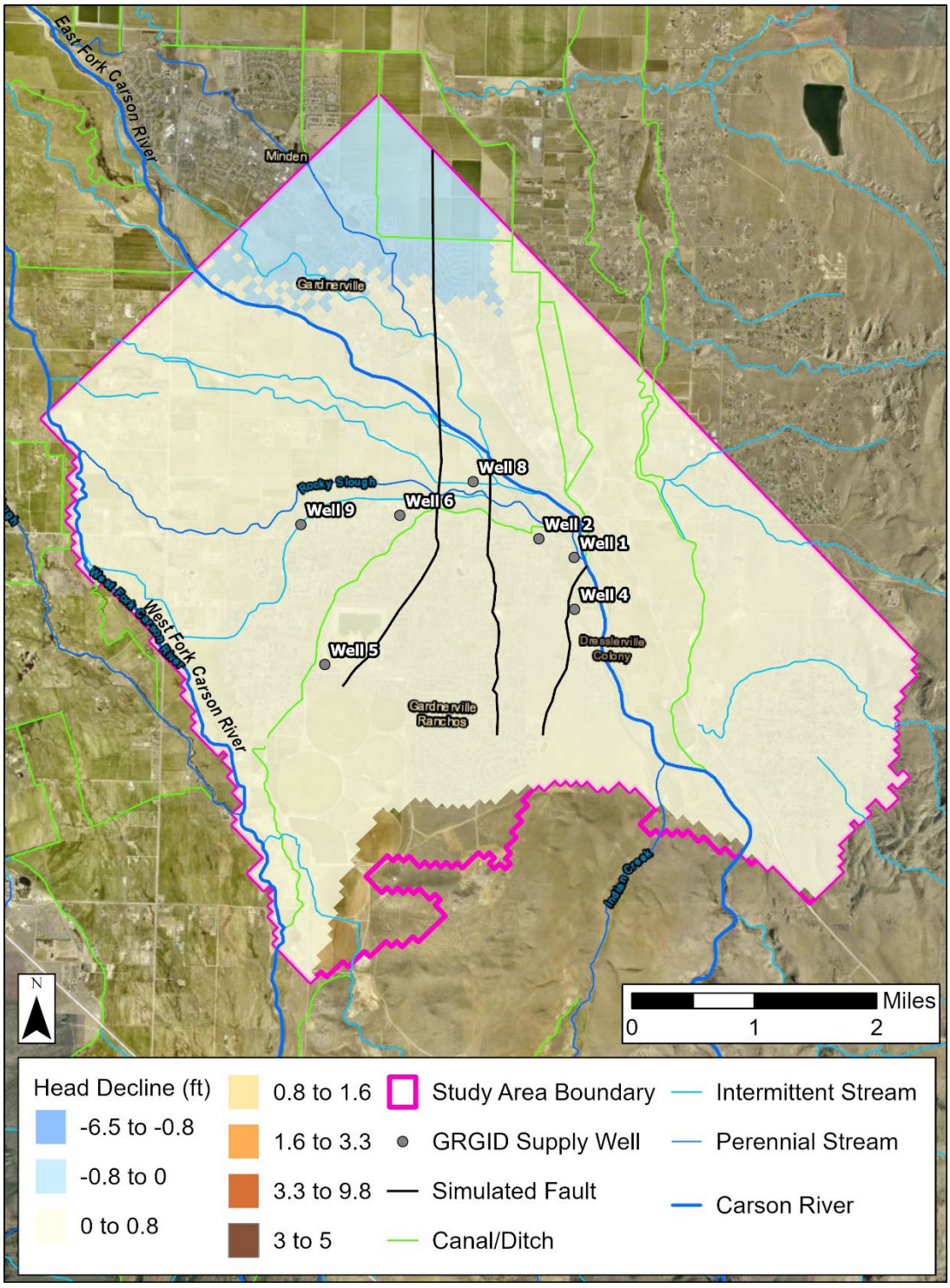

Figure 42D. Map of predictive declines in groundwater levels for simulation C2F in model layer 2 relative to the base-case model for September 2034 under a temperature increase of 0.1°F/yr (0.05°C/yr) from average and pumping rates equal to the 2018-2023 average for Gardnerville Ranchos supply wells. Areas in blue (negative values) have higher groundwater levels compared to the base-case model and areas in orange (positive values) have lower groundwater levels.

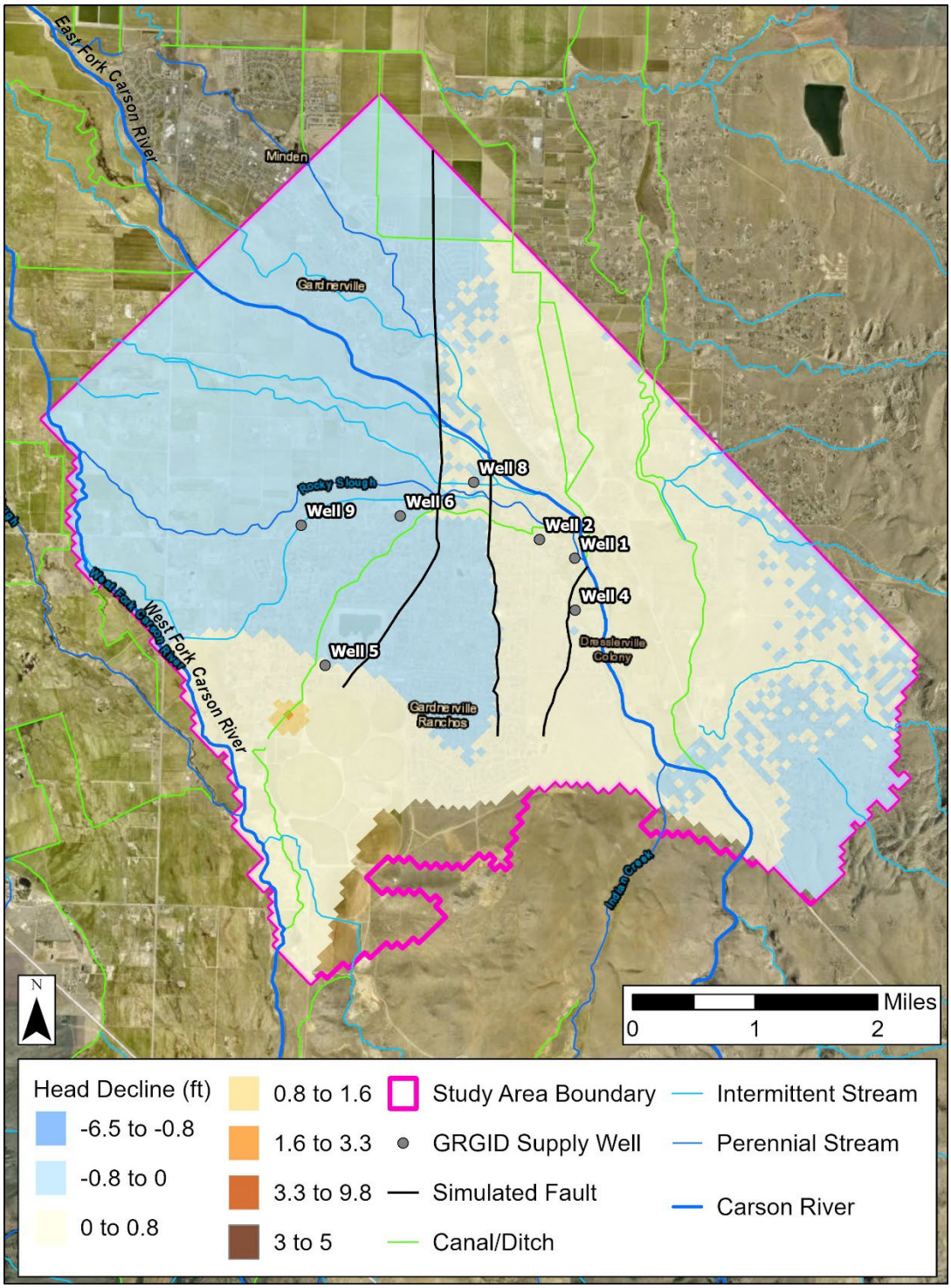

Figure 42E. Map of predictive declines in groundwater levels for simulation C2F in model layer 2 relative to the base-case model for May 2043 under a temperature increase of 0.1°F/yr (0.05°C/yr) from average and pumping rates equal to the 2018-2023 average for Gardnerville Ranchos supply wells. Areas in blue (negative values) have higher groundwater levels compared to the base-case model and areas in orange (positive values) have lower groundwater levels.

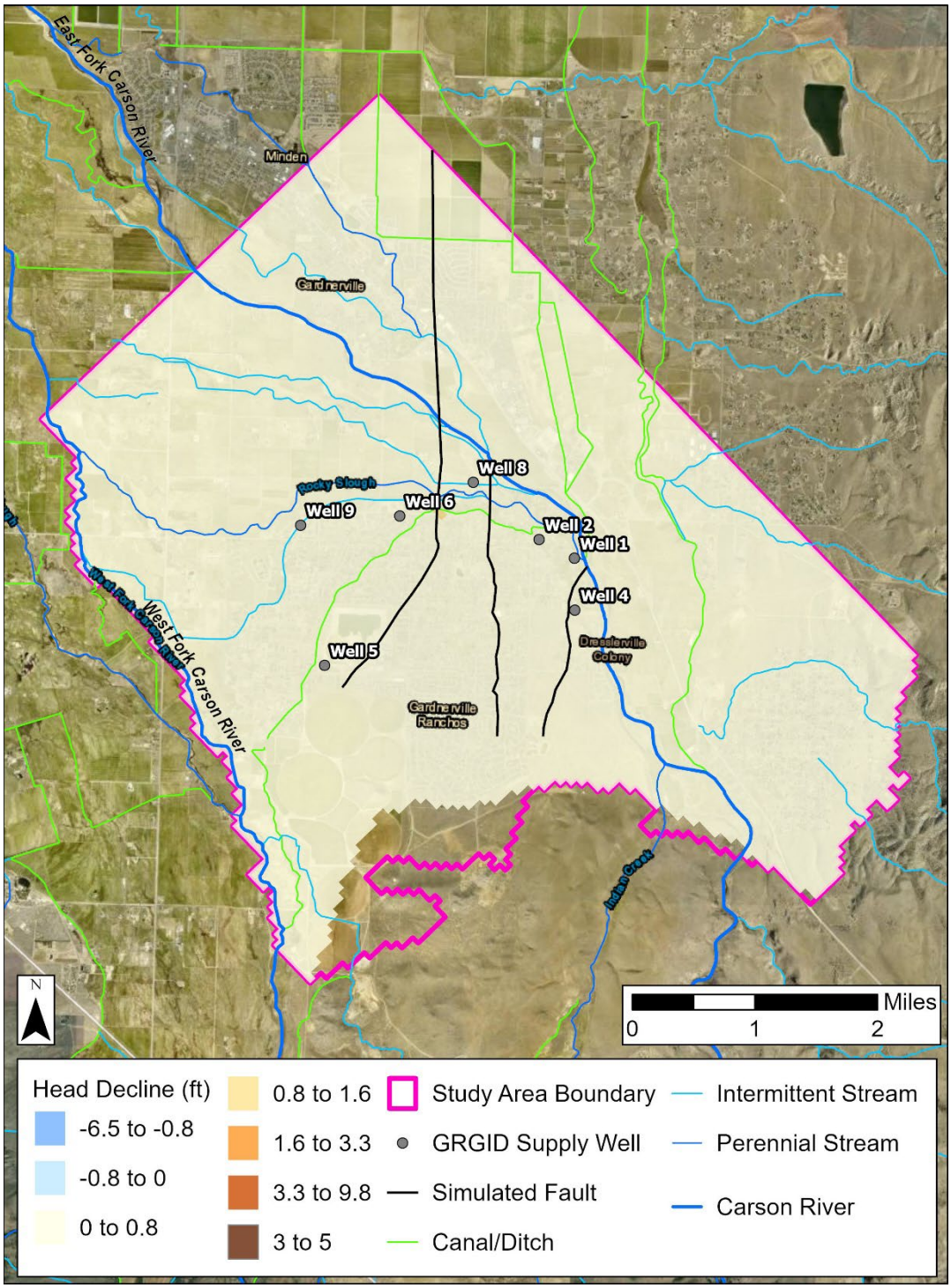

Figure 42F. Map of predictive declines in groundwater levels for simulation C2F in model layer 2 relative to the base-case model for September 2043 under a temperature increase of 0.1°F/yr (0.05°C/yr) from average and pumping rates equal to the 2018-2023 average for Gardnerville Ranchos supply wells. Areas in blue (negative values) have higher groundwater levels compared to the base-case model and areas in orange (positive values) have lower groundwater levels.

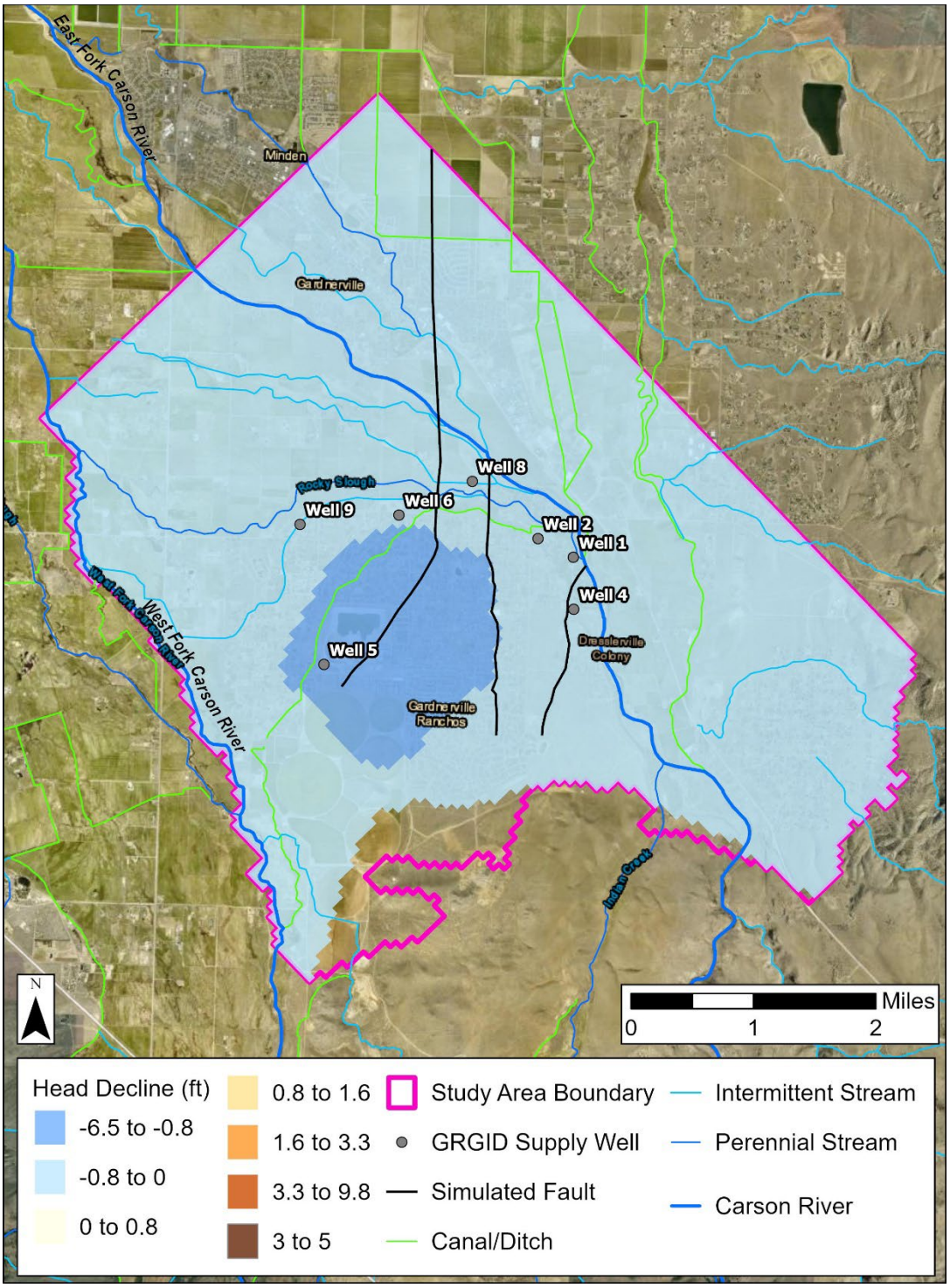

Figure 43A. Map of predictive declines in groundwater levels for simulation C4F in model layer 2 relative to the base-case model for May 2025 under a temperature increase of 0.2°F/yr (0.1°C/yr) from average and pumping rates equal to the 2018-2023 average for Gardnerville Ranchos supply wells. Areas in blue (negative values) have higher groundwater levels compared to the base-case model and areas in orange (positive values) have lower groundwater levels.

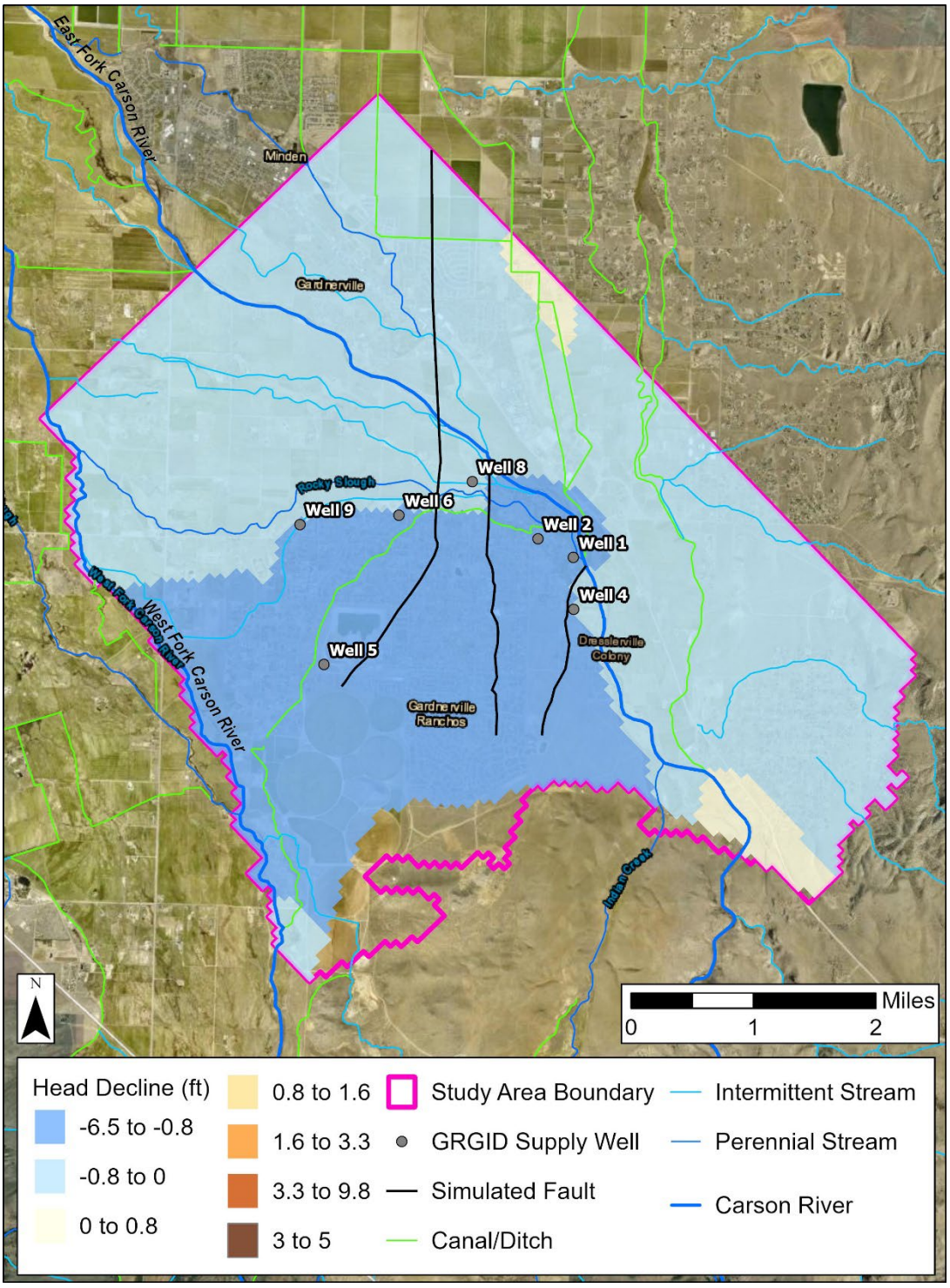

Figure 43B. Map of predictive declines in groundwater levels for simulation C4F in model layer 2 relative to the base-case model for September 2025 under a temperature increase of 0.2°F/yr (0.1°C/yr) from average and pumping rates equal to the 2018-2023 average for Gardnerville Ranchos supply wells. Areas in blue (negative values) have higher groundwater levels compared to the base-case model and areas in orange (positive values) have lower groundwater levels.

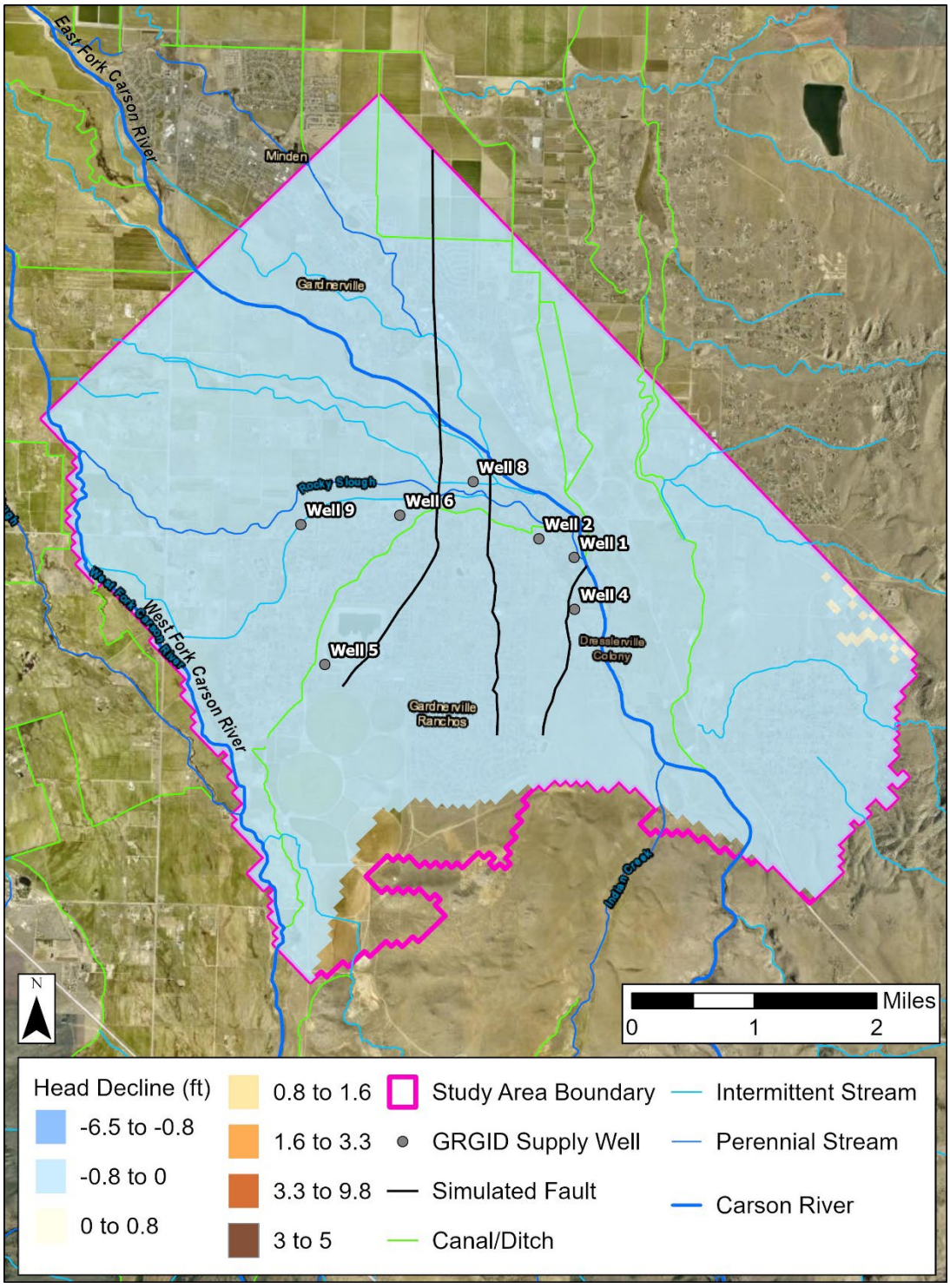

Figure 43C. Map of predictive declines in groundwater levels for simulation C4F in model layer 2 relative to the base-case model for May 2034 under a temperature increase of 0.2°F/yr (0.1°C/yr) from average and pumping rates equal to the 2018-2023 average for Gardnerville Ranchos supply wells. Areas in blue (negative values) have higher groundwater levels compared to the base-case model and areas in orange (positive values) have lower groundwater levels.

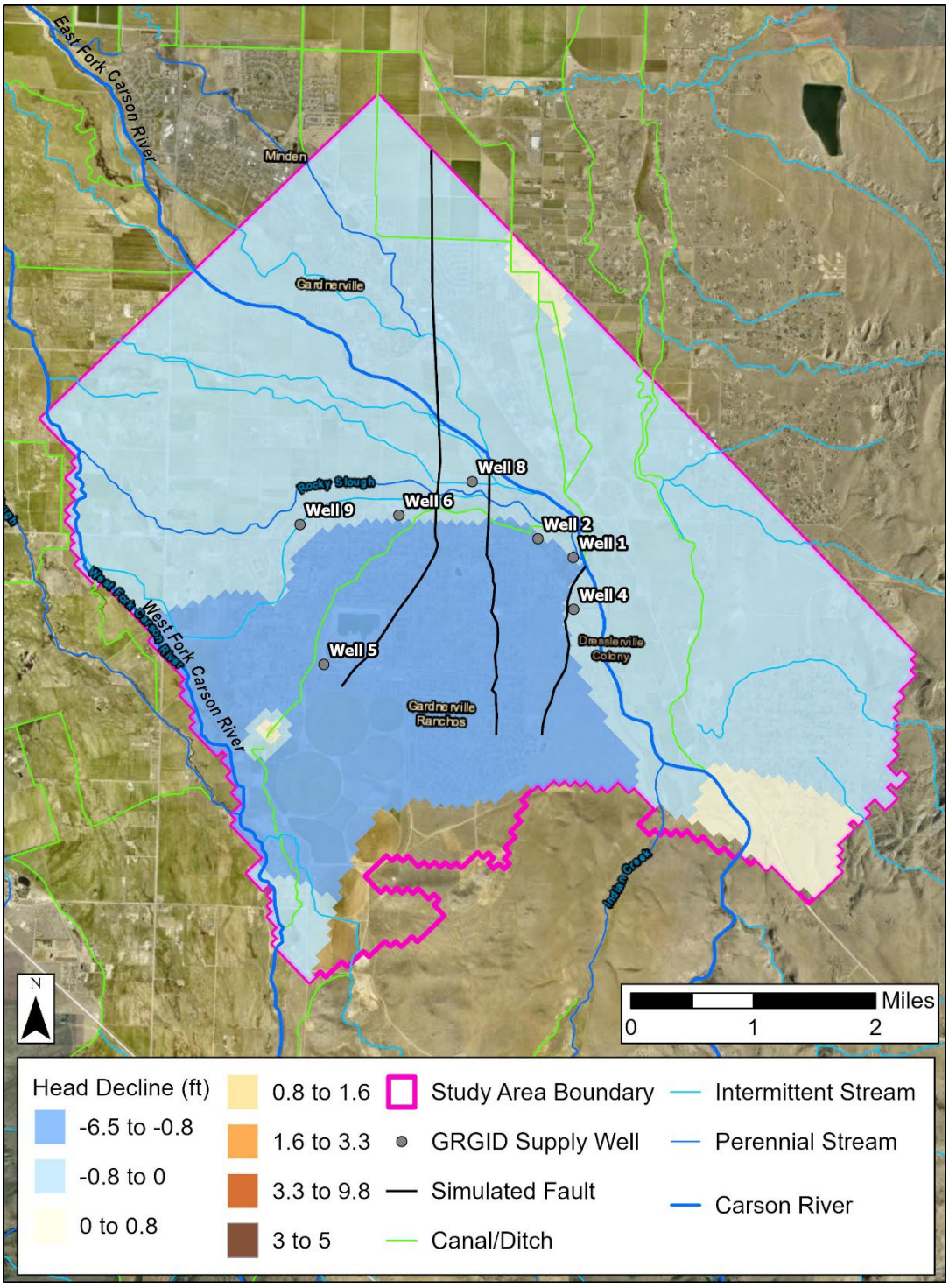

Figure 43D. Map of predictive declines in groundwater levels for simulation C4F in model layer 2 relative to the base-case model for September 2034 under a temperature increase of 0.2°F/yr (0.1°C/yr) from average and pumping rates equal to the 2018-2023 average for Gardnerville Ranchos supply wells. Areas in blue (negative values) have higher groundwater levels compared to the base-case model and areas in orange (positive values) have lower groundwater levels.

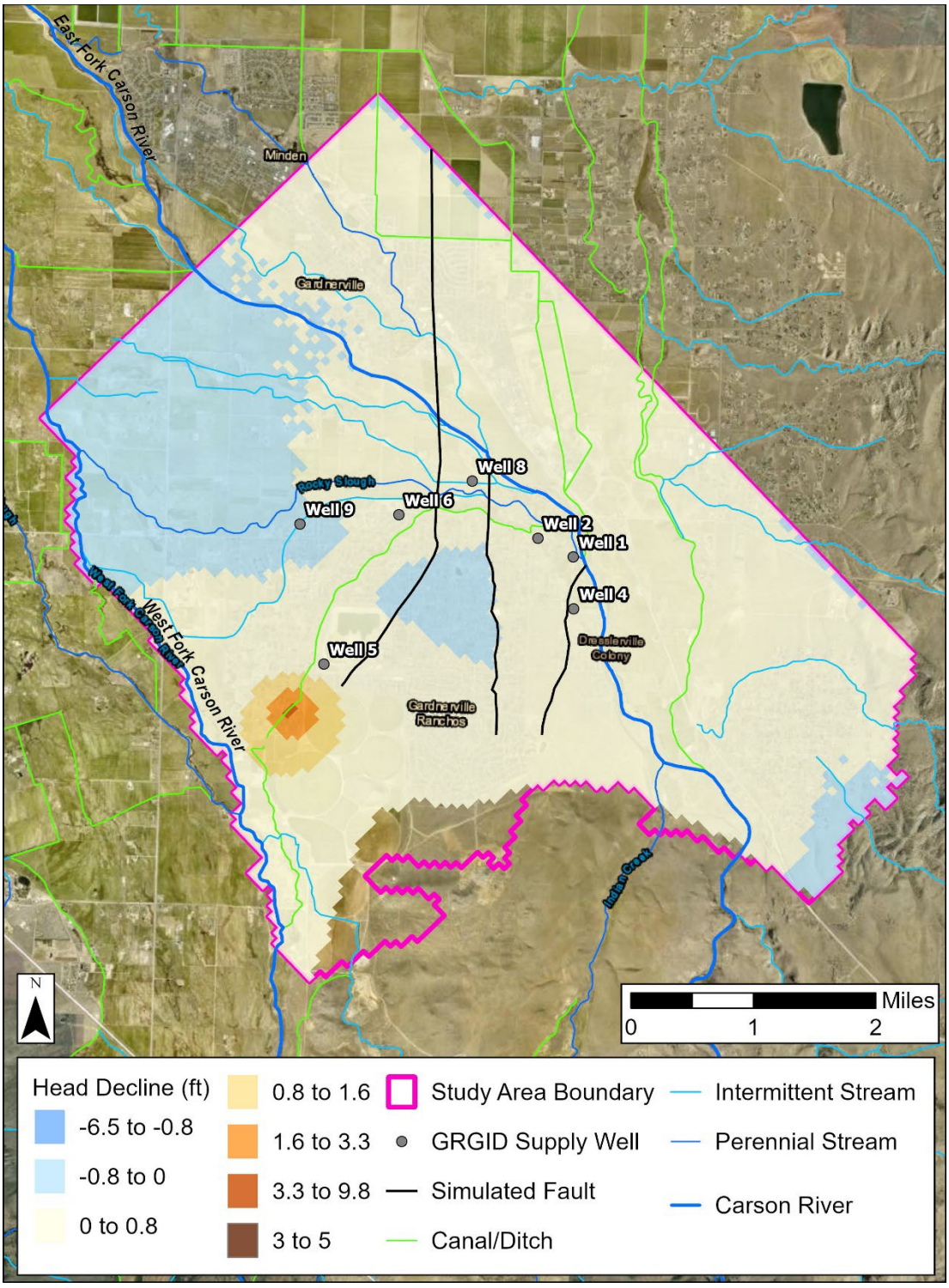

Figure 43E. Map of predictive declines in groundwater levels for simulation C4F in model layer 2 relative to the base-case model for May 2043 under a temperature increase of 0.2°F/yr (0.1°C/yr) from average and pumping rates equal to the 2018-2023 average for Gardnerville Ranchos supply wells. Areas in blue (negative values) have higher groundwater levels compared to the base-case model and areas in orange (positive values) have lower groundwater levels.

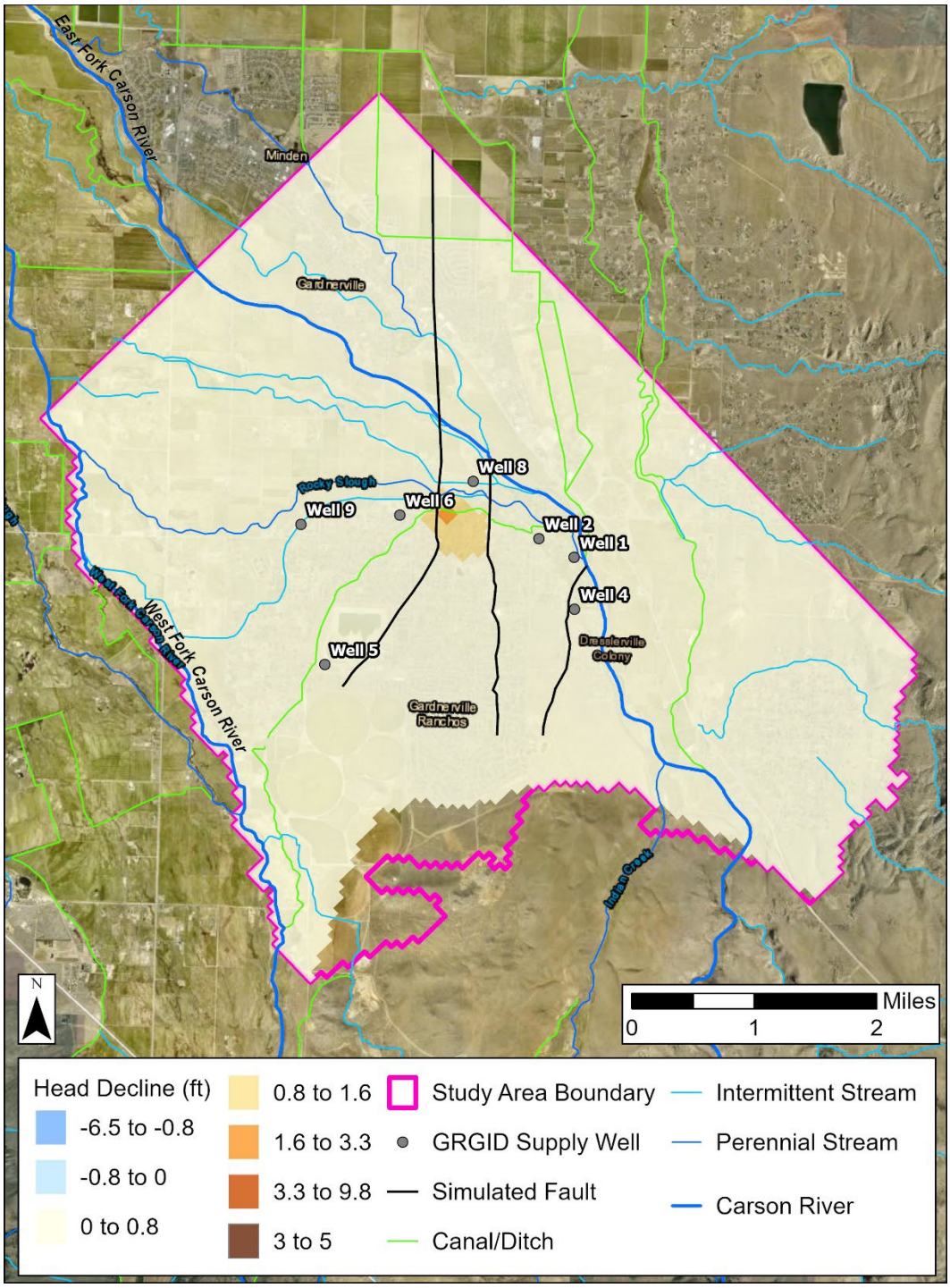

Figure 43F. Map of predictive declines in groundwater levels for simulation C4F in model layer 2 relative to the base-case model for September 2043 under a temperature increase of 0.2°F/yr (0.1°C/yr) from average and pumping rates equal to the 2018-2023 average for Gardnerville Ranchos supply wells. Areas in blue (negative values) have higher groundwater levels compared to the base-case model and areas in orange (positive values) have lower groundwater levels.

3.9.4.3 Pumping-Driven Changes to Groundwater Levels

Pumping simulations P1a and P2a isolate the effects to groundwater levels from annual pumping increases of 1.5% and 0.2%, respectively, at Gardnerville Ranchos supply wells while maintaining base-case streamflow for the duration of the predictive period. Maps of predicted head declines for simulations P1a and P2a are provided as Figures 44 and 45, respectively. Under a 1.5% annual increase in pumping, the effect can be seen throughout the model domain for the duration of the predictive period, with a head decrease of <0.8 ft (<0.25 m) throughout most of the model domain when compared to the base-case model for the month of May 2025 (Figure 44A). The spatial extent and magnitude of head change grows over time. The greatest head change is in eastern and southern Gardnerville Ranchos, where heads decrease by 1.6 to 3.3 ft (0.5 to 1 m) by the summer of 2034 (Figure 44D) and by 3.3 to 9.8 ft (1 to 3 m) by the summer of 2043 (Figure 44F). Localized decreases reach 9.8 to 16 ft (3 to 5 m) near supply wells 1 and 4 in summer 2043.

Over the same time frame and with an annual pumping increase of 0.2%, heads decrease over time but generally do not change by >0.8 ft (>0.25 m) (Figure 45). The most pronounced head change is in eastern and southern Gardnerville Ranchos, as indicated by lowering heads as early as May 2025 (Figure 45A), while heads slightly increase elsewhere in the model domain. The total area experiencing declining heads expands as monthly pumping increases in the summer of 2025 (Figure 45B). Except for localized declines 1.6 ft (<0.5) m near Wells 1 and 4, heads are not expected to decline by more than 0.8 ft (0.25 m) throughout the study area by 2043 (Figure 45F). In comparing head changes between P1a and P2a, realistic growth and water conservation can reduce the overall magnitude and distribution of groundwater level decline in the study area.

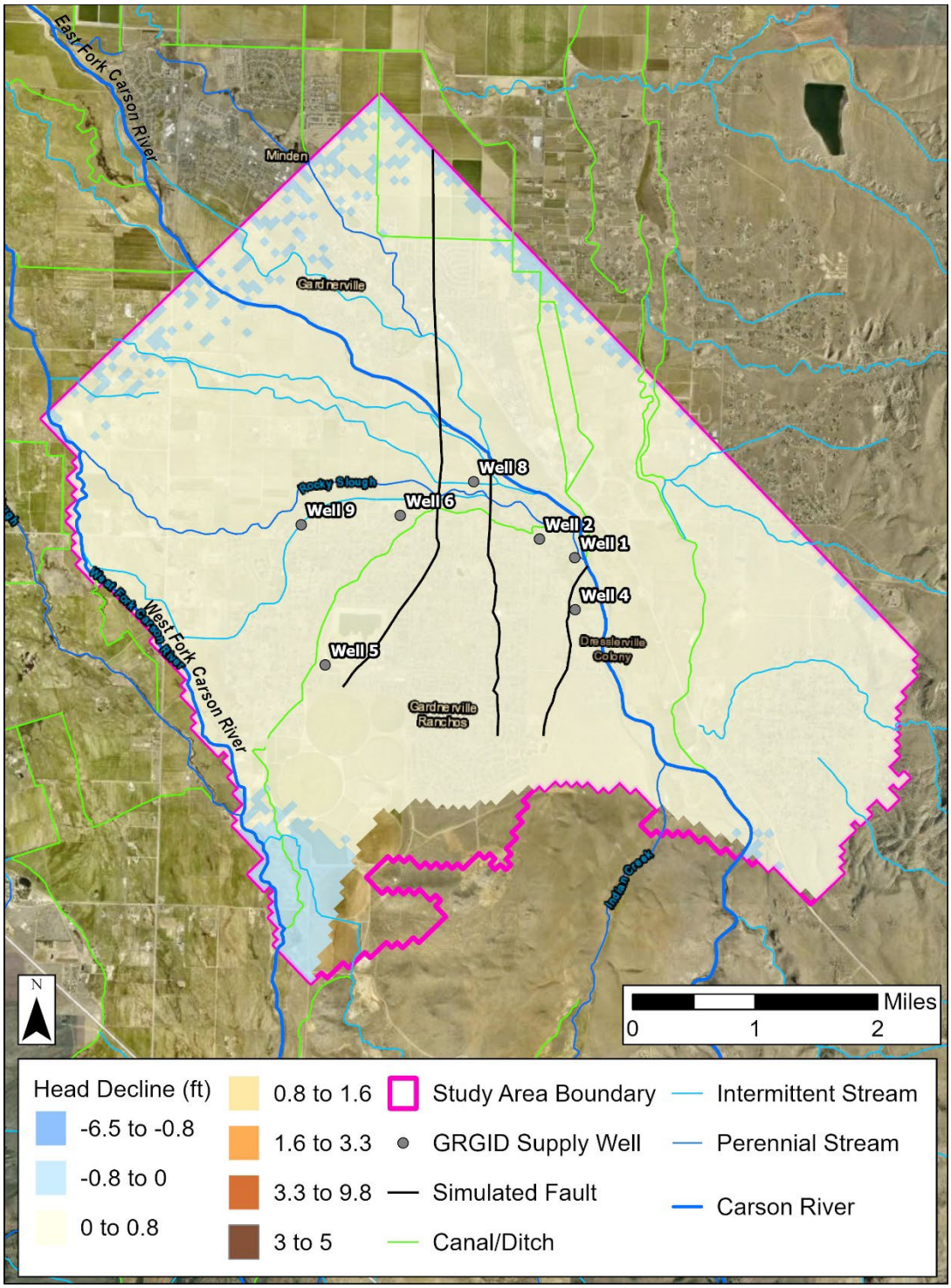

Figure 44A. Map of predictive declines in groundwater levels for simulation P1a in model layer 2 relative to the base-case model for May 2025 under a pumping increase of 1.5% annually at Gardnerville Ranchos supply wells and no temperature change. Areas in blue (negative values) have higher groundwater levels compared to the base-case model and areas in orange (positive values) have lower groundwater levels.

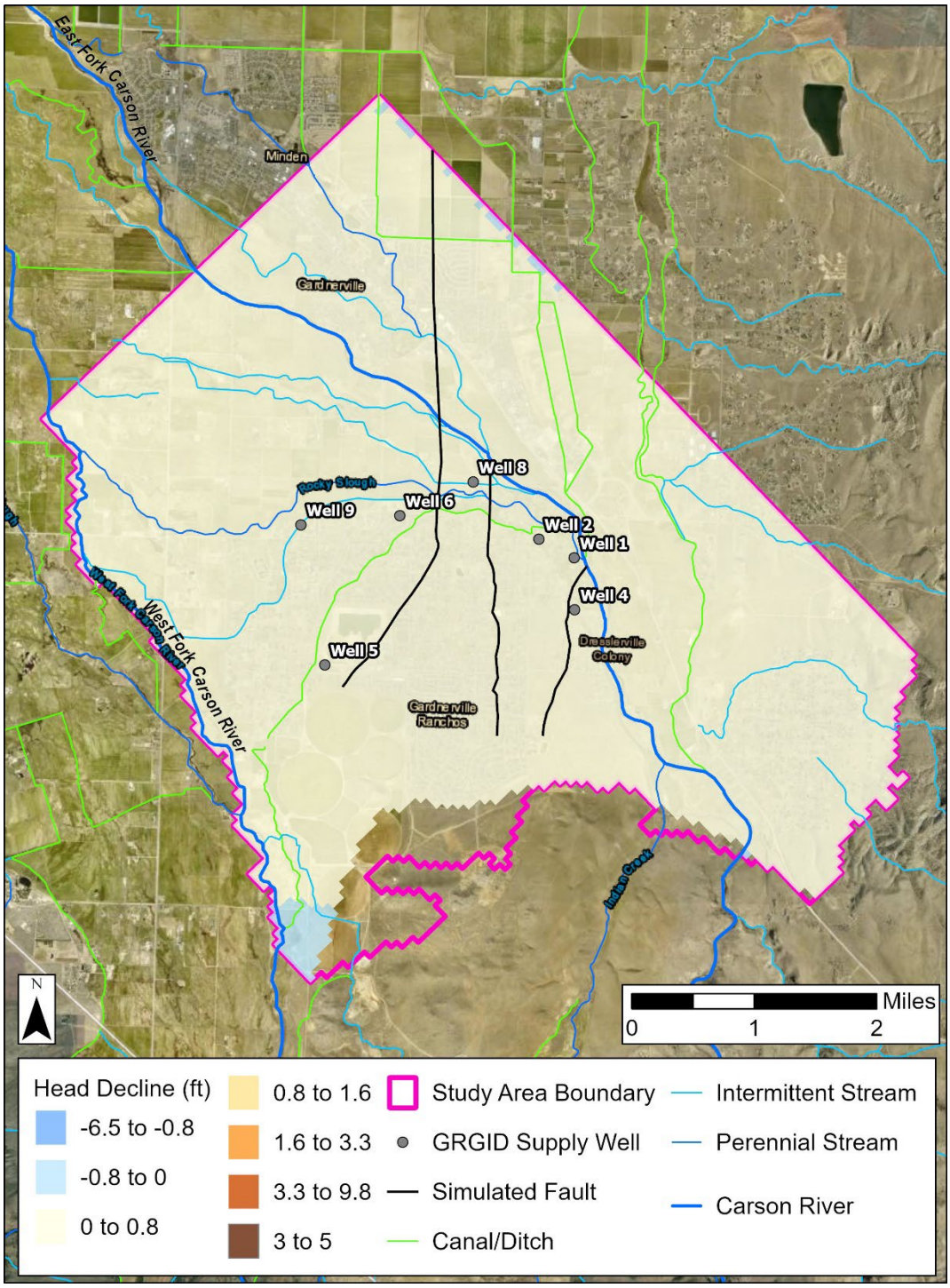

Figure 44B. Map of predictive declines in groundwater levels for simulation P1a in model layer 2 relative to the base-case model for September 2025 under a pumping increase of 1.5% annually at Gardnerville Ranchos supply wells and no temperature change. Areas in blue (negative values) have higher groundwater levels compared to the base-case model and areas in orange (positive values) have lower groundwater levels.

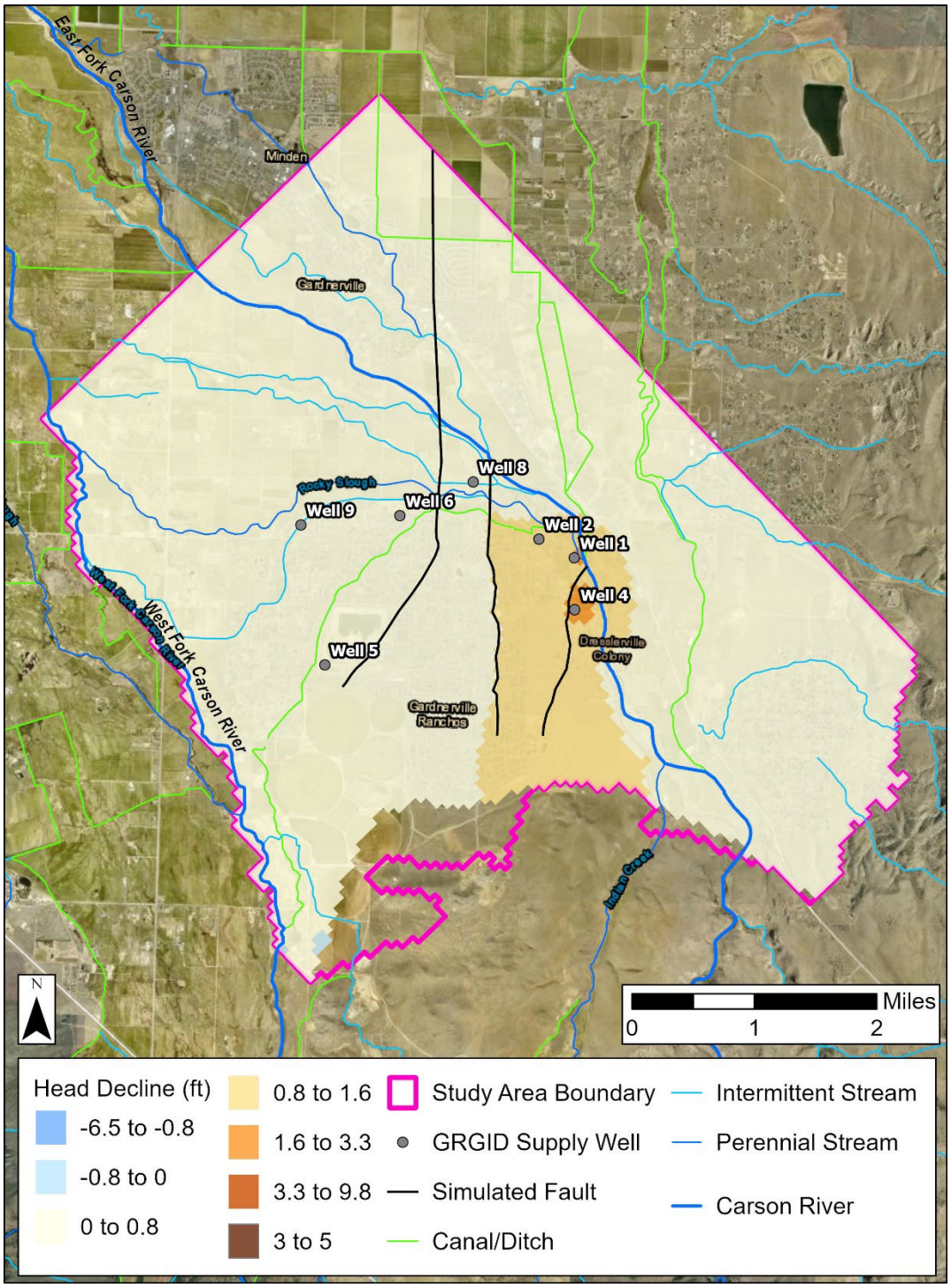

Figure 44C. Map of predictive declines in groundwater levels for simulation P1a in model layer 2 relative to the base-case model for May 2034 under a pumping increase of 1.5% annually at Gardnerville Ranchos supply wells and no temperature change. Areas in blue (negative values) have higher groundwater levels compared to the base-case model and areas in orange (positive values) have lower groundwater levels.

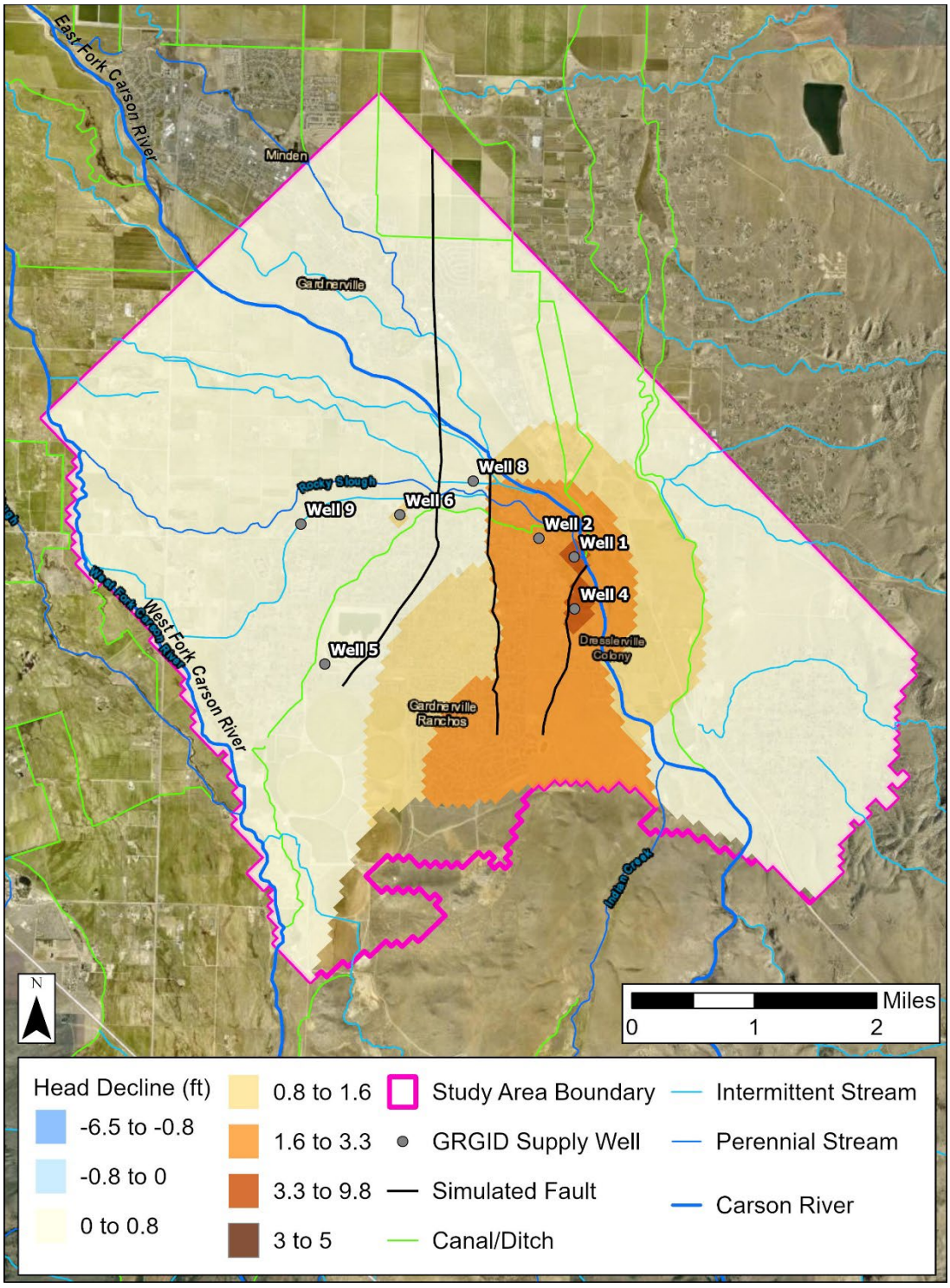

Figure 44D. Map of declines in groundwater levels for simulation P1a in model layer 2 relative to the base-case model for September 2034 under a pumping increase of 1.5% annually at Gardnerville Ranchos supply wells and no temperature change. Areas in blue (negative values) have higher groundwater levels compared to the base-case model and areas in orange (positive values) have lower groundwater levels.

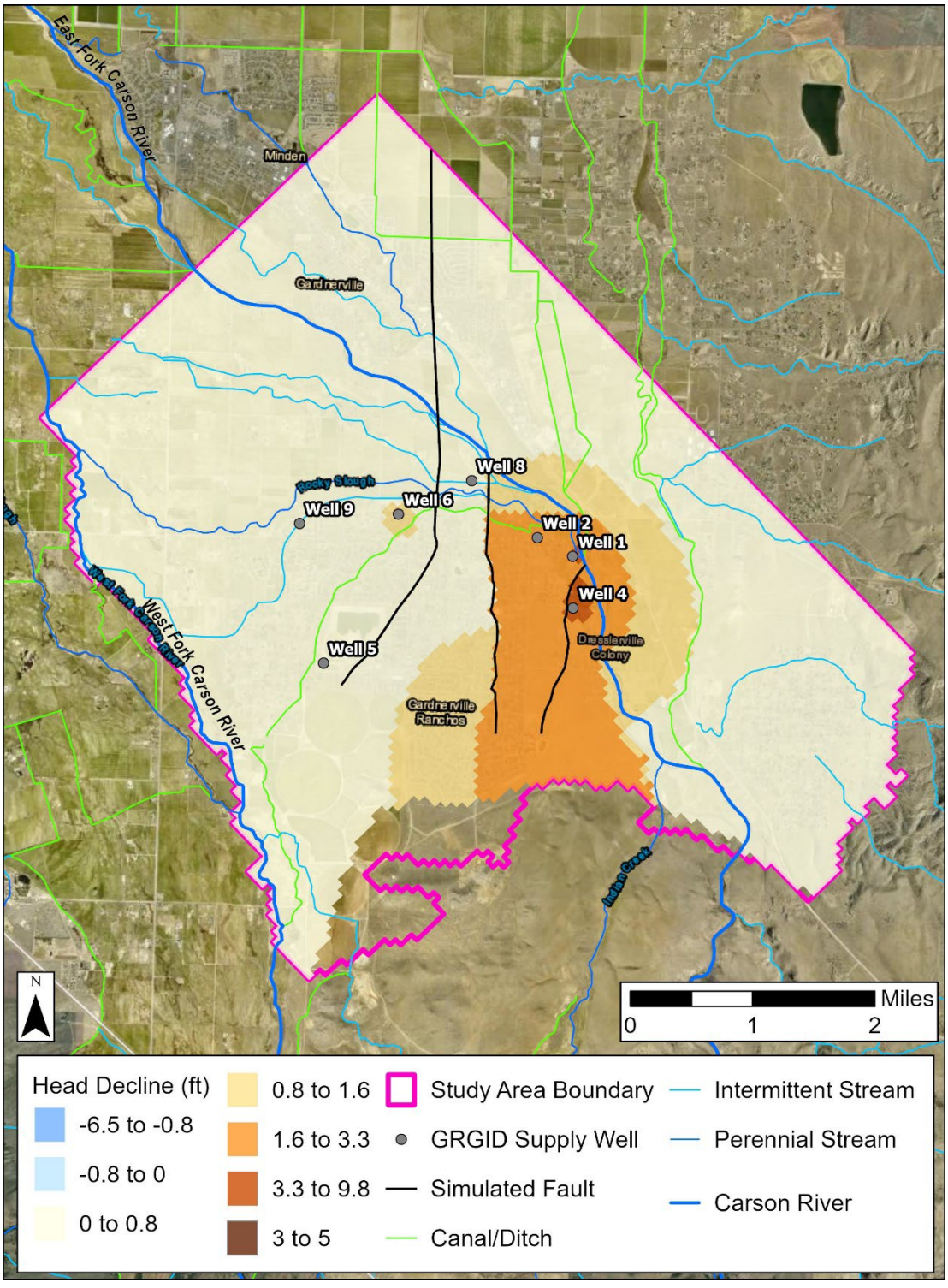

Figure 44E. Map of predictive declines in groundwater levels for simulation P1a in model layer 2 relative to the base-case model for May 2043 under a pumping increase of 1.5% annually at Gardnerville Ranchos supply wells and no temperature change. Areas in blue (negative values) have higher groundwater levels compared to the base-case model and areas in orange (positive values) have lower groundwater levels.

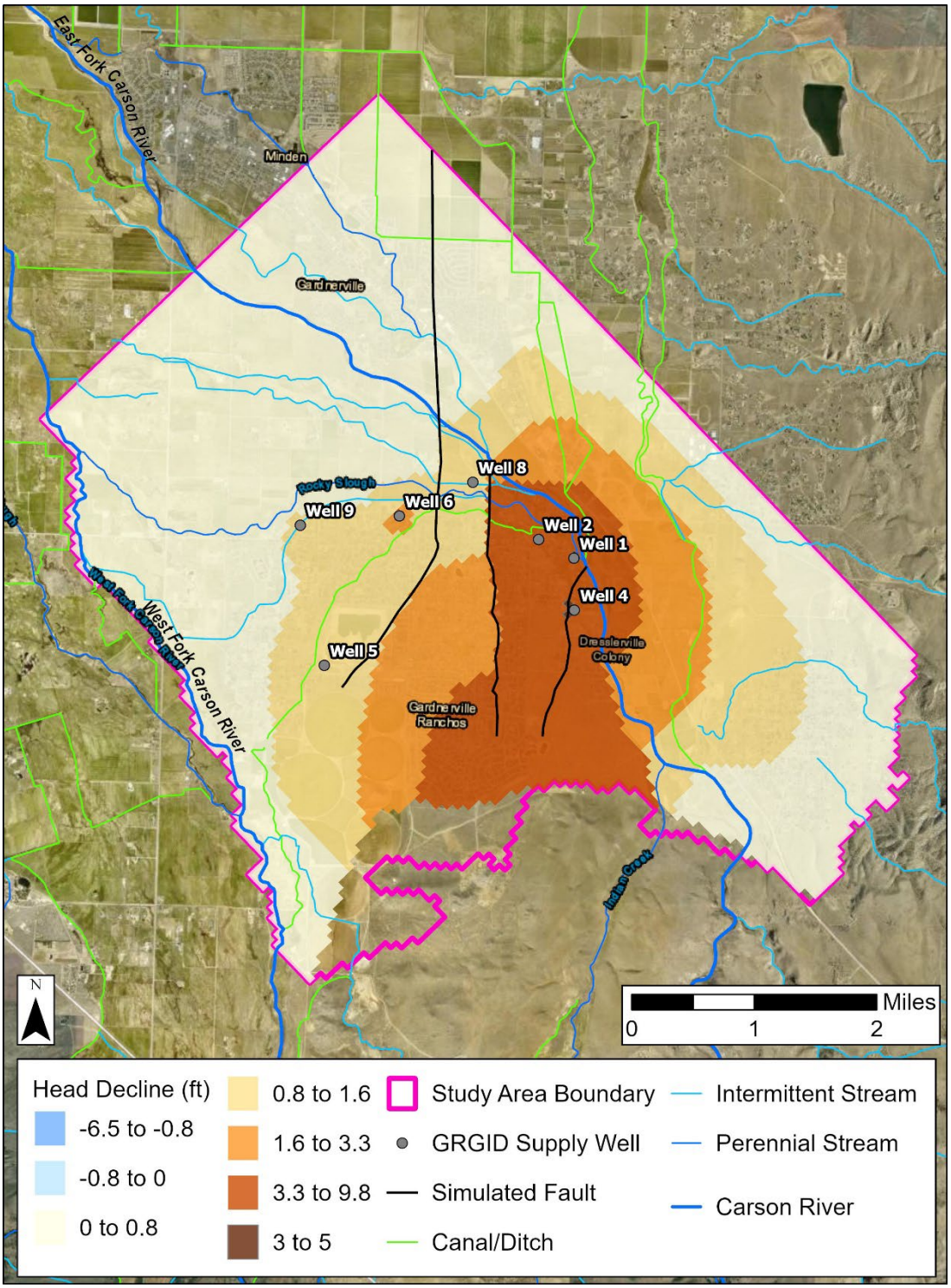

Figure 44F. Map of predictive declines in groundwater levels for simulation P1a in model layer 2 relative to the base-case model for September 2043 under a pumping increase of 1.5% annually at Gardnerville Ranchos supply wells and no temperature change. Areas in blue (negative values) have higher groundwater levels compared to the base-case model and areas in orange (positive values) have lower groundwater levels.

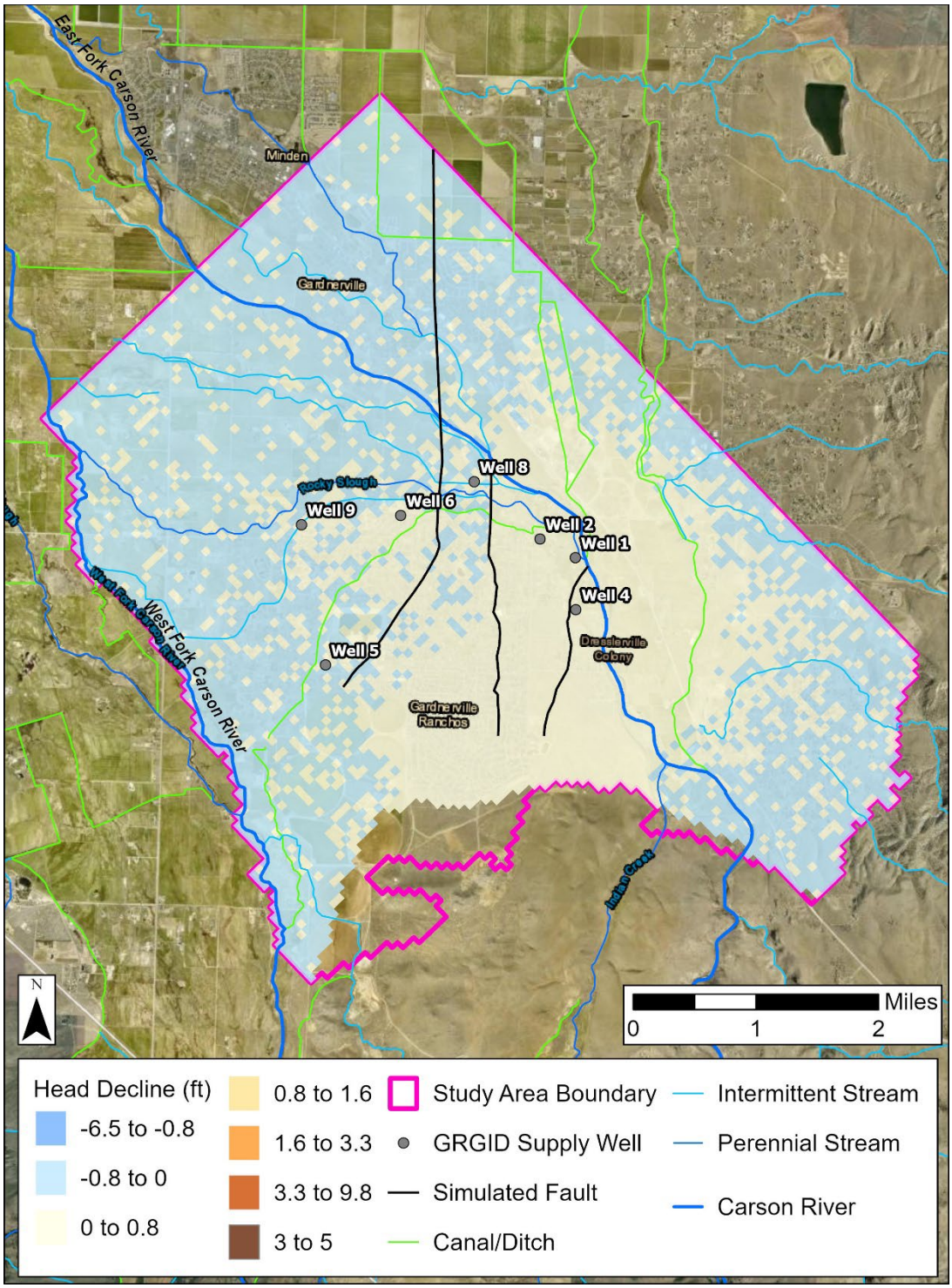

Figure 45A. Map of predictive declines in groundwater levels for simulation P2a in layer 2 relative to the base-case model for May 2025 under a pumping increase of 0.2% annually at Gardnerville Ranchos supply wells and no temperature change. Areas in blue (negative values) have higher groundwater levels compared to the base-case model and areas in orange (positive values) have lower groundwater levels.

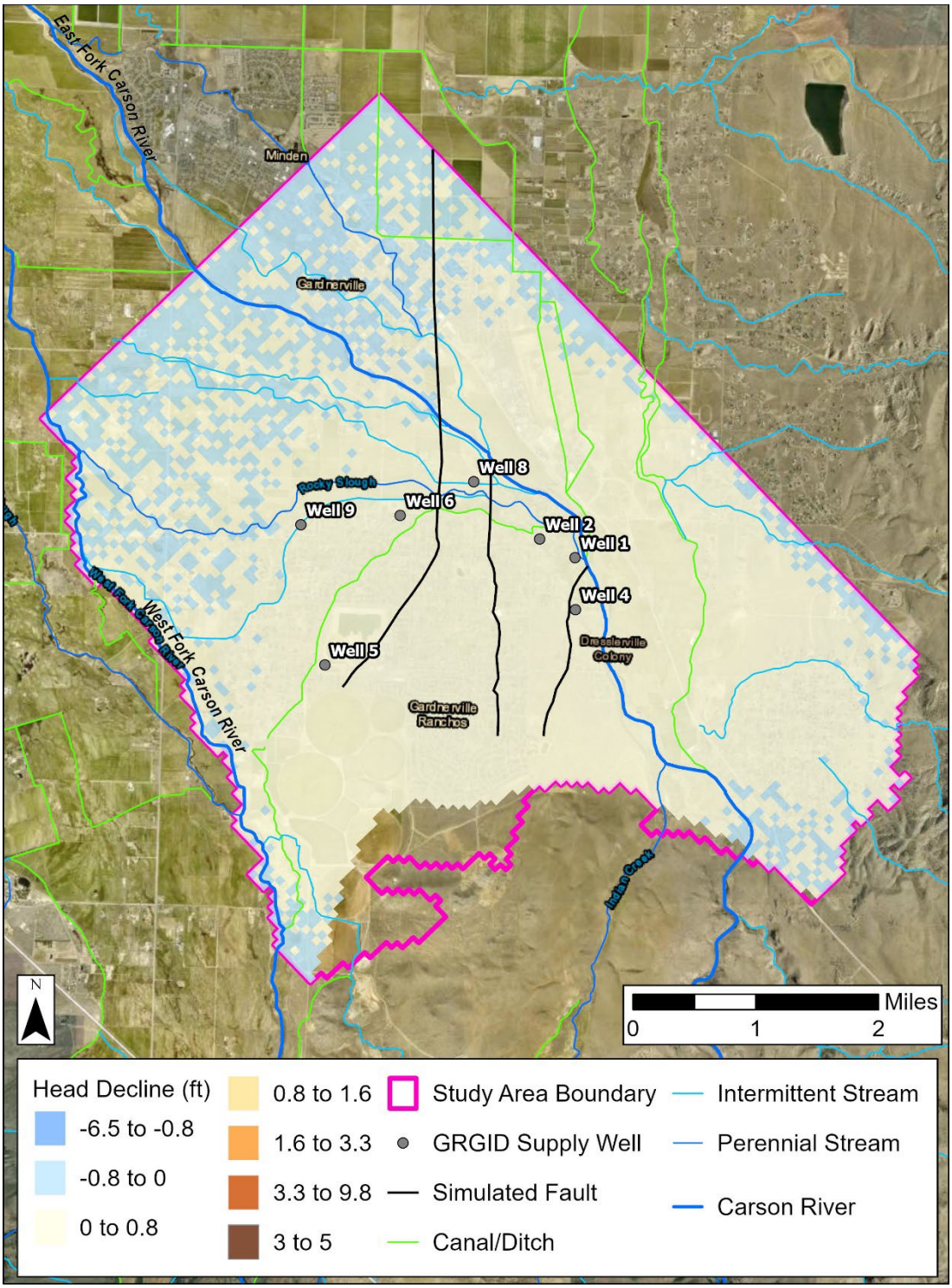

Figure 45B. Map of predictive declines in groundwater levels for simulation P2a in layer 2 relative to the base-case model for September 2025 under a pumping increase of 0.2% annually at Gardnerville Ranchos supply wells and no temperature change. Areas in blue (negative values) have higher groundwater levels compared to the base-case model and areas in orange (positive values) have lower groundwater levels.

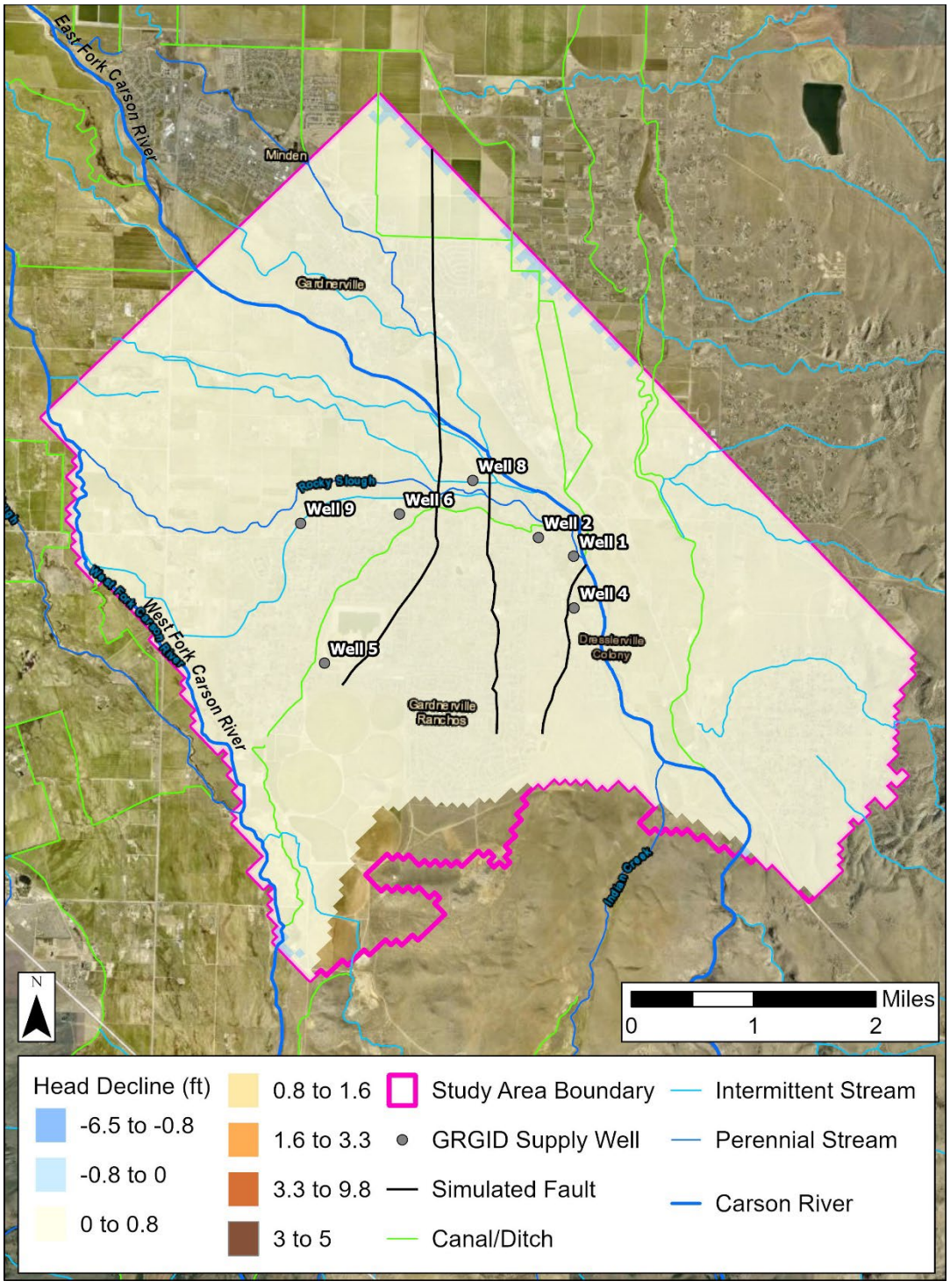

Figure 45C. Map of predictive declines in groundwater levels for simulation P2a in layer 2 relative to the base-case model for May 2034 under a pumping increase of 0.2% annually at Gardnerville Ranchos supply wells and no temperature change. Areas in blue (negative values) have higher groundwater levels compared to the base-case model and areas in orange (positive values) have lower groundwater levels.

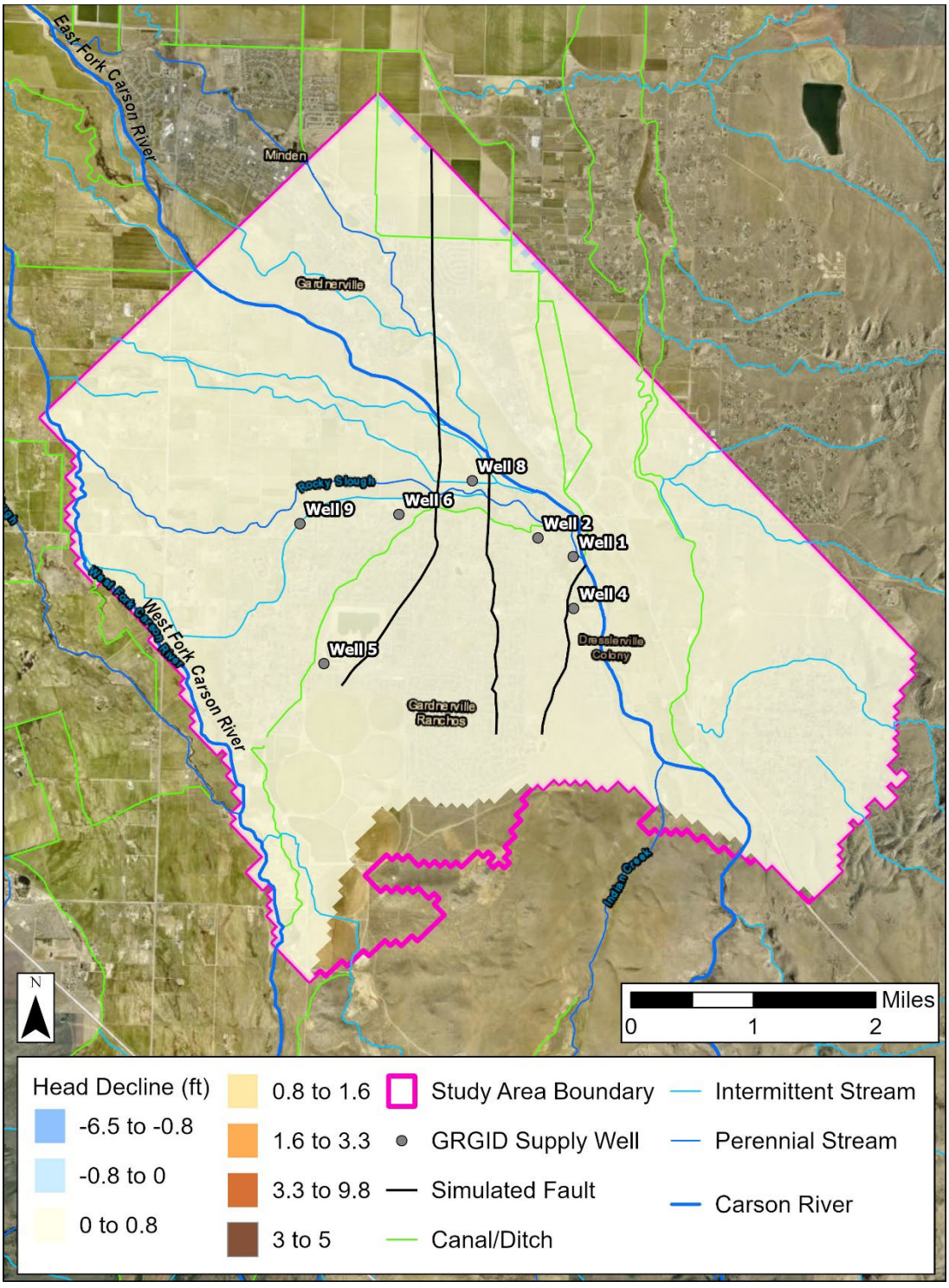

Figure 45D. Map of predictive declines in groundwater levels for simulation P2a in layer 2 relative to the base-case model for September 2034 under a pumping increase of 0.2% annually at Gardnerville Ranchos supply wells and no temperature change. Areas in blue (negative values) have higher groundwater levels compared to the base-case model and areas in orange (positive values) have lower groundwater levels.

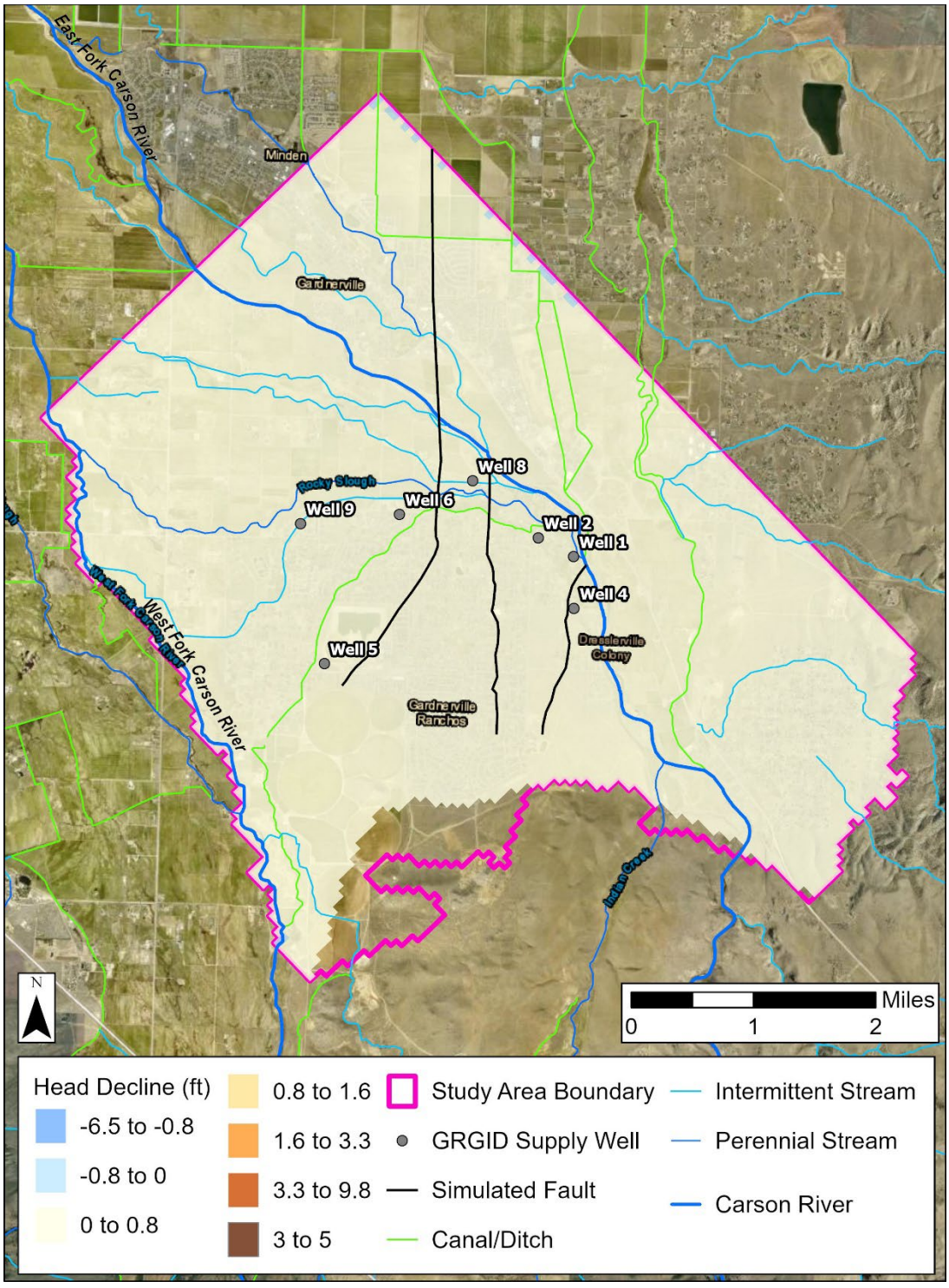

Figure 45E. Map of predictive declines in groundwater levels for simulation P2a in layer 2 relative to the base-case model for May 2043 under a pumping increase of 0.2% annually at Gardnerville Ranchos supply wells and no temperature change. Areas in blue (negative values) have higher groundwater levels compared to the base-case model and areas in orange (positive values) have lower groundwater levels.

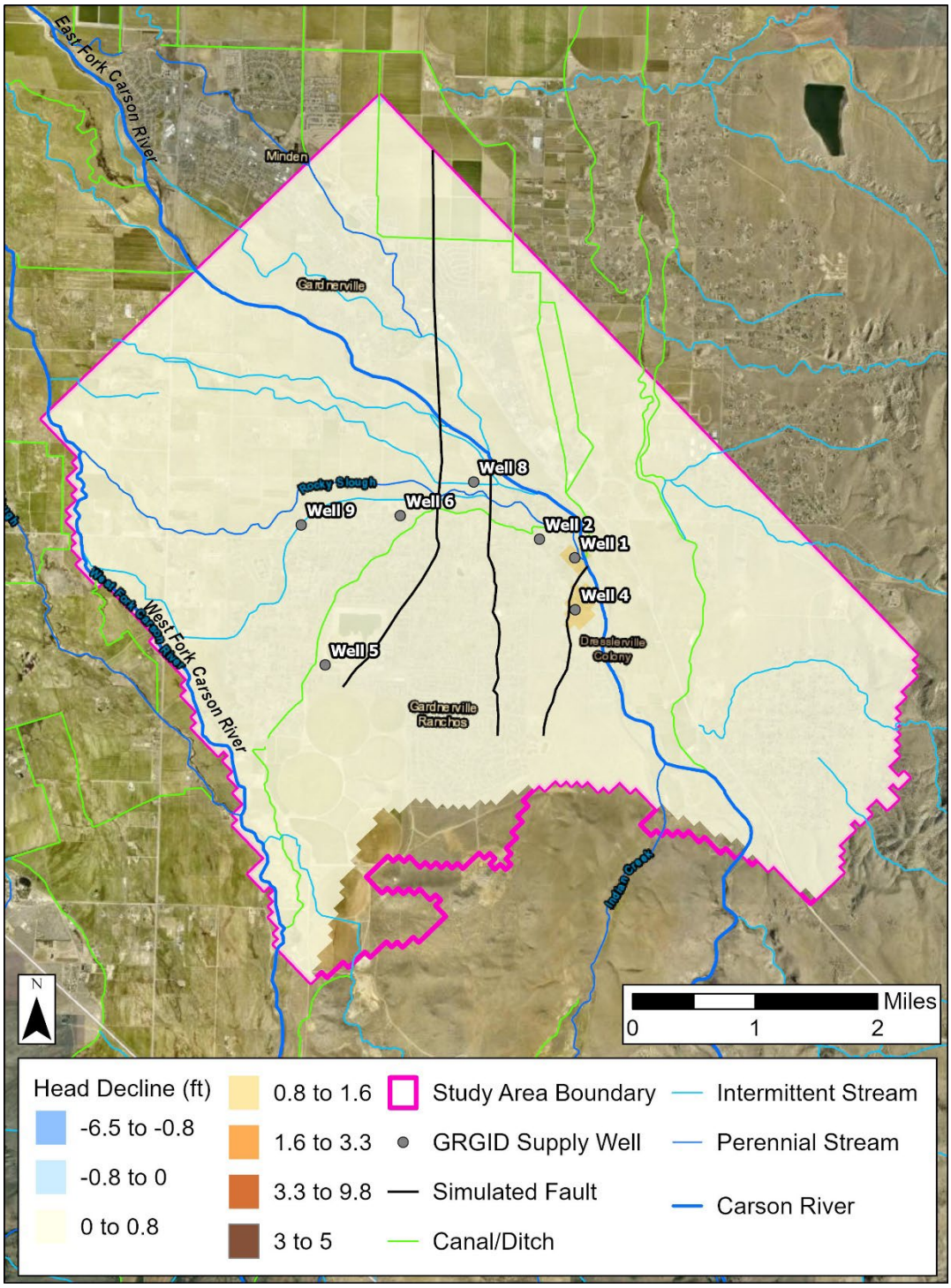

Figure 45F. Map of predictive declines in groundwater levels for simulation P2a in layer 2 relative to the base-case model for September 2043 under a pumping increase of 0.2% annually at Gardnerville Ranchos supply wells and no temperature change. Areas in blue (negative values) have higher groundwater levels compared to the base-case model and areas in orange (positive values) have lower groundwater levels.

3.9.4.4 Combined Effects of Pumping and Climate on Groundwater Levels

Pumping simulations P1b, P1c, P2b, and P2c simulate the combined effects of pumping and temperature increases to groundwater levels. An annual pumping increase of 1.5% is represented in simulations P1b and P1c, and temperature increases of 0.1°F/yr (0.05°C/yr) and 0.2°F/yr (0.1°C/yr) above average are captured by P1b and P1c, respectively.

Simulations P1b and P1c show the impact of increased pumping rates on heads. When compared to climate simulations C2F and C4F (no annual increase in pumping), the magnitude and extent of head decline is greater because of increased pumping rates. Of all predictive simulations, the greatest head change occurs in southern and eastern Gardnerville Ranchos under a pumping increase of 1.5% annually and temperature increase of 0.2°F/yr (0.1°C/yr) (simulation P1c; Figure 47F). This zone of high head change is associated with pumping at Wells 1, 2, and 4 and low permeability of the Central and East Faults. There is a distinct change in the magnitude of head change at the Central Fault; with a 1.6 to 3.3 ft (0.5 to 1 m) decline on the west side and 3.3 to 9.8 ft (1 to 3 m) decline on the east side. The zone of high head change extends east beyond Well 4 because of the combined effects of pumping at Well 4, the East Fault barrier effect, and low transmissivity of the aquifer surrounding Well 4.

Like climate simulations C2F and C4F, there is a balance between earlier streamflow and reduced stream discharge that affect seasonal and long-term water levels in simulations P1b and P1c. In 2025, water levels increase overall as streamflow enters the valley earlier with increasing temperature (Figure 46A-B; Figure 47A-B).

In September 2034, streamflow timing and discharge at different temperatures both play a role in groundwater level changes. Simulation P1b shows that heads decline throughout the model domain in 2034 of <10 ft (<3 m) in response to a +0.1°F/yr (0.05°C/yr) change, with the greatest decreases in eastern and southern Gardnerville Ranchos (Figure 46C-D). In comparison to pumping simulation P1a (no temperature increase), the spatial extent of head decline grows in simulation P1b because of reduced streamflow and stream infiltration. Simulation P1c illustrates that, in September 2034, under a +0.2°F/yr (0.1°C/yr) temperature change, earlier streamflow maintains higher groundwater levels in the southwest portion of the model domain and the spatial extent of head decline in eastern Gardnerville Ranchos is less than P1b (Figure 47D).

In May and September 2043, the magnitude and extent of head change grows throughout the model domain with temperature increase. This suggests that, in 2043, the benefits of earlier streamflow to water levels in the Gardnerville Ranchos area are outweighed by the annual decreases in stream discharge (and stream infiltration) under both a 0.1°F/yr (0.05°C/yr) (Figure 46E-F) and 0.2°F/yr (0.1°C/yr) (Figure 47E-F) temperature increase.

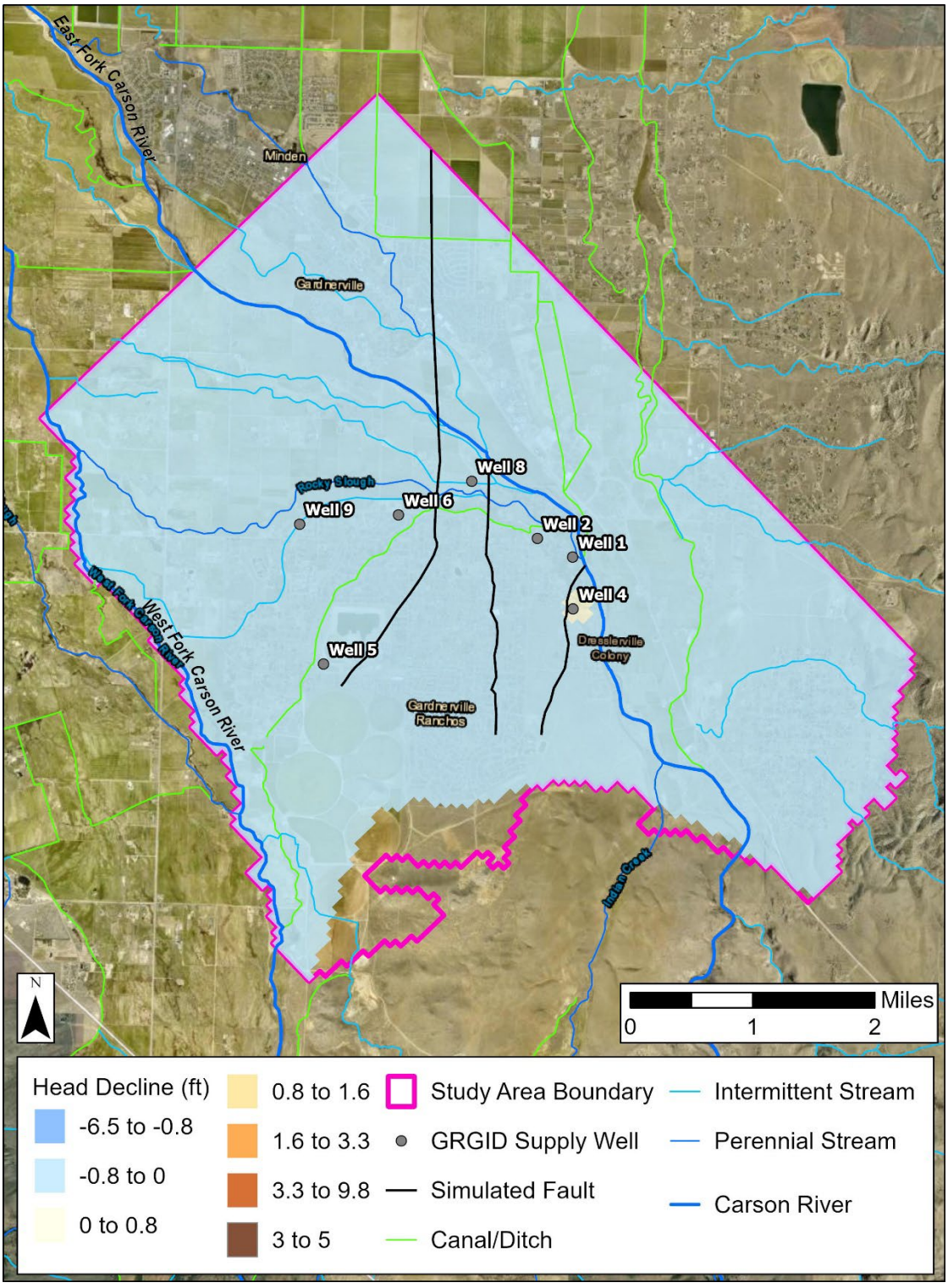

Figure 46A. Map of predictive declines in groundwater levels for simulation P1b in model layer 2 relative to the base-case model for May 2025 under a pumping increase of 1.5% annually at Gardnerville Ranchos supply wells and temperature increase of 0.1°F/yr (0.05°C/yr) above average. Areas in blue (negative values) have higher groundwater levels compared to the base-case model and areas in orange (positive values) have lower groundwater levels.

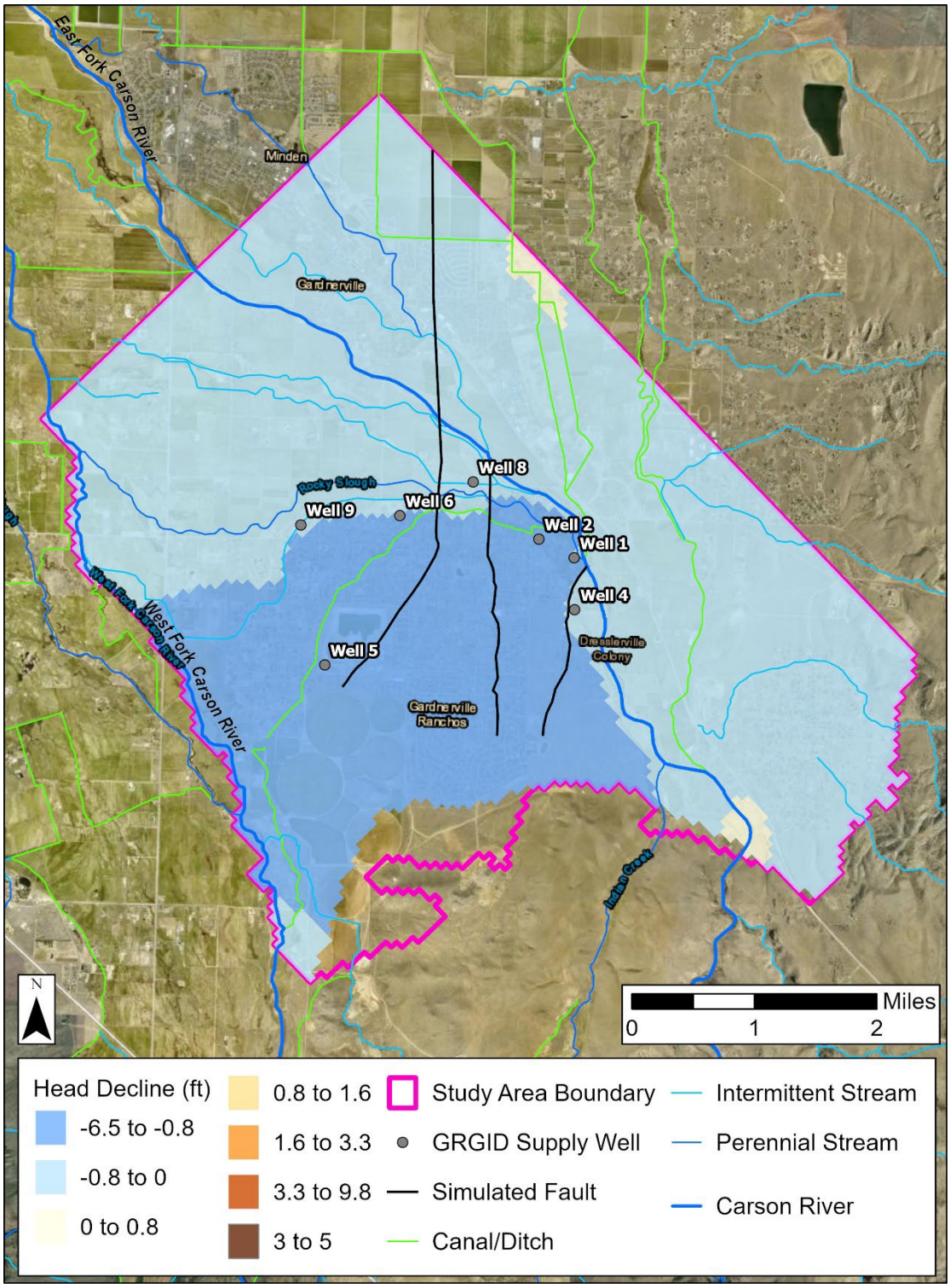

Figure 46B. Map of predictive declines in groundwater levels for simulation P1b in model layer 2 relative to the base-case model for September 2025 under a pumping increase of 1.5% annually at Gardnerville Ranchos supply wells and temperature increase of 0.1°F/yr (0.05°C/yr) above average. Areas in blue (negative values) have higher groundwater levels compared to the base-case model and areas in orange (positive values) have lower groundwater levels.

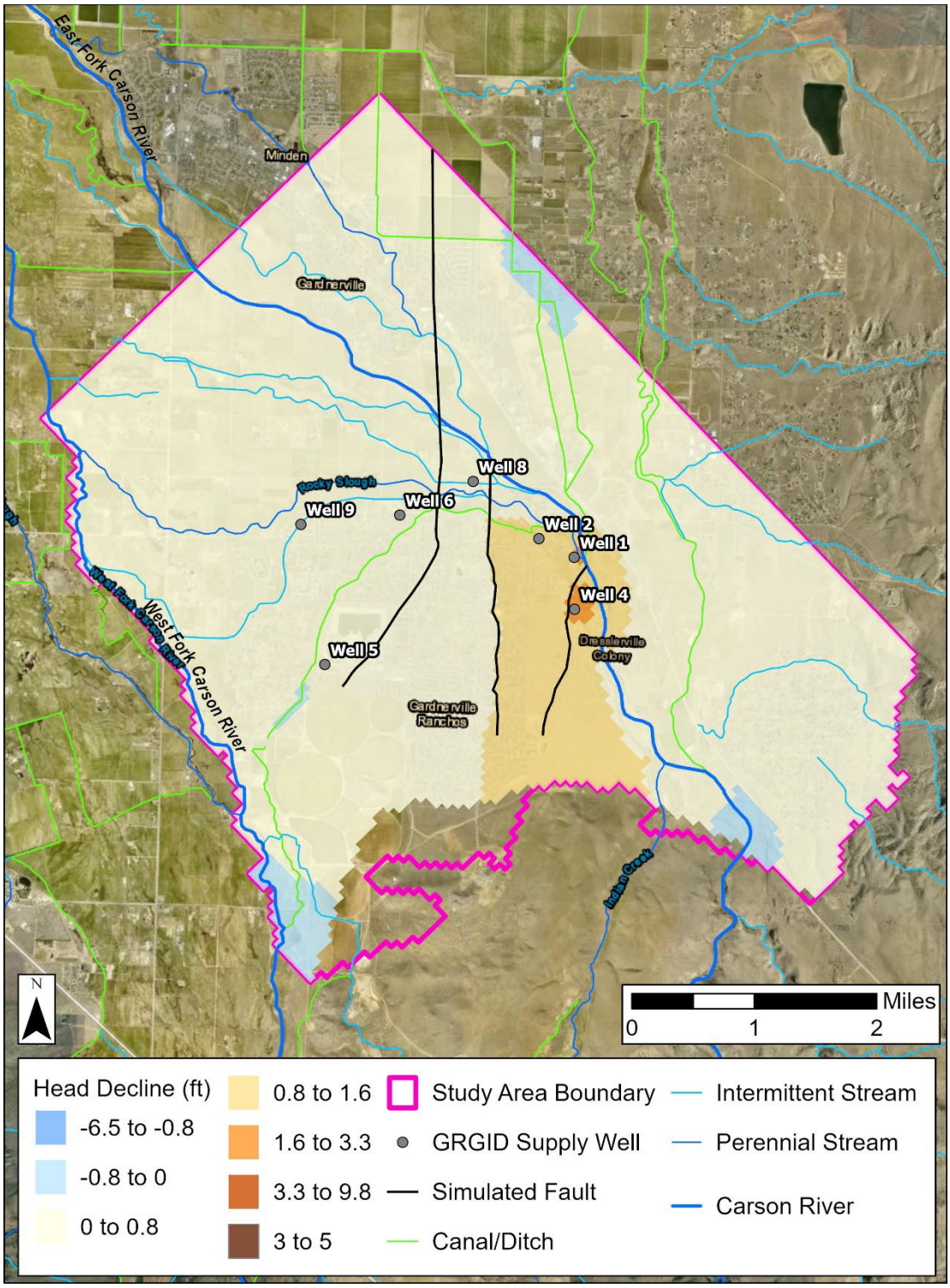

Figure 46C. Map of predictive declines in groundwater levels for simulation P1b in model layer 2 relative to the base-case model for May 2034 under a pumping increase of 1.5% annually at Gardnerville Ranchos supply wells and temperature increase of 0.1°F/yr (0.05°C/yr) above average. Areas in blue (negative values) have higher groundwater levels compared to the base-case model and areas in orange (positive values) have lower groundwater levels.

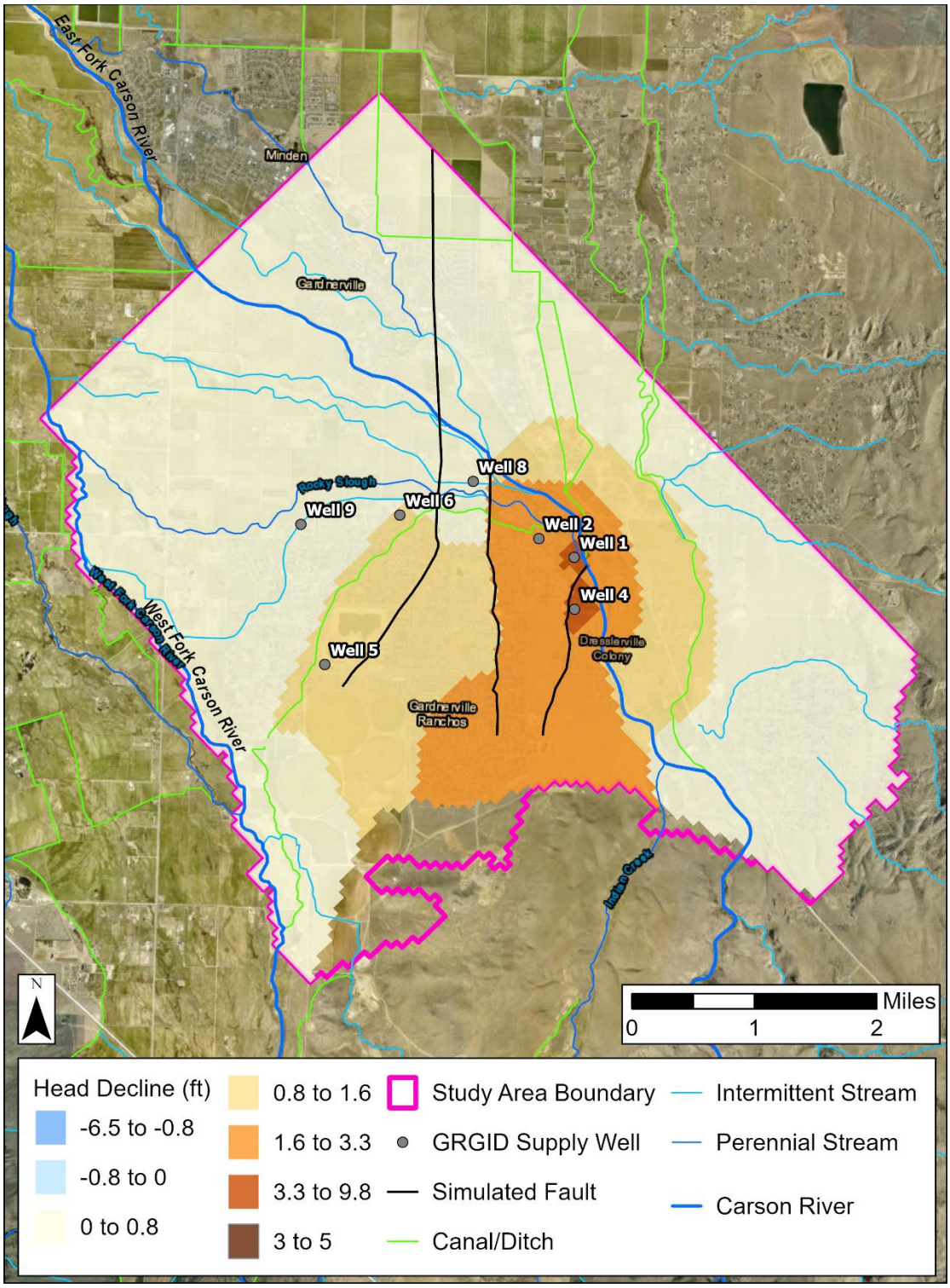

Figure 46D. Map of predictive declines in groundwater levels for simulation P1b in model layer 2 relative to the base-case model for September 2034 under a pumping increase of 1.5% annually at Gardnerville Ranchos supply wells and temperature increase of 0.1°F/yr (0.05°C/yr) above average. Areas in blue (negative values) have higher groundwater levels compared to the base-case model and areas in orange (positive values) have lower groundwater levels.

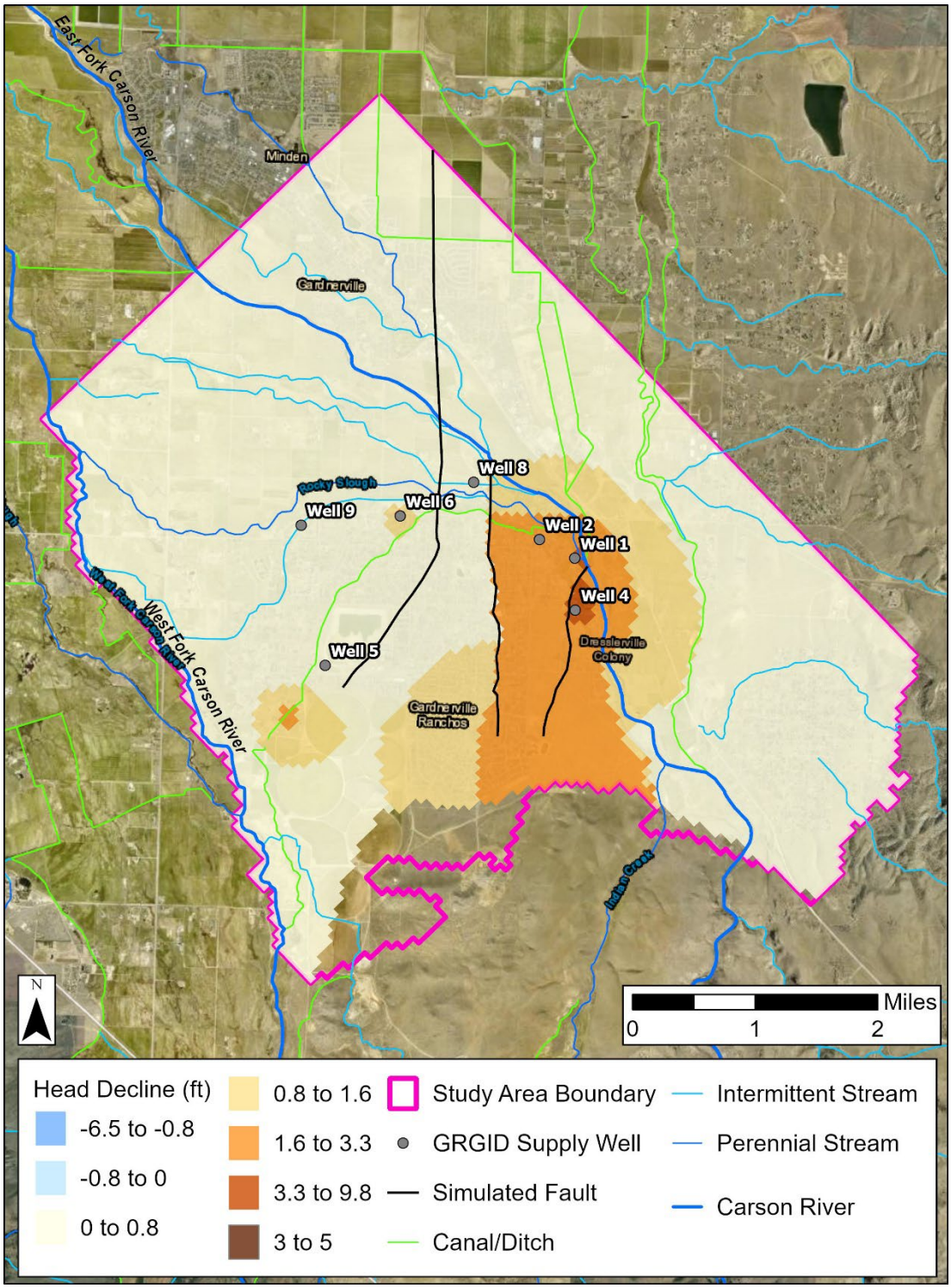

Figure 46E. Map of predictive declines in groundwater levels for simulation P1b in model layer 2 relative to the base-case model for May 2043 under a pumping increase of 1.5% annually at Gardnerville Ranchos supply wells and temperature increase of 0.1°F/yr (0.05°C/yr) above average. Areas in blue (negative values) have higher groundwater levels compared to the base-case model and areas in orange (positive values) have lower groundwater levels.

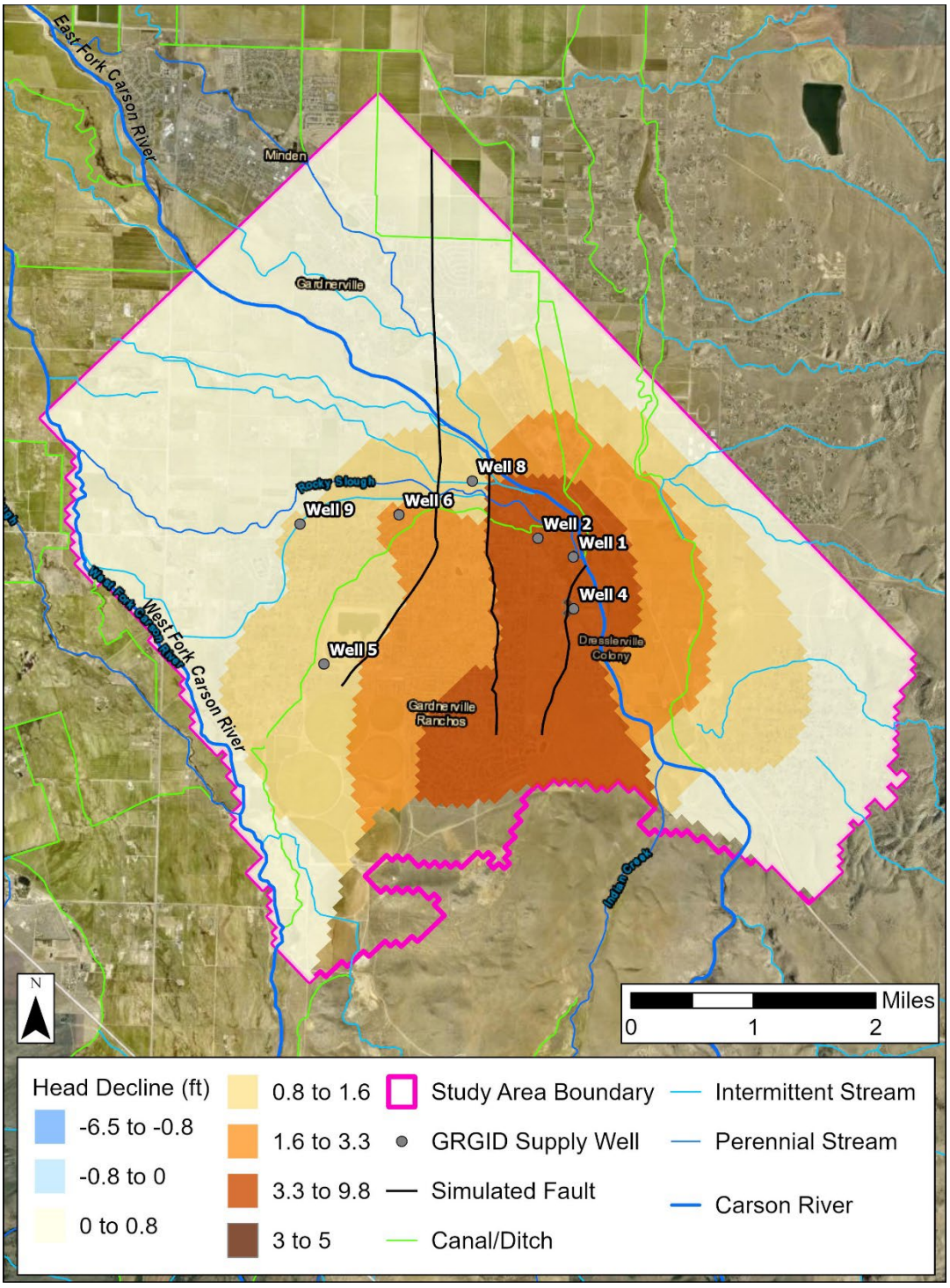

Figure 46F. Map of predictive declines in groundwater levels for simulation P1b in model layer 2 relative to the base-case model for September 2043 under a pumping increase of 1.5% annually at Gardnerville Ranchos supply wells and temperature increase of 0.1°F/yr (0.05°C/yr) above average. Areas in blue (negative values) have higher groundwater levels compared to the base-case model and areas in orange (positive values) have lower groundwater levels.

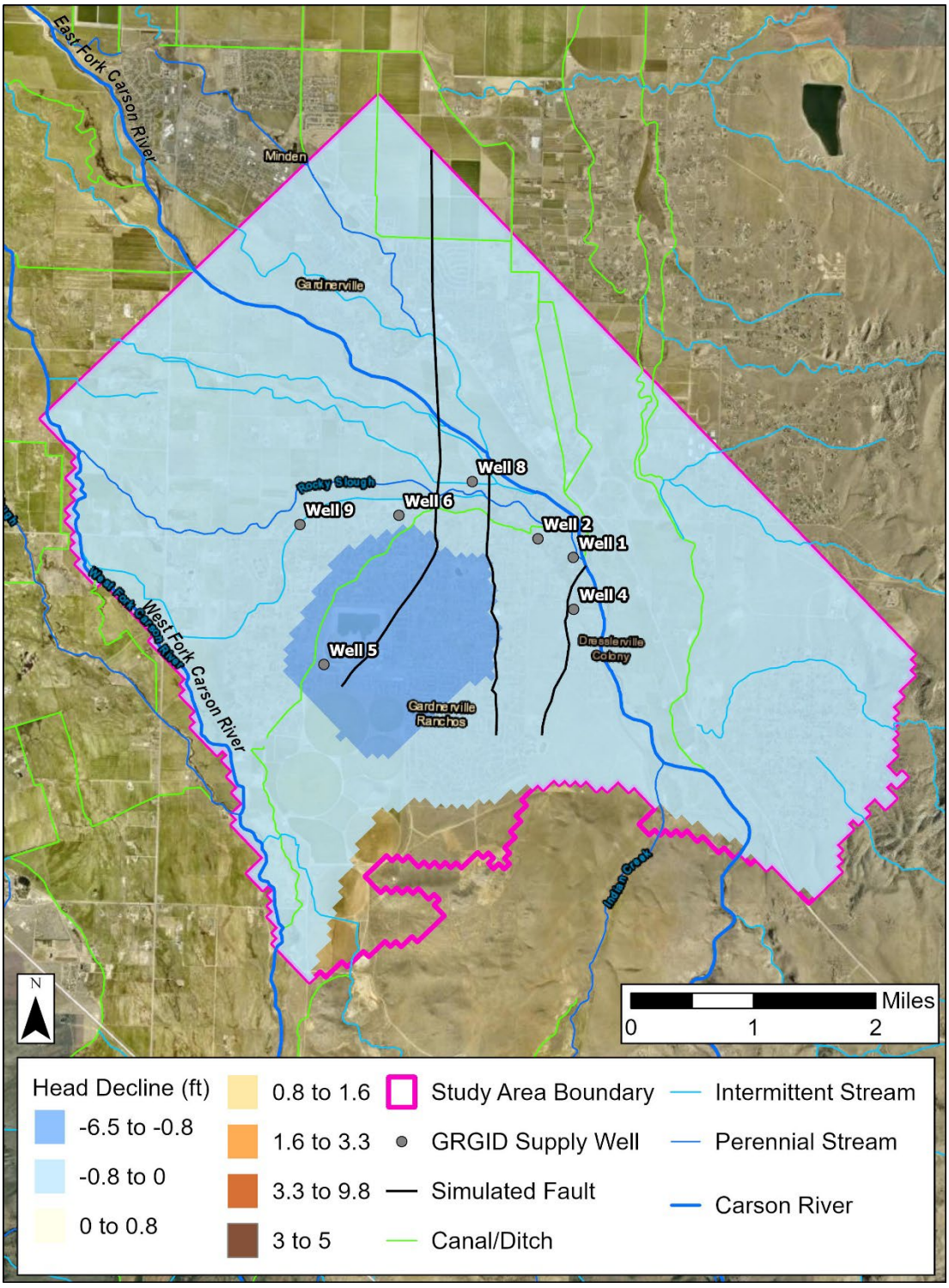

Figure 47A. Map of predictive declines in groundwater levels for simulation P1c in model layer 2 relative to the base-case model for May 2025 under a pumping increase of 1.5% annually at Gardnerville Ranchos supply wells and temperature increase of 0.2°F/yr (0.1°C/yr) above average. Areas in blue (negative values) have higher groundwater levels compared to the base-case model and areas in orange (positive values) have lower groundwater levels.

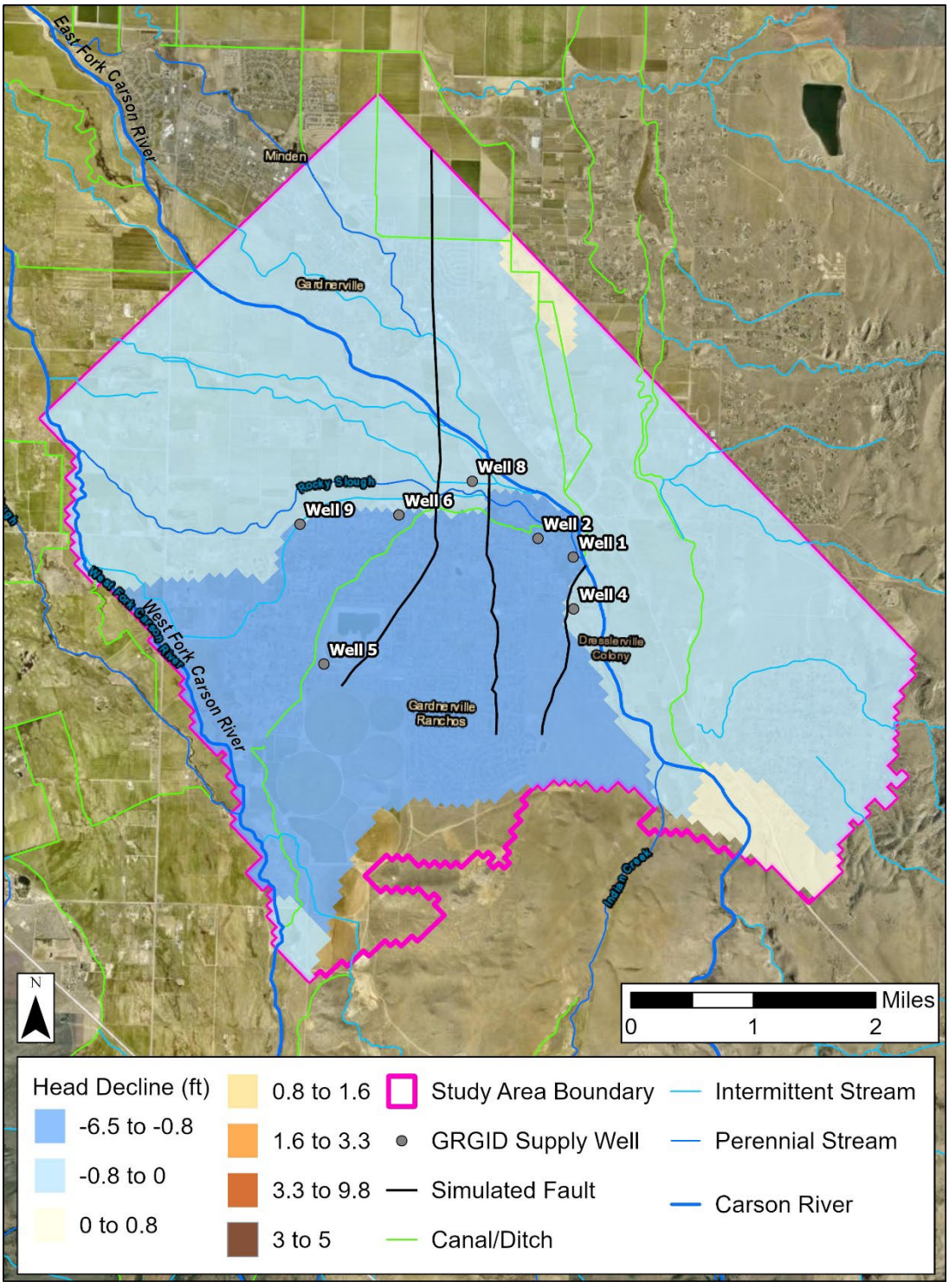

Figure 47B. Map of predictive declines in groundwater levels for simulation P1c in model layer 2 relative to the base-case model for September 2025 under a pumping increase of 1.5% annually at Gardnerville Ranchos supply wells and temperature increase of 0.2°F/yr (0.1°C/yr) above average. Areas in blue (negative values) have higher groundwater levels compared to the base-case model and areas in orange (positive values) have lower groundwater levels.

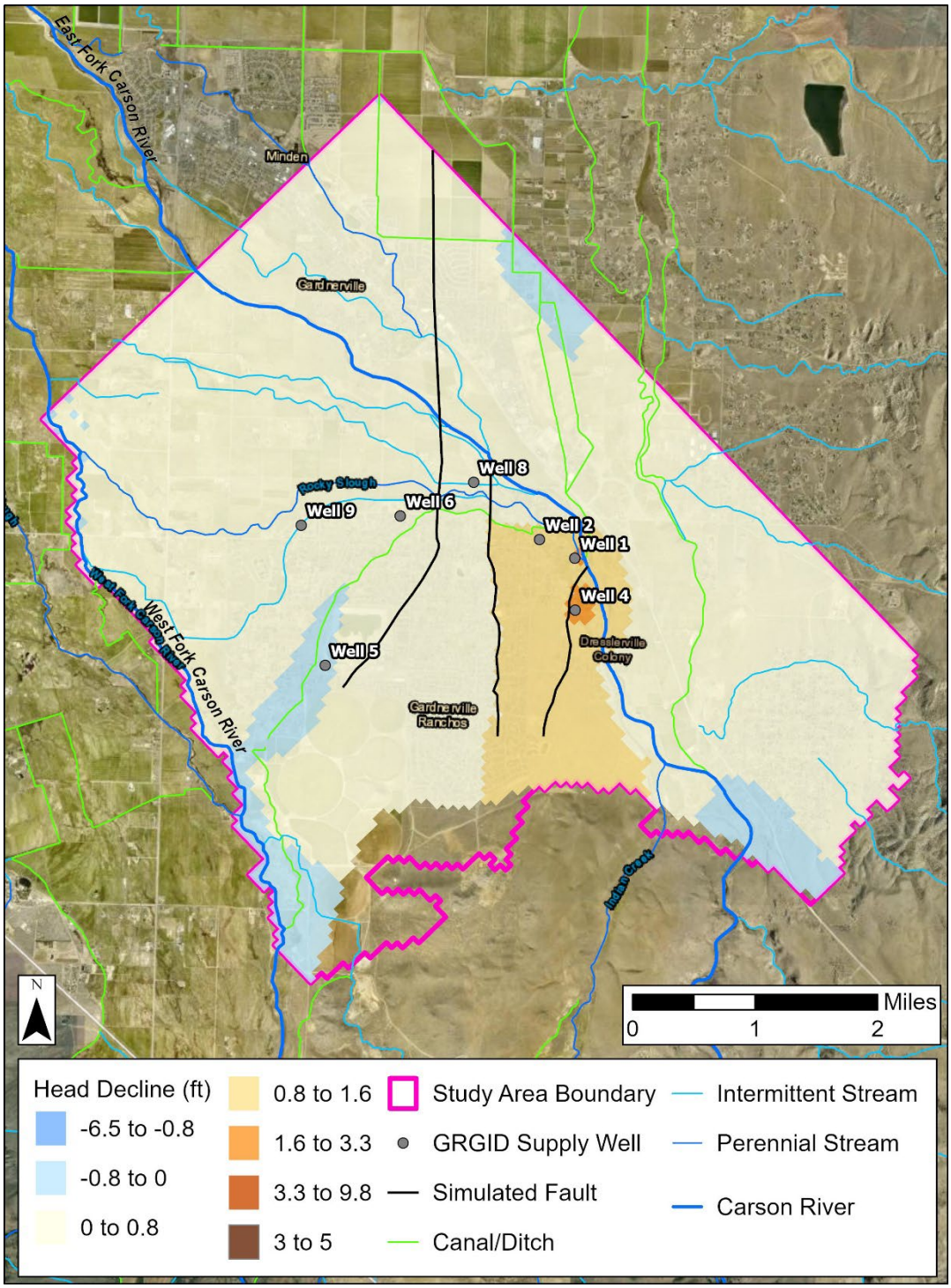

Figure 47C. Map of predictive declines in groundwater levels for simulation P1c in model layer 2 relative to the base-case model for May 2034 under a pumping increase of 1.5% annually at Gardnerville Ranchos supply wells and temperature increase of 0.2°F/yr (0.1°C/yr) above average. Areas in blue (negative values) have higher groundwater levels compared to the base-case model and areas in orange (positive values) have lower groundwater levels.

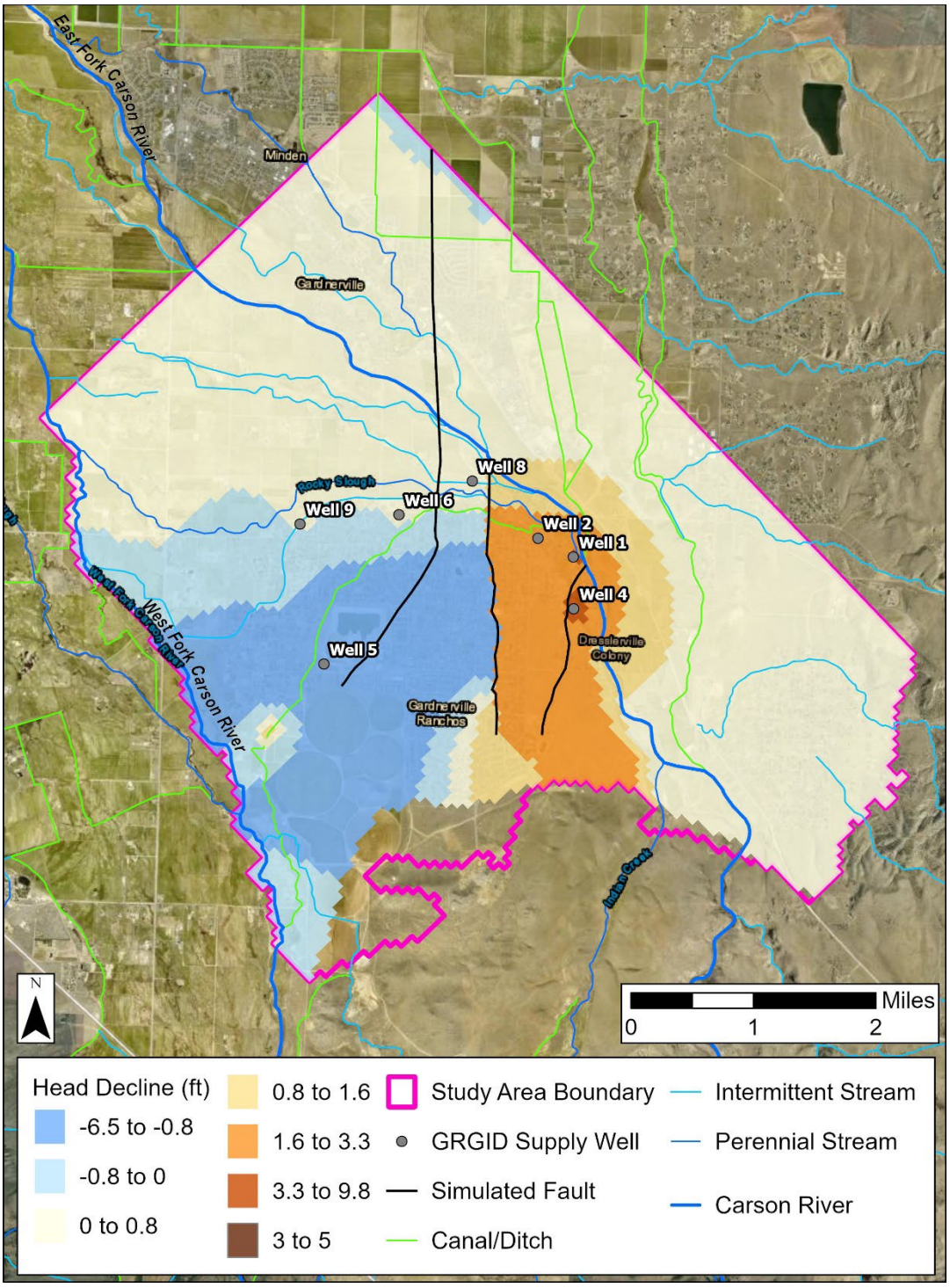

Figure 47D. Map of predictive declines in groundwater levels for simulation P1c in model layer 2 relative to the base-case model for September 2034 under a pumping increase of 1.5% annually at Gardnerville Ranchos supply wells and temperature increase of 0.2°F/yr (0.1°C/yr) above average. Areas in blue (negative values) have higher groundwater levels compared to the base-case model and areas in orange (positive values) have lower groundwater levels.

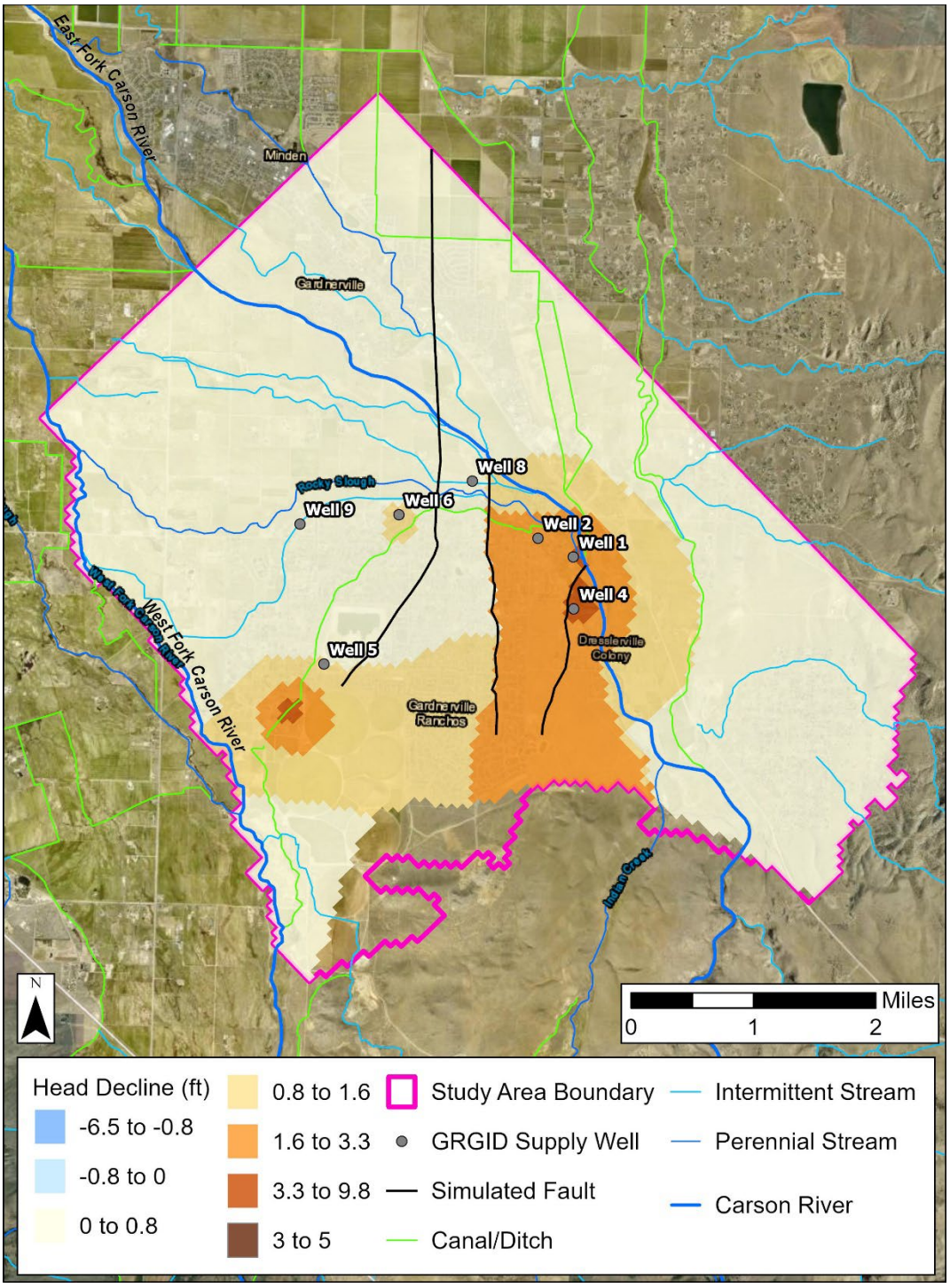

Figure 47E. Map of predictive declines in groundwater levels for simulation P1c in model layer 2 relative to the base-case model for May 2043 under a pumping increase of 1.5% annually at Gardnerville Ranchos supply wells and temperature increase of 0.2°F/yr (0.1°C/yr) above average. Areas in blue (negative values) have higher groundwater levels compared to the base-case model and areas in orange (positive values) have lower groundwater levels.

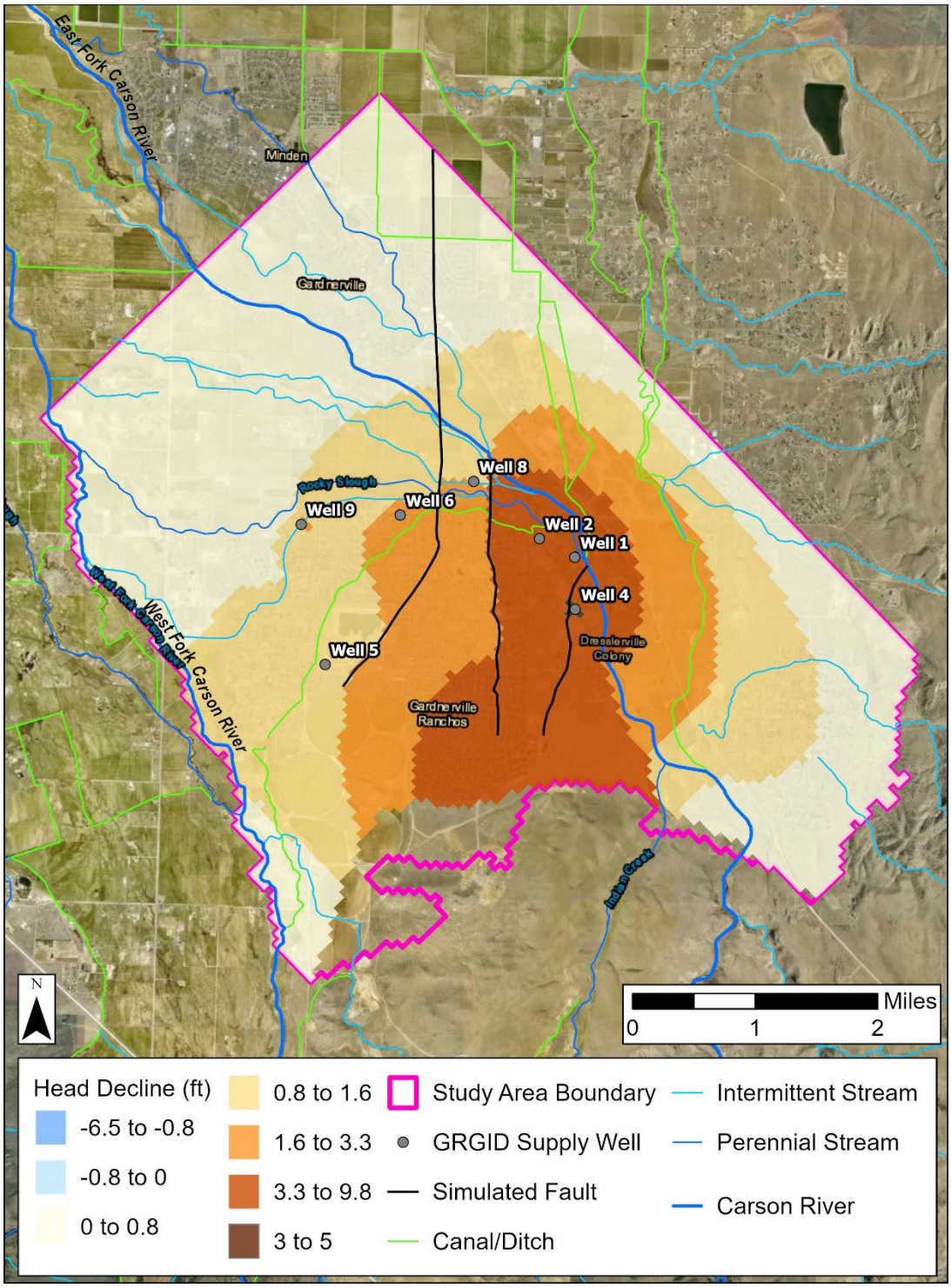

Figure 47F. Map of predictive declines in groundwater levels for simulation P1c in model layer 2 relative to the base-case model for September 2043 under a pumping increase of 1.5% annually at Gardnerville Ranchos supply wells and temperature increase of 0.2°F/yr (0.1°C/yr) above average. Areas in blue (negative values) have higher groundwater levels compared to the base-case model and areas in orange (positive values) have lower groundwater levels.

Under an annual pumping increase of 0.2% with 2F (simulation P2b) and 4F (simulation P2c) temperature increases, similar temporal and spatial trends in head changes exist compared to the 1.5% annual pumping increases (simulations P1b and P1c). The magnitude of head change is less. Earlier streamflow into the valley leads to an overall increase in heads throughout the model domain in 2025 (Figure 48A-B; 49A-B).

In the spring of 2034, heads decline in much of the southeast section of the model domain under both temperature increases (Figure 48C; 45C). In the summer of 2034, heads increase throughout most of the model domain under a 0.2°F/yr (0.1°C/yr) increase, with the greatest increase to the west of the Central Fault (0.8 to 6.5 ft; 0.25 to 2 m) (Figure 49D). Under an increase of 0.1°F/yr (0.05°C/yr) temperature increase, the water levels decrease throughout the model domain by <0.8 ft (<0.25 m) in the summer of 2025 (Figure 48D). The difference in head change between these simulations (Figures 48D and 49D) shows that reduced stream discharge leads to a head reduction under a +0.1°F/yr (+0.05°C/yr) change, while earlier recharge from streamflow contributes to increased heads under a 0.2°F/yr (0.1°C/yr) increase. This is consistent with the observed head changes under the same temperature conditions when pumping increases at 1.5% annually.

By spring 2043, heads decrease throughout the model domain under both temperature change conditions uniformly at <0.25 m (Figure 48E, 49E). Under a 0.2°F/yr (0.1°C/yr) temperature increase, there is a local depression (0.8 to 10 ft; 0.25 to 3 m head reduction) in the southwest corner of the model domain where there are many domestic wells (Figure 49E). In the summer of 2043, eastern Gardnerville Ranchos sees more pronounced head declines (0.8 to 1.6 ft; 0.25 to 0.5 m) than the rest of the model domain (<0.8 ft; <0.25 m) (Figure 48F, 49F). This zone of greater head declines is associated with the pumping of Wells 1, 2, and 4, the barrier effects of the faults, and low transmissivity and storage of the aquifer east of the East Fault near Well 4.

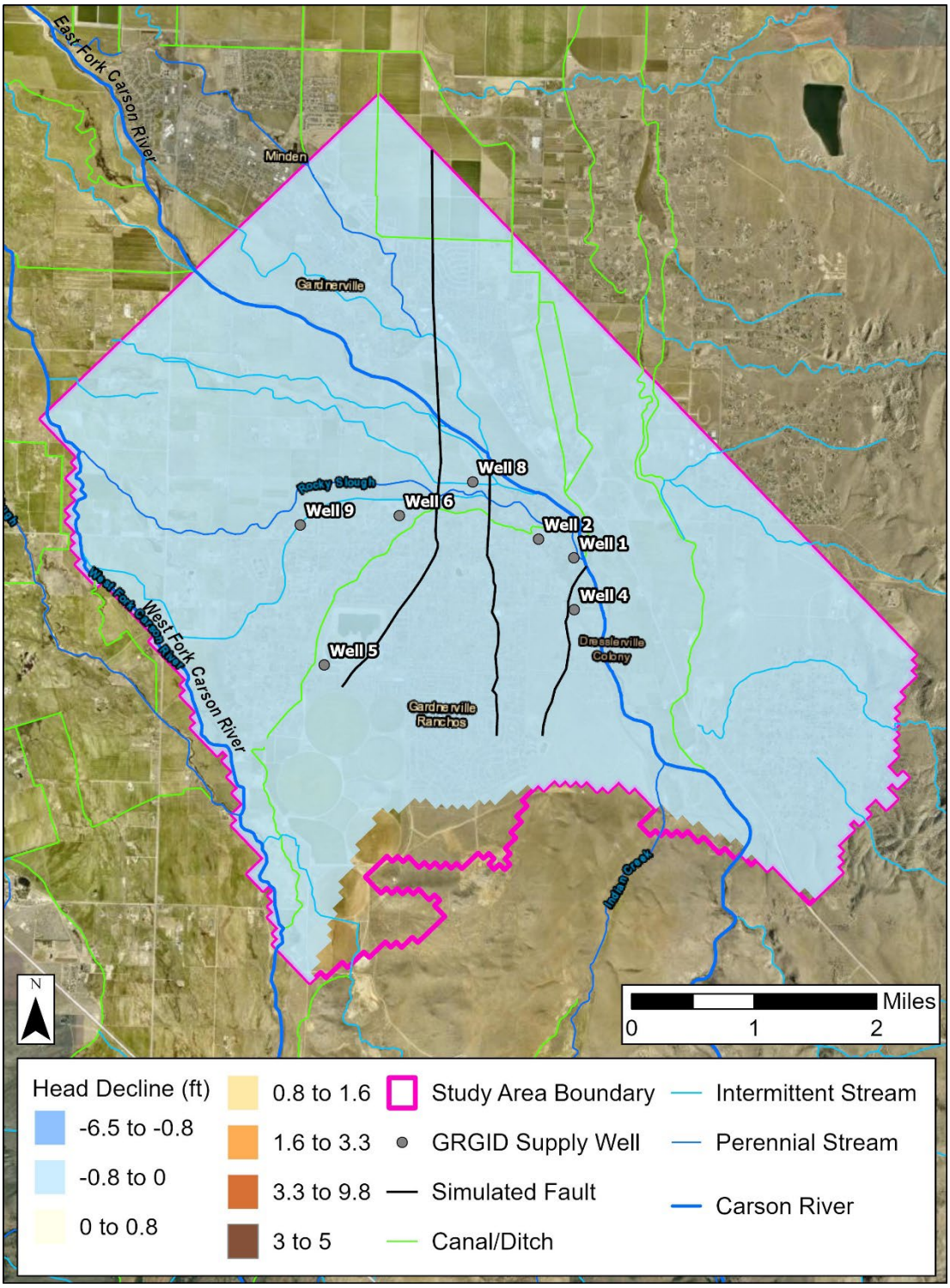

Figure 48A. Map of predictive declines in groundwater levels for simulation P2b in model layer 2 relative to the base-case model for May 2025 under a pumping increase of 0.2% annually at Gardnerville Ranchos supply wells and temperature increase of 0.1°F/yr (0.05°C/yr) above average. Areas in blue (negative values) have higher groundwater levels compared to the base-case model and areas in orange (positive values) have lower groundwater levels.

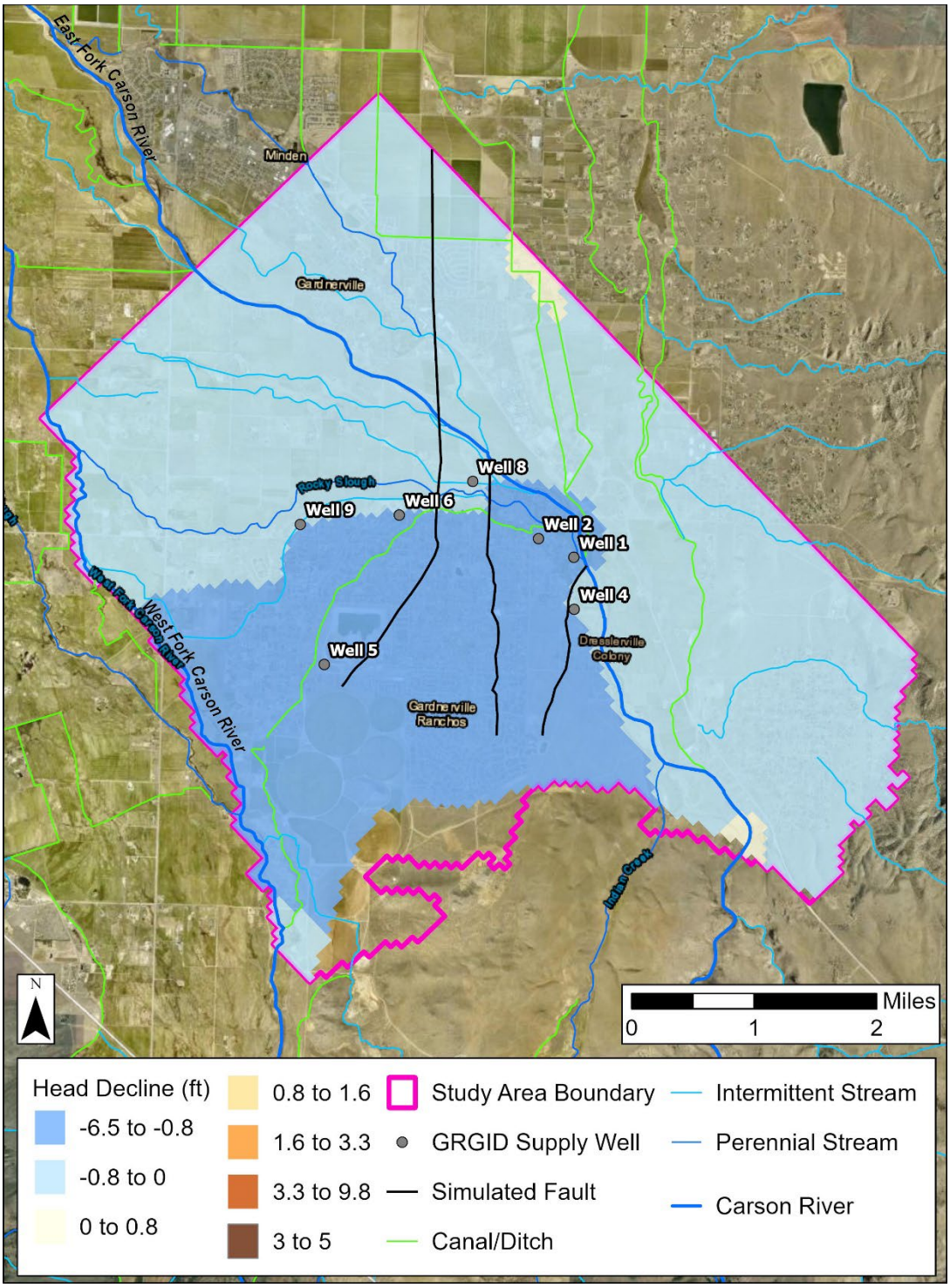

Figure 48B. Map of predictive declines in groundwater levels for simulation P2b in model layer 2 relative to the base-case model for September 2025 under a pumping increase of 0.2% annually at Gardnerville Ranchos supply wells and temperature increase of 0.1°F/yr (0.05°C/yr) above average. Areas in blue (negative values) have higher groundwater levels compared to the base-case model and areas in orange (positive values) have lower groundwater levels.

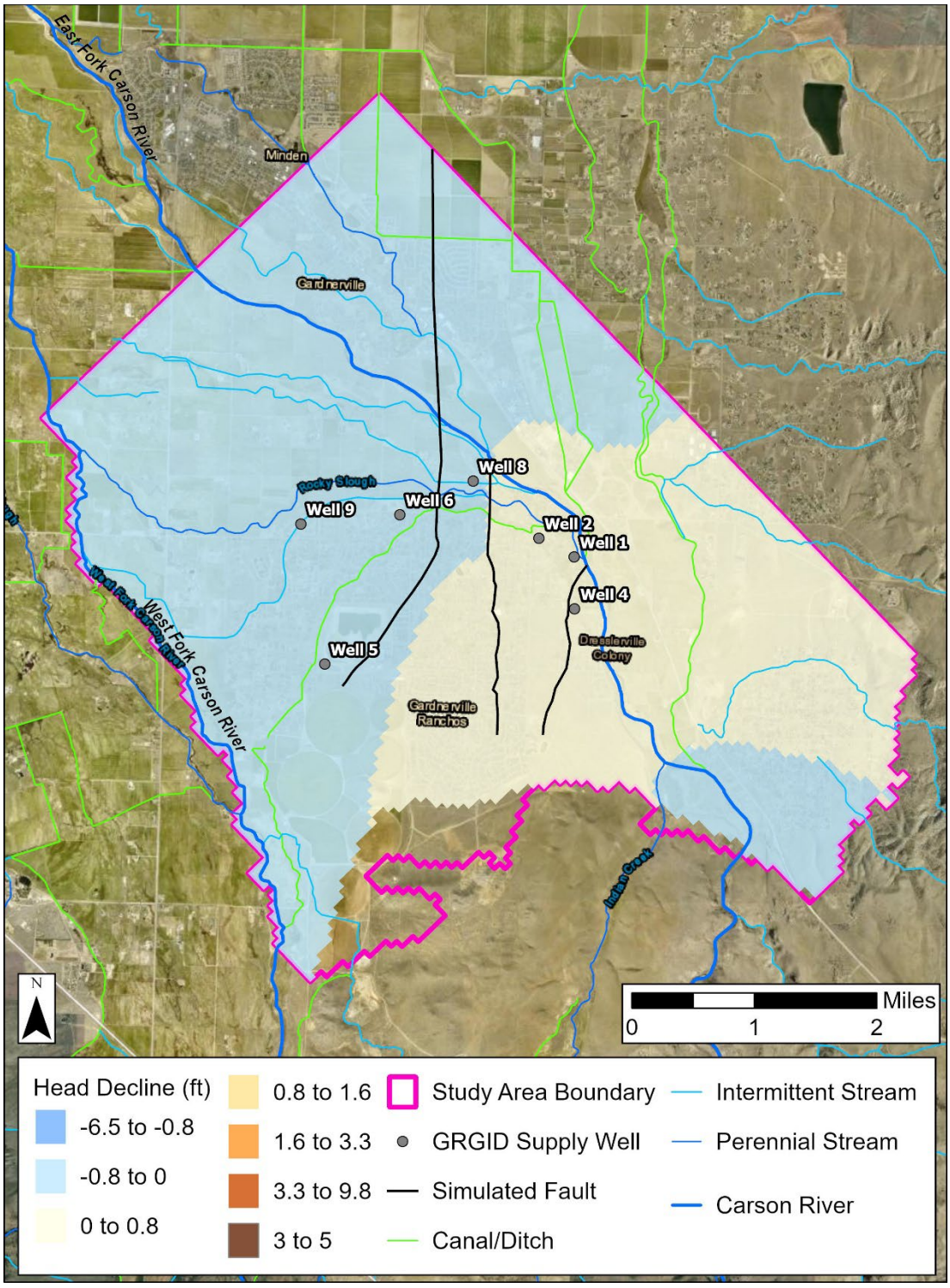

Figure 48C. Map of predictive declines in groundwater levels for simulation P2b in model layer 2 relative to the base-case model for May 2034 under a pumping increase of 0.2% annually at Gardnerville Ranchos supply wells and temperature increase of 0.1°F/yr (0.05°C/yr) above average. Areas in blue (negative values) have higher groundwater levels compared to the base-case model and areas in orange (positive values) have lower groundwater levels.

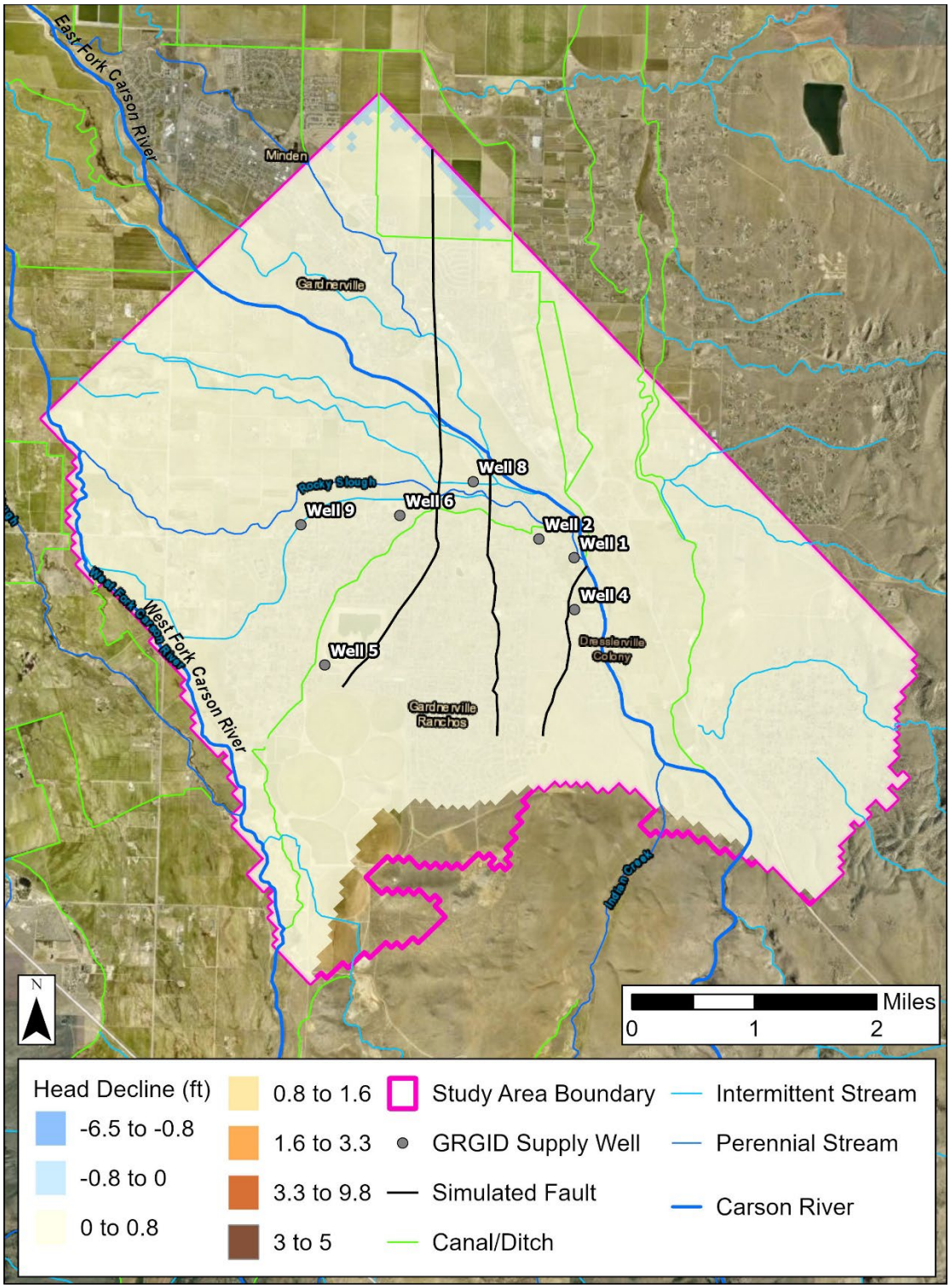

Figure 48D. Map of predictive declines in groundwater levels for simulation P2b in model layer 2 relative to the base-case model for September 2034 under a pumping increase of 0.2% annually at Gardnerville Ranchos supply wells and temperature increase of 0.1°F/yr (0.05°C/yr) above average. Areas in blue (negative values) have higher groundwater levels compared to the base-case model and areas in orange (positive values) have lower groundwater levels.

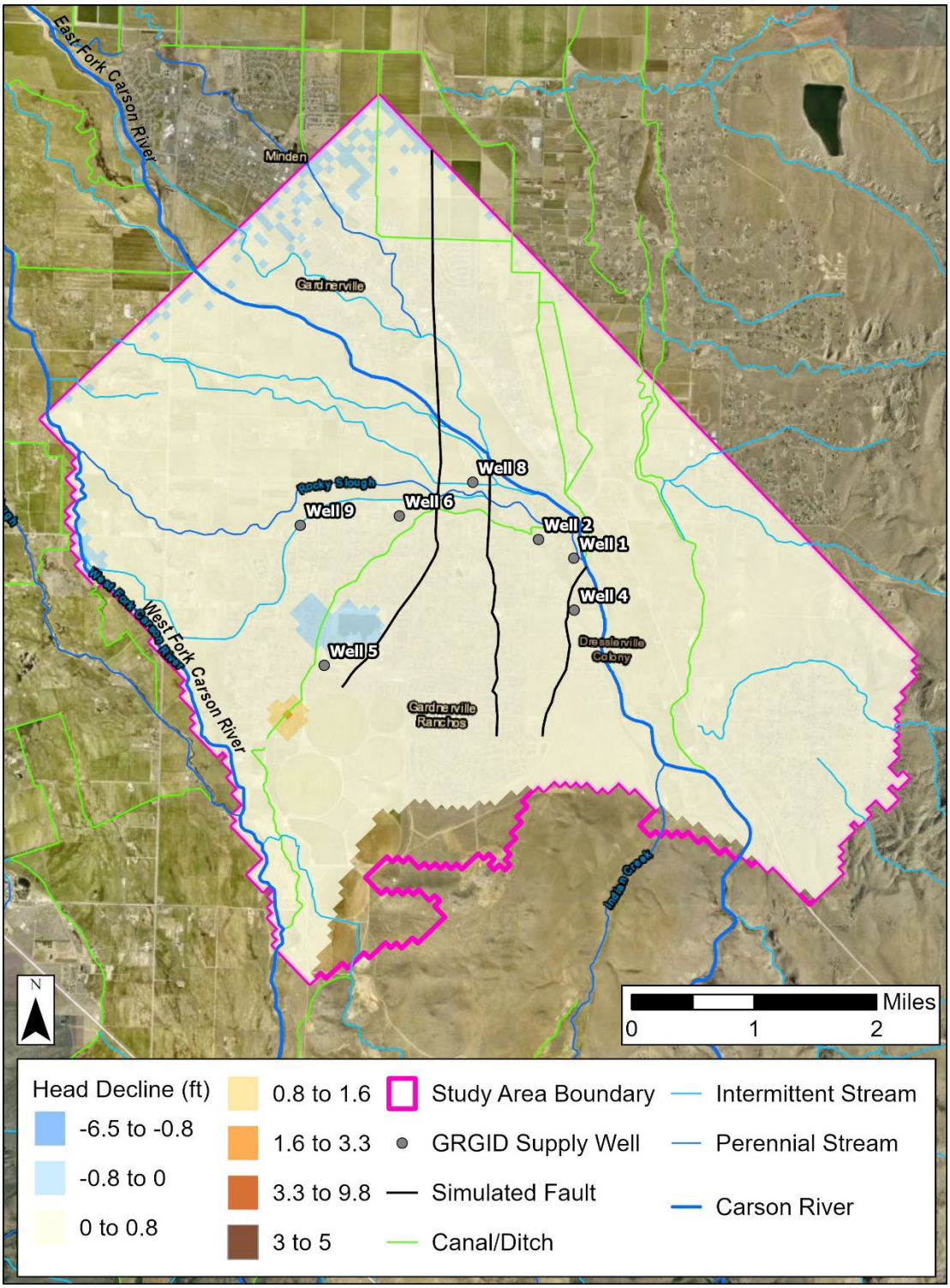

Figure 48E. Map of predictive declines in groundwater levels for simulation P2b in model layer 2 relative to the base-case model for May 2043 under a pumping increase of 0.2% annually at Gardnerville Ranchos supply wells and temperature increase of 0.1°F/yr (0.05°C/yr) above average. Areas in blue (negative values) have higher groundwater levels compared to the base-case model and areas in orange (positive values) have lower groundwater levels.

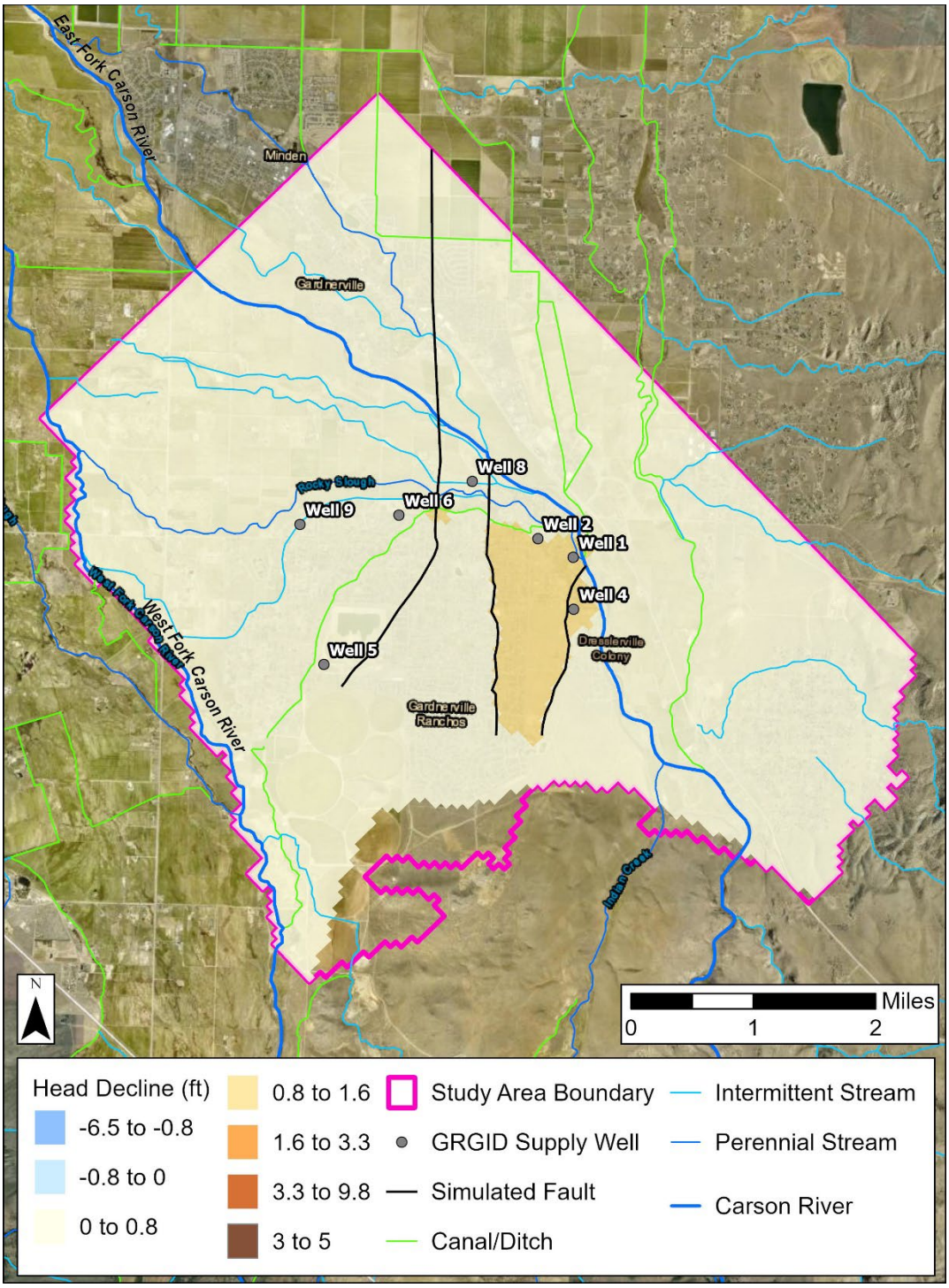

Figure 48F. Map of predictive declines in groundwater levels for simulation P2b in model layer 2 relative to the base-case model for September 2043 under a pumping increase of 0.2% annually at Gardnerville Ranchos supply wells and temperature increase of 0.1°F/yr (0.05°C/yr) above average. Areas in blue (negative values) have higher groundwater levels compared to the base-case model and areas in orange (positive values) have lower groundwater levels.

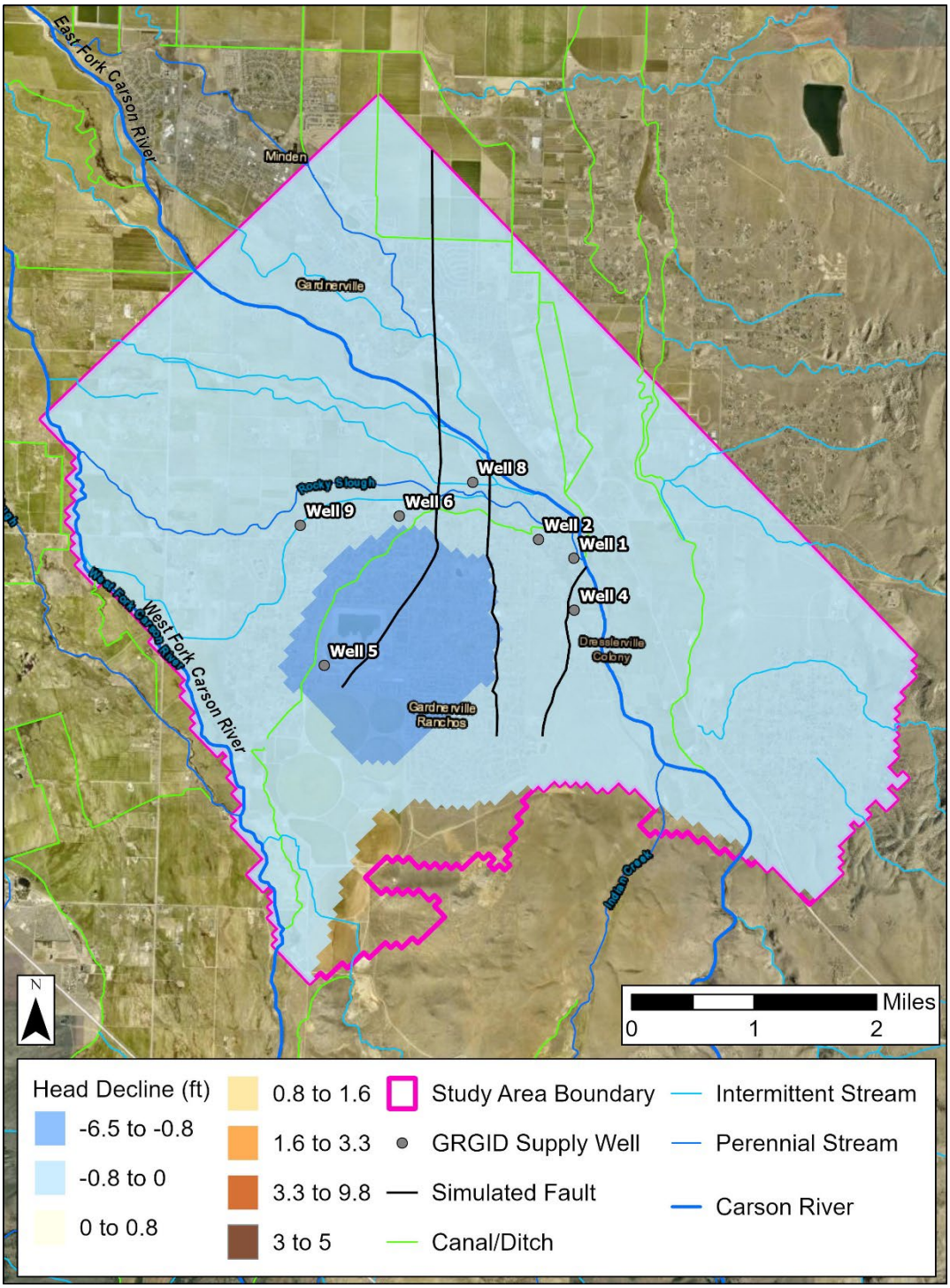

Figure 49A. Map of predictive declines in groundwater levels for simulation P2c in model layer 2 relative to the base-case model for May 2025 under a pumping increase of 0.2% annually at Gardnerville Ranchos supply wells and temperature increase of 0.2°F/yr (0.1°C/yr) above average. Areas in blue (negative values) have higher groundwater levels compared to the base-case model and areas in orange (positive values) have lower groundwater levels.

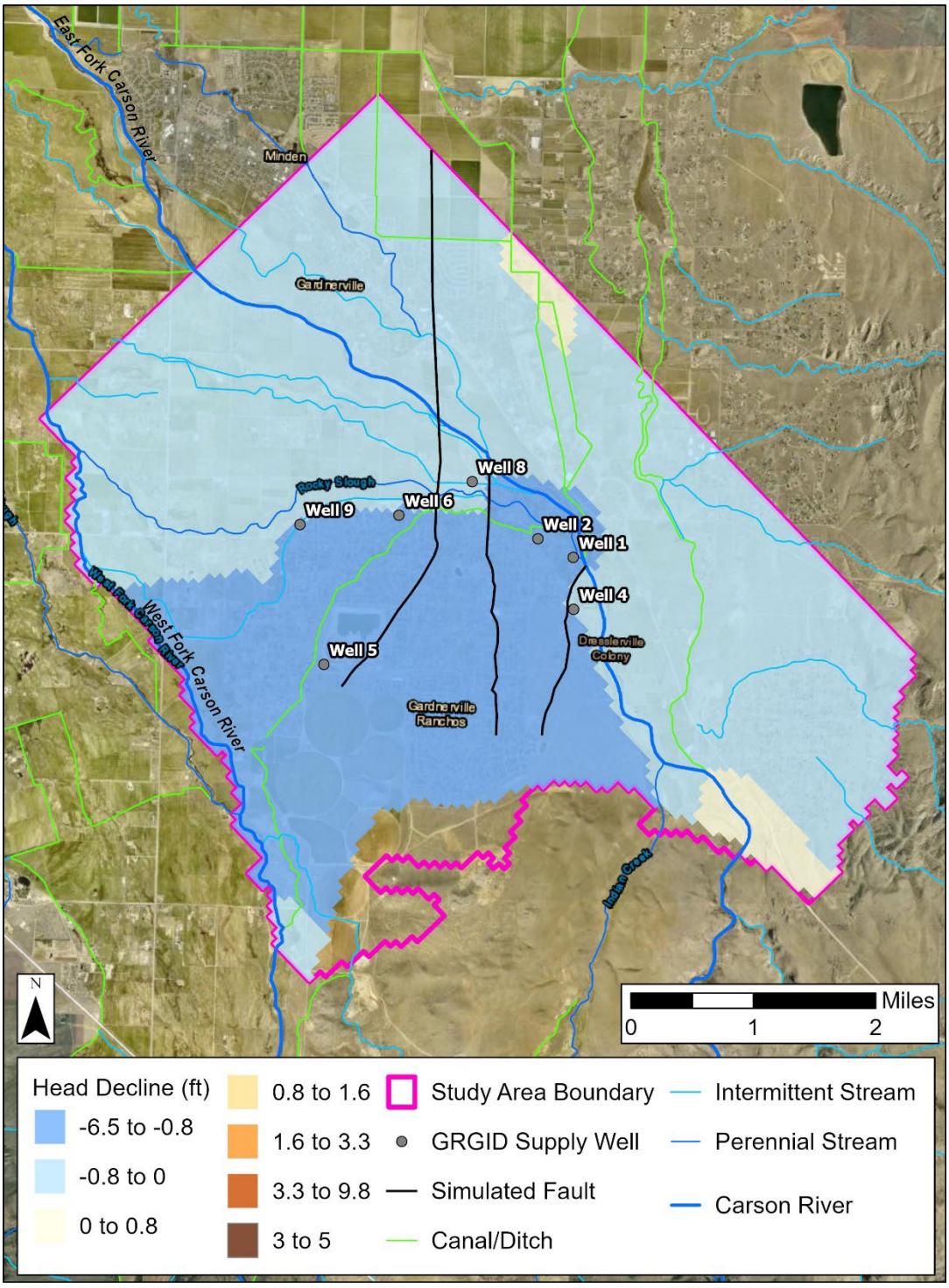

Figure 49B. Map of predictive declines in groundwater levels for simulation P2c in model layer 2 relative to the base-case model for September 2025 under a pumping increase of 0.2% annually at Gardnerville Ranchos supply wells and temperature increase of 0.2°F/yr (0.1°C/yr) above average. Areas in blue (negative values) have higher groundwater levels compared to the base-case model and areas in orange (positive values) have lower groundwater levels.

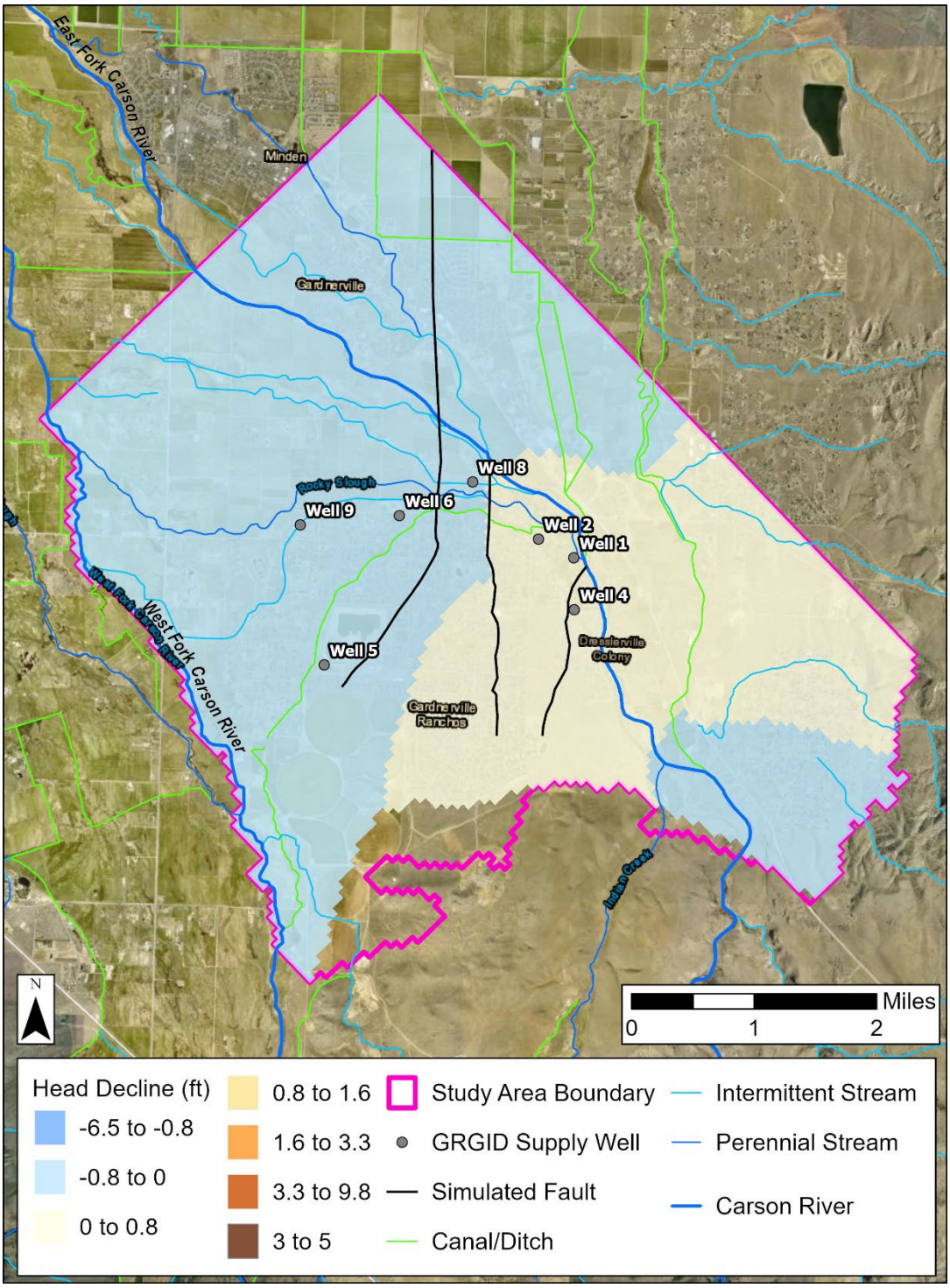

Figure 49C. Map of predictive declines in groundwater levels for simulation P2c in model layer 2 relative to the base-case model for May 2034 under a pumping increase of 0.2% annually at Gardnerville Ranchos supply wells and temperature increase of 0.2°F/yr (0.1°C/yr) above average. Areas in blue (negative values) have higher groundwater levels compared to the base-case model and areas in orange (positive values) have lower groundwater levels.

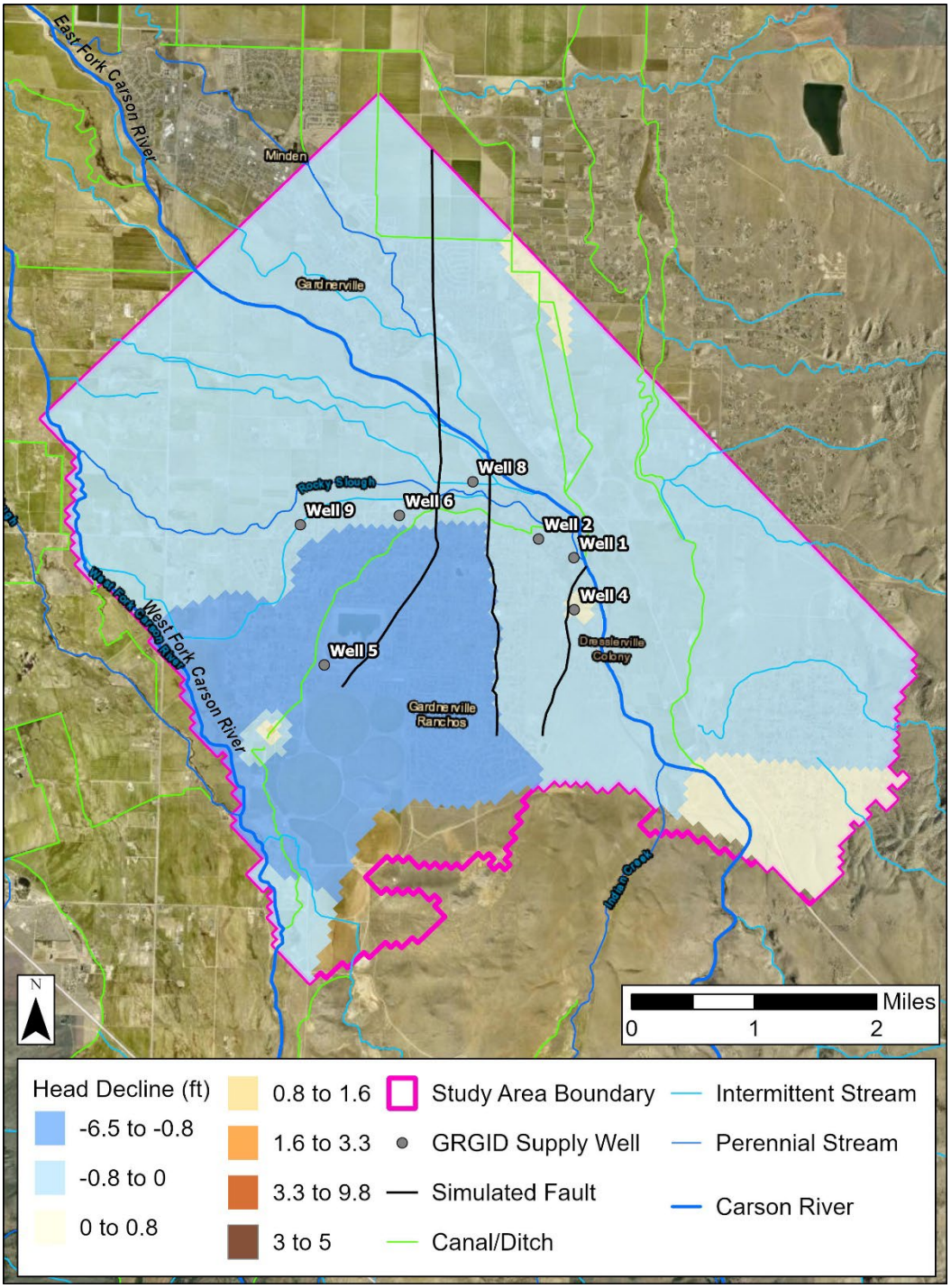

Figure 49D. Map of predictive declines in groundwater levels for simulation P2c in model layer 2 relative to the base-case model for September 2034 under a pumping increase of 0.2% annually at Gardnerville Ranchos supply wells and temperature increase of 0.2°F/yr (0.1°C/yr) above average. Areas in blue (negative values) have higher groundwater levels compared to the base-case model and areas in orange (positive values) have lower groundwater levels.

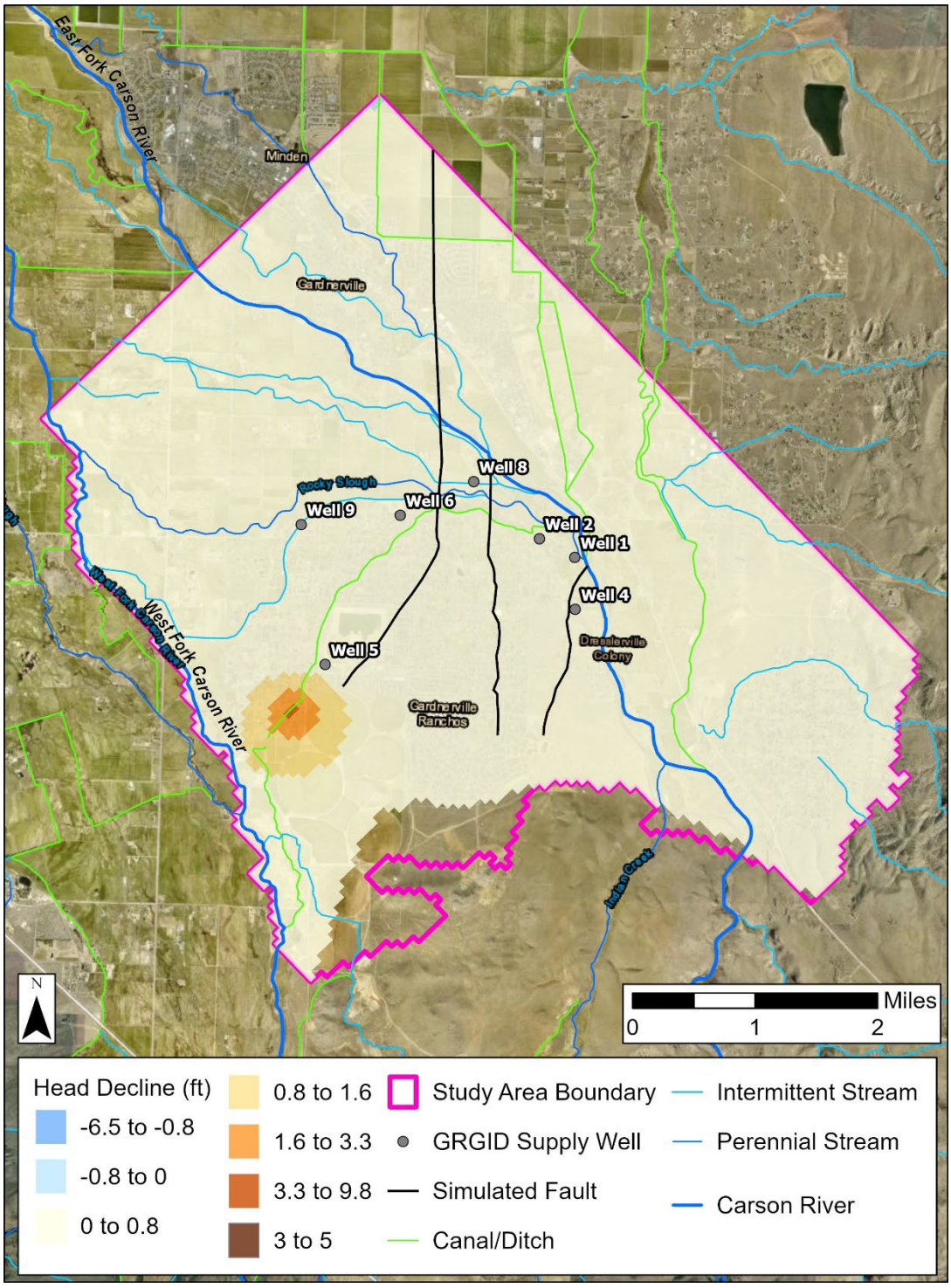

Figure 49E. Map of predictive declines in groundwater levels for simulation P2c in model layer 2 relative to the base-case model for May 2043 under a pumping increase of 0.2% annually at Gardnerville Ranchos supply wells and temperature increase of 0.2°F/yr (0.1°C/yr) above average. Areas in blue (negative values) have higher groundwater levels compared to the base-case model and areas in orange (positive values) have lower groundwater levels.

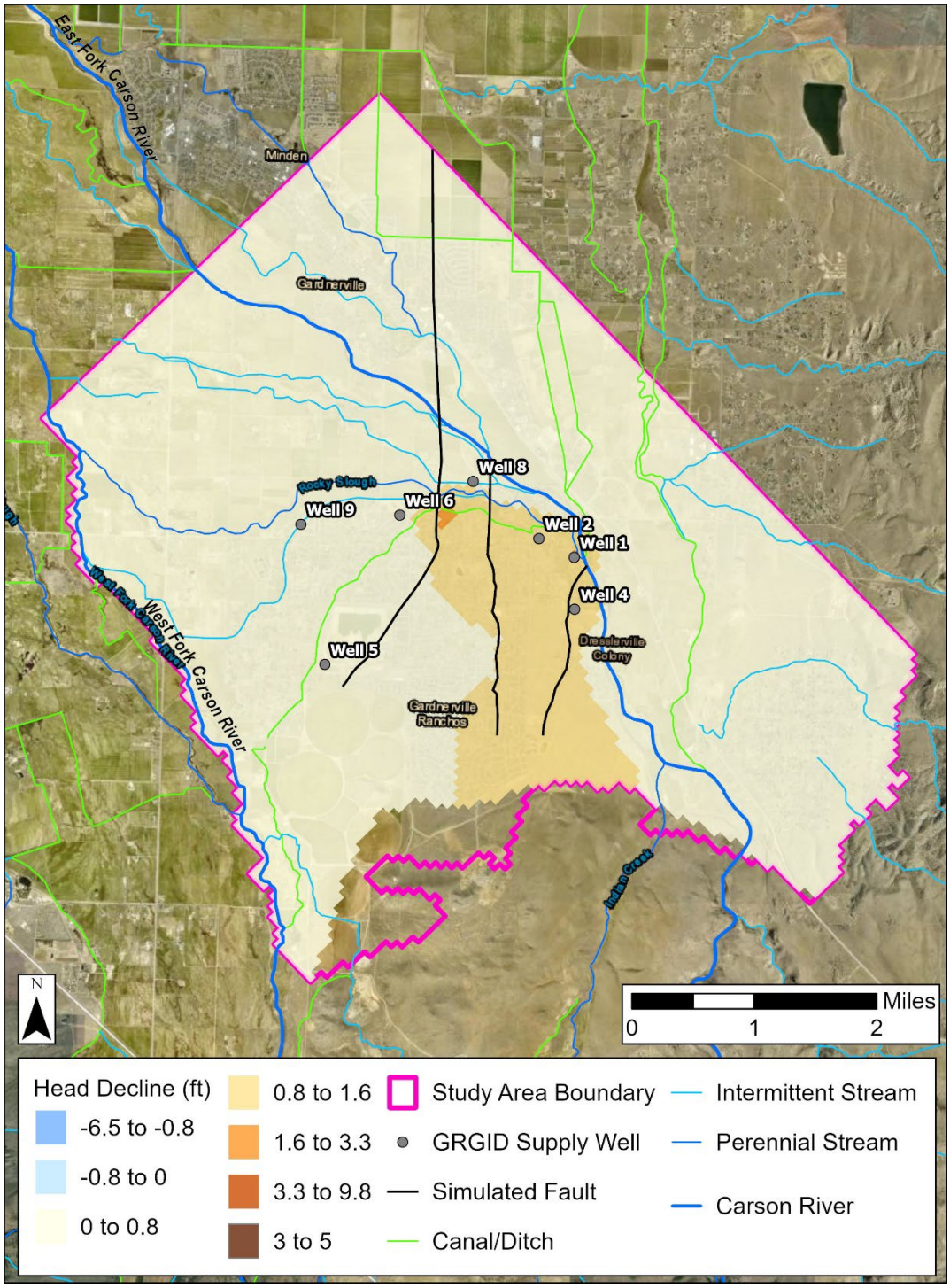

Figure 49F. Map of predictive declines in groundwater levels for simulation P2c in model layer 2 relative to the base-case model for September 2043 under a pumping increase of 0.2% annually at Gardnerville Ranchos supply wells and temperature increase of 0.2°F/yr (0.1°C/yr) above average. Areas in blue (negative values) have higher groundwater levels compared to the base-case model and areas in orange (positive values) have lower groundwater levels.

3.9.5 Predictive Results – Temporal Head Changes

This section focuses on results related to predictive model goal 2 (assess whether the existing GRGID supply well network is expected to meet future monthly demands under projected changes in pumping and temperature). Each simulation is checked for two criteria to assess whether the supply well network is expected to meet the future monthly demand. For the full duration of the simulation period (2024-2043), each GRGID supply well must meet the following criteria:

1) Simulated heads in the supply well (h_{well}) are greater than the minimum head threshold (h_{lim}) under projected average monthly pumping conditions and
2) Simulated monthly pumping rates (Q_{sim}) are within 50 m^3/d (10 gpm) of the targeted monthly pumping rate (Q_{des}).

To assess whether criterion 1 is met, hydrographs of simulated head elevations in GRGID supply wells are compared to h_{lim} for each predictive simulation. To check criterion 2, predictive simulated monthly pumping rates (Q_{sim}) are compared to the targeted monthly pumping rates (Q_{des}) for each supply well and each simulation. As described previously, Q_{sim} is reduced automatically during the simulation to a rate less than Q_{des} if h_{well} drops to a level below h_{lim} or if flow from the aquifer to the well becomes less than Q_{des}. As previously stated, the model simulates average monthly conditions and does not account for submonthly (e.g., hourly or daily) variability in pumping rates. Therefore, model results are discussed in terms of the ability of the supply wells and aquifer to meet average monthly demands and not the ability to meet short-term spikes in demand.

Hydrographs of predicted heads in GRGID supply wells for each simulation are presented in Figures 50-55. For comparison to predicted heads, observed historical heads are also plotted. Historical water levels (black dots in Figures 50-55) are instantaneous water levels (not monthly average water levels) and therefore show greater variability than simulated heads (colored dots). To show the range of predicted head changes in non-pumping wells, hydrographs of predicted heads at GRGID monitoring wells are included (Figures 56-65).

The h_{lim} for each supply well is listed in Table 15, along with the minimum predicted head (h_{min}) for each simulation and each supply well associated with the hydrographs in Figures 50-55. As shown in Table 15, h_{min} is greater than h_{lim} in all supply wells for each simulation. Table 16 summarizes the differences between h_{min} and h_{sim}. As shown, predicted h_{min} values are at least 42 ft (13 m) above h_{lim} for all simulations. The minimum difference between predicted h_{min} and h_{lim} are for Wells 1, 2, 6, and 9 are 42 to 46 ft (13 to 14 m) when simulated pumping increases by 1.5% annually (simulations P1a, P1b, and P1c). Pumping rates are lower for all other simulations, resulting in higher h_{min} values. Because simulated heads remain above the head thresholds for each supply well, water levels in the supply wells are expected to remain at a sufficient level to meet future average monthly pumping requirements for all predictive scenarios. This indicates that criterion 1 is successfully met for each well and each simulation.

Table 15. Minimum predicted head, in feet above sea level, in GRGID supply wells for each predictive simulation from 2024 to 2043 compared to the minimum head threshold (H_{lim}).

Name	Hlim	BC	C2F	C4F	P1a	P1b	P1c	P2a	P2b	P2c
Well 1	4,610	4,678	4,678	4,678	4,652	4,652	4,652	4,675	4,675	4,675
Well 2	4,577	4,652	4,652	4,652	4,619	4,619	4,619	4,649	4,649	4,649
Well 4	4,560	4,682	4,682	4,682	4,665	4,665	4,665	4,678	4,682	4,682
Well 6	4,596	4,659	4,665	4,665	4,639	4,642	4,642	4,656	4,662	4,662
Well 8	4,570	4,731	4,734	4,734	4,724	4,728	4,728	4,731	4,734	4,734
Well 9	4,580	4,646	4,649	4,649	4,623	4,623	4,623	4,642	4,649	4,646

Table 16. Difference between minimum simulated head and minimum head threshold, in feet, for each GRGID supply well and each simulation.

Name	BC	C2F	C4F	P1a	P1b	P1c	P2a	P2b	P2c
Well 1	69	69	69	43	43	43	66	66	66
Well 2	75	75	75	43	43	43	72	72	72
Well 4	121	121	121	105	105	105	118	121	121
Well 6	62	69	69	43	46	46	59	66	66
Well 8	161	164	164	154	157	157	161	164	164
Well 9	66	69	69	43	43	43	62	69	66

The projected rate of water level change in Gardnerville Ranchos is calculated by fitting a linear model to predicted heads for each simulation in all GRGID supply wells (Figures 50-55) and monitoring wells (Figures 56-65). The estimated head change rates for supply wells from 2024 to 2043 are summarized in Table 17. For comparison, head change rates for monitoring wells are included in Table 18. All predictive simulations show that water levels are expected to decline in the future, at rates ranging from -0.04 ft/yr (-0.011 m/yr) at monitoring well 7 during the base-case simulation to 1.1 ft/yr (-0.34 m/yr) at Well 1 during simulation P1b. Overall, head reduction rates are greatest during P1 simulations when the projected annual pumping increase is greatest (1.5% annually). Well 1 has the greatest rate of decline for each P1 simulation. With the exception of Well 8, all supply wells have a similar rate of decline during P2 simulations (annual pumping increase of 0.2%). Well 8 head declines at a lower rate because it is simulated to pump at a reduced capacity compared to all other supply wells. The water level rate of decline is generally greater in supply wells than monitoring wells because of well inefficiencies (greater drawdown inside of the well compared to the surrounding aquifer formation) and because drawdown typically decreases with distance from the pumping source.

In the monitoring wells, water levels are predicted to decline most quickly in all scenarios (>3 ft/yr; >1 m/yr) at MW1_Bing, MW2_Bing, and Well 5. These wells are all located in the West Block and are the greatest distance from the East Fork and irrigation canals, which are major recharge sources in the study area. While the West Fork can also be a recharge source (or a discharge point, depending on groundwater levels), the flow of the West Fork is lower than the East Fork and provides less recharge to the aquifer. Water levels at monitoring wells MW1, 3, 5, and 6 decline at the lowest rate during most scenarios because of their proximity to surface waters that are recharge sources. However, water levels decline much more rapidly at MW3, 5, and 6 during P1 simulations due to their proximity to supply wells 1 and 2 and the increased annual pumping rate of 1.5%.

Table 17. Rate of head change, in feet per year, in GRGID supply wells for each predictive simulation from 2024 to 2043. A negative value indicates lowering of the water table.

Name	BC	C2F	C4F	P1a	P1b	P1c	P2a	P2b	P2c
Well 1	-0.11	-0.14	-0.12	-1.08	-1.11	-1.09	-0.22	-0.25	-0.24
Well 2	-0.13	-0.16	-0.14	-0.95	-0.98	-0.96	-0.23	-0.26	-0.24
Well 4	-0.15	-0.17	-0.16	-0.89	-0.90	-0.89	-0.24	-0.26	-0.25
Well 6	-0.14	-0.15	-0.14	-0.95	-0.97	-0.96	-0.23	-0.25	-0.24
Well 8	-0.09	-0.10	-0.09	-0.23	-0.25	-0.24	-0.10	-0.12	-0.11
Well 9	-0.14	-0.14	-0.13	-0.92	-0.92	-0.92	-0.23	-0.23	-0.23
Mean	-0.12	-0.14	-0.13	-0.84	-0.85	-0.84	-0.21	-0.23	-0.22
Median	-0.13	-0.14	-0.14	-0.94	-0.94	-0.94	-0.23	-0.25	-0.24

Table 18. Rate of head change, in feet per year, in GRGID monitoring wells for each predictive simulation from 2024 to 2043. Negative value indicates heads are declining.

Name	BC	C2F	C4F	P1a	P1b	P1c	P2a	P2b	P2c
MW1	-0.10	-0.09	-0.09	-0.13	-0.12	-0.12	-0.10	-0.09	-0.09
MW2	-0.16	-0.20	-0.18	-0.22	-0.26	-0.24	-0.17	-0.20	-0.19
MW3	-0.07	-0.10	-0.08	-0.25	-0.28	-0.26	-0.09	-0.11	-0.10
MW5	-0.06	-0.08	-0.07	-0.24	-0.27	-0.26	-0.08	-0.10	-0.09
MW6	-0.06	-0.09	-0.08	-0.25	-0.28	-0.26	-0.08	-0.11	-0.10
MW1_Bing	-0.38	-0.44	-0.39	-0.42	-0.48	-0.43	-0.38	-0.44	-0.39
MW2_Bing	-0.34	-0.40	-0.36	-0.38	-0.44	-0.40	-0.35	-0.40	-0.36
Sweetwater	-0.27	-0.31	-0.28	-0.31	-0.35	-0.32	-0.27	-0.31	-0.28
Well 5	-0.34	-0.39	-0.34	-0.38	-0.43	-0.38	-0.34	-0.39	-0.35
Well 7	-0.04	-0.07	-0.04	-0.13	-0.16	-0.13	-0.05	-0.08	-0.05
Mean	-0.18	-0.21	-0.19	-0.27	-0.31	-0.28	-0.19	-0.23	-0.20
Median	-0.13	-0.14	-0.13	-0.25	-0.28	-0.26	-0.13	-0.16	-0.14

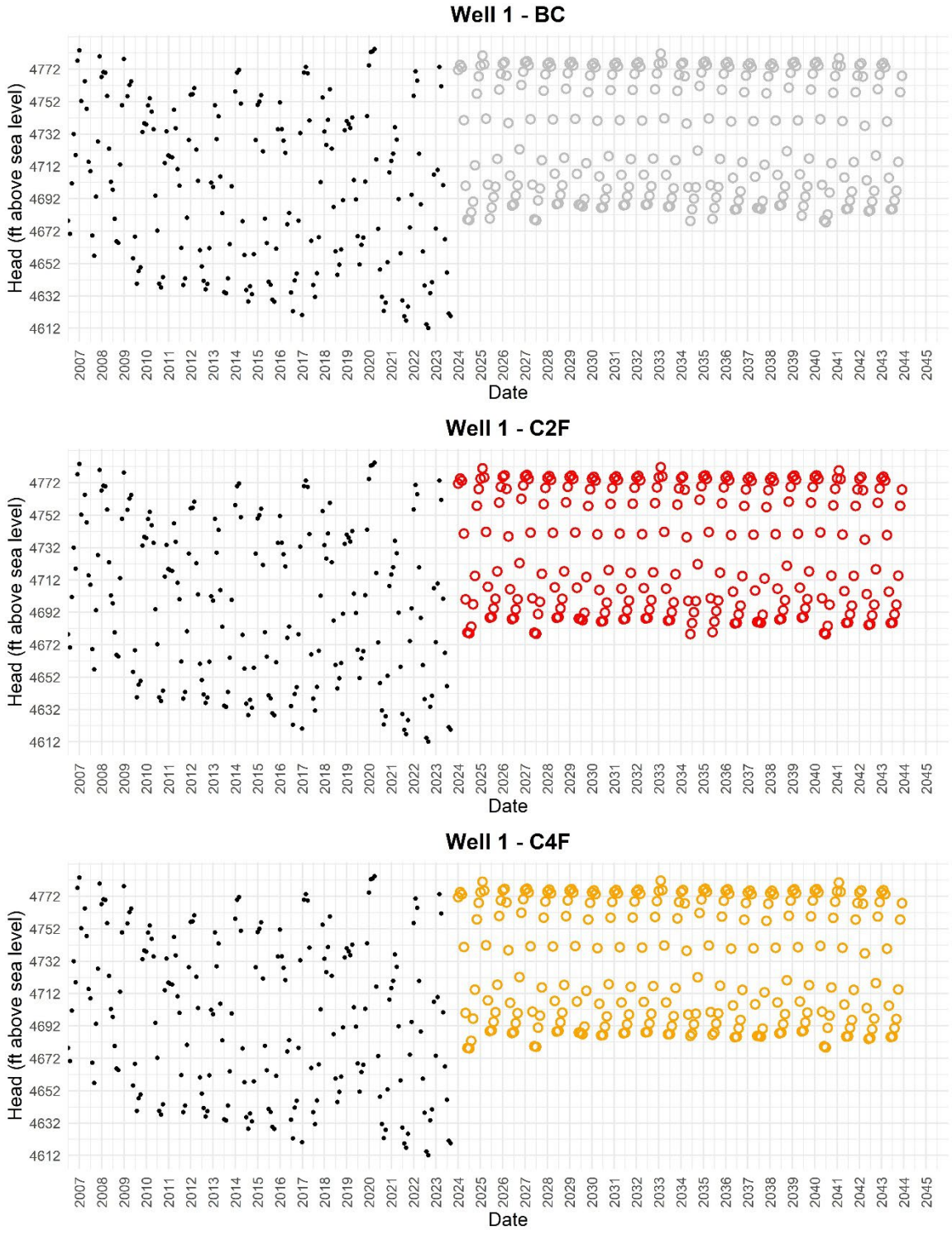

Figure 50A. Time series plots of predicted heads (colored circles) at GRGID supply Well 1 for predictive simulations BC, C2F, and C4F. For comparison to predicted heads, historical observed heads are also plotted (black dots). Simulation details are provided in Table 14. The *x*-axis extent depends on the date range of observed head data. Predicted minimum heads and rate of head change associated with the plots are presented in Table 17.

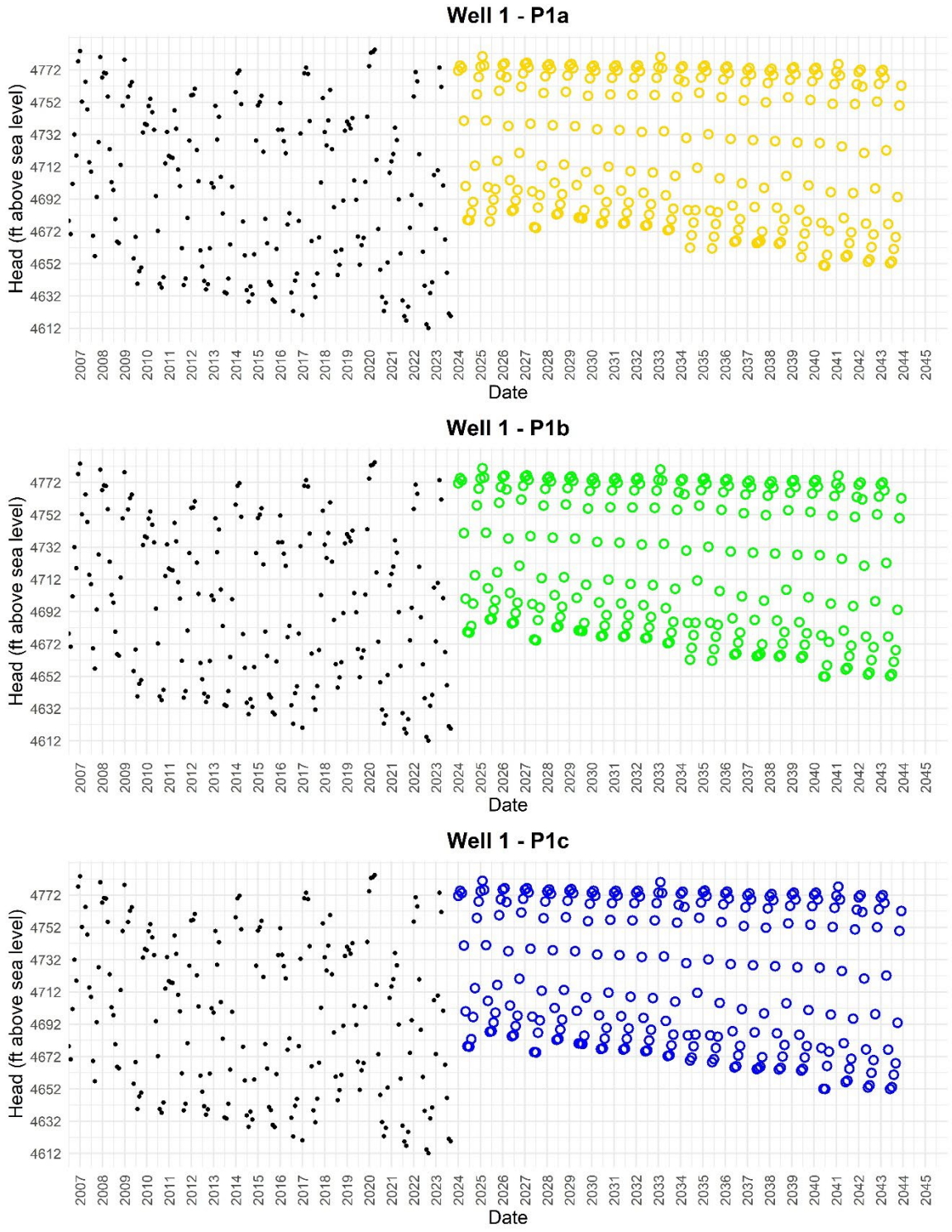

Figure 50B. Time series plots of predicted heads (colored circles) at GRGID supply Well 1 for predictive simulations P1a, P1b, and P1c. For comparison to predicted heads, historical observed heads are also plotted (black dots). Simulation details are provided in Table 14. The *x*-axis extent depends on the date range of observed head data. Predicted minimum heads and rate of head change associated with the plots are presented in Table 17.

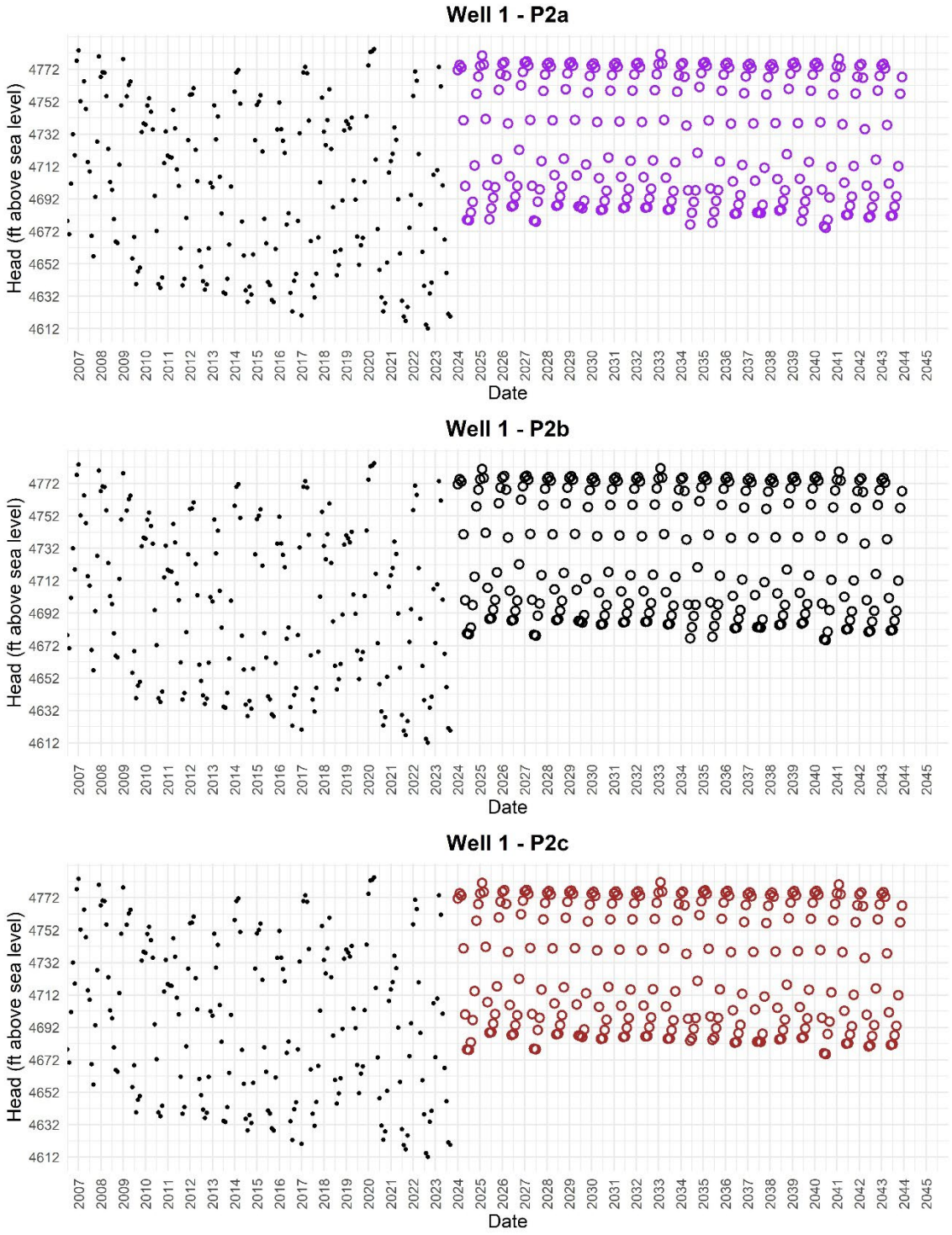

Figure 50C. Time series plots of predicted heads (colored circles) at GRGID supply Well 1 for predictive simulations P2a, P2b, and P2c. For comparison to predicted heads, historical observed heads are also plotted (black dots). Simulation details are provided in Table 14. The *x*-axis extent depends on the date range of observed head data. Predicted minimum heads and rate of head change associated with the plots are presented in Table 17.

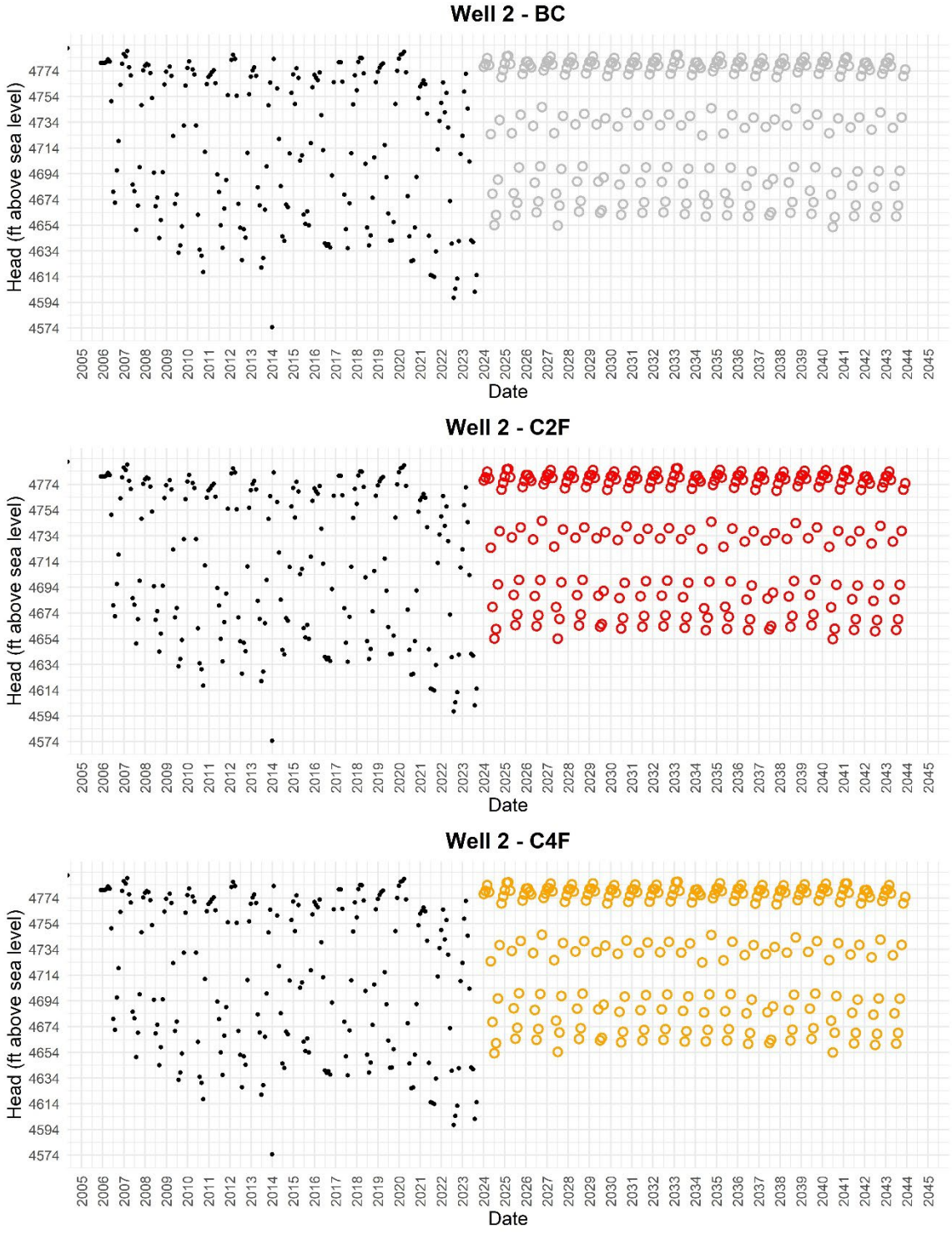

Figure 51A. Time series plots of predicted heads (colored circles) at GRGID supply Well 2 for predictive simulations BC, C2F, and C4F. For comparison to predicted heads, historical observed heads are also plotted (black dots). Simulation details are provided in Table 14. The *x*-axis extent depends on the date range of observed head data. Predicted minimum heads and rate of head change associated with the plots are presented in Table 17.

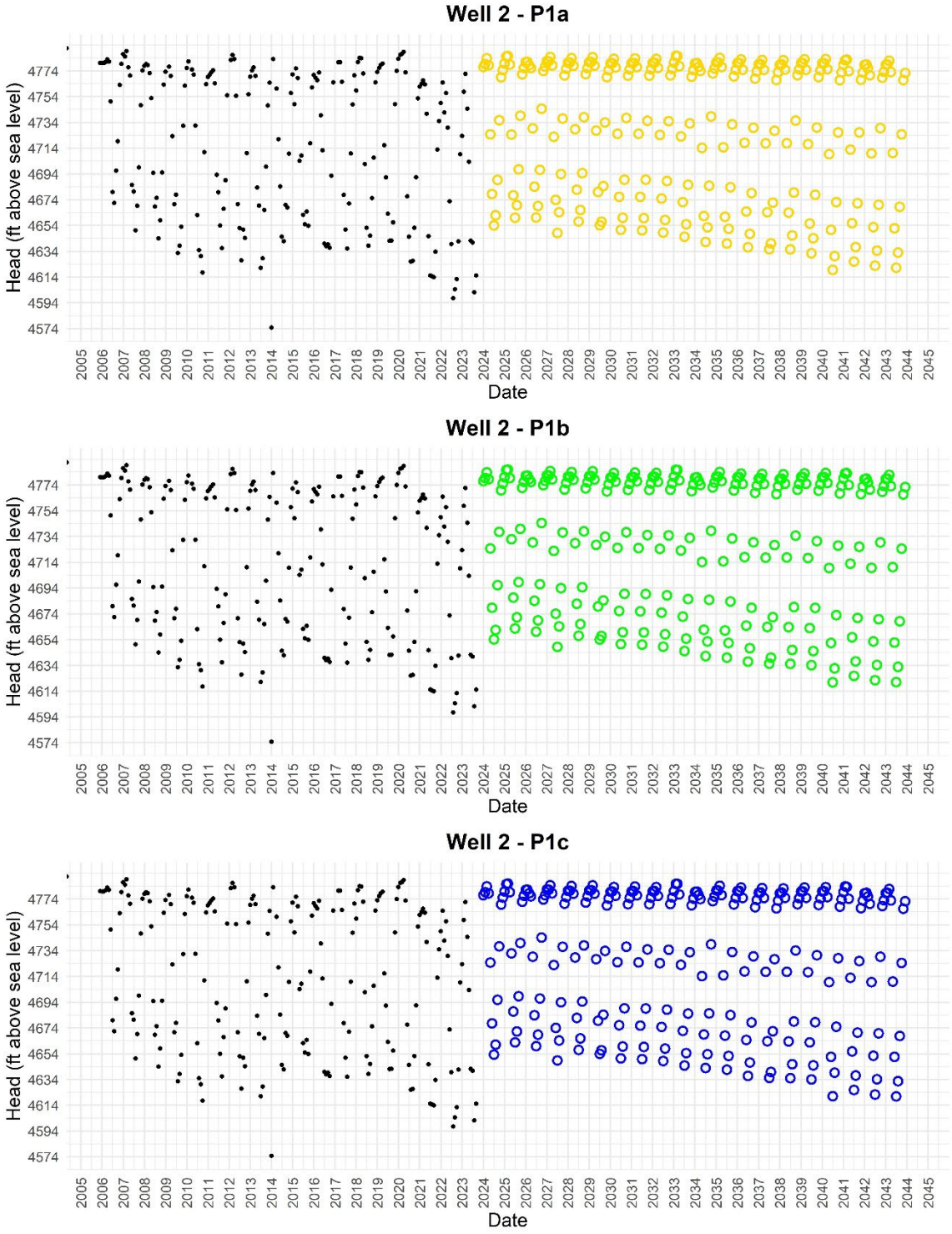

Figure 51B. Time series plots of predicted heads (colored circles) at GRGID supply Well 2 for predictive simulations P1a, P1b, and P1c. For comparison to predicted heads, historical observed heads are also plotted (black dots). Simulation details are provided in Table 14. The *x*-axis extent depends on the date range of observed head data. Predicted minimum heads and rate of head change associated with the plots are presented in Table 17.

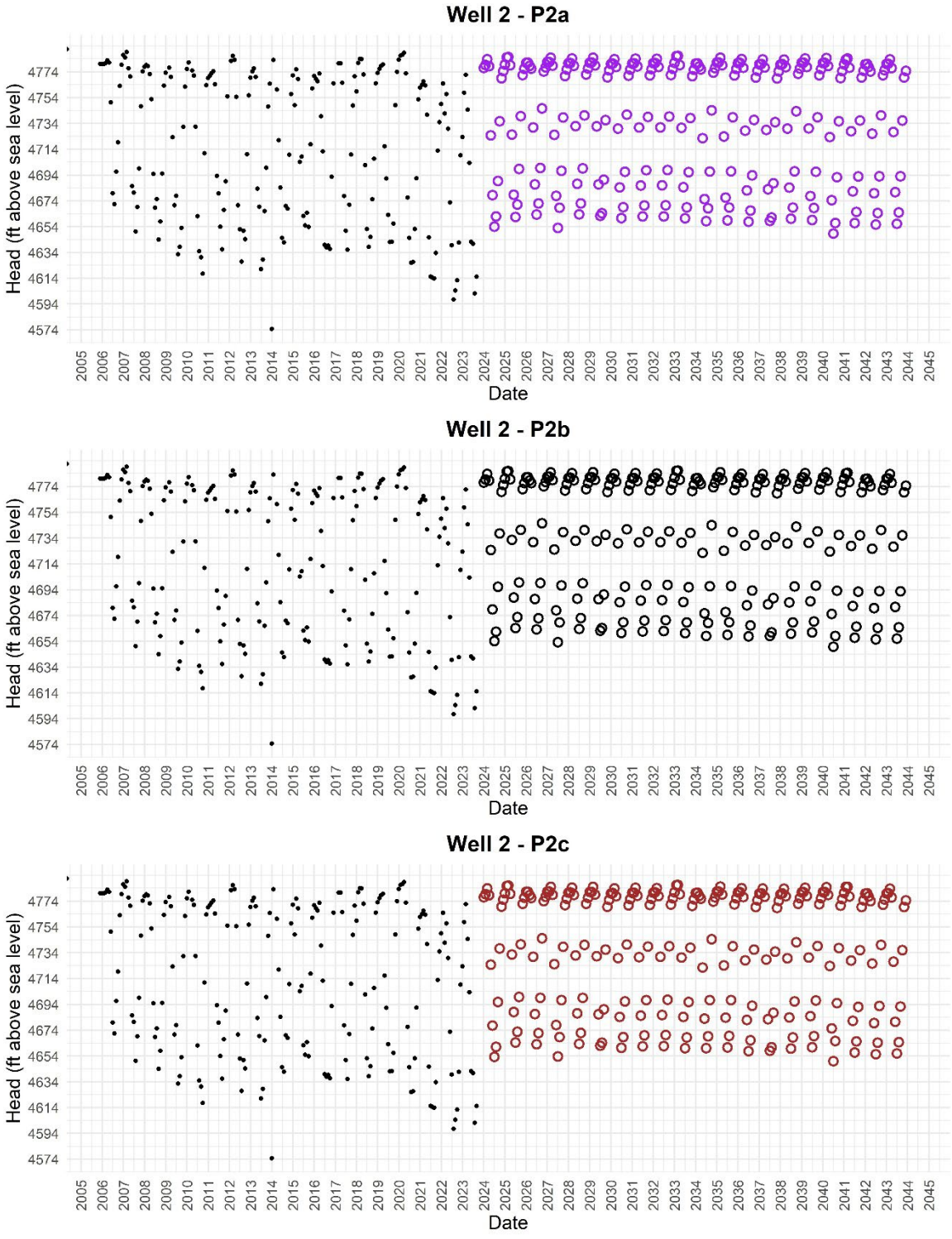

Figure 51C. Time series plots of predicted heads (colored circles) at GRGID supply Well 2 for predictive simulations P2a, P2b, and P2c. For comparison to predicted heads, historical observed heads are also plotted (black dots). Simulation details are provided in Table 14. The *x*-axis extent depends on the date range of observed head data. Predicted minimum heads and rate of head change associated with the plots are presented in Table 17.

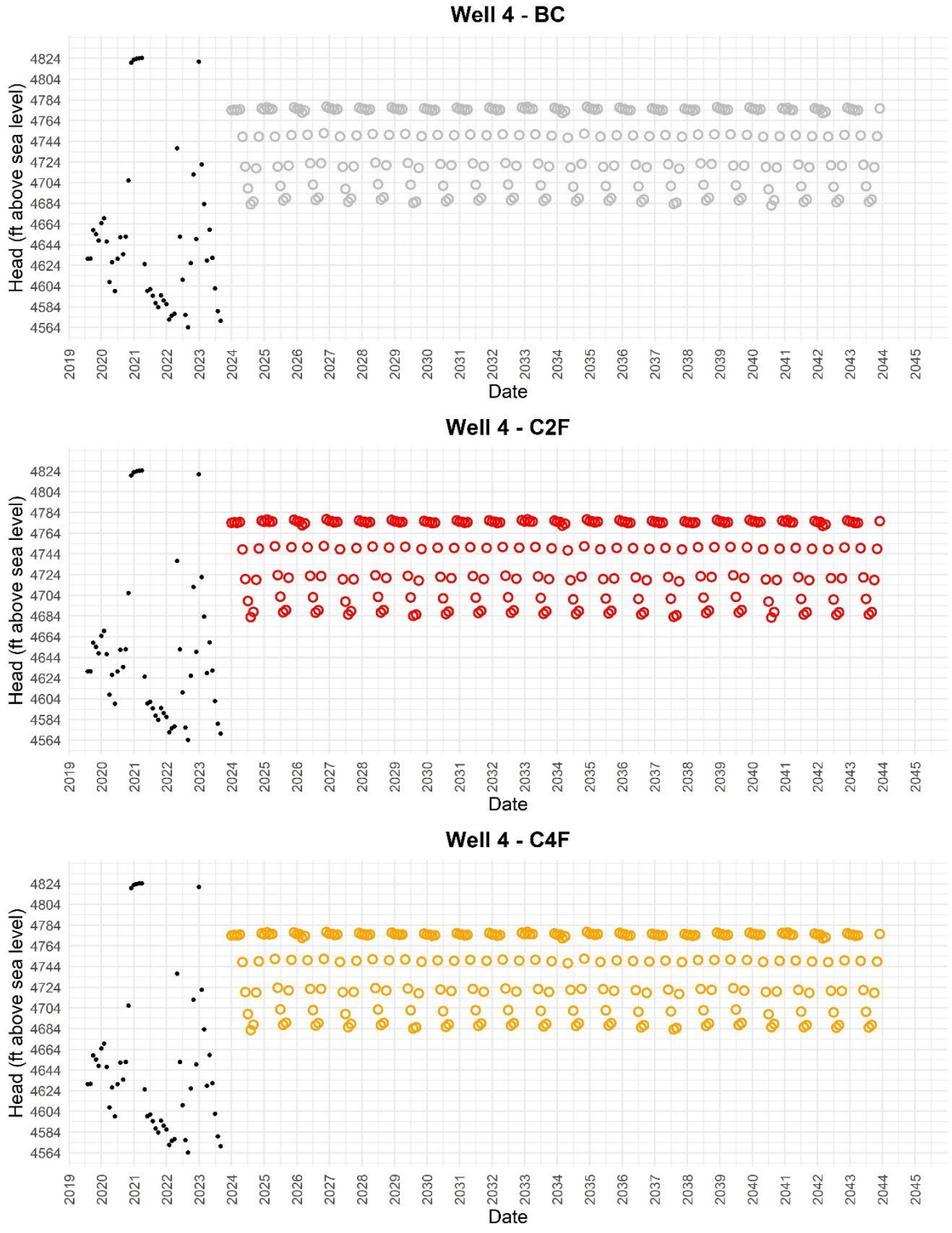

Figure 52A. Time series plots of predicted heads (colored circles) at GRGID supply Well 4 for predictive simulations BC, C2F, and C4F. For comparison to predicted heads, historical observed heads are also plotted (black dots). Simulation details are provided in Table 14. The *x*-axis extent depends on the date range of observed head data. Predicted minimum heads and rate of head change associated with the plots are presented in Table 17.

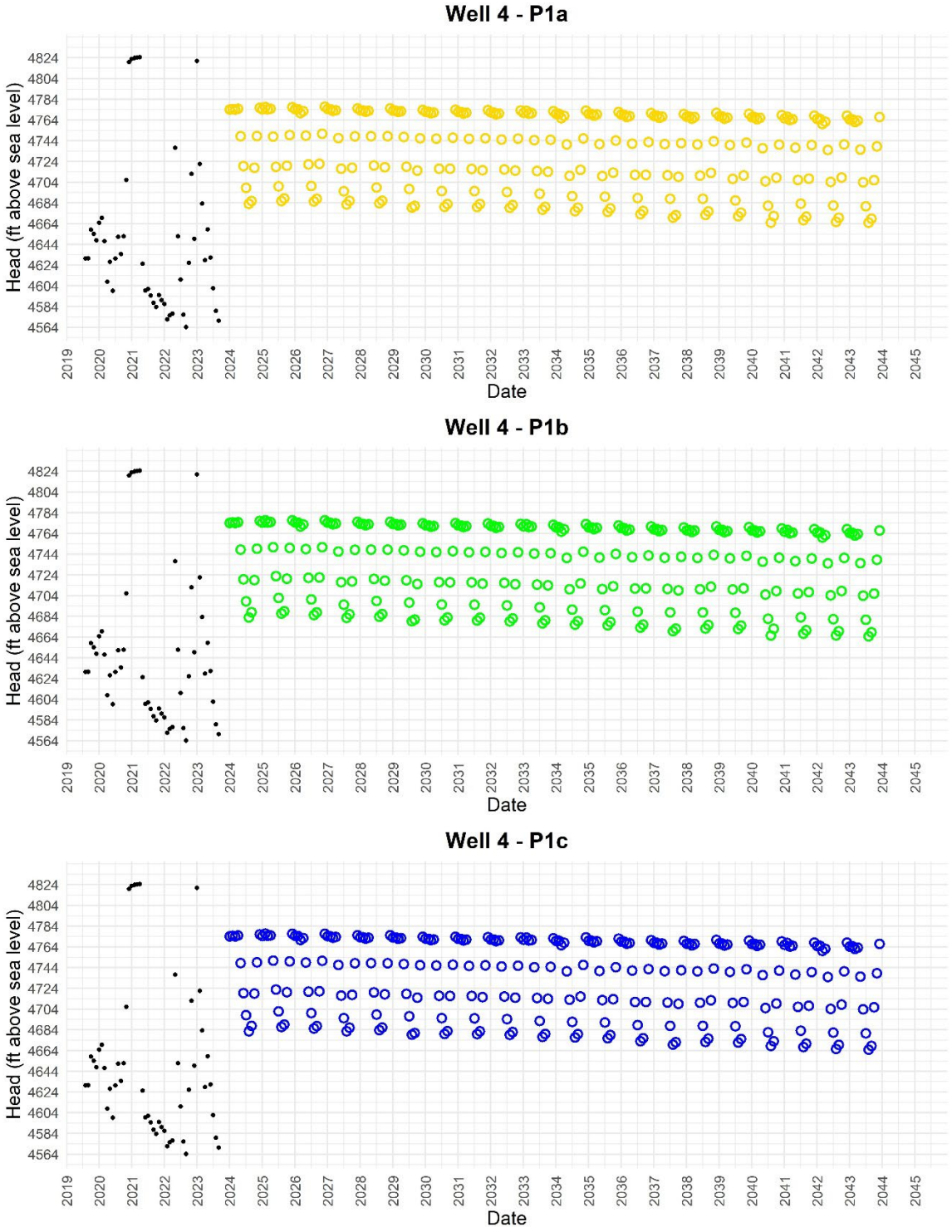

Figure 52B. Time series plots of predicted heads (colored circles) at GRGID supply Well 4 for predictive simulations P1a, P1b, and P1c. For comparison to predicted heads, historical observed heads are also plotted (black dots). Simulation details are provided in Table 14. The *x*-axis extent depends on the date range of observed head data. Predicted minimum heads and rate of head change associated with the plots are presented in Table 17.

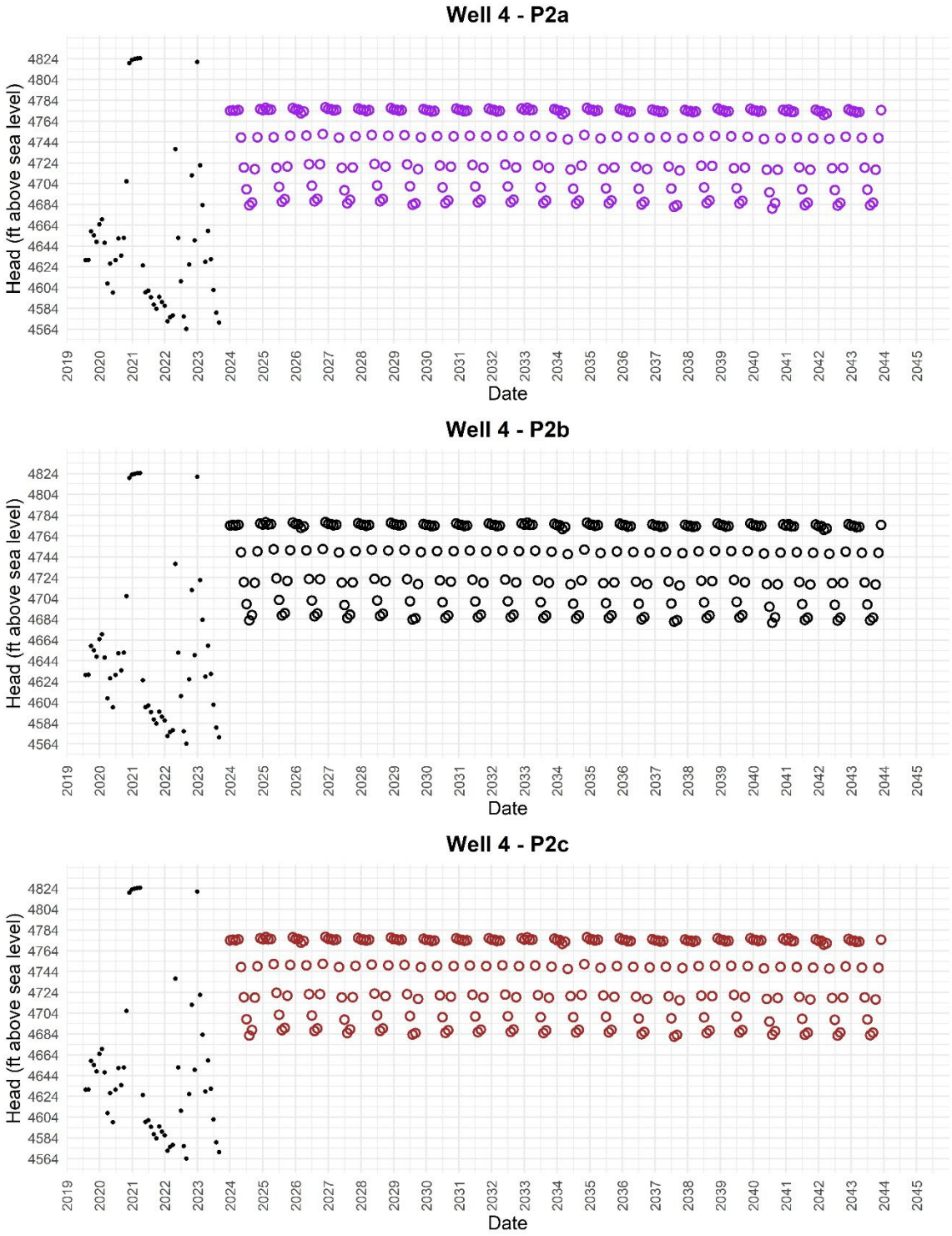

Figure 52C. Time series plots of predicted heads (colored circles) at GRGID supply Well 4 for predictive simulations P2a, P2b, and P2c. For comparison to predicted heads, historical observed heads are also plotted (black dots). Simulation details are provided in Table 14. The *x*-axis extent depends on the date range of observed head data. Predicted minimum heads and rate of head change associated with the plots are presented in Table 17.

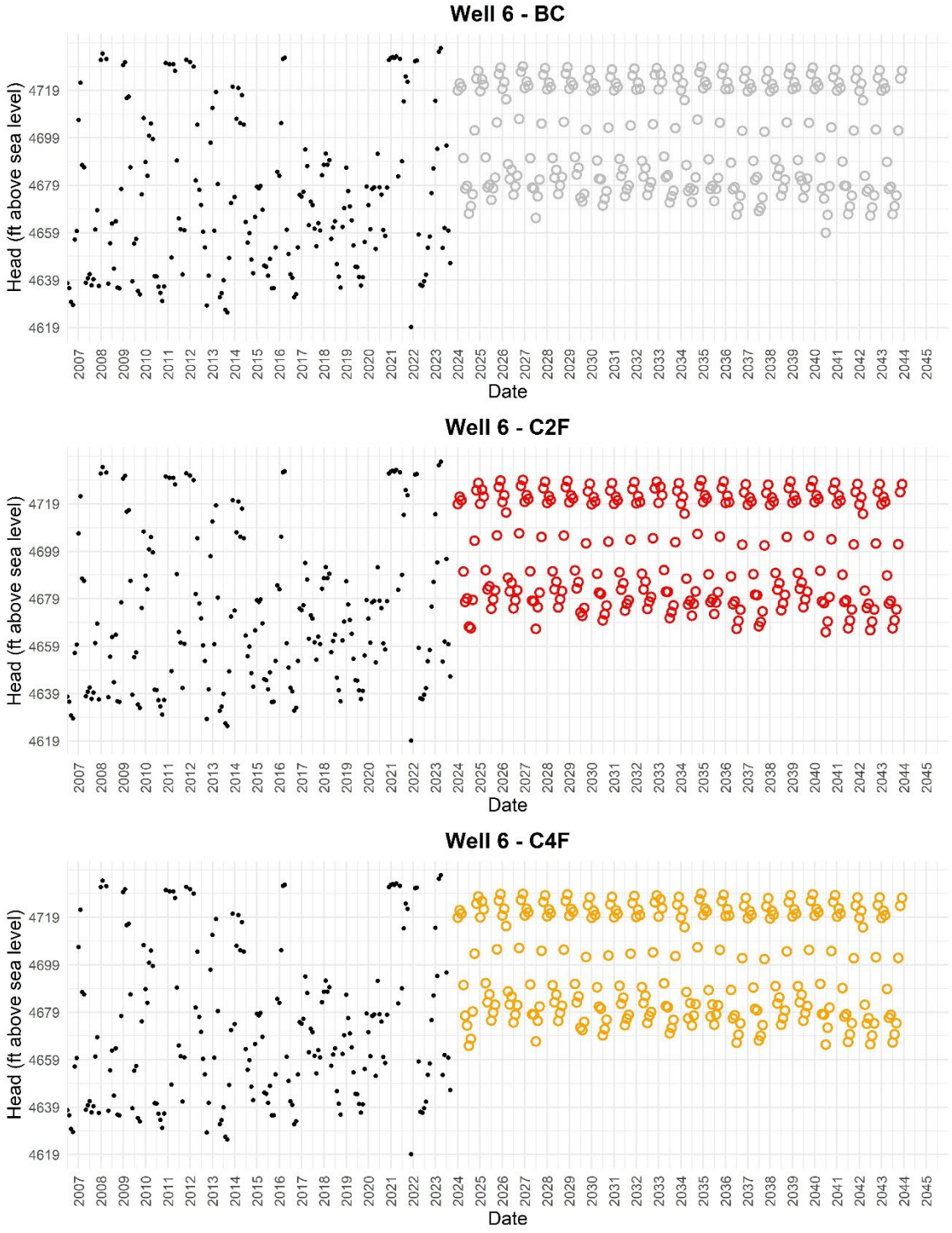

Figure 53A. Time series plots of predicted heads (colored circles) at GRGID supply Well 6 for predictive simulations BC, C2F, and C4F. For comparison to predicted heads, historical observed heads are also plotted (black dots). Simulation details are provided in Table 14. The *x*-axis extent depends on the date range of observed head data. Predicted minimum heads and rate of head change associated with the plots are presented in Table 17.

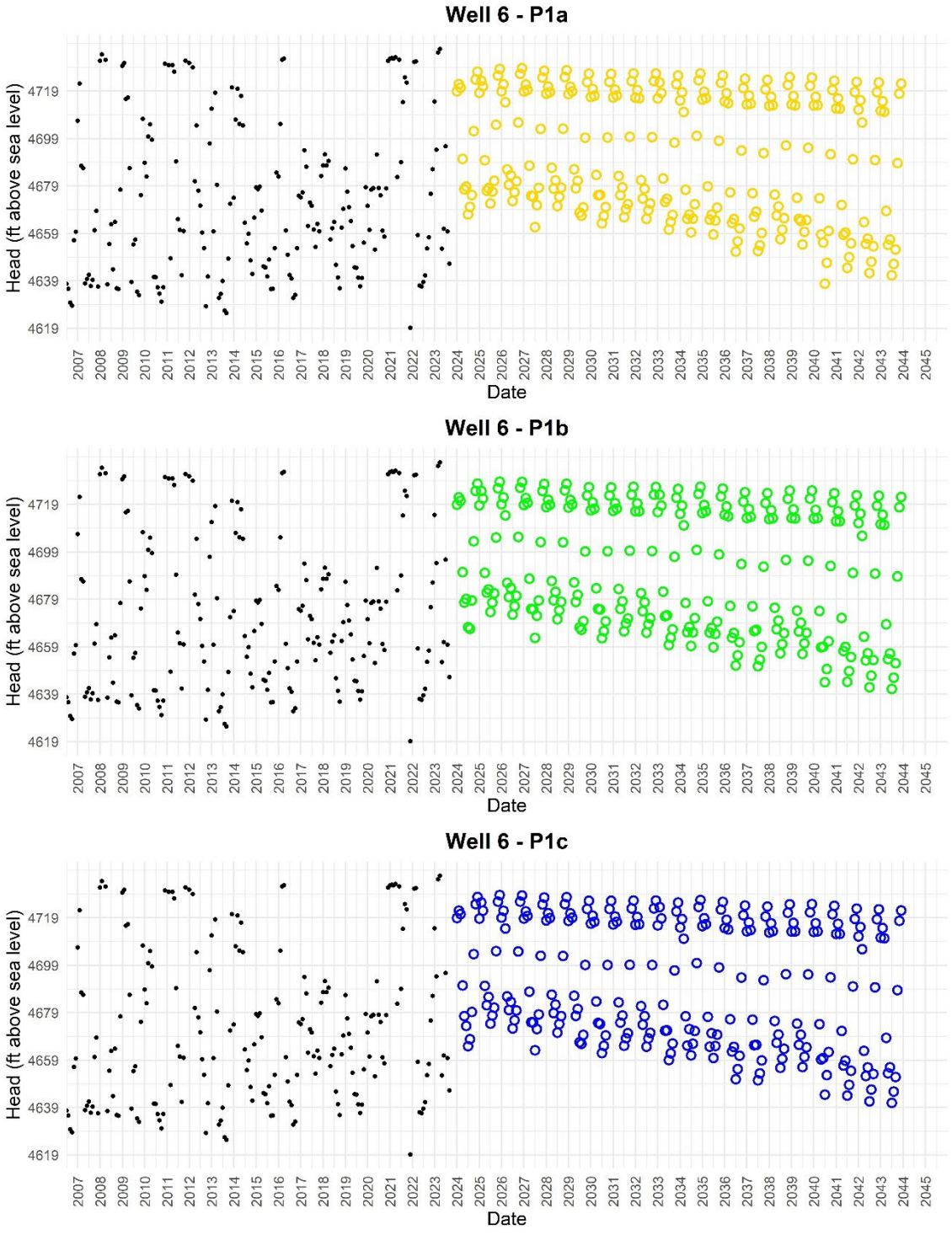

Figure 53B. Time series plots of predicted heads (colored circles) at GRGID supply Well 6 for predictive simulations P1a, P1b, and P1c. For comparison to predicted heads, historical observed heads are also plotted (black dots). Simulation details are provided in Table 14. The *x*-axis extent depends on the date range of observed head data. Predicted minimum heads and rate of head change associated with the plots are presented in Table 17.

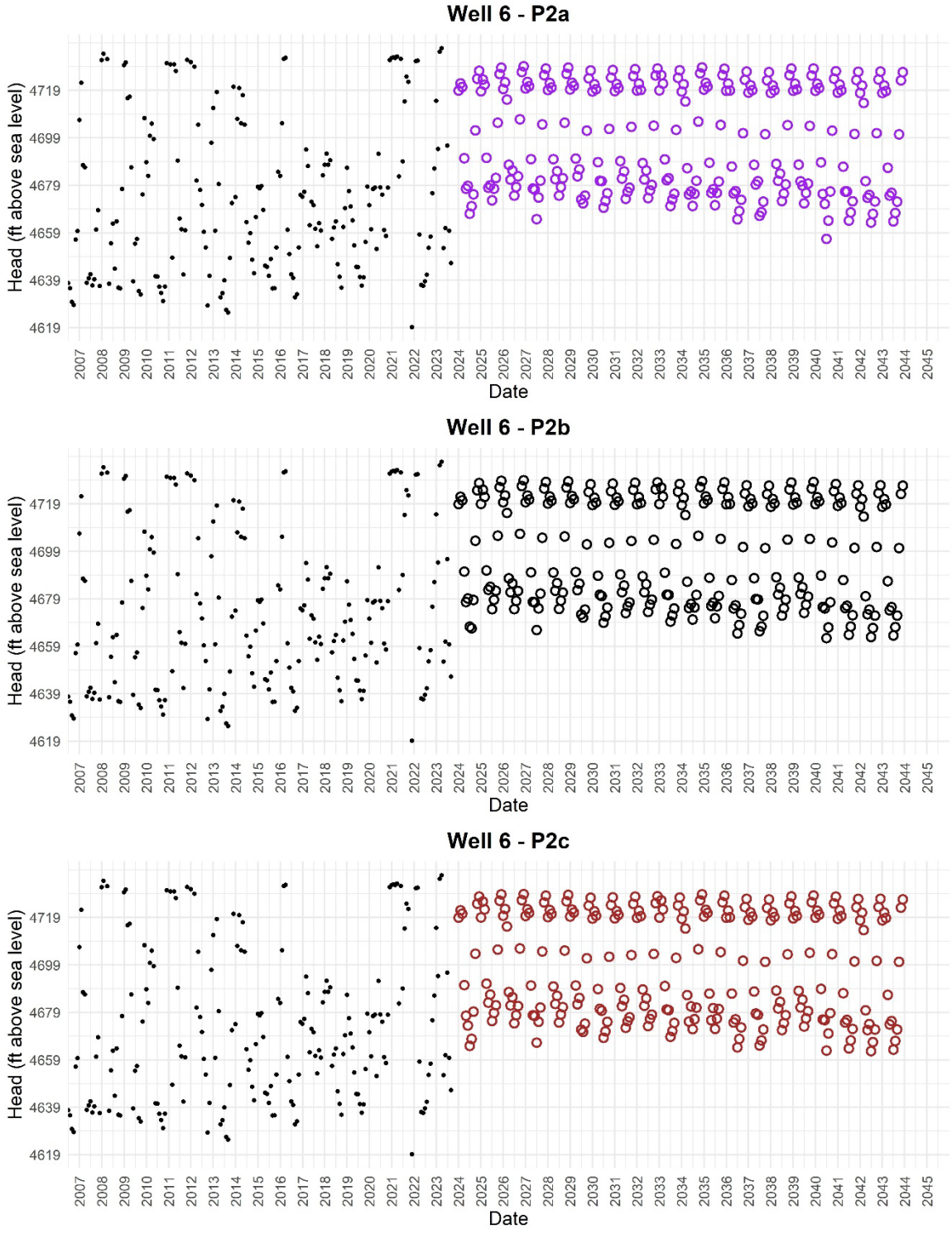

Figure 53C. Time series plots of predicted heads (colored circles) at GRGID supply Well 6 for predictive simulations P2s, P2b, P2c. For comparison to predicted heads, historical observed heads are also plotted (black dots). Simulation details are provided in Table 14. The *x*-axis extent depends on the date range of observed head data. Predicted minimum heads and rate of head change associated with the plots are presented in Table 17.

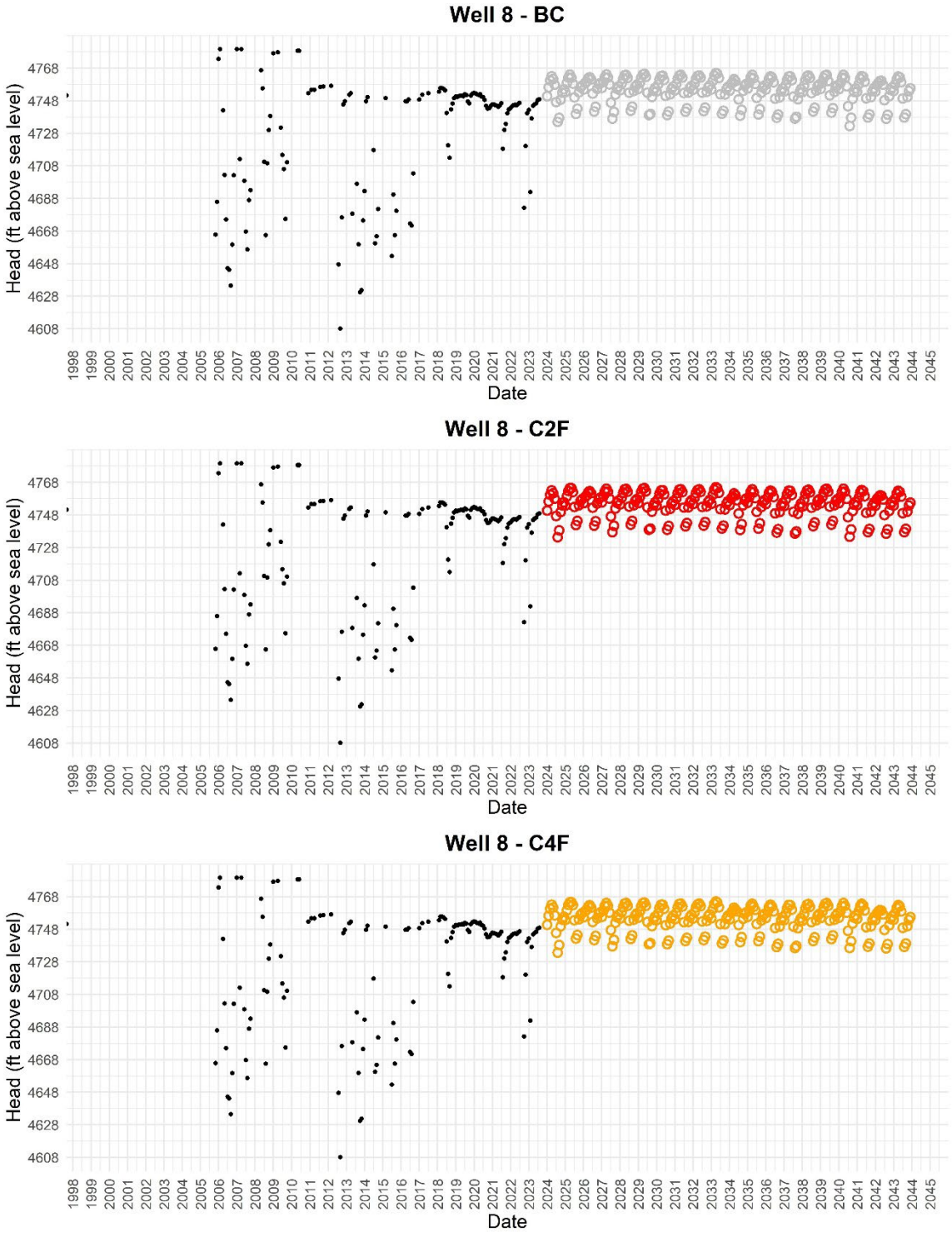

Figure 54A. Time series plots of predicted heads (colored circles) at GRGID supply Well 8 for predictive simulations BC, C2F, and C4F. For comparison to predicted heads, historical observed heads are also plotted (black dots). Simulation details are provided in Table 14. The *x*-axis extent depends on the date range of observed head data. Predicted minimum heads and rate of head change associated with the plots are presented in Table 17.

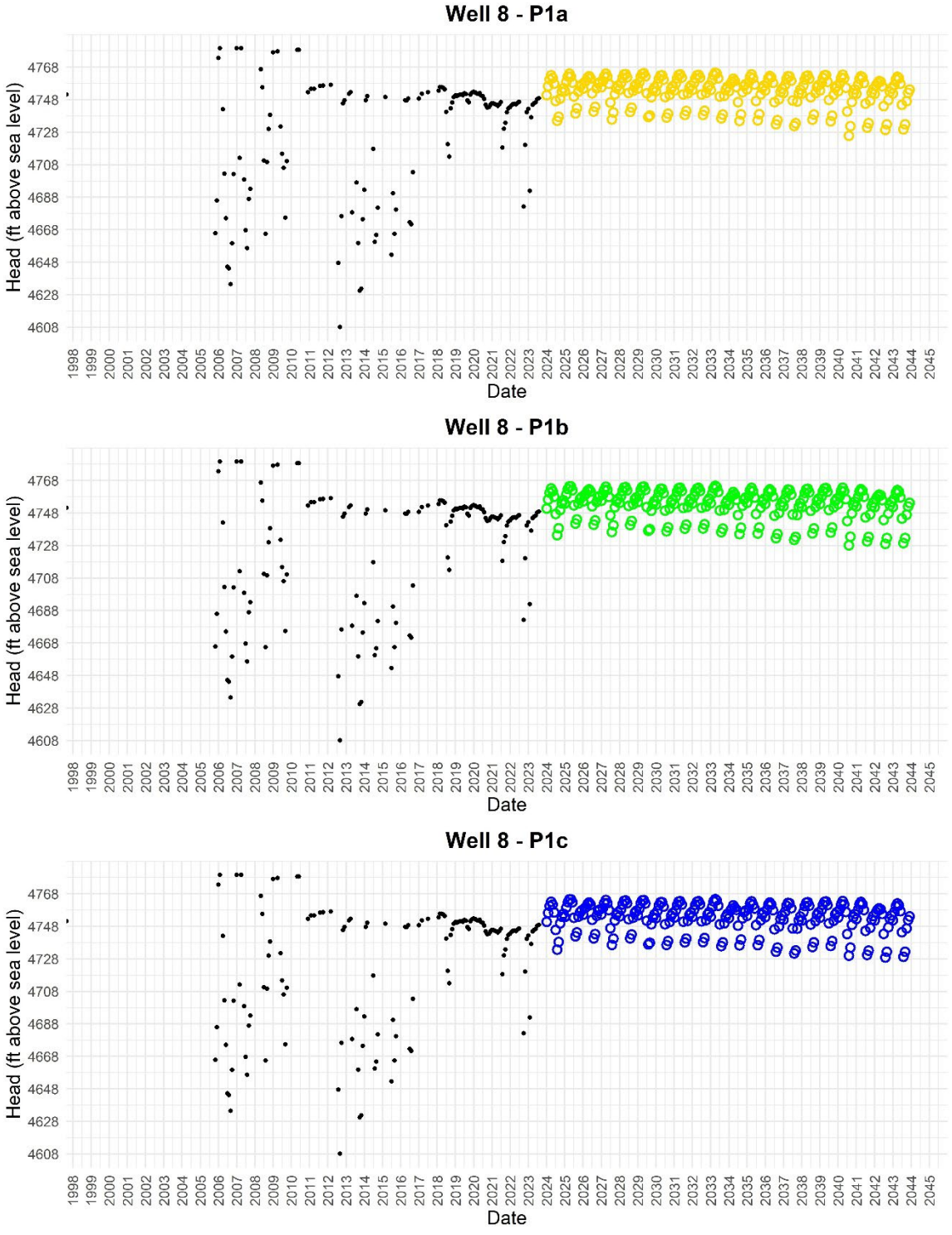

Figure 54B. Time series plots of predicted heads (colored circles) at GRGID supply Well 8 for predictive simulations P1a, P1b, and P1c. For comparison to predicted heads, historical observed heads are also plotted (black dots). Simulation details are provided in Table 14. The *x*-axis extent depends on the date range of observed head data. Predicted minimum heads and rate of head change associated with the plots are presented in Table 17.

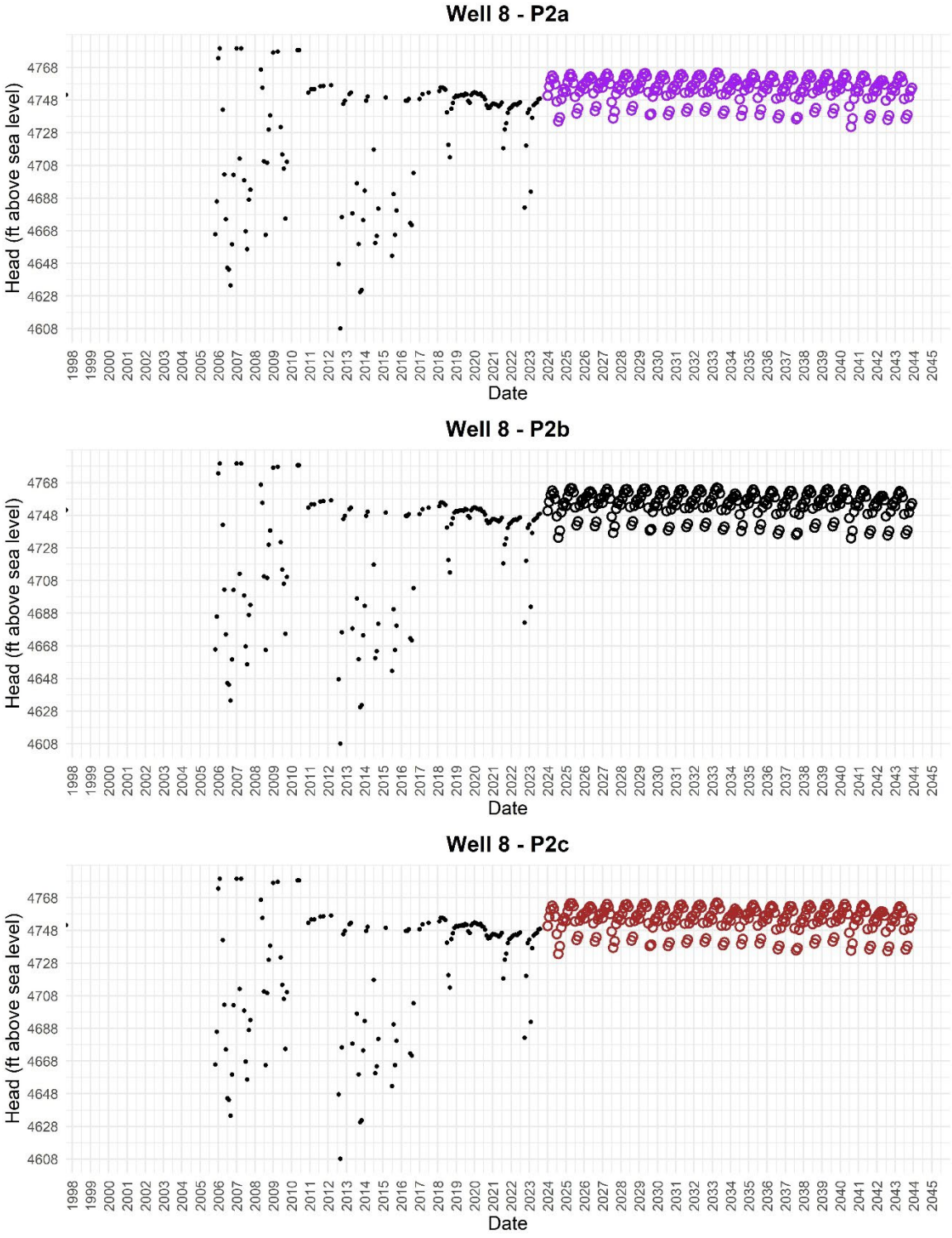

Figure 54C. Time series plots of predicted heads (colored circles) at GRGID supply Well 8 for predictive simulations P2a, P2b, and P2c. For comparison to predicted heads, historical observed heads are also plotted (black dots). Simulation details are provided in Table 14. The *x*-axis extent depends on the date range of observed head data. Predicted minimum heads and rate of head change associated with the plots are presented in Table 17.

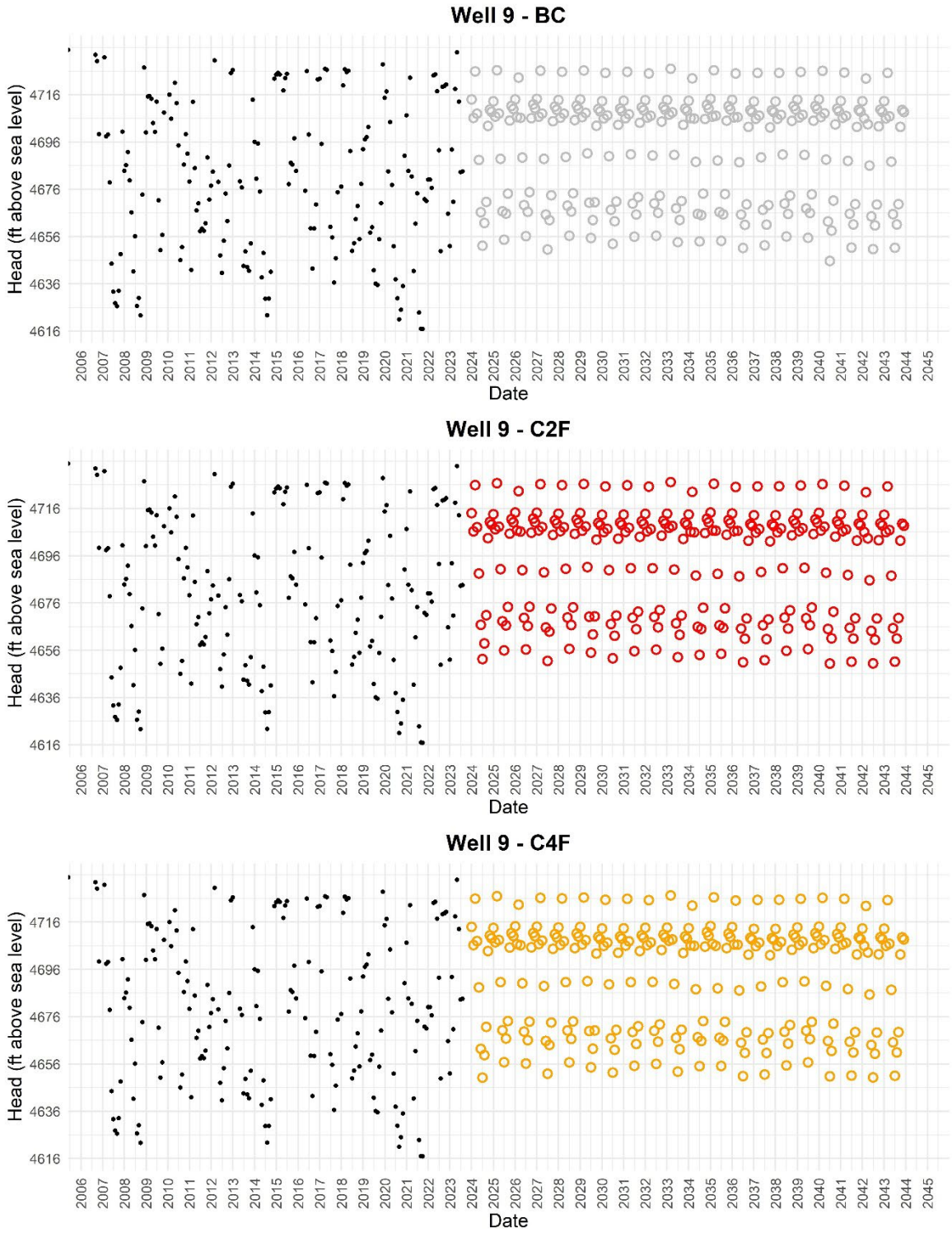

Figure 55A. Time series plots of predicted heads (colored circles) at GRGID supply Well 9 for predictive simulations BC, C2F, and C4F. For comparison to predicted heads, historical observed heads are also plotted (black dots). Simulation details are provided in Table 14. The *x*-axis extent depends on the date range of observed head data. Predicted minimum heads and rate of head change associated with the plots are presented in Table 17.

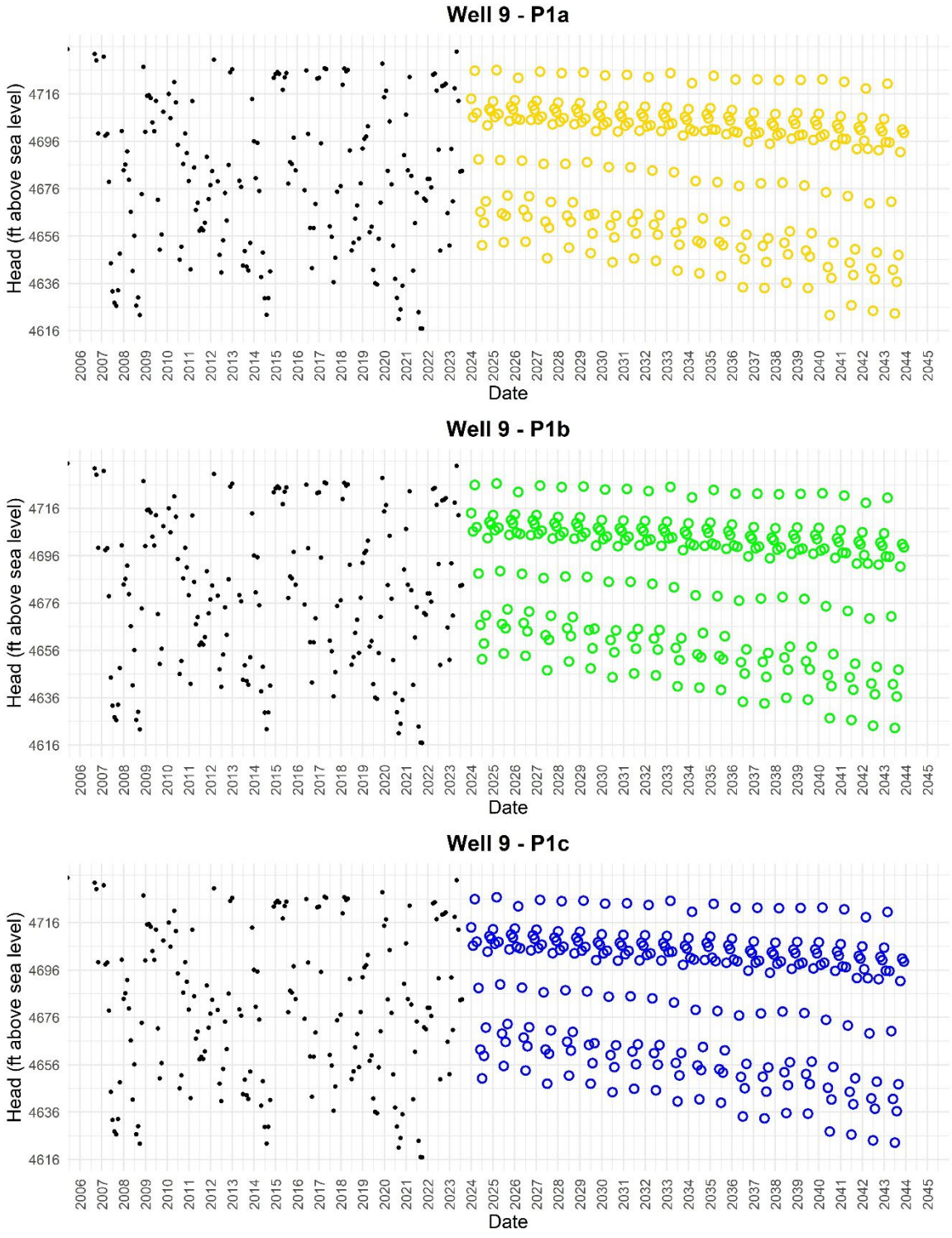

Figure 55B. Time series plots of predicted heads (colored circles) at GRGID supply Well 9 for predictive simulations P1a, P1b, and P1c. For comparison to predicted heads, historical observed heads are also plotted (black dots). Simulation details are provided in Table 14. The *x*-axis extent depends on the date range of observed head data. Predicted minimum heads and rate of head change associated with the plots are presented in Table 17.

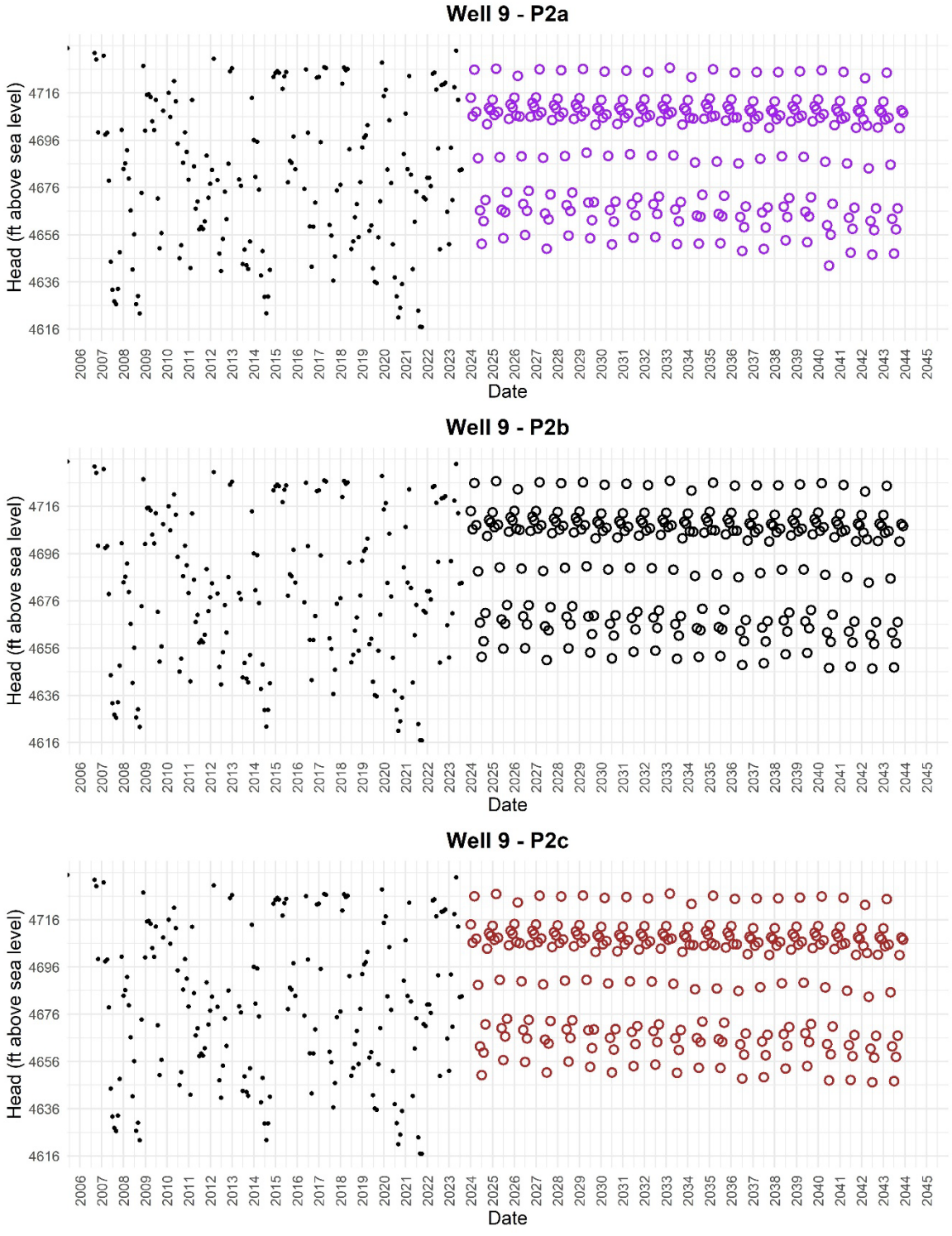

Figure 55C. Time series plots of predicted heads (colored circles) at GRGID supply Well 9 for predictive simulations P2a, P2b, and P2c. For comparison to predicted heads, historical observed heads are also plotted (black dots). Simulation details are provided in Table 14. The *x*-axis extent depends on the date range of observed head data. Predicted minimum heads and rate of head change associated with the plots are presented in Table 17.

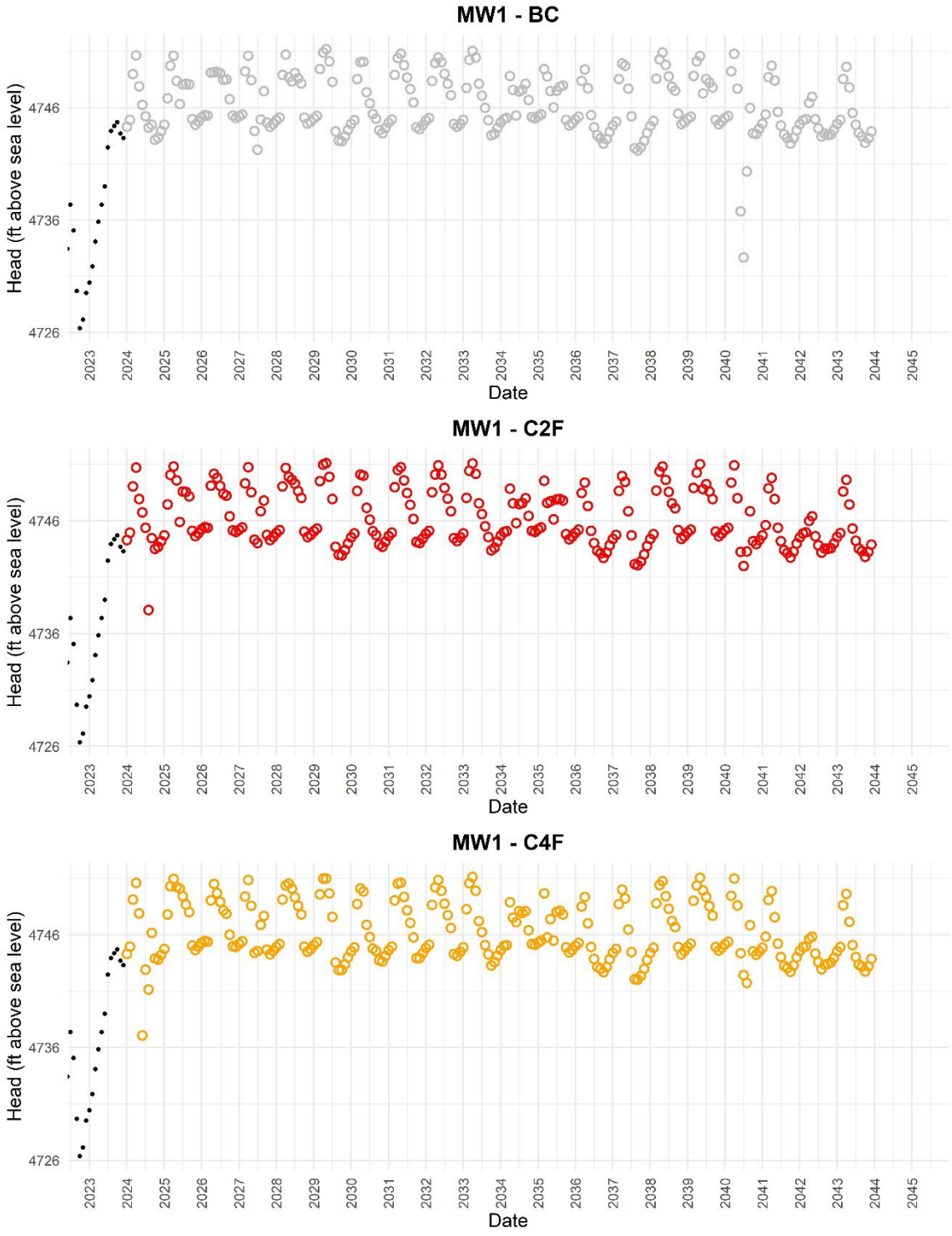

Figure 56A. Time series plots of predicted heads (colored circles) at GRGID Monitoring Well 1 (MW1) for predictive simulations BC, C2F, and C4F. For comparison to predicted heads, historical observed heads are also plotted (black dots). Simulation details are provided in Table 14. The *x*-axis extent depends on the date range of observed head data. Predicted minimum heads and rate of head change associated with the plots are presented in Table 18.

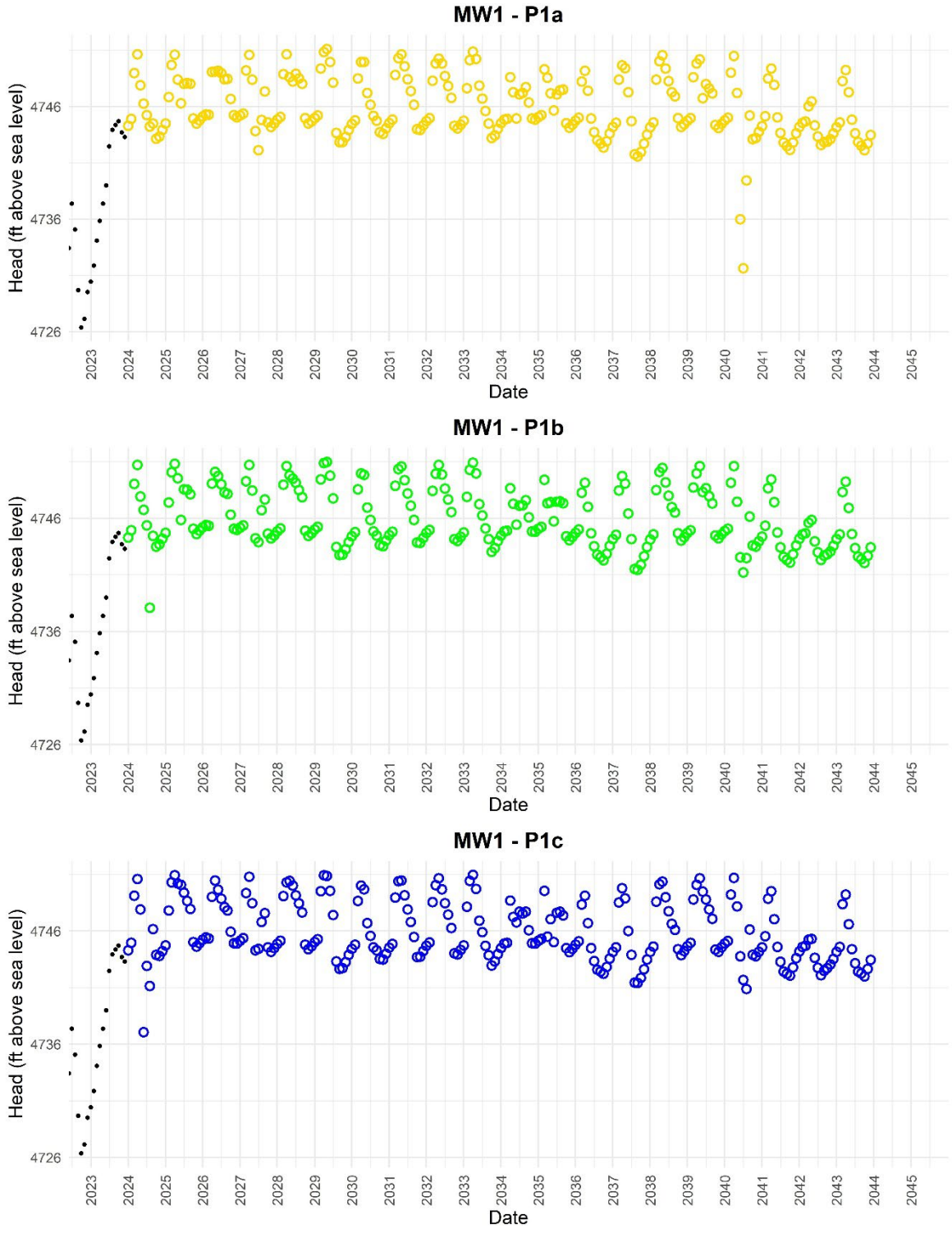

Figure 56B. Time series plots of predicted heads (colored circles) at GRGID MW1 for predictive simulations P1a, P1b, and P1c. For comparison to predicted heads, historical observed heads are also plotted (black dots). Simulation details are provided in Table 14. The *x*-axis extent depends on the date range of observed head data. Predicted minimum heads and rate of head change associated with the plots are presented in Table 18.

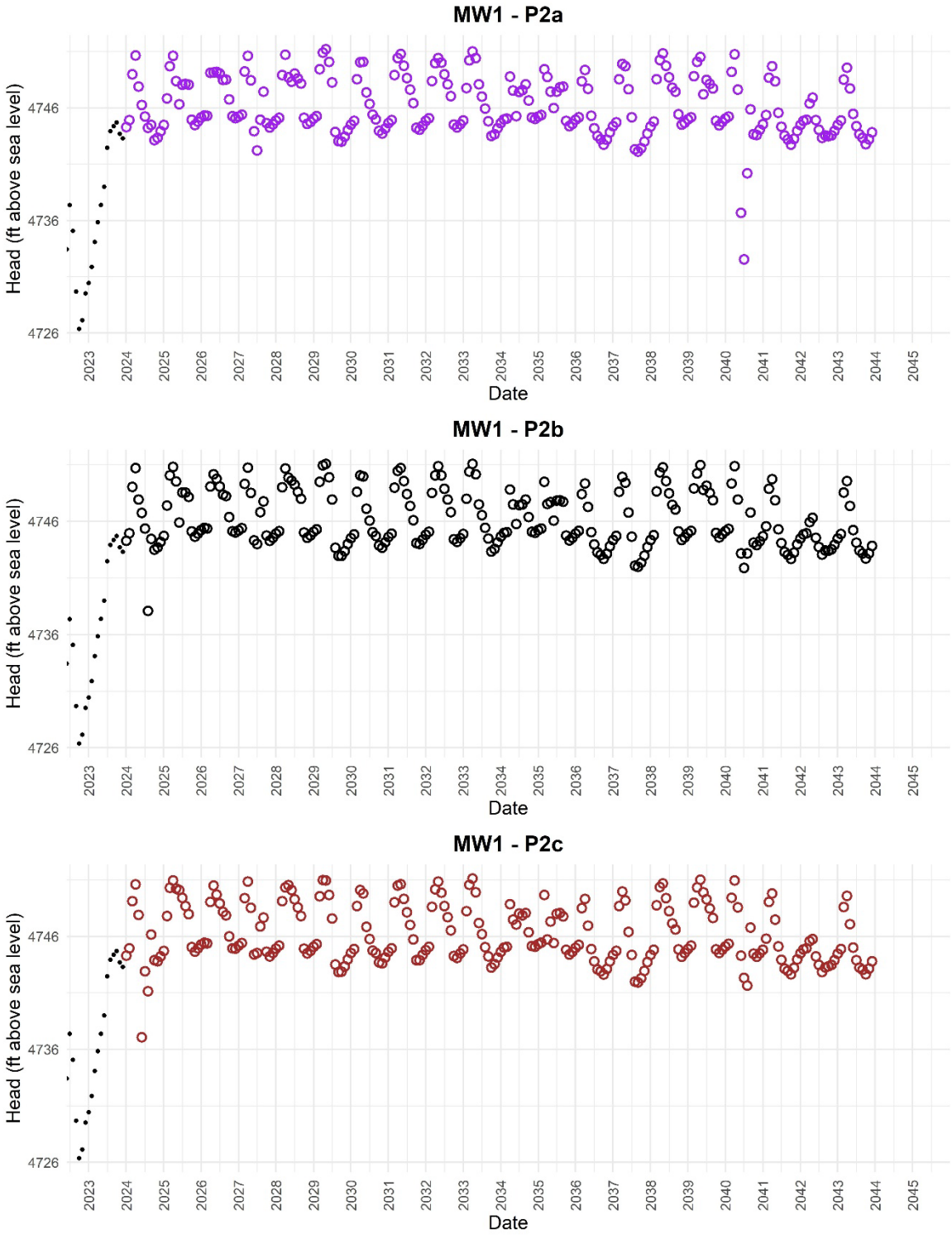

Figure 56C. Time series plots of predicted heads (colored circles) at GRGID MW1 for predictive simulations P2a, P2b, and P2c. For comparison to predicted heads, historical observed heads are also plotted (black dots). Simulation details are provided in Table 14. The *x*-axis extent depends on the date range of observed head data. Predicted minimum heads and rate of head change associated with the plots are presented in Table 18.

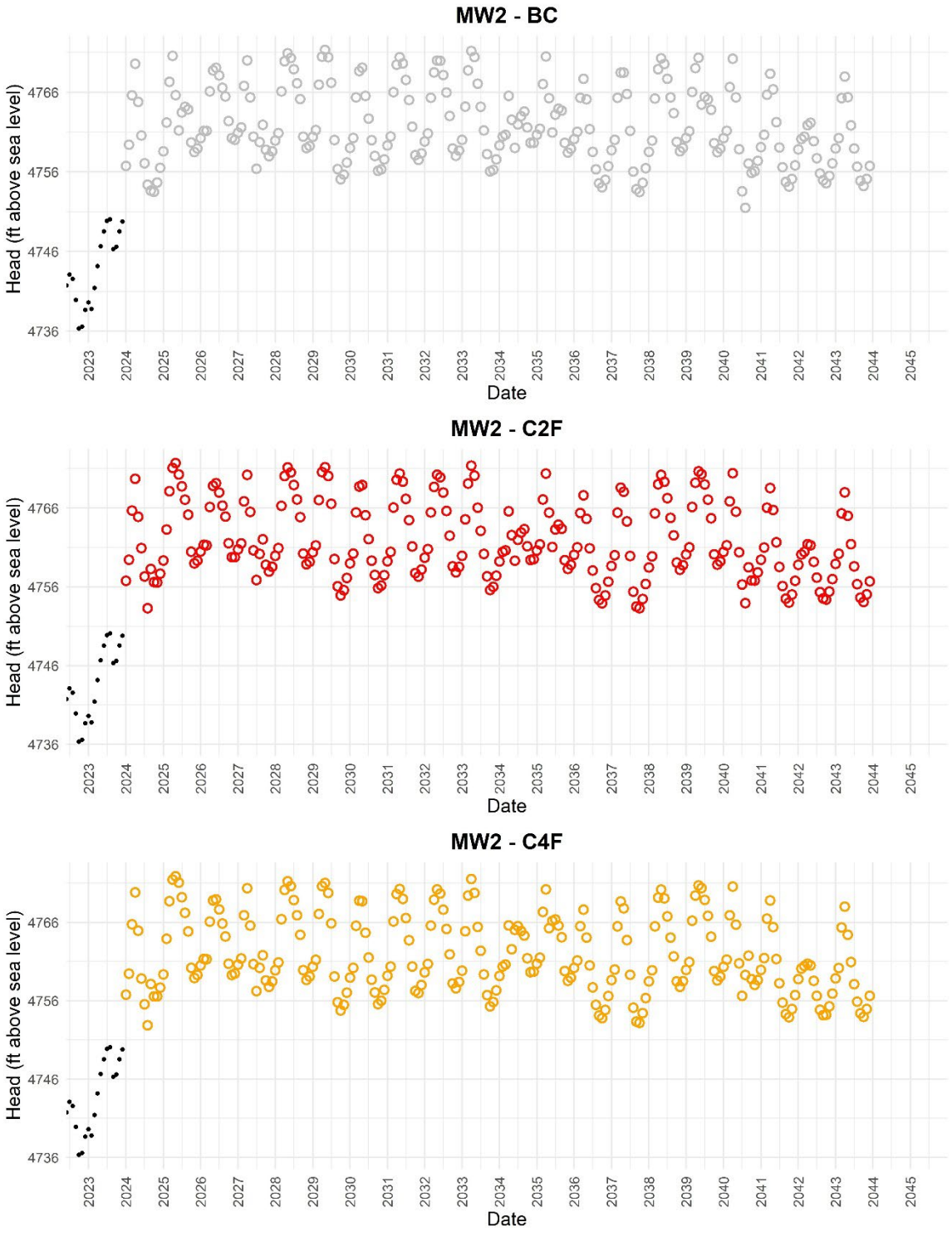

Figure 57A. Time series plots of predicted heads (colored circles) at GRGID Monitoring Well 2 (MW2) for predictive simulations BC, C2F, and C4F. For comparison to predicted heads, historical observed heads are also plotted (black dots). Simulation details are provided in Table 14. The *x*-axis extent depends on the date range of observed head data. Predicted minimum heads and rate of head change associated with the plots are presented in Table 18.

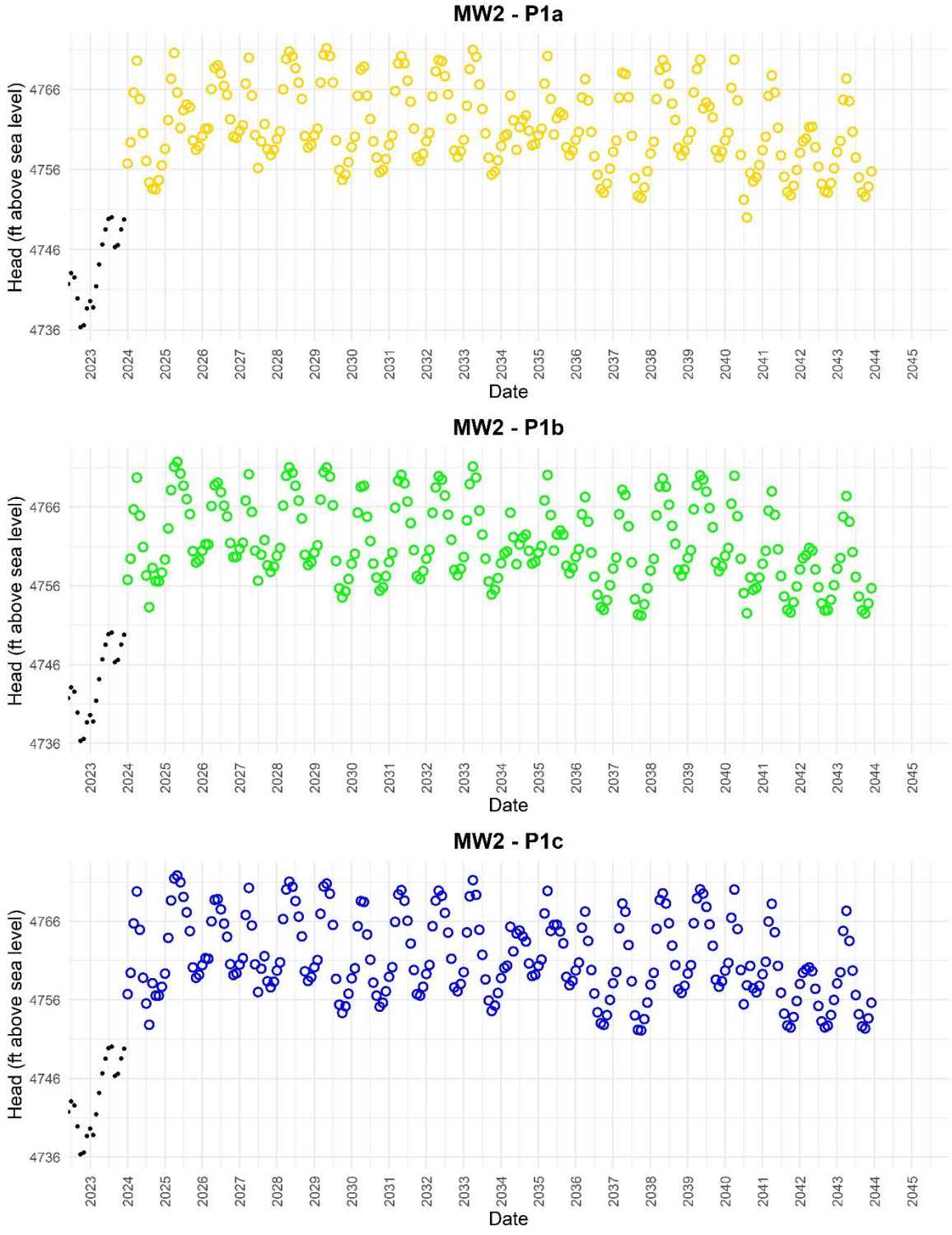

Figure 57B. Time series plots of predicted heads (colored circles) at GRGID MW2 for predictive simulations P1a, P1b, and P1c. For comparison to predicted heads, historical observed heads are also plotted (black dots). Simulation details are provided in Table 14. The *x*-axis extent depends on the date range of observed head data. Predicted minimum heads and rate of head change associated with the plots are presented in Table 18.

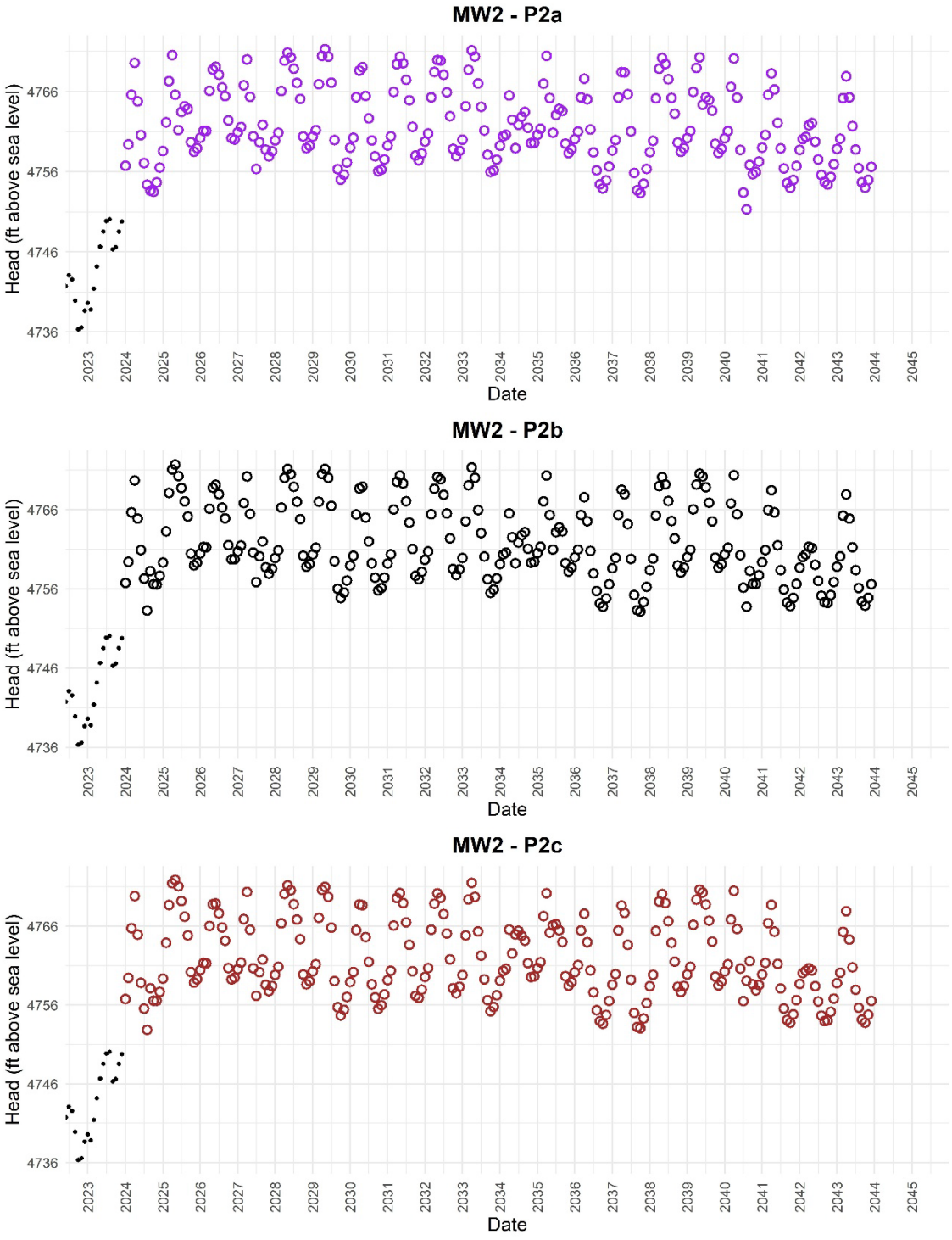

Figure 57C. Time series plots of predicted heads (colored circles) at GRGID MW2 for predictive simulations P2a, P2b, and P2c. For comparison to predicted heads, historical observed heads are also plotted (black dots). Simulation details are provided in Table 14. The *x*-axis extent depends on the date range of observed head data. Predicted minimum heads and rate of head change associated with the plots are presented in Table 18.

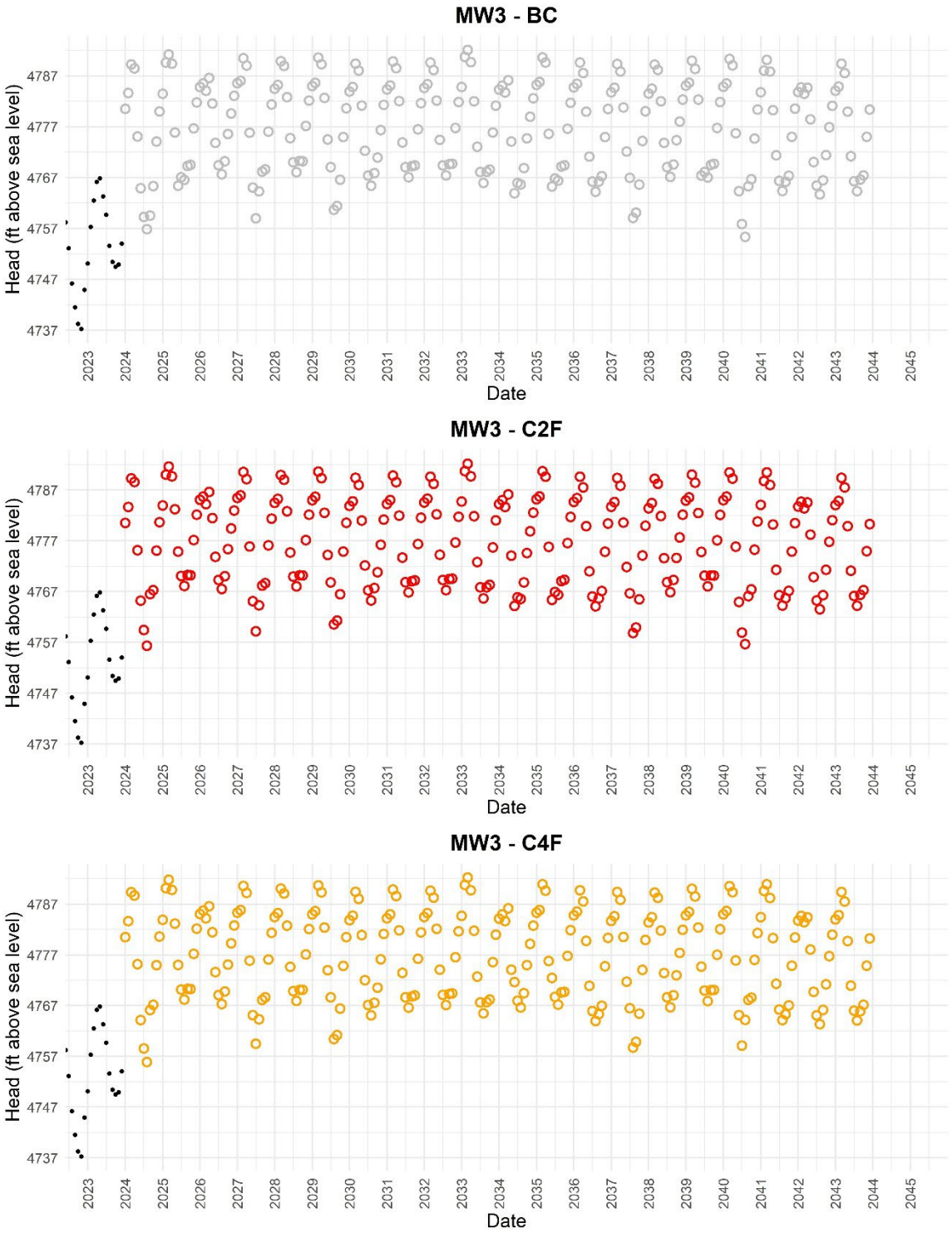

Figure 58A. Time series plots of predicted heads (colored circles) at GRGID Monitoring Well 3 (MW3) for predictive simulations BC, C2F, and C4F. For comparison to predicted heads, historical observed heads are also plotted (black dots). Simulation details are provided in Table 14. The *x*-axis extent depends on the date range of observed head data. Predicted minimum heads and rate of head change associated with the plots are presented in Table 18.

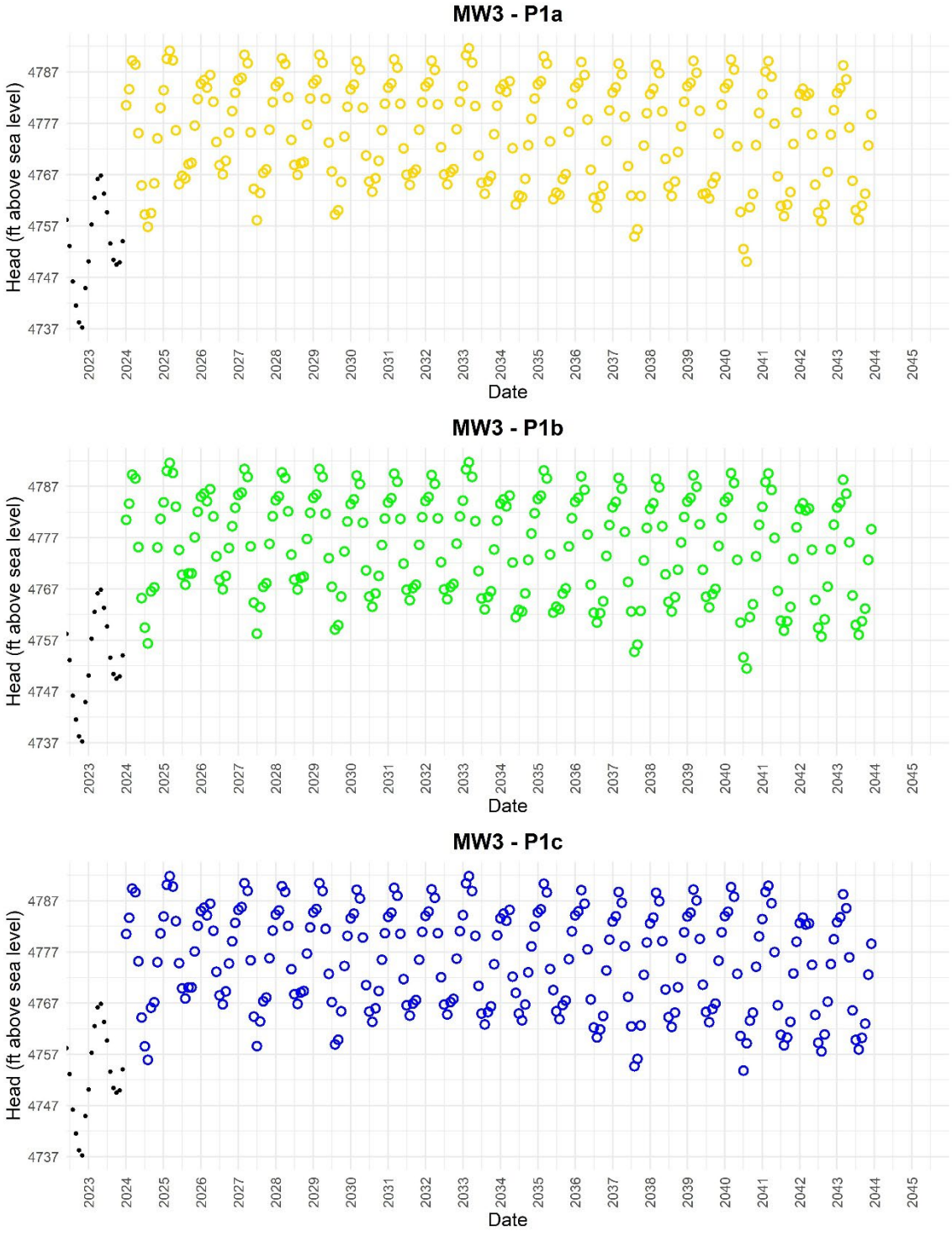

Figure 58B. Time series plots of predicted heads (colored circles) at GRGID MW3 for predictive simulations P1a, P1b, and P1c. For comparison to predicted heads, historical observed heads are also plotted (black dots). Simulation details are provided in Table 14. The *x*-axis extent depends on the date range of observed head data. Predicted minimum heads and rate of head change associated with the plots are presented in Table 18.

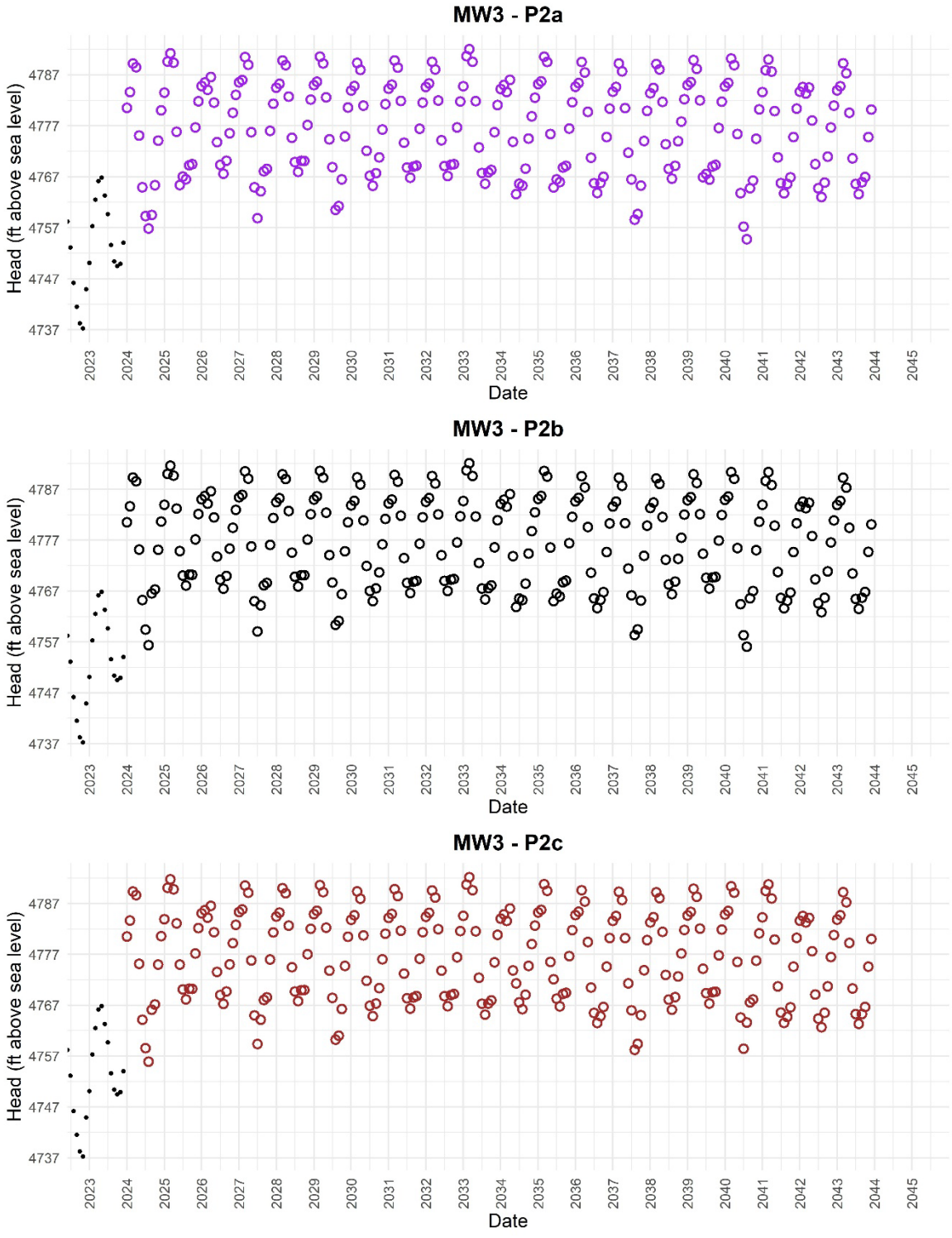

Figure 58C. Time series plots of predicted heads (colored circles) at GRGID MW3 for predictive simulations P2a, P2b, and P2c. For comparison to predicted heads, historical observed heads are also plotted (black dots). Simulation details are provided in Table 14. The *x*-axis extent depends on the date range of observed head data. Predicted minimum heads and rate of head change associated with the plots are presented in Table 18.

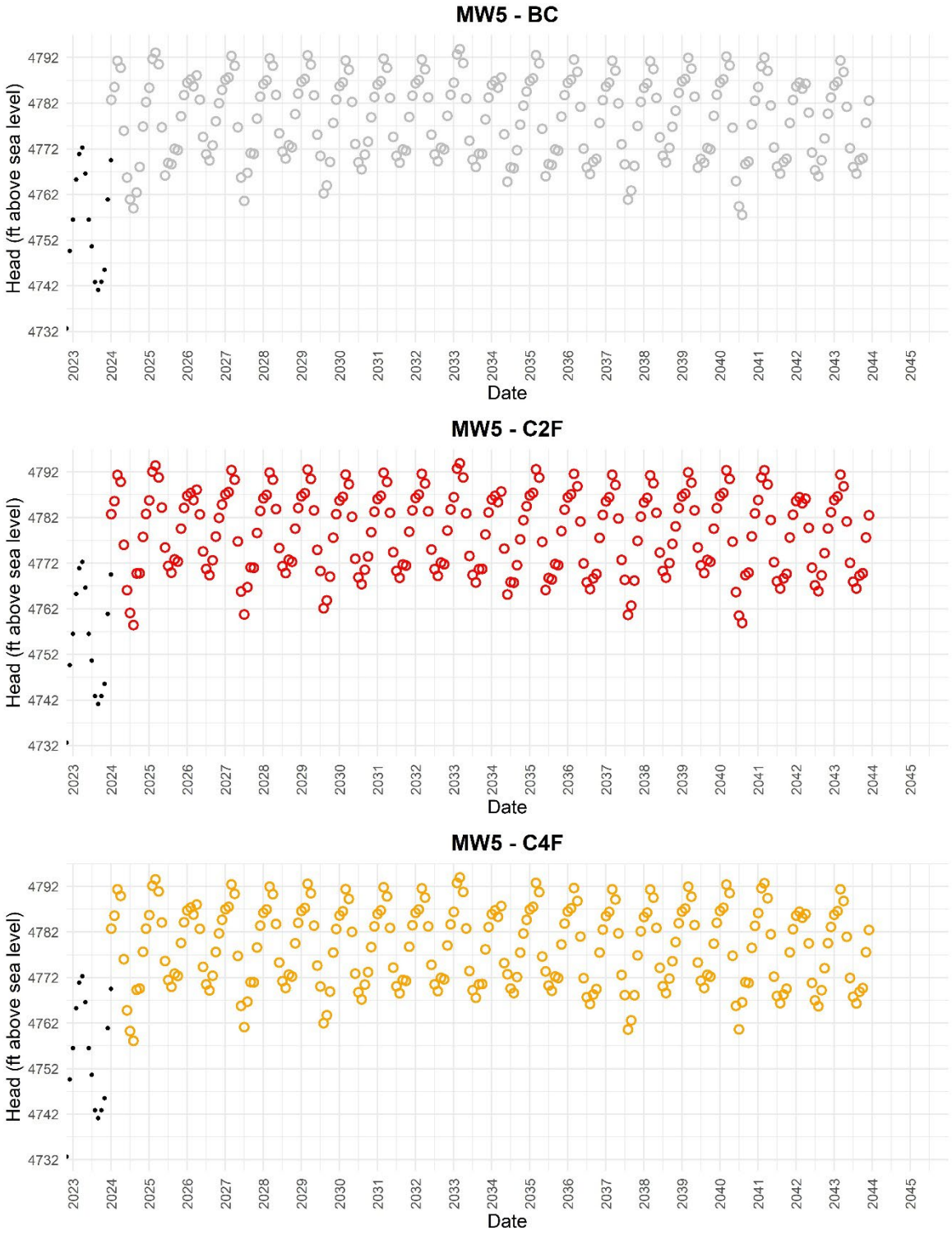

Figure 59A. Time series plots of predicted heads (colored circles) at GRGID Monitoring Well 5 (MW5) for predictive simulations BC, C2F, and C4F. For comparison to predicted heads, historical observed heads are also plotted (black dots). Simulation details are provided in Table 14. The *x*-axis extent depends on the date range of observed head data. Predicted minimum heads and rate of head change associated with the plots are presented in Table 18.

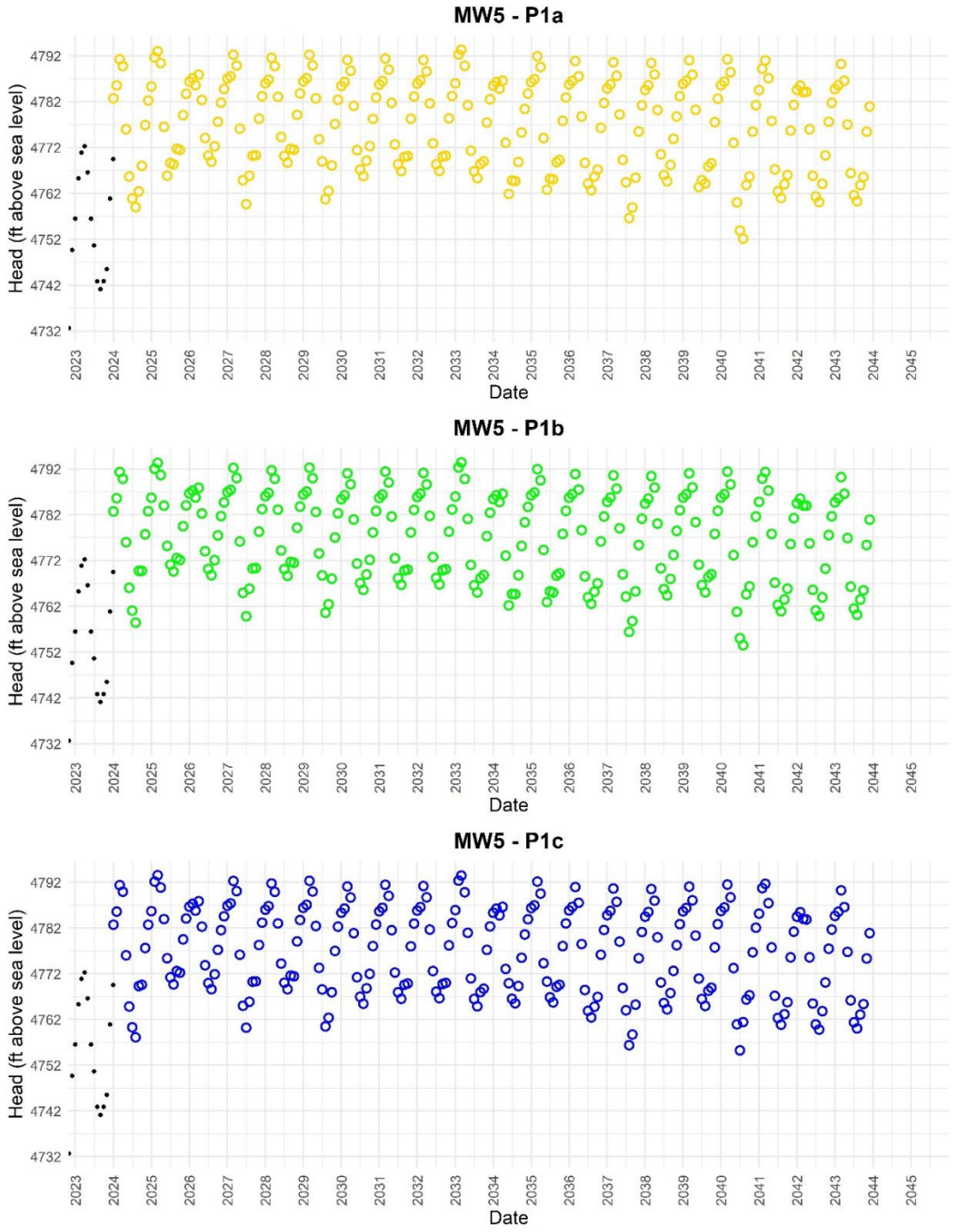

Figure 59B. Time series plots of predicted heads (colored circles) at GRGID MW5 for predictive simulations P1a, P1b, and P1c. For comparison to predicted heads, historical observed heads are also plotted (black dots). Simulation details are provided in Table 14. The *x*-axis varies between wells based on the date range of observed head data. Predicted minimum heads and rate of head change associated with the plots are presented in Table 18.

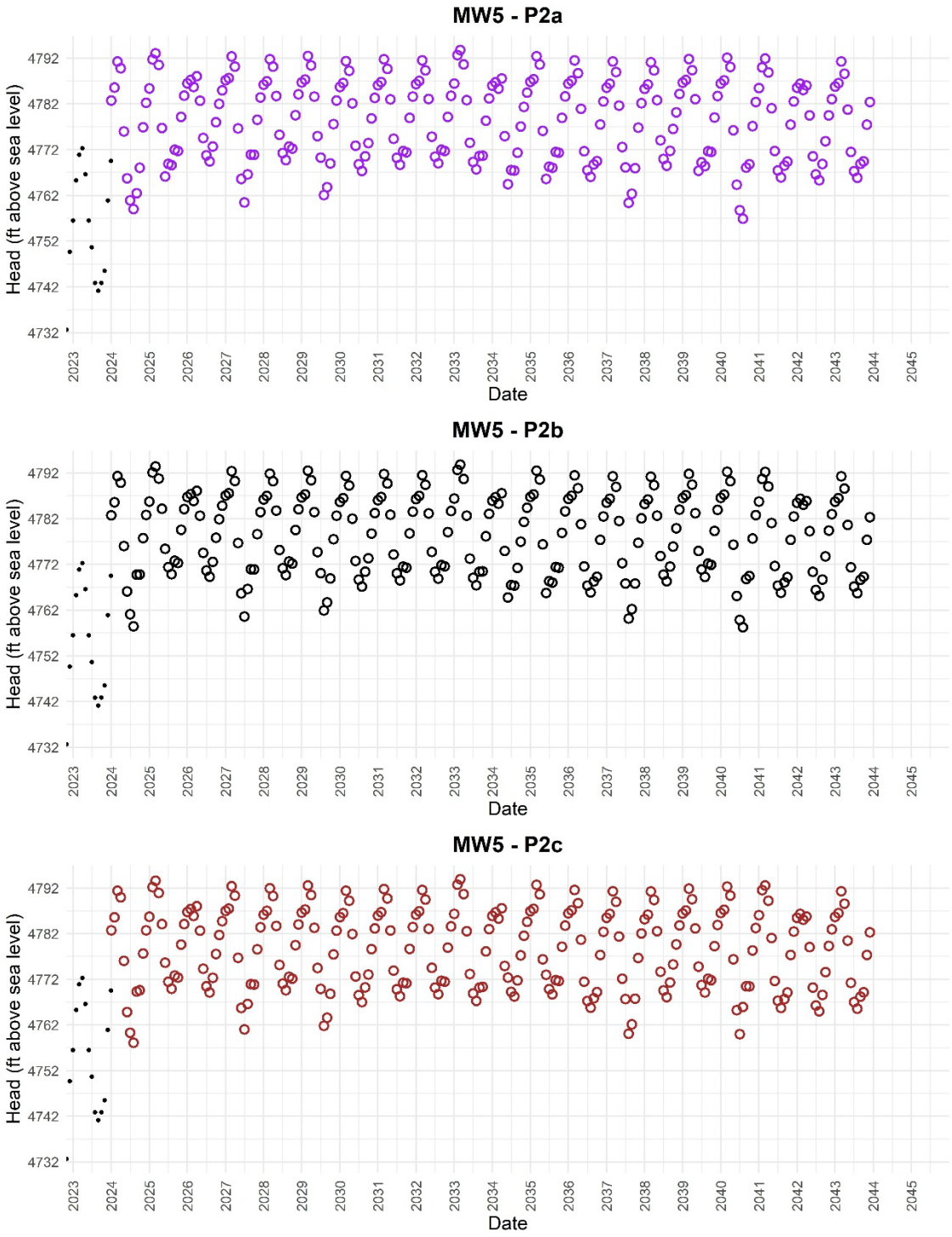

Figure 59C. Time series plots of predicted heads (colored circles) at GRGID MW5 for predictive simulations P2a, P2b, and P2c. For comparison to predicted heads, historical observed heads are also plotted (black dots). Simulation details are provided in Table 14. The *x*-axis varies between wells based on the date range of observed head data. Predicted minimum heads and rate of head change associated with the plots are presented in Table 18.

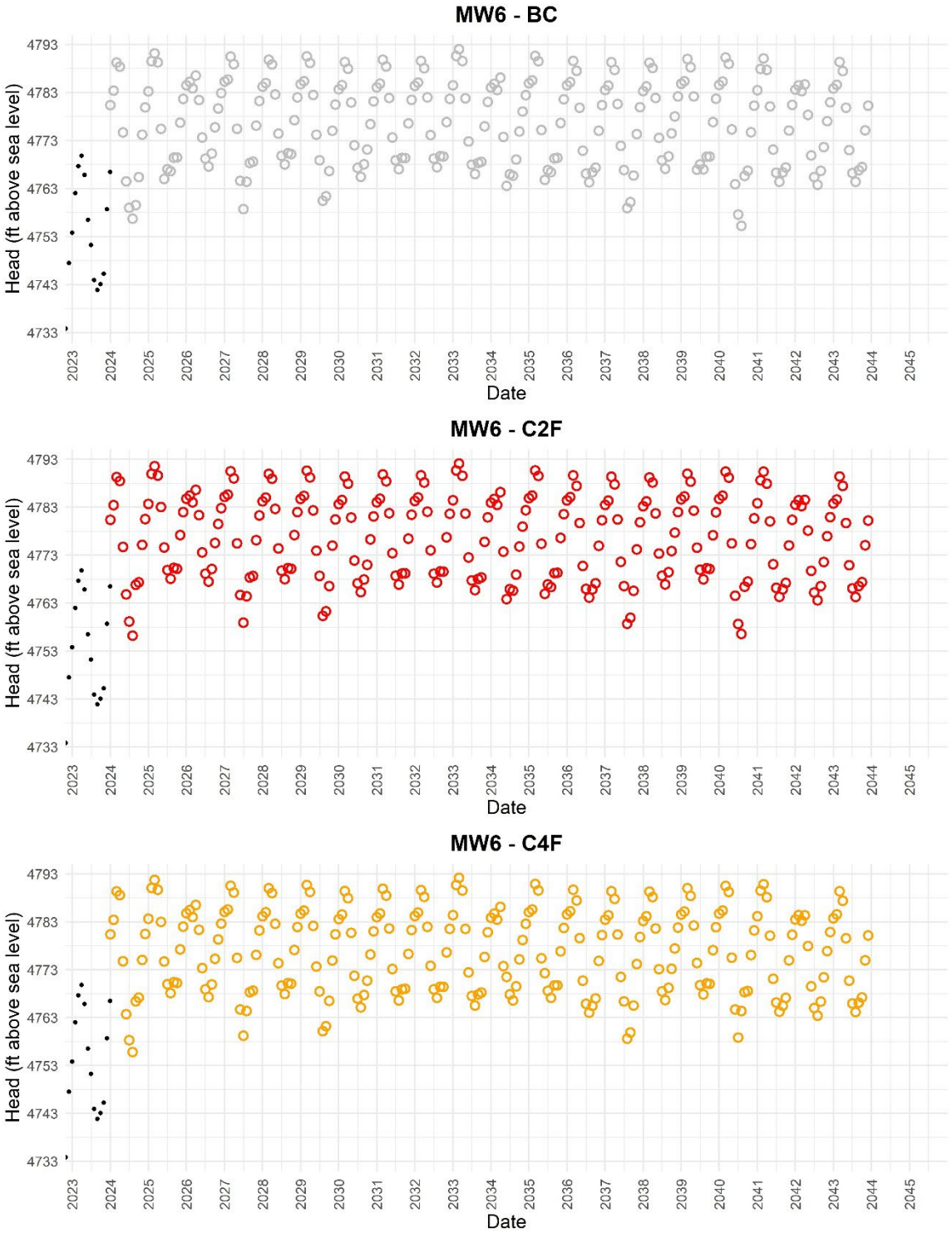

Figure 60A. Time series plots of predicted heads (colored circles) at GRGID Monitoring Well 6 (MW6) for predictive simulations BC, C2F, and C4F. For comparison to predicted heads, historical observed heads are also plotted (black dots). Simulation details are provided in Table 14. The *x*-axis varies between wells based on the date range of observed head data. Predicted minimum heads and rate of head change associated with the plots are presented in Table 18).

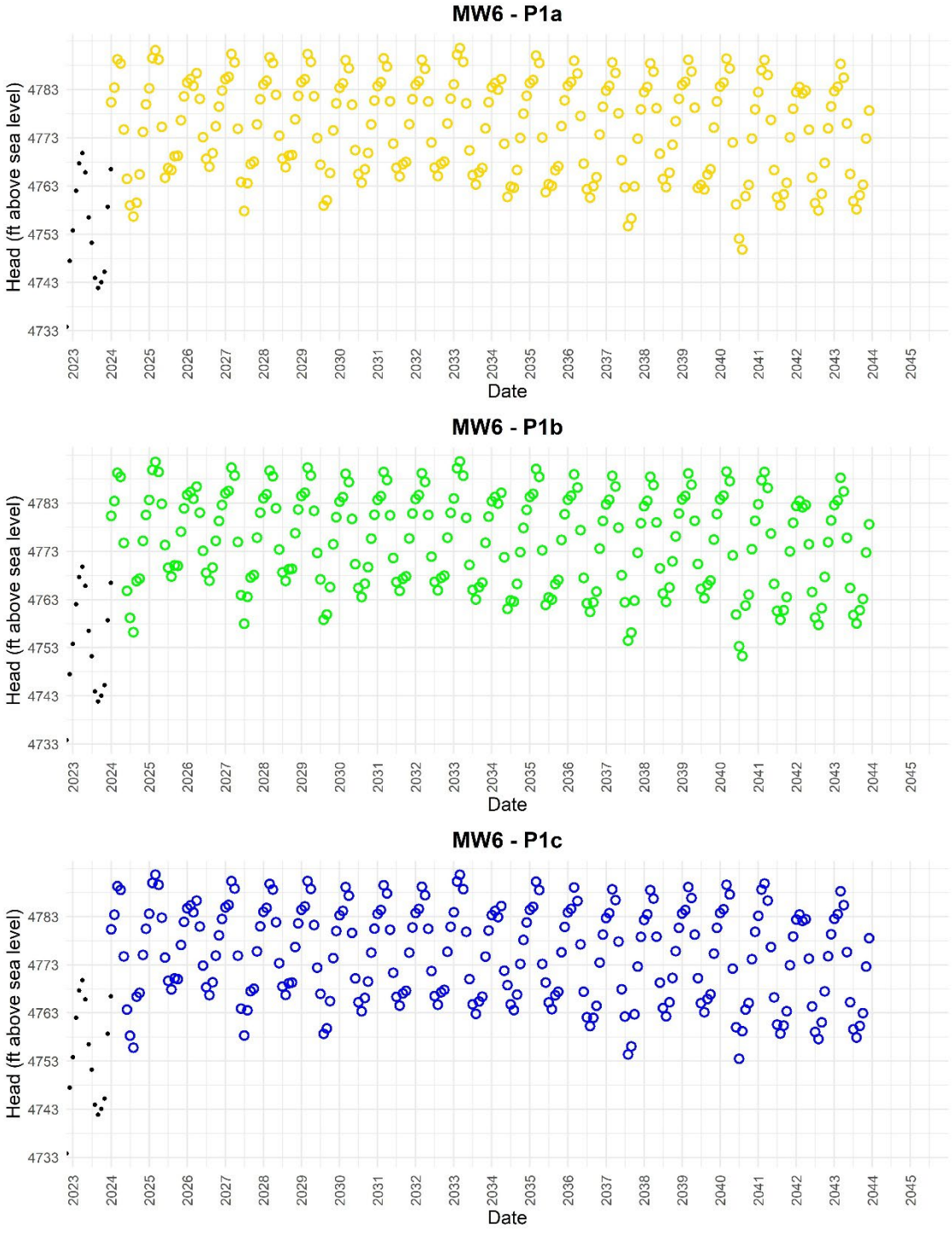

Figure 60B. Time series plots of predicted heads (colored circles) at GRGID MW6 for predictive simulations P1a, P1b, and P1c. For comparison to predicted heads, historical observed heads are also plotted (black dots). Simulation details are provided in Table 14. The *x*-axis varies between wells based on the date range of observed head data. Predicted minimum heads and rate of head change associated with the plots are presented in Table 18.

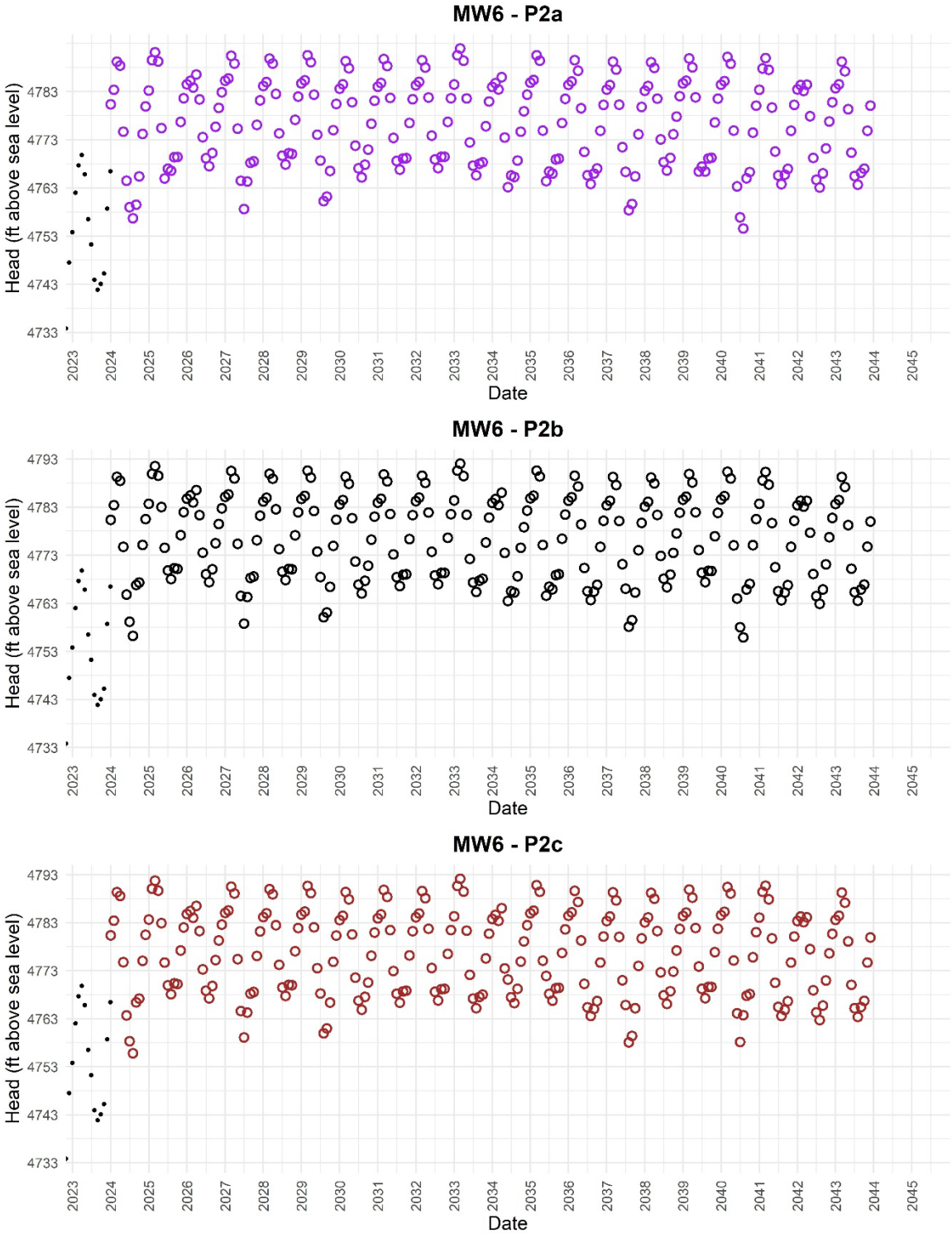

Figure 60C. Time series plots of predicted heads (colored circles) at GRGID MW6 for predictive simulations P2a, P2b, and P2c. For comparison to predicted heads, historical observed heads are also plotted (black dots). Simulation details are provided in Table 14. The *x*-axis varies between wells based on the date range of observed head data. Predicted minimum heads and rate of head change associated with the plots are presented in Table 18.

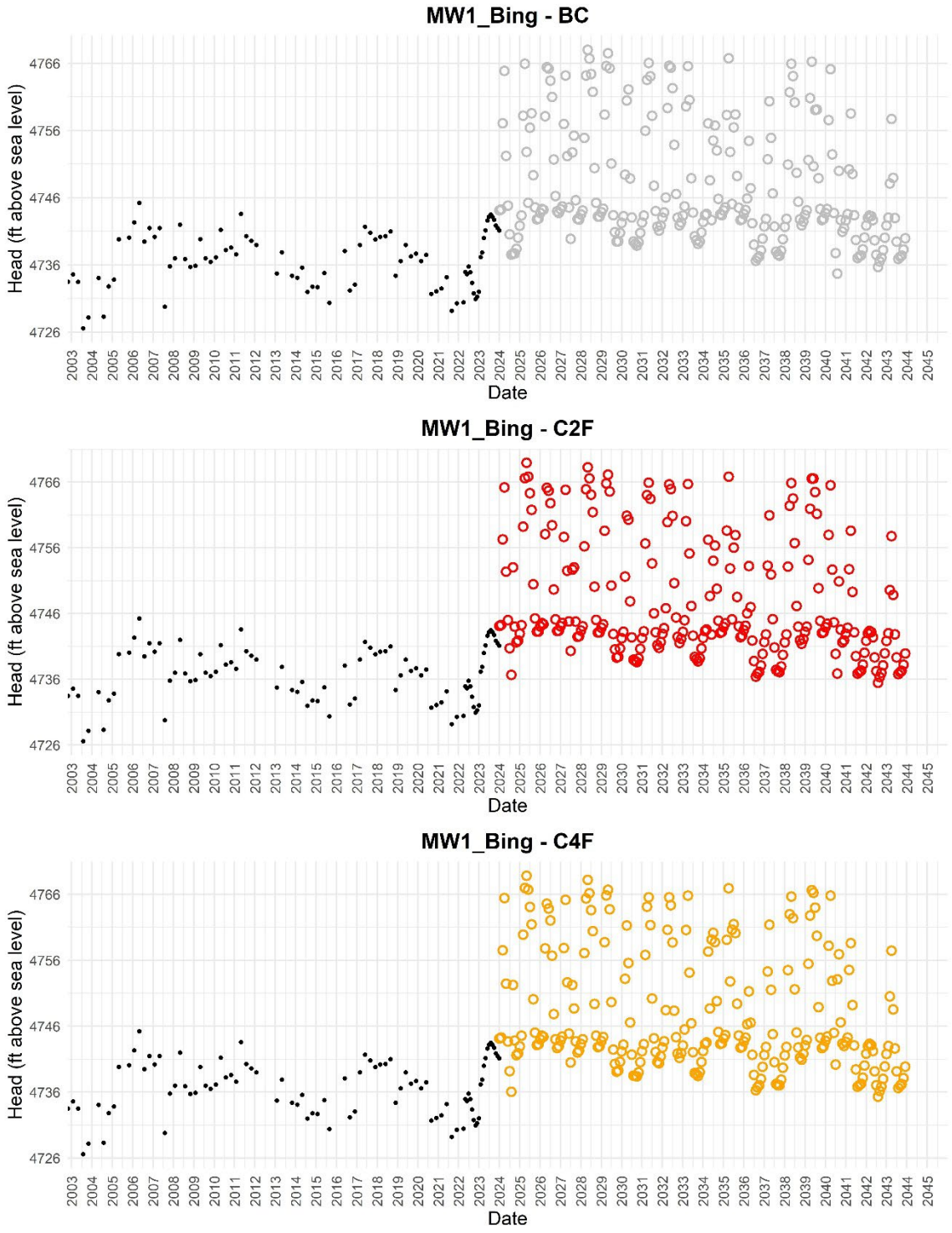

Figure 61A. Time series plots of predicted heads (colored circles) at MW1_Bing for predictive simulations BC, C2F, and C4F. For comparison to predicted heads, historical observed heads are also plotted (black dots). Simulation details are provided in Table 14. The *x*-axis varies between wells based on the date range of observed head data. Predicted minimum heads and rate of head change associated with the plots are presented in Table 18.

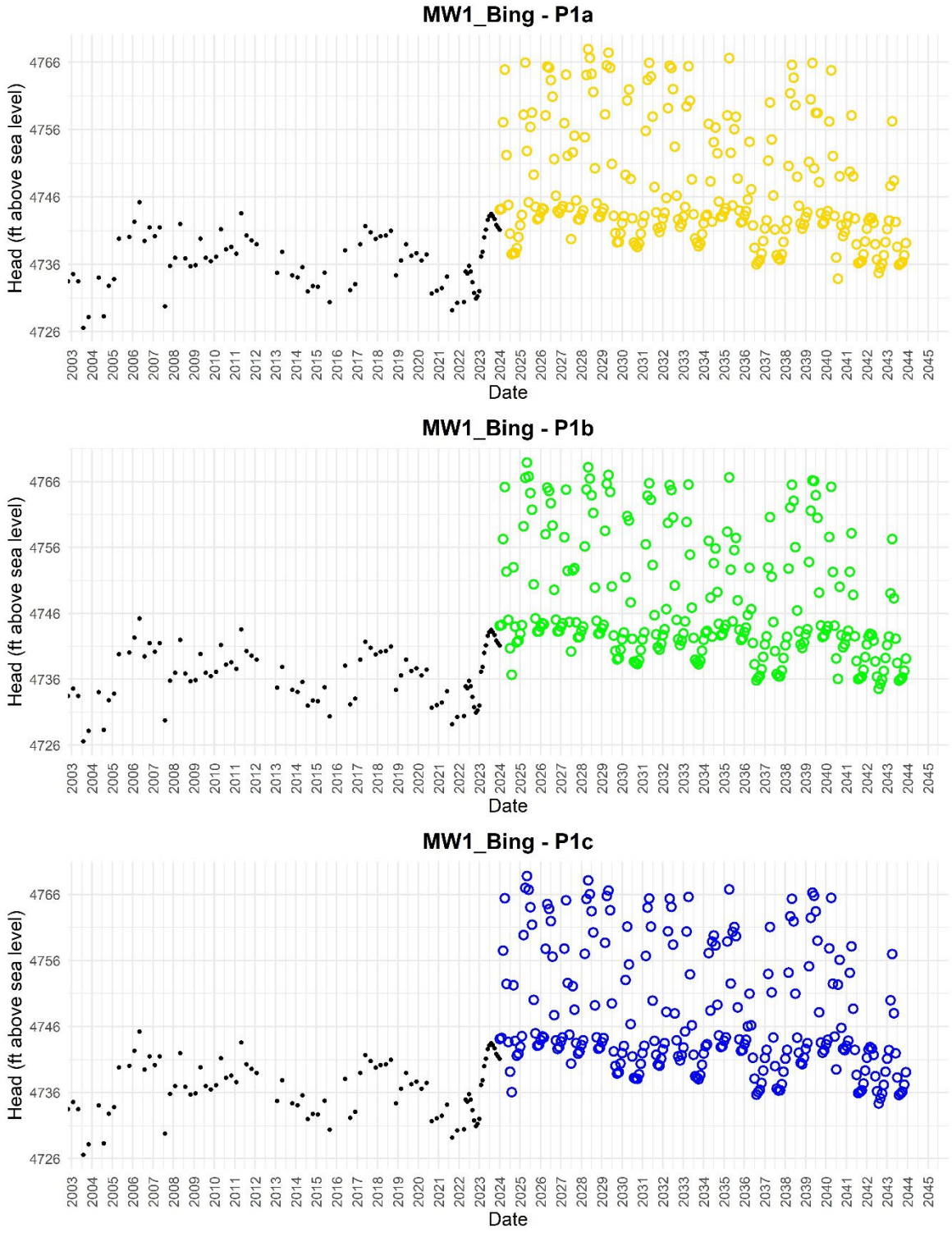

Figure 61B. Time series plots of predicted heads (colored circles) at MW1_Bing for predictive simulations P1a, P1b, and P1c. For comparison to predicted heads, historical observed heads are also plotted (black dots). Simulation details are provided in Table 14. The *x*-axis varies between wells based on the date range of observed head data. Predicted minimum heads and rate of head change associated with the plots are presented in Table 18.

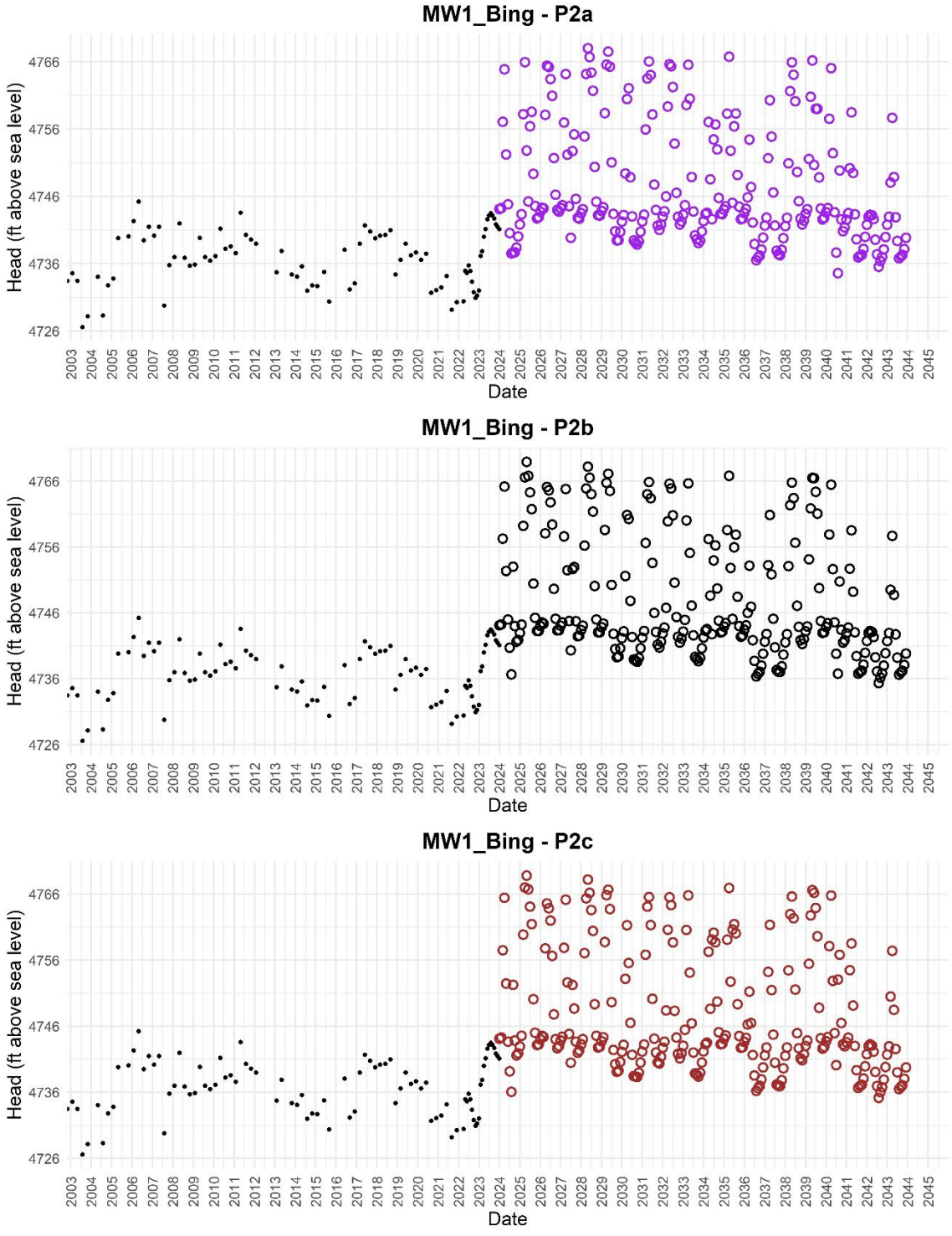

Figure 61C. Time series plots of predicted heads (colored circles) at MW1_Bing for predictive simulations P2a, P2b, and P2c. For comparison to predicted heads, historical observed heads are also plotted (black dots). Simulation details are provided in Table 14. The *x*-axis varies between wells based on the date range of observed head data. Predicted minimum heads and rate of head change associated with the plots are presented in Table 18.

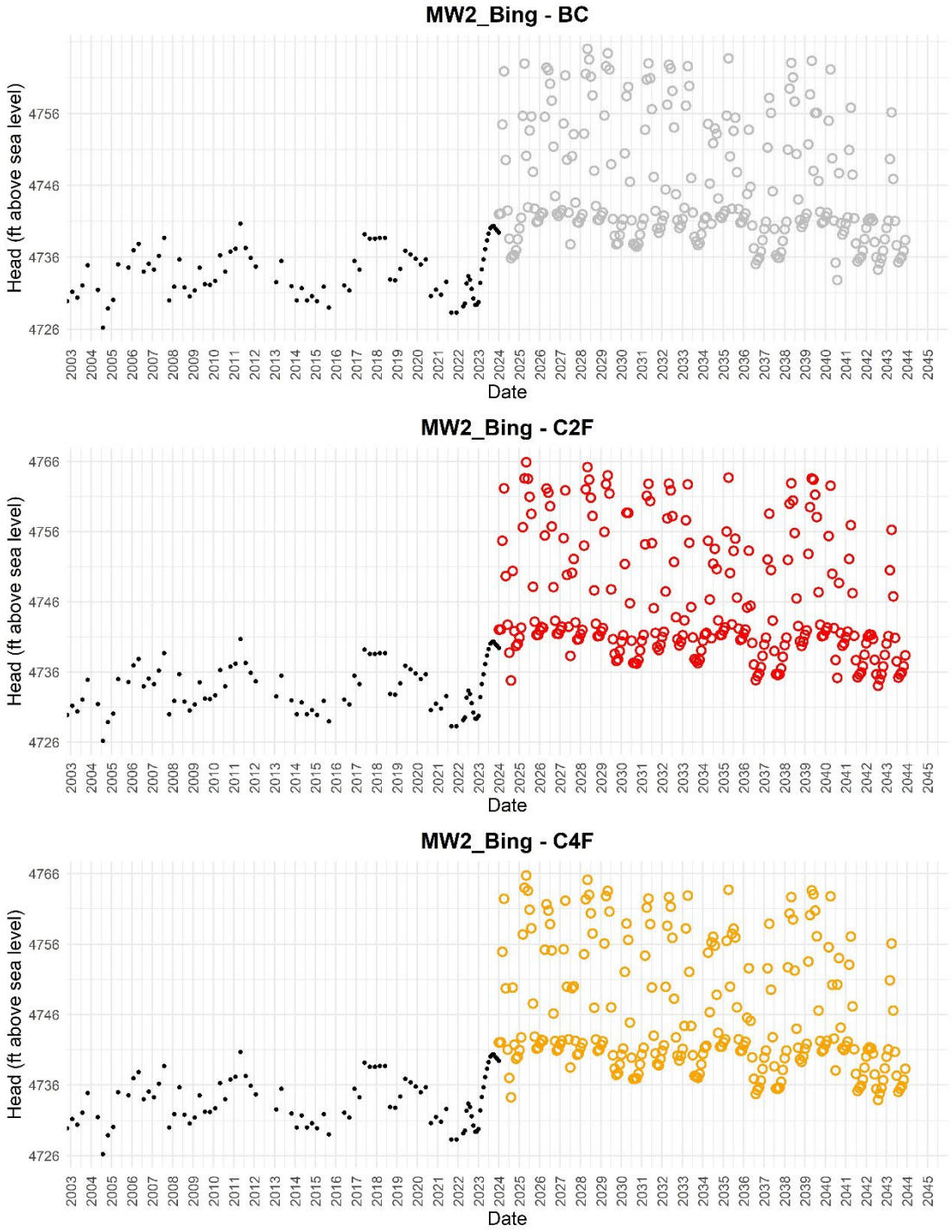

Figure 62A. Time series plots of predicted heads (colored circles) at MW2_Bing for predictive simulations BC, C2F, and C4F. For comparison to predicted heads, historical observed heads are also plotted (black dots). Simulation details are provided in Table 14. The *x*-axis varies between wells based on the date range of observed head data. Predicted minimum heads and rate of head change associated with the plots are presented in Table 18.

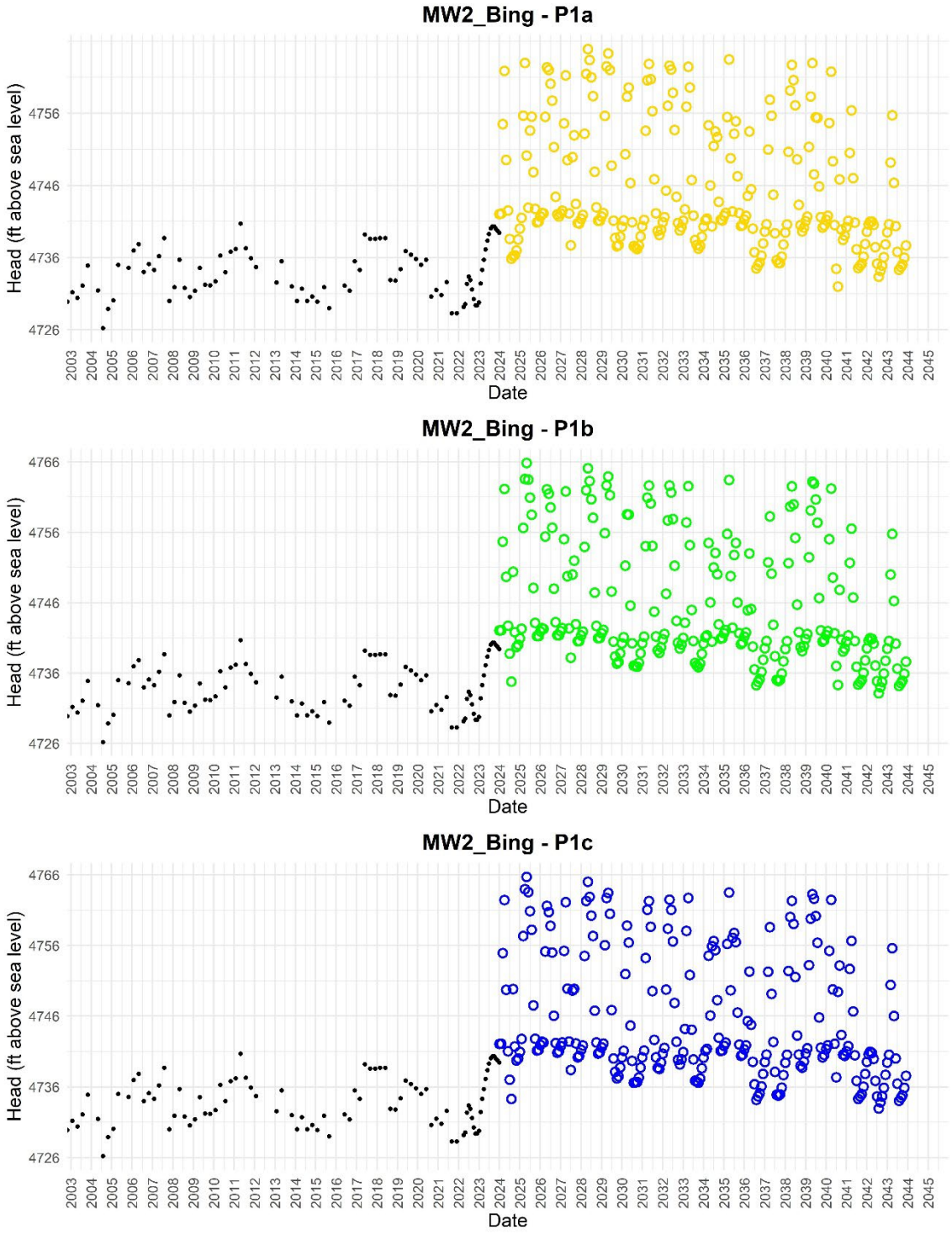

Figure 62B. Time series plots of predicted heads (colored circles) at MW2_Bing for predictive simulations P1a, P1b, and P1c. For comparison to predicted heads, historical observed heads are also plotted (black dots). Simulation details are provided in Table 14. The *x*-axis varies between wells based on the date range of observed head data. Predicted minimum heads and rate of head change associated with the plots are presented in Table 18.

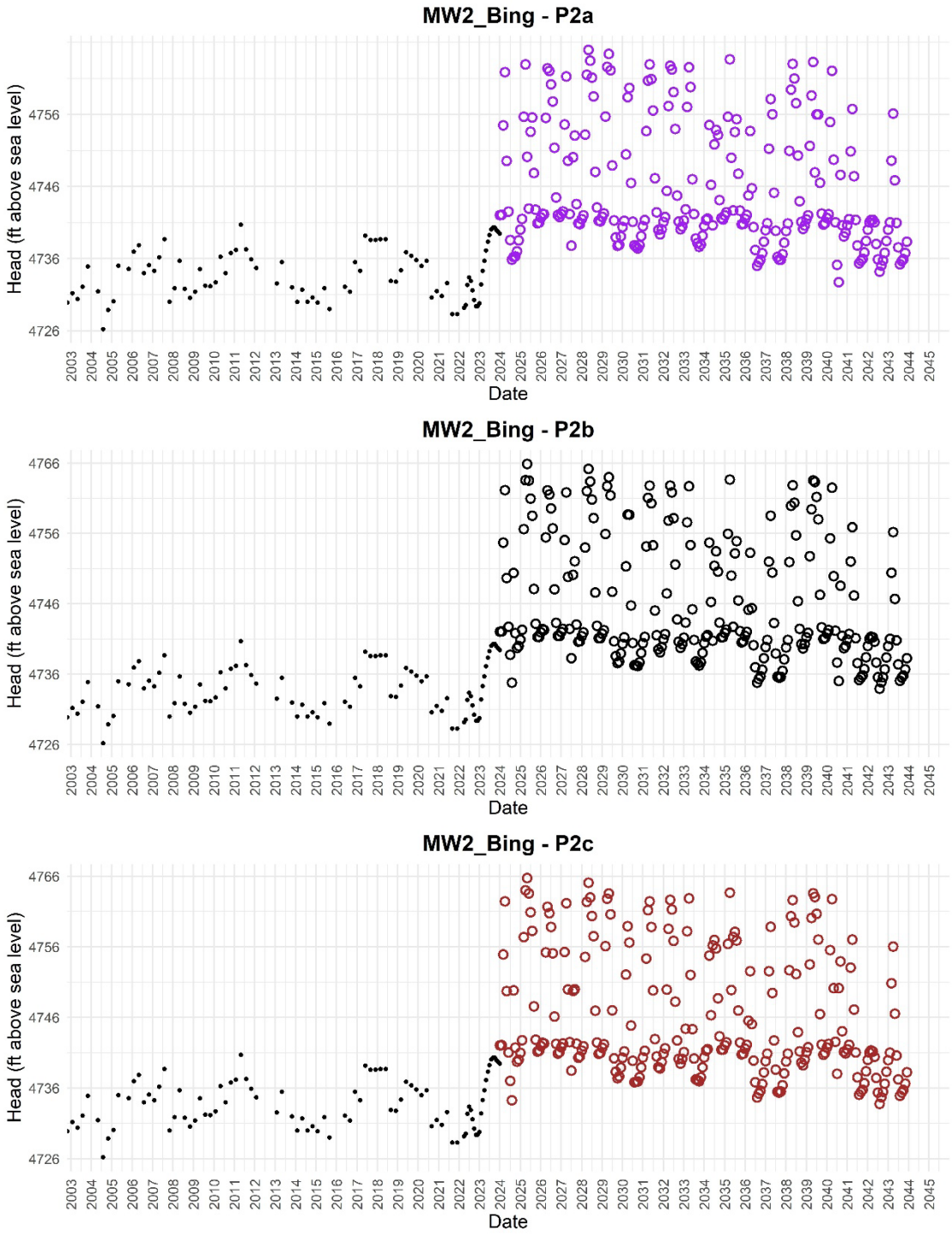

Figure 62C. Time series plots of predicted heads (colored circles) at MW2_Bing for predictive simulations P2a, P2b, and P2c. For comparison to predicted heads, historical observed heads are also plotted (black dots). Simulation details are provided in Table 14. The *x*-axis varies between wells based on the date range of observed head data. Predicted minimum heads and rate of head change associated with the plots are presented in Table 18.

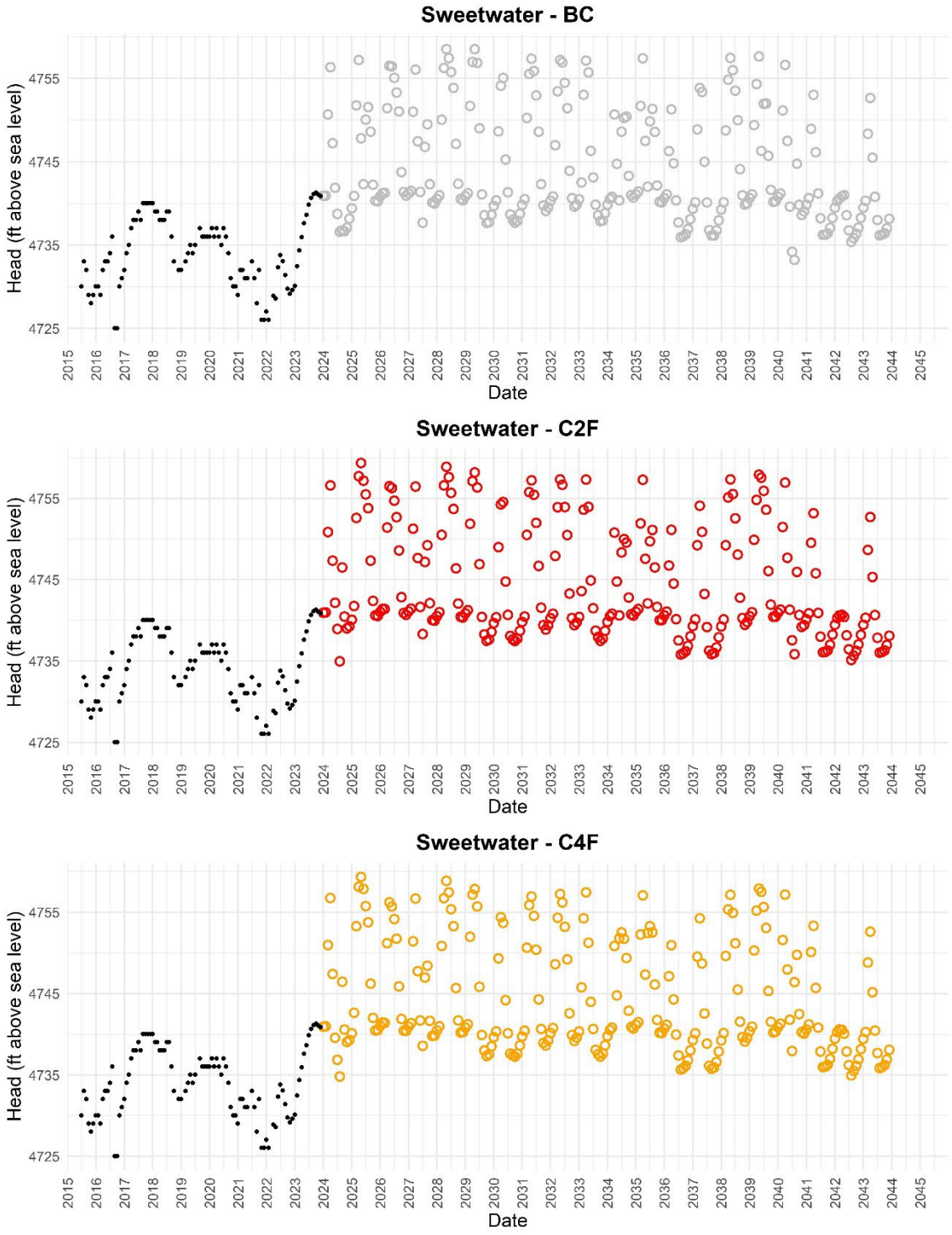

Figure 63A. Time series plots of predicted heads (colored circles) at GRGID Sweetwater monitoring well for predictive simulations BC, C2F, and C4F. For comparison to predicted heads, historical observed heads are also plotted (black dots). Simulation details are provided in Table 14. The *x*-axis varies between wells based on the date range of observed head data. Predicted minimum heads and rate of head change associated with the plots are presented in Table 18.

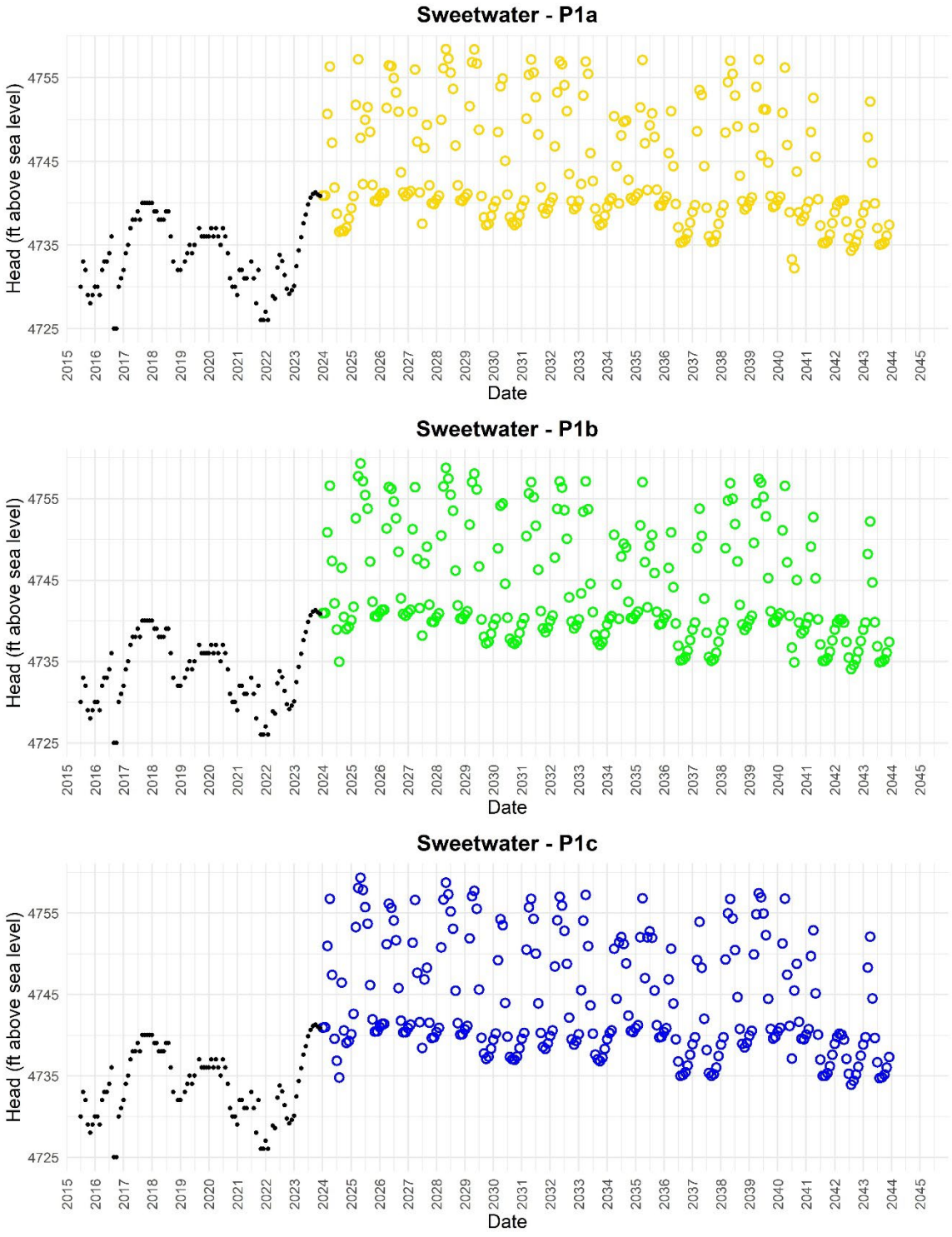

Figure 63B. Time series plots of predicted heads (colored circles) at GRGID Sweetwater monitoring well for predictive simulations P1a, P1b, and P1c. For comparison to predicted heads, historical observed heads are also plotted (black dots). Simulation details are provided in Table 14. The *x*-axis varies between wells based on the date range of observed head data. Predicted minimum heads and rate of head change associated with the plots are presented in Table 18.

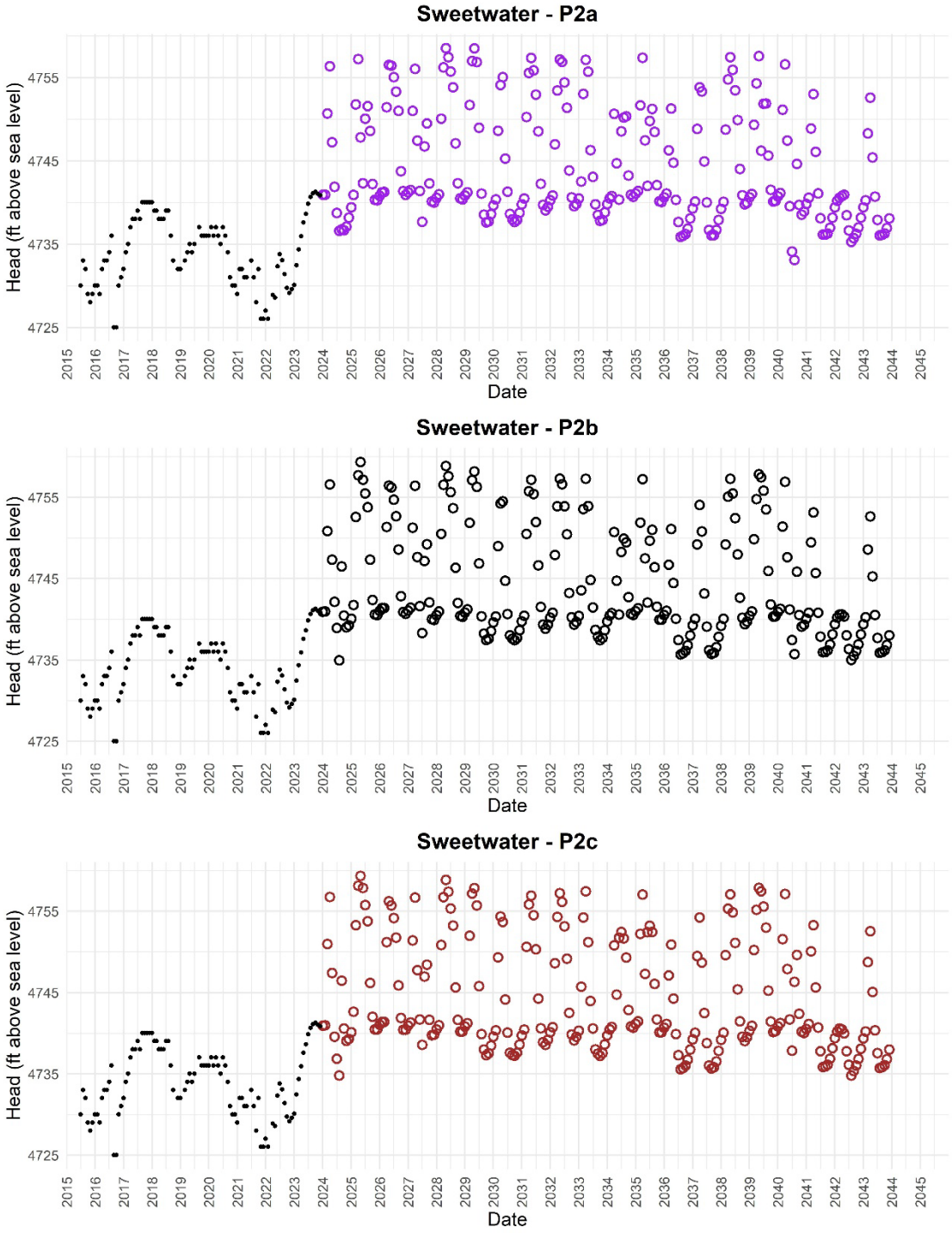

Figure 63C. Time series plots of predicted heads (colored circles) at GRGID Sweetwater monitoring well for predictive simulations P2a, P2b, and P2c. For comparison to predicted heads, historical observed heads are also plotted (black dots). Simulation details are provided in Table 14. The *x*-axis varies between wells based on the date range of observed head data. Predicted minimum heads and rate of head change associated with the plots are presented in Table 18.

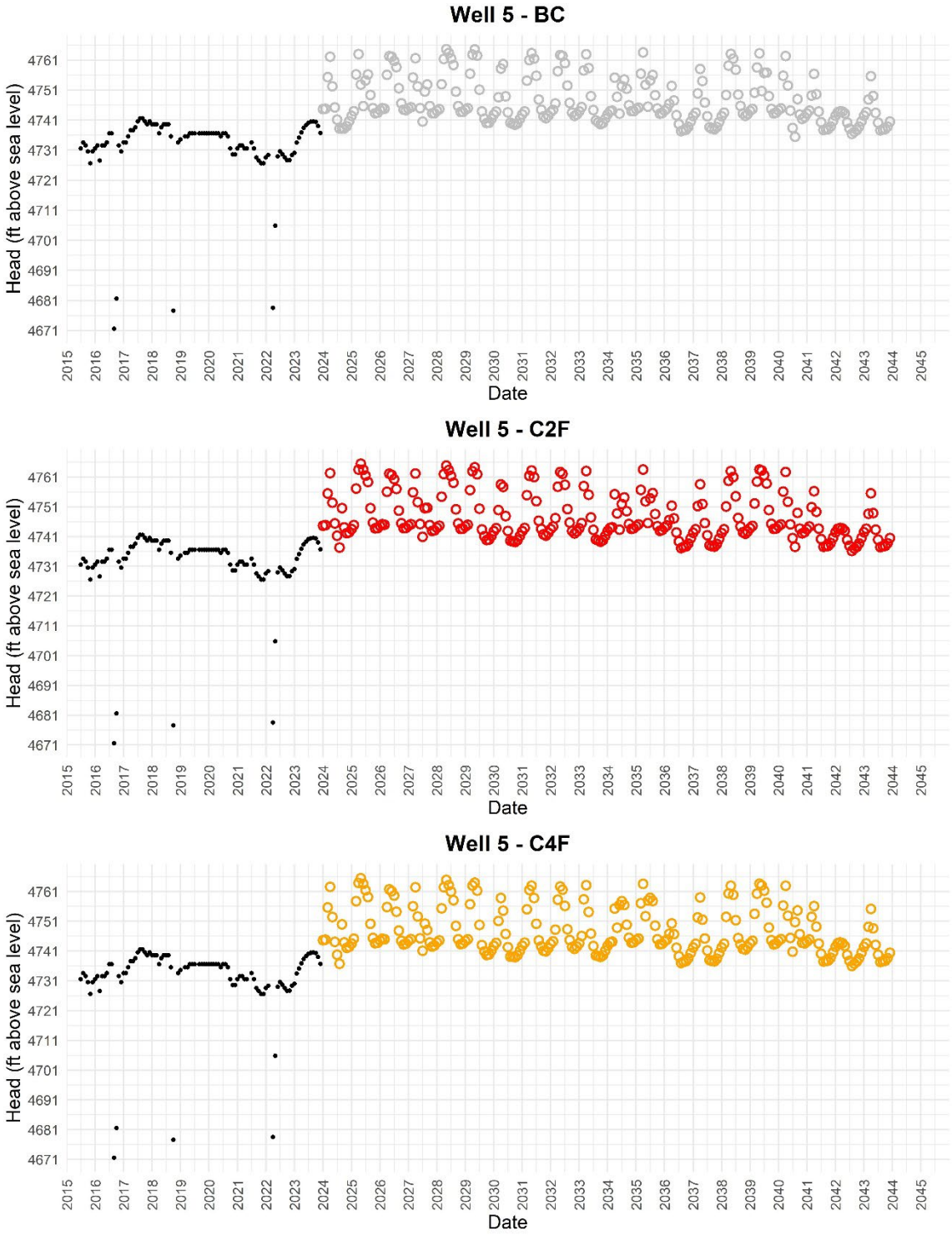

Figure 64A. Time series plots of predicted heads (colored circles) at GRGID Well 5 for predictive simulations BC, C2F, and C4F. For comparison to predicted heads, historical observed heads are also plotted (black dots). Simulation details are provided in Table 14. The *x*-axis varies between wells based on the date range of observed head data. Predicted minimum heads and rate of head change associated with the plots are presented in Table 18.

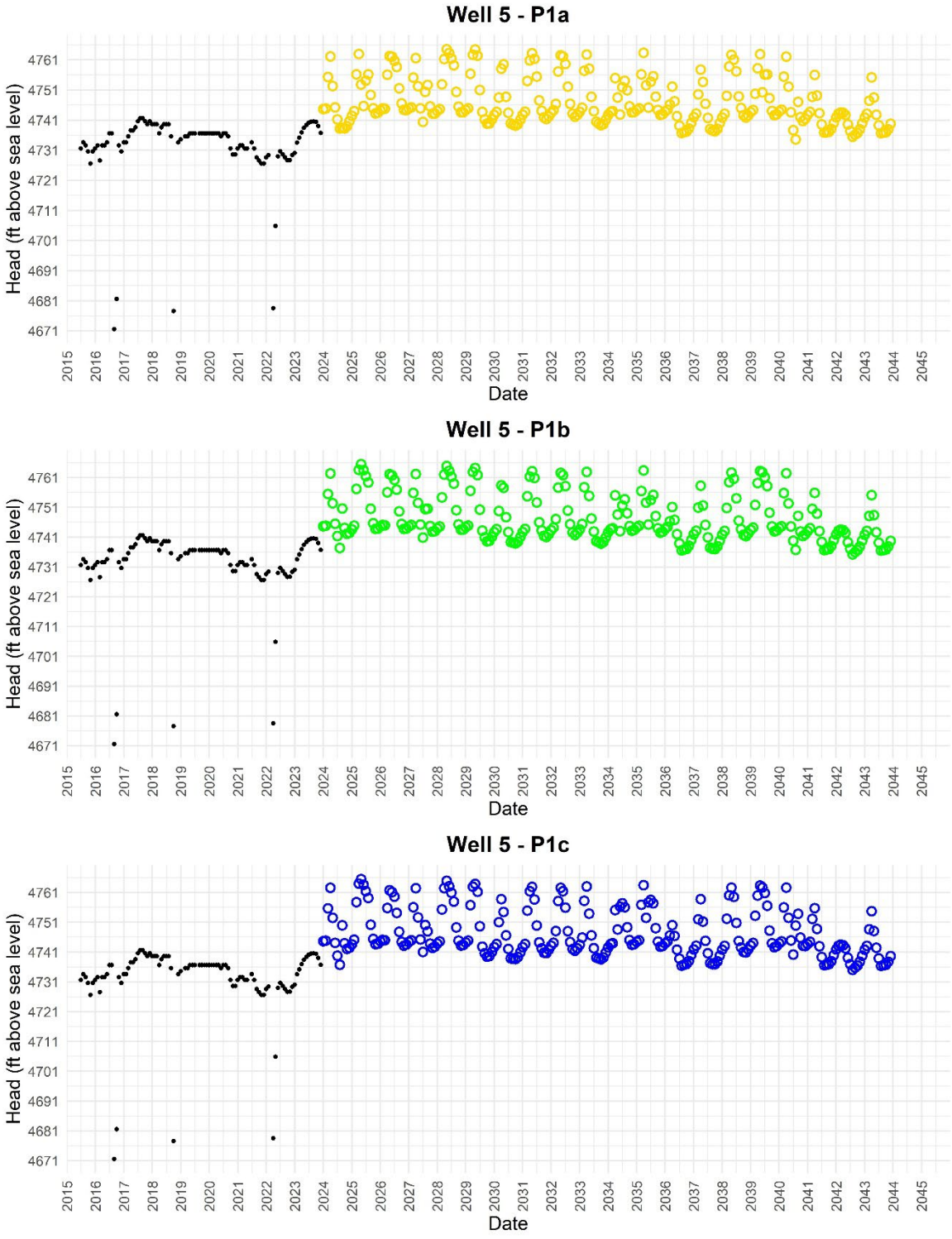

Figure 64B. Time series plots of predicted heads (colored circles) at GRGID Well 5 for predictive simulations P1a, P1b, and P1c. For comparison to predicted heads, historical observed heads are also plotted (black dots). Simulation details are provided in Table 14. The *x*-axis varies between wells based on the date range of observed head data. Predicted minimum heads and rate of head change associated with the plots are presented in Table 18.

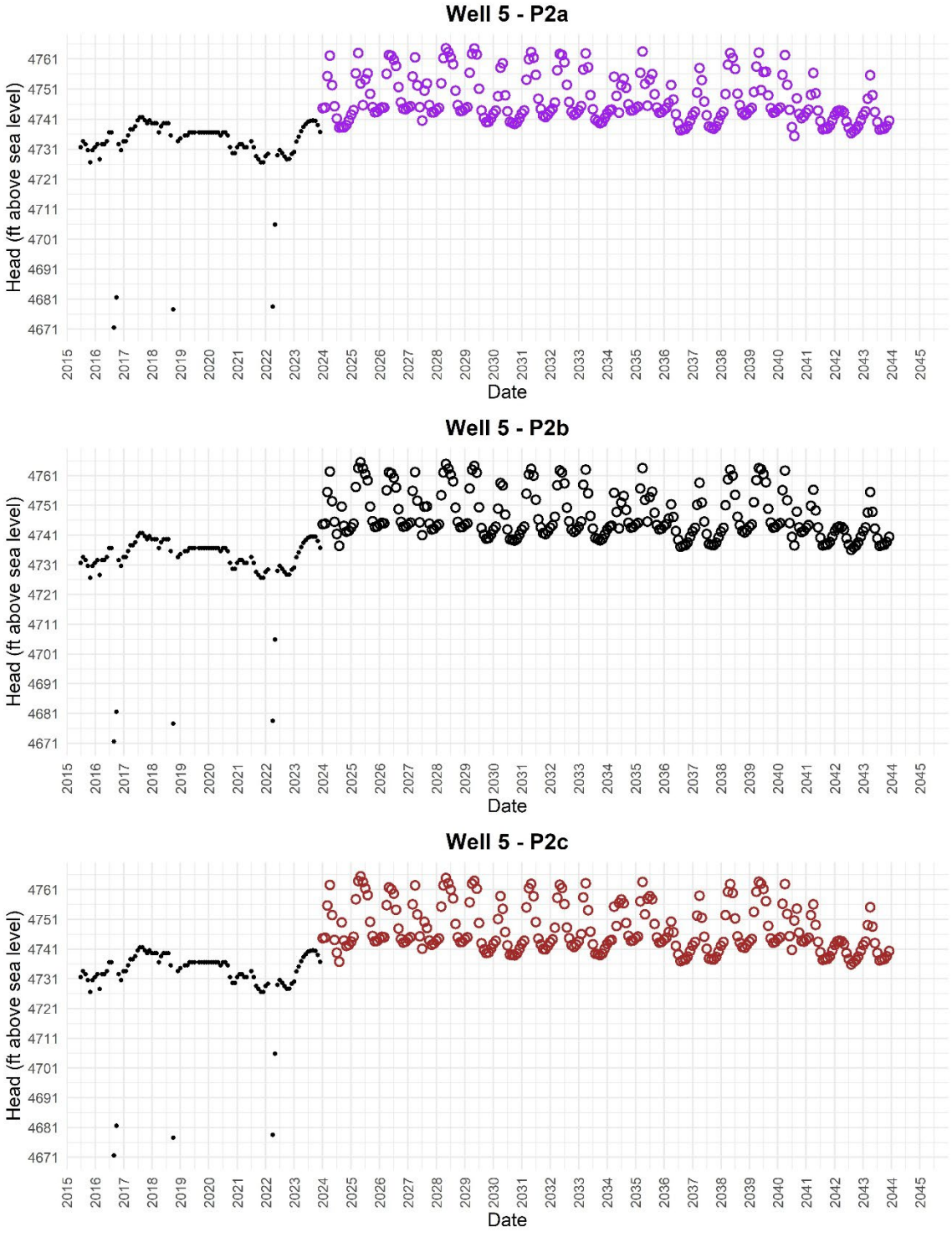

Figure 64C. Time series plots of predicted heads (colored circles) at GRGID Well 5 for predictive simulations P2a, P2b, and P2c. For comparison to predicted heads, historical observed heads are also plotted (black dots). Simulation details are provided in Table 14. The *x*-axis varies between wells based on the date range of observed head data. Predicted minimum heads and rate of head change associated with the plots are presented in Table 18.

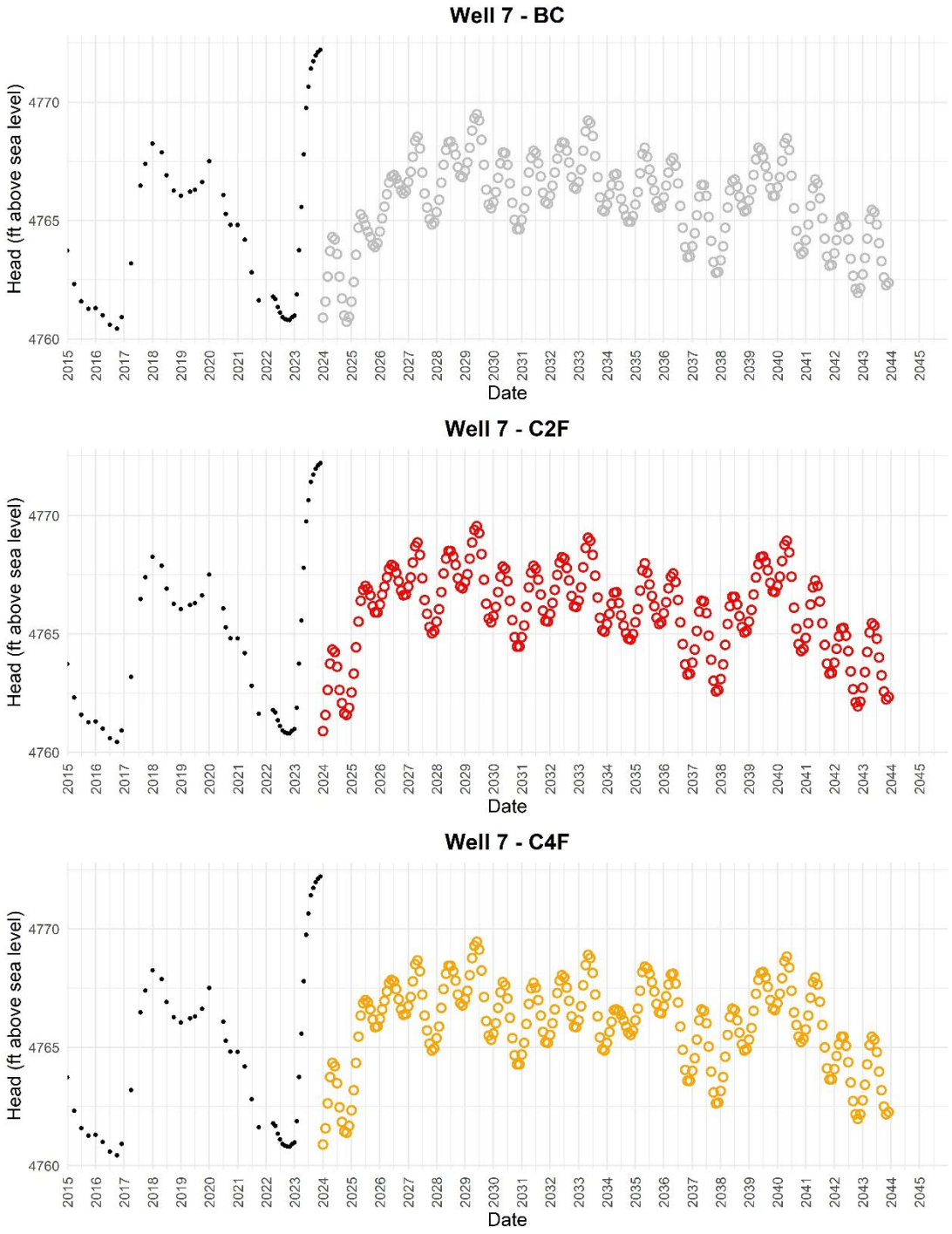

Figure 65A. Time series plots of predicted heads (colored circles) at GRGID Well 7 for predictive simulations BC, C2F, and C4F. For comparison to predicted heads, historical observed heads are also plotted (black dots). Simulation details are provided in Table 14. The *x*-axis varies between wells based on the date range of observed head data. Predicted minimum heads and rate of head change associated with the plots are presented in Table 18.

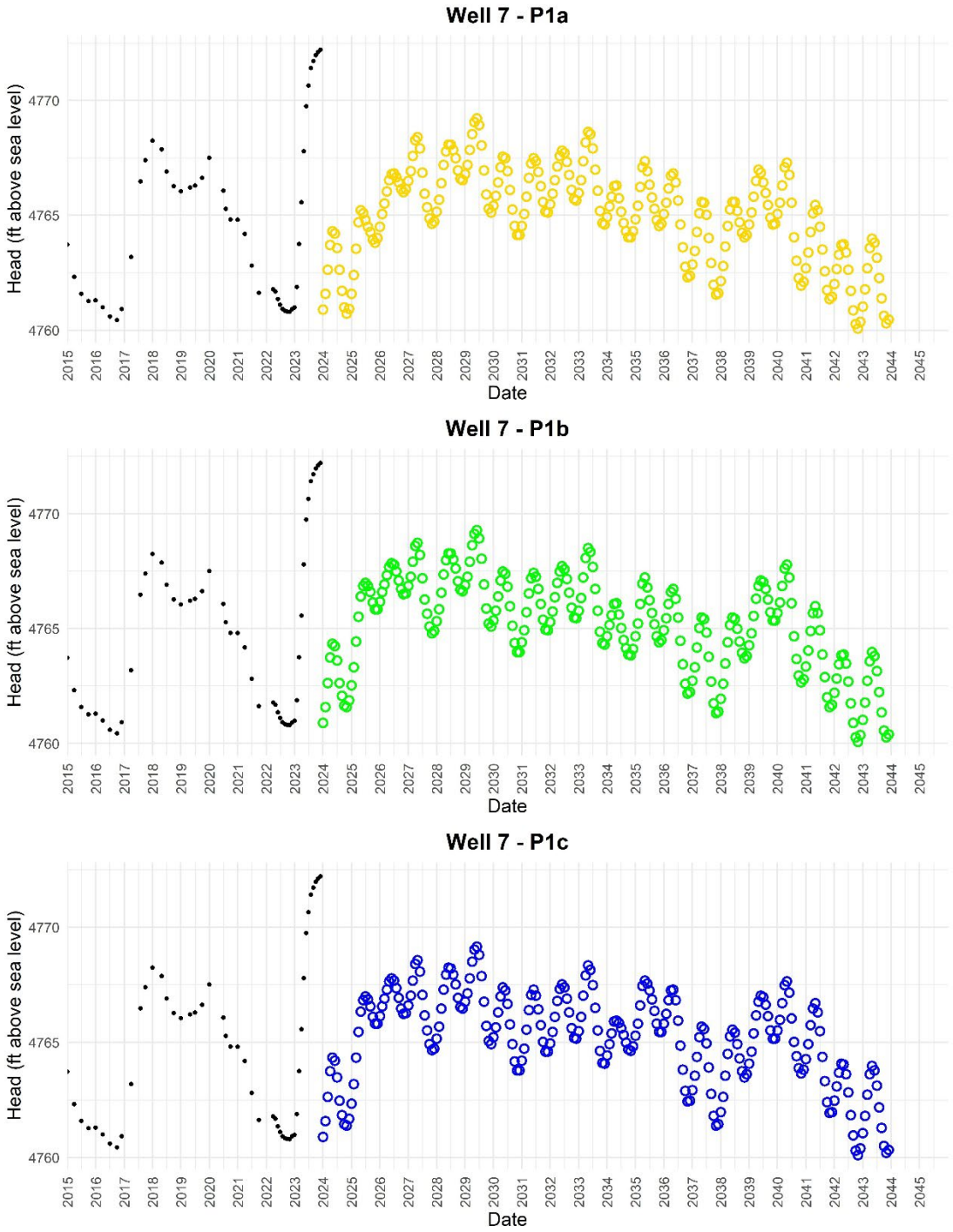

Figure 65B. Time series plots of predicted heads (colored circles) at GRGID Well 7 for predictive simulations P1a, P1b, and P1c. For comparison to predicted heads, historical observed heads are also plotted (black dots). Simulation details are provided in Table 14. The *x*-axis varies between wells based on the date range of observed head data. Predicted minimum heads and rate of head change associated with the plots are presented in Table 18.

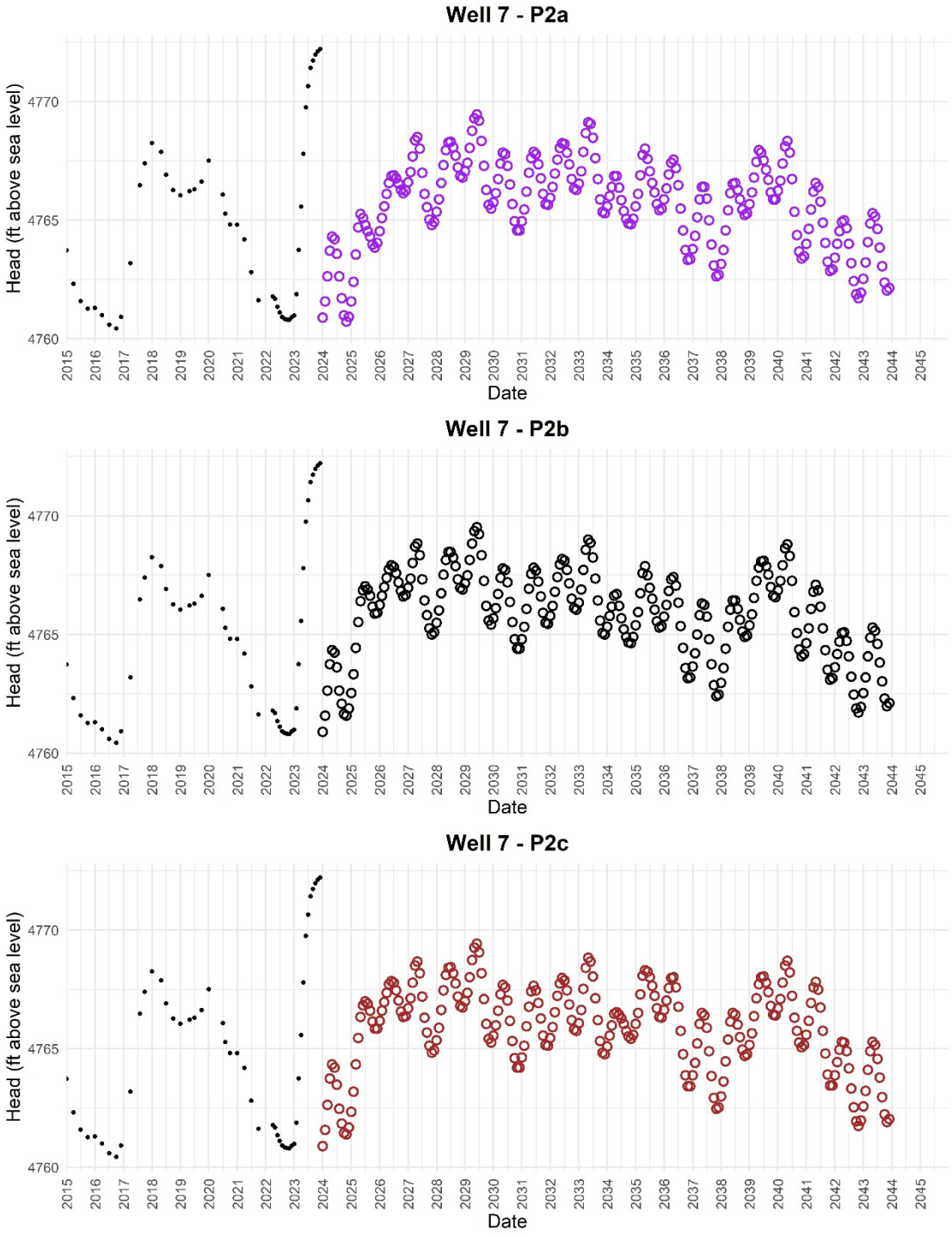

Figure 65C. Time series plots of predicted heads (colored circles) at GRGID Well 7 for predictive simulations P2a, P2b, and P2c. For comparison to predicted heads, historical observed heads are also plotted (black dots). Simulation details are provided in Table 14. The *x*-axis varies between wells based on the date range of observed head data. Predicted minimum heads and rate of head change associated with the plots are presented in Table 18.

Figure 66 compares the targeted (black dot) and simulated (gold circle) pumping rates for each supply well during each simulation. Negative values indicate that water is being pumped (removed) from the aquifer and a lower number (more negative) indicates a greater pumping rate. Each dot-circle pair represents the Q_{des} and Q_{sim} for one stress period during the 20-year predictive period. If the black dot falls inside of the gold circle, then the Q_{sim} is equal to Q_{des} for that stress period. As previously described, Q_{sim} would deviate from Q_{des} if the h_{well} drops below h_{lim} or if the flow from the aquifer to the well is less than Q_{des}. As indicated in Figure 48, the targeted and simulated heads at the GRGID supply wells are effectively equal for all stress periods in each simulation. This suggests that the existing supply well network is expected to meet the future monthly pumping requirements under projected monthly demand and temperature increases, and therefore, criterion 2 is met for all wells and simulations.

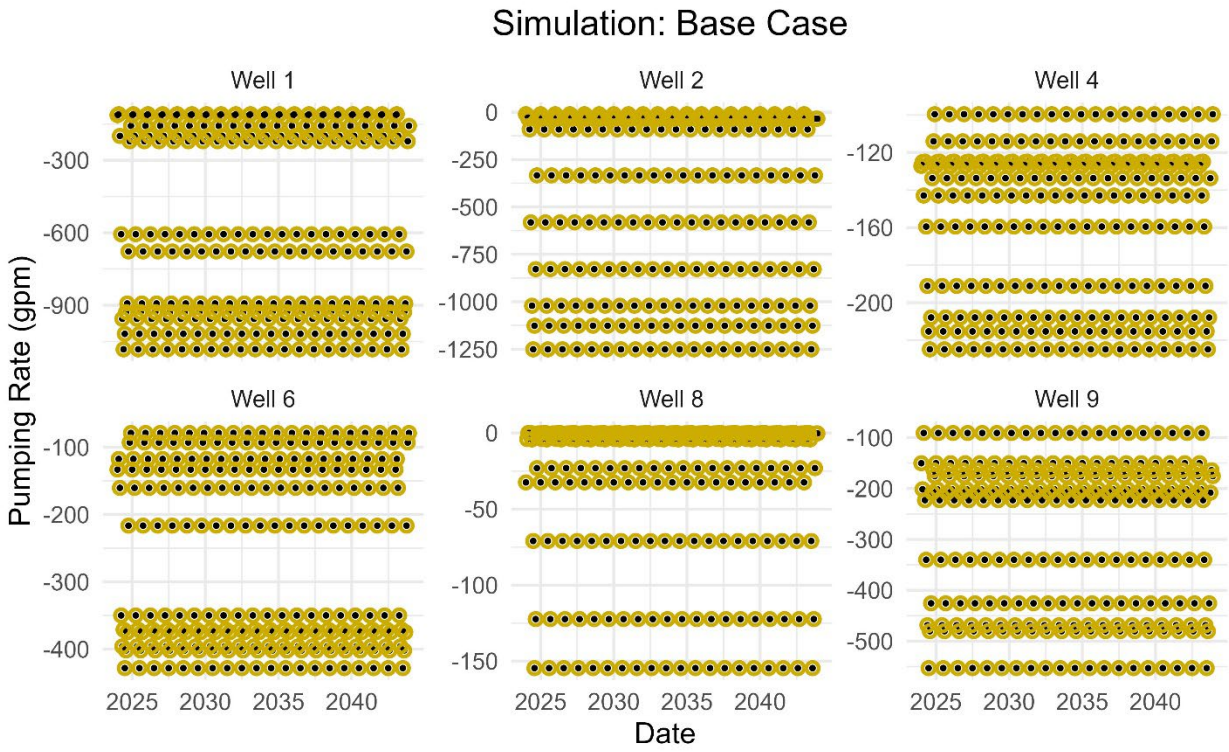

Figure 66A. Comparison of targeted pumping rates (black dots) and simulated pumping rates (gold circles) at GRGID supply wells for the monthly stress periods of the base-case scenario (2024-2043).

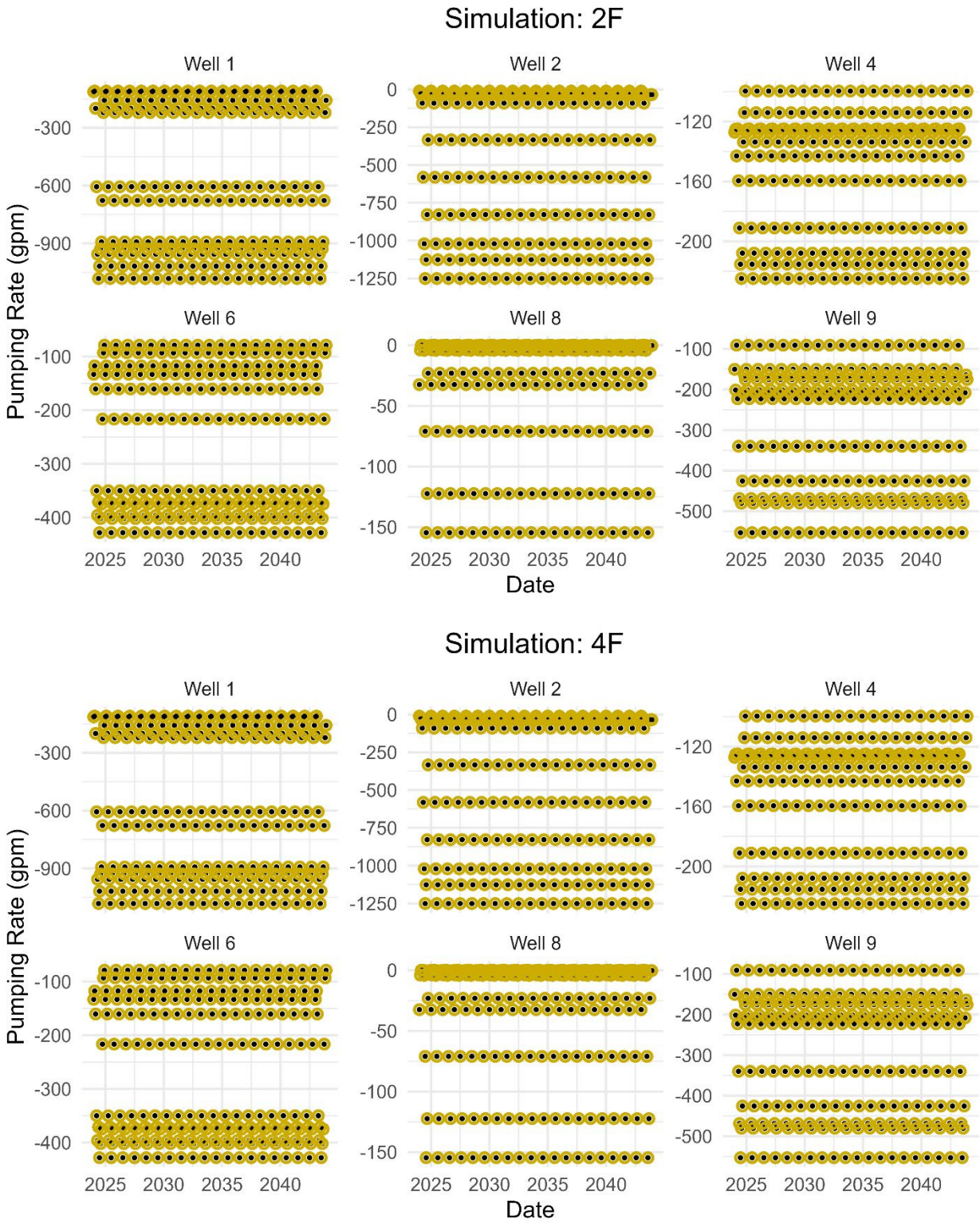

Figure 66B. Comparison of targeted pumping rates (black dots) and simulated pumping rates (gold circles) at GRGID supply wells for the monthly stress periods of the climate scenarios C2F and C4F (2024-2043).

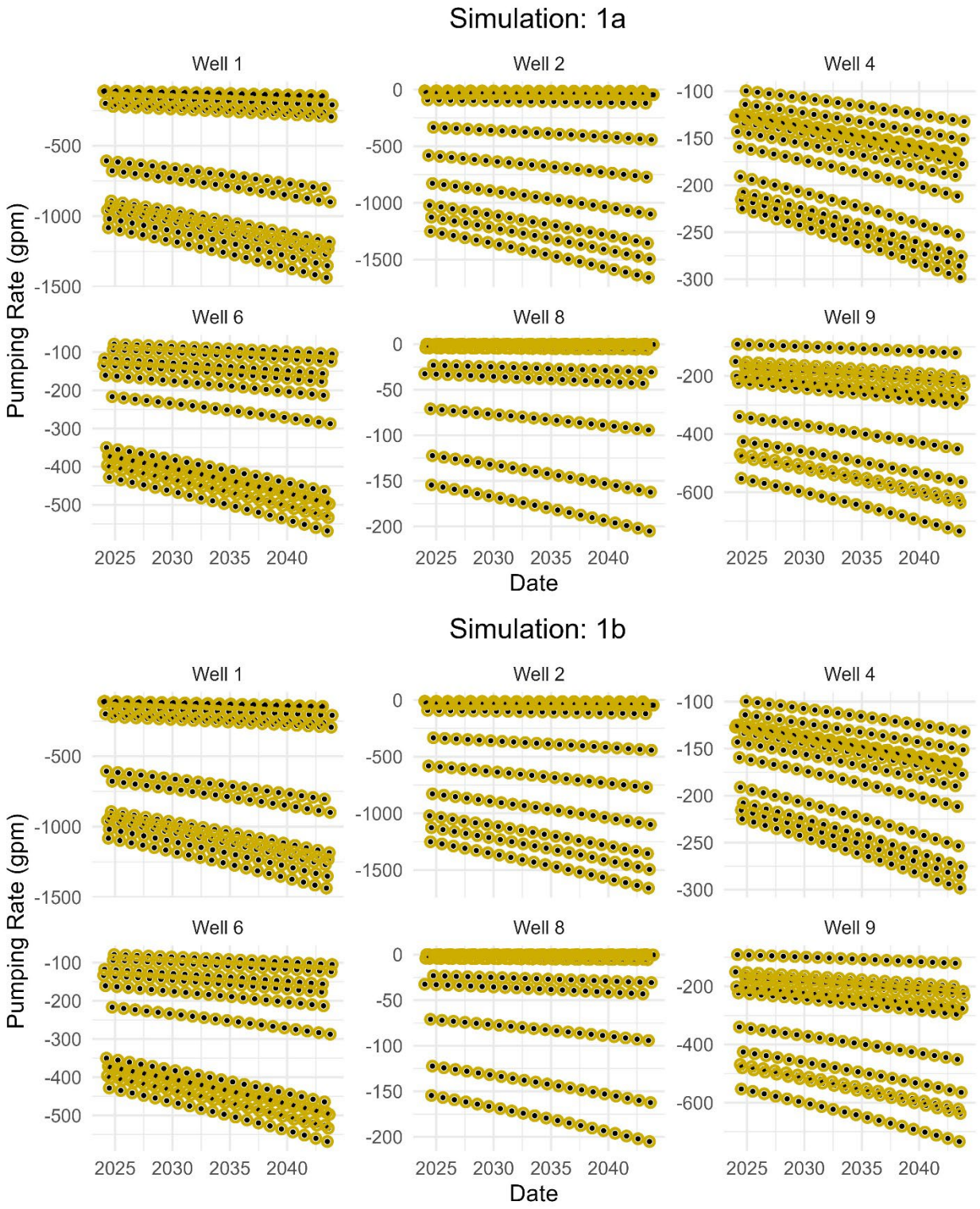

Figure 66C. Comparison of targeted pumping rates (black dots) and simulated pumping rates (gold circles) at GRGID supply wells for the monthly stress periods of pumping scenarios P1a and P1b (2024-2043).

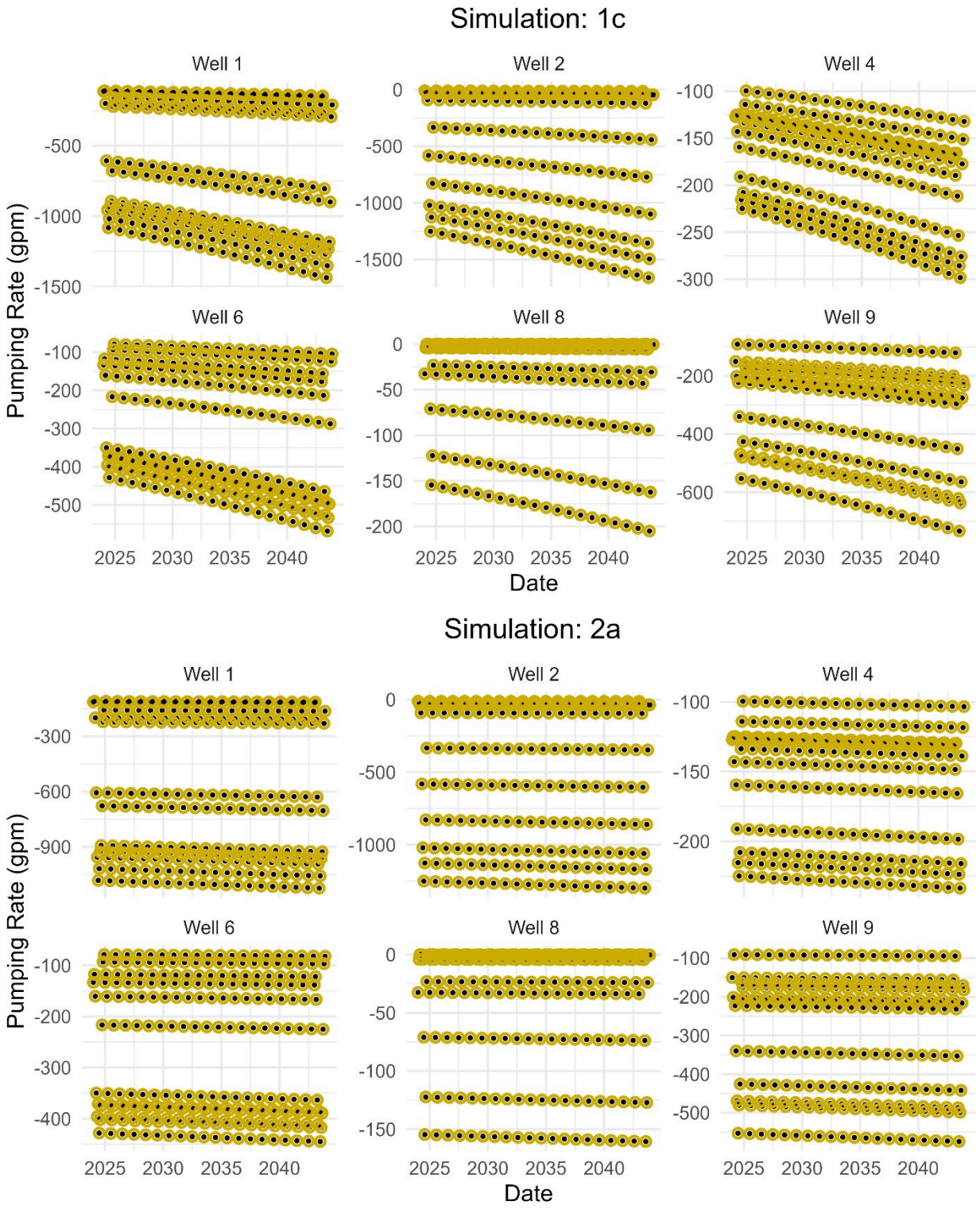

Figure 66D. Comparison of targeted pumping rates (black dots) and simulated pumping rates (gold circles) at GRGID supply wells for the monthly stress periods for pumping scenarios P1c and P2a (2024-2043).

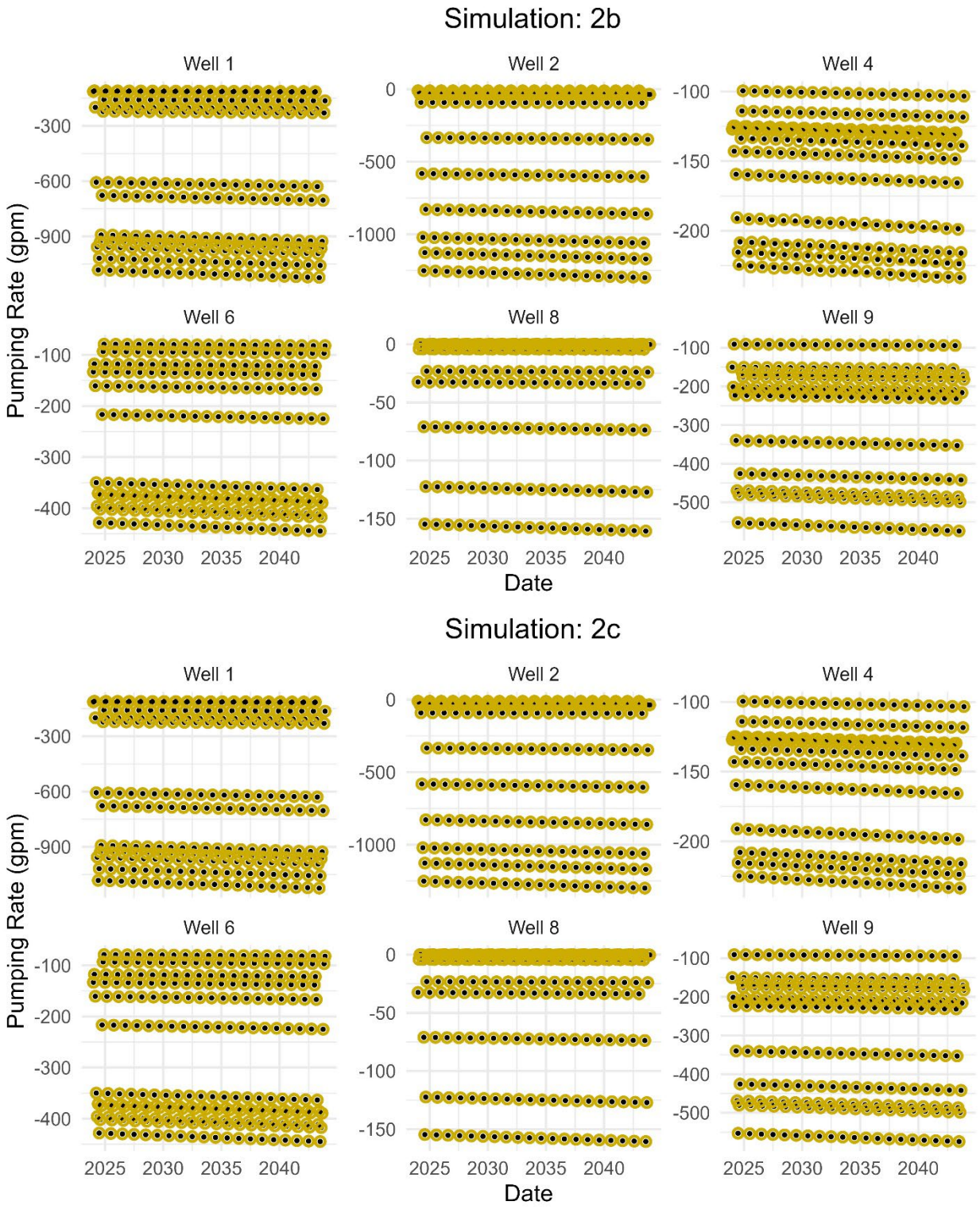

Figure 66E. Comparison of targeted pumping rates (black dots) and simulated pumping rates (gold circles) at GRGID supply wells for the monthly stress periods of pumping scenarios P2b and P2c (2024-2043).

4.0 SUMMARY FOR WATER MANAGEMENT

The groundwater model developed in this study provides a tool for projecting groundwater level trends and supporting sustainable water management in the Gardnerville Ranchos area and the greater Carson Valley. Groundwater levels have declined across much of the basin over the past several decades due to climate shifts and cumulative pumping, particularly for irrigation and public supply. Model results suggest that these declines are expected to continue, especially if groundwater withdrawals increase without mitigation or adaptive planning. Importantly, the study demonstrates that future groundwater conditions are influenced by groundwater extraction, climate-driven changes to groundwater recharge, and aquifer conditions.

Simulations of climate scenarios suggest that earlier snowmelt may temporarily boost spring recharge, but overall stream discharge is likely to decrease, leading to long-term water table declines. This transition may place additional pressure on groundwater supplies, particularly during dry years when surface water becomes less available. Although the Gardnerville Ranchos area is hydraulically upgradient of most agricultural and municipal users in the Carson Valley, it is not insensitive to cumulative drawdown effects. These findings underscore the importance of using this model not only for scenario testing, but also for operational planning and regional collaboration.

The Gardnerville Ranchos supply well network is expected to remain functional through 2043 under the tested scenarios. However, the rate and distribution of groundwater decline varies across the service area. Wells 1, 2, and 4 are projected to experience the steepest drawdowns, particularly under high-demand conditions. This suggests that well yields may degrade over time due to increased drawdown.

4.1 Recommendations for Water Managers

1. **Reduce seasonal reliance on high-demand wells**. Wells 1 and 2 show the most sensitivity to future drawdown. To mitigate localized stress during high-demand summer months, GRGID may consider a) increasing pumping from Wells 1 and 2 during lower-demand months (fall/winter) to fill storage tanks (additional water storage tanks could be considered); b) redistributing summer pumping toward underutilized wells, for example Wells 8 and 5, with appropriate water quality treatment and monitoring; and c) using model output to plan well usage schedules that optimize system-wide drawdown and efficiency.
2. **Use model output to guide future well-siting**. Should new supply wells be considered, future well-siting efforts should prioritize areas with favorable hydraulic properties. Fluvial deposits to the north of Gardnerville Ranchos and west of the West Fault show potential due to higher transmissivity and less drawdown interference.
3. **Evaluate implications of land use conversion**. Land development would change recharge patterns and impact groundwater conditions in Carson Valley. For example, the conversion of agricultural land for urban development may reduce agricultural recharge and irrigation return flows. Land development in Gardnerville Ranchos would also impact recharge patterns. Future model updates could include simulating land-use change scenarios to quantify effects on recharge and groundwater levels.

4. **Integrate conservation planning into scenario analysis**. Future model updates can help test the effects of specific water conservation measures on water use and groundwater levels. Modeling different conservation strategies would inform cost-effective demand reduction policies.
5. **Consider adaptive management and regional coordination**. A coordinated, valley-wide monitoring program and shared model updates would improve forecast accuracy, identify early signs of stress, and promote sustainable basin-scale management.
6. **Continue updating and expanding the model**. To maintain decision-making utility, model updates every 5-10 years would be beneficial as new data become available. Future enhancements could include expanding the model domain to incorporate a greater portion of Carson Valley, expanded stream gaging for groundwater-surface water interaction improvements, and incorporation of future land use.

REFERENCES

Anderson, M.P., W.W. Woessner, and R.J. Hunt, 2015. Applied groundwater modeling: Simulation of flow and advective transport (2nd ed., pp. 535-564). Academic Press.

Berger, D.L., 1987. Ground-water levels in water years 1984-86 and estimated ground-water pumpage in water years 1984-85, Carson Valley, Douglas County, Nevada. U.S. Geological Survey.

Berger, D.L., 1990. Ground-water levels in water year 1987 and estimated ground-water pumpage in water years 1986-87, Carson Valley, Douglas County, Nevada. U.S. Geological Survey Open-File Report 89-70, 9 p.

Bourdet, D., J.A. Ayoub, and Y.M. Pirard, 1989. Use of pressure derivative in well-test interpretation. SPE Formation Evaluation, June 1989, 293-302.

Cashman, P. H., J.H. Trexler Jr., T.W. Muntean, J.E. Faulds, J.N. Louie, and G.L. Oppliger, 2009. Neogene tectonic evolution of the Sierra Nevada-Basin and Range transition zone at the latitude of Carson City, Nevada. In J. S. Oldow and P. H. Cashman (Eds.), Late Cenozoic Structure and Evolution of the Great Basin-Sierra Nevada Transition.

Cooper, H.H., and C.E. Jacob, 1946. A generalized graphical method for evaluating formation constants and summarizing well field history. American Geophysical Union Transactions, 27, 526-534.

dePolo, C.M., A.R. Ramelli, and T. Muntean, 2000. Geologic map of the Gardnerville quadrangle, Douglas County, Nevada (Open-File Report 00-9). Nevada Bureau of Mines and Geology.

Dewitz, J., 2023. National Land Cover Database (NLCD) 2021 Products [Data release]. U.S. Geological Survey. https://doi.org/10.5066/P9JZ7AO3

Dillingham, H.L., 1980. Washoe Project, Nevada-California: Ground-water geology and resources, definite plan appendix, Carson Valley, Nevada. U.S. Bureau of Reclamation.

Doherty, J., and R.J. Hunt, 2010. Approaches to highly parameterized inversion: A guide to using PEST for groundwater-model calibration (U.S. Geological Survey Scientific Investigations Report 2010–5169). https://pubs.usgs.gov/sir/2010/5169

Domenico, P.A., and F.W. Schwartz, 1990. Physical and chemical hydrogeology. John Wiley and Sons.

Federal Water Master, 2015. Truckee River Operating Agreement reports. Carson Arch. http://www.troa.net/

Glancy, P.A., and T.L. Katzer, 1975. Water-resources appraisal of the Carson River Basin, western Nevada (Water Resources Reconnaissance Series Report 59). Nevada Department of Conservation and Natural Resources, Division of Water Resources.

Guitjens, J.C., W.W. Miller, H.M. Joung, and C.N. Mahannah, 1978. Quality monitoring of irrigation water and return flows, irrigation season 1975 (Report 119). Max C. Fleischmann College of Agriculture, University of Nevada, Reno.

Halford, K.J., C.A. Garcia, J.M. Fenelon, and B.B. Mirus, 2012. Advanced methods for modeling water-levels and estimating drawdowns with SeriesSEE, an Excel add-in (U.S. Geological Survey Techniques and Methods 4-F4, 28 p.).

He, M., A. Schwarz, E. Lynn, and M. Anderson, 2018. Drought across California's hydrologic regions in the 21st century. Climate, 6(2), 31. https://doi.org/10.3390/cli6020031

Horton, J.D., San Juan, C.A., and Stoeser, D.B., 2017, The State Geologic Map Compilation (SGMC) geodatabase of the conterminous United States (ver. 1.1, August 2017): U.S. Geological Survey Data Series 1052, 46 p., https://doi.org/10.3133/ds1052

Huntington, J.L., and R.G. Niswonger, 2012. Role of surface and groundwater interactions on projected summertime streamflow in snow dominated regions: An integrated modeling approach. Water Resources Research, 48(11). https://doi.org/10.1029/2012WR012319

HydroSOLVE, Inc., 2008. AQTESOLV for Windows 95/98/NT/2000/XP/Vista (Version 4.50.002 – Professional). Reston, VA.

Jeton, A.E., and D.K. Maurer, 2007. Precipitation and runoff simulations of the Carson Range and Pine Nut Mountains, and updated estimates of ground-water inflow and the ground-water budget for basin-fill aquifers of Carson Valley, Douglas County, Nevada, and Alpine County, California (U.S. Geological Survey Scientific Investigations Report 2007–5205, 56 p.).

Kitlasten, W., E.D. Morway, R.G. Niswonger, M. Gardner, J.T. White, E. Triana, and D. Selkowitz, 2021. Integrated hydrology and operations modeling to evaluate climate change impacts in an agricultural valley irrigated with snowmelt runoff. Water Resources Research, 57, e2020WR027924. https://doi.org/10.1029/2020WR027924

Lumos and Associates, 2024. 2023 Water Master Plan Update, Gardnerville Ranchos General Improvement District (Draft).

Lyles, B.F., C. Pearson, G.D. McCurdy, and J.L. Huntington, 2019. NICE Net Precipitation Summary Report: 2017. Desert Research Institute.

Maurer, D.K., D.L. Berger, M.L. Tumbusch, and M.J. Johnson, 2006. Rates of evapotranspiration, recharge from precipitation beneath selected areas of native vegetation, and streamflow gain and loss in Carson Valley, Douglas County, Nevada, and Alpine County, California (U.S. Geological Survey Scientific Investigations Report 2005–5288, 70 p.). http://pubs.water.usgs.gov/sir2005-5288

Maurer, D.K., and D.L. Berger, 2007. Water budgets and potential effects of land and water-use changes for Carson Valley, Douglas County, Nevada, and Alpine County, California (U.S. Geological Survey Scientific Investigations Report 2006–5305, 64 p.).

Maurer, D.K., and K.J. Halford, 2004. Updated estimates of the distribution of average annual precipitation in Carson Valley, 1971-2000, Douglas County, Nevada, and Alpine County, California. Journal of the Nevada Water Resources Association, 1(1), 20-39.

Maurer, D.K., A.P. Paul, D.L. Berger, and C.J. Mayers, 2009. Analysis of streamflow trends, ground-water and surface-water interactions, and water quality in the upper Carson River basin, Nevada and California (U.S. Geological Survey Scientific Investigations Report 2008–5238, 192 p.).

Maurer, D.K., T.J. Lopes, R.L. Medina, and J.L. Smith, 2004. Hydrogeology and hydrologic landscape regions of Nevada (U.S. Geological Survey Scientific Investigations Report 2004–5131). https://doi.org/10.3133/sir20045131

Maurer, D.K., 1986. Geohydrology and simulated response to ground-water pumpage in Carson Valley, a river-dominated basin in Douglas County, Nevada, and Alpine County, California (U.S. Geological Survey Water-Resources Investigations Report 86–4328). https://doi.org/10.3133/wri864328

Maurer, D.K., 1984. Gravity survey and depth to bedrock in Carson Valley, Nevada-California (U.S. Geological Survey Water-Resources Investigations Report 84–4202). https://doi.org/10.3133/wri844202

McDonald, M.G., and A.W. Harbaugh, 1988. A modular three-dimensional finite-difference ground-water flow model (U.S. Geological Survey Techniques of Water-Resources Investigations, Book 6, Chapter A1). https://pubs.usgs.gov/twri/6a1/report.pdf

Melton, F.S., J. Huntington, R. Grimm, J. Herring, M. Hall, D. Rollison, T. Erickson et al., 2022. OpenET: Filling a critical data gap in water management for the Western United States. Journal of the American Water Resources Association, 58(6), 971-994. https://doi.org/10.1111/1752-1688.12956

Menne, M.J., I. Durre, B. Korzeniewski, S. McNeill, K. Thomas, X. Yin et al., 2012. Global Historical Climatology Network - Daily (GHCN-Daily), Version 3. NOAA National Climatic Data Center. https://doi.org/10.7289/V5D21VHZ

Muntean, T.W., 2001. Evolution and stratigraphy of the Neogene Sunrise Pass Formation of the Gardnerville sedimentary basin, Douglas County, Nevada (master's thesis, University of Nevada, Reno).

Nevada Division of Water Resources, 2024a. Well log search. https://tools.water.nv.gov/WellLogQuery.aspx

Nevada Division of Water Resources, 2024b. Pumpage inventories. https://tools.water.nv.gov/PumpageInventoryFiles.aspx

Neuman, S.P., and P.A. Witherspoon, 1969. Applicability of current theories of flow in leaky aquifers. Water Resources Research, 5(4), 817-829.

Nielsen, K.A., 2007. Fractured aquifers: Formation evaluation by well testing. Trafford Publishing.

Preissler, A.M., M.S. Fadali, and J.M. Thomas, 1999. Estimates of ground-water discharge as base flow to the Walker River, west-central Nevada, using water-temperature and ground-water-flow simulation methods (U.S. Geological Survey Water-Resources Investigations Report 99–4205). https://pubs.usgs.gov/wri/1999/4205/report.pdf

Prudic, D.E., 1989. Documentation of a computer program to simulate stream-aquifer relations using a modular, finite-difference, ground-water flow model (U.S. Geological Survey Open-File Report 88–729, 113 p.).

Prudic, D.E., and J.L. Wood, 1995. Results of hypothetical ground-water pumping in Carson Valley, a river-dominated basin in Douglas County, Nevada, and Alpine County, California (U.S. Geological Survey Water-Resources Investigations Report 95–4174). https://doi.org/10.3133/wri954174

Ramelli, A.R., J.C. Yount, D.A. John, and L.J. Garside, 2014. Geologic map of the Minden quadrangle, Douglas County, Nevada and Alpine County, California (Nevada Bureau of Mines and Geology Map 182).

Shah, A.K., and O.S. Boyd, 2018. Depth to basement and thickness of unconsolidated sediments for the western United States: Initial estimates for layers of the U.S. Geological Survey National Crustal Model (U.S. Geological Survey Open-File Report 2018–1115). https://doi.org/10.3133/ofr20181115

Simpson, E.S., D.B. Thorud, and I. Friedman, 1970. Distinguishing seasonal recharge to groundwater by deuterium analysis in southern Arizona. In Symposium on World Water Balance (Int. Soc. Sci. Hydrol. Publ., 92(3), 623-633).

Smith, G. I., Friedman, I., Veronda, G., and Johnson, C. A., 2002. Stable isotope compositions of waters in the Great Basin, United States, 3: Comparison of groundwaters with modern precipitation. Journal of Geophysical Research: Atmospheres, 107(D19), 4402. https://doi.org/10.1029/2001JD000567

Smith, G.I., I. Friedman, J.D. Gleason, and A. Warden, 1992. Stable isotope composition of waters in southeastern California, 2: Ground waters and their relation to modern precipitation. Journal of Geophysical Research: Atmospheres, 97(D5), 5813-5823.

Spane Jr., F.A., and Wurstner, S.K., 1993. DERIV: A computer program for calculating pressure derivatives for use in hydraulic test analysis. Ground Water, 31(5), 814-822.

Spane, F.A., 1977. Evaluation of factors influencing the inorganic water-quality regimen of Carson River, Carson Valley, Nevada-California (Ph.D. dissertation, University of Nevada, Reno).

Theis, C.V., 1935. The relation between the lowering of the piezometric surface and the rate and duration of discharge of a well using groundwater storage. American Geophysical Union Transactions, 16, 519-524.

U.S. Geological Survey, 2006. Quaternary fault and fold database for the United States. https://earthquakes.usgs.gov/regional/qfaults/

U.S. Geological Survey, 2016. National Water Information System data available on the World Wide Web (USGS Water Data for the Nation). http://waterdata.usgs.gov/nwis/

U.S. Geological Survey, 2024. Watershed Boundary Dataset, version 2.3.1. Released xxxx. Accessed December 10, 2024 from https://www.usgs.gov/national-hydrography/access-national-hydrography-products

Welch, A.H., S.J. Lawrence, M.S. Lico, J.M. Thomas, and D.H. Schaefer, 1990. Ground-water quality assessment of the Carson River basin, Nevada and California: Results of investigations, 1987-91 (U.S. Geological Survey Water-Supply Paper 2356-A). https://doi.org/10.3133/wsp2356A

Welch, A.H., U.S. National Water-Quality Assessment Program, and U.S. Geological Survey, 1994. Ground-water quality and geochemistry in Carson and Eagle Valleys, western Nevada and eastern California. U.S. Geological Survey.

Winograd, I.J., and I. Friedman, 1972. Deuterium as a tracer of regional ground-water flow, southern Great Basin, California and Nevada. Geological Society of America Bulletin, 83, 3691-3708.

Wolff, R.G., 1970. Relationship between horizontal strain near a well and reverse water level fluctuation. Water Resources Research, 6, 1721-1728.

Yager, R.M., D.K. Maurer, and C.J. Mayers, 2012. Assessing potential effects of changes in water use with a numerical groundwater-flow model of Carson Valley, Douglas County, Nevada, and Alpine County, California (U.S. Geological Survey Scientific Investigations Report 2012–5262). https://pubs.usgs.gov/sir/2012/5262/pdf/sir2012-5262.pdf

APPENDIX A. HYDROGEOLOGIC CHARACTERIZATION

THIS PAGE LEFT INTENTIONALLY BLANK

CONTENTS

LIST OF FIGURES

LIST OF TABLES

THIS PAGE LEFT INTENTIONALLY BLANK

INTRODUCTION

A hydrogeologic characterization was conducted by Desert Research Institute (DRI) from fall 2021 through fall 2023, with the goal of refining the understanding of the hydrogeologic conditions of the Gardnerville Ranchos and surrounding areas in the southern segment of the Carson Valley hydrographic basin. Results of the hydrogeologic characterization support the development of a numerical groundwater flow model that is discussed in the main body of the report. The purpose of Appendix A is to provide details on the field data collection and analysis conducted as part of the hydrogeologic characterization activities for this study. Previous hydrogeologic and hydrologic investigations in the study area and the broader Carson Valley are discussed in the main body of the report.

The hydrogeologic characterization consisted of a series of activities covering a broad scope, including:

- Downhole camera inspections of Supply Wells 6, 8, and 9 were performed to assess the degree of well-screen blockage from the accumulation of mineral deposits, sediment, etc.
- Five boreholes were drilled to characterize geology in areas where geologic information was lacking.
- Two-inch monitoring wells were completed in each new borehole.
- New and existing monitoring wells were equipped with a pressure transducer for high-frequency groundwater level data collection to measure background water levels and responses during aquifer tests.
- Seven constant-rate, multiday aquifer pumping and recovery tests were conducted to assess aquifer hydraulic properties and boundary conditions.
- Water samples were collected from several wells and surface water bodies for stable isotope analysis to assess groundwater sources and to quantify groundwater-surface water mixing.
- Hydrologic, hydraulic, and isotope data were analyzed to characterize local aquifer and groundwater conditions.

WELL SCREEN INSPECTION

A “well screen” is a section of perforated pipe installed in a water well that allows groundwater to enter the well while filtering out sediment. Over time, debris, sediment, and mineral deposits can accumulate in the screen of a supply well. This buildup is problematic for water supply management because it can reduce the amount of flow from the aquifer to the well, ultimately resulting in less water production over time. From a hydrogeologic perspective, well screen buildup is problematic because it reduces the hydraulic connection between the well and the surrounding aquifer, which impacts the extent of pressure propagation during aquifer testing. To determine the extent of this issue, downhole camera inspections were performed by DRI at select supply wells on September 28-29, 2021, using a dipper-See Examiner by Heron Instruments, Inc. The inspection was performed by inserting the camera into the interior of the supply well through the appropriate access port. However, some supply wells were not inspected due to access restrictions, including the access port

being too small or the presence of downhole equipment (i.e., pipes, pumps, etc.) that could not be bypassed. As deemed necessary based on results of the well inspections, well screen rehabilitation was performed by Carson Pump (Carson City, NV) using a well screen brush, chemical treatment, air surging, or a combination of these to clear the well screens. The goal of well rehabilitation is to improve a well's pumping efficiency and to maximize hydraulic stress on the aquifer during aquifer testing conducted during the hydrogeologic characterization. Figure A-1 is an example of a relatively clear well screen (Well 9) and Figure A-2 shows a screen with buildup (Well 6). A summary of inspection and rehabilitation activities for each supply well is provided below:

- Well 1: No inspection was carried out at Well 1 because of access restrictions.
- Well 2: No inspection was carried out at Well 2 because of access restrictions.
- Well 4: No inspection was performed at Well 4 because it is a relatively new well completion and therefore was unlikely to have substantial well-screen buildup.
- Well 5: No inspection was carried out at Well 5 because it was out of operation at the time of the inspection. Because Well 5 did not contribute to the water supply, well efficiency was not a concern.
- Well 6: The well screen was inspected and rehabilitated at Well 6 (Figure A-1).
- Well 8: The well screen was inspected and rehabilitated at Well 8.
- Well 9: The well screen was inspected at Well 9. It was determined that the well screen had minimal buildup and therefore did not require rehabilitation (Figure A-2).

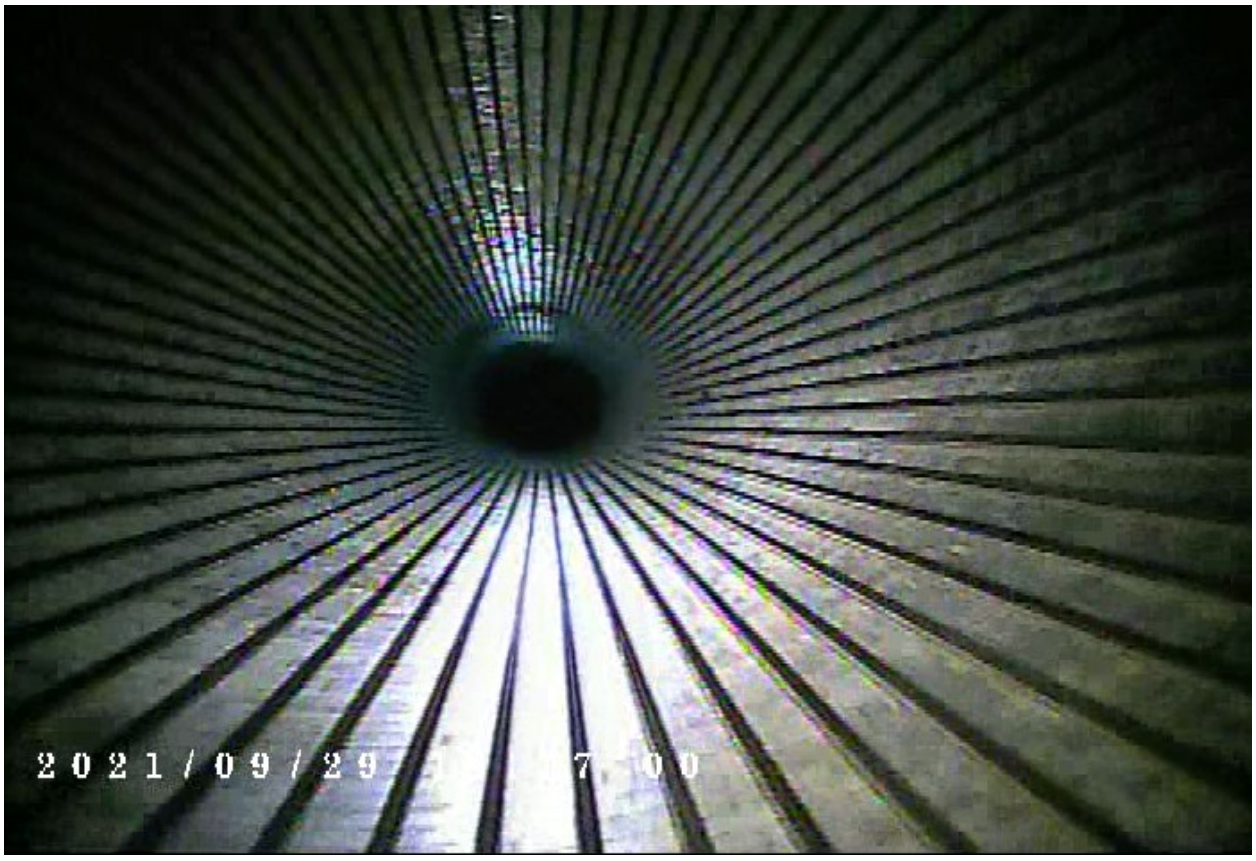

Figure A-1. Downhole image of the interior of Well 9. Well 9 had a relatively clear well screen and rehabilitation was not required.

Figure A-2. Downhole image of the interior of Well 6. Well 6 had a substantial buildup in many sections of the well screen, so the well screen was rehabilitated.

DRILLING AND MONITORING WELL INSTALLATION

The locations of the monitoring wells installed during this study, as well as previously existing monitoring and supply wells, are shown in Figure A-3. New and existing monitoring wells were used to monitor background water levels and responses during aquifer tests. Well completion details are provided in Table A-1 and described in the following subsections.

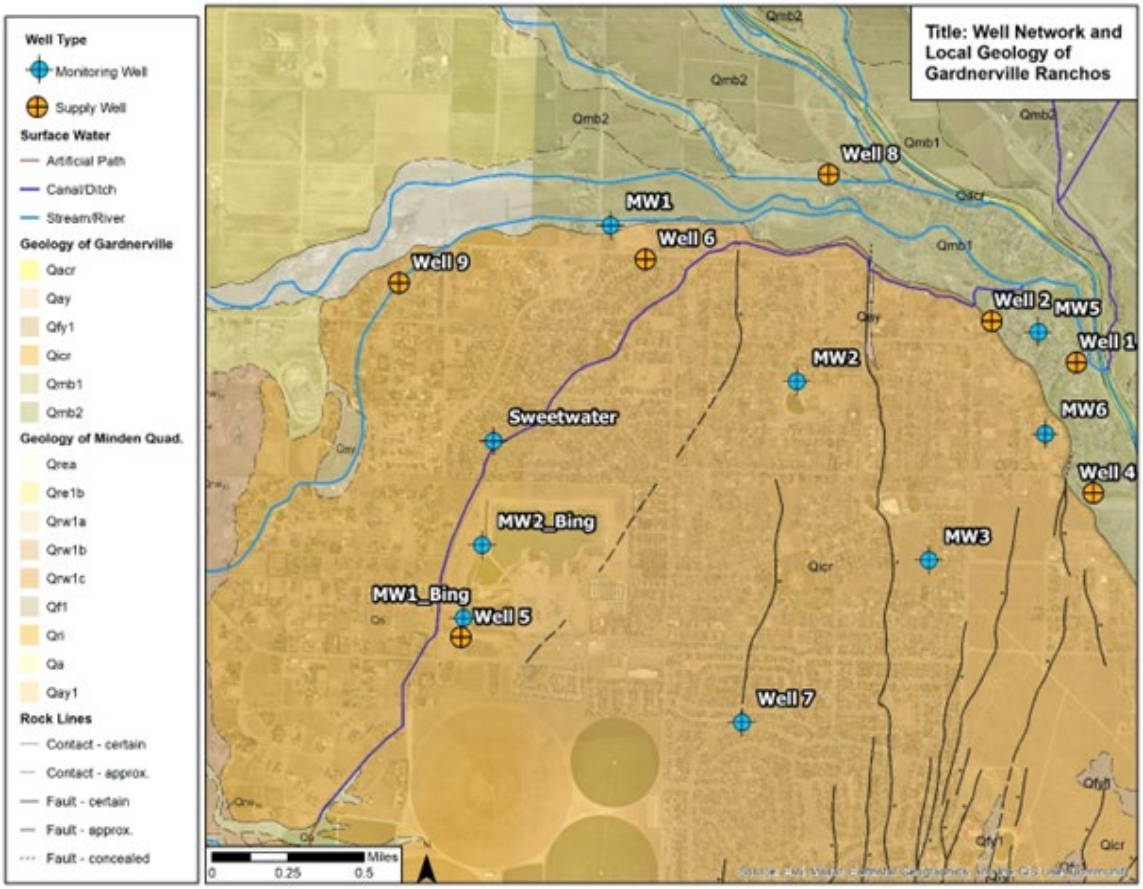

Figure A-3. Map of the well network and local geology of the Gardnerville Ranchos area.

Table A-1. Details of supply wells and monitoring wells in Gardnerville Ranchos

Well ID	Well Type	UTM easting (ft)	UTM Northing (ft)	LS Elev. (ft)	Total depth (ft)	Screen top (ft)	Screen bottom (ft)	Casing diam. (ft)	Pump intake (ft)	SWL (ft amsl)
Well 1	PW	867,348	14,141,295	4,830	420	140	420	1.5	240	4,776
Well 2	PW	865,873	14,142,003	4,824	670	270	650	1.3	268	4,775
Well 4	PW	867,638	14,139,060	4,844	375	183	372	1.3	214	4,827
Well 5	PW	856,633	14,136,593	4,804	450	200	450	1.3	214	4,736
Well 6	PW	859,870	14,143,059	4,794	434	210	430	1.5	216	4,736
Well 8	PW	863,049	14,144,507	4,798	500	260	500	1.3	245	4,744
Well 9	PW	855,593	14,142,654	4,763	390	240	390	1.0	202	4,729
MW1	MW	859,252	14,143,636	4,772	121	100	120	0.2	n/a	4,735
MW2	MW	862,488	14,140,968	4,849	151	130	150	0.2	n/a	4,744
MW3	MW	864,774	14,137,911	4,875	153	130	150	0.2	n/a	4,766
MW5	MW	866,680	14,141,813	4,823	125	105	125	0.2	n/a	4,774
MW6	MW	866,799	14,140,074	4,871	198	180	198	0.2	n/a	4,771
MW1_Bing	MW	856,726	14,136,892	4,802	120	88	108	0.4	n/a	4,738
MW2_Bing	MW	857,021	14,138,268	4,803	120	88	108	0.4	n/a	4,735
Sweetwater	MW	857,222	14,139,938	4,796	100	n/a	n/a	0.5	n/a	4,735
Well 7	MW	861,533	14,135,137	4,866	480	300	480	0.7	n/a	4,765

LS Elev.	land surface elevation
SWL	static groundwater elevation measured on March 8, 2023
ft amsl	feet above mean sea level
PW	production (supply) well
MW	monitoring well
UTM	Universal Transverse Mercator

The field program included drilling of five boreholes and installation of 2-inch monitoring wells MW1, MW2, MW3, MW5, and MW6. Monitoring wells were drilled, constructed, and developed by Gregory Drilling of northern California. Figure A-4 shows the site during drilling of the borehole at MW-3. The completed monitoring well at MW-3 is shown in Figure A-5. Schematics for monitoring wells installed during this study are provided as Figures A-6 and A-7. Boreholes were drilled with a diameter of 7.25 inches using resonant sonic drilling. Continuous core samples were obtained at 2.5-foot intervals and preserved in sample bags in preparation for lithologic descriptions. The well casing is 2-inch inner diameter schedule 40 PVC for both blank and perforated sections (perforation size = 0.020 inches). The annular space between the casing and borehole wall is filled with sand around the perforations, bentonite along blank casing sections, and a cement seal from the land surface to 20 ft depth. The wells were developed via airlifting for several hours to remove sediment and drilling materials from the well until formation water was produced with stabilized levels of turbidity, pH, and total dissolved solids measurements. A concrete pad and steel casing completion with locking lid were installed at the land surface to protect the wellheads that extend above the land surface (i.e., MW-1, MW-2, MW-3). MW-5 and MW-6 are in residential areas near the road and were completed so that the wellheads are flush with the land surface.

Figure A-4 The drill site at MW-3.

Figure A-5. The completed monitoring well head at MW-3.

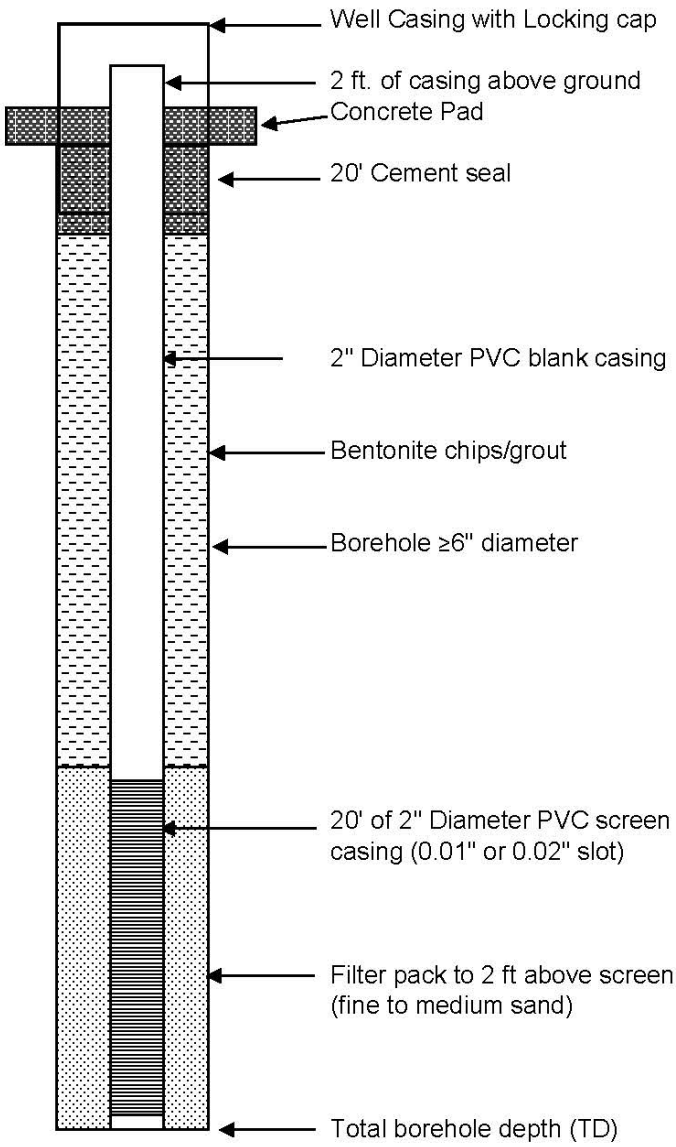

Figure A-6. Generalized well construction diagram for monitoring wells MW1, MW2, and MW3.

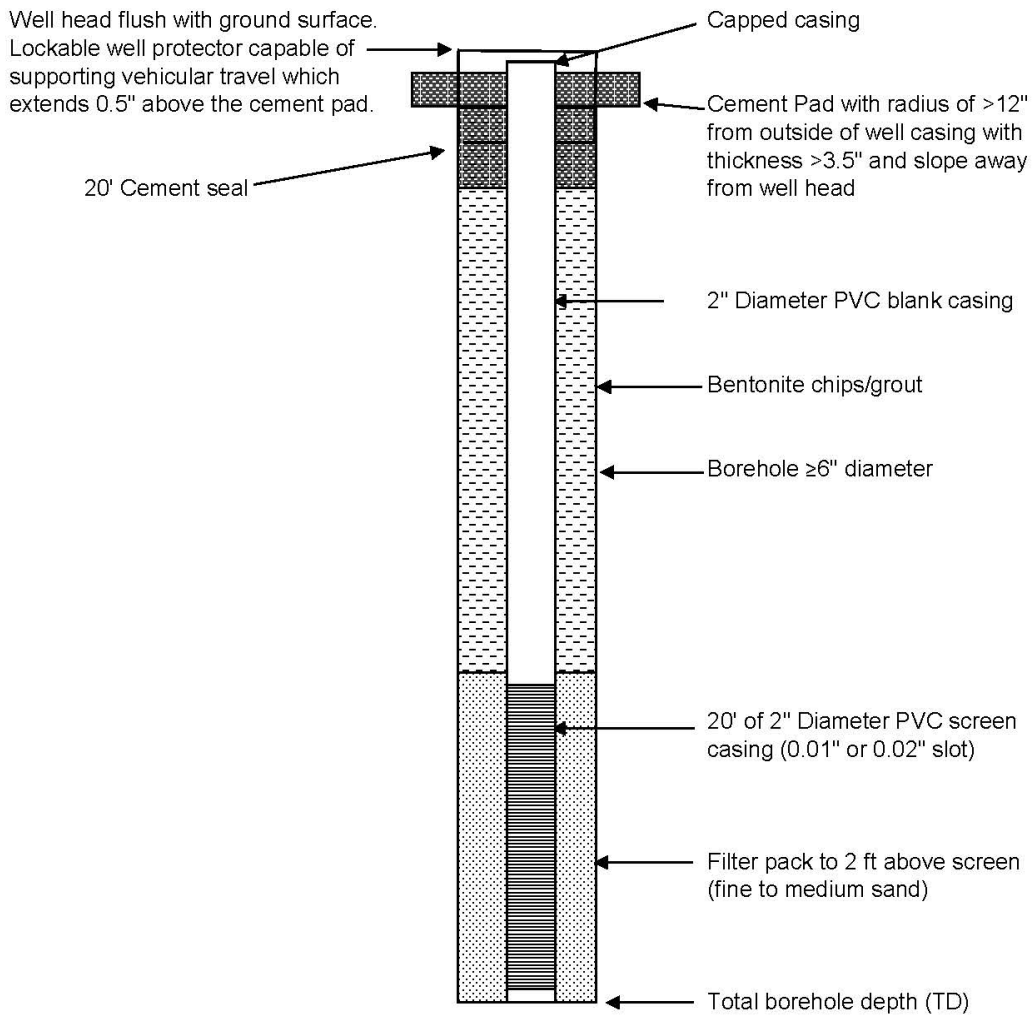

Figure A-7. Generalized well construction diagram for monitoring wells MW5 and MW6.

The location and depth of each new monitoring well targets a particular aquifer, geologic unit, or geologic fault to inform the hydrogeologic conceptual model. Lithology logs for monitoring wells and supply wells are provided in Attachment 1. The lithology, location, and goal of each monitoring well is described below:

- MW1 is located north of Well 6 and northeast of Well 9 and is completed in fluvial deposits (Qmb1) with the goal of assessing the hydraulic connection between the undivided Carson River deposits (Qri) of the western portion of the river terrace (unit pumped by Wells 6 and 9) and the down- and cross-gradient fluvial deposits. The fluvial deposits at MW1 consist primarily of sandy gravel with thin lenses of clayey gravels.
- MW2 is in the north-central section of the river terrace with the goal of assessing the hydraulic connection between the pumped fluvial deposits (Qmb1) of Well 8 and the alluvial deposits (Qicr). MW2 is situated between the West and Central Faults with

the goal of estimating the permeability of these faults by monitoring groundwater level responses to pumping at supply wells on the opposite sides of the faults, including Well 6 (west of the West Fault), and Wells 1 and 2 (east of the Central Fault). From land surface to 60 ft below ground surface, the alluvial deposits at MW2 consist primarily of sandy gravel with minor silt. Clayey and silty gravel predominate from 60 ft to 140 ft bgs before transitioning into massive silt from 140 to 160 ft.

- MW3 is completed in a zone of high fault density within the alluvial deposits (Qicr) on the east side of the river terrace. MW3 is southwest of Wells 1, 2, and 4 with the goal of assessing the hydraulic connection between the pumped fluvial deposits (Qmb1) and the eastern river terrace (Qicr) and estimating the permeability of the East Fault zone between Well 4 and MW3. The alluvial deposits at MW3 alternate between sandy gravels (0-50 ft bgs; 90-110 ft bgs) and silty to clayey gravels and clayey sands (50-90 ft bgs; 110-220 ft bgs).
- MW5 is completed in shallow fluvial deposits (Qmb1) between Wells 1 and 2 with the goal of characterizing the hydraulic connection between the deep fluvial deposits (pumped aquifer) and the shallow fluvial deposits. The fluvial deposits at MW5 consist primarily of silty gravel with interfingering thin layers of sandy gravels and clayey gravels.
- MW6 is located at the northeastern edge of the river terrace and completed primarily in alluvial deposits (Qicr) with the goal of assessing the connection between the fluvial deposits pumped by Wells 1, 2, and 4 and to estimate the permeability of the East Fault zone that extends between Well 4 and MW6. The alluvial deposits at MW6 consist primarily of silty gravel with interfingering layers of clayey gravel and sandy gravels.

Paleosols, or buried ancient soils, were identified in core samples from several boreholes drilled during the field campaign. Paleosols represent transition zones into new geologic units and geomorphic environments and are useful in developing geologic models and establishing hydrostratigraphic units. Depths and descriptions of paleosols in the MW3 borehole include:

- 125 ft below ground surface (ft bgs): Volcanic ash on top of weathered (red) Quaternary alluvium
- 147.5 ft bgs: Change in fluvial conditions indicated by normal grading, fining-upward fluvial deposits that represent flood-no flood sequences (present-day Qmb2 deposits); interbedded silt and silty sand (each bed ~2 inch thick) from 147.5 to 149 ft bgs; well-sorted gravelly sands with trace fines from 149 to 150 ft bgs.
- 157.5 ft bgs: prismatic block soil texture (“peds”) that are commonly found in lower soil horizons.
- 187.5 to 190 ft bgs: interbedded silty gravel-silt-silty gravel in equal thirds. Silt layer indicates transition back into fluvial depositional environment.
- 210 ft bgs: Tertiary sediments consisting of silty gravels that are hard and weathered (red).

GROUNDWATER LEVEL MONITORING

Monitoring Equipment

New and existing monitoring wells were equipped with LevelTROLL pressure transducers manufactured by In-Situ, Inc for continuous water level measurements to determine background and seasonal variability in water levels and to determine the effects of pumping on water levels during aquifer testing. Pressure transducers make high-frequency measurements (up to 4 per second). Vented Rugged Twist-lock cables were used to provide real-time data communication for the vented cables. The vent tube of the Rugged cable pairs with the vented transducer to mechanically compensate for barometric pressure changes to improve overall measurement accuracy.

Additionally, the Gardnerville Ranchos supply wells are equipped with a Supervisory Control and Data Acquisition (SCADA) system that gathers, analyses, and transmits real-time data to monitor pumping rates, system pressure, and water levels. The SCADA system is managed by Sierra Controls of Reno, NV. Through Sierra Controls, DRI accessed historical water level and pumpage data for the supply wells.

Groundwater Level Trends

Hydrographs for the monitoring wells are provided as Figure A-8. The period of record for each monitoring well is dependent on when the well was drilled and when monitoring equipment was installed. The hydrographs were prepared to evaluate flow directions and seasonal water level trends in the Gardnerville Ranchos area, in addition to the effects of pumping.

Overall, groundwater elevations range from about 4,724 to 4,773 ft amsl (1,440 to 1,455 mamsl). Generally, seasonal groundwater level trends in the alluvial aquifer are consistent with typical trends of snowmelt dominated watersheds of the Great Basin. In Gardnerville Ranchos, water levels increase during the spring and early summer, with magnitude and timing dependent on annual snowmelt dynamics, followed by decreasing water levels during late summer and fall when precipitation is lower, and ET is higher. The thick snowpack of the winter of 2022-2023 resulted in a greater increase in groundwater levels throughout the study area in spring/summer of 2023 when compared to 2022.

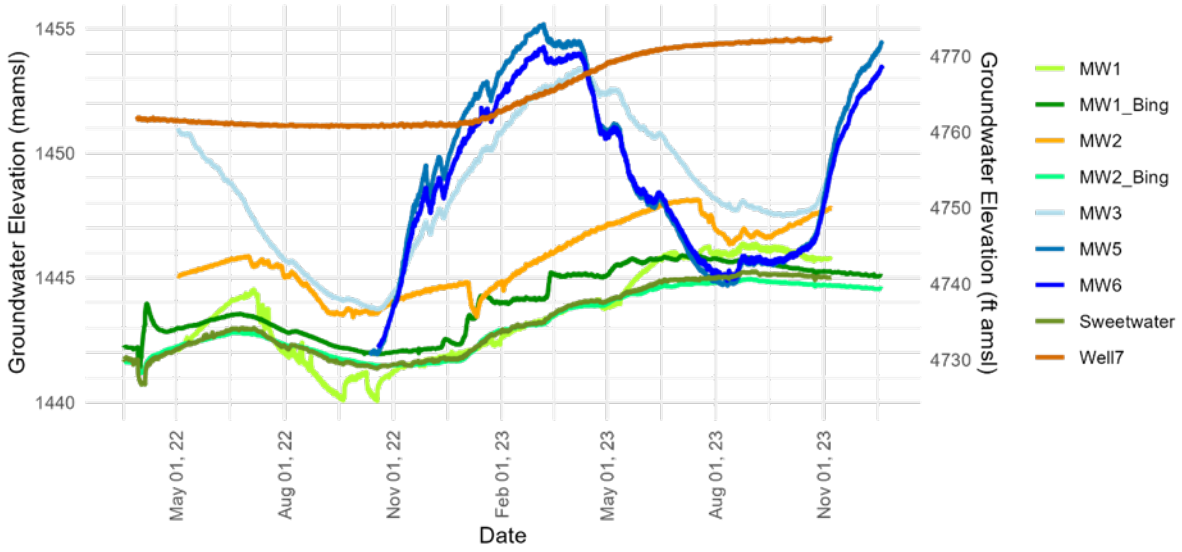

Figure A-8. Hydrographs of groundwater elevation over time at monitoring wells in Gardnerville Ranchos. Wells are colored by hydrogeologic block: West Block wells (green): MW1, MW1_Bing, MW2_Bing, Sweetwater; Central Block wells (orange): MW2, Well 7; East Block wells (blue): MW3, MW5, MW6.

There are also spatial trends in seasonal water levels throughout the study area. The magnitude and timing of seasonal water level variability is consistent between monitoring wells in the west (MW1, MW2_Bing, Sweetwater) and central area (MW-2). Even though MW1_Bing and MW2_Bing are neighboring wells and are completed at the same depth in gravel deposits, water levels at MW1_Bing respond to precipitation events more rapidly than MW2_Bing, suggesting coarser sediment at MW1_Bing and greater infiltration capacity. Also, MW1_Bing is located immediately adjacent to the discharge basin of Well 5, which collects runoff during precipitation events and induces localized infiltration.

Seasonal water level trends are also controlled by proximity to the East Fork Carson River and irrigation canals. Water levels in eastern monitoring wells MW5 and MW6 show the greatest magnitude of seasonal variability because of their proximity to the East Fork Carson River, where streamflow infiltrates to the water table. Moving farther away from the recharge source of the East Fork, there is a lag in the timing of response to streamflow infiltration at MW3. MW1 in northwest Gardnerville Ranchos shows a greater magnitude of seasonal variability than other monitoring wells in west Ranchos (i.e., Sweetwater) because of its proximity to recharge sources of the Edna Ditch and Rocky Slough. Well 7 in south central Gardnerville Ranchos does not show the same seasonal trends as other wells in 2022; a relatively flat hydrograph shows low seasonal variability from March to December 2022. Water levels at Well 7 increased in response to snowmelt during the spring of 2023, consistent with other monitoring wells. Well 7 is a deep monitoring well and is completed within a fault zone with increased clay content, likely resulting in less seasonal recharge.

AQUIFER TESTING

Hydraulic testing of the alluvial aquifer in the Gardnerville Ranchos area was conducted through multi-day constant-rate aquifer pumping and recovery tests. A constant rate aquifer test consists of pumping a well at a specific discharge rate for a length of time and recording water level changes in response to pumping ("drawdown") in both the pumping well and in nearby monitoring wells at specific times. The aquifer testing program was undertaken from March 2022 through February 2023. These tests, in conjunction with previous tests conducted in the study area, provide information on the conditions of the local alluvial aquifer, including the spatial distribution of aquifer hydraulic conductivity, storativity, and boundary conditions.

Site Setup

Gardnerville Ranchos public supply wells were used as test wells for each aquifer test. At each well, discharge was measured using a totalizing flow meter. Additionally, real-time data transmission of pumping rates and system pressures during each test were transmitted through the SCADA system. Pumping rates were measured hourly via the SCADA system and controlled as required by adjusting the variable frequency drive (VFD) or butterfly valve, depending on the well. Each well has an access port to install a pressure transducer to measure groundwater levels before, during, and after each test. If possible, an In Situ Level Troll was installed in the test well for the ability to measure water levels on a log-decaying scale and for real time transmission of water level data via the VuLink telemetry system. If an In Situ transducer could not be installed (typically from limited space in the access port), water levels were measured in the test well using previously installed transducers linked to the GRGID SCADA system.

The existing Gardnerville Ranchos pipeline network was used to convey discharge water during aquifer testing activities from the supply well to two water storage tanks. The storage capacities of the tanks are 1.5 million gallons and 3.0 million gallons. Prior to each aquifer test, water levels in the storage tanks were depleted to the lowest level permissible by the GRGID operations team to maximize available storage space for discharge water produced during aquifer testing. In some cases, water was conveyed between the storage tanks to increase storage capacity during testing. If the storage tank(s) reached capacity during testing, they were allowed to overflow. The storage tanks are >7,400 feet away from the nearest monitoring well (Well 7) and >7,900 feet from the nearest supply well connected to the distribution pipeline (Well 4), minimizing the likelihood that the infiltration of discharge water impacted groundwater levels during testing activities. Well 5 is no longer in use for GRGID's water supply and therefore is not connected to the distribution system. Discharge water produced during the Well 5 test was sent directly to the basin adjacent to the well.

Aquifer Testing Design

A summary of each aquifer test is provided in Table A-2, including test duration, discharge, maximum drawdown in the test well, and specific capacity of the test well. During testing, one test well was pumped at a time to make for clear drawdown signals, pumping rates were held constant to the degree possible, and pumping-well discharge was routed far from the testing and monitoring network to avoid recharging the aquifer. The range of discharge rates achieved ranged from 225 gpm (1,226 m^3/d) at Well 4 to 1,300 gpm

(7,090 m^3/d) at Well 2 and test durations ranged from four to seven days. Targeted long-term discharge rates were determined prior to each test by reviewing and analyzing historical discharge and drawdown data for each well. The optimal pumping rate reduces the pressure head in the aquifer to the maximum extent possible, while leaving sufficient head above the pump inlet. To maximize pressure propagation in the aquifer, pumping rates were increased during testing at Wells 2 and 4.

Table A-2. Summary of aquifer test details.

Test Well	Test Start	Test End	Test Duration (days)	Average Discharge (gpm)	Maximum Drawdown (ft)	Specific Capacity (gpm/ft)	Specific Discharge (ft/gpm)
Well 1	12/9/22 14:00	12/13/22 15:00	4.0	950	73.4	12.9	0.08
Well 2[a]	11/28/22 15:45	12/2/22 15:00	4.0	1300	90.42	14.4	0.07
Well 4[b]	2/8/23 14:00	2/15/23 11:30	6.9	225	246.3	0.9	1.09
Well 5	3/29/22 9:00	4/4/22 13:00	6.2	1216	70.8	17.2	0.06
Well 6	1/23/23 14:30	1/30/23 13:00	6.9	695	101.9	6.8	0.15
Well 8	1/3/23 15:00	1/10/23 16:35	7.1	862	129	6.7	0.15
Well 9	11/9/22 15:00	11/16/22 15:00	7.0	775	90.38	8.6	0.12

gpm - gallons per minute

ft - feet

a - Initial discharge of 1,700 gpm for first 19 minutes of test, then reduced to 1,300 gpm for remainder.

b - Initial discharge of 210 for the first 46 hours of test, then increased to 240 gpm for remainder.

Maximum drawdown is the difference between the pre-test water level and lowest water level in the pumping well.

Specific Capacity - Average Discharge/Maximum Drawdown

Specific Discharge - Maximum Drawdown/Average Discharge

During the pumping periods, continuous groundwater level measurements were made in all wells, including supply wells and monitoring wells, using pressure transducers. For wells with In-Situ transducers, datalogging frequencies during aquifer testing were determined based on anticipated timing and magnitude of drawdown at each observation point associated with distance and an understanding of the hydrogeology. The radial distance between test wells and monitoring wells are shown in Table A-3. Monitoring locations were grouped by tiers:

- Tier 1 locations were generally located near the pumping well and were anticipated to show a rapid water level response to pumping. Pressure transducers at tier 1 monitoring locations were programmed to record on a log-decaying schedule from the start of pumping and start of aquifer recovery, starting at four measurements per

second and reducing frequency over time to a 20-minute interval. High frequency measurements at the start of pumping and recovery are meant to capture early-time water level responses that can provide key data for analyzing aquifer properties.

- Tier 2 locations were generally farther from the pumping well or were located on the opposite side of a fault from the pumping well and were therefore not anticipated to have an early response to pumping. Pressure transducers at Tier 2 locations were programmed at a linear schedule with measurements at 20-minute intervals.

Table A-3. Distances, in feet, between test wells and monitoring locations.

		Test Well							
		Well 1	**Well 2**	**Well 4**	**Well 5**	**Well 6**	**Well 7**	**Well 8**	**Well 9**
Monitoring Location	**Well 1**	0	1,739	2,235	11,723	7,742	8,460	5,461	11,882
	Well 2	1,739	0	3,424	10,721	6,073	8,154	3,753	10,279
	Well 4	2,235	3,424	0	11,053	8,563	7,042	7,046	12,369
	Well 5	11,723	10,721	11,053	0	7,213	5,110	10,175	6,137
	Well 6	7,742	6,073	8,563	7,213	0	8,073	3,482	4,288
	Well 7	8,460	8,154	7,042	5,110	8,073	0	9,488	9,564
	Well 8	5,461	3,753	7,046	10,175	3,482	9,488	0	7,658
	Well 9	11,882	10,279	12,369	6,137	4,288	9,564	7,658	0
	MW1	8,507	6,812	9,407	7,515	873	8,806	3,886	3,773
	MW1_Bing	11,530	10,493	10,915	338	6,886	5,146	9,874	5,825
	MW2	4,926	3,547	5,324	7,309	3,324	5,917	3,571	7,077
	MW2_Bing	10,820	9,654	10,433	1,624	5,641	5,434	8,732	4,692
	MW3	4,224	4,263	2,859	8,247	7,082	4,274	6,808	10,312
	MW4	13,935	12,563	13,835	4,111	7,279	8,992	10,751	3,851
	MW5	942	837	2,930	11,322	6,906	8,438	4,520	11,100
	MW6	1,292	2,165	1,261	10,745	7,523	7,226	5,802	11,478
	Sweetwater	10,264	8,898	10,251	3,409	4,072	6,465	7,385	3,137

Aquifer Test Data Corrections and Processing

Time-series drawdown data are required 1) to estimate aquifer hydraulic properties and 2) to use as temporal head targets during transient model calibration. To isolate the effects of pumping on water levels, and to produce time-series drawdown datasets for each monitoring well during each aquifer test, background water level trends were removed from the temporal water level data using SeriesSEE, a Microsoft Excel add-in developed by the United States Geological Survey (USGS) for modeling water levels and estimating drawdown during aquifer pumping (Halford et al., 2012).

Prior to estimating drawdown, complete and continuous water level datasets were produced by correcting raw water level data in SeriesSEE for outliers, data gaps, and offsets, which reduces the likelihood of producing erroneous simulated water levels. Processed water level datasets were then reduced from high-frequency water levels (<20 minutes) to twelve-hour averaged water levels. Frequency reduction was performed because high-frequency water levels may capture subtle fluctuations that cannot be accounted for by the environmental and pumping variables included in SeriesSEE.

The SeriesSEE model assumes that measured water level fluctuations can be approximated by summing multiple component fluctuations, including background water level trends and pumping. Input series of water levels from monitoring wells unimpacted by pumping during the field program were used to estimate background water level trends. The pressure transducers are vented to the atmosphere, so barometric pressure data were not required. Water level model components are summarized in Table A-4.

Table A-4. Water level model components, input datasets, and coefficients to transform input datasets.

WLM component	Time Series Input	Coeff. 1	Coeff. 2	Coeff. 3	Coeff. 4	Coeff. 5
Moving Average	Any series	Multiplier	Phase	Averaging Period	-	-
Theis transform	Pumping schedule	Transmissivity	Storage coefficient	Radial distance	Flow-rate conversion	-

Water levels from background wells were transformed by averaging over periods of hours to days because a broad range of averaging periods are more likely to simulate environmental fluctuations (Halford et al., 2012). The averaging periods used to transform background water levels are 0.04, 0.08, 0.125, 0.25, 0.5, 1, 2, 4, and 7 days. This equates to nine water level model components created for each input series of background water levels.

Input series of pumping schedules at the test wells are transformed to water level fluctuations with the Theis (1935) solution:

$$s = \frac{Q}{4\pi T} W(U) = \frac{Q}{4\pi T} W\left(\frac{r^2 S}{4T\Delta t}\right) \quad \text{(A-1)}$$

where s is drawdown, Q is the pumping rate, T is the transmissivity, $W(U)$ is the exponential integral solution, U is dimensionless time, r is radial distance between the observation well and the pumping well, S is the storage coefficient, and Δt is the elapsed time since the flow rate changed.

Values for all variables above are known, except for transmissivity and the storage coefficient. Aquifer transmissivity and storage coefficients are adjusted to minimize the differences between synthetic and measured water levels. SeriesSEE water level models are calibrated using PEST (Doherty and Hunt, 2010) to derive a statistically suitable solution to explain and differentiate between pumping responses and environmental fluctuations. Model performance is reported using the root-mean-square error (RMSE) because RMSE has units of length and is easily compared to the actual water level measurements. A lower RMSE indicates a better model fit in this application.

In cases where aquifer conditions honor the assumptions of the Theis solution (i.e., infinite areal extent, homogenous, isotropic, confined, uniform thickness, horizontal and unsteady flow), the estimates of aquifer transmissivity and storage are representative of aquifer conditions and are considered during conceptual model development. If assumptions of the Theis solution are broken (e.g., in cases where a low permeability fault separates the monitoring well from the test well), then estimated aquifer hydraulic properties are not considered representative of actual aquifer conditions and not used for conceptual model development. Rather, the estimated hydraulic properties are simply curve fitting parameters to produce the drawdown datasets for additional hydraulic property analysis and transient model calibration.

After correcting groundwater level data for the effects of environmental fluctuations, drawdown data were analyzed to determine aquifer hydraulic properties using AQTESOLV, the industry-standard software package for the interpretation of aquifer tests (HydroSOLVE, 2008). Water levels were analyzed in AQTESOLV if an apparent change in water level over time was observed in response to pumping based on SeriesSEE analysis. Drawdown analysis in AQTESOLV began with conventional log-log diagnostic derivative and flow analysis (Theis, 1935) to analyze pumping test data and identify flow regimes. Derivative analysis of the water level drawdown was used to assist in determining aquifer conditions (Nielsen, 2007), including confined or unconfined aquifers, nonleaky or leaky aquifers, recharge boundaries (e.g., stream leakage), and no-flow boundaries (e.g., faults). The analytical graphing technique of water level derivatives is also useful in determining which analytical technique is appropriate for estimating hydraulic parameters (Bourdet et al., 1989; Spane 1993; Nielsen, 2007).

In aquifer test diagnostics, it is typically assumed that the pumping rate is constant, the only unnatural stress on groundwater levels is pumping at the test well, and that the aquifer is homogenous. The assumption of aquifer homogeneity is rarely accurate. Heterogeneities that can influence pumping test responses include varying hydraulic properties with depth, by geologic unit, or with radial distance from the pumping well, or the presence of recharge and no-flow linear boundaries.

Methods developed by Theis (1935) and Cooper-Jacob (1946) were used to analyze drawdown data in wells in the pumped aquifer (the confined aquifer) when diagnostic analyses showed infinite-acting radial flow. These methods involve fitting a line through drawdown data as a function of log time, the slope of which is used to calculate hydraulic properties. Only water level recovery (“residual drawdown”) data collected after the termination of pumping were used to estimate aquifer properties at the pumped well.

Overall, drawdown responses in shallow monitoring wells of the unpumped aquifer (unconfined aquifer) closely match the Neuman and Witherspoon (1969) solution for leaky confined aquifer systems. The Neuman and Witherspoon solution accounts for drawdown in both the pumped and unpumped aquifers and estimates aquifer properties for each. Additionally, the Neuman and Witherspoon solution estimates a vertical leakage factor through the aquitard. An example of the output from an AQTESOLV model for MW-5 during the Well 1 aquifer test is shown as Figure A-9.

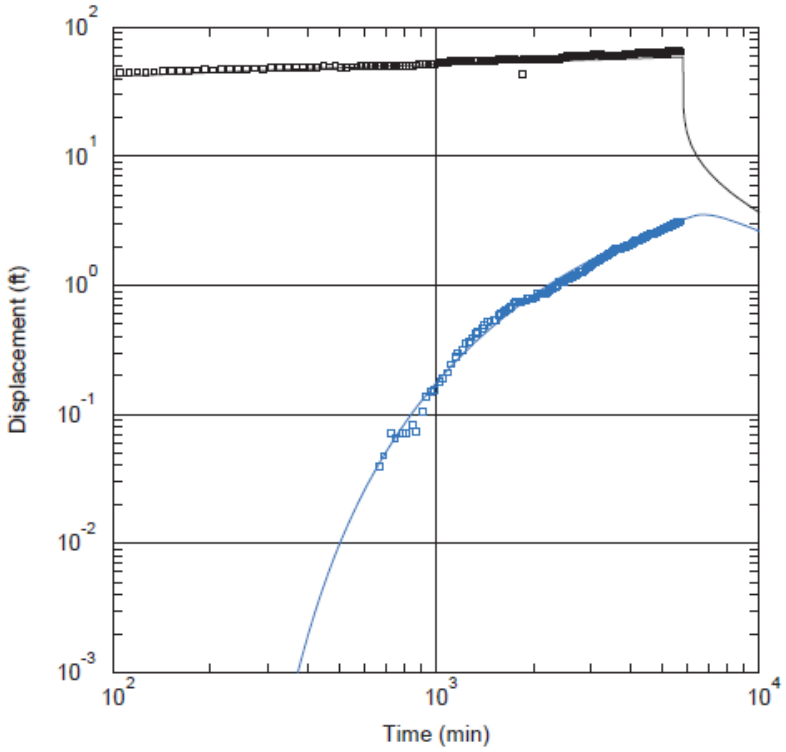

WELL TEST ANALYSIS

Data Set: D:\Projects\GRGID\modeling\aqtesolv\well1_test\well1test_dd_mw5_neumanwitherspoon.aqt
Date: 01/19/24 Time: 15:15:05

PROJECT INFORMATION

Company: DRI
Client: GRGID
Location: Gardnerville Ranchos
Test Well: Well 1
Test Date: 12/9/23 - 12/13/22

AQUIFER DATA

Saturated Thickness: 290. ft
Aquitard Thickness (b'): 1. ft
Anisotropy Ratio (Kz/Kr): 0.0009616
Aquitard Thickness (b"): 1. ft

WELL DATA

Pumping Wells

Well Name	X (ft)	Y (ft)
Well 1	867347.9024	14141295.63

Observation Wells

Well Name	X (ft)	Y (ft)
Well 1	867347.9024	14141295.63
MW5	866680.3329	14141813.32

SOLUTION

Aquifer Model: Leaky
T = 3395.4 ft^2/day
1/B = 0.4057 ft^{-1}
T2 = 51.33 ft^2/day
Solution Method: Neuman-Witherspoon
S = 0.006469
ß/r = 0.1871 ft^{-1}
S2 = 3.449E-5

Figure A-9. AQTESOLV analytical graph for MW5 for the Well 1 aquifer test.

Aquifer Testing Results

Summary of Results

Observations made during each aquifer test that contribute to development of the conceptual model are described in detail in the following subsections. The summary provided here introduces key concepts and takeaways that are referred to in the following subsections. Additionally, the hydraulic properties calculated using aquifer test data are summarized here.

Attachment 2 documents the transformed values of the input series for each SeriesSEE model and output plots of simulated water levels and calculated drawdown. Attachment 2 includes SeriesSEE output plots for monitoring wells that either 1) show drawdown from pumping or 2) are located close to the pumping well and do not show drawdown. The estimated drawdown from SeriesSEE was then used as the input dataset for additional analysis in AQTESOLV. Attachment 3 includes analytical graphs and aquifer properties estimated in AQTESOLV. Hydraulic properties estimated for each monitoring well and summarized by hydrogeologic block (discussed below) are provided as Tables A-5 through A-8.

Results of the aquifer tests suggest the presence of four hydrogeologic blocks that are bound by north-south trending, low-permeability faults. Hydrogeologic block delineations are illustrated on Figure A-10, along with the faults that define their boundaries. The hydrogeologic blocks are characterized by relatively high transmissivity in the north-south direction (parallel to the faults) and lower transmissivity in the east-west directions (perpendicular to the faults). Overall, drawdown is limited to the pumped hydrogeologic block, with either little or no drawdown extending across the fault boundaries.

The West, Central, and East Faults mapped by the U.S. Geological Survey are marked by lineaments at the land surface of the alluvial deposits (Qri, Qicr). The spatial distribution of drawdown during aquifer testing suggests that the West, Central, and East Faults extend to the north through the fluvial deposits (Qmb1, Qmb2) beyond what the surface geology maps indicate. While these faults are represented as individual fault planes with depth in the conceptual model, they represent a more complex network of interconnected faults and fractures at depth that control groundwater flow. For example, the high density of faults in the southern portion of the East block may interconnect at depth with the east-dipping Central Fault.

Aquifer testing results and borehole lithology data suggest the presence of a two-aquifer system throughout the study area that includes a deeper confined aquifer and a shallow unconfined aquifer with leakage through the aquitard that separates the two aquifers. The deep confined aquifer is the primary aquifer pumped by supply wells in the Gardnerville Ranchos area.

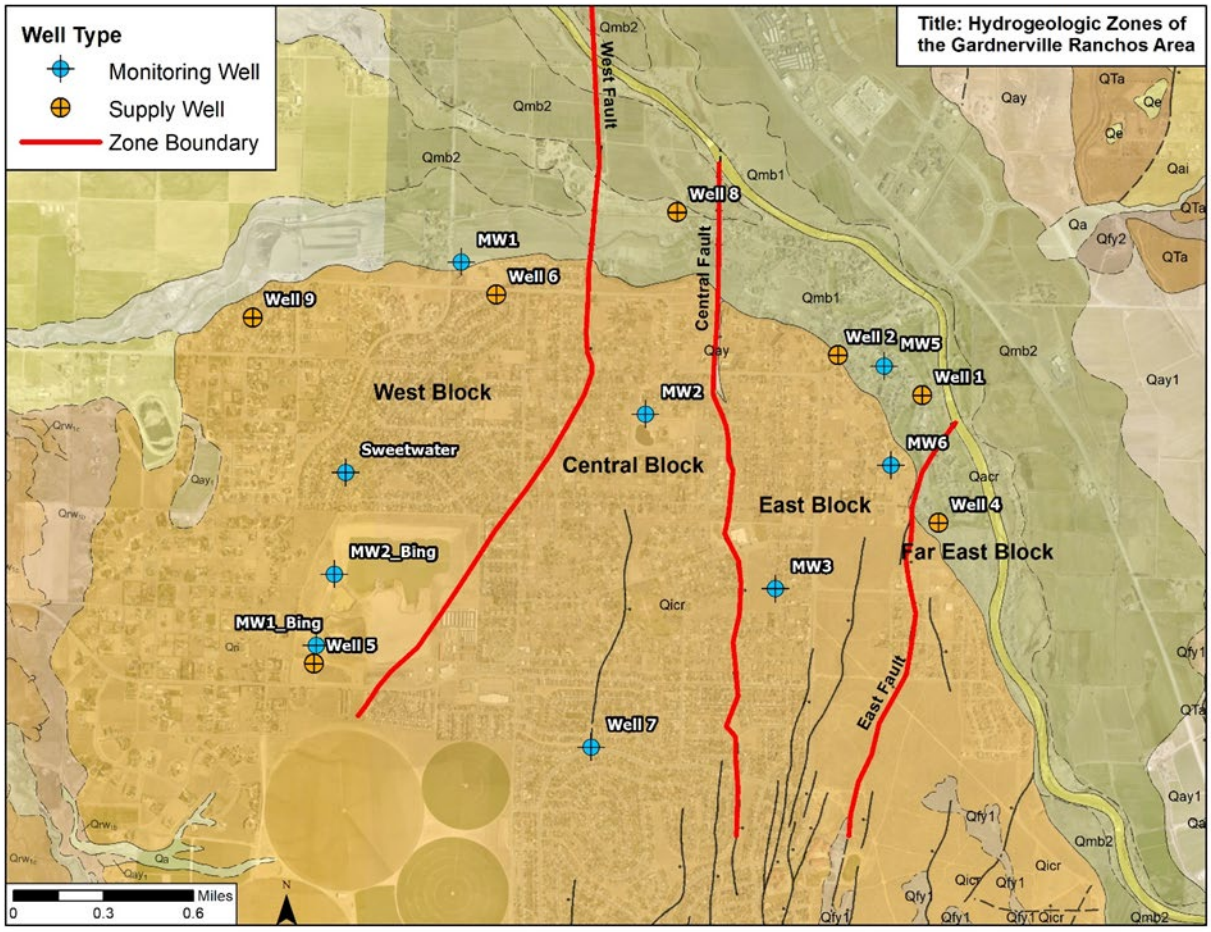

Figure A-10. Aquifer test results suggest that the local aquifer is divided into four hydrogeologic blocks that are bound by low-permeability faults. The locations of the blocks and faults are shown here.

Summary tables of hydraulic properties for the pumped aquifer and unpumped aquifer are provided in Tables A-5 and A-6. For each aquifer test, only estimates of hydraulic properties at monitoring wells in the same hydrogeologic block as the pumping well are included. Summary statistics of hydraulic properties by hydrogeologic block are provided in Tables A-7 and A-8. Field-tested transmissivity values in the pumped aquifer range from 419 ft^2/d (39 m^2/d) (Well 4) to 4.91E+04 ft^2/d (4,560 m^2/d) (Well 9) and in the unpumped aquifer range from 0.0148 ft^2/d (0.001 m^2/d) (MW6) to 6.32E+05 ft^2/d (5.87E+04 m^2/d) (MW2_Bing). Overall, transmissivity is lower in the east and far east blocks, where there is increased clay content, and higher in the Western Block where the aquifer consists primarily of sandy gravels.

Table A-5. Hydraulic properties of basin-fill materials derived from drawdown in the pumped aquifer.

Well Info				AQTESOLV (Theis)					AQTESOLV (Theis Recovery)		
Test Well	**Penetrated Aquifer Thickness (ft)**	**Hydrogeologic Block**	**Monitoring Well**	**T1 (ft2/d)**	**K1 (ft/d)**	**S1 (unitless)**	**Ss1 (ft-1)**	**Kz/Kr**	**T1 (ft2/d)**	**K1 (ft/d)**	**S/S' (unitless)**
Well 1	260	East	Well 2	4.52E+03	1.74E+01	2.74E-04	1.05E-06	9.62E-04	-	-	-
Well 2	380	East	Well 1	3.52E+03	1.35E+01	3.75E-04	1.44E-06	1.00E+00	-	-	-
			Well 2	-	-	-	-	-	2.19E+03	5.77E+00	1.74E+00
Well 4	189	Far East	Well 4	4.19E+02	1.10E+00	2.27E-06	5.97E-09	1.00E+00	-	-	-
Well 6	220	West	Well 5*	1.33E+03	6.05E+00	1.60E-03	7.27E-06	-	-	-	-
			Well 6	-	-	-	-	-	4.09E+03	1.86E+01	1.01E+01
Well 8	240	Central	Well 8	-	-	-	-	-	2.08E+03	8.68E+00	7.62E-01
Well 9	150	West	Well 5	4.91E+04	3.27E+02	2.92E-03	1.94E-05	1.00E+00	-	-	-

T1 transmissivity of pumped aquifer

K1 hydraulic conductivity of pumped aquiver = T1/aquifer thickness

S1 storativity in pumped aquifer

Ss1 specific storage in a pumped aquifer = S1/aquifer thickness

Kz/Kr vertical to horizontal conductivity anisotropy

S/S' ratio of storativity during pumping (S) to storativity during recovery (S')

* We5 T1 and S1 calculated in SeriesSEE

Table A-6. Hydraulic properties of basin-fill materials derived from drawdown in the unpumped aquifer.

Test Well	Penetrated Aquifer Thickness (ft)	Hydrogeologic Block	Monitoring Well	T_1 (ft^2/d)	K_1 (ft/d)	S_1 (unitless)	Ss_1 (ft^{-1})	1/B (ft^{-1})	β/r (ft^{-1})	T_2 (ft2/d)	K_2 (ft/d)	S_2 (ft2/d)	Ss_2 (ft^{-1})
			MW3	2.94E+03	1.13E+01	4.32E-04	1.66E-06	4.28E-01	1.92E-01	1.49E-02	5.72E-05	3.20E-08	1.23E-10
Well 1	260	East	MW5	3.40E+03	1.31E+01	6.47E-03	2.49E-05	4.06E-01	1.87E-01	5.13E+01	1.97E-01	3.45E-05	1.33E-07
			MW6	3.92E+03	1.51E+01	3.58E-03	1.38E-05	4.31E-01	1.86E-01	1.44E-02	5.54E-05	3.33E-08	1.28E-10
			MW3	3.45E+04	9.08E+01	1.05E-03	2.76E-06	5.24E-01	1.40E-01	5.45E+03	1.44E+01	8.52E-15	2.24E-17
Well 2	380	East	MW5	6.35E+01	1.67E-01	1.87E-03	4.92E-06	8.43E-02	7.10E-02	9.04E+03	2.38E+01	5.81E-12	1.53E-14
			MW6	1.59E+03	4.18E+00	2.13E-05	5.61E-08	5.23E-01	2.17E+00	1.69E+03	4.44E+00	1.38E-03	3.62E-06
Well 6	220	West	MW1	3.31E+04	1.51E+02	2.59E-03	1.18E-05	6.03E-02	4.82E-02	1.26E+04	5.71E+01	4.04E-04	1.84E-06
Well 8	240	Central	MW2	5.32E+03	2.22E+01	1.27E-05	5.28E-08	7.15E-02	9.83E-02	2.02E+03	8.42E+00	5.44E-04	2.27E-06
Well 9	150	West	MW2_Bing	8.41E+04	5.60E+02	1.11E-02	7.42E-05	2.17E-09	3.45E-05	6.32E+05	4.22E+03	1.00E+00	6.67E-03
			Sweetwater	9.57E+03	6.38E+01	2.13E-03	1.42E-05	2.17E-03	3.51E-04	9.97E+04	6.64E+02	1.01E-10	6.71E-13

Hydraulic property estimated for monitoring wells using the Neuman-Witherspoon (1969) method

T1	transmissivity of pumped aquifer	T2	transmissivity of unpumped aquifer
K1	hydraulic conductivity of pumped aquifer = T1/aquifer thickness	K2	hydraulic conductivity of unpumped aquifer = T2/aquifer thickness
S1	storativity in pumped aquifer	S2	storativity in unpumped aquifer
Ss1	specific storage in pumped aquifer = S1/aquifer thickness	Ss2	specific storage in unpumped aquifer = S2/aquifer thickness
1/B	aquitard leakage parameter		
β/r	aquitard leakage parameter		

Table A-7. Summary of hydraulic properties by hydrogeologic block in the pumped aquifer.

Block	Statistic	T_1 (ft^2/d)	K_1 (ft/d)	S_1 (unitless)	Ss_1 (ft^{-1})	Kz/Kr
Far East (n=1)	All	4.19E+02	1.10E+00	2.27E-06	5.97E-09	1.00E+00
East (n=3)	Max	4.52E+03	1.74E+01	3.75E-04	1.44E-06	1.00E+00
	Min	2.19E+03	5.77E+00	2.74E-04	1.05E-06	9.62E-04
	Mean	3.41E+03	1.22E+01	3.24E-04	1.25E-06	5.00E-01
	Geomean	3.27E+03	1.11E+01	3.20E-04	1.23E-06	3.10E-02
	Med	3.52E+03	1.35E+01	3.24E-04	1.25E-06	5.00E-01
Central (n=1)	All	2.08E+03	8.68E+00	-	-	-
West (n=3)	Max	4.91E+04	3.27E+02	2.92E-03	1.94E-05	1.00E+00
	Min	1.33E+03	6.05E+00	1.60E-03	7.27E-06	1.00E+00
	Mean	1.82E+04	1.17E+02	2.26E-03	1.34E-05	1.00E+00
	Geomean	6.44E+03	3.33E+01	2.16E-03	1.19E-05	1.00E+00
	Med	4.09E+03	1.86E+01	2.26E-03	1.34E-05	1.00E+00

Table A-8. Summary of hydraulic properties by hydrogeologic block in the unpumped aquifer.

Block	Statistic	T_1 (ft^2/d)	K_1 (ft/d)	S_1 (unitless)	Ss_1 (ft^{-1})	1/B (ft^{-1})	β/r (ft^{-1})	T_2 (ft2/d)	K_2 (ft/d)	S_2 (ft^2/d)	Ss_2 (ft^{-1})
East (n=8)	Max	3.45E+04	9.08E+01	6.47E-03	2.49E-05	5.24E-01	2.17E+00	9.04E+03	2.38E+01	1.38E-03	3.62E-06
	Min	6.35E+01	1.67E-01	2.13E-05	5.61E-08	8.43E-02	7.10E-02	1.44E-02	5.70E-05	8.52E-15	2.24E-17
	Mean	7.74E+03	2.24E+01	2.21E-03	7.89E-06	3.98E-01	4.91E-01	2.71E+03	7.13E+00	2.35E-04	6.26E-07
	Geomean	2.27E+03	7.22E+00	8.55E-04	2.72E-06	3.45E-01	2.30E-01	3.13E+01	9.97E-02	1.16E-08	3.69E-11
	Med	3.16E+03	1.22E+01	1.46E-03	3.84E-06	4.26E-01	1.89E-01	8.70E+02	2.32E+00	3.22E-08	1.24E-10
Central (n=1)	All	5.32E+03	2.22E+01	1.27E-05	5.28E-08	7.15E-02	9.83E-02	2.02E+03	8.42E+00	5.44E-04	2.27E-06
West (n=3)	Max	8.41E+04	5.60E+02	1.11E-02	7.42E-05	6.03E-02	4.82E-02	6.32E+05	4.22E+03	1.00E+00	6.67E-03
	Min	9.57E+03	6.38E+01	2.13E-03	1.18E-05	2.17E-09	3.45E-05	1.26E+04	5.71E+01	1.01E-10	6.71E-13
	Mean	4.22E+04	2.58E+02	5.28E-03	3.34E-05	2.08E-02	1.62E-02	2.48E+05	1.65E+03	3.33E-01	2.22E-03
	Geomean	2.99E+04	1.75E+02	3.94E-03	2.31E-05	6.57E-05	8.35E-04	9.25E+04	5.43E+02	3.44E-05	2.02E-07
	Med	3.31E+04	1.51E+02	2.59E-03	1.42E-05	2.17E-03	3.51E-04	9.97E+04	6.64E+02	4.04E-04	1.84E-06

Well 1 Test

Aquifer testing at Well 1 took place from December 9-13, 2022. During the test, drawdown in monitoring wells to the northwest of Well 1 increased with distance; the maximum drawdown at MW5 (844 ft from the pumping well) was approximately 3.4 ft, while the maximum drawdown at Well 2 (1,635 ft away from the pumping well) was approximately 18 ft. This drawdown distribution is explained by a confined two-aquifer system in the East Block, where Supply Well 1 is screened in the deeper confined aquifer (pumped aquifer). A greater magnitude of drawdown was measured in Well 2 because it is screened in the pumped aquifer when compared to shallow monitoring wells that are screened in the overlying unconfined aquifer (i.e., MW3, MW5, MW6). Lithology logs for boreholes in the East Block suggest the presence of low permeability clay layers, which form an aquitard that limits the hydraulic connection between the confined and unconfined aquifers. Consistently, there is a delayed drawdown effect in the shallow wells, where the maximum drawdown measured in each well occurs after pumping has ceased, which can be attributed to a low permeability aquitard that reduces/delays flow between the two aquifers. Drawdown in the shallow aquifer indicates that the two aquifers are hydraulically connected. Drawdown was observed up to 4,246 feet away (MW-3) in the unpumped aquifer. Maps showing the maximum drawdown contours for both aquifers during the Well 1 test are provided as Figures A-11 and A-12. No drawdown response was measured at Well 4 (2,253 ft from Well 1 in the pumped aquifer), which is a result of inhibited flow across the East Fault and because the aquifer at Well 4 has a lower hydraulic conductivity than Well 1. The dashed-line extension of the East Fault to the northeast through fluvial deposits (Qmb1) between Well 1 and 4 is an approximation based on results of the aquifer test. Specific capacity data from Well 4, and other wells to the east of Gardnerville Ranchos (NDWR, 2024a), show that the aquifer at Well 4 has a lower hydraulic conductivity than at Well 1 (Figure A-13). No drawdown was detected in the pumped aquifer at Well 8 (distance = 5,461 ft), which may suggest that the Central Fault propagates to the north through the fluvial deposits (dashed lined east of Well 8) and inhibits flow between Wells 1 and 8.

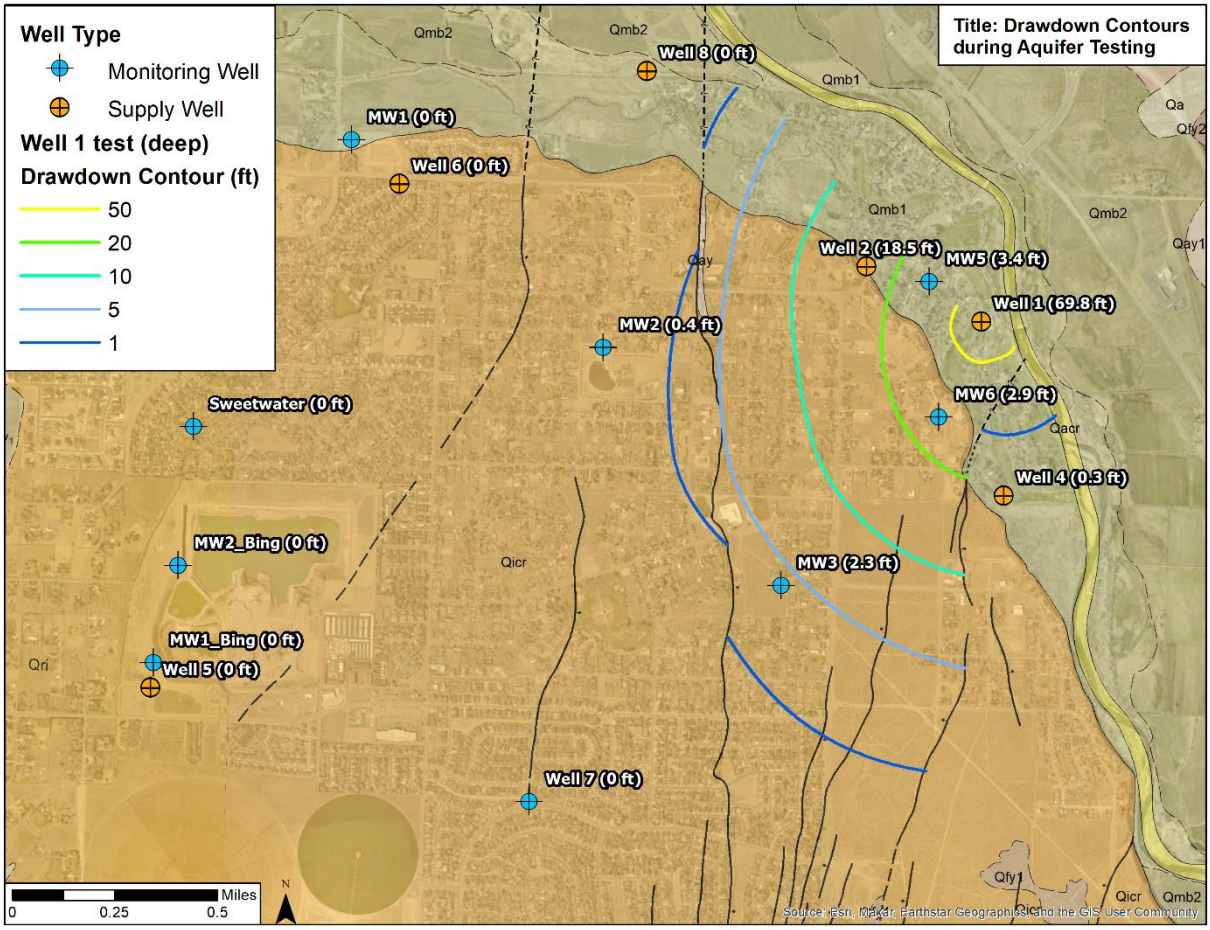

Figure A-11. Drawdown contours for the confined aquifer during the Well 1 test. Maximum drawdown measured in each well (including shallow and deep wells) is shown next to the well name.

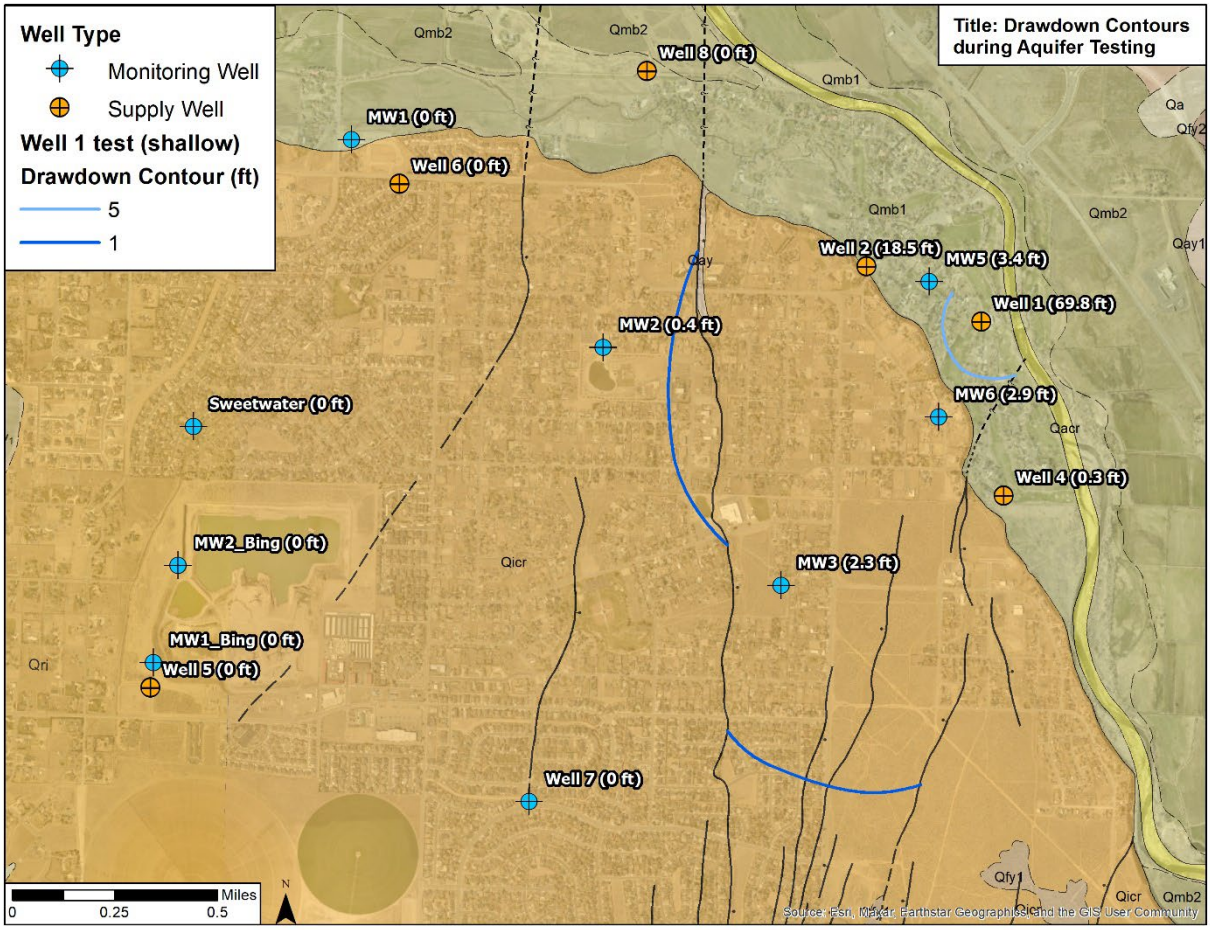

Figure A-12. Drawdown contours for the unconfined aquifer during the Well 1 test. Maximum drawdown measured in each well (including shallow and deep wells) is shown next to the well name.

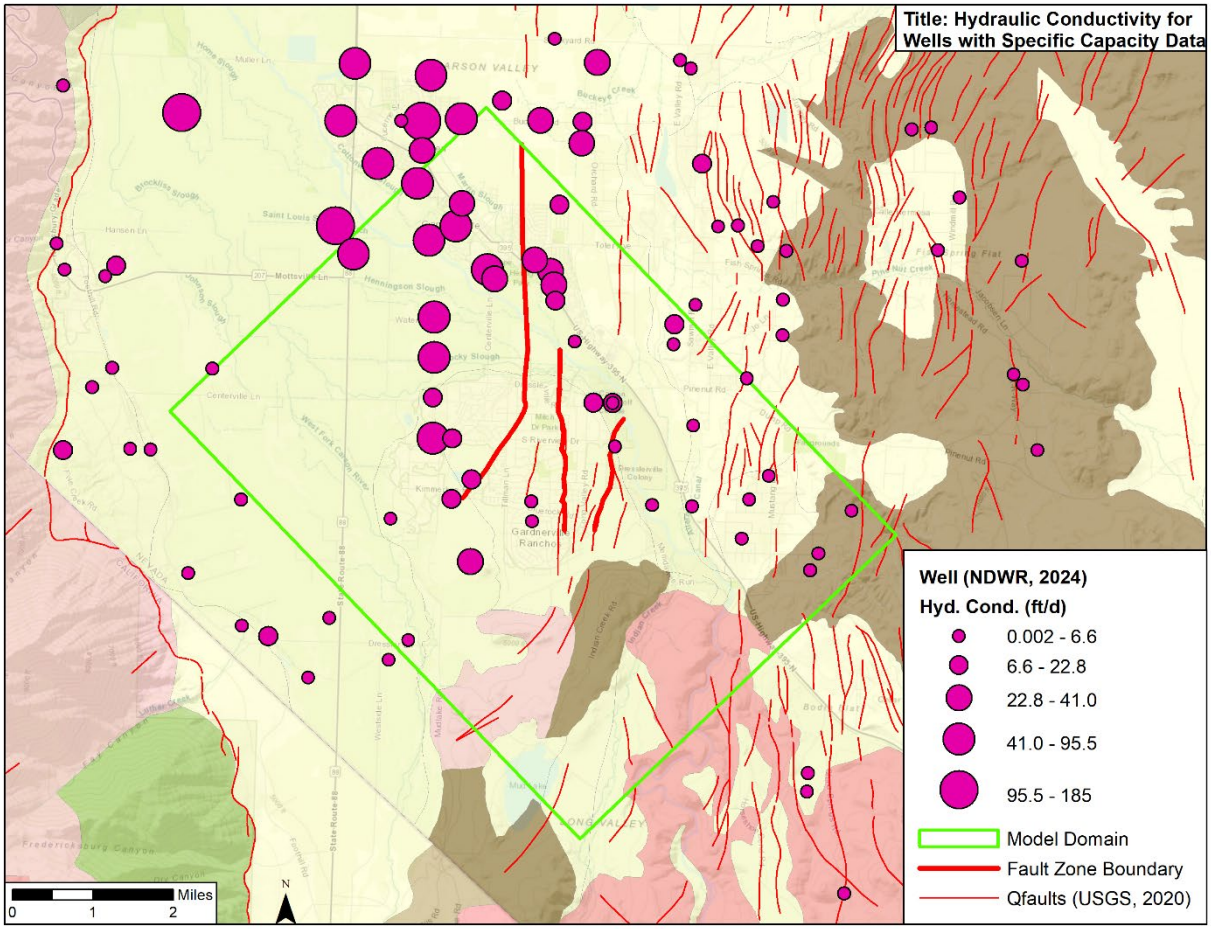

Figure A-13. Estimated hydraulic conductivity at wells with specific capacity data in southern Carson Valley. Surface geology from the USGS State Geologic Map Compilation (Horton et al., 2017). Geologic units listed in Figure 3 of the main text.

To estimate bulk hydraulic properties in the pumped aquifer of the Eastern Block during the Well 1 test, time-drawdown data at Well 2 were used. The slope of the time-drawdown at Well 2 steepens near the end of the test (Attachment 2), which may suggest that the cone of depression reached a no-flow boundary, such as the Central Fault or a low transmissivity hydrostratigraphic unit.

Drawdown responses in the shallow unconfined aquifer at MW3, MW5, and MW6 during Well 1 pumping closely match the Neuman and Witherspoon (1969) solution for leaky confined aquifer systems. Results suggest that the pumped aquifer has a higher transmissivity and lower storativity than the unpumped aquifer in the East Block.

Well 2 Test

Results of the Well 2 test corroborate the observations of Well 1 test. Well 2 is completed in the confined aquifer of the East Block and the relationship between drawdown magnitude with radial distance from the pumping well supports a layered aquifer system; drawdown at Well 1 (24.7 ft; distance = 1,738 ft) was greater than drawdown at MW5 (4 ft;

distance = 836 ft). Drawdown was observed in monitoring wells completed in the shallow unpumped aquifer (i.e., MW3, MW5, MW6), with 1.13 ft of drawdown up to 4,251 ft from the pumping well (MW-3). A slope change in the time-drawdown curve for each of the shallow monitoring wells occurred on December 1, 2022 (~3 days into the test) suggesting that a no-flow boundary was reached, which could be a fault (i.e., Central or East Fault) or a low permeability hydrostratigraphic unit. No drawdown was measured in the pumped aquifer at Wells 4 and 8, reaffirming that the Central and East Faults are flow barriers. Approximated maximum drawdown contours from the Well 2 test for the deep and shallow aquifers are shown in Figures A-14 and A-15.

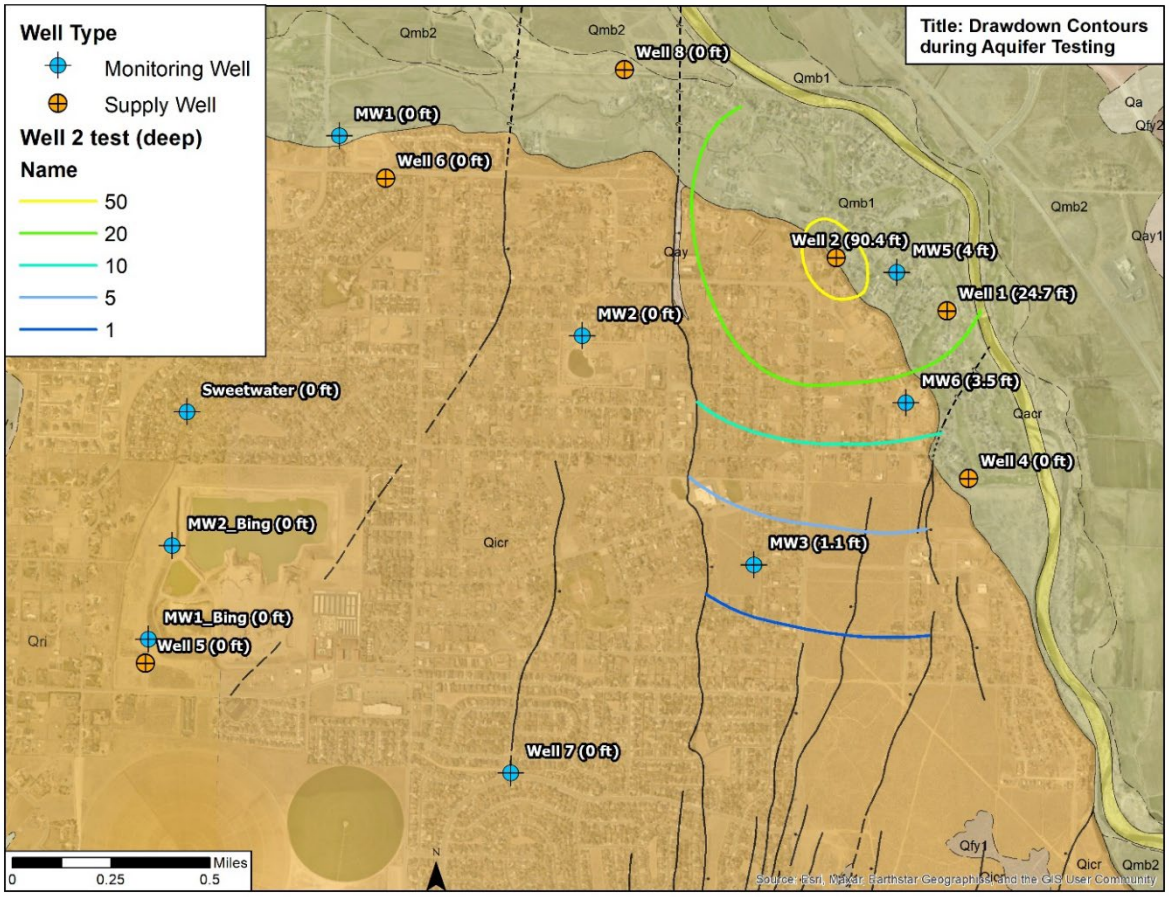

Figure A-14. Drawdown contours for the confined aquifer during the Well 2 test. Maximum drawdown measured in each well (including shallow and deep wells) is shown next to the well name.

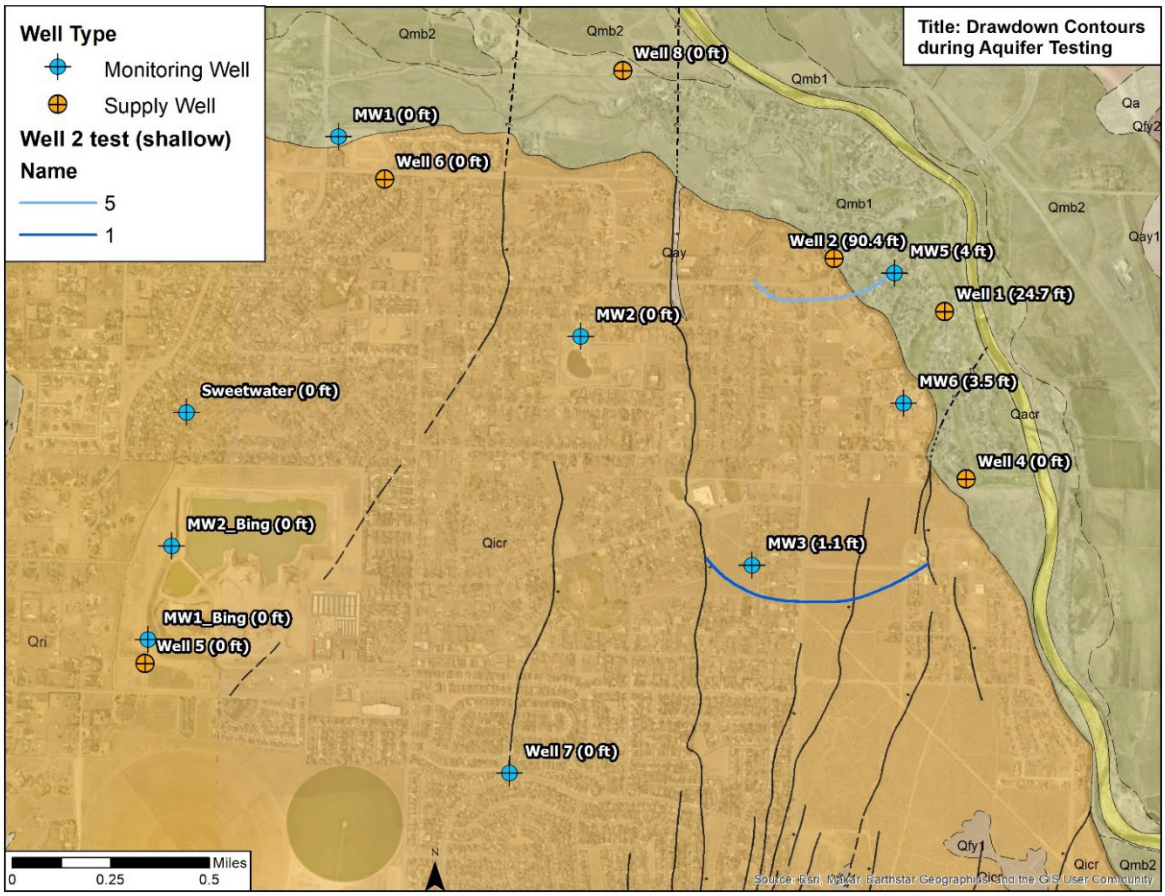

Figure A-15. Drawdown contours for the unconfined aquifer during the Well 2 test. Maximum drawdown measured in each well (including shallow and deep wells) is shown next to the well name.

To estimate bulk hydraulic properties in the pumped aquifer, drawdown data in Well 1 (Theis solution) and recovery data from Well 2 (Theis recovery solution) were analyzed. The Theis recovery solution was used to analyze water level recovery data for the pumping well because discharge rates varied during the first twenty minutes of pumping. Shallow well drawdown data were matched to the Neuman-Witherspoon solution. Estimated hydraulic properties from the pumped and unpumped aquifers during the Well 2 test are summarized in Tables A-5 and A-6.

Well 4 Test

The aquifer test at Well 4 was performed from 2/8/23 to 2/15/23. A discharge rate of 210 gpm was sustained from the start of the test until 2/10/23 at 12:00, at which point, the discharge was increased to approximately 240 gpm (1,300 m^3/d) for the remainder of the test to enhance the likelihood of drawdown at the neighboring monitoring wells. No drawdown was measured at any monitoring wells in the vicinity of Well 4. Time-drawdown and recovery data illustrate that the aquifer in the immediate area of Well 4 has a low transmissivity (T = 418.6 ft^2/d; 38.9 m^2/d) and low storativity (S = 2.267E-6). These aquifer

characteristics are consistent with a cone of depression that is narrow (does not propagate a great distance laterally) and deep (max drawdown = 246.3 ft) under a low discharge rate (210-240 gpm; 1,145 to 1,300 m^3/d) (Figure A-16). In agreement, an assessment of aquifer transmissivity using specific capacity data from well driller's reports (Figure A-13) suggests low transmissivity values throughout the southeast segment of the model domain. The borehole lithology of Well 4 shows alternating sandy gravels and clayey gravels in the screened interval of the well, with clay content increasing with depth. The low transmissivity is associated with the clay layers. Additionally, the East Fault is a low-permeability boundary that limits horizontal groundwater flow, as evidenced by results of the aquifer tests conducted in the East and Far East Blocks. The lack of a drawdown response at Well 1 (~2,235 ft to the north in the pumped aquifer) may corroborate that the East Fault extends to the north below the floodplain deposits (Figure A-10) and limits horizontal flow. Additionally, seven consecutive days of pumping at Well 4 did not induce a drawdown response at MW-6 (1,261 ft northwest in the unpumped aquifer). This may be explained by the barrier effect of East Fault and/or that there is limited hydraulic connection between the pumped confined aquifer and overlying unconfined aquifer near Well 4.

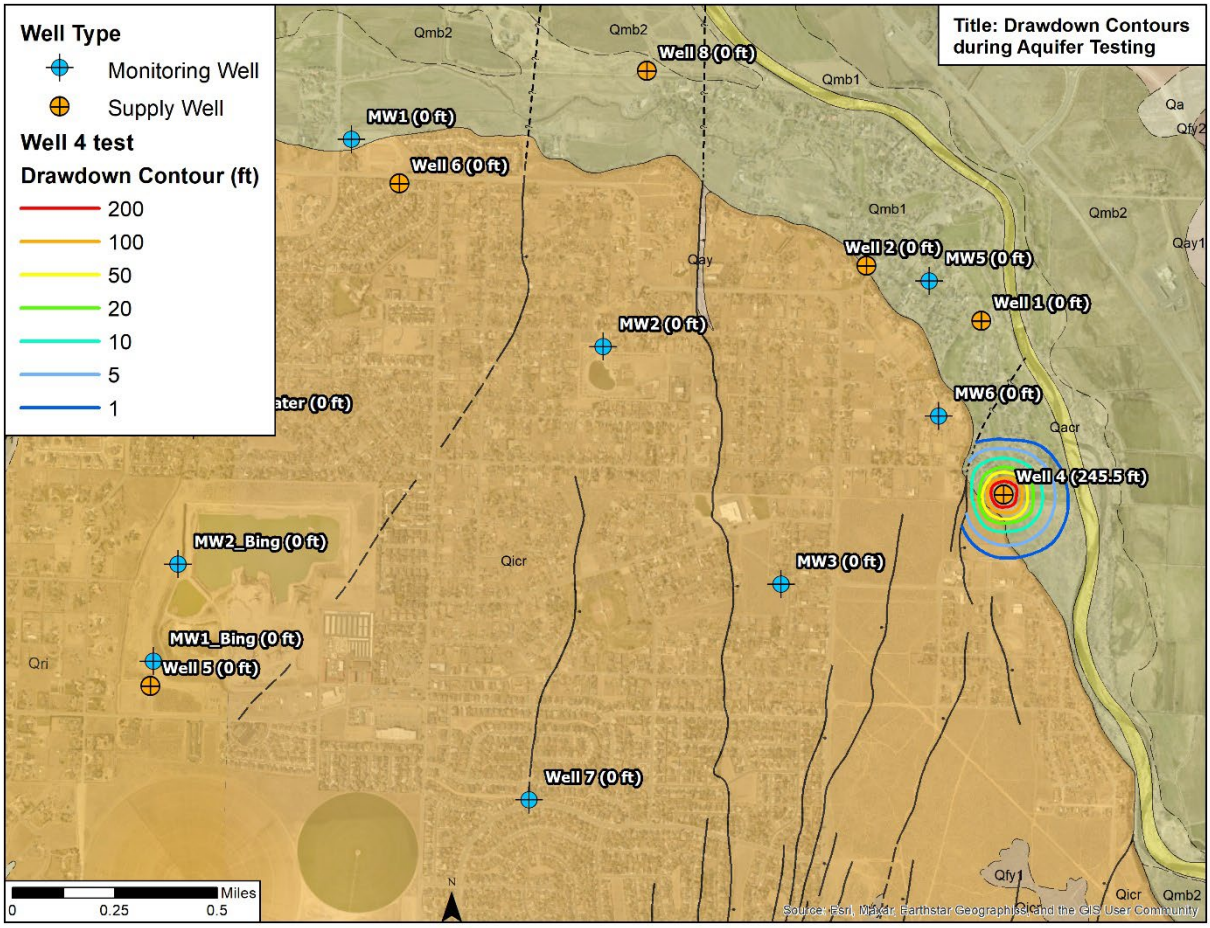

Figure A-16. Drawdown contours for the Well 4 test. Maximum drawdown measured in each well (including shallow and deep wells) is shown next to the well name.

Well 5 Test

The Well 5 test was conducted from 3/29/22 to 4/4/22. Well 5 is no longer in use for GRGID's water distribution system and as such, water produced during the test was discharged to the basin immediately adjacent to the well. The discharge water infiltrated to the aquifer and impacted water levels during the test. As a result, the data produced during the Well 5 test were used for qualitative analysis only and not to quantify aquifer properties or boundary conditions. Shallow monitoring wells MW1_Bing, MW2_Bing, and Sweetwater all displayed a clear drawdown response to pumping at Well 5 (Figure A-17), with a drawdown of >3.6 ft at 3,400 ft from the pumping well (Sweetwater). All three of these monitoring wells were impacted by the "slug" of infiltration water. The infiltration reached MW1_Bing on 3/31/22 (two days into the test) and resulted in a groundwater mound six feet higher than the pre-test static water level. As the groundwater mound spread laterally, drawdown rates were impacted at MW2_Bing and Sweetwater as indicated by the change in slope of the drawdown curves on 3/31/22. The drawdown curve eventually had an increasing slope for the last two days of the test at MW2_Bing, while the drawdown curve became flat at Sweetwater. A slope change was also observed in the drawdown curve in Well 5 on the second day of the test, indicating that the slug of water infiltrated as deep as 140 ft. This also suggests that there may not be a confining clay layer in the vicinity of Well 5. Drawdown was also measured in the pumped aquifer at Well 9, approximately 6,100 ft north of the test Well 5. Key takeaways from this test are that the West Block is characterized by high infiltration capacity and high transmissivity.

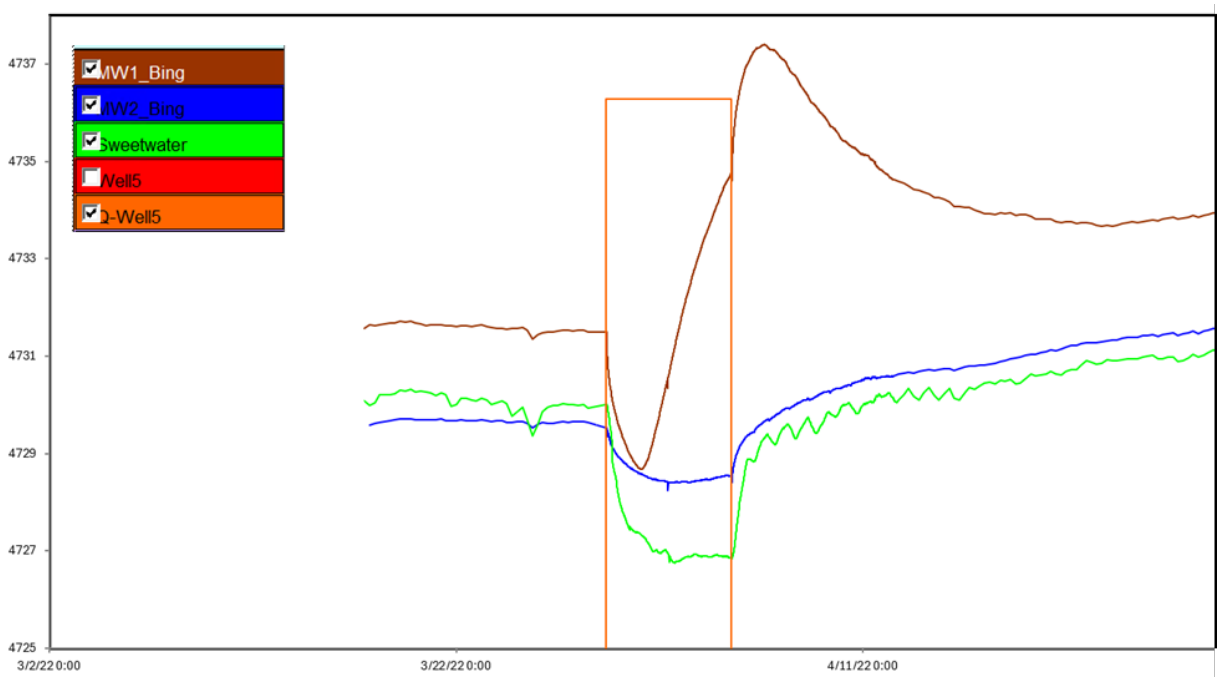

Figure A-17. Water levels in a) shallow monitoring wells impacted by the infiltration of discharge water during the Well 5 test.

Well 6 Test

The average constant rate at Well 6 was 695 gpm (3,788 m^3/d) from 1/23/23 through 1/30/23. A reverse water level fluctuation was observed in the pumping well when the pump was started and stopped in which the water level responses in the pumping well were opposite of that predicted (Wolff, 1970). This phenomenon may also be attributed to a column loading, compaction of aquifer material in response to vibration of the pumping engine, dilatancy (when fluid viscosity increases under pressure), the Noordbergum effect (pressure increases in an aquifer at the beginning of water pumping due to overburden load transfers), or the development of radial strains near a pumping well from compression near the well to tension farther away from the well (Wolff, 1970). Because this phenomenon may not be directly associated with aquifer conditions, data from the first five minutes of pumping and recovery were removed from the dataset prior to aquifer test analysis. During the long-term test, the booster pump was utilized on occasion to maintain water system pressure. The pressure change in the system translated to water level changes of up to three feet in the pumping well. Because these water level changes are not associated with changes in pumping rate, the difference between simulated and measured water levels is impacted in both the SeriesSEE and AQTESOLV models. However, on average, the curve matching approach to estimating hydraulic properties is still deemed to be representative of overall aquifer conditions.

During the constant-rate test, the maximum drawdown during testing in the pumping well was 94.5 ft. Water levels declined rapidly at the start of the test, followed a much gentler and linear decline for the remainder of the test, with a constant rate of head change of approximately 1 ft/day. This drawdown plateau might suggest the presence of a recharge boundary, which could either be high transmissivity aquifer materials and/or the presence of hydraulically connected surface water in streams and canals to the north of the pumping well. At the end of pumping, water levels recovered rapidly, recovering to 95% of pre-testing levels within 2.5 hours and 99% within 14.5 hours. Based on an analysis of recovery data, the estimated transmissivity in the immediate vicinity of Well 6 is 4,090 ft^2/d (380 m^2/d). A ratio of storativity during pumping (S) to storativity during recovery (S') of 10.09 is a strong indication of a recharge boundary.

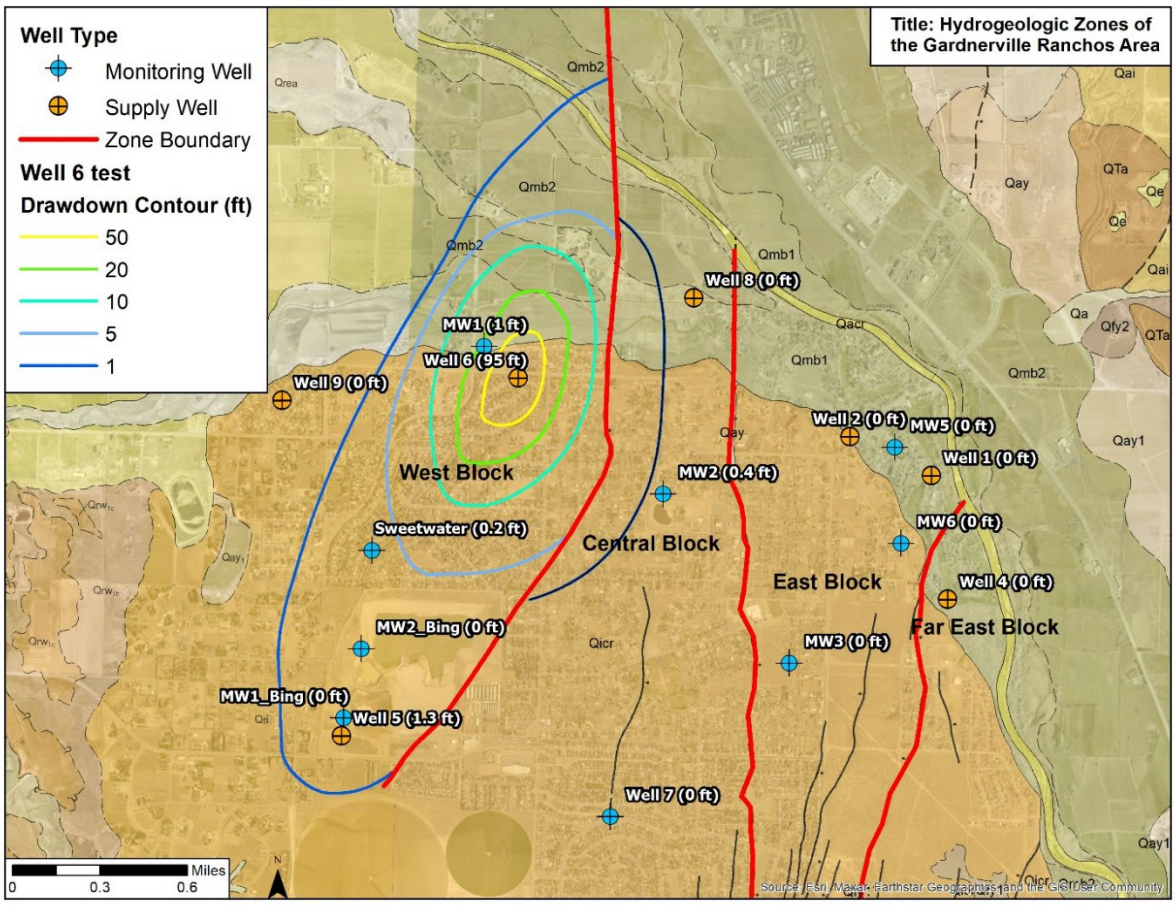

Figure A-18. Drawdown contours for the confined aquifer during the Well 6 test. Maximum drawdown measured in each well (including shallow and deep wells) is shown next to the well name.

A drawdown response up to 1.0 ft was measured at MW-1, which is approximately 870 ft to the northwest of Well 6. The low magnitude of drawdown at a low radial distance from the pumping well suggest the presence of a layered aquifer system in the West Block and that MW1 is completed in the shallow unconfined (unpumped) aquifer. The screened interval of Well 6 (210-430 ft bgs) is deeper than that of MW-1 (100-120). Time drawdown data for MW-1 closely matches the Neuman-Witherspoon solution for leaky confined aquifers, in agreement with a layered aquifer. Infiltration of local precipitation (rainfall and snowmelt) reached the local water table at MW1 during the Well 6 test, as evidenced by the increase in water levels from 1/26/23 to 1/28/23 at MW-1, and other monitoring wells outside the area of influence (i.e., MW3 and Well 7). The infiltration effect corroborates that MW-1 and several other shallow monitoring wells are completed in an unconfined aquifer segment. The borehole log for MW-1 indicates predominantly sandy gravels with lenses of clayey gravel, so it is possible that there is a clay zone limiting vertical flow between Well 6 and MW-1.

Potential drawdown was measured 4,000 ft to the southwest at Sweetwater (<0.1 ft) and 7,200 ft at Well 5 (<0.5 ft). To the west, there was no detected drawdown at Well 9 (4,290 ft). Consistent with other aquifer tests, the spatial extent of the cone of depression (Figure A-18) suggests horizontal anisotropy, with higher transmissivity in the north-south direction and lower transmissivity east-west. There are no mapped faults between Wells 6 and 9, so the anisotropy may be caused by layered sediments of varying hydraulic conductivities related to paleo-depositional environments. Potential drawdown (<0.4 ft) was measured at MW-2. The West Fault extends north-south between MW-2 and Well 6, so a delayed drawdown response at MW-2 would suggest that the West Fault restricts flow but is not a complete barrier.

Well 8 Test

An average discharge of 862 gpm (4,700 m^3/d) was achieved for the duration of the Well 8 test from 1/3/23 through 1/10/23. Groundwater levels measured during the test show a cone of depression that extends in the north-south direction and limited propagation in the east-west directions, suggesting a north-south orientation of high transmissivity (Figure A-19). The magnitude and timing of groundwater level response at MW-2 illustrate a direct hydraulic connection between the fluvial deposits at Well 8 and alluvial deposits at MW-2 (3,570 ft south). Water levels at MW-2 showed a delayed response to the pump starting (approximately 40 minutes) and stopping (approximately two hours) at Well 8 and a maximum drawdown of 4.2 ft was measured by the end of the test. Potential drawdown of up to 0.2 ft was measured at Well 7 (9,480 ft south of Well 8). A delayed response to pumping at MW-2 might be explained by differences in hydraulic conductivity between the pumped aquifer (fluvial) and monitored aquifer (alluvial) and/or a layered and leaky aquifer system, with MW-2 completed in the overlying unconfined aquifer and pumping from the deeper confined aquifer.

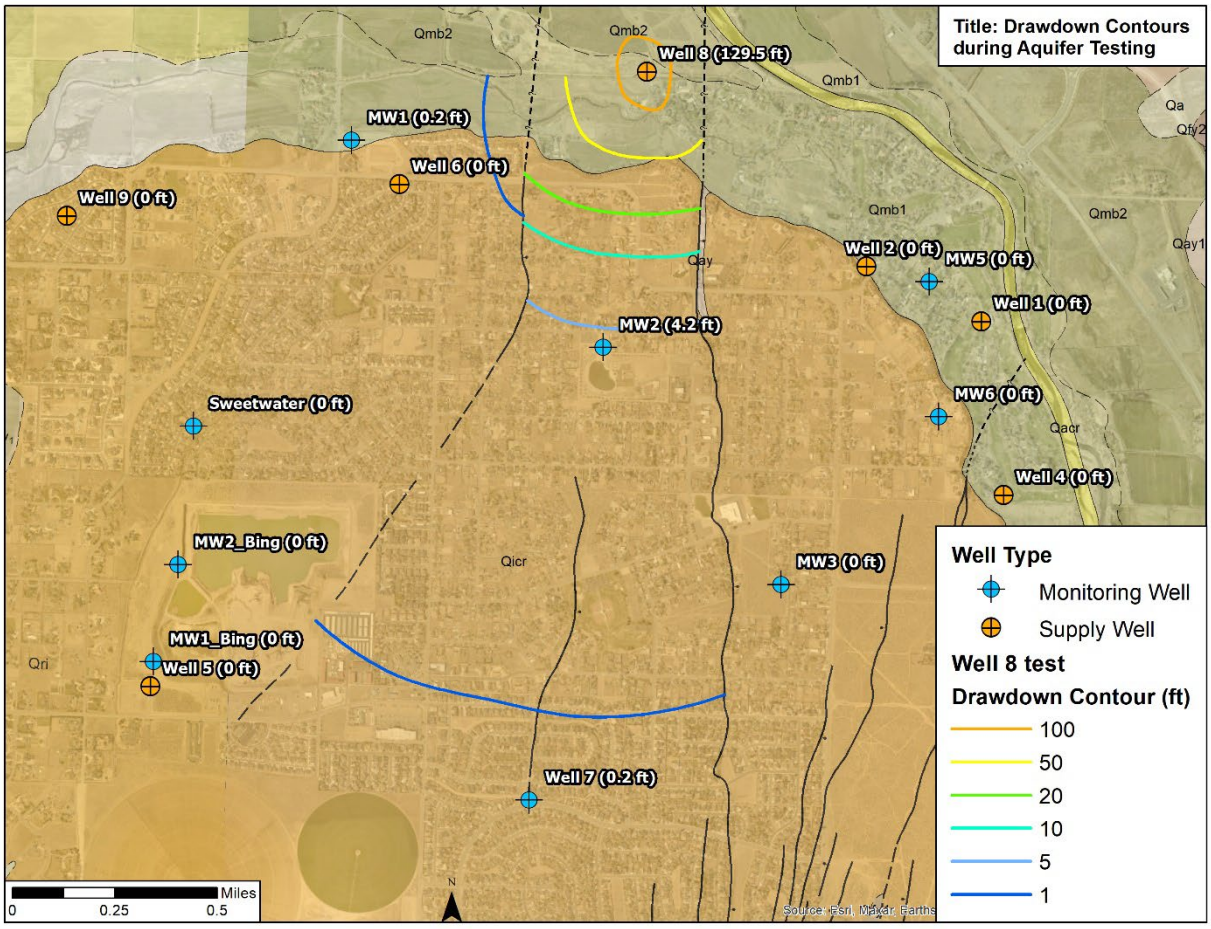

Figure A-19. Drawdown contours for the confined aquifer during the Well 8 test. Maximum drawdown measured in each well (including shallow and deep wells) is shown next to the well name.

The Neuman-Witherspoon solution for a leaky confined aquifer closely matches the observation data at MW-2. Estimates of hydraulic properties in the pumped aquifer based on time-drawdown data at MW-2 and include transmissivity of 5,320 ft^2/d (495 m^2/d) and storativity of 1.27E-05. The unpumped shallow aquifer has an estimated transmissivity of 2,020 ft^2/d (188 m^2/d) and storativity of 5.4E-04. The zone of high transmissivity extends in the north-south direction, parallel to the orientation of West and Central Faults that bound MW-2. Drawdown to the west of Well 8 was limited, with potential drawdown magnitudes of <0.1 ft in both Well 6 (3,480 ft) and MW1 (3,890 ft). The low transmissivity to the east-west of Well 8 is likely associated with low permeability of the West and Central Faults, which limit flow in the east-west direction and bound the central aquifer zone that includes Well 8, MW-2, and Well 7.

Well 9 Test

The Well 9 test was conducted from 11/9/22 to 11/16/22 and the average constant rate achieved was 775 gpm (4,224 m^3/d). Overall, the Well 9 test corroborates the results of the Well 6 test. Both Well 9 and Well 6 are in the western segment of Gardnerville Ranchos and drawdown was detected in the same monitoring wells during both tests. The cone of depression produced during the Well 9 test is elongated in north-south direction (Figure A-20). The maximum drawdown at Well 5 (6,129 ft) was approximately 0.53 ft, exceeding the maximum drawdown of shallow monitoring wells closer to the pumping well (i.e., Sweetwater, MW2_Bing, MW1_Bing). Well 5 and Well 9 are both deep supply wells that are screened in the deeper aquifer and the timing and magnitude of drawdown at Well 5 indicates a direct hydraulic connection. The lower magnitude of drawdown in the shallow monitoring wells support the conceptual model that these wells are in the shallow unconfined aquifer. The lithology logs for Wells 9 and 5 indicates predominantly gravelly sands with interfingering clay layers, with two distinct clay zones (116-119 and 287-299 ft bgs). Although the lateral extent of these clay zones is unknown, low conductivity clay layers appear to separate the confined aquifer from the shallow unconfined aquifer. Drawdown in the unconfined aquifer indicates a hydraulic connection between the deep and shallow aquifers.

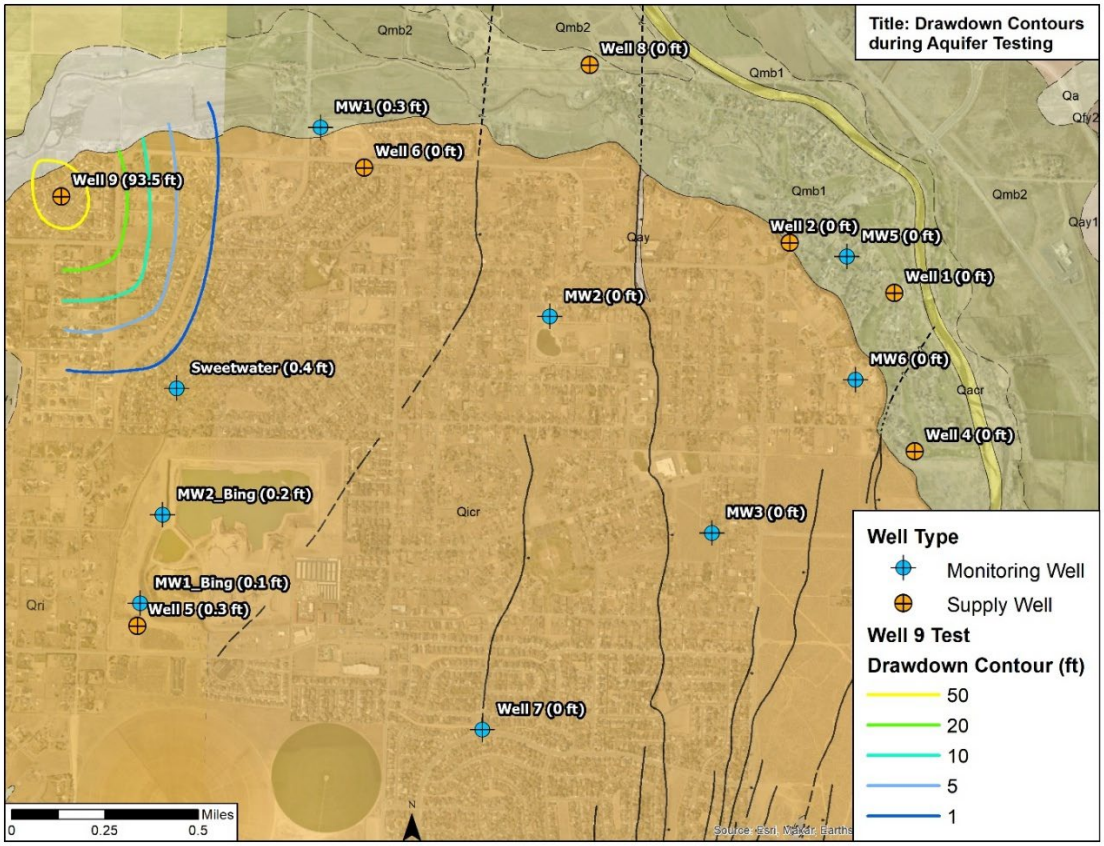

Figure A-20. Drawdown contours for the confined aquifer during the Well 9 test. Maximum drawdown measured in each well (including shallow and deep wells) is shown next to the well name.

For the pumped aquifer, estimated transmissivity (4.91E+04 ft^2/d; 4,560 m^2/d) and storativity (0.0029) for the deeper confined aquifer were estimated using drawdown data at Well 5. No drawdown was detected in Well 6, which corroborates results of the Well 9 test that suggested low transmissivity in the east-west direction in the West Block. This anisotropy may be attributed to layered sediments of varying hydraulic conductivity. Time-drawdown data in the shallow monitoring wells closely match the Neuman-Witherspoon (1969) solution for a confined two-aquifer system with leakage. Estimated aquifer transmissivity values for the unpumped aquifer (shallow unconfined) is 9.97E+04 based on the drawdown data at Sweetwater.

STABLE ISOTOPE ASSESSMENT

Water molecules contain varying concentrations of stable hydrogen (^2H) and oxygen (^{18}O) isotopes. Deuterium concentration is expressed relative to hydrogen-1 ($^2H/^1H$) and is reported as delta deuterium (δD) and oxygen-18 concentration is expressed relative to oxygen-16 ($^{18}O/^{16}O$) and reported as delta oxygen-18 ($\delta^{18}O$). Both isotopes are reported relative to Vienna Standard Mean Ocean Water (VSMOW) in parts per thousand (permil). The δD and $\delta^{18}O$ concentrations can be used to help determine sources of groundwater. Samples for stable isotopes were collected from surface water, groundwater, and precipitation in the study area to identify sources of water to the study area, estimate the amount of mixing of water sources in the unconfined and confined aquifers, and to determine whether surface waters from rivers, creeks, and canals leak into the aquifers.

Sampling Design

To assess spatial variability of mixing, surface water samples were collected from five locations and groundwater samples were collected from eleven wells (four monitoring wells and seven supply wells), and a bulk precipitation sample was collected at Well 5. All supply wells were sampled from in-line sampling ports. Monitoring wells MW-1, MW-2, MW-3, and Sweetwater were sampled using a submersible pump. All wells were purged of stagnant water in the well casing prior to sample collection. A glass funnel was used to route rainwater into a plastic pipe near Well 5. To prevent sample evaporation, mineral oil was added to the plastic pipe during installation. The bulk precipitation sample included rainwater that accumulated throughout August and September 2022. All samples were collected in September and October 2022 in 20 mL glass vials with a Polyseal cap to prevent sample evaporation. Stable isotopes analysis was performed at the UNR Stable Isotope Laboratory using a Picarro L2130-i spectroscopic water isotope analyzer.

Stable Isotope Data Analysis

To aid with identification of water sources and seasonal atmospheric processes, stable isotope compositions were plotted against the global meteoric water line (Craig, 1961) and a regional meteoric water line for Nevada (Lyles et al., 2019). To quantify the degree of mixing of surface water and groundwater at each sampled well, a linear mixing equation is applied to estimate the proportion of groundwater:

$$F_{GW} = \frac{\delta_{sample} - \delta_{SW}}{\delta_{GW} - \delta_{SW}} \quad \text{(A-2)}$$

where F_{GW} is the fraction (as a percentage) of water sourced from groundwater for a given groundwater sample, δ_{sample} is the measured isotopic ratio of the water sample, δ_{SW} is the measured isotopic ratio in the surface water end member, and δ_{GW} is the measured isotopic ratio in the groundwater end member.

This two-endmember model assumes that sources are known, their isotopic compositions are known, and their isotopic signatures do not overlap. The surface water and groundwater samples assigned as endmembers were selected based on their isotopic composition relative to other samples and based on an understanding of the local and regional hydrology. The end-members used here are understood to be mixtures of surface water and groundwater but are the most representative endmember samples available. As such, the mixing percentages calculated here are estimates used to provide a general sense of relative surface water-groundwater contributions and are not considered exact. The surface water and groundwater end members are described in more detail later in the report.

Precipitation water is indirectly accounted for in these calculations because streamflow is sourced primarily from winter precipitation. The relative proportion of surface water (F_{SW}) is equal $1 - F_{GW}$. The proportion of groundwater and surface water is estimated for each sample by calculating the F_{GW} and F_{SW} for both oxygen-18 and deuterium concentrations and taking the average. The mixing percentages for each sample are provided in Table A-9. The estimated F_{GW} can be negative if δ_{SW} is greater than δ_{GW} or δ_{sample}. This would result in an estimated F_{SW} that exceeds 100%. As stated in the previous paragraph, percentages are not considered to be exact but are used as qualitative measures of mixing.

Stable isotope data collected in this study were evaluated to assess sources of water to shallow and deep aquifers. Isotope data were compared to previous data from Lyles et al. (2019) and plotted with the global meteoric water line (Craig 1961) and a regional meteoric water line (RMWL) for Nevada (Lyles et al., 2019) to assess seasonal and elevation effects on isotopic composition (Figure A-21).

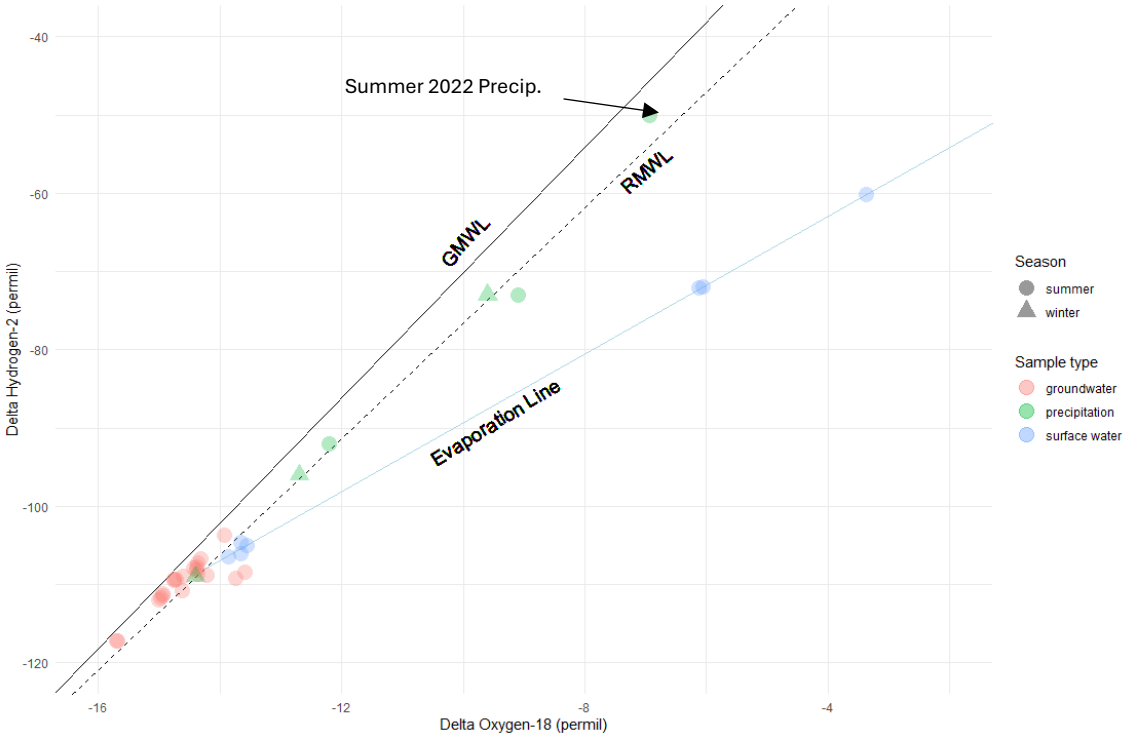

Figure A-21. Plot of delta Hydrogen-2 versus delta oxygen-18 for surface water, groundwater, and precipitation in the study area. Data are compared to the global meteoric water line (GMWL) and regional meteoric water line (RMWL).

Table A-9. Surface water-groundwater mixing percentages.

Sample	F_{GW} δ18O (%)	F_{sw} δ18O (%)	F_{GW} δD (%)	F_{sw} δD (%)	F_{GW} mean (%)	F_{sw} mean (%)
MW1_isot_28Sept_1126	12	88	-15	115	-2	102
MW2_isot_27Sept_1345	-5	105	25	75	10	90
MW3_isot_28Sept_1415	3	97	32	68	17	83
Well1_isot_28Sept_0942	62	38	49	51	56	44
Well2_isot_27Sept_1507	46	54	29	71	37	63
Well2_isot_28Sept_1003	62	38	50	50	56	44
Well2_isot_28Sept_1655	64	36	53	47	59	41
Well2_isot_29Sept_1641	66	34	55	45	60	40
Well4_isot_27Sept_0937	32	68	10	90	21	79
Well4_isot_28Sept_0927	54	46	32	68	43	57
Well4_isot_28Sept_1645	54	46	33	67	43	57
Well4_isot_29Sept_1112	52	48	32	68	42	58
Well5_isot_07Oct_1200	26	74	28	72	27	73
Well6_isot_27Sept_0850	34	66	15	85	24	76
Well6_isot_28Sept_0905	35	65	20	80	27	73
Well6_isot_28Sept_1625	37	63	21	79	29	71
Well6_isot_29Sept_1540	35	65	23	77	29	71
Well8_isot_29Sept_1211	47	53	44	56	46	54
Well9_isot_28Sept_1555	34	66	27	73	31	69

The global and regional meteoric water lines provide an important key to the interpretation of the oxygen-18 and deuterium data. Water with an isotopic composition plotting on or along RMWL are assumed to have originated from the atmosphere and to be unaffected by other isotopic processes (Domenico and Schwartz, 1990). The primary process that causes isotopic compositions to plot away from the meteoric water line is evaporation. As shown in Figures A-21 and A-22, waters collected during this study generally plot along the RMWL, with the exception of water from the Bing Pit lake, Mitch Pond, MW2, and MW3. Groundwater from several wells (i.e., Sweetwater, Well 1, Well 2, Well 4, Well 6, MW1) plot above the RMWL by about -0.1 to -0.2 permil for oxygen-18 or about +1 to +2 permil for deuterium. This uniform shift is likely explained by the fact that the RMWL was developed using isotope data collected throughout Nevada, including regions with isotopic compositions that are different from the study area.

During evaporation, lighter isotopes tend to evaporate more readily than heavier isotopes, leading to an enrichment of oxygen-18 and deuterium. Samples that plot below the RMWL, including all surface water samples collected in this study (i.e., rivers, diversions, ponds/lakes) are impacted by evaporation to varying degrees. A local evaporation line is plotted as a linear line through all the surface water samples (Figure A-21). Waters in Bing Pit and Mitch Pond are the most enriched in oxygen-18 because of heightened evaporation in stagnant surface waters. River and canal water samples are also impacted by evaporation, but

to a lesser degree than the ponds due to higher flows and being sourced primarily from recent snowmelt. Shallow observation wells MW2 and MW3 plot near river and diversion samples but are relatively depleted of deuterium, suggesting the groundwater in northeast Gardnerville Ranchos is likely sourced by the infiltration of evaporated surface waters. Shallow well MW1 is likely sourced by the infiltration of surface water from the Rocky Slough diversion. Deep supply Wells 5 and 9 may receive some inflow of evaporated waters as indicated by their compositions plotting near the evaporation line. This might be explained by the location of these wells relative to the Bing Pit. The Bing Pit lake is in hydraulic connection with the surrounding aquifer and therefore, the evaporated water that flows through and out of the pit area eventually returns to the aquifer and may impact isotopic composition of down gradient and cross-gradient wells.

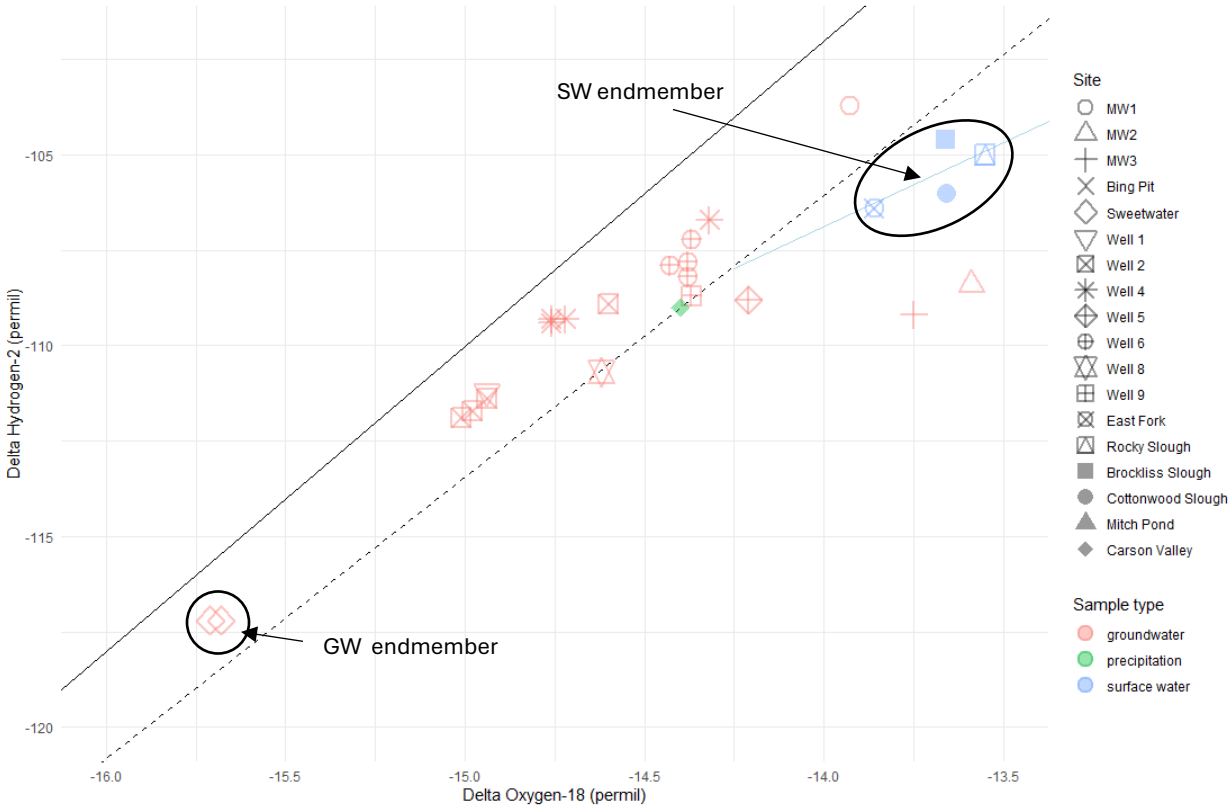

Figure A-22. Plot of delta Hydrogen-2 versus delta oxygen-18 zoomed in to surface water and groundwater endmembers. Data are compared to the global meteoric water line (GMWL) and regional meteoric water line (RMWL).

The point of intersection of the evaporation line with the meteoric water line generally represents the isotopic composition of unaltered precipitation (Domenico and Schwartz, 1990). Any deviations from this intersection point that fall along the RMWL is likely explained by temperature-dependent isotopic fractionation. The season during which precipitation occurs strongly influences air temperatures, which in turn, impacts isotopic

composition of precipitation (Smith et al., 2002). When precipitation falls as rain during the summer, evaporation and fractionation occur as the rain falls to the ground and while it remains on the ground surface. Essentially no isotopic fractionation occurs when precipitation falls as snow and before percolating below land surface toward the water table (Smith et al., 2002). As a result, summer precipitation is isotopically heavier than winter precipitation. which is shown to be the case throughout Nevada (Lyles et al., 2019). Consistent with this, a bulk summer precipitation sample (accumulated rainwater from August and September 2022) collected during this study plots just above the RMWL and is enriched in oxygen-18 and deuterium compared to river water, canal water, groundwater, and previous winter and summer Carson Valley precipitation samples (Lyles et al., 2019). The summer precipitation samples collected by Lyles et al (2019) may be relatively depleted because the bulk precipitation accumulated over a six-month period with greater variability than the two-month bulk precipitation collected in this study.

The river water and groundwater samples collected in this study are depleted of oxygen-18 and deuterium compared to the summer 2022 precipitation sample. These samples have isotopic compositions that are similar to the 2017 winter precipitation sample from Carson Valley and other winter waters throughout Nevada (Lyles et al., 2019). This suggests that winter precipitation and snowmelt-dominated streamflow is an important source of recharge to the study area. The deuterium values of river and groundwater samples are all greater than -130 permil, suggesting present-day recharge (Smith et al., 2002). Consistent with this observation, surface water and groundwater isotopic compositions are in the range of compositions of upland surface waters in the Carson Range measured by Welch et al. (1994). This is also consistent with the consensus that recharge in arid areas of the western U.S. occurs mostly or completely in winter and that summer precipitation evaporates before reaching the water table (Simpson et al., 1970; Winograd and Friedman, 1972, Smith et al., 1992).

The isotopic composition of shallow groundwater near the East Fork Carson River at MW1-MW3 is similar to the composition of surface waters collected in this study. The average of the four river and canal samples is used to define the “surface water” isotopic endmember used to calculate mixing ratios (Table A-9). Surface water proportions of the shallow groundwater samples at MW1-MW3 range from 83-100%, indicating that the shallow aquifer receives recharge via leakage from surface water (Welch et al., 1994).

Sweetwater is another shallow aquifer observation well but has the lightest isotopic composition of all samples collected in this study. Sweetwater is situated approximately at the mid-way point between the East and West Forks and is less likely to receive recharge from surface water leakage compared to MW1-3 which are closer to the East Fork and active canals. Because of its depleted isotopic composition and location relative to potential recharge sources (i.e., surface water), data from Sweetwater is the “groundwater” isotopic endmember for the mixing calculations. The deuterium value at Sweetwater (-117.20 permil) is lighter than present-day winter precipitation in the Carson Pass (-110 permil). Typically, precipitation at higher elevations (i.e., Sierra Nevada) has lighter isotopic compositions than lower elevations (i.e., Carson Valley), with a vertical change of -5 to -10 permil/km in the region. The light isotopic composition of Sweetwater may suggest that the groundwater in this area was recharged during a period of greater precipitation and/or cooler air temperature.

Based on the location of Sweetwater (and all of Gardnerville Ranchos) near mountainous recharge areas, it is likely that the light isotopic composition at Sweetwater is from a period of cooler precipitation during recent times (Holocene rather than Pleistocene).

Deep supply well samples from the confined aquifer are isotopically lighter than surface water and shallow well samples and heavier than the groundwater endmember. This suggests that the supply wells are sourced from a mixture of groundwater and surface water. This illustrates that isotopic composition in the Gardnerville Ranchos area is a function of both depth and position relative to surface water. Supply wells are relatively deep and therefore tap groundwater; however all supply wells (except Well 5) are completed in fluvial deposits that receive recharge from stream leakage. Time series data collected at Wells 2 and 4 (Figure A-23) suggest that, when pumping commences, and groundwater levels are static, infiltrated surface water is the primary source of water to these wells which are next to the East Fork Carson River (63% for Well 2 and 79% for Well 4). An analysis of hydrogen-isotope data by Welch et al. (1994) found that at least some of the recharge to the deeper aquifer in the Minden-Gardnerville area is from the Carson River and tritium data shows that recharge has occurred since about 1952. Recharge of the deeper aquifer through shallow basin-fill sediment is likely enhanced by hydraulic gradients created by pumping (Welch et al., 1994). The downward movement of groundwater may occur through buried channel deposits (Welch et al., 1994). Time series data from supply Wells 2 and 4 show that, as pumping continues, isotopic compositions trend towards the groundwater endmember (Figure A-23) and the proportion of surface water decreases to 40% and 58% for Wells 2 and 4, respectively. At the start of pumping, these wells may extract water from both the shallow unconfined aquifer (enriched isotopic composition) and deeper confined aquifer (depleted isotopic composition), and as the water table lowers, there is increased input from the depleted groundwater endmember. The temporal trend towards depleted groundwater is consistent with the conceptual model that the deeper confined aquifer is not hydraulically connected to surface water and that pumping from wells near the East Fork Carson River does not induce recharge from the river.

Wells 5, 6, 8, and 9 are also supply wells sourced from the deeper confined aquifer. The percentage of surface water in these wells range from 54 to 76%. A winter precipitation sample from Lyles et al. (2019) plots withing the range of data for these wells, suggesting that winter precipitation and streamflow are likely recharge sources. Similar isotopic compositions for Wells 6 and 9 suggest a common groundwater source under the northwestern section of Gardnerville Ranchos. Time series data show minimal variability during pumping at Well 6, suggesting the relative contributions of source waters remain constant over time.

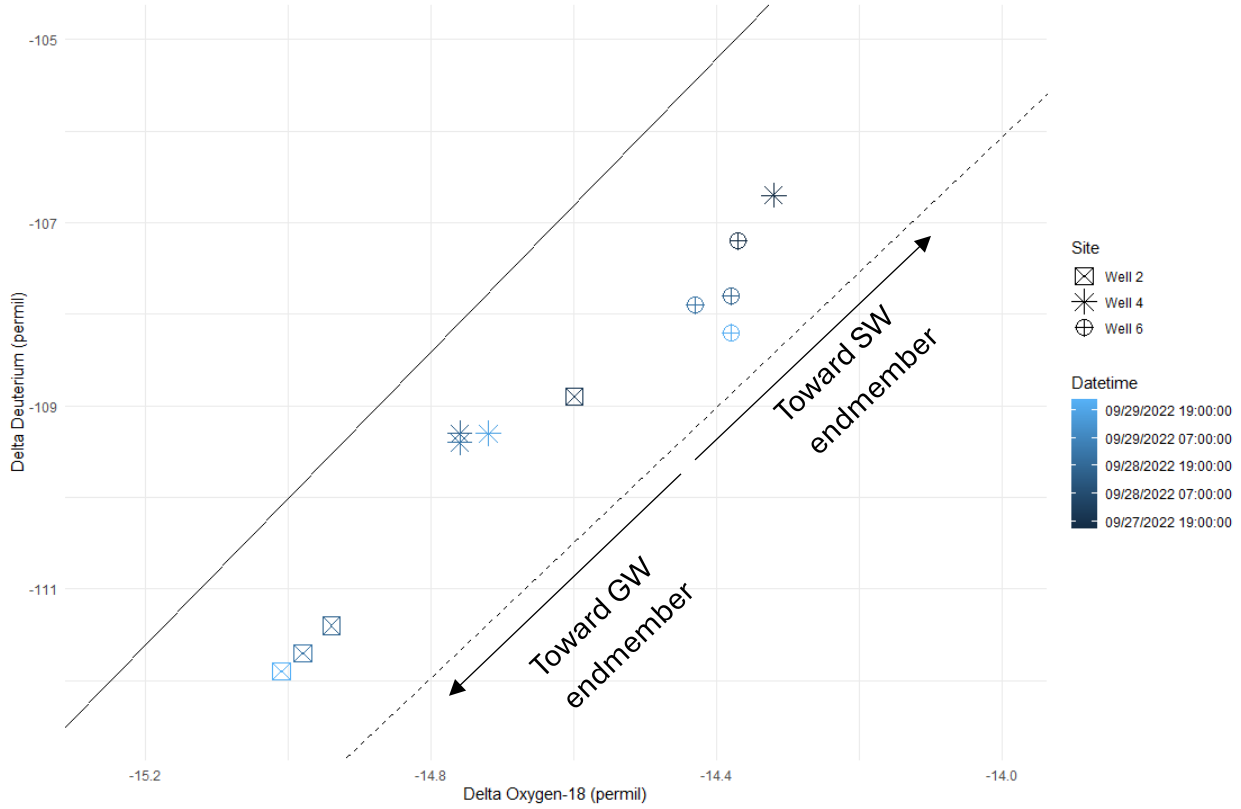

Figure A-23. Plot of delta Hydrogen-2 versus delta oxygen-18 showing time series data during active pumping of supply wells.

ATTACHMENTS. **(1) LITHOLOGY LOGS, (2) SERIESSEE OUTPUT PLOTS, AND (3) AQTESOLV AQUIFER PROPERTIES GRAPHS**

THIS PAGE LEFT INTENTIONALLY BLANK

MW1_Bing

Attachment 1: Lithology Logs

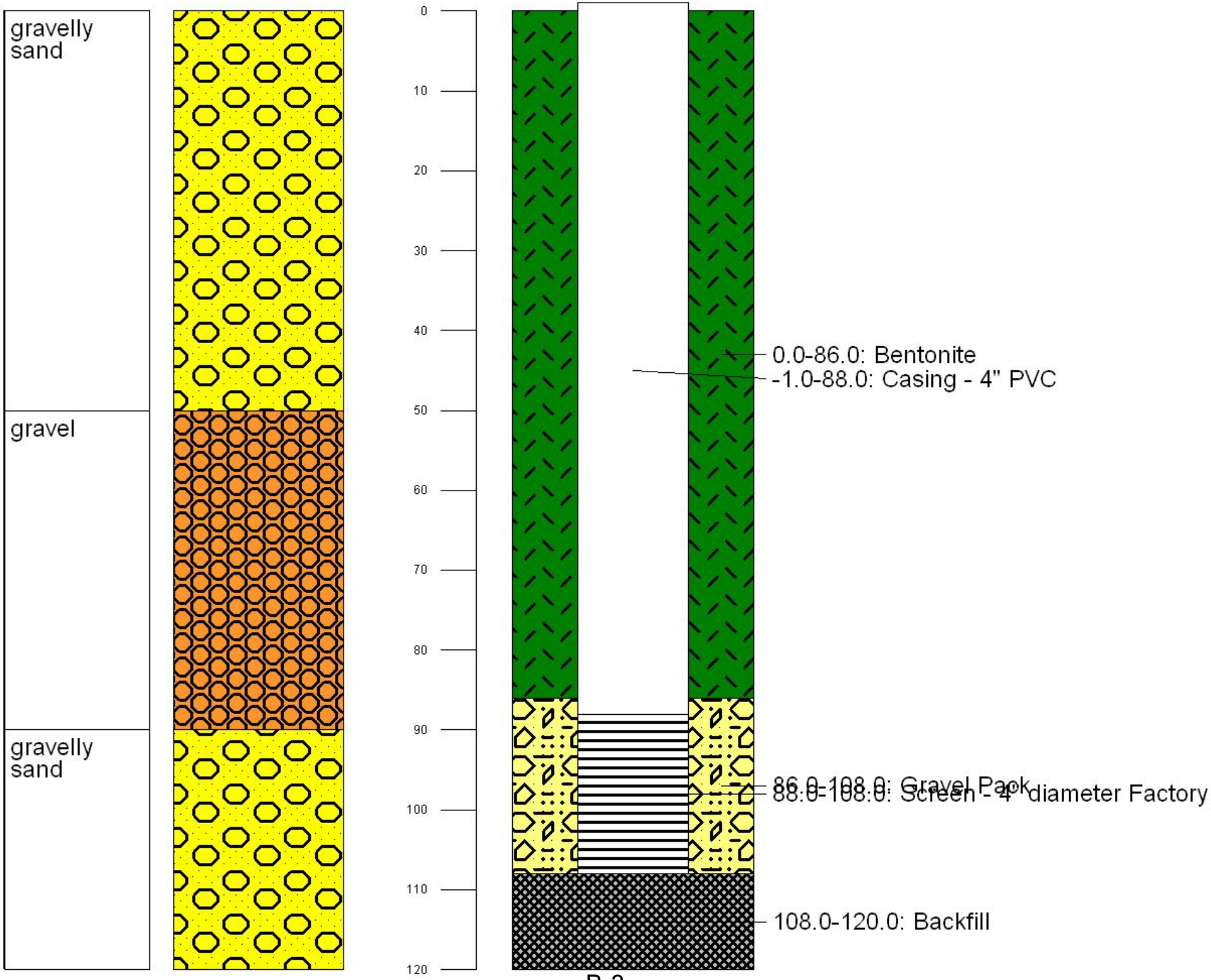

MW1

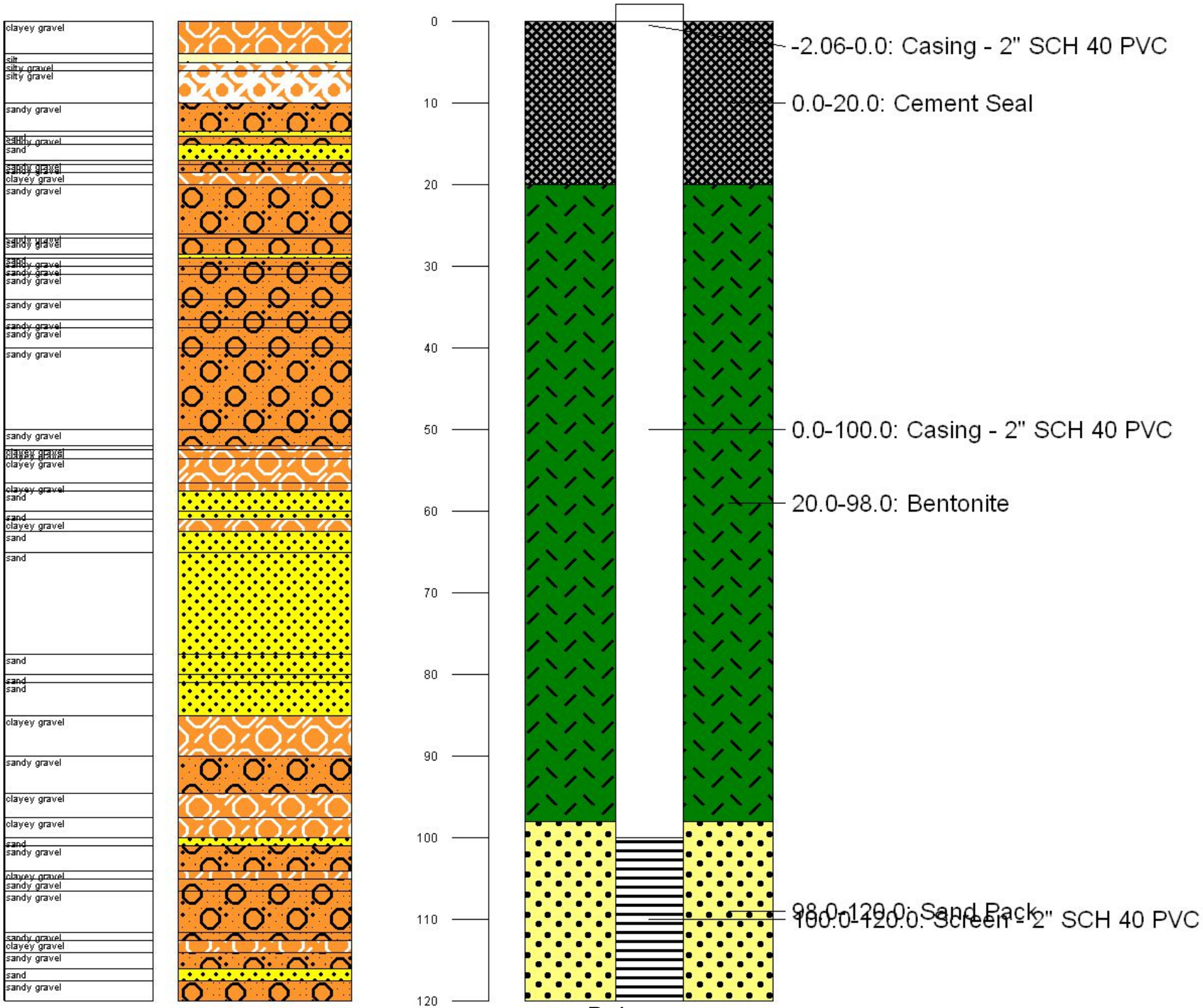
clayey gravel
silt
silty gravel
silty gravel
sandy gravel
sand
sandy gravel
sand
clayey gravel
sandy gravel
sandy gravel
sandy gravel
sand
sandy gravel
sandy gravel
sandy gravel
sandy gravel
sandy gravel
sandy gravel
clayey gravel
clayey gravel
clayey gravel
sand
sand
clayey gravel
sand
sand
sand
sand
clayey gravel
sandy gravel
clayey gravel
clayey gravel
sand
sandy gravel
clayey gravel
sandy gravel
sandy gravel
sandy gravel
clayey gravel
sandy gravel
sand
sandy gravel
0
10
20
30
40
50
60
70
80
90
100
110
120
-2.06-0.0: Casing - 2" SCH 40 PVC
0.0-20.0: Cement Seal
0.0-100.0: Casing - 2" SCH 40 PVC
20.0-98.0: Bentonite
98.0-120.0: Sand Pack
100.0-120.0: Screen - 2" SCH 40 PVC

MW2_Bing

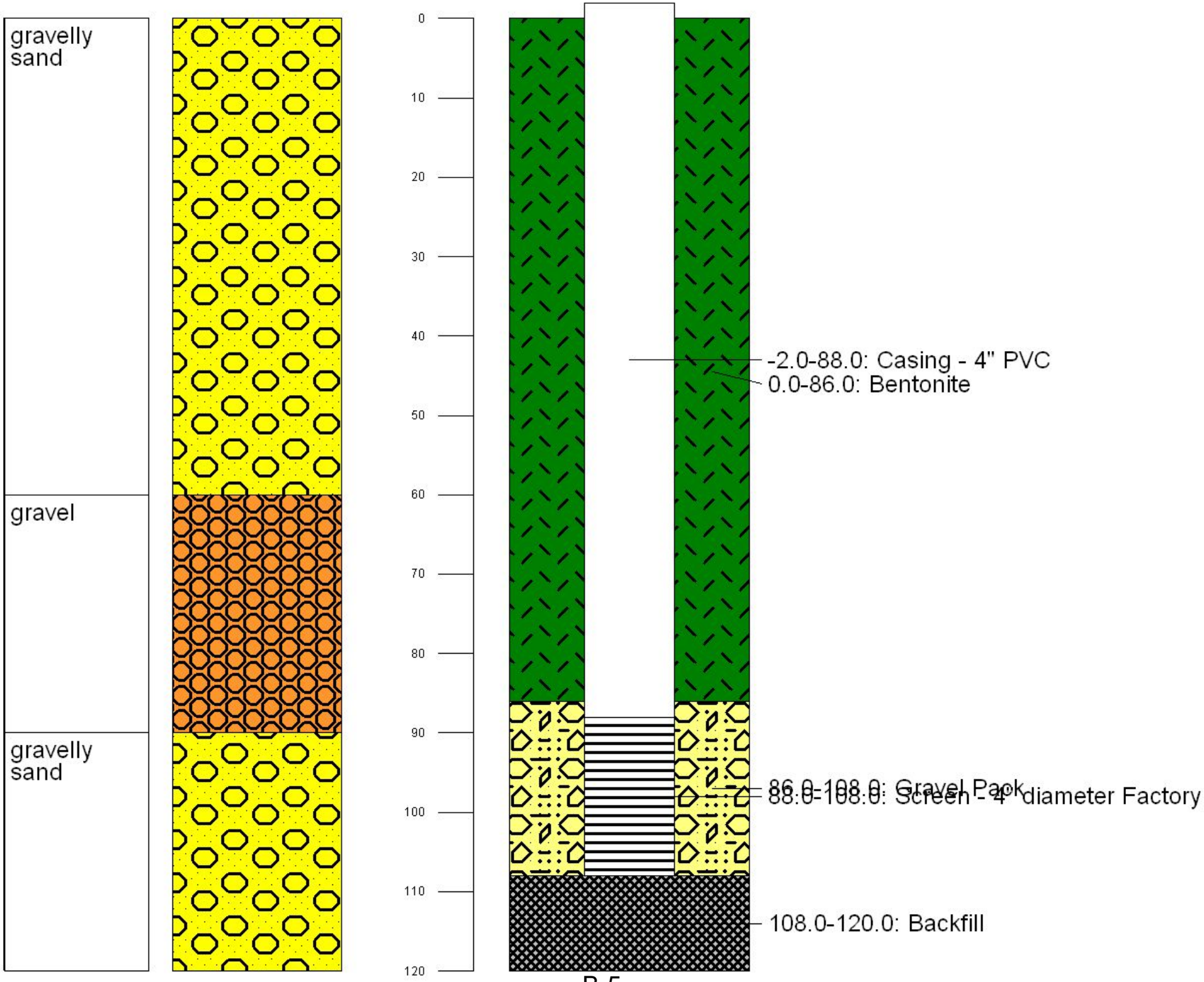
gravelly sand
gravel
gravelly sand
0
10
20
30
40
50
60
70
80
90
100
110
120
-2.0-88.0: Casing - 4" PVC
0.0-86.0: Bentonite
86.0-108.0: Gravel Pack
88.0-108.0: Screen - 4" diameter Factory
108.0-120.0: Backfill

MW2

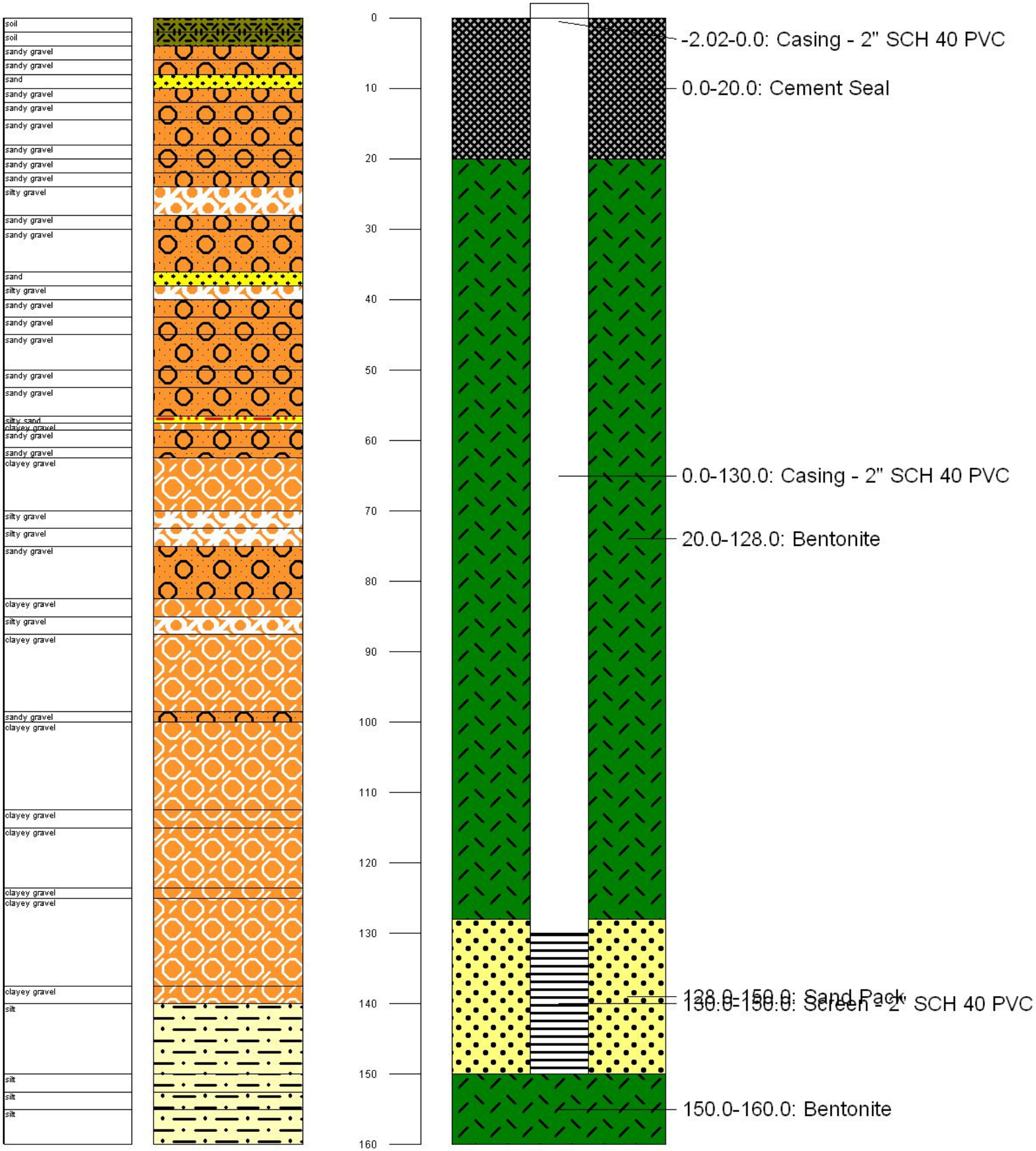
soil
soil
sandy gravel
sandy gravel
sand
sandy gravel
sandy gravel
sandy gravel
sandy gravel
sandy gravel
sandy gravel
silty gravel
sandy gravel
sandy gravel
sand
silty gravel
sandy gravel
sandy gravel
sandy gravel
sandy gravel
sandy gravel
silty sand
clayey gravel
sandy gravel
sandy gravel
clayey gravel
silty gravel
silty gravel
sandy gravel
clayey gravel
silty gravel
clayey gravel
sandy gravel
clayey gravel
clayey gravel
clayey gravel
clayey gravel
clayey gravel
clayey gravel
silt
silt
silt
silt
0
10
20
30
40
50
60
70
80
90
100
110
120
130
140
150
160
-2.02-0.0: Casing - 2" SCH 40 PVC
0.0-20.0: Cement Seal
0.0-130.0: Casing - 2" SCH 40 PVC
20.0-128.0: Bentonite
128.0-150.0: Sand Pack
130.0-150.0: Screen - 2" SCH 40 PVC
150.0-160.0: Bentonite

MW3

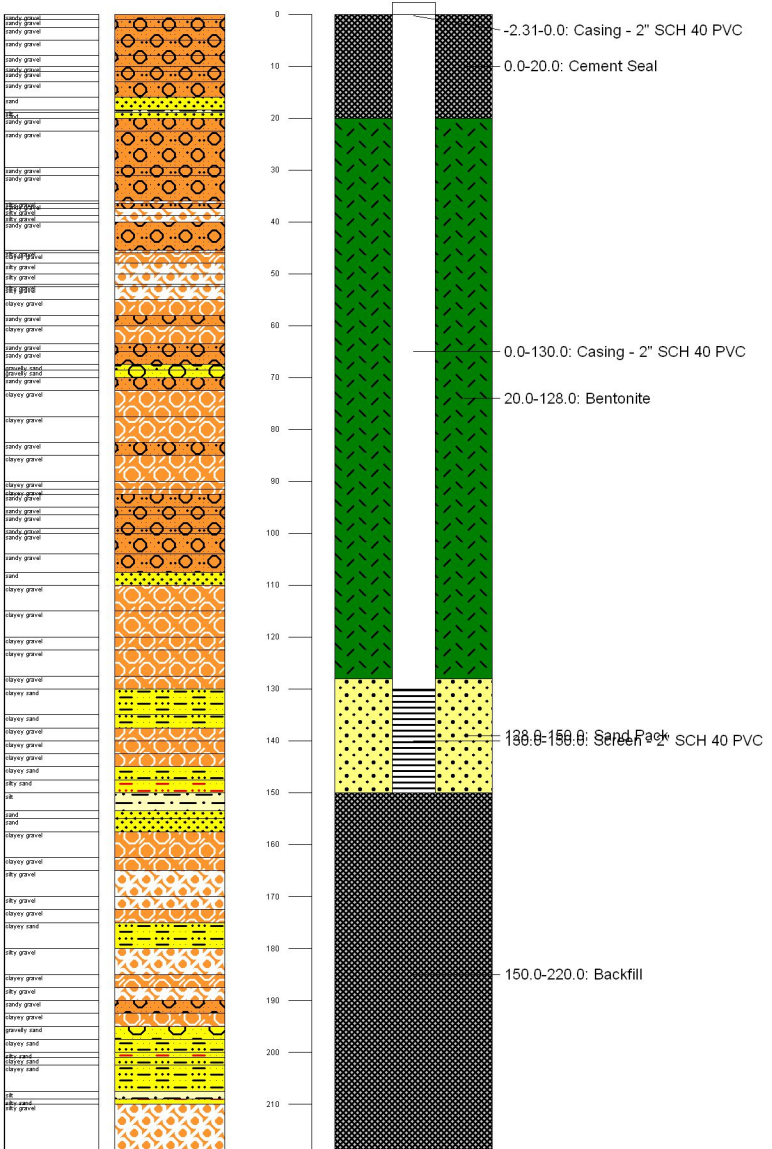
-2.31-0.0: Casing - 2" SCH 40 PVC
0.0-20.0: Cement Seal
0.0-130.0: Casing - 2" SCH 40 PVC
20.0-128.0: Bentonite
128.0-150.0: Sand Pack
130.0-150.0: Screen - 2" SCH 40 PVC
150.0-220.0: Backfill
0
10
20
30
40
50
60
70
80
90
100
110
120
130
140
150
160
170
180
190
200
210
220

Well 1

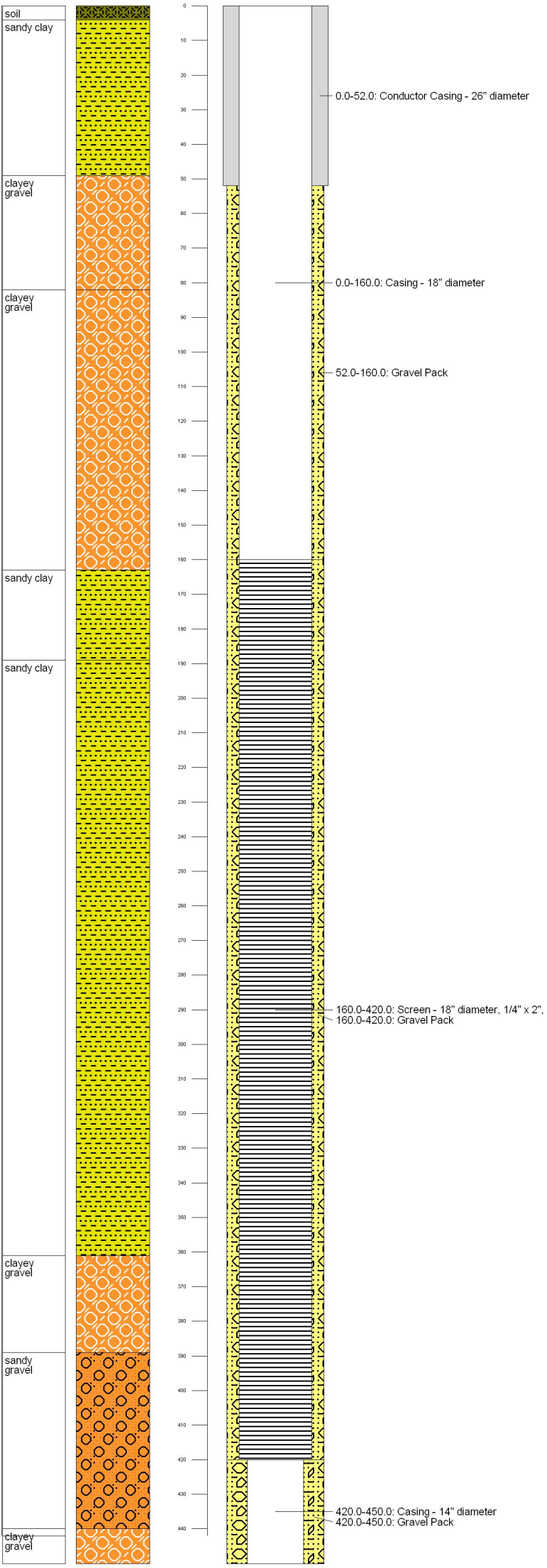
soil
sandy clay
clayey gravel
clayey gravel
sandy clay
sandy clay
clayey gravel
sandy gravel
clayey gravel
0
10
20
30
40
50
60
70
80
90
100
110
120
130
140
150
160
170
180
190
200
210
220
230
240
250
260
270
280
290
300
310
320
330
340
350
360
370
380
390
400
410
420
430
440
0.0-52.0: Conductor Casing - 26" diameter
0.0-160.0: Casing - 18" diameter
52.0-160.0: Gravel Pack
160.0-420.0: Screen - 18" diameter, 1/4" x 2",
160.0-420.0: Gravel Pack
420.0-450.0: Casing - 14" diameter
420.0-450.0: Gravel Pack

Well 2

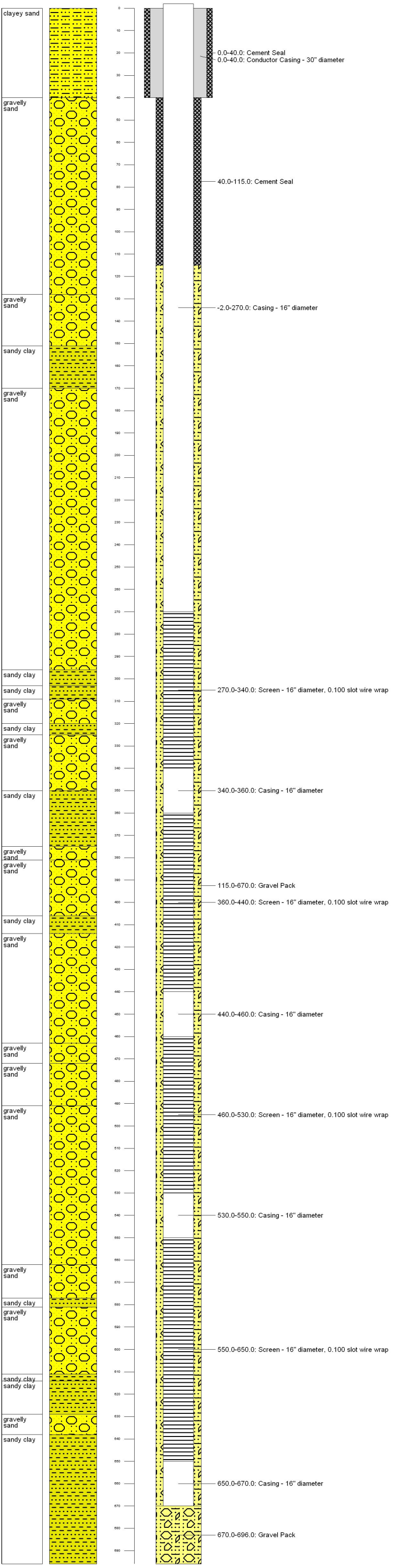
clayey sand
gravelly sand
gravelly sand
sandy clay
gravelly sand
sandy clay
sandy clay
gravelly sand
sandy clay
gravelly sand
sandy clay
gravelly sand
gravelly sand
gravelly sand
gravelly sand
sandy clay
gravelly sand
sandy clay
sandy clay
gravelly sand
sandy clay
0.0-40.0: Cement Seal
0.0-40.0: Conductor Casing - 30" diameter
40.0-115.0: Cement Seal
-2.0-270.0: Casing - 16" diameter
270.0-340.0: Screen - 16" diameter, 0.100 slot wire wrap
340.0-360.0: Casing - 16" diameter
115.0-670.0: Gravel Pack
360.0-440.0: Screen - 16" diameter, 0.100 slot wire wrap
440.0-460.0: Casing - 16" diameter
460.0-530.0: Screen - 16" diameter, 0.100 slot wire wrap
530.0-550.0: Casing - 16" diameter
550.0-650.0: Screen - 16" diameter, 0.100 slot wire wrap
650.0-670.0: Casing - 16" diameter
670.0-696.0: Gravel Pack

Well 4

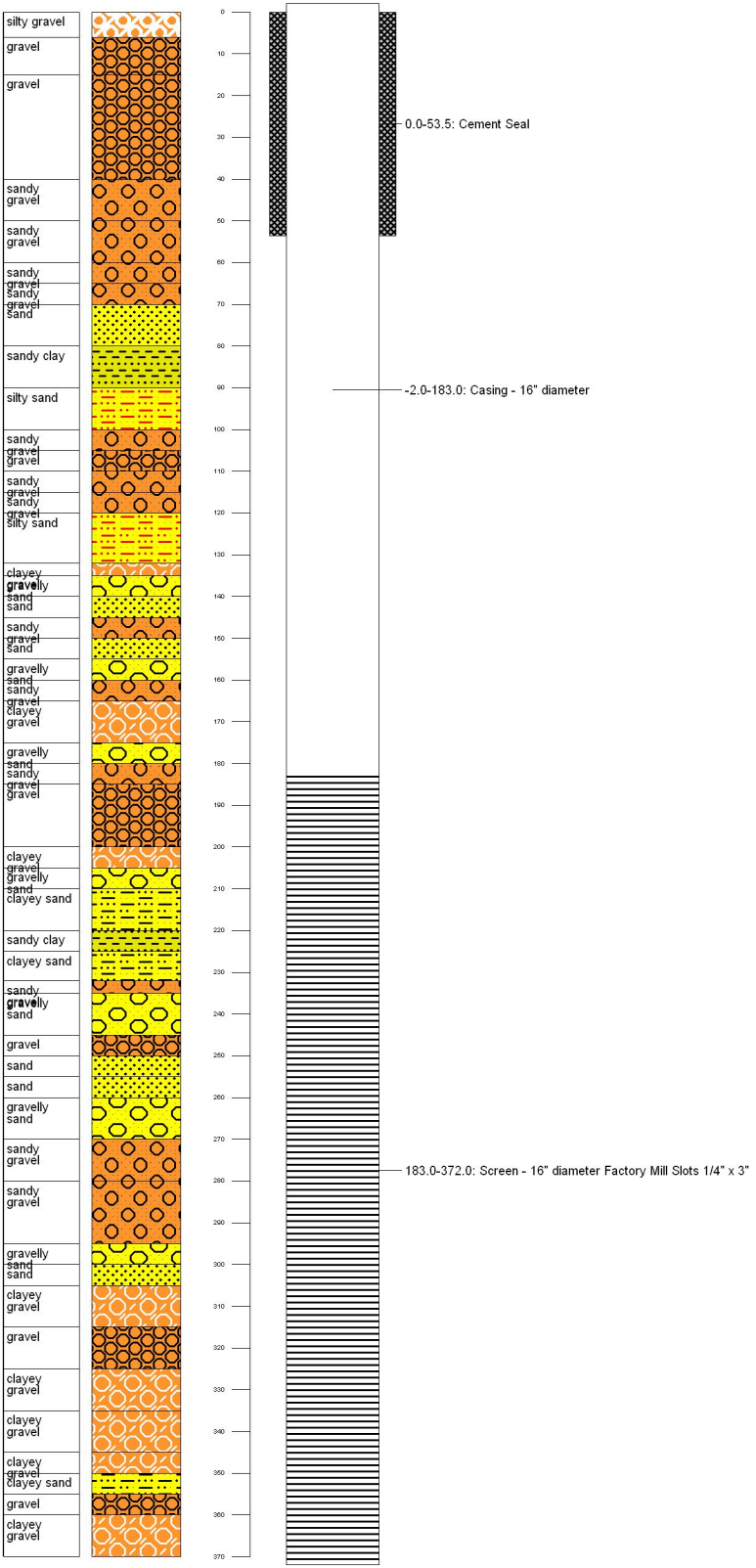
silty gravel
gravel
gravel
sandy gravel
sandy gravel
sandy gravel
sandy gravel
sand
sandy clay
silty sand
sandy gravel
sandy gravel
sandy gravel
silty sand
clayey gravelly sand
sandy gravel
sand
gravelly sand
sandy gravel
clayey gravel
gravelly sand
sandy gravel
clayey gravel
gravelly sand
clayey sand
sandy clay
clayey sand
sandy gravelly sand
gravel
sand
sand
gravelly sand
sandy gravel
sandy gravel
gravelly sand
clayey gravel
gravel
clayey gravel
clayey gravel
clayey gravel
clayey sand
gravel
clayey gravel
0
10
20
30
40
50
60
70
80
90
100
110
120
130
140
150
160
170
180
190
200
210
220
230
240
250
260
270
280
290
300
310
320
330
340
350
360
370
0.0-53.5: Cement Seal
-2.0-183.0: Casing - 16" diameter
183.0-372.0: Screen - 16" diameter Factory Mill Slots 1/4" x 3"

Well 5

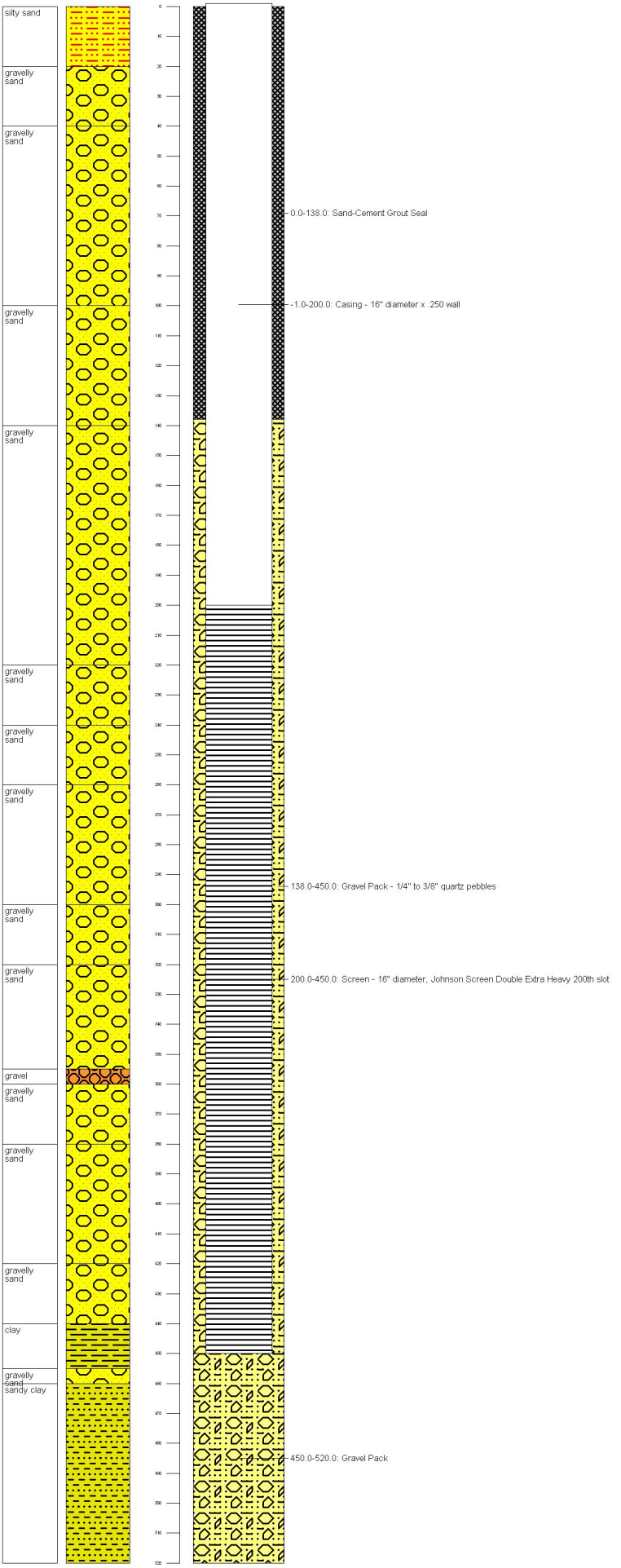
silty sand
gravelly sand
gravelly sand
gravelly sand
gravelly sand
gravelly sand
gravelly sand
gravelly sand
gravelly sand
gravelly sand
gravel
gravelly sand
gravelly sand
gravelly sand
clay
gravelly sand
sandy clay
0.0-138.0: Sand-Cement Grout Seal
-1.0-200.0: Casing - 16" diameter x .250 wall
138.0-450.0: Gravel Pack - 1/4" to 3/8" quartz pebbles
200.0-450.0: Screen - 16" diameter, Johnson Screen Double Extra Heavy 200th slot
450.0-520.0: Gravel Pack

Well 6

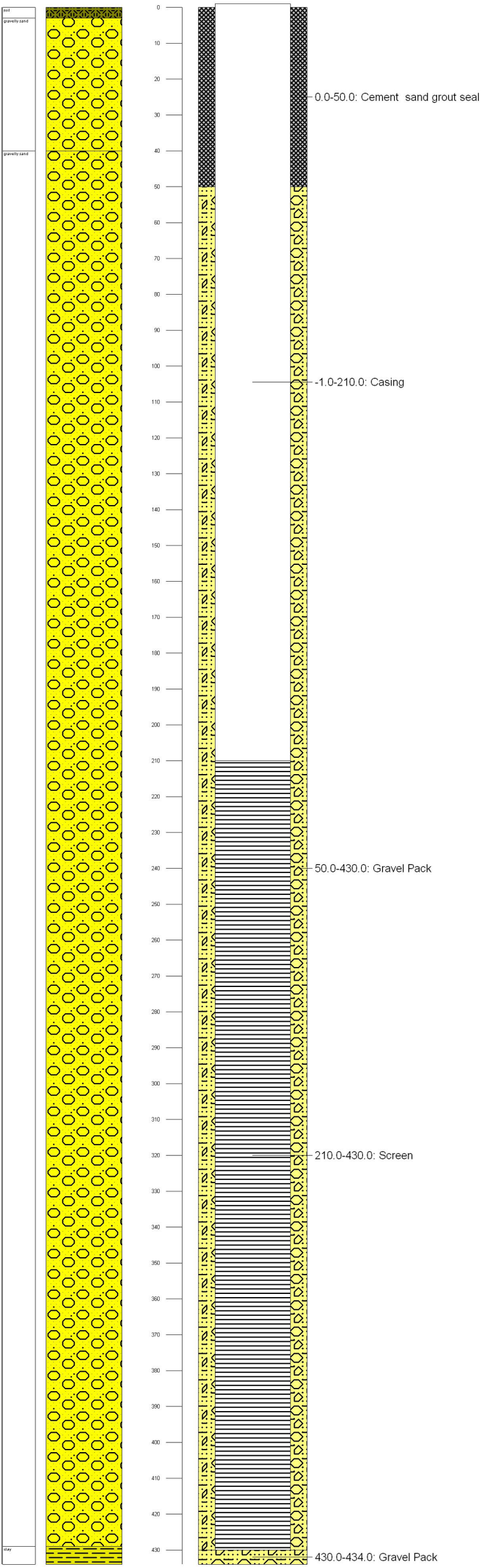
soil
gravelly sand
gravelly sand
clay
0
10
20
30
40
50
60
70
80
90
100
110
120
130
140
150
160
170
180
190
200
210
220
230
240
250
260
270
280
290
300
310
320
330
340
350
360
370
380
390
400
410
420
430
0.0-50.0: Cement sand grout seal
-1.0-210.0: Casing
50.0-430.0: Gravel Pack
210.0-430.0: Screen
430.0-434.0: Gravel Pack

Well 7

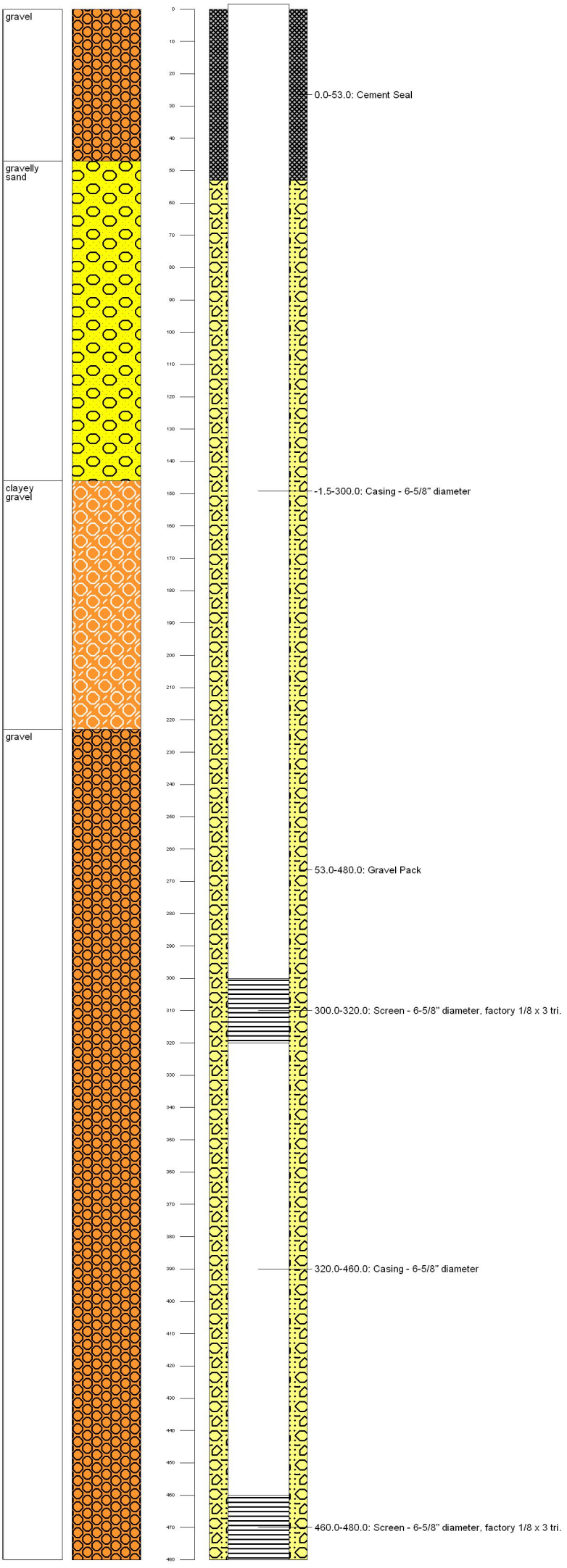
gravel
gravelly sand
clayey gravel
gravel
0
10
20
30
40
50
60
70
80
90
100
110
120
130
140
150
160
170
180
190
200
210
220
230
240
250
260
270
280
290
300
310
320
330
340
350
360
370
380
390
400
410
420
430
440
450
460
470
480
0.0-53.0: Cement Seal
-1.5-300.0: Casing - 6-5/8" diameter
53.0-480.0: Gravel Pack
300.0-320.0: Screen - 6-5/8" diameter, factory 1/8 x 3 tri.
320.0-460.0: Casing - 6-5/8" diameter
460.0-480.0: Screen - 6-5/8" diameter, factory 1/8 x 3 tri.

Well 8

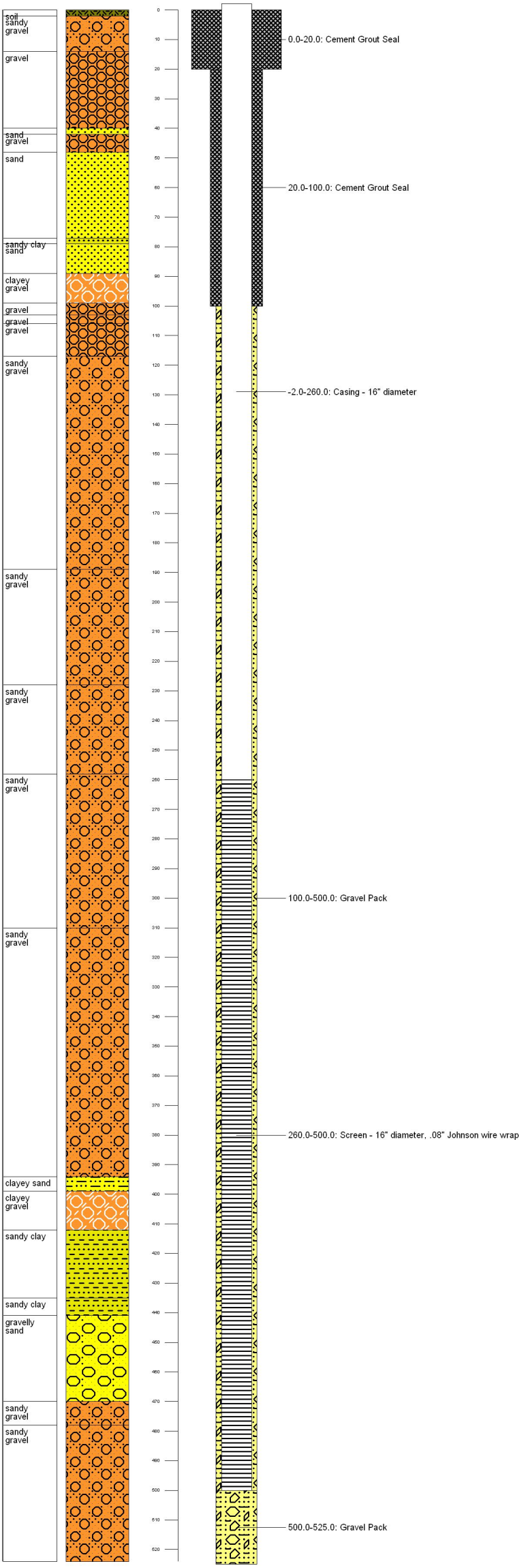
soil
sandy gravel
gravel
sand gravel
sand
sandy clay sand
clayey gravel
gravel
gravel
gravel
sandy gravel
sandy gravel
sandy gravel
sandy gravel
sandy gravel
clayey sand
clayey gravel
sandy clay
sandy clay
gravelly sand
sandy gravel
sandy gravel
0
10
20
30
40
50
60
70
80
90
100
110
120
130
140
150
160
170
180
190
200
210
220
230
240
250
260
270
280
290
300
310
320
330
340
350
360
370
380
390
400
410
420
430
440
450
460
470
480
490
500
510
520
0.0-20.0: Cement Grout Seal
20.0-100.0: Cement Grout Seal
-2.0-260.0: Casing - 16" diameter
100.0-500.0: Gravel Pack
260.0-500.0: Screen - 16" diameter, .08" Johnson wire wrap
500.0-525.0: Gravel Pack

Well 9

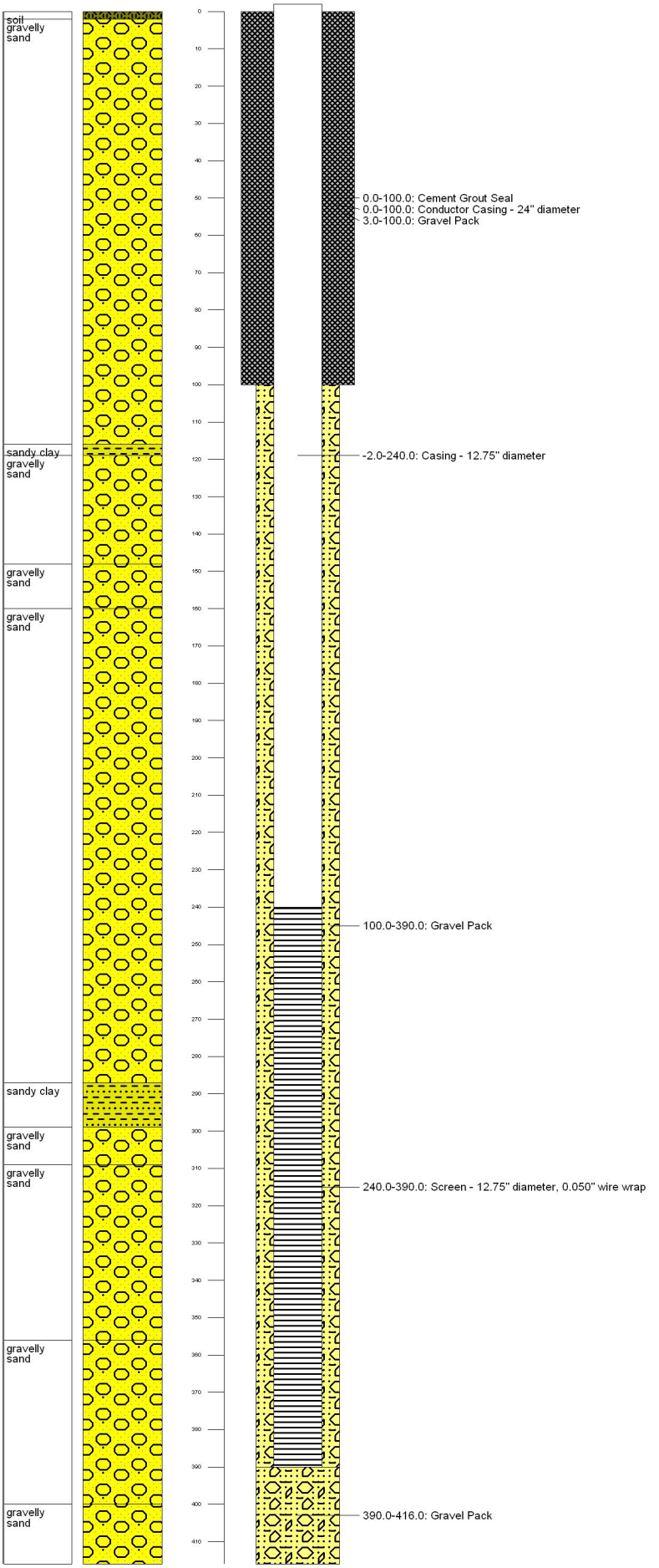
soil
gravelly sand
sandy clay
gravelly sand
gravelly sand
gravelly sand
sandy clay
gravelly sand
gravelly sand
gravelly sand
gravelly sand
0
10
20
30
40
50
60
70
80
90
100
110
120
130
140
150
160
170
180
190
200
210
220
230
240
250
260
270
280
290
300
310
320
330
340
350
360
370
380
390
400
410
0.0-100.0: Cement Grout Seal
0.0-100.0: Conductor Casing - 24" diameter
3.0-100.0: Gravel Pack
-2.0-240.0: Casing - 12.75" diameter
100.0-390.0: Gravel Pack
240.0-390.0: Screen - 12.75" diameter, 0.050" wire wrap
390.0-416.0: Gravel Pack

Attachment 2: SeriesSEE Output Plots

RMS = 0.0317

VIEW:

RMS Expected:	0.0030	Maximum:	0.1071
Max Iter:	30	Minimum:	-0.4833
Time Begin:	11/20/2022 14:46	Average:	-0.12
Time End:	01/01/2023 13:38	Std. Dev.:	0.1601
Interval:	0:30:00	Count:	2013

Measured: MW2_GRGID

Transform	Time Series	Coeff.1	Est	Coeff.2	Est	Coeff.3	Coeff.4	Coeff.5
Slope+Offset		**0**	**fixed**	4.7946	none			
SERIES	Well7	-0.035831184	none	0.1018	none	0.04167		
SERIES	Well7	-0.38243692	none	-0.1399	none	0.08333		
SERIES	Well7	0.3211239	none	0.2616	none	0.125		
SERIES	Well7	0.9299061	none	-0.0439	none	0.25		
SERIES	Well7	-0.78133739	none	0.1736	none	0.5		
SERIES	Well7	1.0983114	none	0.4395	none	1		
SERIES	Well7	0.43892726	none	1.9668	none	2		
SERIES	Well7	-0.31259931	none	0.834	none	4		
SERIES	Well7	-0.58167562	none	-1.1339	none	7		
SERIES	MW2_Bing	1.0440999	none	-0.0052	none	0.04167		
SERIES	MW2_Bing	0.038533692	none	0.0314	none	0.08333		
SERIES	MW2_Bing	-0.019867849	none	0.1419	none	0.125		
SERIES	MW2_Bing	-1.2494196	none	-0.252	none	0.25		
SERIES	MW2_Bing	2.0228843	none	-0.289	none	0.5		
SERIES	MW2_Bing	-0.17264392	none	-3.3257	none	1		
SERIES	MW2_Bing	1.5972264	none	-2.137	none	2		
SERIES	MW2_Bing	-2.3724026	none	-0.2757	none	4		
SERIES	MW2_Bing	1.6403067	none	-8.2411	none	7		
THEIS	Q-Well1	2.90E+03	log	0.0093	log	4925	-193	

DD-MW2_GRGID | Q-Well1 | 09/01/2010 00:00:00 | 10/24/2010 00:00:00

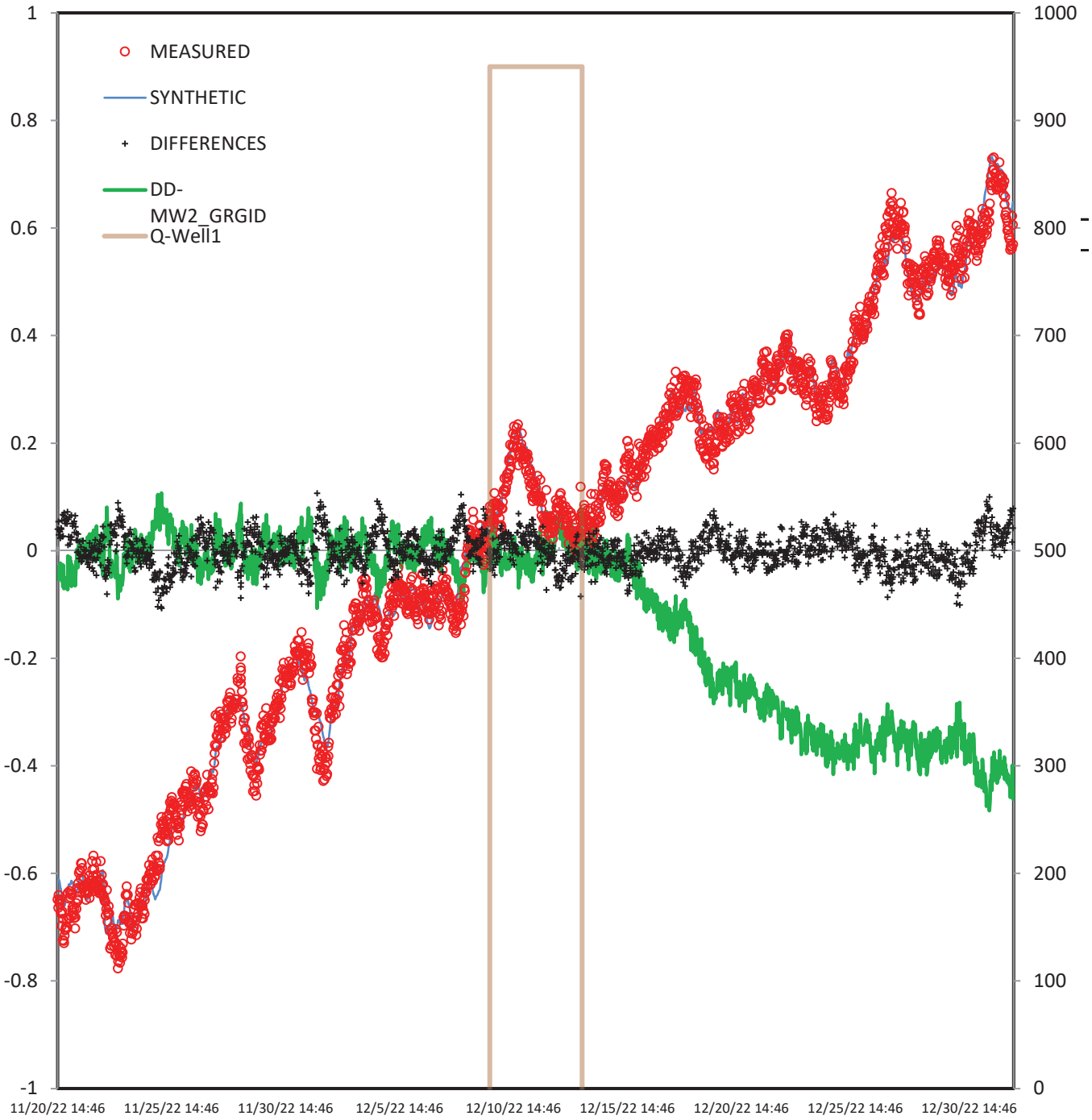

RMS = 0.0369

VIEW:

RMS Expected:	0.0030	Maximum:	0.0909435
Max Iter:	30	Minimum:	-2.4468054
Time Begin:	12/04/2022 23:01	Average:	-1.097275
Time End:	12/19/2022 23:01	Std. Dev.:	1.0039053
Interval:	0:30:00	Count:	719

Measured: MW3

Transform	Time Series	Coeff.1	Est	Coeff.2	Est	Coeff.3	Coeff.4	Coeff.5
Slope+Offset		**0**	**fixed**	-6.9025837	none			
SERIES	Well7	2.02E-01	none	5.77E-02	none	0.04167		
SERIES	Well7	2.81E-01	none	-2.39E-01	none	0.08333		
SERIES	Well7	-7.88E-02	none	1.29E-01	none	0.125		
SERIES	Well7	-5.27E-01	none	3.00E-01	none	0.25		
SERIES	Well7	-1.33E+00	none	-1.75E-01	none	0.5		
SERIES	Well7	-4.22E+00	none	3.06E-01	none	1		
SERIES	Well7	-4.27E+00	none	-1.21E+00	none	2		
SERIES	MW2_GRGID	7.86E-01	none	1.24E-02	none	0.04167		
SERIES	MW2_GRGID	7.34E-01	none	-5.34E-02	none	0.08333		
SERIES	MW2_GRGID	5.80E-01	none	-2.41E-01	none	0.125		
SERIES	MW2_GRGID	3.90E-01	none	2.26E-01	none	0.25		
SERIES	MW2_GRGID	9.04E-01	none	-6.17E-01	none	0.5		
SERIES	MW2_GRGID	2.81E+00	none	-1.79E+00	none	1		
SERIES	MW2_GRGID	5.59E+00	none	-2.34E-01	none	2		
THEIS	Q-Well1	2.94E+03	log	0.0018491	log	4220	-193	

DD-MW3 | Q-Well1 | 09/01/2010 00:00:00 | 10/24/2010 00:00:00

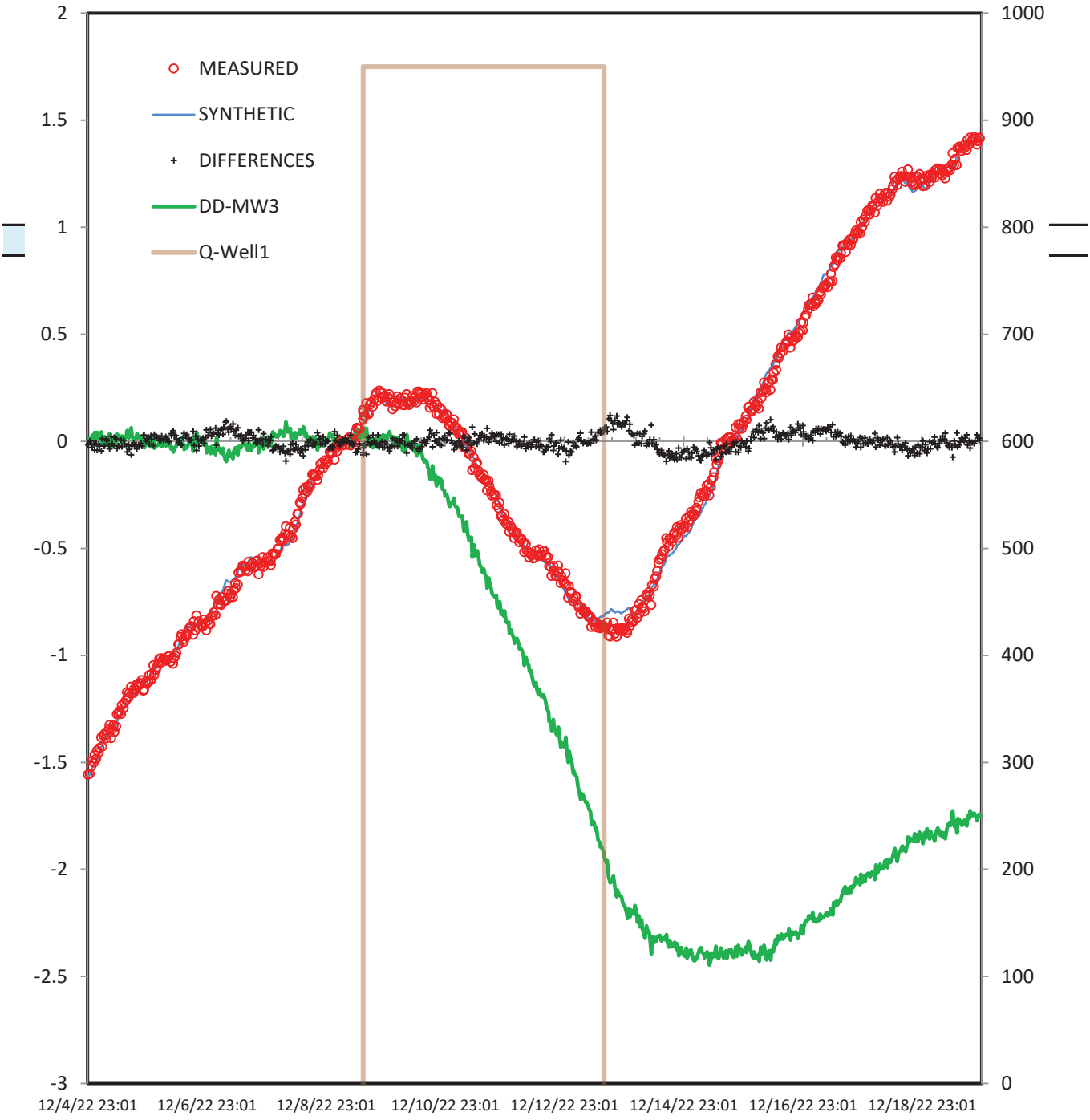

RMS = 0.0492

VIEW:

RMS Expected:	0.0030	Maximum:	0.0739
Max Iter:	30	Minimum:	-3.3989
Time Begin:	12/04/2022 23:39	Average:	-1.4539
Time End:	12/19/2022 23:39	Std. Dev.:	1.2484
Interval:	0:30:00	Count:	719

Measured: MW5

Transform	Time Series	Coeff.1	Est	Coeff.2	Est	Coeff.3	Coeff.4	Coeff.5
Slope+Offset		**0**	**fixed**	-5.0462	none			
SERIES	Well7	-0.406504	none	0.0156	none	0.04167		
SERIES	Well7	-0.37047	none	-1.0376	none	0.08333		
SERIES	Well7	0.9486357	none	-1.0244	none	0.125		
SERIES	Well7	0.1627507	none	2.357	none	0.25		
SERIES	Well7	2.4243278	none	-1.2468	none	0.5		
SERIES	Well7	-3.038778	none	-4.4823	none	1		
SERIES	Well7	3.7340826	none	-4.4776	none	2		
SERIES	MW2_GRGID	0.5008831	none	0.0672	none	0.04167		
SERIES	MW2_GRGID	0.7932028	none	-0.0115	none	0.08333		
SERIES	MW2_GRGID	0.5255423	none	-0.2955	none	0.125		
SERIES	MW2_GRGID	1.9002571	none	0.4688	none	0.25		
SERIES	MW2_GRGID	-1.791237	none	-1.1967	none	0.5		
SERIES	MW2_GRGID	4.5624146	none	-0.5892	none	1		
SERIES	MW2_GRGID	6.3712148	none	2.2642	none	2		
THEIS	Q-Well1	3.52E+03	log	0.024	log	942	-193	

DD-MW5 | Q-Well1 | 09/01/2010 00:00:00 | 10/24/2010 00:00:00

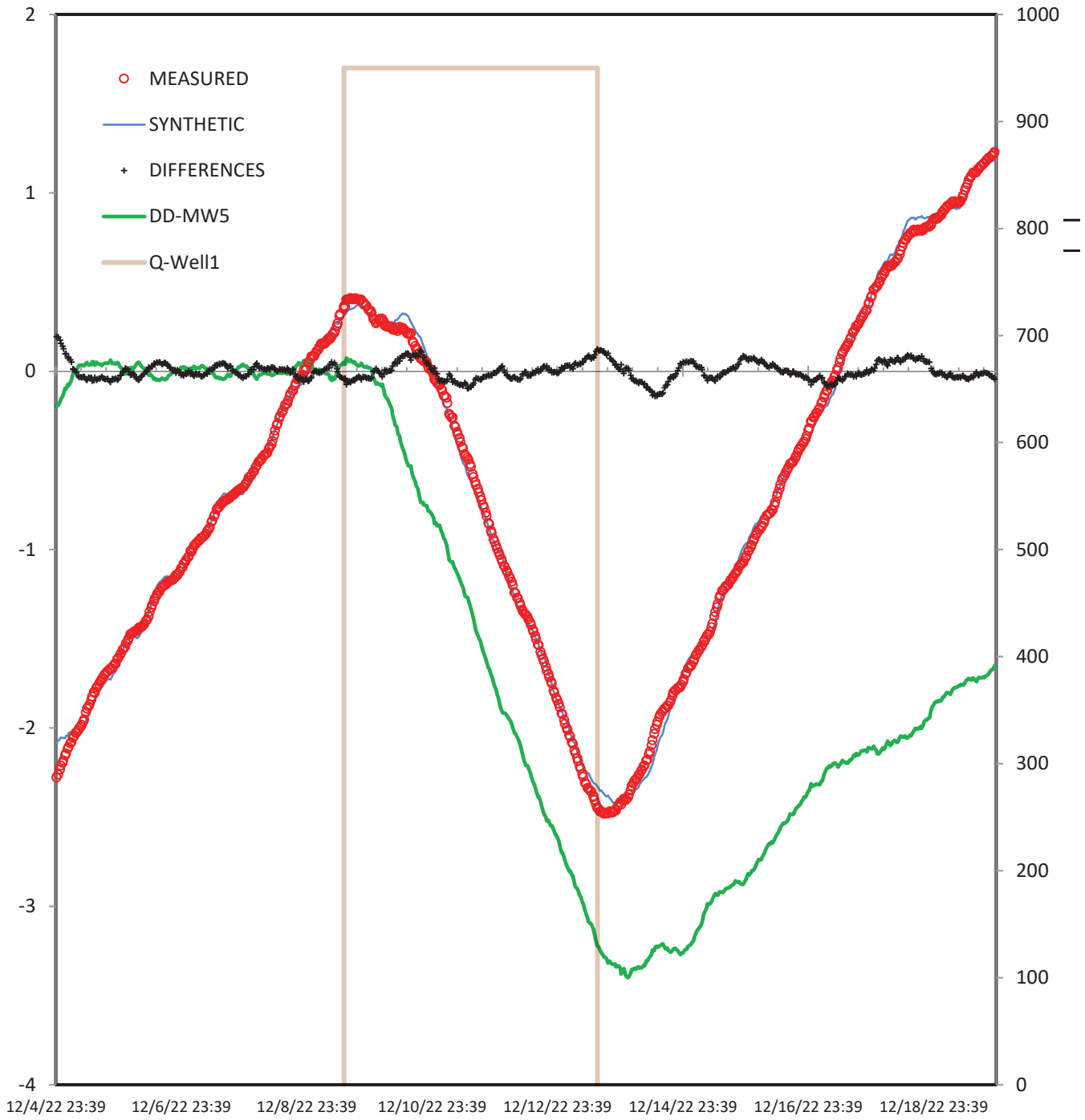

RMS = 0.0640

VIEW:

RMS Expected:	0.0030	Maximum:	0.1272
Max Iter:	30	Minimum:	-2.895
Time Begin:	12/04/2022 23:01	Average:	-1.2301
Time End:	12/19/2022 23:01	Std. Dev.:	1.0651
Interval:	0:30:00	Count:	719

Measured: MW6

Transform	Time Series	Coeff.1	Est	Coeff.2	Est	Coeff.3	Coeff.4	Coeff.5
Slope+Offset		**0**	**fixed**	-5.0747	none			
SERIES	Well7	1.02E+00	none	-0.0787	none	0.04167		
SERIES	Well7	7.70E-01	none	-0.3417	none	0.08333		
SERIES	Well7	1.00E+00	none	-1.1195	none	0.125		
SERIES	Well7	1.59E+00	none	0.1852	none	0.25		
SERIES	Well7	2.49E+00	none	1.5266	none	0.5		
SERIES	Well7	-4.56E+00	none	0.1233	none	1		
SERIES	Well7	-1.49E+00	none	0.0892	none	2		
SERIES	MW2_GRGID	5.47E-01	none	0.4053	none	0.04167		
SERIES	MW2_GRGID	8.55E-01	none	-0.1355	none	0.08333		
SERIES	MW2_GRGID	-1.31E-03	none	-0.4843	none	0.125		
SERIES	MW2_GRGID	9.03E-01	none	-1.5843	none	0.25		
SERIES	MW2_GRGID	1.47E+00	none	-0.6014	none	0.5		
SERIES	MW2_GRGID	3.36E+00	none	2.8619	none	1		
SERIES	MW2_GRGID	4.72E+00	none	-0.01	none	2		
THEIS	Q-Well1	3.98E+03	log	0.0152	log	1300	-193	

DD-MW6 | Q-Well1 | 09/01/2010 00:00:00 | 10/24/2010 00:00:00

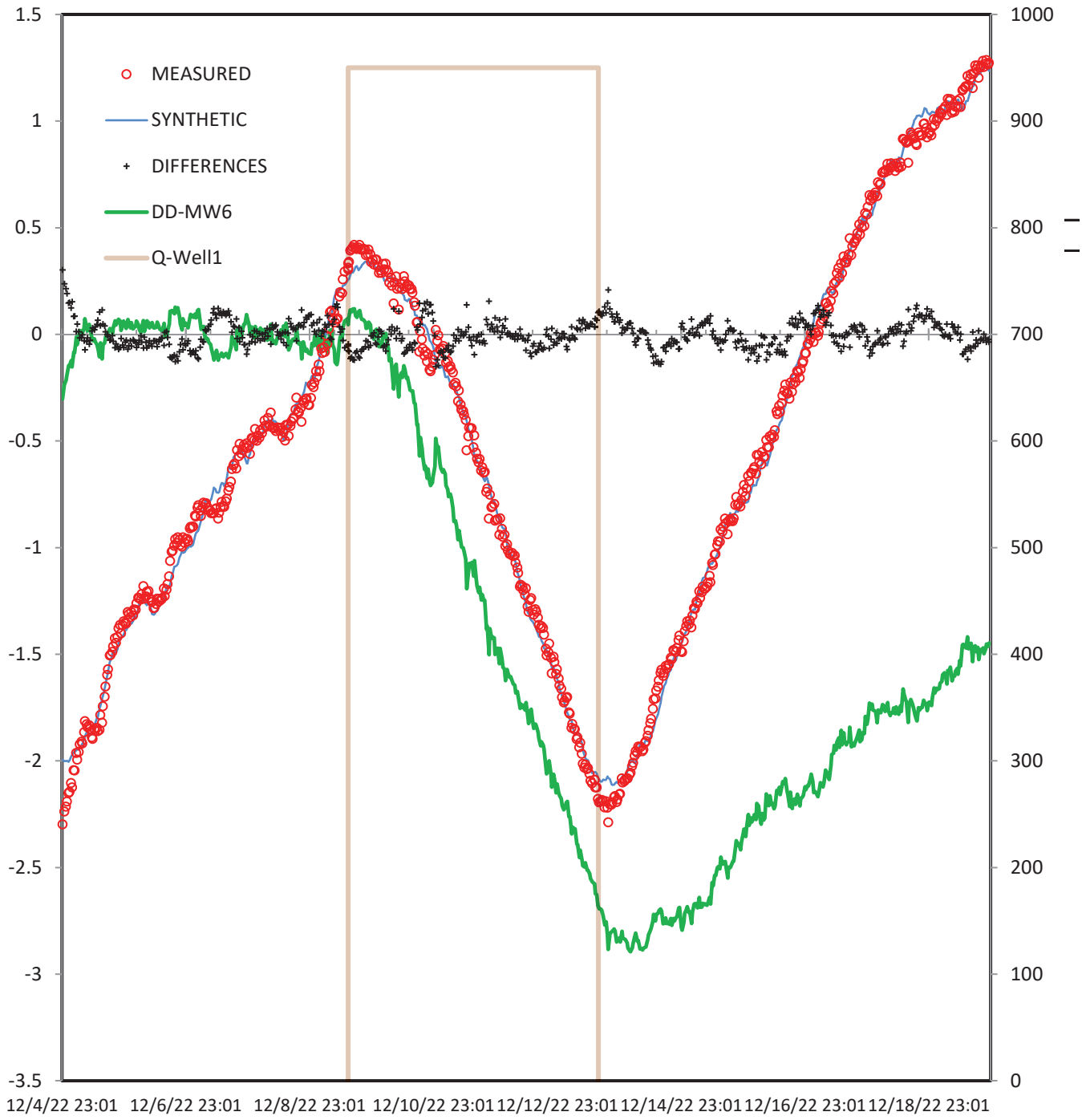

FIT | LOAD | MS = 0.1489 | ☑ Offset to average | VIEW:

☐ Remove steps drawdown

RMS Expected:	0.0030	Maximum:	1.5812
Max Iter:	30	Minimum:	-33.025
Time Begin:	12/07/2022 00:22	Average:	-5.9772
Time End:	12/22/2022 00:22	Std. Dev.:	5.2623
Interval:	0:30:00	Count:	268

Measured: Well2

Transform	Time Series	Coeff.1	Est	Coeff.2	Est	Coeff.3	Coeff.4	Coeff.5
Slope+Offset		0	fixed	18.502	none			
SERIES	Well7	0.4163511	none	3.0299	none	0.04167		
SERIES	Well7	0.4921069	none	3.8058	none	0.08333		
SERIES	Well7	3.5883254	none	3.0107	none	0.125		
SERIES	Well7	-4.000389	none	4.0899	none	0.25		
SERIES	Well7	-6.211725	none	2.7982	none	0.5		
SERIES	Well7	2.1553687	none	2.2917	none	1		
SERIES	Well7	-8.704234	none	4.8563	none	2		
SERIES	Well7	-10.55171	none	6.884	none	4		
SERIES	Well7	4.8887512	none	-2.3073	none	7		
SERIES	MW2_Bing	-0.090182	none	4.339	none	0.04167		
SERIES	MW2_Bing	7.9535467	none	2.628	none	0.08333		
SERIES	MW2_Bing	-4.340556	none	-0.3737	none	0.125		
SERIES	MW2_Bing	-7.535483	none	5.3215	none	0.25		
SERIES	MW2_Bing	-4.909943	none	-0.3483	none	0.5		
SERIES	MW2_Bing	-2.76823	none	0.2178	none	1		
SERIES	MW2_Bing	-7.258128	none	2.3385	none	2		
SERIES	MW2_Bing	13.2817	none	-5.1987	none	4		
SERIES	MW2_Bing	20.606149	none	-3.4354	none	7		
THEIS	Q-Well1	3649.06	log	0.0003	log	1750	-193	

DD-Well2

Q-Well1

09/01/2010 00:00:00 | 10/24/2010 00:00:00

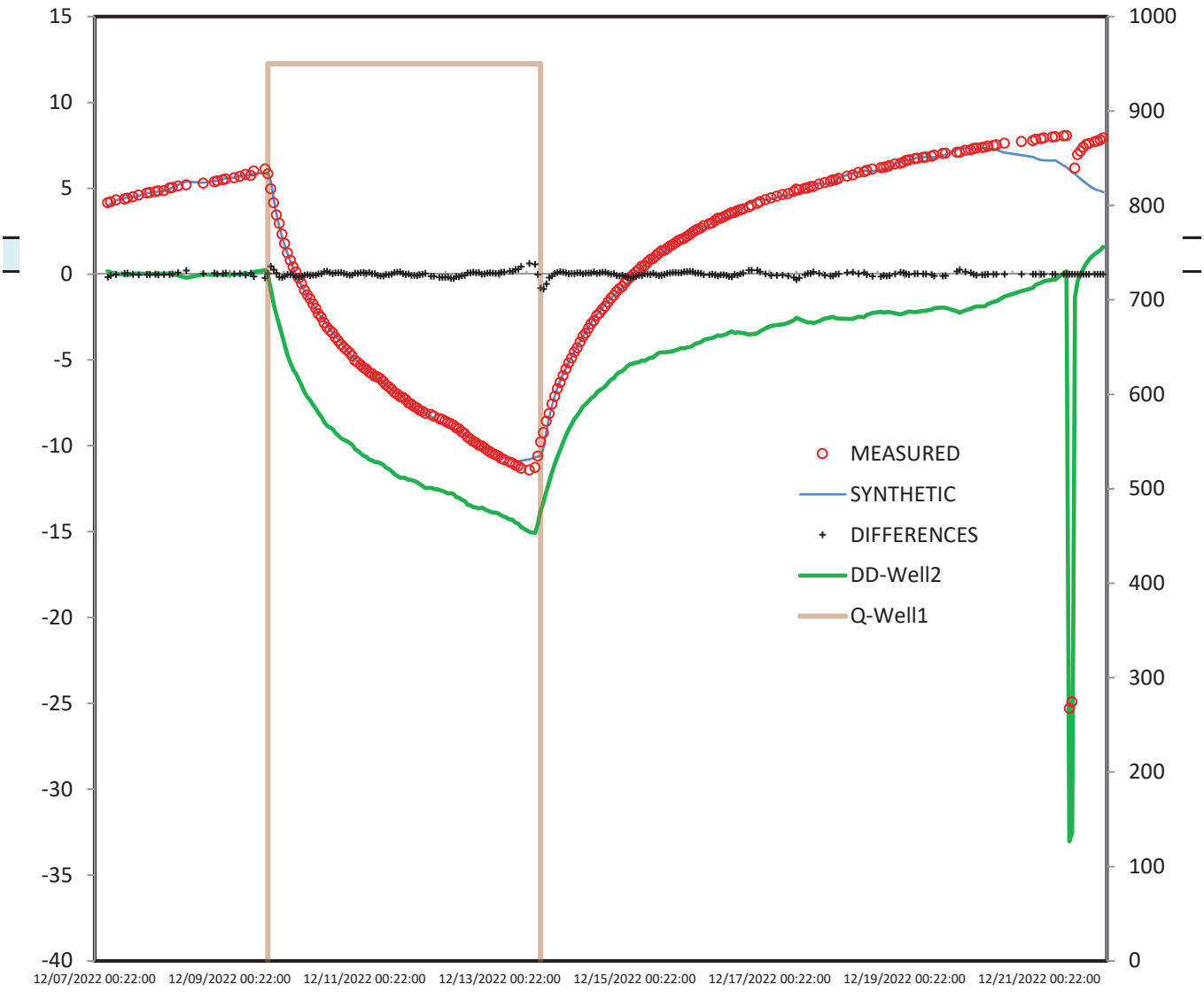

RMS = 0.1066

VIEW:

RMS Expected:	0.0030	Maximum:	0.2222
Max Iter:	30	Minimum:	-0.2737
Time Begin:	11/28/2022 00:24	Average:	-0.0176
Time End:	12/28/2022 00:24	Std. Dev.:	0.1054
Interval:	0:30:00	Count:	199

Measured: Well4

Transform	Time Series	Coeff.1	Est	Coeff.2	Est	Coeff.3	Coeff.4	Coeff.5
Slope+Offset		**0**	**fixed**	2.3316	none			
SERIES	Well7	0.4123982	none	-0.7618	none	0.04167		
SERIES	Well7	-0.785849	none	-0.8133	none	0.08333		
SERIES	Well7	-0.2478	none	-1.1629	none	0.125		
SERIES	Well7	0.4250022	none	0.0227	none	0.25		
SERIES	Well7	0.2931139	none	-0.8699	none	0.5		
SERIES	Well7	-0.172473	none	-1.3395	none	1		
SERIES	Well7	-0.394225	none	2.1464	none	2		
SERIES	Well7	-2.857623	none	-0.2587	none	4		
SERIES	Well7	-3.60688	none	1.0244	none	7		
SERIES	MW2_Bing	-0.176856	none	-0.8165	none	0.04167		
SERIES	MW2_Bing	-0.121026	none	-0.4258	none	0.08333		
SERIES	MW2_Bing	-0.83092	none	-1.7769	none	0.125		
SERIES	MW2_Bing	0.6557687	none	-0.2712	none	0.25		
SERIES	MW2_Bing	-0.151646	none	-0.6393	none	0.5		
SERIES	MW2_Bing	2.0933338	none	4.6965	none	1		
SERIES	MW2_Bing	-2.43353	none	-0.5447	none	2		
SERIES	MW2_Bing	2.9803986	none	-5.6978	none	4		
SERIES	MW2_Bing	2.7862064	none	2.3975	none	7		
THEIS	Q-Well1	3.60E+02	log	0.098	log	2230	-193	

DD-Well4 | Q-Well1 | 09/01/2010 00:00:00 | 10/24/2010 00:00:00

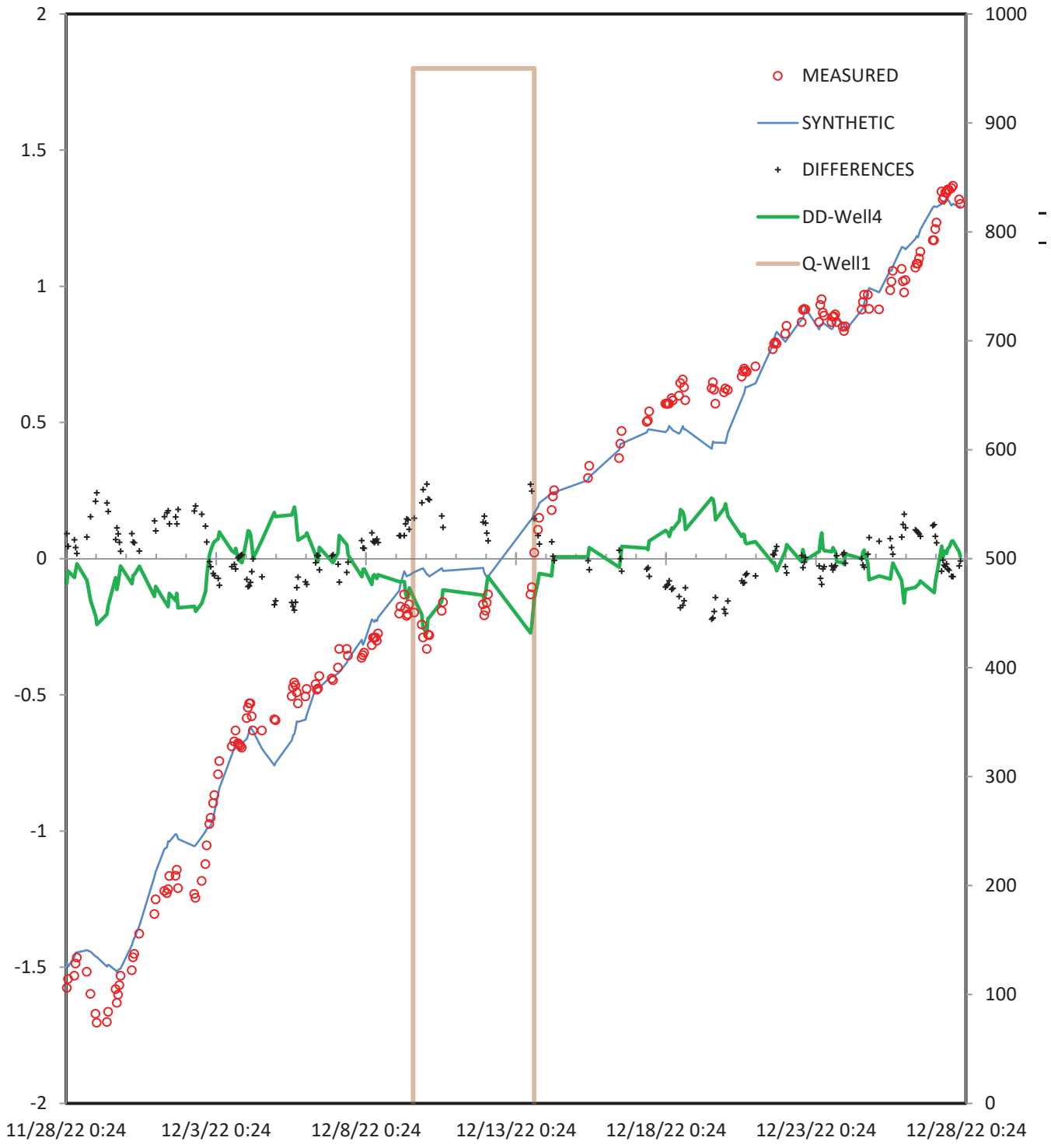

RMS = 0.0845

VIEW:

RMS Expected:	0.0030	Maximum:	0.2029
Max Iter:	30	Minimum:	-0.1624
Time Begin:	11/26/2022 23:47	Average:	0.0224
Time End:	12/26/2022 23:47	Std. Dev.:	0.0815
Interval:	0:30:00	Count:	565

Measured: Well8

Transform	Time Series	Coeff.1	Est	Coeff.2	Est	Coeff.3	Coeff.4	Coeff.5
Slope+Offset		**0**	**fixed**	1.2507	none			
SERIES	Well7	0.0066346	none	-0.6909	none	0.0417		
SERIES	Well7	-0.231138	none	-0.6947	none	0.0833		
SERIES	Well7	-0.049506	none	-0.4105	none	0.125		
SERIES	Well7	-0.021575	none	-0.989	none	0.25		
SERIES	Well7	-0.36612	none	-1.4254	none	0.5		
SERIES	Well7	-0.643995	none	-0.244	none	1		
SERIES	Well7	-0.743767	none	0.2621	none	2		
SERIES	Well7	-0.962218	none	-1.9738	none	4		
SERIES	Well7	0.0752391	none	3.0714	none	7		
SERIES	MW2_Bing	0.0152402	none	-0.805	none	0.0417		
SERIES	MW2_Bing	-0.020006	none	-0.9226	none	0.0833		
SERIES	MW2_Bing	-0.011829	none	-0.6199	none	0.125		
SERIES	MW2_Bing	0.0676693	none	-0.6855	none	0.25		
SERIES	MW2_Bing	0.1603259	none	-0.8112	none	0.5		
SERIES	MW2_Bing	0.302969	none	-0.8555	none	1		
SERIES	MW2_Bing	0.3882188	none	-4.7538	none	2		
SERIES	MW2_Bing	0.4881963	none	-4.8576	none	4		
SERIES	MW2_Bing	0.7582697	none	1.3767	none	7		
THEIS	Q-Well1	2.86E+01	log	28.552	log	5460	-193	

DD-Well8 | Q-Well1 | 09/01/2010 00:00:00 | 10/24/2010 00:00:00

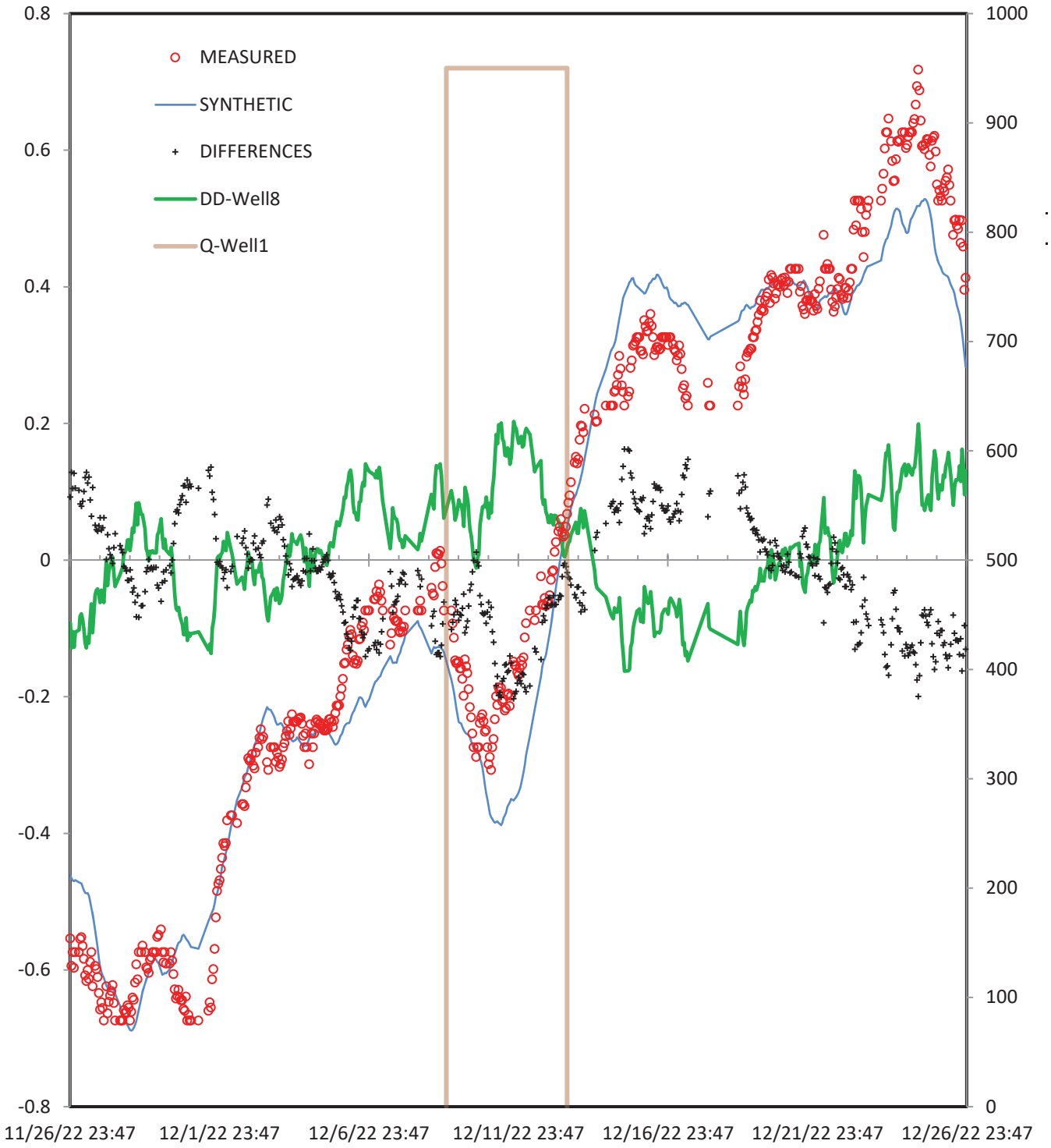

RMS = 0.1279

VIEW:

RMS Expected:	0.0030	Maximum:	0.3335
Max Iter:	30	Minimum:	-0.3566
Time Begin:	11/14/2022 23:16	Average:	0.0001
Time End:	12/14/2022 23:16	Std. Dev.:	0.1279
Interval:	0:30:00	Count:	1437

Measured: MW2_GRGID

Transform	Time Series	Coeff.1	Est	Coeff.2	Est	Coeff.3	Coeff.4	Coeff.5
Slope+Offset		**0**	**fixed**	1.6242	none			
SERIES	Well7	0.5752511	none	0.0615	none	0.0417		
SERIES	Well7	-0.843244	none	-0.4722	none	0.0833		
SERIES	Well7	0.6918973	none	-0.2307	none	0.125		
SERIES	Well7	2.368341	none	0.5364	none	0.25		
SERIES	Well7	-1.957897	none	0.5606	none	0.5		
SERIES	Well7	-0.080993	none	1.7918	none	1		
SERIES	Well7	-0.551653	none	5.999	none	2		
SERIES	Well7	1.7925338	none	-1.0098	none	4		
SERIES	Well7	3.8723918	none	-6.0612	none	7		
THEIS	Q-Well2	50	log	1	log	3547	-193	

DD-MW2_GRGID

Q-Well2

09/01/2010 00:00:00 | 10/24/2010 00:00:00

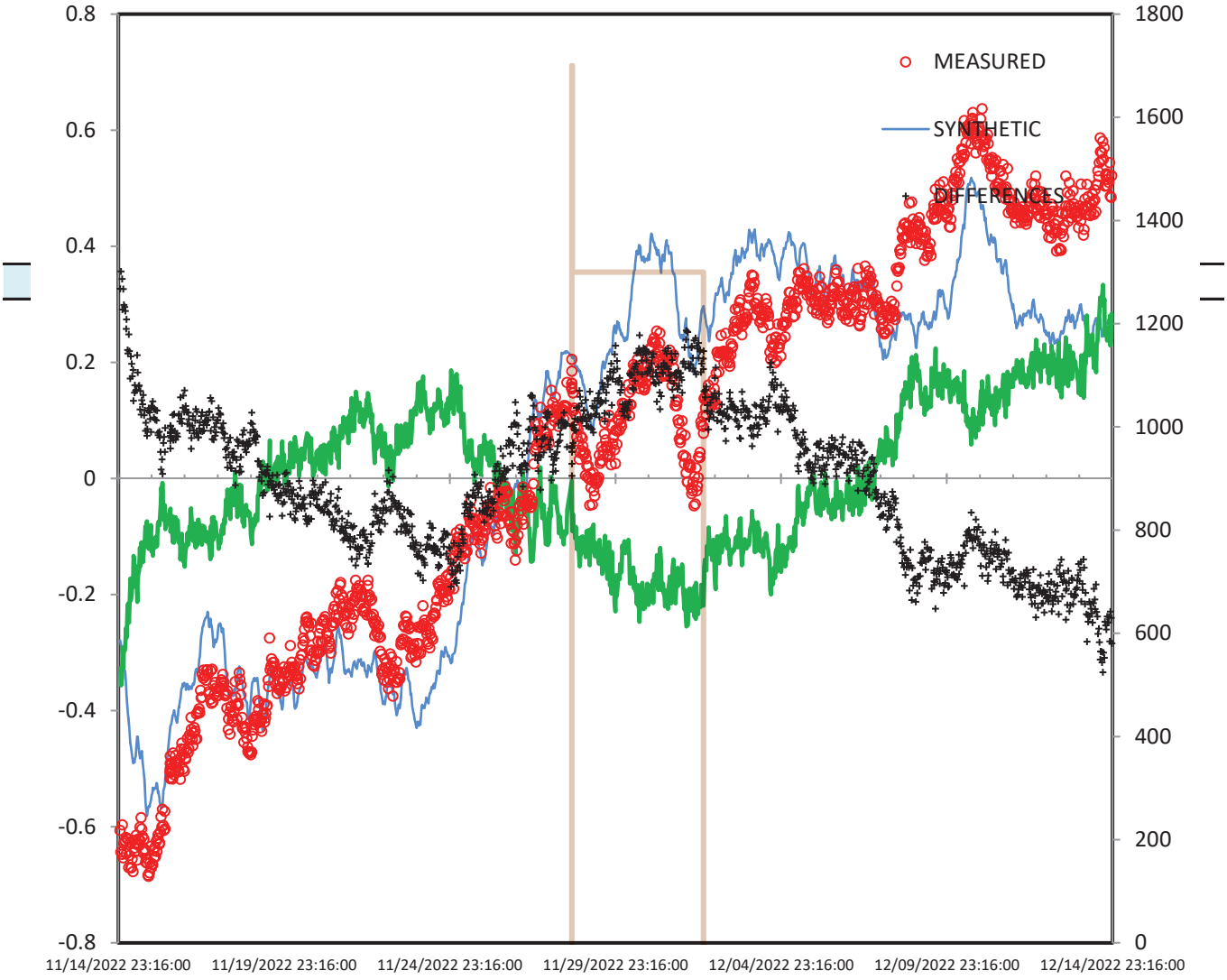

RMS = 0.0586

VIEW:

RMS Expected:	0.0030	Maximum:	0.1518
Max Iter:	30	Minimum:	-1.1446
Time Begin:	###############	Average:	-0.2284
Time End:	###############	Std. Dev.:	0.3114
Interval:	0:30:00	Count:	1439

Measured: MW3

Transform	Time Series	Coeff.1	Est	Coeff.2	Est	Coeff.3	Coeff.4	Coeff.5
Slope+Offset		**0**	**fixed**	2.0955	none			
SERIES	MW2_GRGID	-0.38511	none	0.1671	none	0.04167		
SERIES	MW2_GRGID	0.4646005	none	-0.0125	none	0.08333		
SERIES	MW2_GRGID	0.0307857	none	-0.7875	none	0.125		
SERIES	MW2_GRGID	-1.152713	none	0.3665	none	0.25		
SERIES	MW2_GRGID	-0.876862	none	0.9051	none	0.5		
SERIES	MW2_GRGID	0.0934709	none	-0.339	none	1		
SERIES	MW2_GRGID	2.8106272	none	-0.2536	none	2		
SERIES	MW2_GRGID	5.8848809	none	-0.6216	none	4		
SERIES	MW2_GRGID	-2.194063	none	-1.8382	none	7		
SERIES	Well7	-0.083521	none	-0.1153	none	0.04167		
SERIES	Well7	0.1716838	none	-0.0238	none	0.08333		
SERIES	Well7	0.4797876	none	0.1652	none	0.125		
SERIES	Well7	1.0285922	none	0.4223	none	0.25		
SERIES	Well7	1.8202123	none	1.9032	none	0.5		
SERIES	Well7	3.7906365	none	1.0842	none	1		
SERIES	Well7	5.2387664	none	3.0333	none	2		
SERIES	Well7	-7.22626	none	1.6866	none	4		
SERIES	Well7	3.4348378	none	2.7299	none	7		
THEIS	Q-Well2	39731.006	log	0.0022	log	4262	-193	

DD-MW3 | Q-Well2 | 09/01/2010 00:00:00 | 10/24/2010 00:00:00

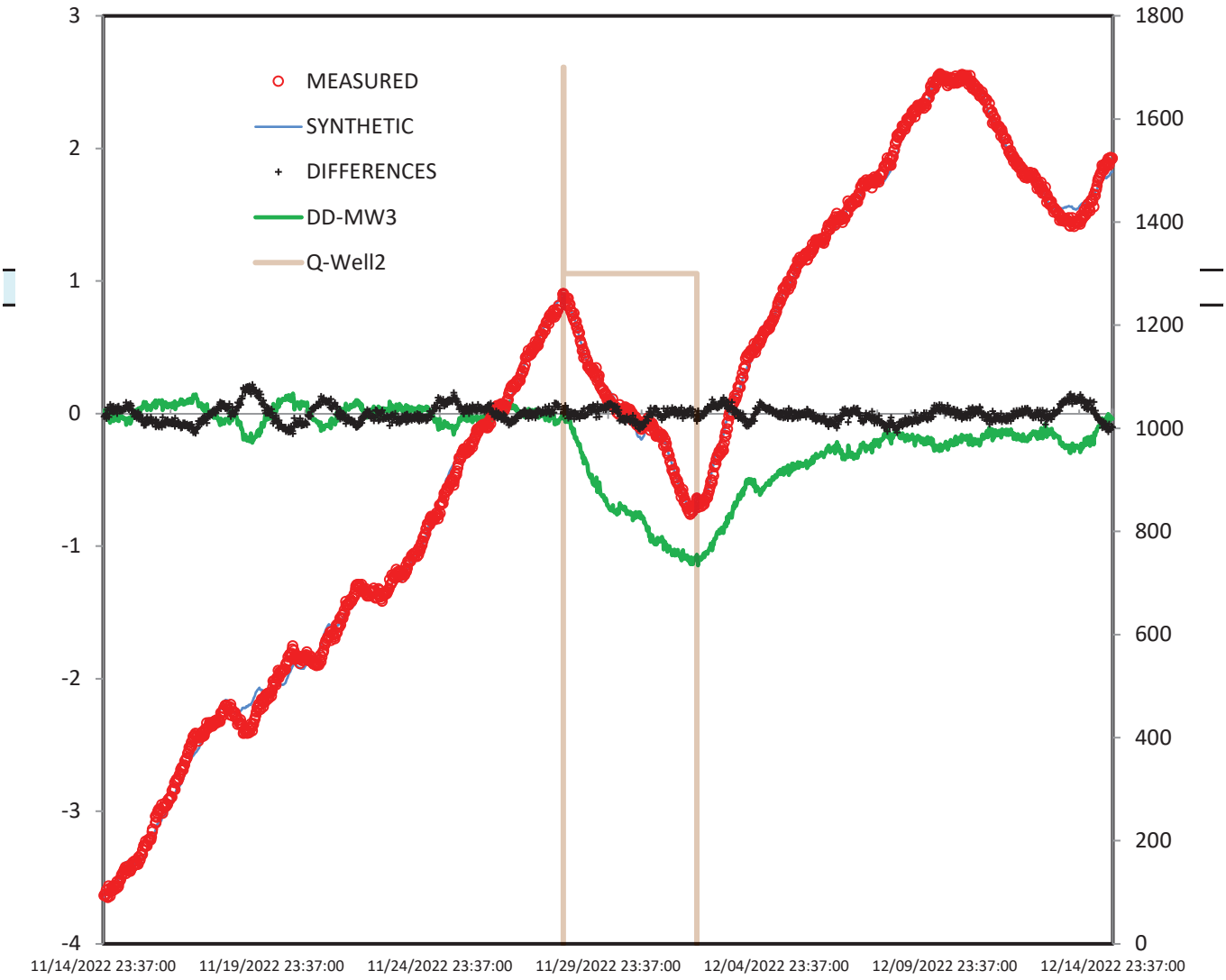

RMS = 0.0524

VIEW:

RMS Expected:	0.0030	Maximum:	0.2191
Max Iter:	30	Minimum:	-3.9852
Time Begin:	11/22/2022 23:28	Average:	-1.3314
Time End:	12/07/2022 23:28	Std. Dev.:	1.288
Interval:	0:30:00	Count:	720

Measured: MW5

Transform	Time Series	Coeff.1	Est	Coeff.2	Est	Coeff.3	Coeff.4	Coeff.5
Slope+Offset		**0**	**fixed**	-0.4867	none			
SERIES	Well7	0.8709364	none	-0.3345	none	0.04167		
SERIES	Well7	0.0995496	none	-1.4789	none	0.08333		
SERIES	Well7	0.2134119	none	-0.6183	none	0.125		
SERIES	Well7	1.2289599	none	-0.6493	none	0.25		
SERIES	Well7	2.7504689	none	0.0155	none	0.5		
SERIES	Well7	1.9011658	none	-0.9874	none	1		
SERIES	Well7	2.2663691	none	3.7332	none	2		
SERIES	MW2_GRGID	0.5152021	none	-0.005	none	0.04167		
SERIES	MW2_GRGID	0.1785246	none	-0.159	none	0.08333		
SERIES	MW2_GRGID	-0.550484	none	-1.2569	none	0.125		
SERIES	MW2_GRGID	-1.328982	none	-0.7629	none	0.25		
SERIES	MW2_GRGID	0.646281	none	-0.1101	none	0.5		
SERIES	MW2_GRGID	3.192807	none	0.4549	none	1		
SERIES	MW2_GRGID	4.8605861	none	1.9692	none	2		
THEIS	Q-Well2	8.98E+03	log	0.0219	log	860	-193	

DD-MW5 | Q-Well2 | 09/01/2010 00:00:00 | 10/24/2010 00:00:00

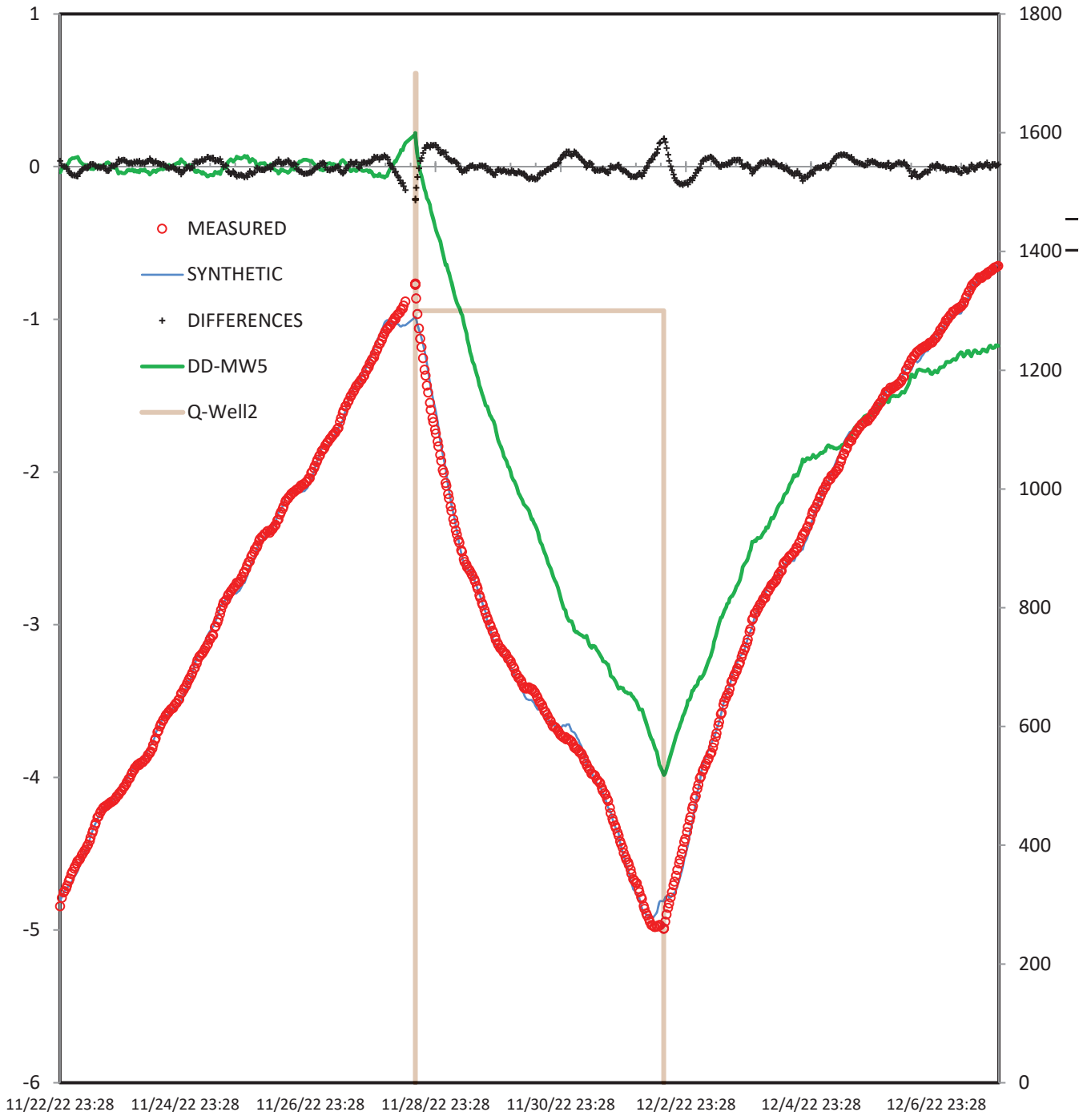

RMS = 0.0813

VIEW:

RMS Expected:	0.0030	Maximum:	0.1492
Max Iter:	30	Minimum:	-3.5754
Time Begin:	11/22/2022 22:51	Average:	-1.3021
Time End:	12/07/2022 22:51	Std. Dev.:	1.3568
Interval:	0:30:00	Count:	719

Measured: MW6

Transform	Time Series	Coeff.1	Est	Coeff.2	Est	Coeff.3	Coeff.4	Coeff.5
Slope+Offset		**0**	**fixed**	-6.2	none			
SERIES	Well7	-1.3912848	none	0.0859	none	0.04167		
SERIES	Well7	-1.0947867	none	-0.2425	none	0.08333		
SERIES	Well7	-0.51325345	none	-0.5675	none	0.125		
SERIES	Well7	-0.0134061	none	-1.2531	none	0.25		
SERIES	Well7	0.13321115	none	0.1497	none	0.5		
SERIES	Well7	-2.5459816	none	-4.0435	none	1		
SERIES	Well7	-13.426598	none	-2.4287	none	2		
SERIES	MW2_GRGID	-0.69282265	none	-0.2321	none	0.04167		
SERIES	MW2_GRGID	-0.41472828	none	-0.1616	none	0.08333		
SERIES	MW2_GRGID	-0.33597777	none	-1.3918	none	0.125		
SERIES	MW2_GRGID	-0.84721191	none	-0.4617	none	0.25		
SERIES	MW2_GRGID	2.5721793	none	-0.1128	none	0.5		
SERIES	MW2_GRGID	6.1986512	none	-0.2275	none	1		
SERIES	MW2_GRGID	5.3448019	none	-2.7354	none	2		
THEIS	Q-Well2	3051.6094	log	0.0068	log	2200	-193	

DD-MW6 | Q-Well2 | 09/01/2010 00:00:00 | 10/24/2010 00:00:00

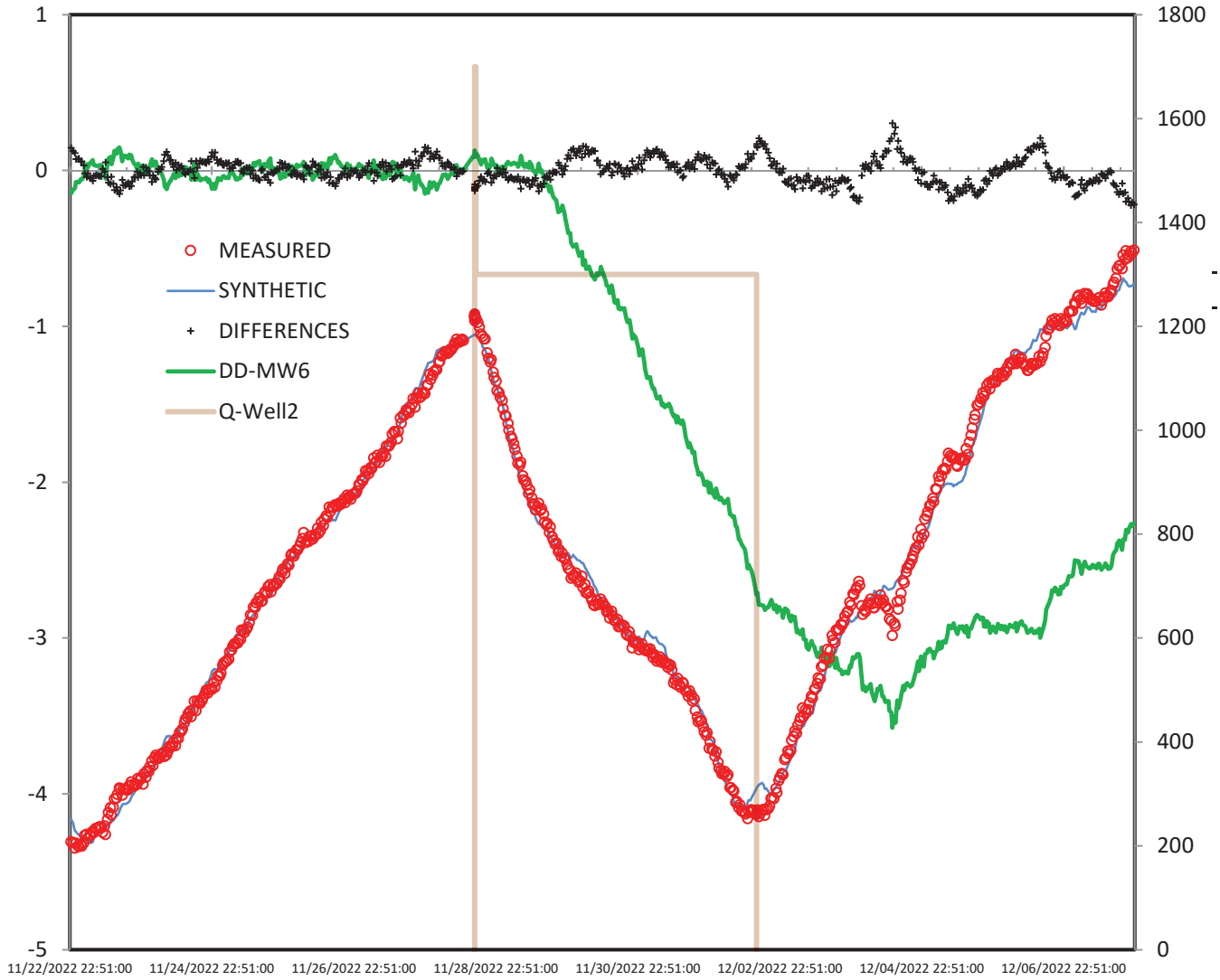

RMS = 0.1164

VIEW:

RMS Expected:	0.0030	Maximum:	0.243
Max Iter:	30	Minimum:	-19.867
Time Begin:	11/23/2022 23:58	Average:	-7.4422
Time End:	12/09/2022 00:28	Std. Dev.:	6.3833
Interval:	0:30:00	Count:	274

Measured: Well1

Transform	Time Series	Coeff.1	Est	Coeff.2	Est	Coeff.3	Coeff.4	Coeff.5
Slope+Offset		**0**	**fixed**	45.316	none			
SERIES	Sweetwater	-2.653342	none	1.2211	none	0.04167		
SERIES	Sweetwater	2.4268188	none	0.4216	none	0.08333		
SERIES	Sweetwater	-2.946001	none	-0.5071	none	0.125		
SERIES	Sweetwater	-2.394418	none	-0.2138	none	0.25		
SERIES	Sweetwater	-9.601575	none	0.322	none	0.5		
SERIES	Sweetwater	-1.58639	none	0.4172	none	1		
SERIES	Sweetwater	-6.529185	none	1.7274	none	2		
SERIES	Sweetwater	-0.708613	none	-8.0377	none	4		
SERIES	Sweetwater	-1.709816	none	-1.6842	none	7		
SERIES	MW1_GRGID	0.2613585	none	2.0004	none	0.04167		
SERIES	MW1_GRGID	0.6257249	none	1.0111	none	0.08333		
SERIES	MW1_GRGID	-0.177749	none	1.2632	none	0.125		
SERIES	MW1_GRGID	-0.350972	none	0.9643	none	0.25		
SERIES	MW1_GRGID	0.6080601	none	0.102	none	0.5		
SERIES	MW1_GRGID	1.4843369	none	-0.3457	none	1		
SERIES	MW1_GRGID	-1.865181	none	1.8038	none	2		
SERIES	MW1_GRGID	5.6362728	none	1.4679	none	4		
SERIES	MW1_GRGID	5.6502308	none	1.0015	none	7		
SERIES	MW2_Bing	-3.271428	none	0.8399	none	0.04167		
SERIES	MW2_Bing	3.8300957	none	0.2036	none	0.08333		
SERIES	MW2_Bing	-0.413401	none	-0.2235	none	0.125		
SERIES	MW2_Bing	1.9873406	none	1.2856	none	0.25		
SERIES	MW2_Bing	1.099629	none	-0.2743	none	0.5		
SERIES	MW2_Bing	2.4024738	none	-3.3302	none	1		
SERIES	MW2_Bing	-0.716292	none	3.5299	none	2		
SERIES	MW2_Bing	9.6918728	none	1.9048	none	4		
SERIES	MW2_Bing	7.3522525	none	-7.0271	none	7		
SERIES	Well7	-0.445874	none	-0.2759	none	0.04167		
SERIES	Well7	-1.327423	none	-0.3761	none	0.08333		
SERIES	Well7	1.9030953	none	-0.4249	none	0.125		
SERIES	Well7	-1.553179	none	-1.0362	none	0.25		
SERIES	Well7	1.0669307	none	-0.8284	none	0.5		
SERIES	Well7	2.1890771	none	2.4558	none	1		
SERIES	Well7	3.1468414	none	-0.1665	none	2		
SERIES	Well7	17.255472	none	0.5617	none	4		

SERIES	Well7	-4.048235	none	2.9219	none	7	
THEIS	Q-Well2	3524.102	log	0.0003	log	2000	-193

DD-Well1

Q-Well2

09/01/2010 00:00:00 | 10/24/2010 00:00:00

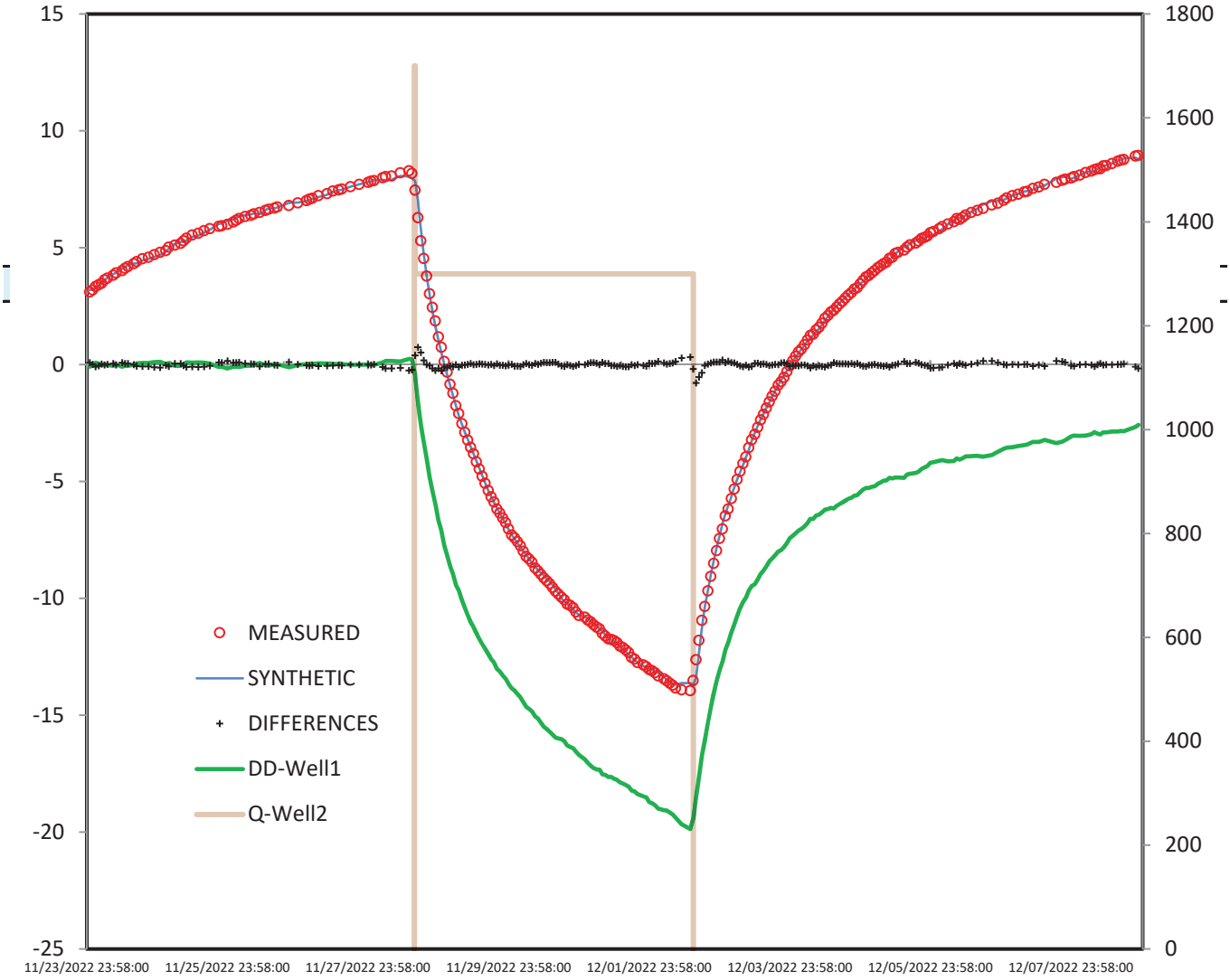

RMS = 0.3270

VIEW:

RMS Expected:	0.0030	Maximum:	0.7591
Max Iter:	30	Minimum:	-0.7423
Time Begin:	11/26/2022 00:07	Average:	1E-04
Time End:	12/14/2022 23:24	Std. Dev.:	0.3282
Interval:	0:30:00	Count:	134

Measured: Well4

Transform	Time Series	Coeff.1	Est	Coeff.2	Est	Coeff.3	Coeff.4	Coeff.5
Slope+Offset		**0**	**fixed**	3.0048	none			
SERIES	Well7	0.3246919	none	-2.1304	none	0.04167		
SERIES	Well7	0.3246896	none	-2.1303	none	0.08333		
SERIES	Well7	0.3246904	none	-2.1304	none	0.125		
SERIES	Well7	0.3246923	none	-2.1305	none	0.25		
SERIES	Well7	0.3247101	none	-2.1305	none	0.5		
SERIES	Well7	0.3247287	none	-2.1305	none	1		
SERIES	Well7	0.3247344	none	-2.1305	none	2		
SERIES	Well7	0.3247847	none	-2.1305	none	4		
SERIES	Well7	0.3248957	none	-2.1305	none	7		
SERIES	MW2_GRGID	0.3251422	none	-2.1302	none	0.04167		
SERIES	MW2_GRGID	0.3251487	none	-2.1305	none	0.08333		
SERIES	MW2_GRGID	0.3251492	none	-2.1304	none	0.125		
SERIES	MW2_GRGID	0.3251595	none	-2.1305	none	0.25		
SERIES	MW2_GRGID	0.3251809	none	-2.1305	none	0.5		
SERIES	MW2_GRGID	0.3251988	none	-2.1305	none	1		
SERIES	MW2_GRGID	0.3252301	none	-2.1305	none	2		
SERIES	MW2_GRGID	0.3252593	none	-2.1304	none	4		
SERIES	MW2_GRGID	0.3253357	none	-2.1305	none	7		
THEIS	Q-Well2	6.05E+02	log	604.52	log	3400	-193	

DD-Well4 | Q-Well2 | 09/01/2010 00:00:00 | 10/24/2010 00:00:00

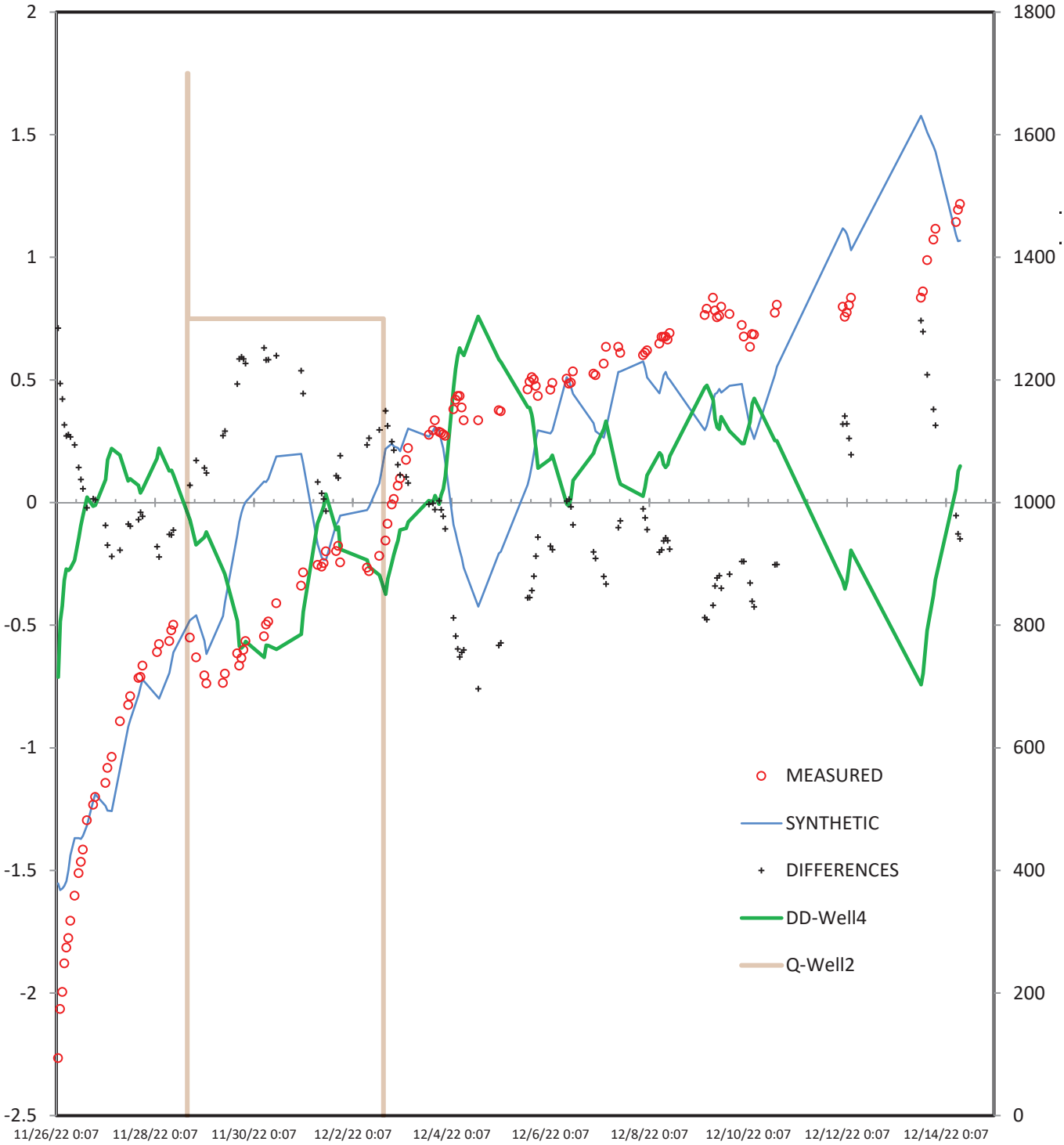

RMS = 0.0410

VIEW:

RMS Expected:	0.0030	Maximum:	0.2115
Max Iter:	30	Minimum:	-65.59
Time Begin:	11/15/2022 00:07	Average:	-0.3146
Time End:	12/15/2022 00:07	Std. Dev.:	3.7279
Interval:	0:30:00	Count:	591

Measured: Well8

Transform	Time Series	Coeff.1	Est	Coeff.2	Est	Coeff.3	Coeff.4	Coeff.5
Slope+Offset		**0**	**fixed**	-1.3802	none			
SERIES	Well7	-0.394797	none	0.3703	none	0.04167		
SERIES	Well7	0.1829978	none	0.6068	none	0.08333		
SERIES	Well7	-0.506368	none	0.7035	none	0.125		
SERIES	Well7	-0.35514	none	0.0473	none	0.25		
SERIES	Well7	0.1110662	none	1.3192	none	0.5		
SERIES	Well7	-0.591792	none	0.5188	none	1		
SERIES	Well7	-0.094074	none	11.335	none	2		
SERIES	Well7	2.406075	none	4.4619	none	4		
SERIES	Well7	-2.510237	none	12.259	none	7		
SERIES	MW2_GRGID	-0.377985	none	0.6019	none	0.04167		
SERIES	MW2_GRGID	0.0298333	none	0.4746	none	0.08333		
SERIES	MW2_GRGID	0.0130601	none	0.779	none	0.125		
SERIES	MW2_GRGID	0.5165932	none	0.2458	none	0.25		
SERIES	MW2_GRGID	0.6145531	none	0.5775	none	0.5		
SERIES	MW2_GRGID	-0.112913	none	-2.5755	none	1		
SERIES	MW2_GRGID	0.5118834	none	-5.3242	none	2		
SERIES	MW2_GRGID	-3.975948	none	4.1035	none	4		
SERIES	MW2_GRGID	4.9468749	none	12.179	none	7		
THEIS	Q-Well2	14.98794	log	14.988	log	3750	-193	

DD-Well8	Q-Well2	09/01/2010 00:00:00 | 10/24/2010 00:00:00

SeriesSEEfileNAME: SeriesSee.V1.30.xlam
SourceBOOK: all_wells_25Apr23_offset.xlsm
PESTmodule: SSmodule_WLmodel.SerSee
ULreferenceDATA: C3

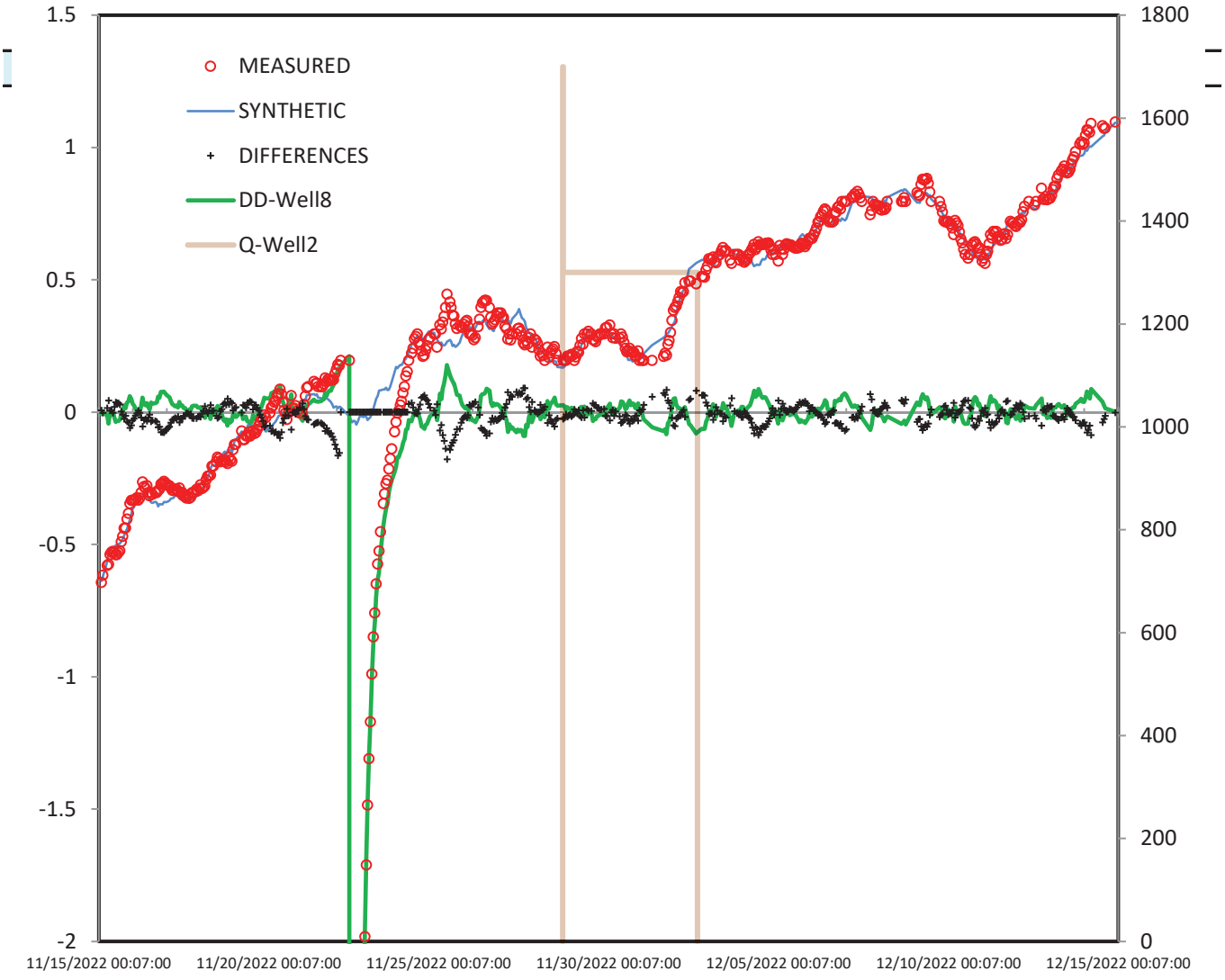

RMS = 0.1019

VIEW:

RMS Expected:	0.0030	Maximum:	0.2276
Max Iter:	30	Minimum:	-0.387
Time Begin:	01/23/2023 14:24	Average:	-0.0362
Time End:	02/22/2023 14:24	Std. Dev.:	0.0916
Interval:	0:30:00	Count:	1433

Measured: MW3

Transform	Time Series	Coeff.1	Est	Coeff.2	Est	Coeff.3	Coeff.4	Coeff.5
Slope+Offset		0	fixed	2.1422	none			
SERIES	MW1_GRGID	0.0865878	none	0.287	none	0.04167		
SERIES	MW1_GRGID	-0.071127	none	0.3552	none	0.08333		
SERIES	MW1_GRGID	0.0353117	none	0.2718	none	0.125		
SERIES	MW1_GRGID	-0.098459	none	0.2638	none	0.25		
SERIES	MW1_GRGID	0.345717	none	-0.1486	none	0.5		
SERIES	MW1_GRGID	0.1989004	none	0.514	none	1		
SERIES	MW1_GRGID	-0.416245	none	0.2166	none	2		
SERIES	MW1_GRGID	-0.019798	none	-0.0975	none	4		
SERIES	MW1_GRGID	-0.073951	none	-0.1634	none	7		
SERIES	Well7	0.1389396	none	0.2321	none	0.04167		
SERIES	Well7	0.1378967	none	0.265	none	0.08333		
SERIES	Well7	0.0696389	none	0.2123	none	0.125		
SERIES	Well7	0.1448095	none	0.2394	none	0.25		
SERIES	Well7	0.5174113	none	0.2037	none	0.5		
SERIES	Well7	0.8619095	none	0.3535	none	1		
SERIES	Well7	0.2592296	none	0.6681	none	2		
SERIES	Well7	-0.004191	none	0.844	none	4		
SERIES	Well7	0.079159	none	0.1066	none	7		
SERIES	MW2_Bing	-0.034911	none	0.2462	none	0.04167		
SERIES	MW2_Bing	-0.090607	none	0.3179	none	0.08333		
SERIES	MW2_Bing	-0.119178	none	0.3268	none	0.125		
SERIES	MW2_Bing	-0.004161	none	0.136	none	0.25		
SERIES	MW2_Bing	0.1313207	none	-0.5268	none	0.5		
SERIES	MW2_Bing	0.2093317	none	-0.0503	none	1		
SERIES	MW2_Bing	-0.028633	none	0.0688	none	2		
SERIES	MW2_Bing	0.0992781	none	0.3503	none	4		
SERIES	MW2_Bing	0.8373366	none	0.1648	none	7		
THEIS	Q-Well4	1.00E+04	log	0.1	log	2850	193	

DD-MW3 | Q-Well4 | 09/01/2010 00:00:00 | 10/24/2010 00:00:00

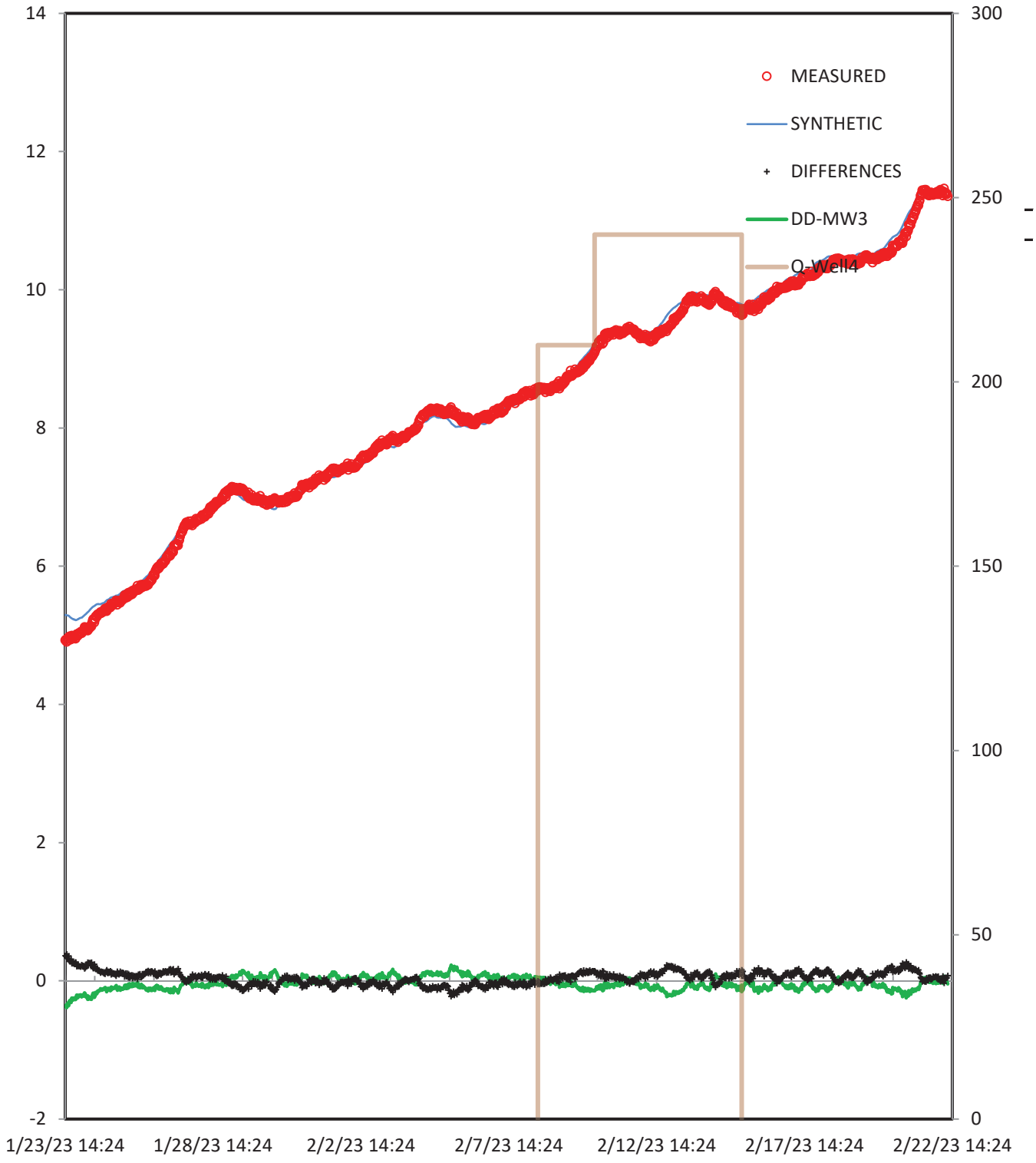

RMS = 0.0840

VIEW:

RMS Expected:	0.0030	Maximum:	0.3952
Max Iter:	30	Minimum:	-0.8343
Time Begin:	01/23/2023 14:24	Average:	-0.039
Time End:	02/22/2023 14:24	Std. Dev.:	0.1493
Interval:	0:30:00	Count:	1432

Measured: MW6

Transform	Time Series	Coeff.1	Est	Coeff.2	Est	Coeff.3	Coeff.4	Coeff.5
Slope+Offset		**0**	**fixed**	-3.392	none			
SERIES	MW1_GRGID	0.0555351	none	0.5975	none	0.04167		
SERIES	MW1_GRGID	0.0770802	none	0.3053	none	0.08333		
SERIES	MW1_GRGID	0.0032359	none	0.171	none	0.125		
SERIES	MW1_GRGID	0.503247	none	0.0692	none	0.25		
SERIES	MW1_GRGID	0.7752665	none	0.0116	none	0.5		
SERIES	MW1_GRGID	-1.270009	none	-0.054	none	1		
SERIES	MW1_GRGID	-0.121853	none	-0.0661	none	2		
SERIES	MW1_GRGID	-0.157089	none	0.1557	none	4		
SERIES	MW1_GRGID	0.235118	none	1.1842	none	7		
SERIES	Well7	0.2868699	none	0.2499	none	0.04167		
SERIES	Well7	0.4194743	none	0.4559	none	0.08333		
SERIES	Well7	0.3455408	none	0.5801	none	0.125		
SERIES	Well7	0.7314994	none	0.1481	none	0.25		
SERIES	Well7	1.1873942	none	-0.2151	none	0.5		
SERIES	Well7	-0.91846	none	0.5155	none	1		
SERIES	Well7	-0.059558	none	-0.2281	none	2		
SERIES	Well7	0.0503084	none	-0.0403	none	4		
SERIES	Well7	-1.255321	none	-3.1905	none	7		
SERIES	MW2_Bing	-0.079629	none	0.2059	none	0.04167		
SERIES	MW2_Bing	0.169711	none	-0.0077	none	0.08333		
SERIES	MW2_Bing	0.01055	none	0.053	none	0.125		
SERIES	MW2_Bing	-0.127985	none	0.2005	none	0.25		
SERIES	MW2_Bing	0.3186347	none	0.9959	none	0.5		
SERIES	MW2_Bing	0.0752024	none	0.5256	none	1		
SERIES	MW2_Bing	1.0060494	none	0.4352	none	2		
SERIES	MW2_Bing	-0.100689	none	-0.3688	none	4		
SERIES	MW2_Bing	2.6328022	none	-4.1423	none	7		
THEIS	Q-Well4	10000	log	0.5	log	1300	193	

DD-MW6 | Q-Well4 | 09/01/2010 00:00:00 | 10/24/2010 00:00:00

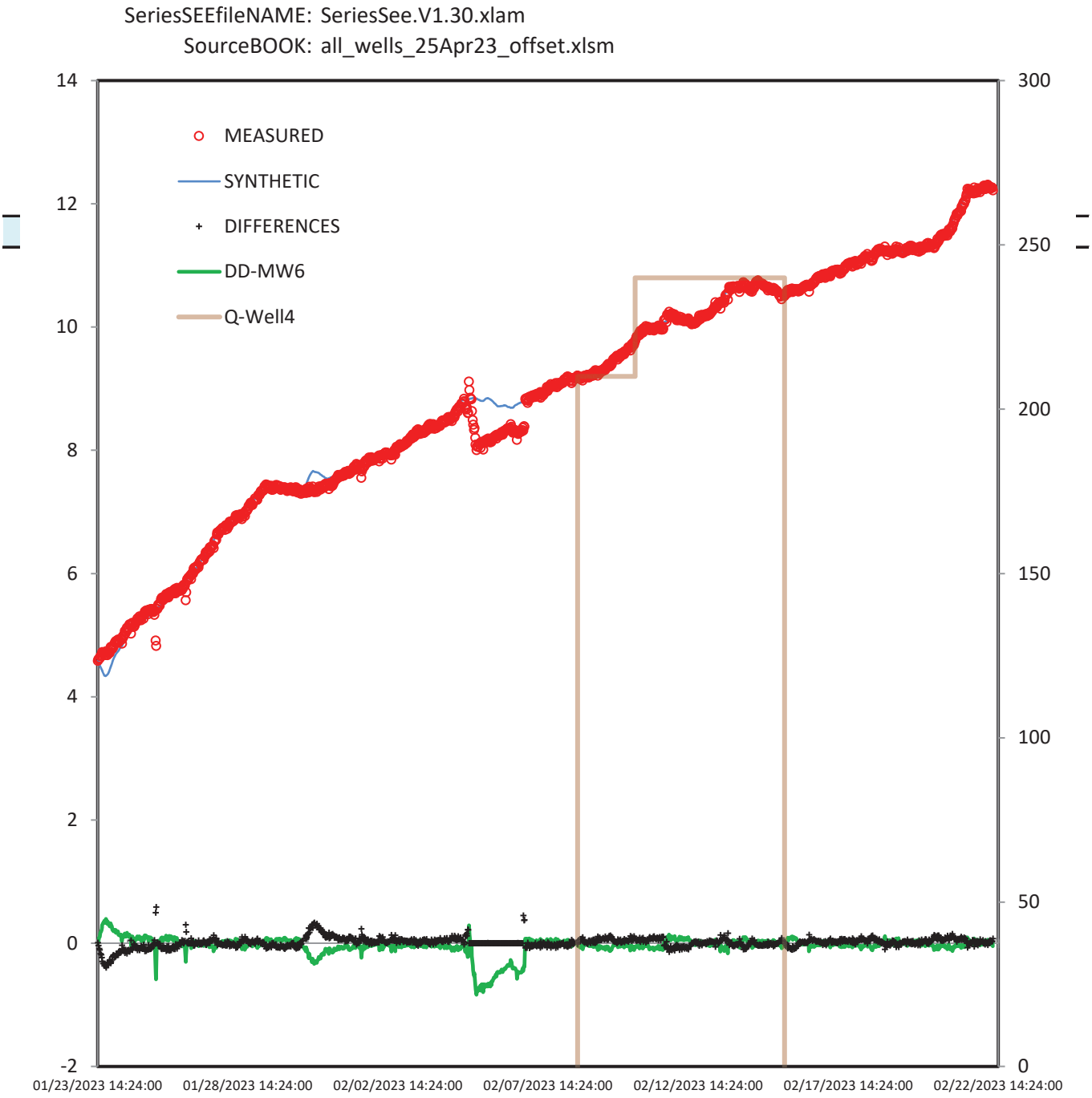

RMS = 0.0861

VIEW:

RMS Expected:	0.0030	Maximum:	0.1974
Max Iter:	30	Minimum:	-0.2182
Time Begin:	01/30/2023 15:30	Average:	-9E-07
Time End:	02/22/2023 08:55	Std. Dev.:	0.0864
Interval:	0:30:00	Count:	148

Measured: Well1

Transform	Time Series		Coeff.1	Est	Coeff.2	Est	Coeff.3	Coeff.4	Coeff.5
Slope+Offset			**0**	**fixed**	-4.6661	none			
SERIES	Well7		0.2830778	none	0.044	none	0.04167		
SERIES	Well7		0.2830776	none	0.0439	none	0.08333		
SERIES	Well7		0.2830776	none	0.044	none	0.125		
SERIES	Well7		0.2830778	none	0.0439	none	0.25		
SERIES	Well7		0.2830778	none	0.0439	none	0.5		
SERIES	Well7		0.2830793	none	0.0439	none	1		
SERIES	Well7		0.2830845	none	0.0439	none	2		
SERIES	Well7		0.283094	none	0.044	none	4		
SERIES	Well7		0.2831096	none	0.044	none	7		
THEIS		Q-Well4	1.00E+02	log	0.01	log	2230	-193	

DD-Well1

Q-Well4

09/01/2010 00:00:00 | 10/24/2010 00:00:00

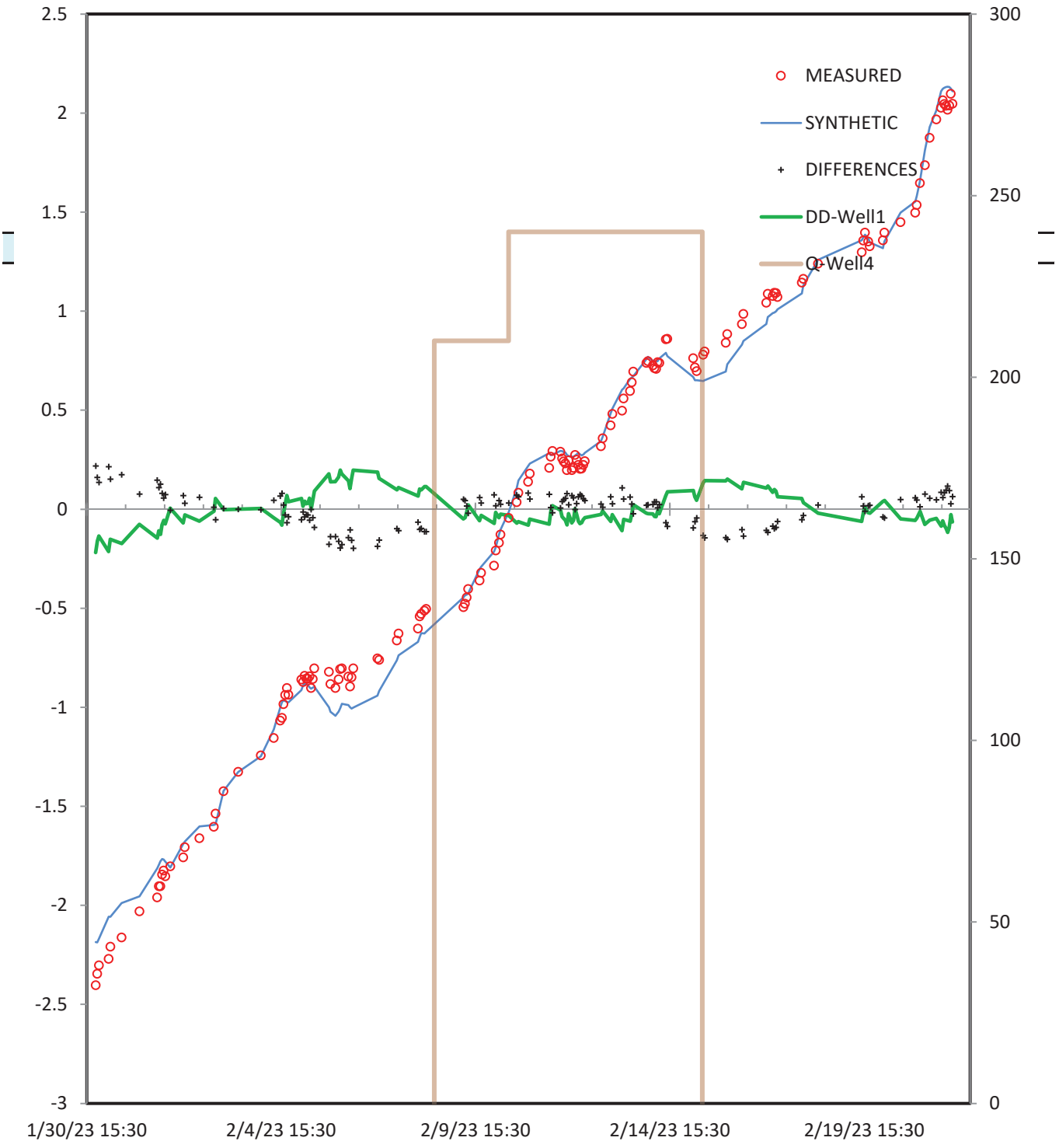

RMS = 0.3538

VIEW:

RMS Expected:	0.0030	Maximum:	0.8823
Max Iter:	30	Minimum:	-0.9944
Time Begin:	03/15/2022 07:49	Average:	-5E-07
Time End:	04/15/2022 07:49	Std. Dev.:	0.354
Interval:	0:30:00	Count:	570

Measured: Well9

Transform	Time Series	Coeff.1	Est	Coeff.2	Est	Coeff.3	Coeff.4	Coeff.5
Slope+Offset		**0**	**fixed**	-3.2172	none			
SERIES	Well8	0.0243547	none	5.1031	none	0.04167		
SERIES	Well8	0.0243547	none	5.1031	none	0.08333		
SERIES	Well8	0.0243486	none	5.1031	none	0.125		
SERIES	Well8	0.0243234	none	5.1031	none	0.25		
SERIES	Well8	0.0242886	none	5.1031	none	0.5		
SERIES	Well8	0.0243	none	5.1031	none	1		
SERIES	Well8	0.0243227	none	5.1031	none	2		
SERIES	Well8	0.0243328	none	5.1031	none	4		
SERIES	Well8	0.0242954	none	5.1031	none	7		
SERIES	Well7	0.022829	none	5.1031	none	0.04167		
SERIES	Well7	0.0230997	none	5.1031	none	0.08333		
SERIES	Well7	0.0231416	none	5.1031	none	0.125		
SERIES	Well7	0.0233964	none	5.1031	none	0.25		
SERIES	Well7	0.0235534	none	5.1031	none	0.5		
SERIES	Well7	0.0236073	none	5.1031	none	1		
SERIES	Well7	0.0236657	none	5.1031	none	2		
SERIES	Well7	0.0236658	none	5.1031	none	4		
SERIES	Well7	0.0236291	none	5.1031	none	7		
THEIS	Q-Well5	1.00E+04	log	0.1	log	6100	-193	

DD-Well9 | Q-Well5 | 09/01/2010 00:00:00 | 10/24/2010 00:00:00

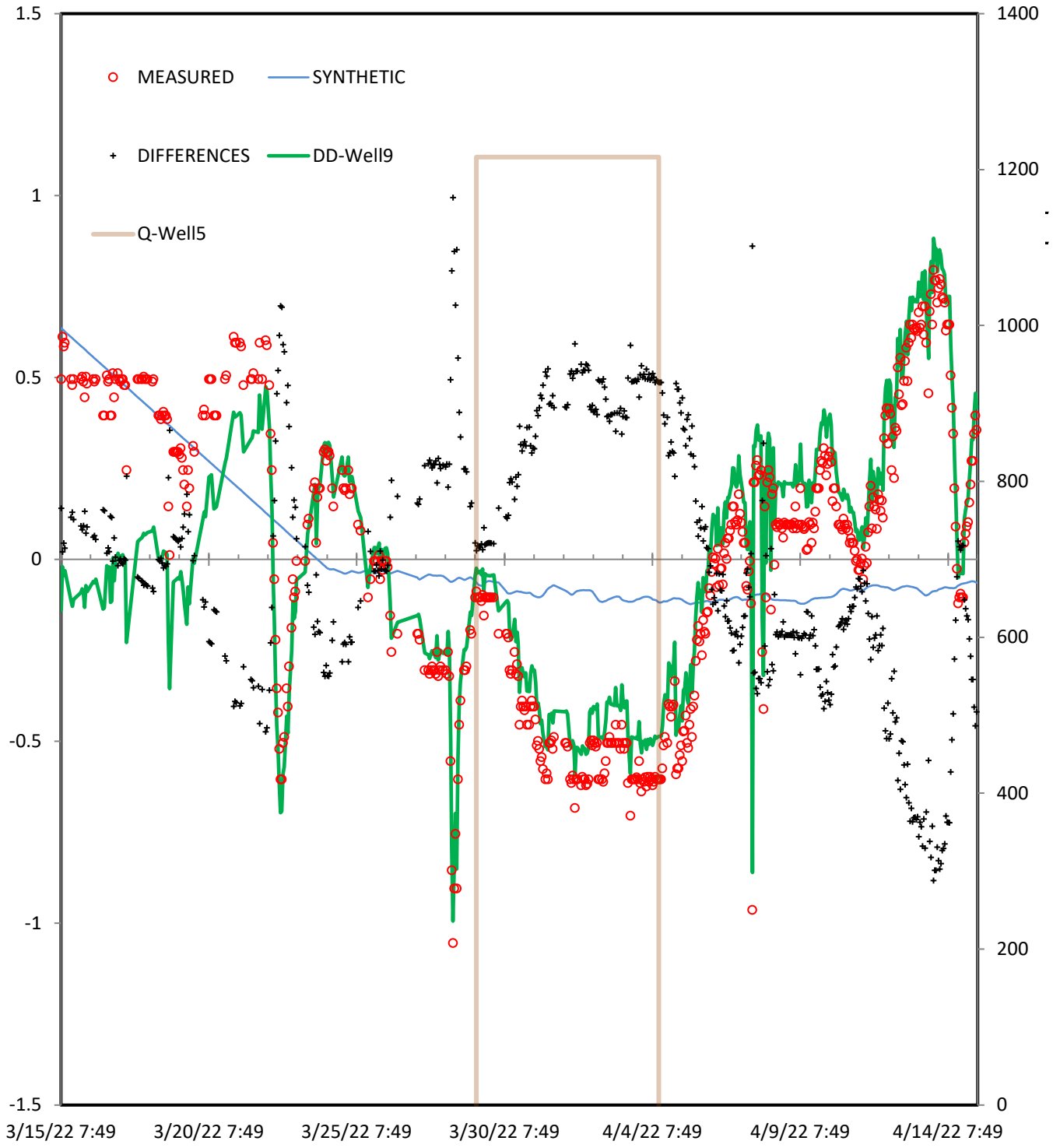

RMS = 0.1107

VIEW:

RMS Expected:	0.0030	Maximum:	0.4421
Max Iter:	30	Minimum:	-1.0007
Time Begin:	01/10/2023 13:59	Average:	-0.1666
Time End:	02/21/2023 14:51	Std. Dev.:	0.25
Interval:	0:30:00	Count:	2017

Measured: MW1_GRGID

Transform	Time Series	Coeff.1	Est	Coeff.2	Est	Coeff.3	Coeff.4	Coeff.5
Slope+Offset		**0**	**fixed**	-0.3265	none			
SERIES	Well7	-2.70E-02	none	-0.7155	none	0.04167		
SERIES	Well7	-0.013554	none	-0.7363	none	0.08333		
SERIES	Well7	-3.18E-02	none	-0.7377	none	0.125		
SERIES	Well7	-6.91E-02	none	-0.759	none	0.25		
SERIES	Well7	-1.34E-01	none	-0.7616	none	0.5		
SERIES	Well7	-0.120152	none	-0.7913	none	1		
SERIES	Well7	0.0863698	none	-0.8705	none	2		
SERIES	Well7	2.81E-01	none	-1.1695	none	4		
SERIES	Well7	4.43E-01	none	-1.0998	none	7		
SERIES	MW3	-4.50E-02	none	-0.9748	none	0.04167		
SERIES	MW3	-5.90E-02	none	-1.0173	none	0.08333		
SERIES	MW3	-3.90E-02	none	-1.091	none	0.125		
SERIES	MW3	-5.51E-02	none	-1.1275	none	0.25		
SERIES	MW3	-1.40E-01	none	-1.0567	none	0.5		
SERIES	MW3	0.1063055	none	-0.8637	none	1		
SERIES	MW3	0.3409492	none	-0.4524	none	2		
SERIES	MW3	1.86E-01	none	-1.3265	none	4		
SERIES	MW3	-0.041768	none	-0.7557	none	7		
THEIS	Q-Well6	5.92E+04	log	0.0198	log	872	-193	

DD-MW1_GRGID | Q-Well6 | 09/01/2010 00:00:00 | 10/24/2010 00:00:00

RMS = 0.1918

VIEW:

RMS Expected:	0.0030	Maximum:	0.3914
Max Iter:	30	Minimum:	-0.6923
Time Begin:	01/12/2023 15:49	Average:	-0.1377
Time End:	02/21/2023 14:51	Std. Dev.:	0.3001
Interval:	0:30:00	Count:	1917

Measured: MW2_Bing

Transform	Time Series	Coeff.1	Est	Coeff.2	Est	Coeff.3	Coeff.4	Coeff.5
Slope+Offset		**0**	**fixed**	0.6529	none			
SERIES	MW3	0.0346222	none	-0.0399	none	0.04167		
SERIES	MW3	0.032518	none	-0.028	none	0.08333		
SERIES	MW3	0.030061	none	-0.0435	none	0.125		
SERIES	MW3	0.0231297	none	-0.0443	none	0.25		
SERIES	MW3	0.0120943	none	-0.063	none	0.5		
SERIES	MW3	0.0207184	none	-0.0752	none	1		
SERIES	MW3	0.0400174	none	-0.0889	none	2		
SERIES	MW3	-0.01871	none	-0.0975	none	4		
SERIES	MW3	0.0086988	none	-0.076	none	7		
SERIES	Well7	0.0283808	none	-0.0095	none	0.04167		
SERIES	Well7	0.027523	none	-0.0071	none	0.08333		
SERIES	Well7	0.0280435	none	-0.0123	none	0.125		
SERIES	Well7	0.0269926	none	-0.0194	none	0.25		
SERIES	Well7	0.0248279	none	-0.0304	none	0.5		
SERIES	Well7	0.023155	none	-0.0348	none	1		
SERIES	Well7	0.0476986	none	-0.0417	none	2		
SERIES	Well7	0.0879098	none	-0.0462	none	4		
SERIES	Well7	0.239984	none	-0.0381	none	7		
THEIS	Q-Well6	2471.1157	log	0.0085	log	5640	-193	

DD-MW2_Bing	Q-Well6	09/01/2010 00:00:00 | 10/24/2010 00:00:00

SeriesSEEfileNAME: SeriesSee.V1.30.xlam
SourceBOOK: all_wells_25Apr23_offset.xlsm
PESTmodule: SSmodule_WLmodel.SerSee
ULreferenceDATA: C3

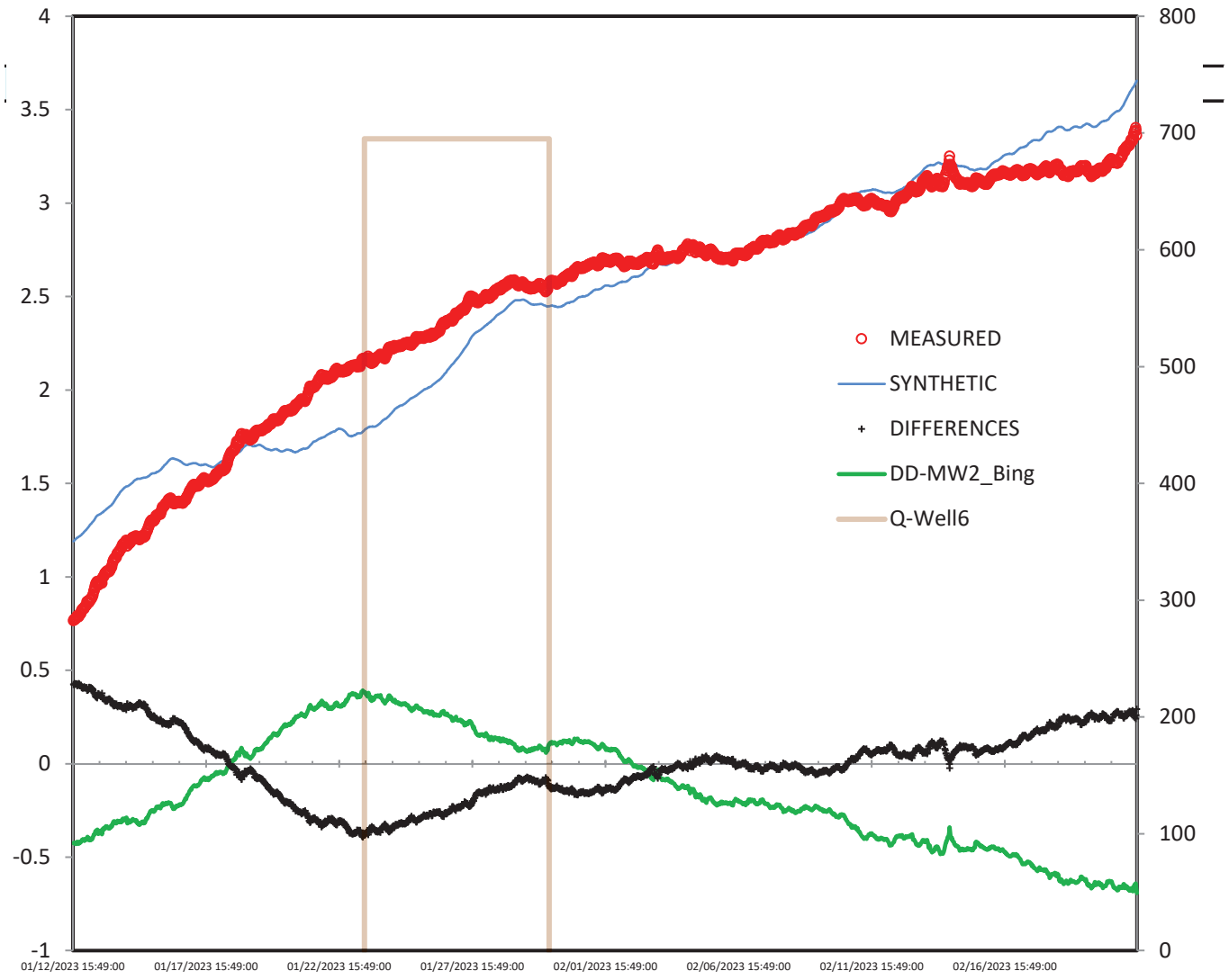

RMS = 0.1489

VIEW:

RMS Expected:	0.0030	Maximum:	0.0937
Max Iter:	30	Minimum:	-1.5282
Time Begin:	01/17/2023 15:13	Average:	-0.4932
Time End:	02/21/2023 14:24	Std. Dev.:	0.3602
Interval:	0:30:00	Count:	1678

Measured: MW2_GRGID

Transform	Time Series	Coeff.1	Est	Coeff.2	Est	Coeff.3	Coeff.4	Coeff.5
Slope+Offset		**0**	**fixed**	-2.6924	none			
SERIES	MW3	-0.18135	none	0.257	none	0.04167		
SERIES	MW3	-0.1182	none	0.6561	none	0.08333		
SERIES	MW3	-0.078063	none	0.0644	none	0.125		
SERIES	MW3	0.0171187	none	0.3489	none	0.25		
SERIES	MW3	0.9169354	none	0.1746	none	0.5		
SERIES	MW3	-0.230454	none	1.4354	none	1		
SERIES	MW3	-0.250776	none	-0.1287	none	2		
SERIES	MW3	-0.646771	none	1.3391	none	4		
SERIES	MW3	0.9172536	none	2.3313	none	7		
SERIES	Well7	0.0017053	none	0.378	none	0.04167		
SERIES	Well7	-0.149065	none	0.2386	none	0.08333		
SERIES	Well7	-0.21712	none	0.253	none	0.125		
SERIES	Well7	0.1269605	none	0.579	none	0.25		
SERIES	Well7	-0.122125	none	0.5095	none	0.5		
SERIES	Well7	-0.130287	none	0.8243	none	1		
SERIES	Well7	1.0747593	none	0.569	none	2		
SERIES	Well7	0.0033242	none	-0.668	none	4		
SERIES	Well7	0.3059139	none	3.3561	none	7		
THEIS	Q-Well6	3.71E+03	log	0.0113	log	3323	-193	

DD-MW2_GRGID | Q-Well6 | 09/01/2010 00:00:00 | 10/24/2010 00:00:00

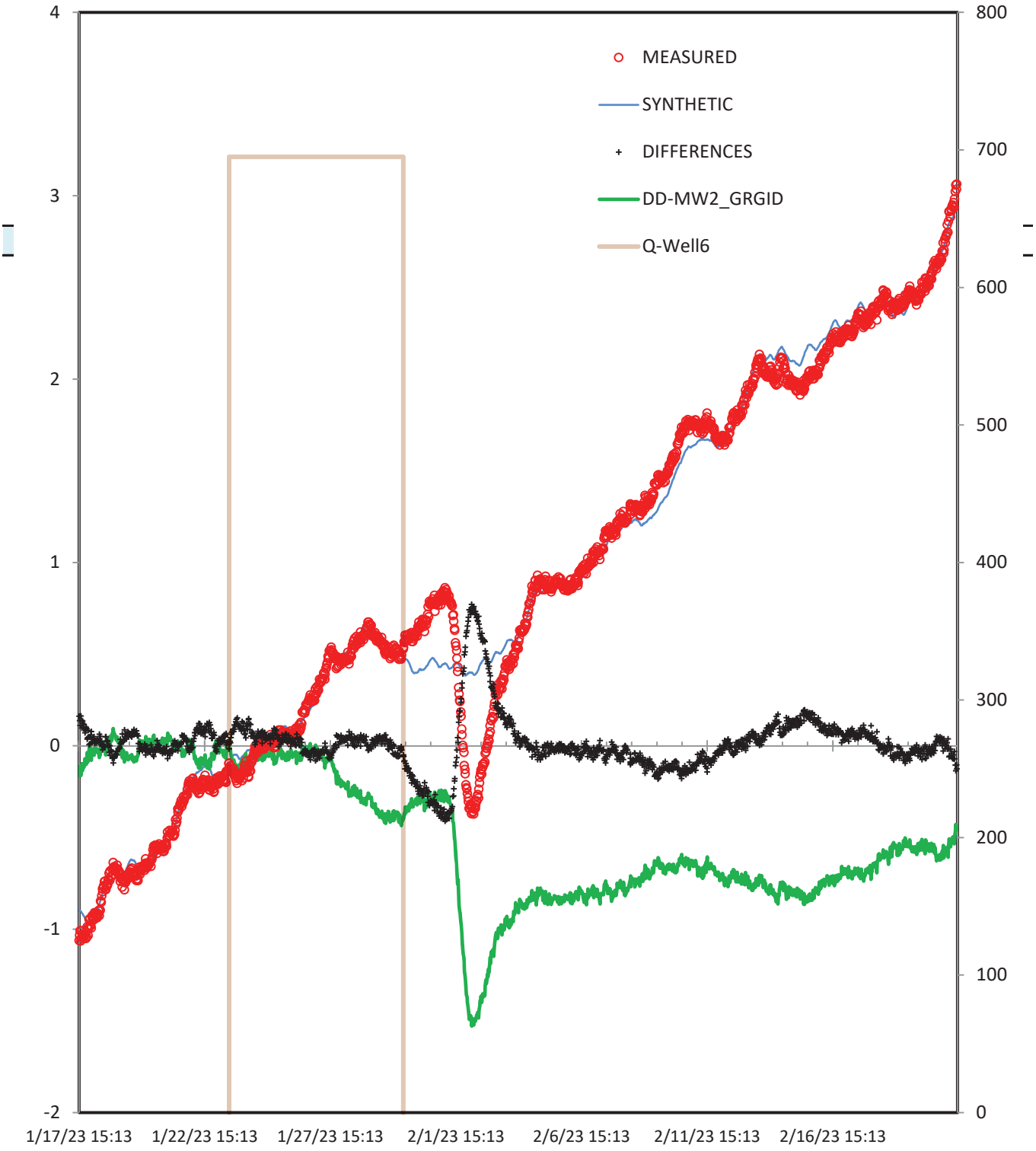

RMS = 0.0530

VIEW:

RMS Expected:	0.0030	Maximum:	0.1335
Max Iter:	30	Minimum:	-0.1736
Time Begin:	01/11/2023 14:24	Average:	-0.0008
Time End:	02/22/2023 14:24	Std. Dev.:	0.0513
Interval:	0:30:00	Count:	2009

Measured: Sweetwater

Transform	Time Series	Coeff.1	Est	Coeff.2	Est	Coeff.3	Coeff.4	Coeff.5
Slope+Offset		**0**	**fixed**	0.4648	none			
SERIES	MW3	-0.206023	none	-0.5674	none	0.04167		
SERIES	MW3	-0.082495	none	-0.4818	none	0.08333		
SERIES	MW3	-0.096735	none	0.1493	none	0.125		
SERIES	MW3	-0.099082	none	-0.2966	none	0.25		
SERIES	MW3	0.1877586	none	-2.8628	none	0.5		
SERIES	MW3	0.2390836	none	-12.922	none	1		
SERIES	MW3	0.2980871	none	-5.3815	none	2		
SERIES	MW3	0.3944909	none	-1.0201	none	4		
SERIES	MW3	-0.412166	none	0.5945	none	7		
SERIES	Well7	0.0339473	none	-0.1115	none	0.04167		
SERIES	Well7	0.7065824	none	0.0235	none	0.08333		
SERIES	Well7	-0.092969	none	-0.4713	none	0.125		
SERIES	Well7	-0.150696	none	-1.626	none	0.25		
SERIES	Well7	1.0320073	none	-0.5986	none	0.5		
SERIES	Well7	0.2471426	none	9.202	none	1		
SERIES	Well7	0.4468705	none	1.7865	none	2		
SERIES	Well7	-1.432882	none	-6.8128	none	4		
SERIES	Well7	-0.711554	none	-14.49	none	7		
THEIS	Q-Well6	3000	log	0.0582	log	4071	-193	

DD-Sweetwater | Q-Well6 | 09/01/2010 00:00:00 | 10/24/2010 00:00:00

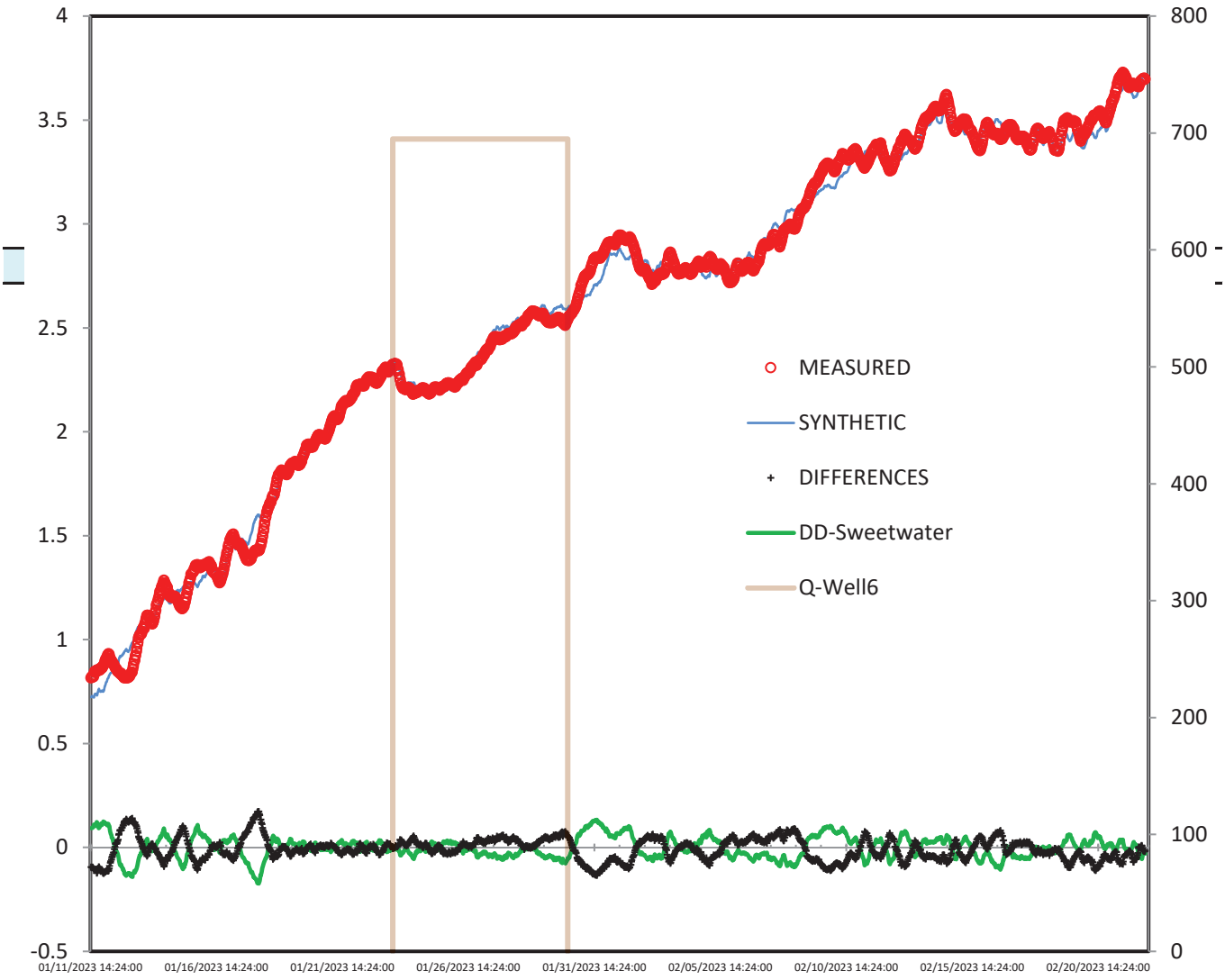

RMS = 0.1315

VIEW:

RMS Expected:	0.0030	Maximum:	0.239
Max Iter:	30	Minimum:	-1.4469
Time Begin:	01/01/2023 13:59	Average:	-0.476
Time End:	02/20/2023 13:38	Std. Dev.:	0.5727
Interval:	0:30:00	Count:	2399

Measured: Well5

Transform	Time Series	Coeff.1	Est	Coeff.2	Est	Coeff.3	Coeff.4	Coeff.5
Slope+Offset		**0**	**fixed**	-3.9971	none			
SERIES	MW3	0.009936	none	0.3463	none	0.04167		
SERIES	MW3	0.260884	none	0.0338	none	0.08333		
SERIES	MW3	0.1233598	none	-0.1125	none	0.125		
SERIES	MW3	0.0338372	none	######	none	0.25		
SERIES	MW3	-0.395734	none	-1.5212	none	0.5		
SERIES	MW3	0.0027948	none	0.0354	none	1		
SERIES	MW3	-0.004531	none	-0.5093	none	2		
SERIES	MW3	-0.713811	none	0.978	none	4		
SERIES	MW3	1.4271295	none	-1.2151	none	7		
SERIES	Well7	0.5363908	none	######	none	0.04167		
SERIES	Well7	-0.208528	none	######	none	0.08333		
SERIES	Well7	-0.135159	none	0.667	none	0.125		
SERIES	Well7	-0.540575	none	0.2279	none	0.25		
SERIES	Well7	-2.402958	none	######	none	0.5		
SERIES	Well7	0.9030536	none	-0.062	none	1		
SERIES	Well7	1.2366075	none	-0.8827	none	2		
SERIES	Well7	-1.954613	none	-3.0316	none	4		
SERIES	Well7	2.0596333	none	2.5769	none	7		
THEIS	Q-Well6	1332.1148	log	0.0016	log	7200	-193	

DD-Well5 | Q-Well6 | 09/01/2010 00:00:00 | 10/24/2010 00:00:00

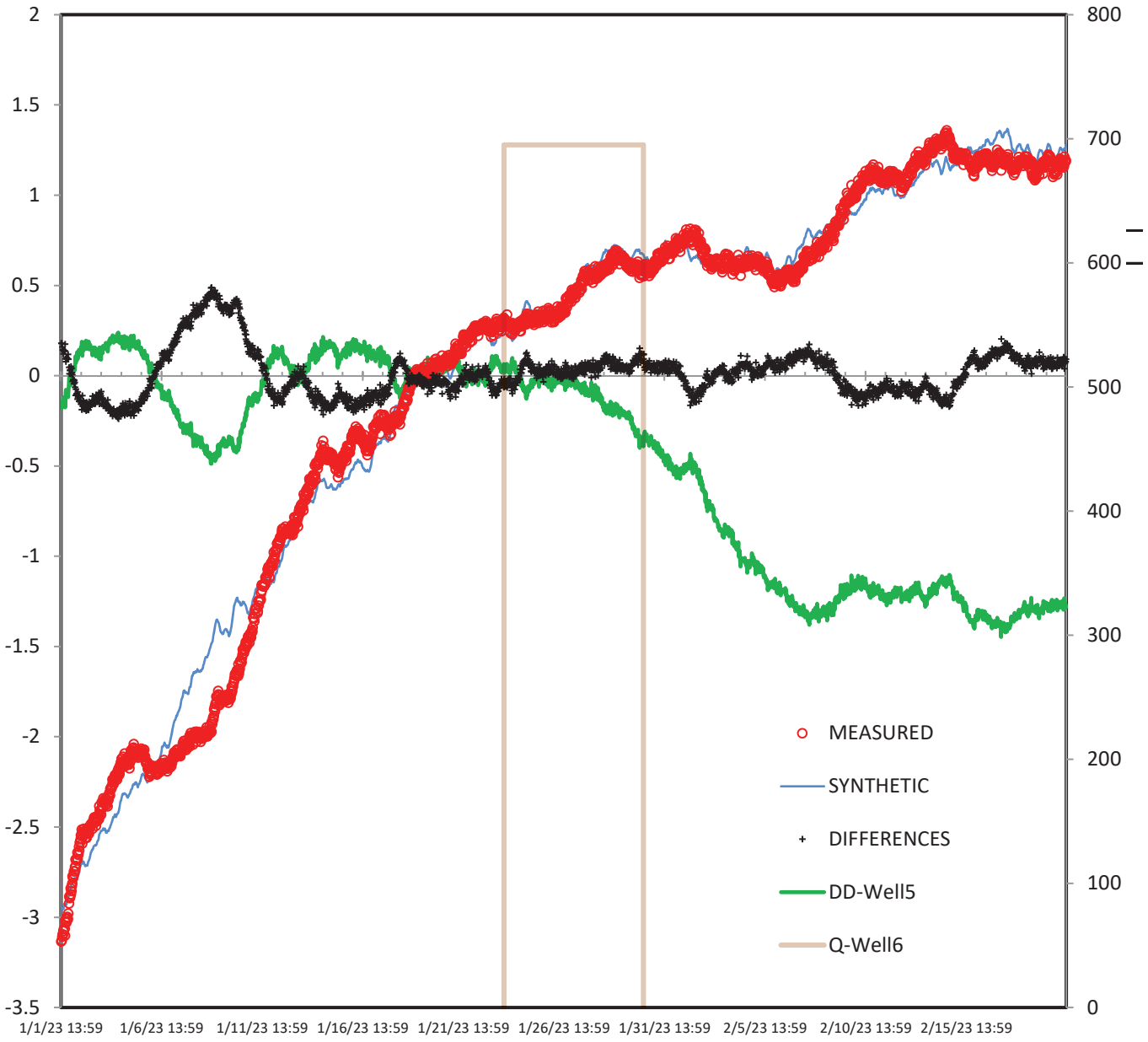

RMS = 0.2920

VIEW:

RMS Expected:	0.0030	Maximum:	0.496
Max Iter:	30	Minimum:	-143.5
Time Begin:	01/16/2023 20:14	Average:	-4.8549
Time End:	02/16/2023 21:08	Std. Dev.:	19.437
Interval:	0:30:00	Count:	628

Measured: Well8

Transform	Time Series	Coeff.1	Est	Coeff.2	Est	Coeff.3	Coeff.4	Coeff.5
Slope+Offset		**0**	**fixed**	4.452	none			
SERIES	MW3	0.0892907	none	4.3847	none	0.04167		
SERIES	MW3	0.0892829	none	4.3852	none	0.08333		
SERIES	MW3	0.0892815	none	4.3851	none	0.125		
SERIES	MW3	0.0892736	none	4.3853	none	0.25		
SERIES	MW3	0.0892431	none	4.3852	none	0.5		
SERIES	MW3	0.0891163	none	4.3853	none	1		
SERIES	MW3	0.0890783	none	4.3854	none	2		
SERIES	MW3	0.0903039	none	4.3855	none	4		
SERIES	MW3	0.0913319	none	4.3854	none	7		
SERIES	Well7	0.090579	none	4.3847	none	0.04167		
SERIES	Well7	0.0905876	none	4.3847	none	0.08333		
SERIES	Well7	0.0905931	none	4.3847	none	0.125		
SERIES	Well7	0.0906365	none	4.3847	none	0.25		
SERIES	Well7	0.0907735	none	4.3848	none	0.5		
SERIES	Well7	0.0910057	none	4.3848	none	1		
SERIES	Well7	0.0911429	none	4.3849	none	2		
SERIES	Well7	0.0918401	none	4.385	none	4		
SERIES	Well7	0.0930542	none	4.3852	none	7		
THEIS	Q-Well6	758.00174	log	0.0038	log	3480	-193	

DD-Well8	Q-Well6	09/01/2010 00:00:00 | 10/24/2010 00:00:00

SeriesSEEfileNAME: SeriesSee.V1.30.xlam
SourceBOOK: all_wells_25Apr23_offset.xlsm

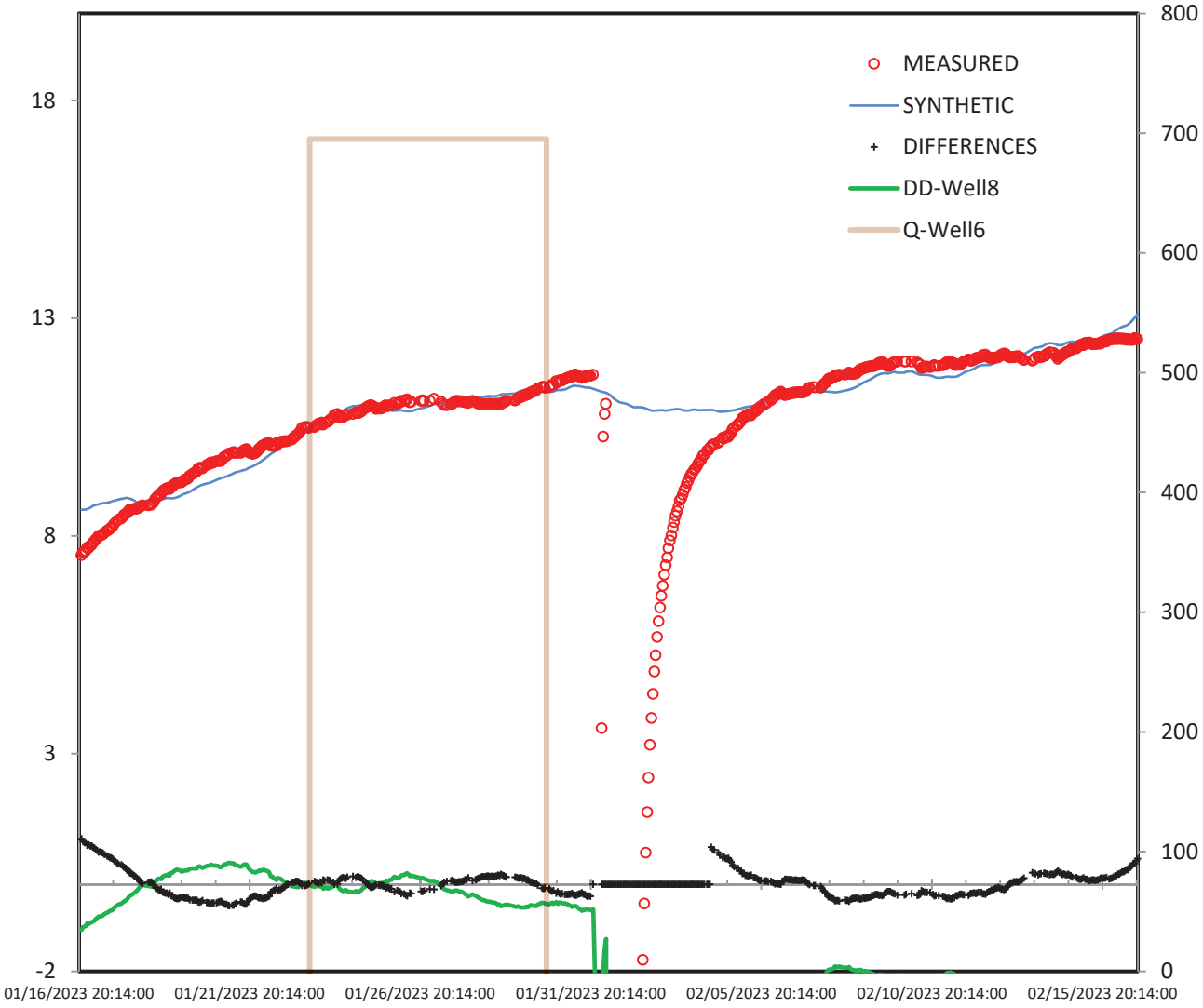

RMS = 0.0874

VIEW:

RMS Expected:	0.0030	Maximum:	0.2067
Max Iter:	30	Minimum:	-0.402
Time Begin:	01/19/2023 01:00	Average:	-0.0082
Time End:	02/01/2023 22:00	Std. Dev.:	0.0869
Interval:	0:30:00	Count:	312

Measured: Well9

Transform	Time Series	Coeff.1	Est	Coeff.2	Est	Coeff.3	Coeff.4	Coeff.5
Slope+Offset		**0**	**fixed**	2.5784	none			
SERIES	MW3	0.116519	none	2.7413	none	0.04167		
SERIES	MW3	0.1310984	none	2.4477	none	0.08333		
SERIES	MW3	-0.365468	none	2.4295	none	0.125		
SERIES	MW3	0.1932391	none	2.5346	none	0.25		
SERIES	MW3	0.1516695	none	0.8618	none	0.5		
SERIES	MW3	-1.381276	none	3.196	none	1		
SERIES	MW3	-0.282933	none	3.798	none	2		
SERIES	MW3	1.6439556	none	4.1678	none	4		
SERIES	MW3	-1.354619	none	2.6047	none	7		
SERIES	Well7	-0.510904	none	2.839	none	0.04167		
SERIES	Well7	0.2959621	none	2.7488	none	0.08333		
SERIES	Well7	0.2931539	none	2.2984	none	0.125		
SERIES	Well7	0.1450747	none	2.4788	none	0.25		
SERIES	Well7	0.7528086	none	3.1413	none	0.5		
SERIES	Well7	1.6187219	none	3.0996	none	1		
SERIES	Well7	0.9328361	none	2.2898	none	2		
SERIES	Well7	2.478087	none	3.6445	none	4		
SERIES	Well7	-0.88606	none	3.1815	none	7		
THEIS	Q-Well6	3000	log	0.02	log	4280	-193	

DD-Well9

Q-Well6

09/01/2010 00:00:00 | 10/24/2010 00:00:00

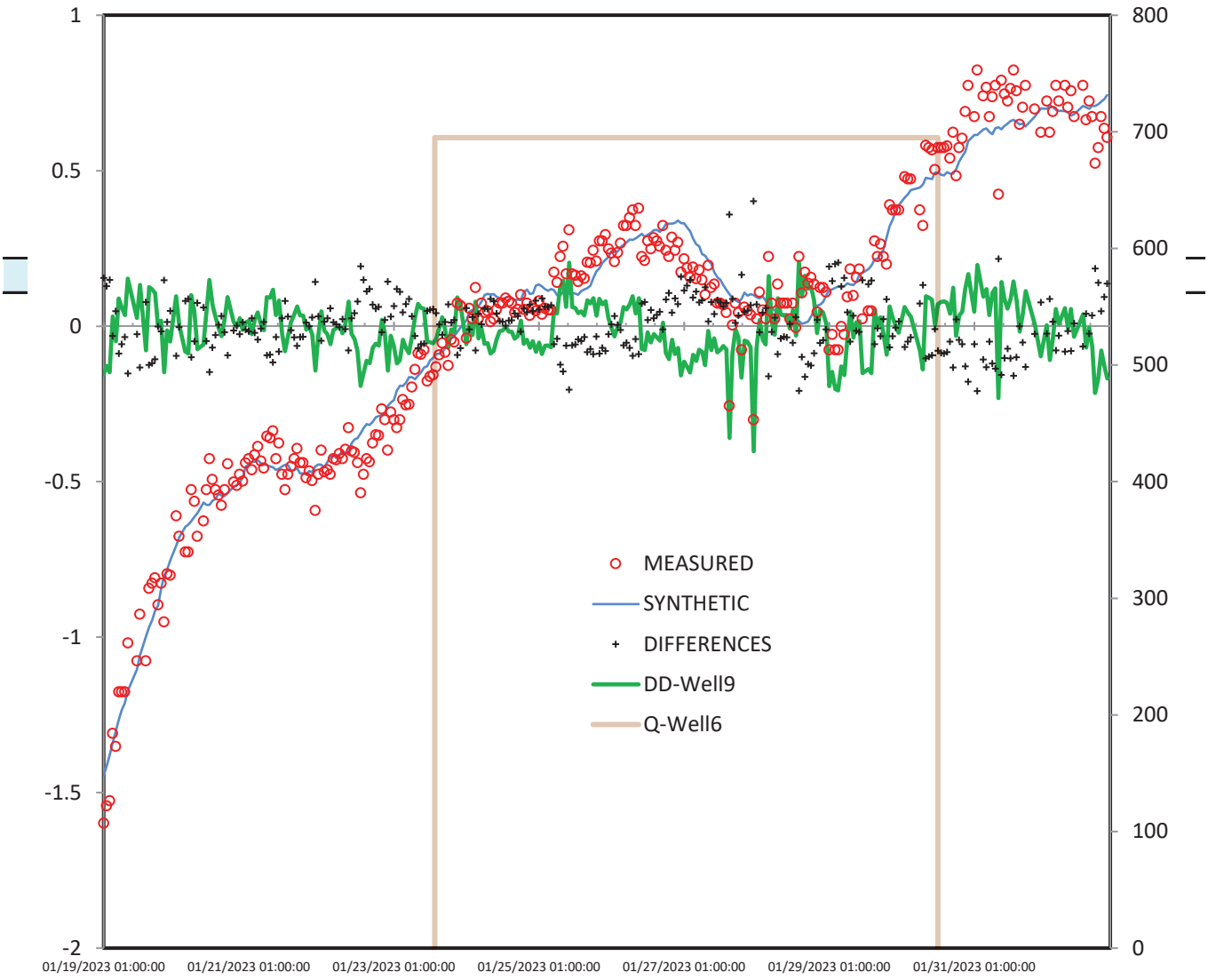

RMS = 0.0429

VIEW:

RMS Expected:	0.0030	Maximum:	0.1262
Max Iter:	30	Minimum:	-0.1108
Time Begin:	12/20/2022 23:48	Average:	0.0006
Time End:	01/19/2023 23:48	Std. Dev.:	0.0429
Interval:	0:30:00	Count:	1439

Measured: MW1_GRGID

Transform	Time Series	Coeff.1	Est	Coeff.2	Est	Coeff.3	Coeff.4	Coeff.5
Slope+Offset		**0**	**fixed**	0.0549	none			
SERIES	MW3	-0.06079	none	1.8229	none	0.04167		
SERIES	MW3	0.244621	none	-0.0009	none	0.08333		
SERIES	MW3	0.6231259	none	0.0366	none	0.125		
SERIES	MW3	0.219942	none	0.4542	none	0.25		
SERIES	MW3	0.4201222	none	0.2474	none	0.5		
SERIES	MW3	-1.121484	none	0.1422	none	1		
SERIES	MW3	0.1336511	none	2.3361	none	2		
SERIES	MW3	-0.127982	none	3.8464	none	4		
SERIES	MW3	-0.232924	none	15.408	none	7		
THEIS	Q-Well8	340.00426	log	1.1638	log	3886	-193	

DD-MW1_GRGID	Q-Well8	09/01/2010 00:00:00 | 10/24/2010 00:00:00

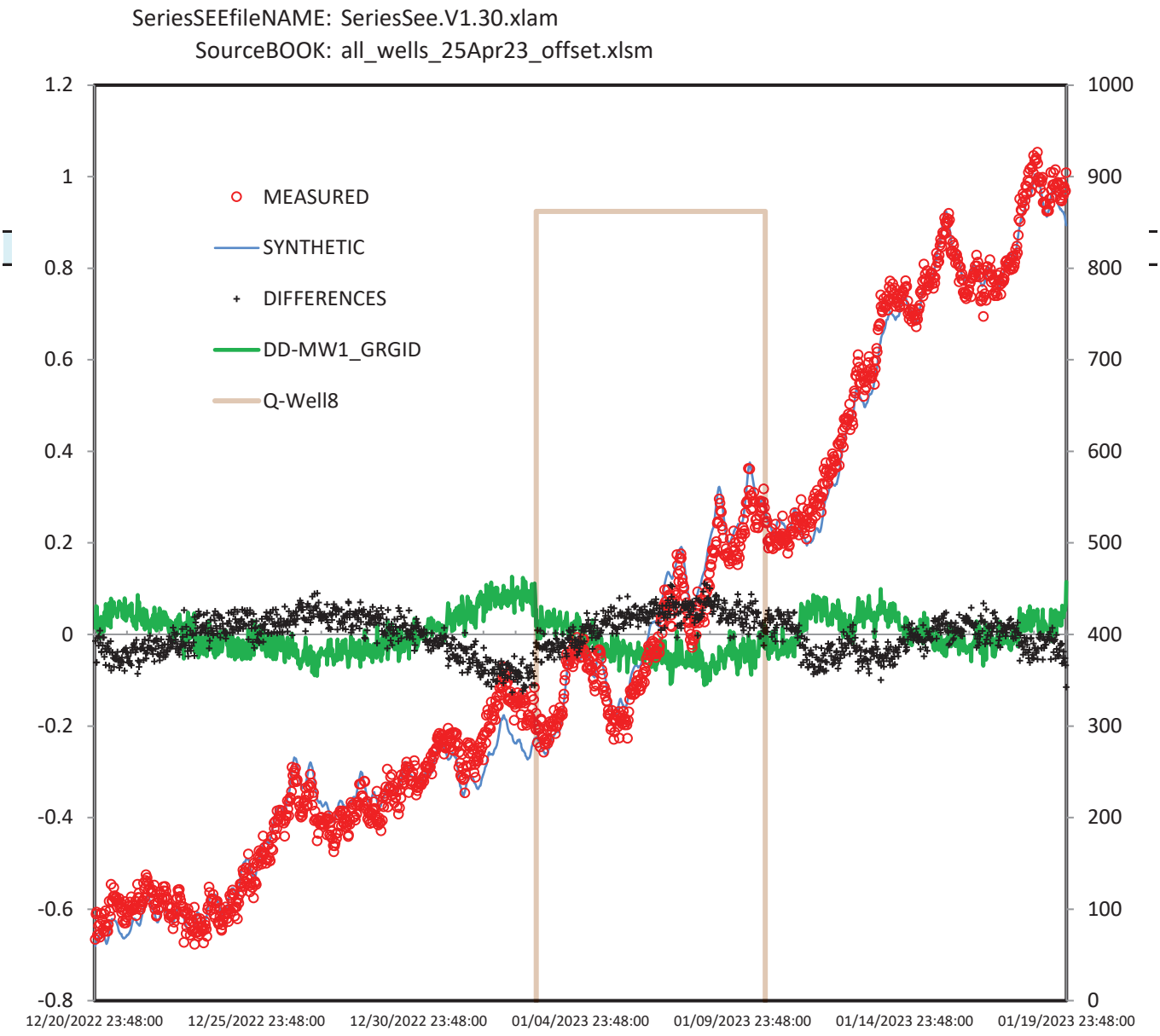

RMS = 0.1073

VIEW:

RMS Expected:	0.0030	Maximum:	0.2372
Max Iter:	30	Minimum:	-4.2214
Time Begin:	12/20/2022 23:28	Average:	-1.2804
Time End:	01/19/2023 23:28	Std. Dev.:	1.4262
Interval:	0:30:00	Count:	1439

Measured: MW2_GRGID

Transform	Time Series	Coeff.1	Est	Coeff.2	Est	Coeff.3	Coeff.4	Coeff.5
Slope+Offset		**0**	**fixed**	0.8396	none			
SERIES	MW3	0.2340194	none	0.0031	none	0.04167		
SERIES	MW3	0.1788391	none	0.0479	none	0.08333		
SERIES	MW3	0.1918916	none	-0.0076	none	0.125		
SERIES	MW3	0.1431637	none	0.047	none	0.25		
SERIES	MW3	0.1466767	none	0.2215	none	0.5		
SERIES	MW3	-0.415826	none	-0.1084	none	1		
SERIES	MW3	-0.30681	none	0.1522	none	2		
SERIES	MW3	0.0556554	none	0.2314	none	4		
SERIES	MW3	-0.221375	none	0.3406	none	7		
THEIS	Q-Well8	6.43E+03	log	0.0011	log	3570	-193	

DD-MW2_GRGID | Q-Well8 | 09/01/2010 00:00:00 | 10/24/2010 00:00:00

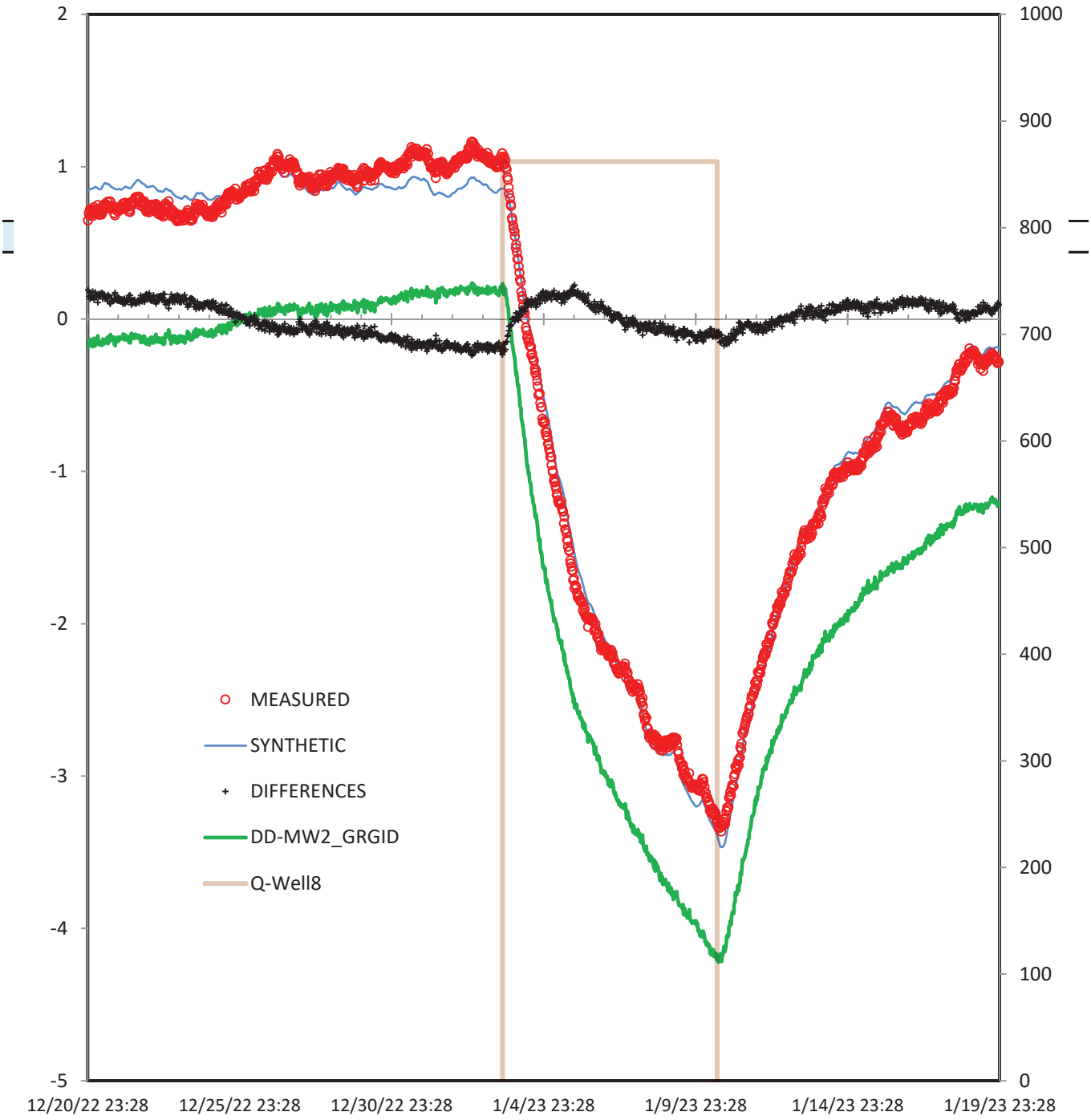

RMS = 0.2914

VIEW:

RMS Expected:	0.0030	Maximum:	0.8082
Max Iter:	30	Minimum:	-10.087
Time Begin:	12/15/2022 23:24	Average:	-0.737
Time End:	01/21/2023 23:24	Std. Dev.:	2.1443
Interval:	0:30:00	Count:	634

Measured: Well1

Transform	Time Series	Coeff.1	Est	Coeff.2	Est	Coeff.3	Coeff.4	Coeff.5
Slope+Offset		**0**	**fixed**	-0.6559	none			
SERIES	MW3	2.3918489	none	2.051	none	0.04167		
SERIES	MW3	3.3757606	none	1.1758	none	0.08333		
SERIES	MW3	-1.124952	none	4.6683	none	0.125		
SERIES	MW3	-1.526573	none	2.5938	none	0.25		
SERIES	MW3	0.1279804	none	1.8031	none	0.5		
SERIES	MW3	-5.866472	none	1.3733	none	1		
SERIES	MW3	-0.189592	none	3.2341	none	2		
SERIES	MW3	5.476025	none	-0.357	none	4		
SERIES	MW3	-1.198518	none	-9.1238	none	7		
THEIS	Q-Well8	1.89E+01	log	0.0001	log	5460	-193	

DD-Well1 | Q-Well8 | 09/01/2010 00:00:00 | 10/24/2010 00:00:00

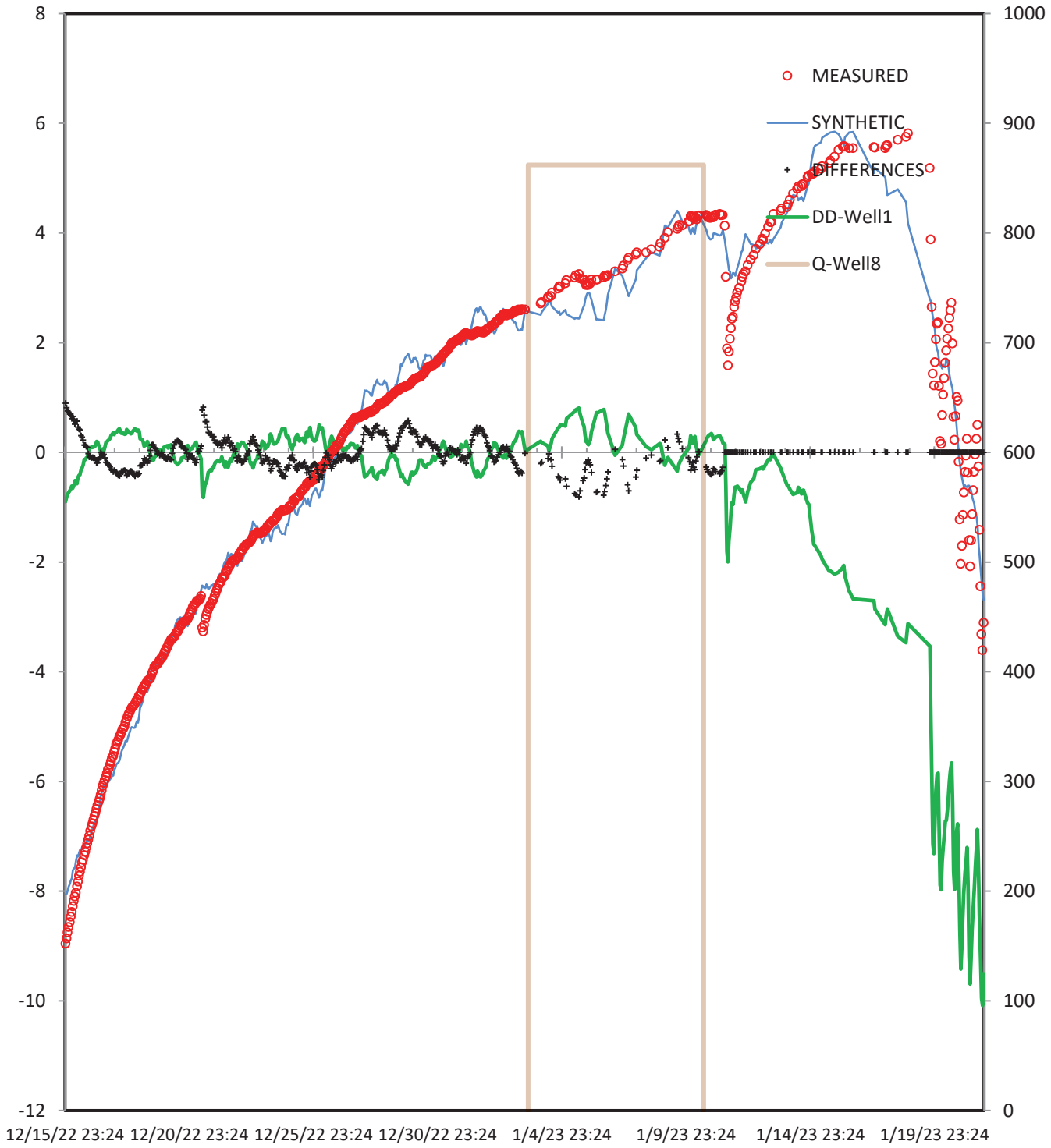

RMS = 0.1614

VIEW:

RMS Expected:	0.0030	Maximum:	0.3859
Max Iter:	30	Minimum:	-0.3098
Time Begin:	12/10/2022 00:26	Average:	0.0007
Time End:	01/17/2023 07:13	Std. Dev.:	0.1617
Interval:	0:30:00	Count:	216

Measured: Well6

Transform	Time Series	Coeff.1	Est	Coeff.2	Est	Coeff.3	Coeff.4	Coeff.5
Slope+Offset		**0**	**fixed**	0.2499	none			
SERIES	MW3	0.5559313	none	-3.5849	none	0.04167		
SERIES	MW3	-0.238764	none	-3.3454	none	0.08333		
SERIES	MW3	0.0605134	none	-3.6415	none	0.125		
SERIES	MW3	-0.254167	none	-3.7103	none	0.25		
SERIES	MW3	0.0094356	none	-3.0201	none	0.5		
SERIES	MW3	-0.098723	none	-3.3311	none	1		
SERIES	MW3	-1.020628	none	-3.7397	none	2		
SERIES	MW3	1.3640295	none	-3.9561	none	4		
SERIES	MW3	-0.162199	none	-4.1507	none	7		
THEIS	Q-Well8	6.03E+04	log	5.809	log	3500	-193	

DD-Well6 | Q-Well8 | 09/01/2010 00:00:00 | 10/24/2010 00:00:00

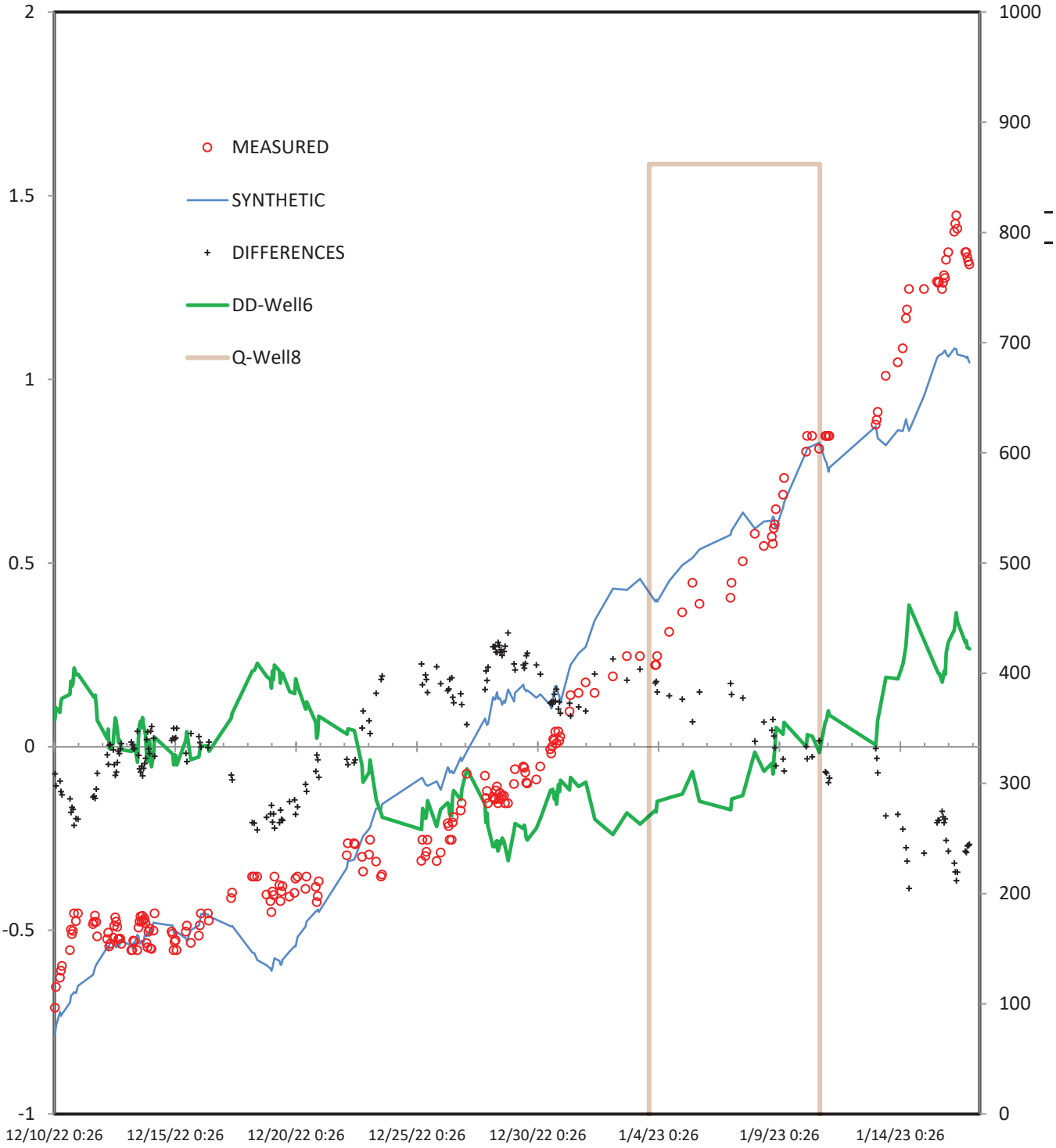

RMS = 0.0512

VIEW:

RMS Expected:	0.0030	Maximum:	0.1458
Max Iter:	30	Minimum:	-0.2638
Time Begin:	12/20/2022 23:48	Average:	-0.03
Time End:	01/19/2023 23:48	Std. Dev.:	0.0701
Interval:	0:30:00	Count:	1440

Measured: Well7

Transform	Time Series	Coeff.1	Est	Coeff.2	Est	Coeff.3	Coeff.4	Coeff.5
Slope+Offset		**0**	**fixed**	-0.6237	none			
SERIES	MW3	0.257037	none	0.0038	none	0.04167		
SERIES	MW3	0.2287848	none	-0.091	none	0.08333		
SERIES	MW3	0.2399593	none	-0.0473	none	0.125		
SERIES	MW3	0.020002	none	-0.1204	none	0.25		
SERIES	MW3	-0.503043	none	-0.1138	none	0.5		
SERIES	MW3	0.3178604	none	-0.1488	none	1		
SERIES	MW3	-0.17447	none	-0.0164	none	2		
SERIES	MW3	0.3320128	none	-0.2091	none	4		
SERIES	MW3	-0.572546	none	-0.1562	none	7		
THEIS	Q-Well8	2.32E+06	log	3E-10	log	9487	-193	

DD-Well7 | Q-Well8 | 09/01/2010 00:00:00 | 10/24/2010 00:00:00

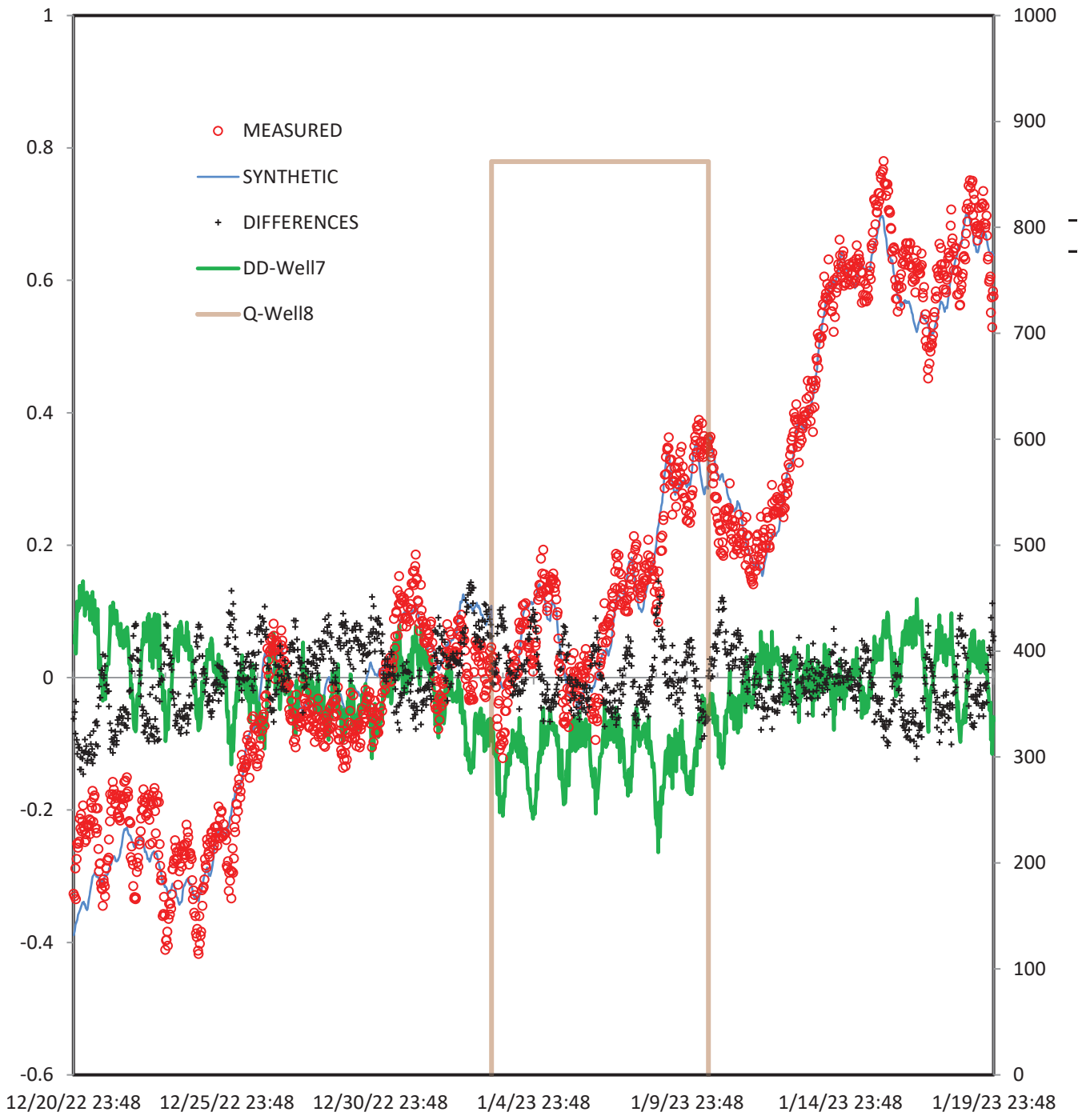

RMS = 0.0219

VIEW:

RMS Expected:	0.0030	Maximum:	0.1515
Max Iter:	30	Minimum:	-0.4561
Time Begin:	10/27/2022 00:08	Average:	-0.0712
Time End:	11/26/2022 00:08	Std. Dev.:	0.0495
Interval:	0:30:00	Count:	1428

Measured: MW1_Bing

Transform	Time Series	Coeff.1	Est	Coeff.2	Est	Coeff.3	Coeff.4	Coeff.5
Slope+Offset		**0**	**fixed**	-1.1231	none			
SERIES	Well7	0.0784019	none	0.6007	none	0.04167		
SERIES	Well7	0.0784019	none	0.6007	none	0.08333		
SERIES	Well7	-2.37E-01	none	0.6146	none	0.125		
SERIES	Well7	-2.11E-01	none	0.5446	none	0.25		
SERIES	Well7	1.22E-01	none	0.4596	none	0.5		
SERIES	Well7	4.61E-01	none	-0.0385	none	1		
SERIES	Well7	1.91E-01	none	-0.7902	none	2		
SERIES	Well7	5.35E-01	none	1.1705	none	4		
SERIES	Well7	-9.68E-01	none	2.7471	none	7		
SERIES	MW3	-1.34E-01	none	0.2877	none	0.04167		
SERIES	MW3	-1.34E-01	none	0.2877	none	0.08333		
SERIES	MW3	1.78E-01	none	0.5025	none	0.125		
SERIES	MW3	7.21E-02	none	0.2425	none	0.25		
SERIES	MW3	-2.62E-01	none	0.7187	none	0.5		
SERIES	MW3	4.08E-01	none	0.5222	none	1		
SERIES	MW3	2.93E-01	none	0.9616	none	2		
SERIES	MW3	-3.78E-01	none	0.8285	none	4		
SERIES	MW3	4.54E-03	none	0.5762	none	7		
THEIS	Q-Well9	1.35E+05	log	0.0156	log	6000	-193	

DD-MW1_Bing | Q-Well9 | 09/01/2010 00:00:00 | 10/24/2010 00:00:00

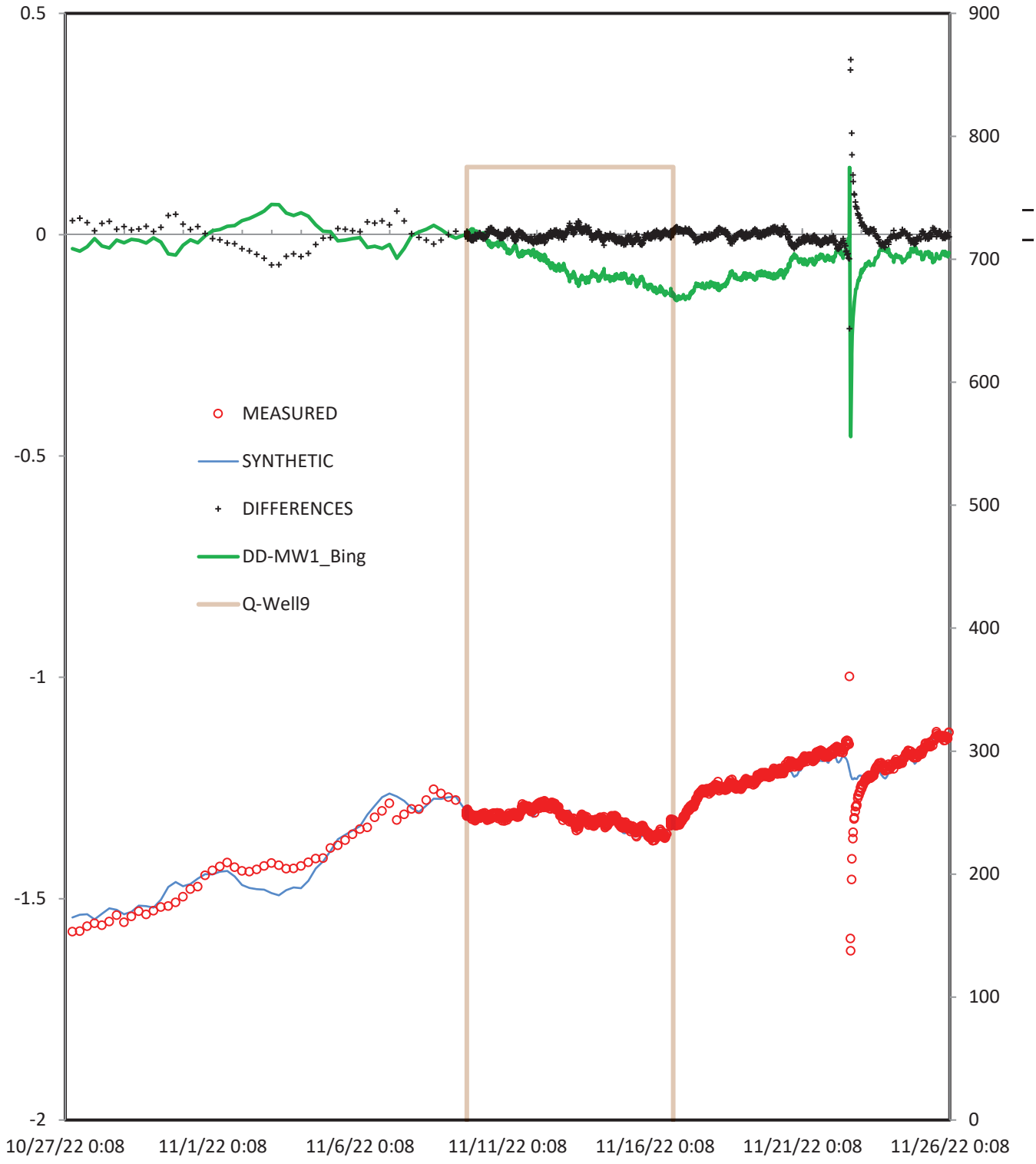

RMS = 0.2615

VIEW:

RMS Expected:	0.0030	Maximum:	0.0964
Max Iter:	30	Minimum:	-0.8904
Time Begin:	10/27/2022 00:08	Average:	-0.1544
Time End:	11/26/2022 00:08	Std. Dev.:	0.2361
Interval:	0:30:00	Count:	443

Measured: MW1_GRGID

Transform	Time Series	Coeff.1	Est	Coeff.2	Est	Coeff.3	Coeff.4	Coeff.5
Slope+Offset		**0**	**fixed**	0.9939	none			
SERIES	Well7	3.91E-01	none	0.2535	none	0.04167		
SERIES	Well7	1.33E-01	none	0.5214	none	0.08333		
SERIES	Well7	-4.43E-01	none	0.2319	none	0.125		
SERIES	Well7	3.90E-01	none	-0.7038	none	0.25		
SERIES	Well7	6.35E-01	none	0.3789	none	0.5		
SERIES	Well7	4.67E-01	none	-0.4675	none	1		
SERIES	Well7	-1.18E+00	none	0.1342	none	2		
SERIES	Well7	8.41E-01	none	0.6506	none	4		
SERIES	Well7	3.54E+00	none	-0.4926	none	7		
SERIES	MW3	3.49E-03	none	0.3756	none	0.04167		
SERIES	MW3	3.49E-03	none	0.3756	none	0.08333		
SERIES	MW3	2.27E-01	none	-0.0023	none	0.125		
SERIES	MW3	-7.66E-01	none	0.3362	none	0.25		
SERIES	MW3	8.93E-01	none	0.2221	none	0.5		
SERIES	MW3	4.15E-01	none	0.7651	none	1		
SERIES	MW3	4.24E-01	none	1.0384	none	2		
SERIES	MW3	-2.20E+00	none	0.7214	none	4		
SERIES	MW3	1.19E+00	none	1.3041	none	7		
THEIS	Q-Well9	1.50E+05	log	0.05	log	3000	-193	

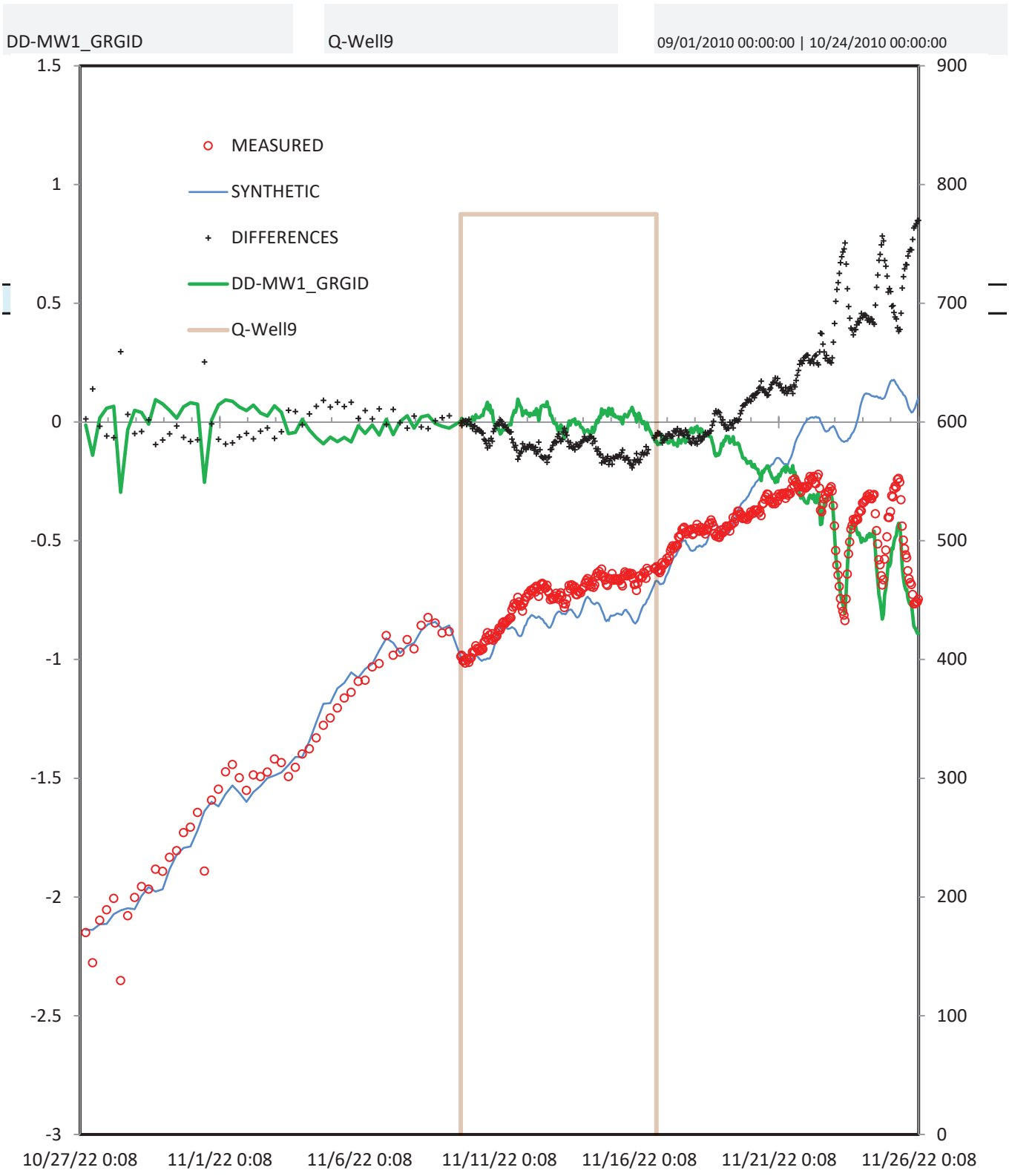
DD-MW1_GRGID
Q-Well9
09/01/2010 00:00:00 | 10/24/2010 00:00:00
MEASURED
SYNTHETIC
DIFFERENCES
DD-MW1_GRGID
Q-Well9
1.5
1
0.5
0
-0.5
-1
-1.5
-2
-2.5
-3
900
800
700
600
500
400
300
200
100
0
10/27/22 0:08
11/1/22 0:08
11/6/22 0:08
11/11/22 0:08
11/16/22 0:08
11/21/22 0:08
11/26/22 0:08

RMS = 0.0115

VIEW:

RMS Expected:	0.0030	Maximum:	0.026
Max Iter:	30	Minimum:	-0.1815
Time Begin:	10/27/2022 00:08	Average:	-0.0767
Time End:	11/26/2022 00:08	Std. Dev.:	0.0499
Interval:	0:30:00	Count:	445

Measured: MW2_Bing

Transform	Time Series	Coeff.1	Est	Coeff.2	Est	Coeff.3	Coeff.4	Coeff.5
Slope+Offset		**0**	**fixed**	-0.2592	none			
SERIES	Well7	2.82E-02	none	0.1321	none	0.04167		
SERIES	Well7	2.82E-02	none	0.1321	none	0.08333		
SERIES	Well7	3.16E-02	none	0.1432	none	0.125		
SERIES	Well7	1.91E-02	none	0.1477	none	0.25		
SERIES	Well7	1.64E-02	none	0.1595	none	0.5		
SERIES	Well7	3.76E-02	none	0.1551	none	1		
SERIES	Well7	7.06E-02	none	0.1455	none	2		
SERIES	Well7	7.53E-02	none	0.1354	none	4		
SERIES	Well7	-4.64E-02	none	0.1561	none	7		
SERIES	MW3	-3.76E-03	none	0.1513	none	0.04167		
SERIES	MW3	-3.76E-03	none	0.1513	none	0.08333		
SERIES	MW3	8.34E-04	none	0.1559	none	0.125		
SERIES	MW3	1.45E-02	none	0.1701	none	0.25		
SERIES	MW3	4.73E-03	none	0.1583	none	0.5		
SERIES	MW3	1.99E-02	none	0.1805	none	1		
SERIES	MW3	-1.19E-03	none	0.1587	none	2		
SERIES	MW3	3.10E-02	none	0.1567	none	4		
SERIES	MW3	-3.81E-02	none	0.1209	none	7		
THEIS	Q-Well9	1.62E+05	log	0.0118	log	5000	-193	

DD-MW2_Bing | Q-Well9 | 09/01/2010 00:00:00 | 10/24/2010 00:00:00

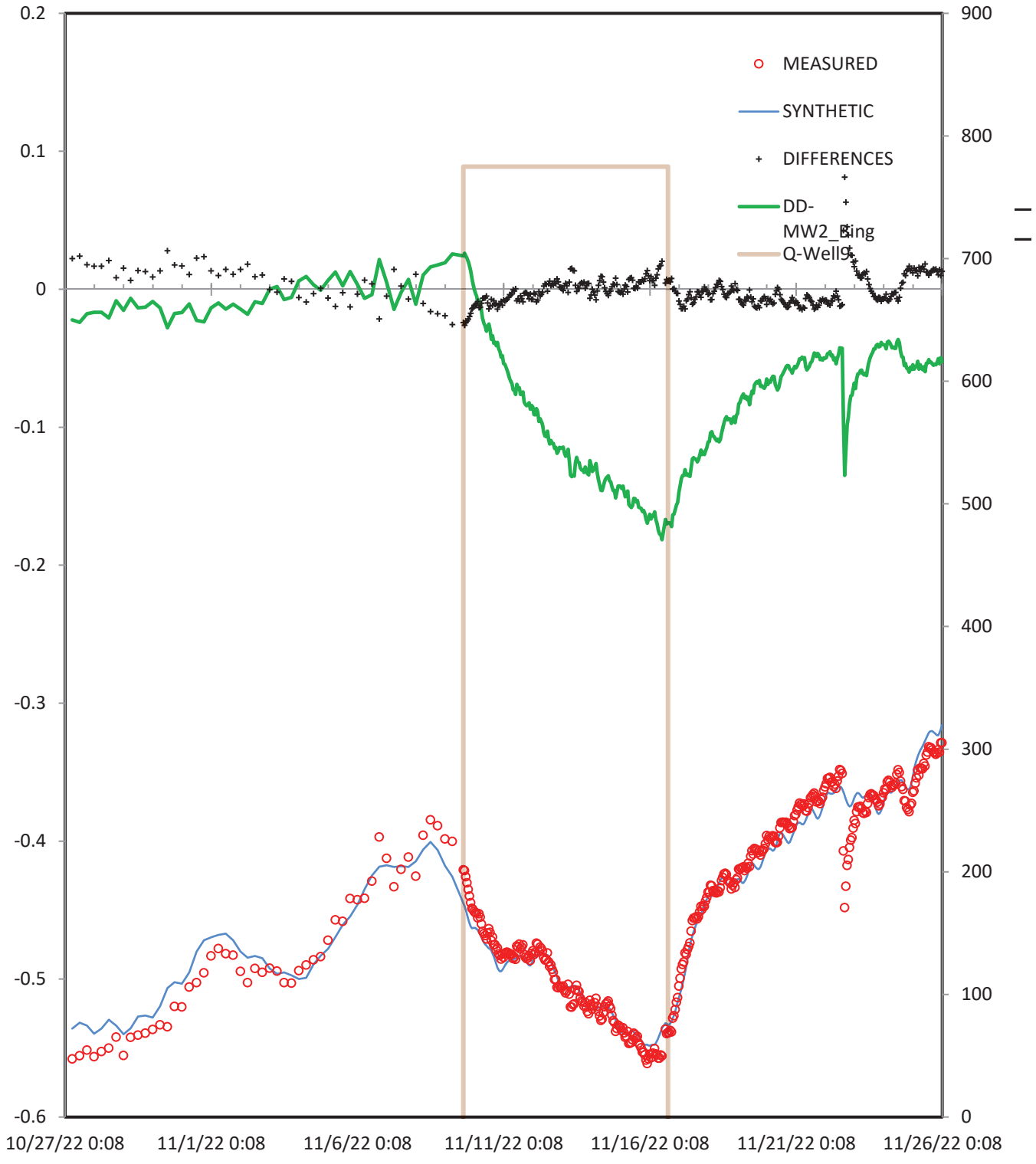

RMS = 0.0138

VIEW:

RMS Expected:	0.0030	Maximum:	0.0539
Max Iter:	30	Minimum:	-0.4464
Time Begin:	10/27/2022 00:08	Average:	-0.1892
Time End:	11/26/2022 00:08	Std. Dev.:	0.1424
Interval:	0:30:00	Count:	442

Measured: Sweetwater

Transform	Time Series	Coeff.1	Est	Coeff.2	Est	Coeff.3	Coeff.4	Coeff.5
Slope+Offset		**0**	**fixed**	0.2766	none			
SERIES	MW2_GRGID	0.2064993	none	-0.3039	none	0.04167		
SERIES	MW2_GRGID	0.1842309	none	-0.4539	none	0.08333		
SERIES	MW2_GRGID	0.2648357	none	-0.0643	none	0.125		
SERIES	MW2_GRGID	-0.303295	none	-0.5597	none	0.25		
SERIES	MW2_GRGID	0.963378	none	-1.5933	none	0.5		
SERIES	MW2_GRGID	-2.195977	none	-1.5711	none	1		
SERIES	MW2_GRGID	1.3694592	none	-0.9435	none	2		
SERIES	MW2_GRGID	-0.754905	none	-1.2852	none	4		
SERIES	MW2_GRGID	1.4603513	none	-1.3236	none	7		
SERIES	Well7	0.1293201	none	-0.9192	none	0.04167		
SERIES	Well7	0.1293201	none	-0.9192	none	0.08333		
SERIES	Well7	-0.244658	none	-0.2995	none	0.125		
SERIES	Well7	0.1331398	none	1.0638	none	0.25		
SERIES	Well7	0.3956617	none	2.2215	none	0.5		
SERIES	Well7	-0.628927	none	-3.2422	none	1		
SERIES	Well7	0.7333346	none	-2.039	none	2		
SERIES	Well7	0.5362908	none	-3.8324	none	4		
SERIES	Well7	-2.706717	none	-0.3092	none	7		
SERIES	MW3	0.1317642	none	0.0296	none	0.04167		
SERIES	MW3	0.1317642	none	0.0296	none	0.08333		
SERIES	MW3	-0.051202	none	0.1103	none	0.125		
SERIES	MW3	-0.287686	none	0.106	none	0.25		
SERIES	MW3	0.3033652	none	-1.8435	none	0.5		
SERIES	MW3	0.5747094	none	-3.3603	none	1		
SERIES	MW3	-0.270774	none	-2.4255	none	2		
SERIES	MW3	0.702202	none	-0.1988	none	4		
SERIES	MW3	-1.359732	none	-1.092	none	7		
THEIS	Q-Well9	107345.72	log	0.0036	log	3000	-193	

DD-Sweetwater | Q-Well9 | 09/01/2010 00:00:00 | 10/24/2010 00:00:00

SeriesSEEfileNAME: SeriesSee.V1.30.xlam
SourceBOOK: all_wells_25Apr23_offset.xlsm

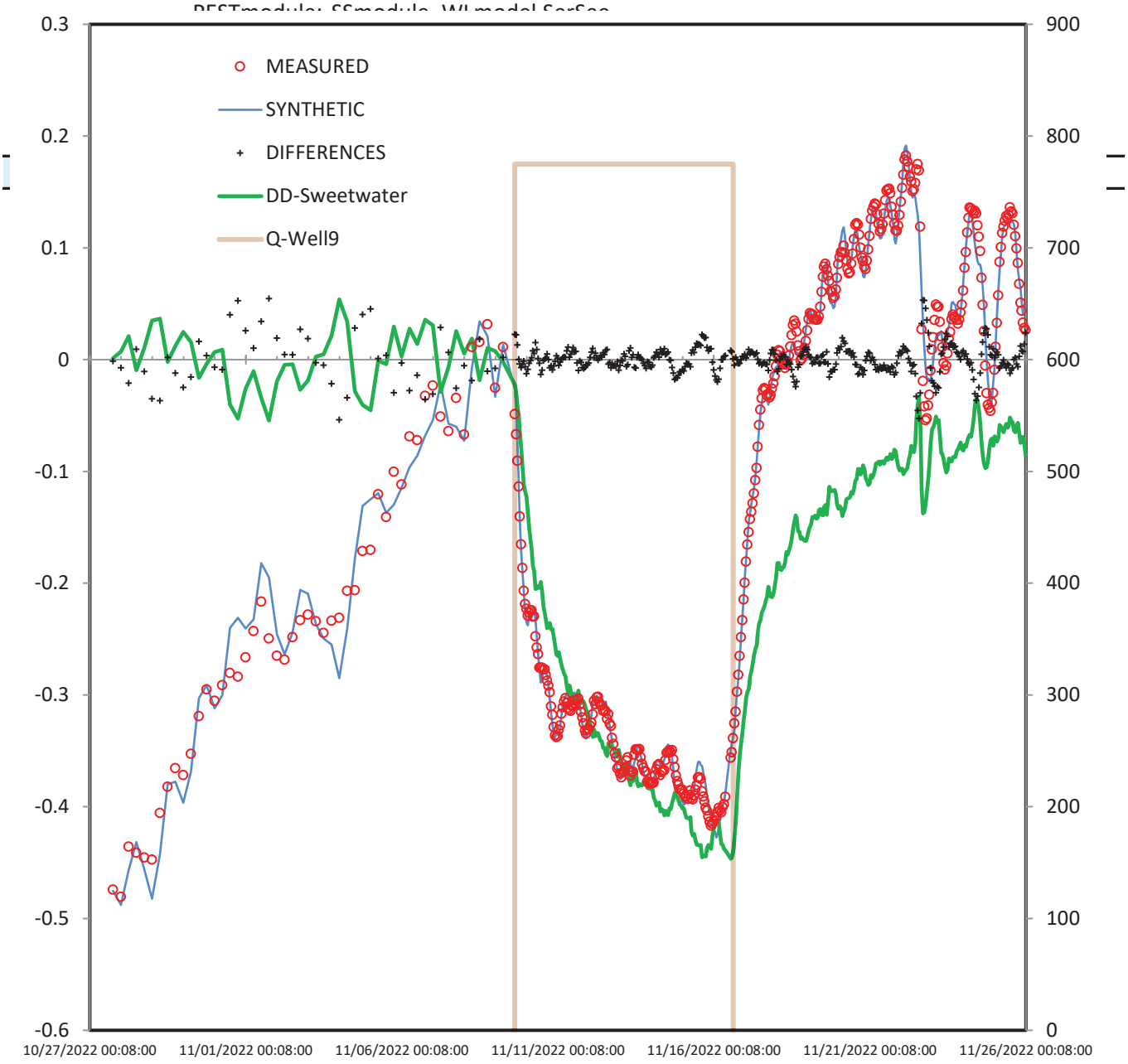

RMS = 0.0265

VIEW:

RMS Expected:	0.0030	Maximum:	0.0921
Max Iter:	30	Minimum:	-0.5403
Time Begin:	10/23/2022 00:56	Average:	-0.3131
Time End:	11/22/2022 00:56	Std. Dev.:	0.1563
Interval:	0:30:00	Count:	643

Measured: Well5

Transform	Time Series		Coeff.1	Est	Coeff.2	Est	Coeff.3	Coeff.4	Coeff.5
Slope+Offset			**0**	**fixed**	-4729.2	none			
SERIES		Well7	0.0993187	none	-0.008	none	0.04167		
SERIES		Well7	0.0996392	none	-0.0035	none	0.08333		
SERIES		Well7	0.100387	none	-0.0045	none	0.125		
SERIES		Well7	0.1019467	none	-0.0042	none	0.25		
SERIES		Well7	0.1034179	none	-0.0122	none	0.5		
SERIES		Well7	0.1118236	none	-0.0116	none	1		
SERIES		Well7	0.1136692	none	-0.015	none	2		
SERIES		Well7	0.1084807	none	-0.0145	none	4		
SERIES		Well7	0.1147834	none	-0.0147	none	7		
SERIES		MW6	-0.011765	none	-0.016	none	0.04167		
SERIES		MW6	-0.01084	none	-0.0161	none	0.08333		
SERIES		MW6	-0.009034	none	-0.0158	none	0.125		
SERIES		MW6	-0.00511	none	-0.0156	none	0.25		
SERIES		MW6	0.0068996	none	-0.0156	none	0.5		
SERIES		MW6	0.0473081	none	-0.016	none	1		
SERIES		MW6	0.1065737	none	-0.0181	none	2		
SERIES		MW6	0.0185748	none	-0.0159	none	4		
SERIES		MW6	-0.05241	none	-0.0167	none	7		
SERIES		MW3	-0.009758	none	-0.0154	none	0.04167		
SERIES		MW3	-0.009194	none	-0.0142	none	0.08333		
SERIES	MW3		-0.008676	none	-0.0152	none	0.125		
SERIES	MW3		-0.007677	none	-0.0148	none	0.25		
SERIES	MW3		-0.004353	none	-0.0154	none	0.5		
SERIES	MW3		0.0154378	none	-0.0169	none	1		
SERIES	MW3		0.0307514	none	-0.0168	none	2		
SERIES	MW3		-0.00915	none	-0.0167	none	4		
SERIES	MW3		-0.047539	none	-0.0167	none	7		
THEIS		Q-Well9	4.86E+04	log	0.0031	log	6100	-193	

DD-Well5 | Q-Well9 | 09/01/2010 00:00:00 | 10/24/2010 00:00:00

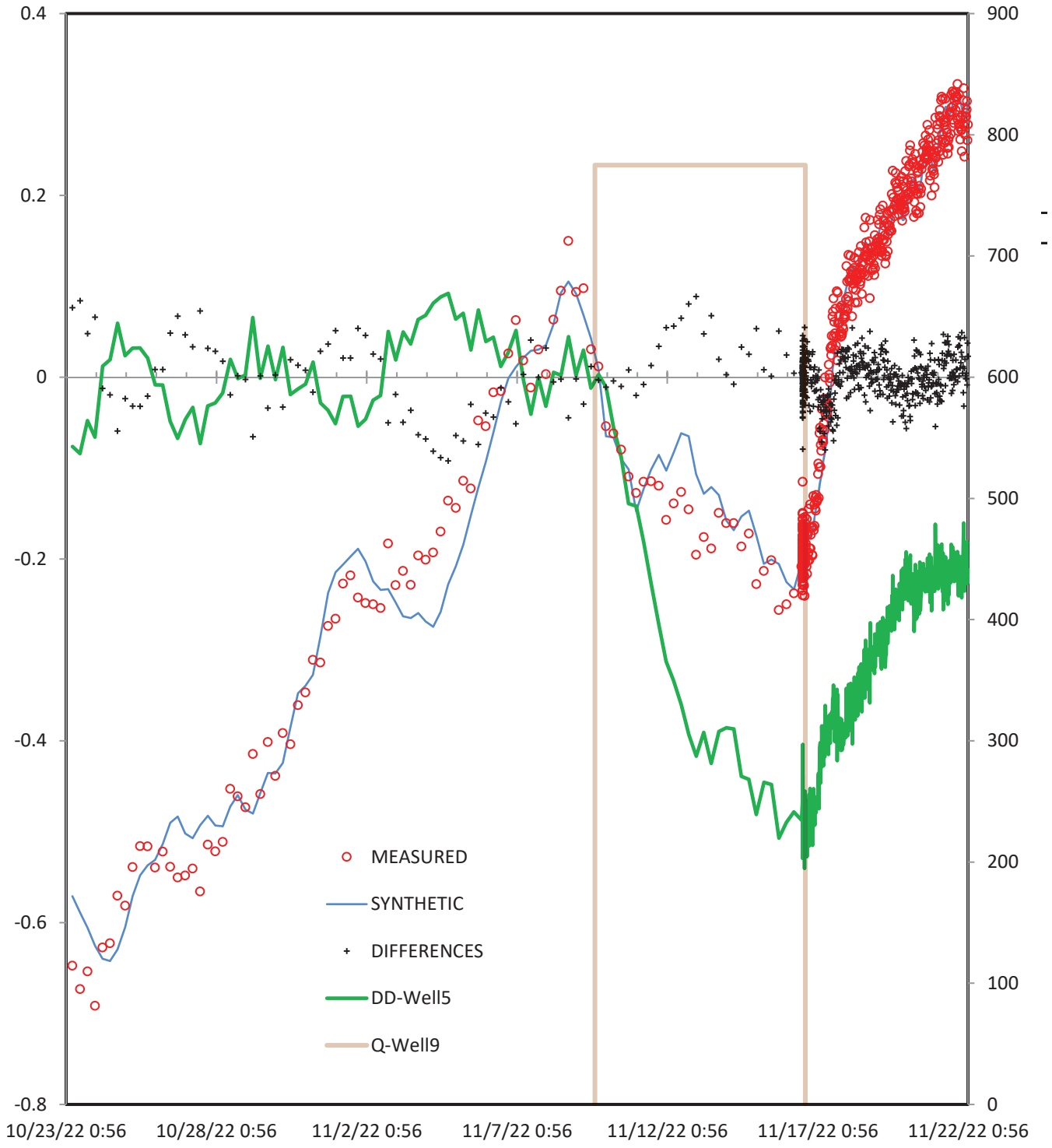

RMS = 0.0618

VIEW:

RMS Expected:	0.0030	Maximum:	0.1371
Max Iter:	30	Minimum:	-0.1499
Time Begin:	11/05/2022 11:48	Average:	-0.0028
Time End:	11/21/2022 11:48	Std. Dev.:	0.0622
Interval:	0:30:00	Count:	61

Measured: Well6

Transform	Time Series	Coeff.1	Est	Coeff.2	Est	Coeff.3	Coeff.4	Coeff.5
Slope+Offset		**0**	**fixed**	2.7794	none			
SERIES	MW3	0.026173	none	-0.4597	none	0.04167		
SERIES	MW3	-0.11944	none	-0.3802	none	0.08333		
SERIES	MW3	0.0206314	none	-0.3332	none	0.125		
SERIES	MW3	0.098831	none	-0.3854	none	0.25		
SERIES	MW3	-0.046066	none	-0.3772	none	0.5		
SERIES	MW3	0.0065335	none	-0.3861	none	1		
SERIES	MW3	-0.041397	none	-0.4009	none	2		
SERIES	MW3	-0.188656	none	-0.5452	none	4		
SERIES	MW3	0.4038169	none	-0.5262	none	7		
SERIES	Well7	0.0043394	none	-0.5844	none	0.04167		
SERIES	Well7	0.0655631	none	-0.4622	none	0.08333		
SERIES	Well7	0.1785646	none	-0.5568	none	0.125		
SERIES	Well7	0.1288938	none	-0.295	none	0.25		
SERIES	Well7	0.0865481	none	-0.7079	none	0.5		
SERIES	Well7	0.2313437	none	-0.3811	none	1		
SERIES	Well7	0.3385311	none	-0.2064	none	2		
SERIES	Well7	0.2554055	none	-0.3059	none	4		
SERIES	Well7	0.2381367	none	-0.3318	none	7		
THEIS	Q-Well9	25367.942	log	0.9	log	4300	-193	

DD-Well6 | Q-Well9 | 09/01/2010 00:00:00 | 10/24/2010 00:00:00

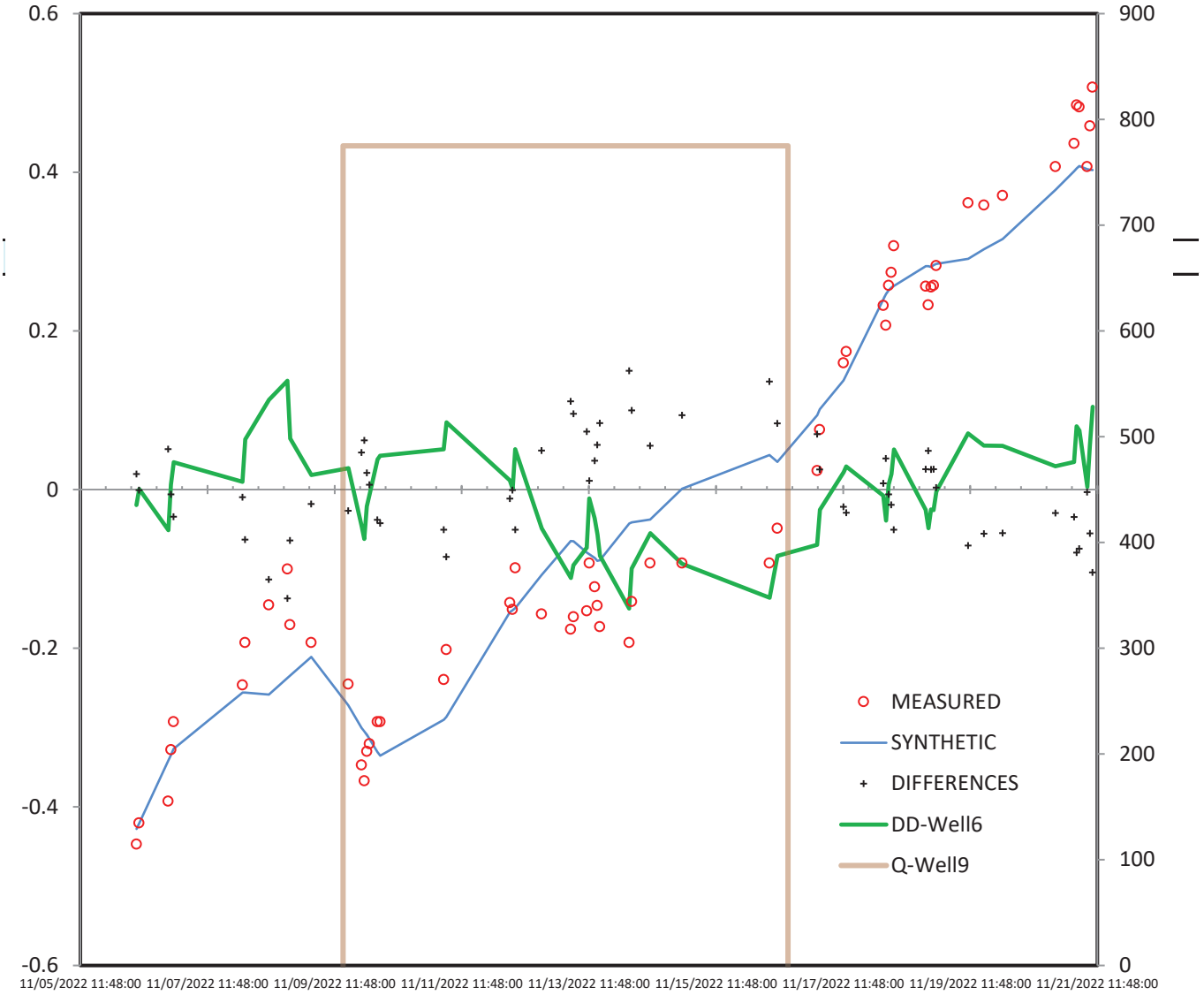

Attachment 3: AQTESOLV Aquifer Properties Graphs

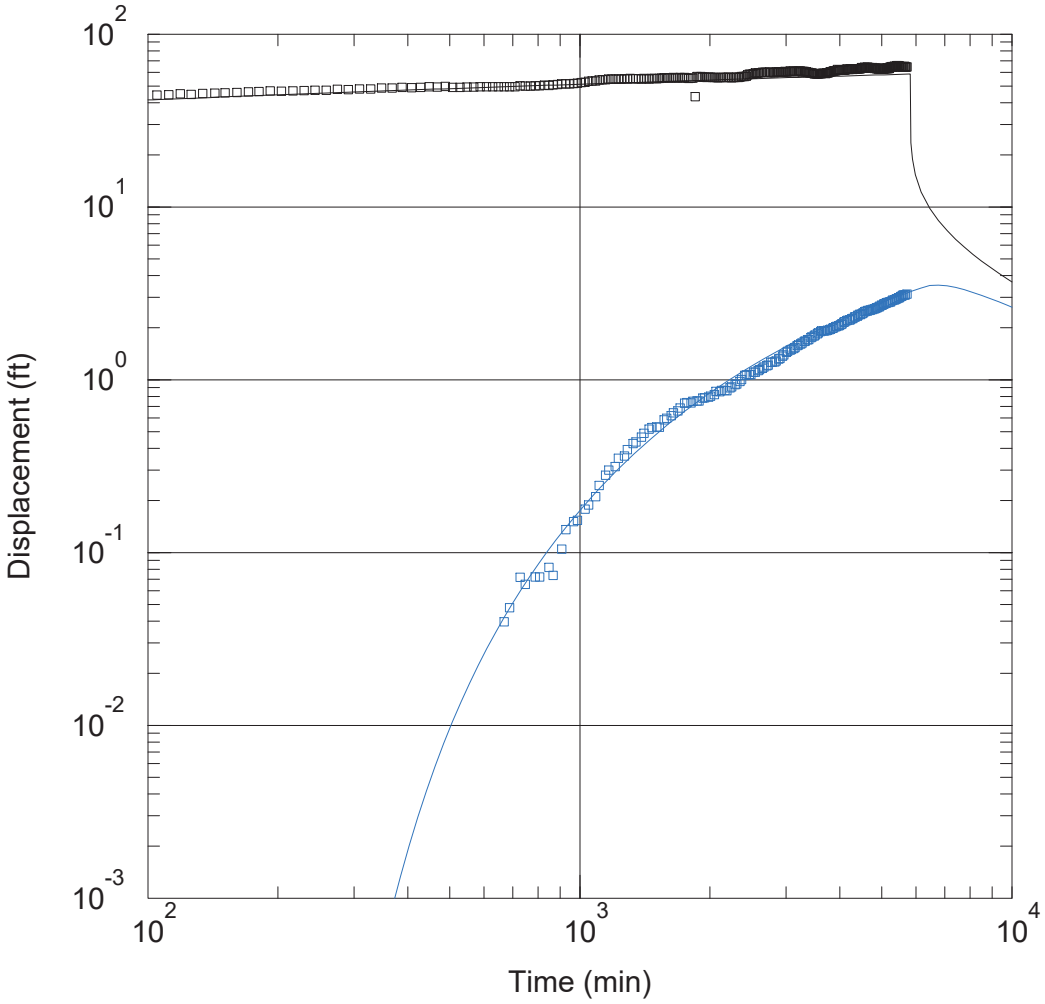

WELL TEST ANALYSIS

Data Set: D:\Projects\GRGID\modeling\aqtesolv\well1_test\well1test_dd_mw5_neumanwitherspoon.aqt
Date: 01/19/24 Time: 15:15:05

PROJECT INFORMATION

Company: DRI
Client: GRGID
Location: Gardnerville Ranchos
Test Well: Well 1
Test Date: 12/9/23 - 12/13/22

AQUIFER DATA

Saturated Thickness: 290. ft
Aquitard Thickness (b'): 1. ft
Anisotropy Ratio (Kz/Kr): 0.0009616
Aquitard Thickness (b"): 1. ft

WELL DATA

Pumping Wells

Well Name	X (ft)	Y (ft)
Well 1	867347.9024	14141295.63

Observation Wells

Well Name	X (ft)	Y (ft)
Well 1	867347.9024	14141295.63
MW5	866680.3329	14141813.32

SOLUTION

Aquifer Model: Leaky
Solution Method: Neuman-Witherspoon

T = 3395.4 ft^2/day
1/B = 0.4057 ft^{-1}
T2 = 51.33 ft^2/day

S = 0.006469
ß/r = 0.1871 ft^{-1}
S2 = 3.449E-5

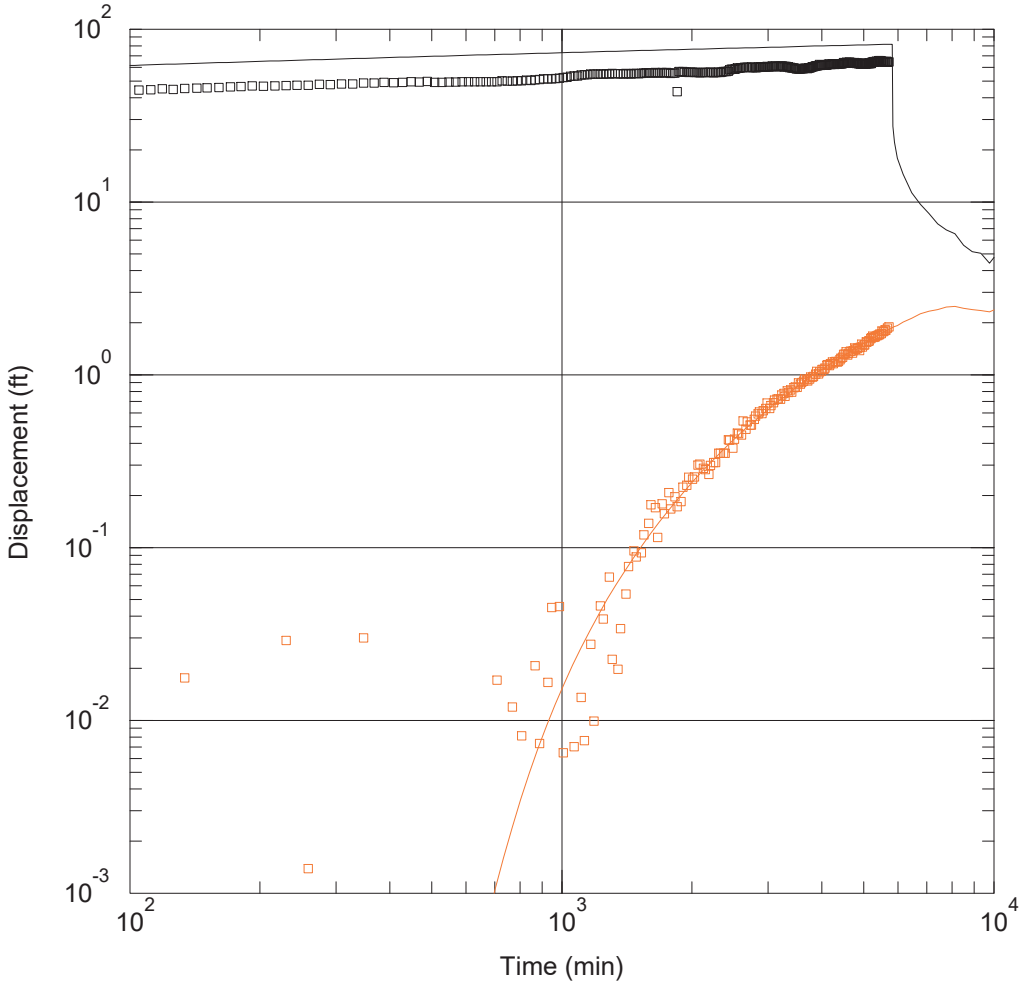

WELL TEST ANALYSIS

Data Set: D:\Projects\GRGID\modeling\aqtesolv\well1_test\well1test_mw3_neumanwitherspoon.aqt
Date: 01/19/24 Time: 15:41:53

PROJECT INFORMATION

Company: DRI
Client: GRGID
Location: Gardnerville Ranchos
Test Well: Well 1
Test Date: 12/9/23 - 12/13/22

AQUIFER DATA

Saturated Thickness: 290. ft
Aquitard Thickness (b'): 1. ft
Anisotropy Ratio (Kz/Kr): 0.0009616
Aquitard Thickness (b"): 1. ft

WELL DATA

Pumping Wells

Well Name	X (ft)	Y (ft)
Well 1	867347.9024	14141295.63

Observation Wells

Well Name	X (ft)	Y (ft)
Well 1	867347.9024	14141295.63
MW3	864774.109	14137911.67

SOLUTION

Aquifer Model: Leaky
Solution Method: Neuman-Witherspoon

T = 2936.7 ft^2/day
1/B = 0.4283 ft^{-1}
T2 = 0.01487 ft^2/day

S = 0.000432
ß/r = 0.1922 ft^{-1}
S2 = 3.197E-8

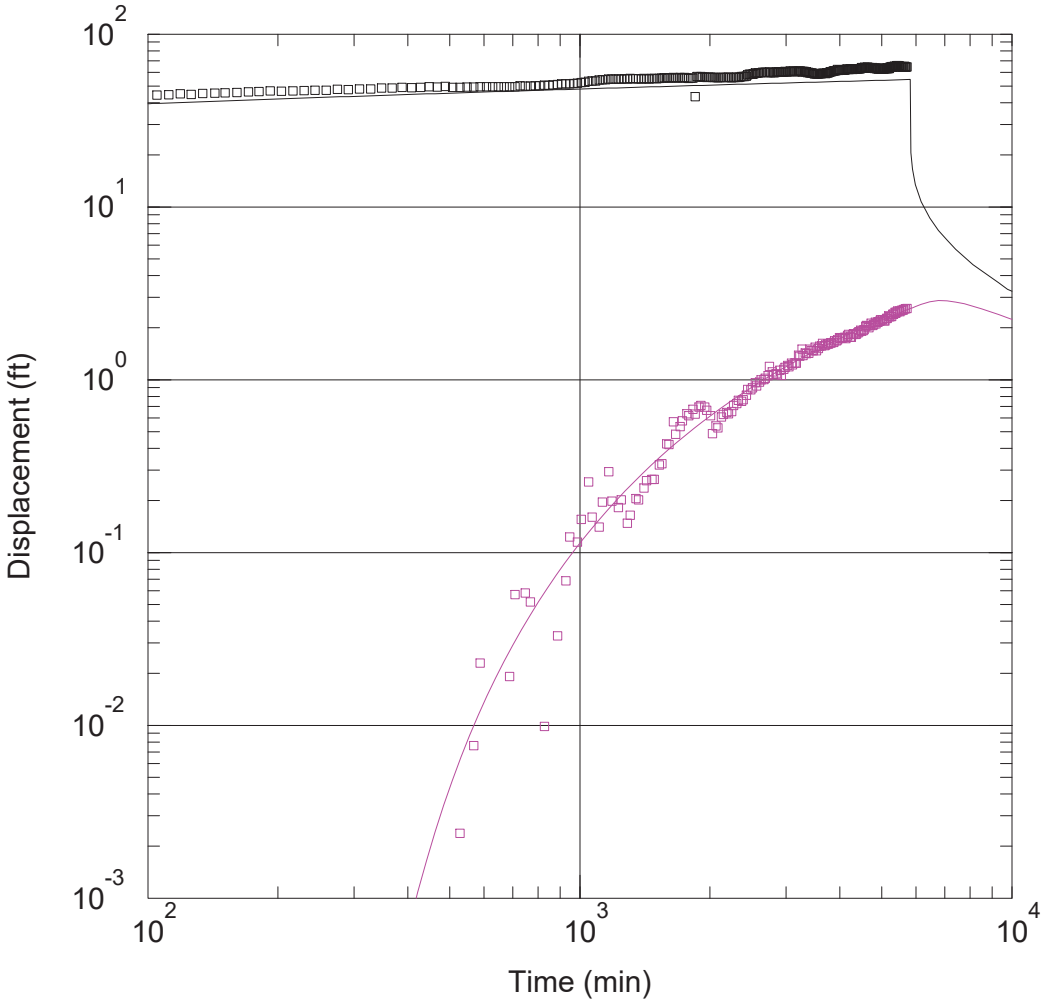

WELL TEST ANALYSIS

Data Set: D:\Projects\GRGID\modeling\aqtesolv\well1_test\well1test_mw6_neumanwitherspoon.aqt
Date: 01/19/24 Time: 15:37:00

PROJECT INFORMATION

Company: DRI
Client: GRGID
Location: Gardnerville Ranchos
Test Well: Well 1
Test Date: 12/9/23 - 12/13/22

AQUIFER DATA

Saturated Thickness: 290. ft
Aquitard Thickness (b'): 1. ft
Anisotropy Ratio (Kz/Kr): 0.0009616
Aquitard Thickness (b"): 1. ft

WELL DATA

Pumping Wells

Well Name	X (ft)	Y (ft)
Well 1	867347.9024	14141295.63

Observation Wells

Well Name	X (ft)	Y (ft)
□ Well 1	867347.9024	14141295.63
□ MW6	866798.9123	14140074.05

SOLUTION

Aquifer Model: Leaky
Solution Method: Neuman-Witherspoon

T = 3923.7 ft^2/day
1/B = 0.4307 ft^{-1}
T2 = 0.0144 ft^2/day
S = 0.00358
ß/r = 0.1861 ft^{-1}
S2 = 3.326E-8

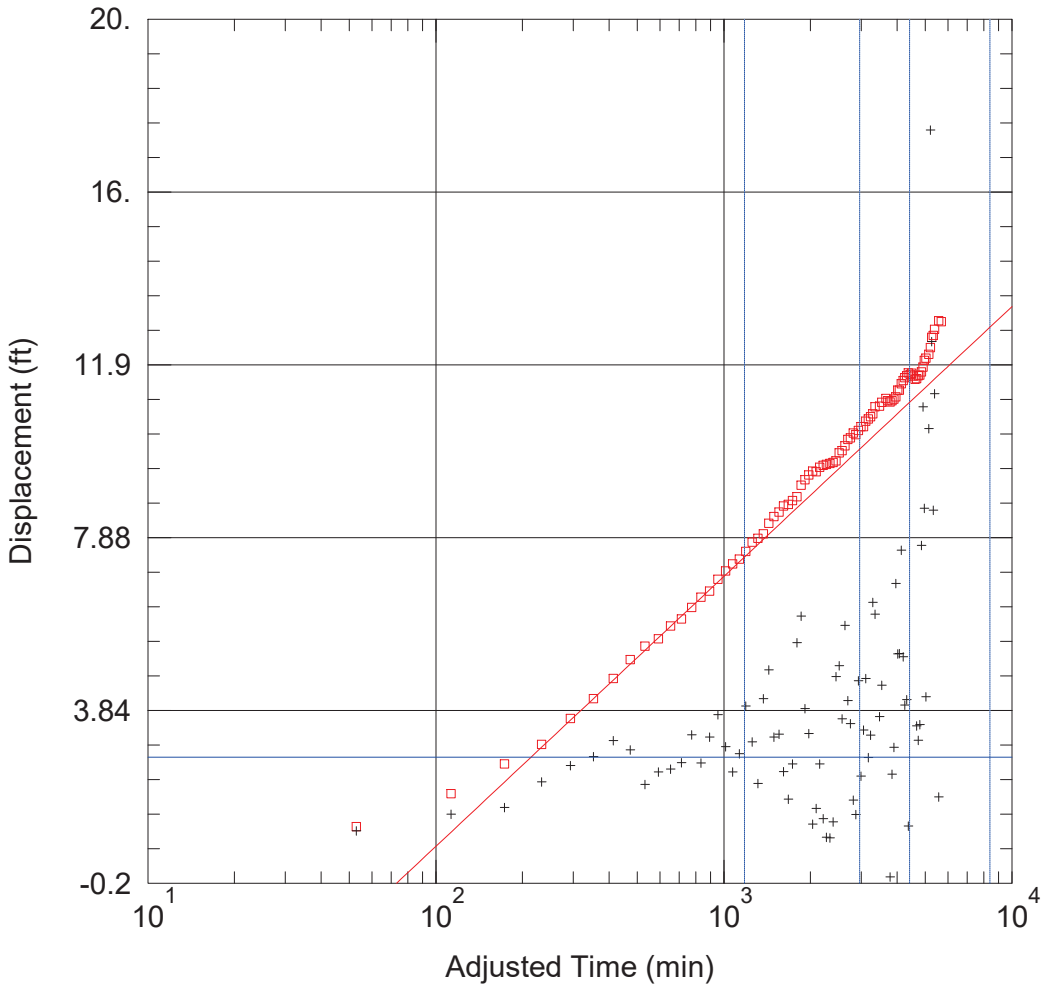

WELL TEST ANALYSIS

Data Set: D:\Projects\GRGID\modeling\aqtesolv\well1_test\well1test_well2_cj.aqt
Date: 01/19/24 Time: 15:55:10

PROJECT INFORMATION

Company: DRI
Client: GRGID
Location: Gardnerville Ranchos
Test Well: Well 1
Test Date: 12/9/23 - 12/13/22

AQUIFER DATA

Saturated Thickness: 290. ft Anisotropy Ratio (Kz/Kr): 0.0009616

WELL DATA

Pumping Wells

Well Name	X (ft)	Y (ft)
Well 1	867347.9024	14141295.63

Observation Wells

Well Name	X (ft)	Y (ft)
Well 2	865873.0392	14142003.03

SOLUTION

Aquifer Model: Confined Solution Method: Cooper-Jacob

T = 5309.3 ft^2/day S = 0.0002435

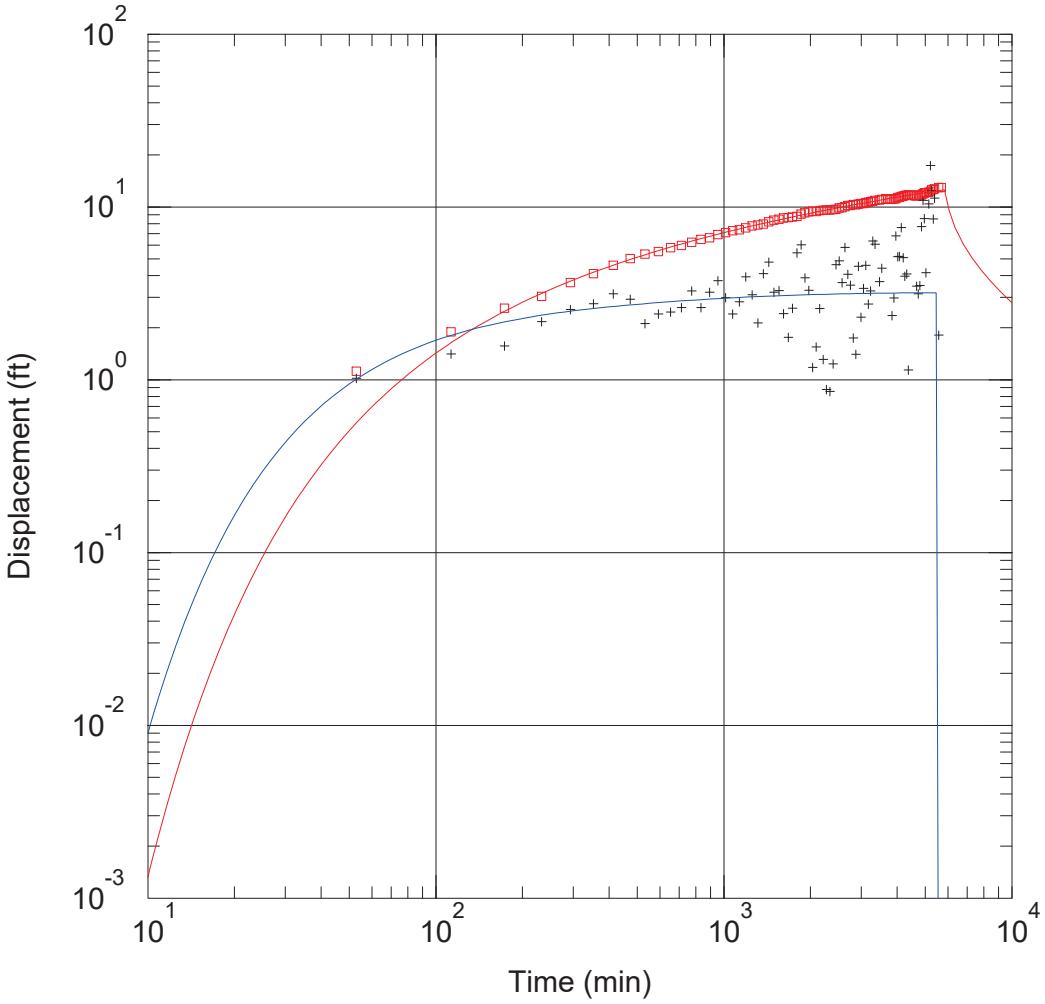

WELL TEST ANALYSIS

Data Set: D:\Projects\GRGID\modeling\aqtesolv\well1_test\well1test_well2_theis.aqt
Date: 01/19/24 Time: 15:49:13

PROJECT INFORMATION

Company: DRI
Client: GRGID
Location: Gardnerville Ranchos
Test Well: Well 1
Test Date: 12/9/23 - 12/13/22

WELL DATA

Pumping Wells

Well Name	X (ft)	Y (ft)
Well 1	867347.9024	14141295.63

Observation Wells

Well Name	X (ft)	Y (ft)
▫ Well 2	865873.0392	14142003.03

SOLUTION

Aquifer Model: Confined
Solution Method: Theis

T = 4516.1 ft^2/day
S = 0.0002735
Kz/Kr = 0.0009616
b = 290. ft

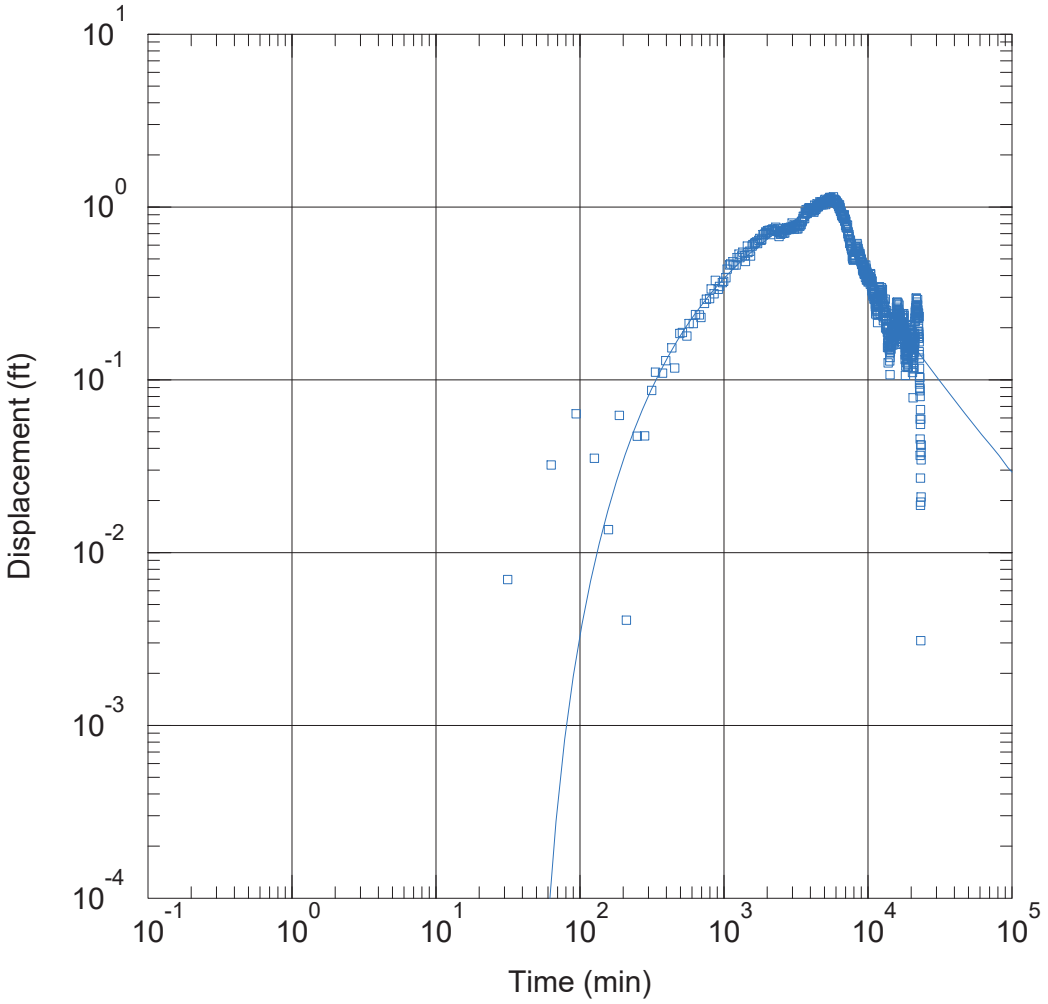

WELL TEST ANALYSIS

Data Set: D:\Projects\GRGID\modeling\aqtesolv\well2_test\well2_test_mw3_neumanwitherspoon.aqt
Date: 01/20/24 Time: 09:53:15

PROJECT INFORMATION

Company: DRI
Client: GRGID
Location: Gardnerville Ranchos
Test Well: Well 2
Test Date: 11/28/22 - 12/2/22

AQUIFER DATA

Saturated Thickness: 526. ft
Aquitard Thickness (b'): 20. ft
Anisotropy Ratio (Kz/Kr): 1.
Aquitard Thickness (b"): 50. ft

WELL DATA

Pumping Wells

Well Name	X (ft)	Y (ft)
Well 2	865873.0392	14142003.03

Observation Wells

Well Name	X (ft)	Y (ft)
MW3	864774.109	14137911.67

SOLUTION

Aquifer Model: Leaky
Solution Method: Neuman-Witherspoon

T = 3.45E+4 ft^2/day
1/B = 0.5242 ft^{-1}
T2 = 5453. ft^2/day

S = 0.001047
ß/r = 0.14 ft^{-1}
S2 = 8.526E-15

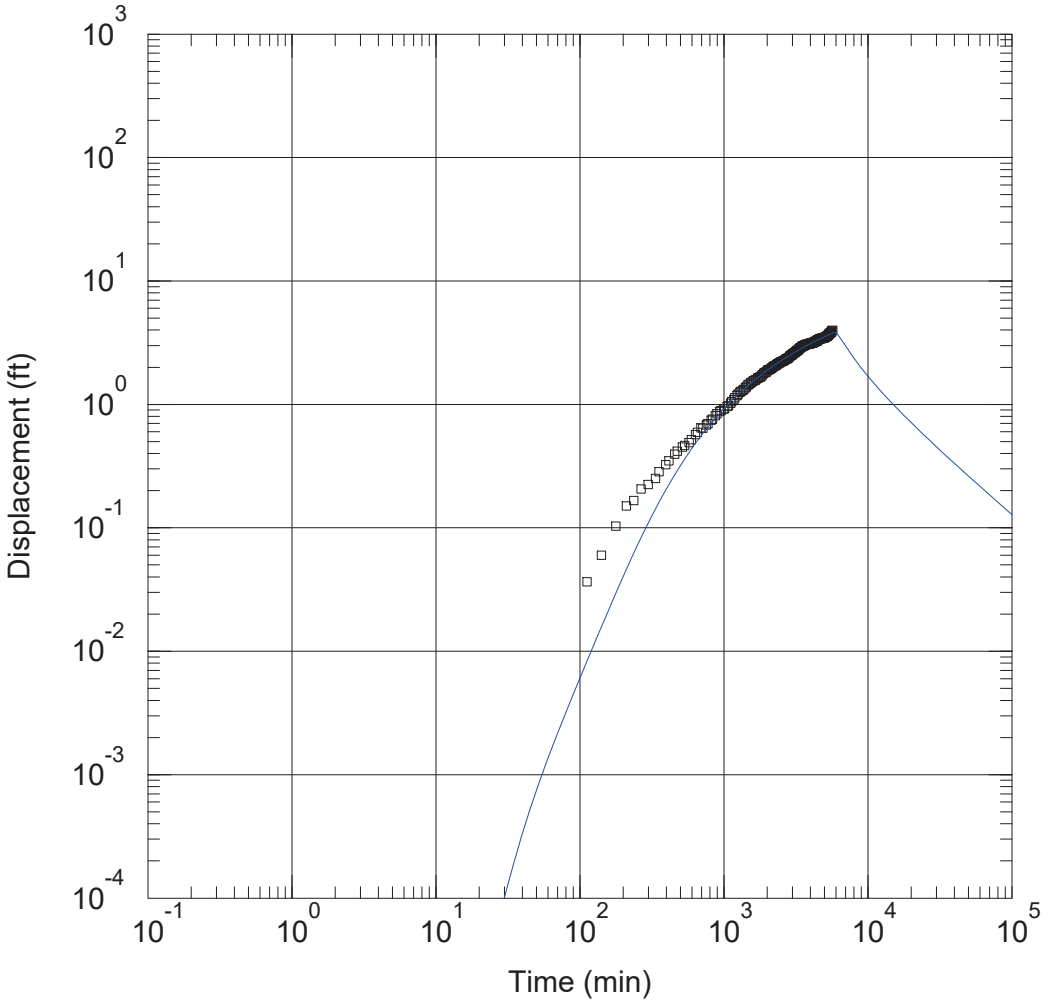

WELL TEST ANALYSIS

Data Set: D:\Projects\GRGID\modeling\aqtesolv\well2_test\well2_test_dd_mw5_neumanwitherspoon_v2.aqt
Date: 01/20/24 Time: 09:22:08

PROJECT INFORMATION

Company: DRI
Client: GRGID
Location: Gardnerville Ranchos
Test Well: Well 2
Test Date: 11/28/22 - 12/2/22

AQUIFER DATA

Saturated Thickness: 526. ft
Aquitard Thickness (b'): 20. ft
Anisotropy Ratio (Kz/Kr): 1.
Aquitard Thickness (b"): 50. ft

WELL DATA

Pumping Wells

Well Name	X (ft)	Y (ft)
Well 2	865873.0392	14142003.03

Observation Wells

Well Name	X (ft)	Y (ft)
MW5	866680.3329	14141813.32

SOLUTION

Aquifer Model: Leaky
Solution Method: Neuman-Witherspoon

T = 63.54 ft^2/day
1/B = 0.08428 ft^{-1}
T2 = 9039. ft^2/day
S = 0.001868
ß/r = 0.07095 ft^{-1}
S2 = 5.808E-12

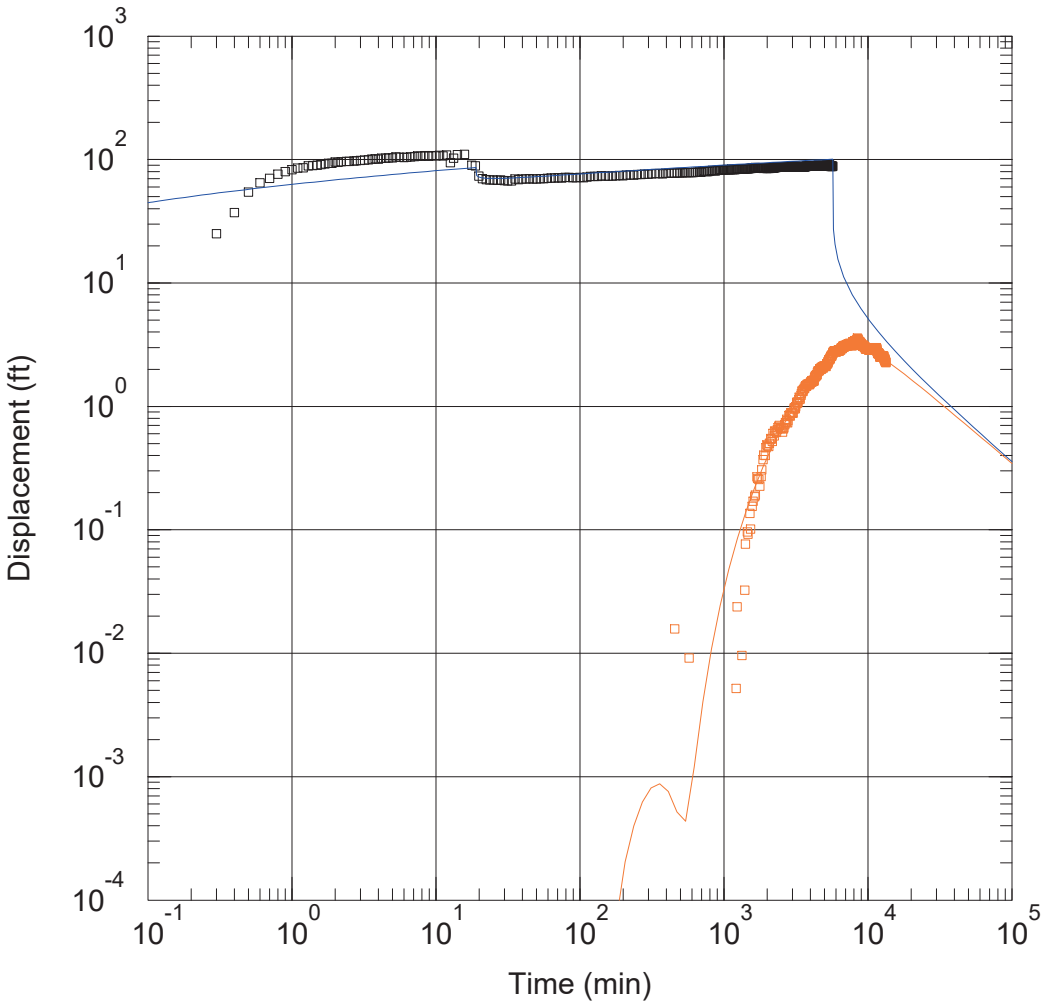

WELL TEST ANALYSIS

Data Set: D:\Projects\GRGID\modeling\aqtesolv\well2_test\revised\well2_test_dd_mw6_neumanwitherspoon_v2.aqt
Date: 01/20/24 Time: 09:31:31

PROJECT INFORMATION

Company: DRI
Client: GRGID
Location: Gardnerville Ranchos
Test Well: Well 2
Test Date: 11/28/22 - 12/2/22

AQUIFER DATA

Saturated Thickness: 526. ft
Aquitard Thickness (b'): 20. ft
Anisotropy Ratio (Kz/Kr): 1.
Aquitard Thickness (b"): 50. ft

WELL DATA

Pumping Wells

Well Name	X (ft)	Y (ft)
Well 2	865873.0392	14142003.03

Observation Wells

Well Name	X (ft)	Y (ft)
Well 2	865873.0392	14142003.03
MW6	866798.9123	14140074.05

SOLUTION

Aquifer Model: Leaky
Solution Method: Neuman-Witherspoon

T = 1586.5 ft^2/day
1/B = 0.5228 ft^{-1}
T2 = 1689.9 ft^2/day

S = 2.13E-5
ß/r = 2.165 ft^{-1}
S2 = 0.001377

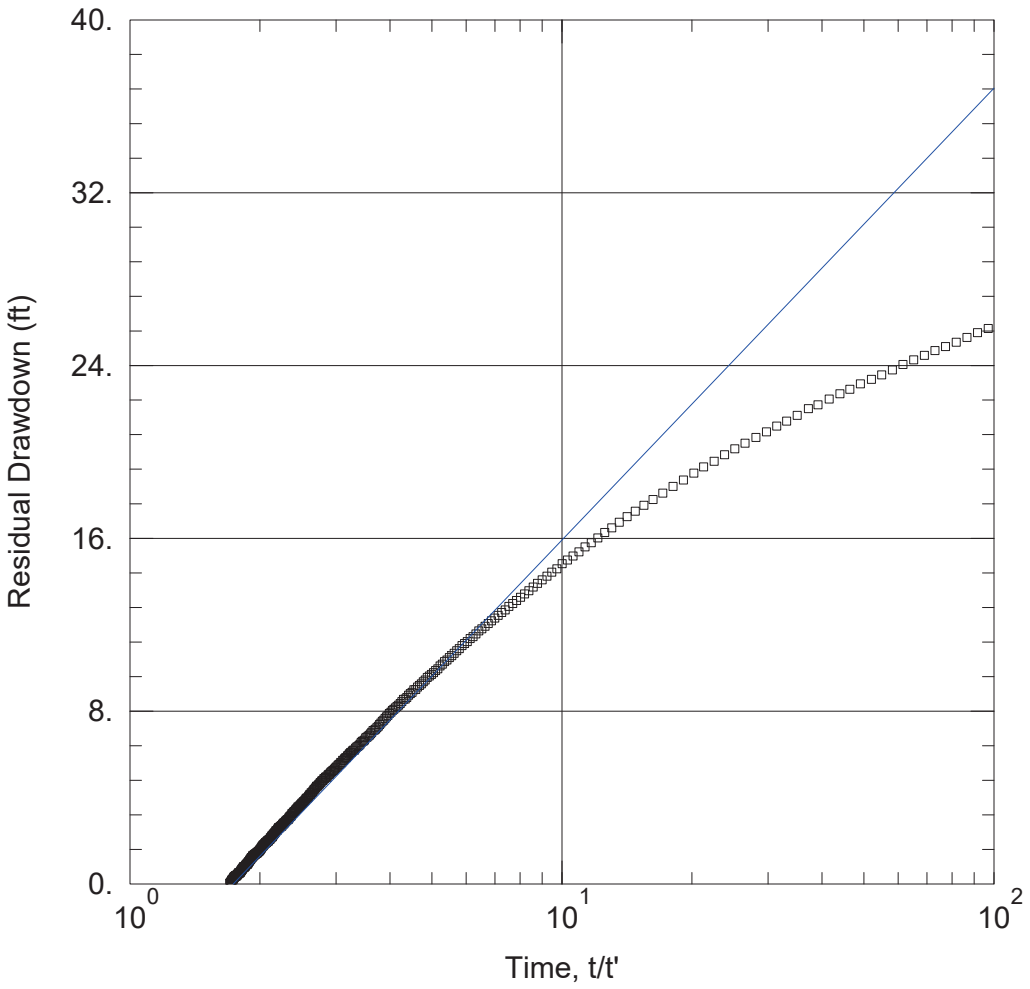

WELL TEST ANALYSIS

Data Set: D:\Projects\GRGID\modeling\aqtesolv\well2_test\well2_test_recovery.aqt
Date: 10/30/23 Time: 16:07:02

PROJECT INFORMATION

Company: DRI
Client: GRGID
Location: Gardnerville Ranchos
Test Well: Well 2
Test Date: 11/28/22 - 12/2/22

AQUIFER DATA

Saturated Thickness: 526. ft Anisotropy Ratio (Kz/Kr): 1.

WELL DATA

Pumping Wells

Well Name	X (ft)	Y (ft)
Well 2	865873.039	14142003.03

Observation Wells

Well Name	X (ft)	Y (ft)
Well 2	865873.039	14142003.03

SOLUTION

Aquifer Model: Confined Solution Method: Theis (Recovery)

T = 2191.9 ft^2/day S/S' = 1.735

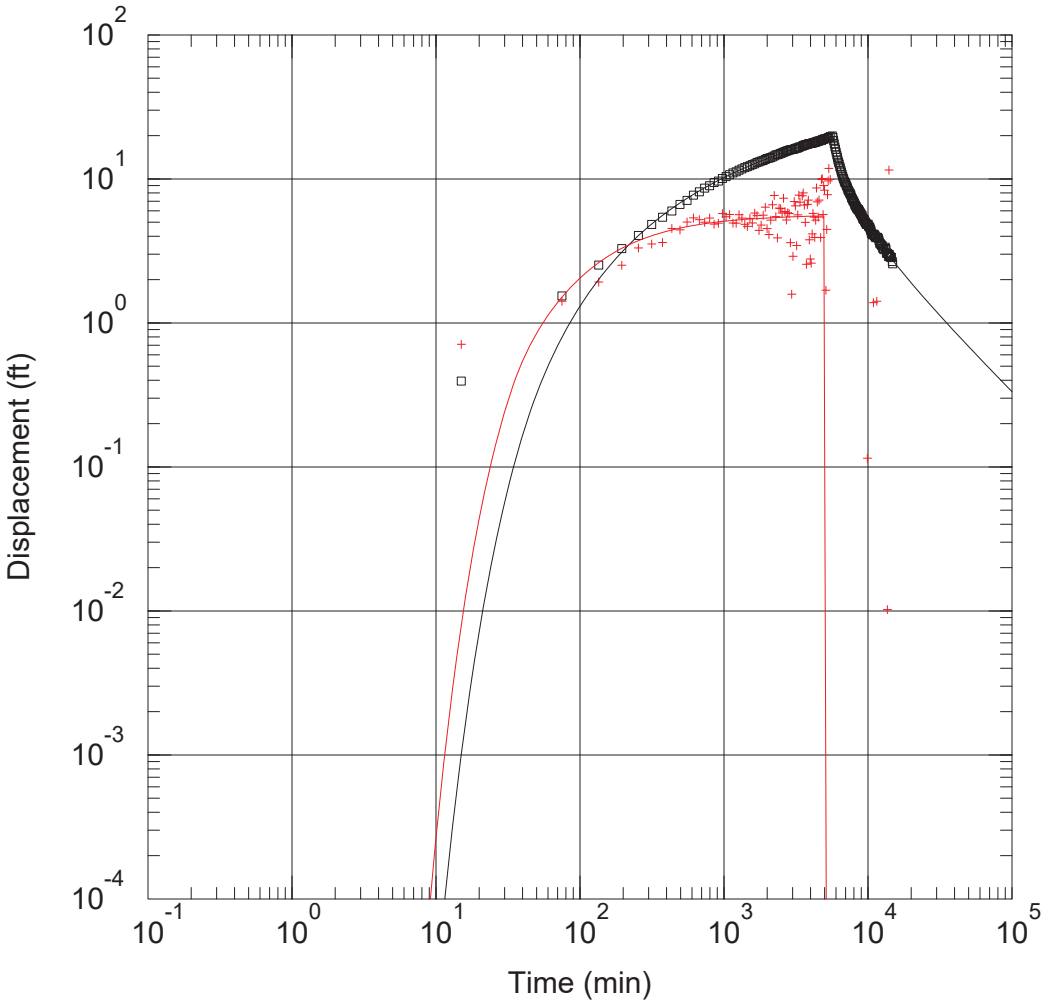

WELL TEST ANALYSIS

Data Set: D:\Projects\GRGID\modeling\aqtesolv\well2_test\well2_test_well1_theis.aqt
Date: 10/30/23 Time: 21:27:36

PROJECT INFORMATION

Company: DRI
Client: GRGID
Location: Gardnerville Ranchos
Test Well: Well 2
Test Date: 11/28/22 - 12/2/22

WELL DATA

Pumping Wells

Well Name	X (ft)	Y (ft)
Well 2	865873.0392	14142003.03

Observation Wells

Well Name	X (ft)	Y (ft)
▫ Well 1	867347.9024	14141295.63

SOLUTION

Aquifer Model: Confined
Solution Method: Theis

T = 3518. ft^2/day
S = 0.0003748
Kz/Kr = 1.
b = 526. ft

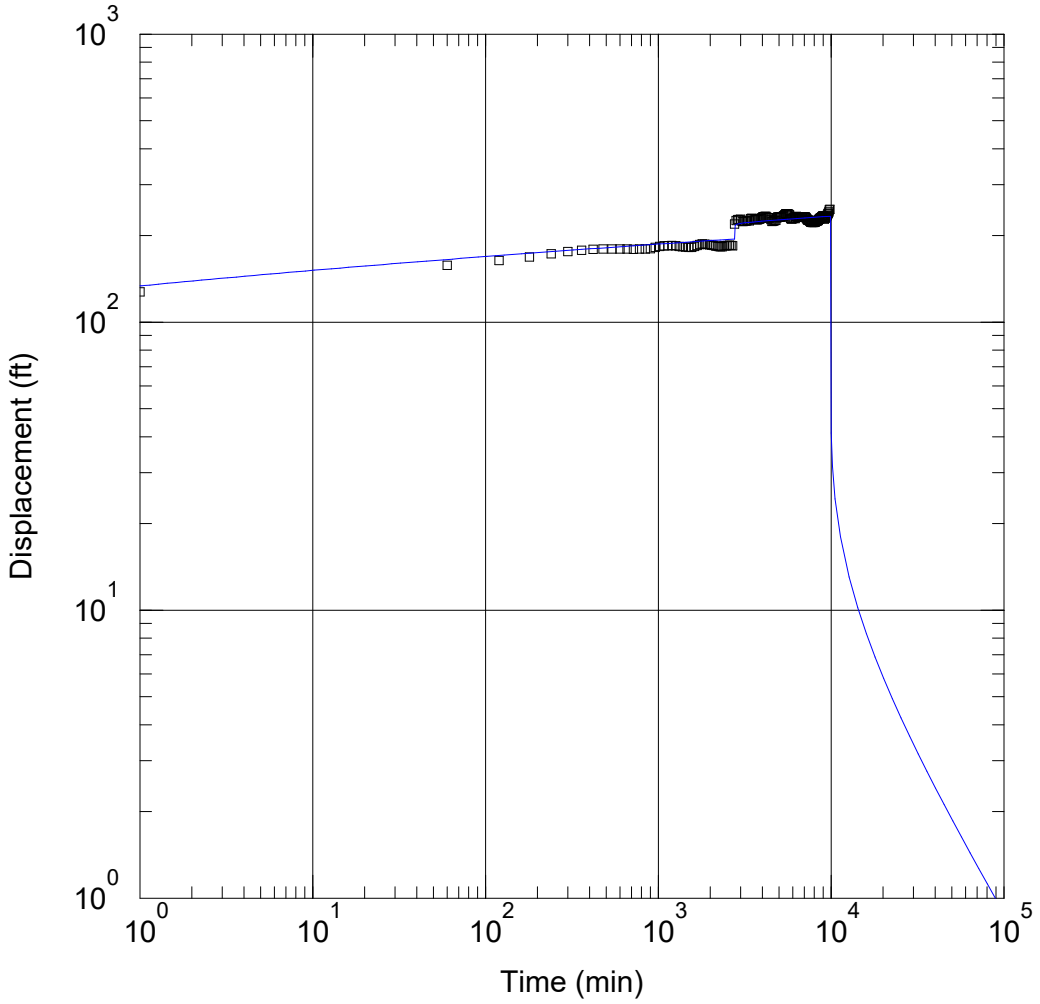

WELL TEST ANALYSIS

Data Set: D:\Projects\GRGID\modeling\aqtesolv\well4_test\well4test_dd_well4_theis.aqt
Date: 01/23/24 Time: 14:29:05

PROJECT INFORMATION

Company: DRI
Client: GRGID
Location: Gardnerville Ranchos
Test Well: Well 4
Test Date: 2/8/23 - 2/15/23

WELL DATA

Pumping Wells

Well Name	X (ft)	Y (ft)
Well 4	867638.5237	14139060.62

Observation Wells

Well Name	X (ft)	Y (ft)
Well 4	867638.5237	14139060.62

SOLUTION

Aquifer Model: Confined
Solution Method: Theis

T = 418.6 ft^2/day
S = 2.267E-6
Kz/Kr = 1.
b = 297. ft

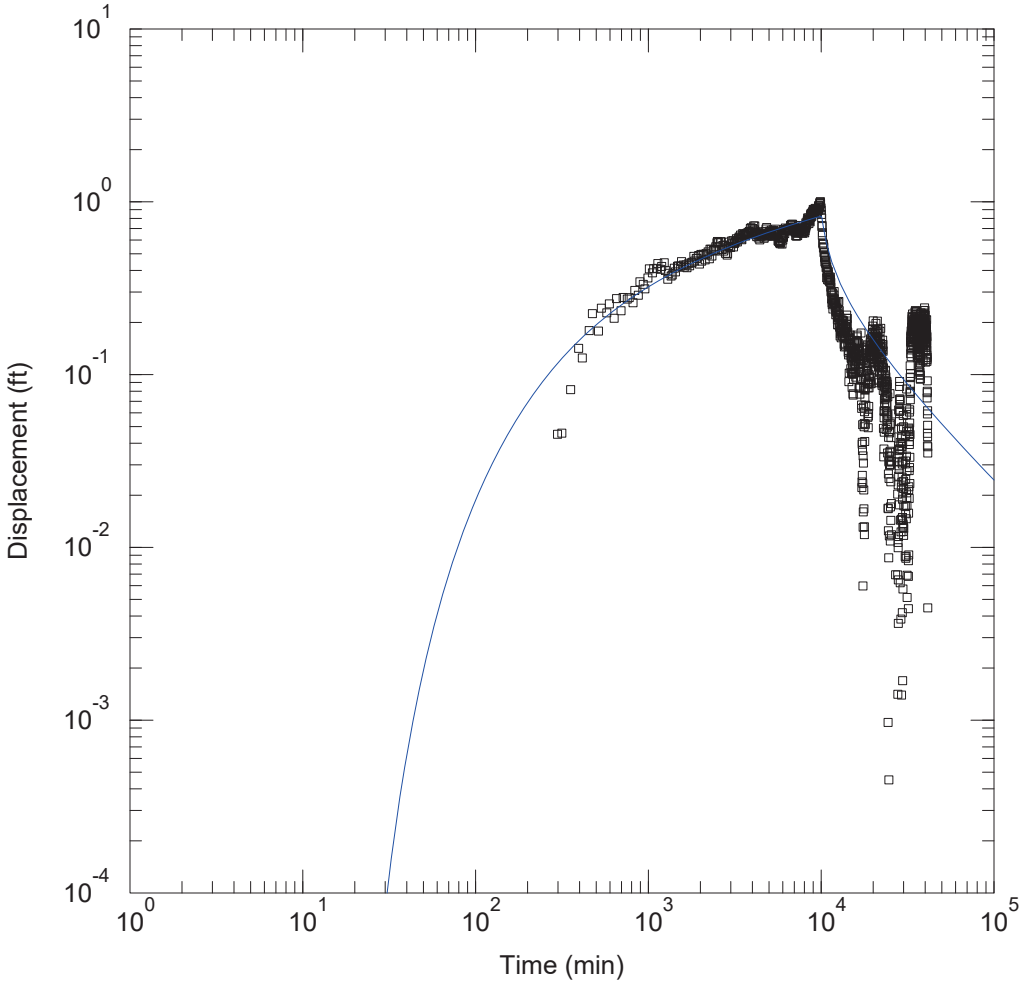

WELL TEST ANALYSIS

Data Set: D:\Projects\GRGID\modeling\aqtesolv\well6_test\revised\well6test_mw1_dd_neumanwitherspoon_v2.aqt
Date: 02/20/25 Time: 20:59:21

PROJECT INFORMATION

Company: DRI
Client: GRGID
Location: Gardnerville Ranchos
Test Well: Well 6
Test Date: 1/23/23 - 1/30/23

AQUIFER DATA

Saturated Thickness: 324. ft
Aquitard Thickness (b'): 1. ft
Anisotropy Ratio (Kz/Kr): 0.09175
Aquitard Thickness (b"): 1. ft

WELL DATA

Pumping Wells

Well Name	X (ft)	Y (ft)
Well 6	859869.6565	14143059.32

Observation Wells

Well Name	X (ft)	Y (ft)
MW-1	859252.5209	14143636.57

SOLUTION

Aquifer Model: Leaky
Solution Method: Neuman-Witherspoon

T = 3.311E+4 ft^2/day
1/B = 0.06028 ft^{-1}
T2 = 1.256E+4 ft^2/day

S = 0.002586
ß/r = 0.04822 ft^{-1}
S2 = 0.0004042

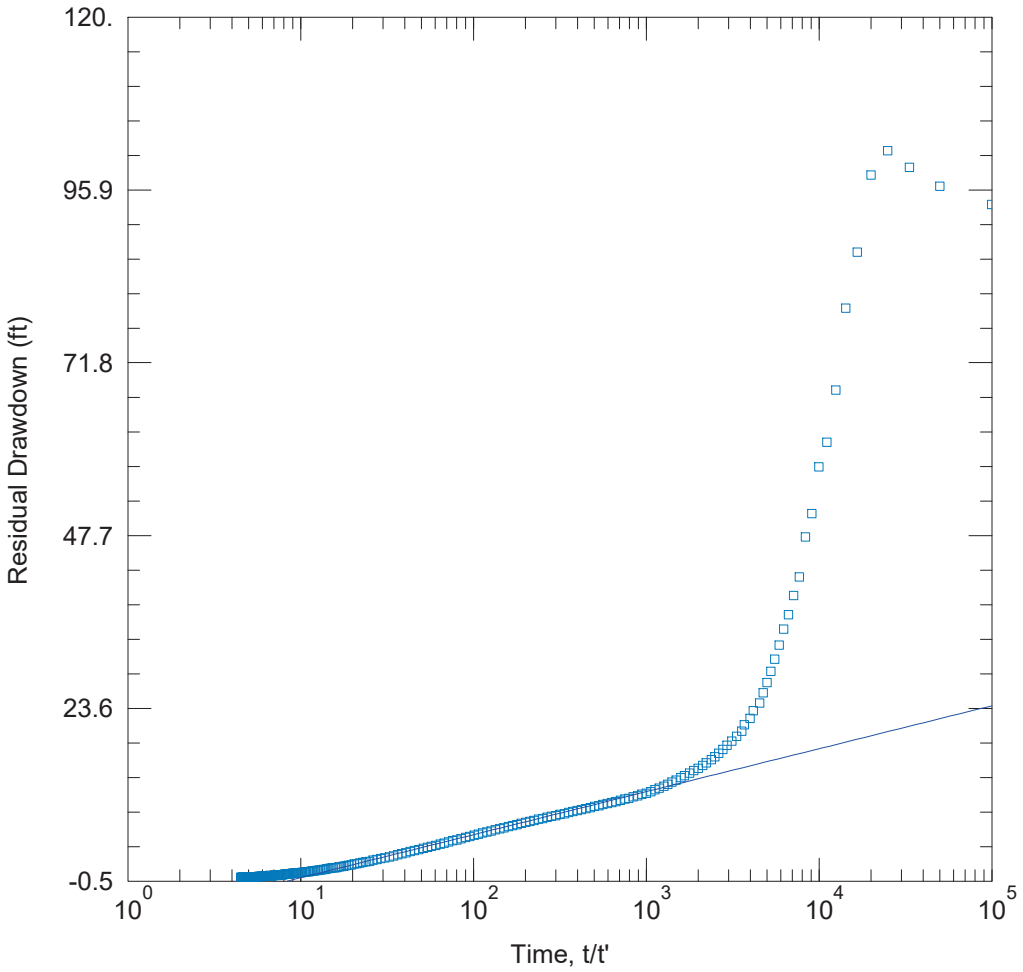

WELL TEST ANALYSIS

Data Set: D:\Projects\GRGID\modeling\aqtesolv\well6_test\well6test_well6_resdd.aqt
Date: 02/05/24 Time: 19:08:28

PROJECT INFORMATION

Company: DRI
Client: GRGID
Location: Gardnerville Ranchos
Test Well: Well 6
Test Date: 1/23/23 - 1/30/23

AQUIFER DATA

Saturated Thickness: 324. ft Anisotropy Ratio (Kz/Kr): 1.0E-5

WELL DATA

Pumping Wells

Well Name	X (ft)	Y (ft)
Well 6	859869.656	14143059.32

Observation Wells

Well Name	X (ft)	Y (ft)
Well 6	859869.656	14143059.32

SOLUTION

Aquifer Model: Confined Solution Method: Theis (Recovery)

T = 4089.8 ft^2/day S/S' = 10.09

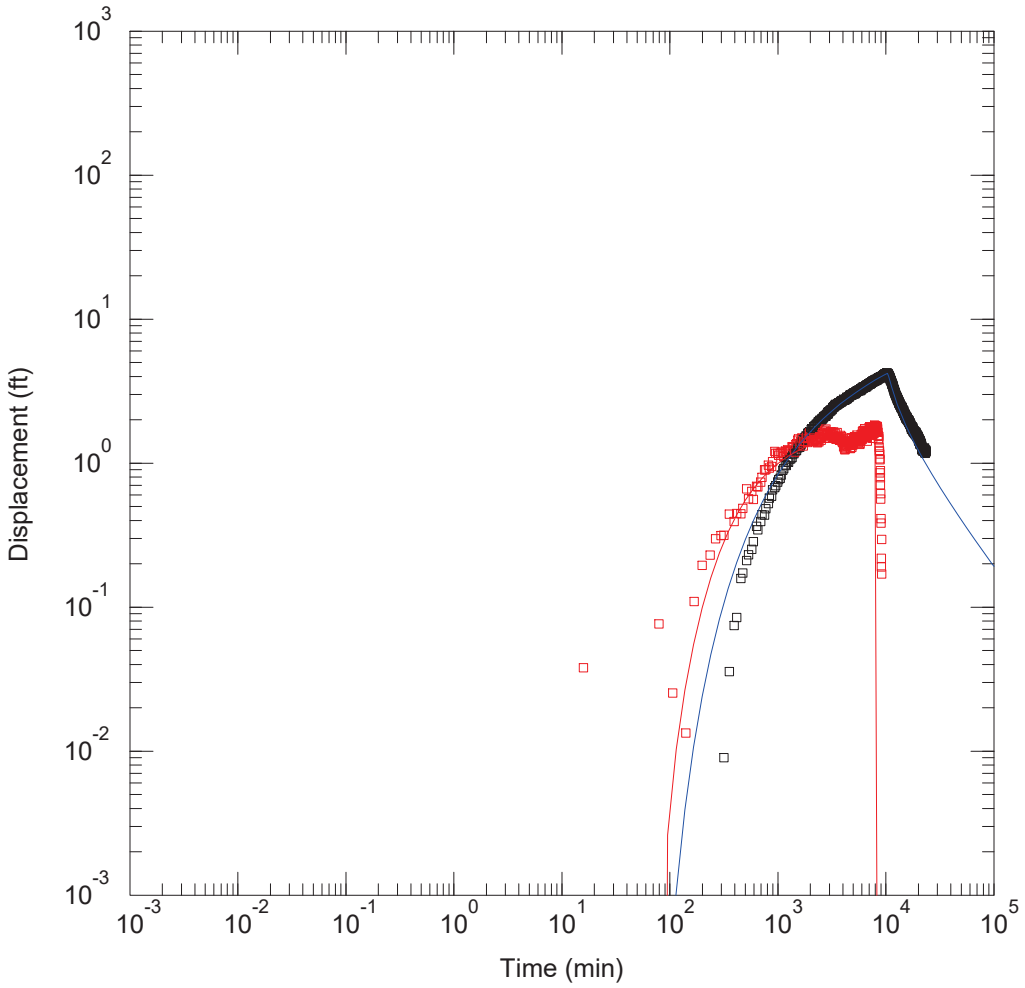

WELL TEST ANALYSIS

Data Set: D:\Projects\GRGID\modeling\aqtesolv\well8_test\well8test_dd_mw2_neumanwitherspoon_v2.aqt
Date: 02/05/24 Time: 12:22:19

PROJECT INFORMATION

Company: DRI
Client: GRGID
Location: Garnderville Ranchos
Test Well: Well 8
Test Date: 1/3/23 - 1/10/23

AQUIFER DATA

Saturated Thickness: 400. ft
Aquitard Thickness (b'): 1. ft
Anisotropy Ratio (Kz/Kr): 0.005506
Aquitard Thickness (b"): 1. ft

WELL DATA

Pumping Wells

Well Name	X (ft)	Y (ft)
Well 8	863049.0355	14144507.3

Observation Wells

Well Name	X (ft)	Y (ft)
MW2	862487.6916	14140968.92

SOLUTION

Aquifer Model: Leaky
Solution Method: Neuman-Witherspoon

T = 5319.5 ft^2/day
1/B = 0.0715 ft^{-1}
T2 = 2020.9 ft^2/day

S = 1.267E-5
ß/r = 0.09825 ft^{-1}
S2 = 0.0005437

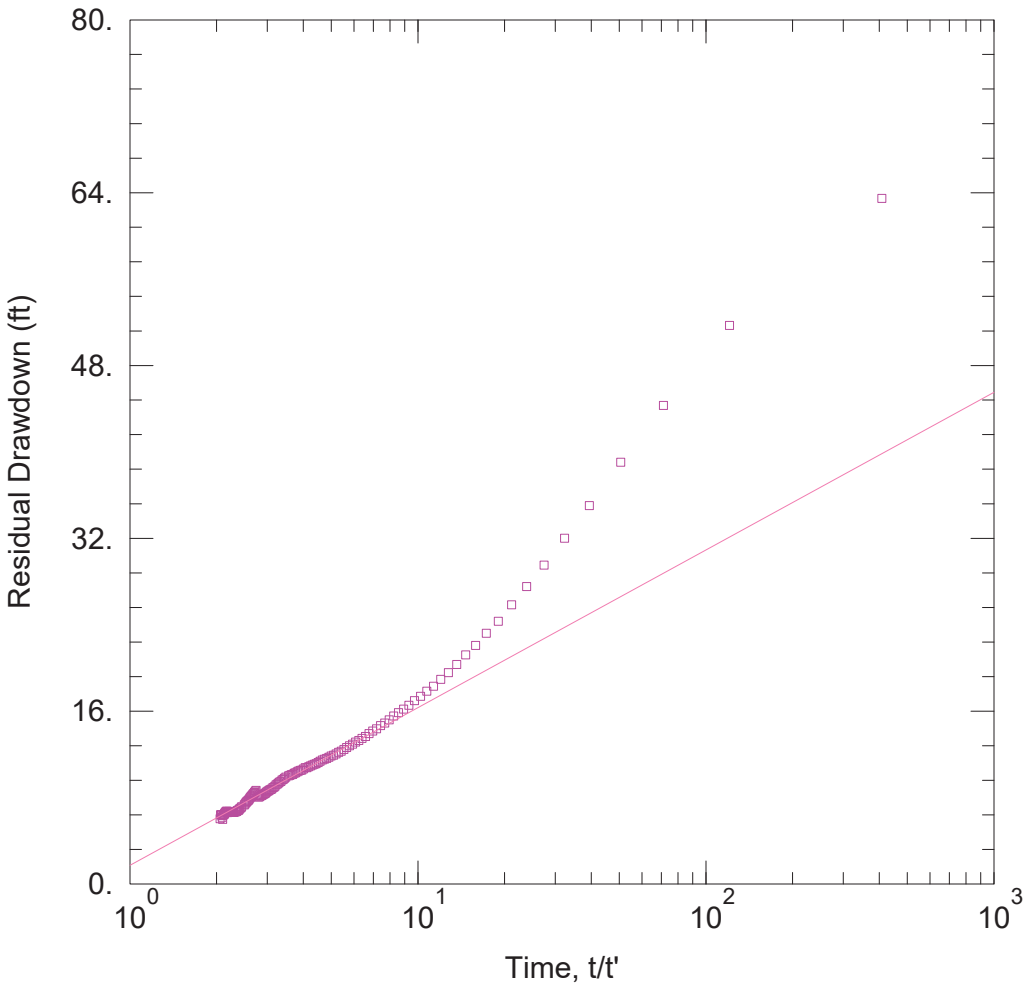

WELL TEST ANALYSIS

Data Set: D:\Projects\GRGID\modeling\aqtesolv\well8_test\well8test_well8_theis_recovery.aqt
Date: 10/31/23 Time: 15:52:29

PROJECT INFORMATION

Company: DRI
Client: GRGID
Location: Garnderville Ranchos
Test Well: Well 8
Test Date: 1/3/23 - 1/10/23

AQUIFER DATA

Saturated Thickness: 400. ft Anisotropy Ratio (Kz/Kr): 0.768

WELL DATA

Pumping Wells

Well Name	X (ft)	Y (ft)
Well 8	863049.0355	14144507.3

Observation Wells

Well Name	X (ft)	Y (ft)
Well 8	863049.0355	14144507.3

SOLUTION

Aquifer Model: Confined Solution Method: Theis (Recovery)

T = 2083.4 ft^2/day S/S' = 0.7618

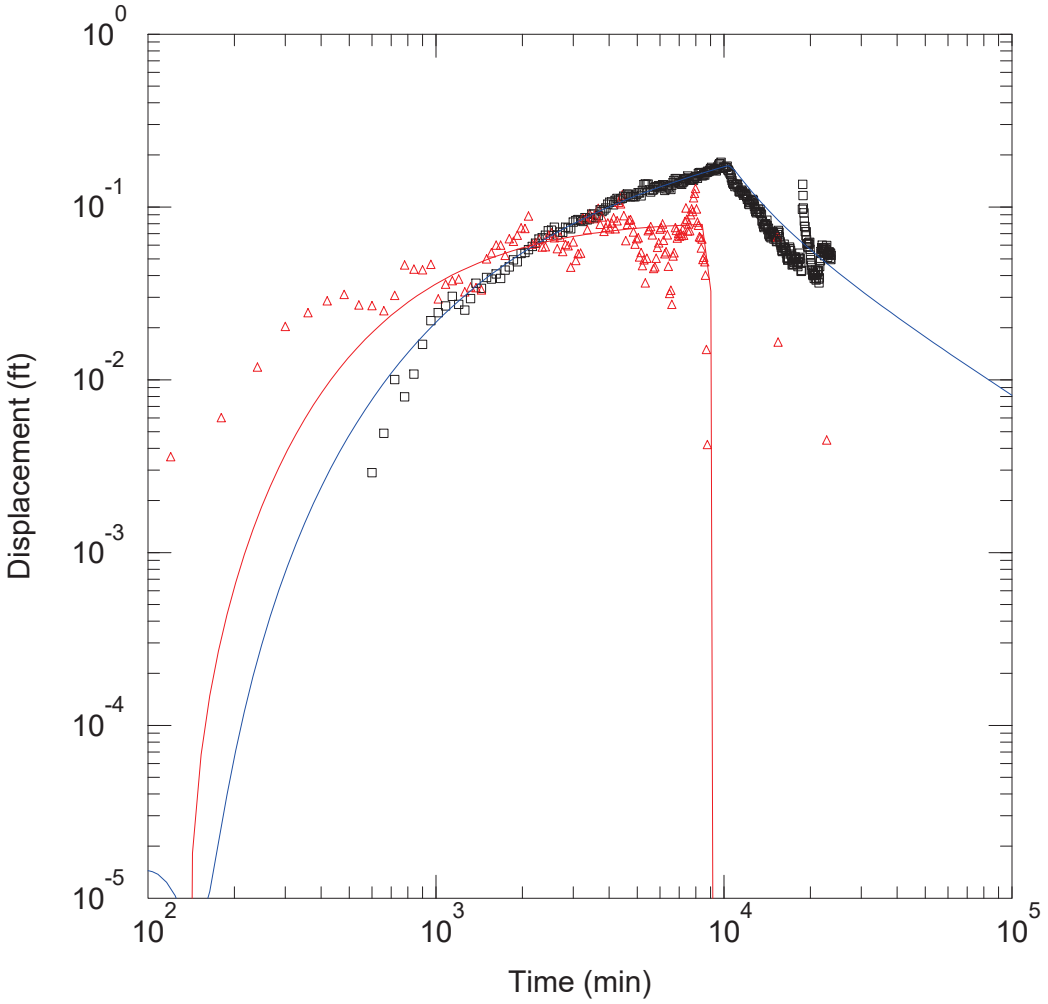

WELL TEST ANALYSIS

Data Set: D:\Projects\GRGID\modeling\aqtesolv\well9_test\well9_test_MW2Bing_dd_neumanwitherspoon.aqt
Date: 02/13/24 Time: 16:25:05

PROJECT INFORMATION

Company: DRI
Client: GRGID
Location: Garnderville Ranchos
Test Well: Well 5
Test Date: 3/29/22-4/4/22

AQUIFER DATA

Saturated Thickness: 315. ft
Aquitard Thickness (b'): 1. ft
Anisotropy Ratio (Kz/Kr): 1.
Aquitard Thickness (b"): 1. ft

WELL DATA

Pumping Wells

Well Name	X (ft)	Y (ft)
Well 9	855593.1842	14142654.9

Observation Wells

Well Name	X (ft)	Y (ft)
MW2_Bing	857021.0576	14138268.27

SOLUTION

Aquifer Model: Leaky
Solution Method: Neuman-Witherspoon

T = 8.407E+4 ft^2/day
1/B = 2.168E-9 ft^{-1}
T2 = 6.323E+5 ft^2/day
S = 0.01113
ß/r = 3.447E-5 ft^{-1}
S2 = 1.

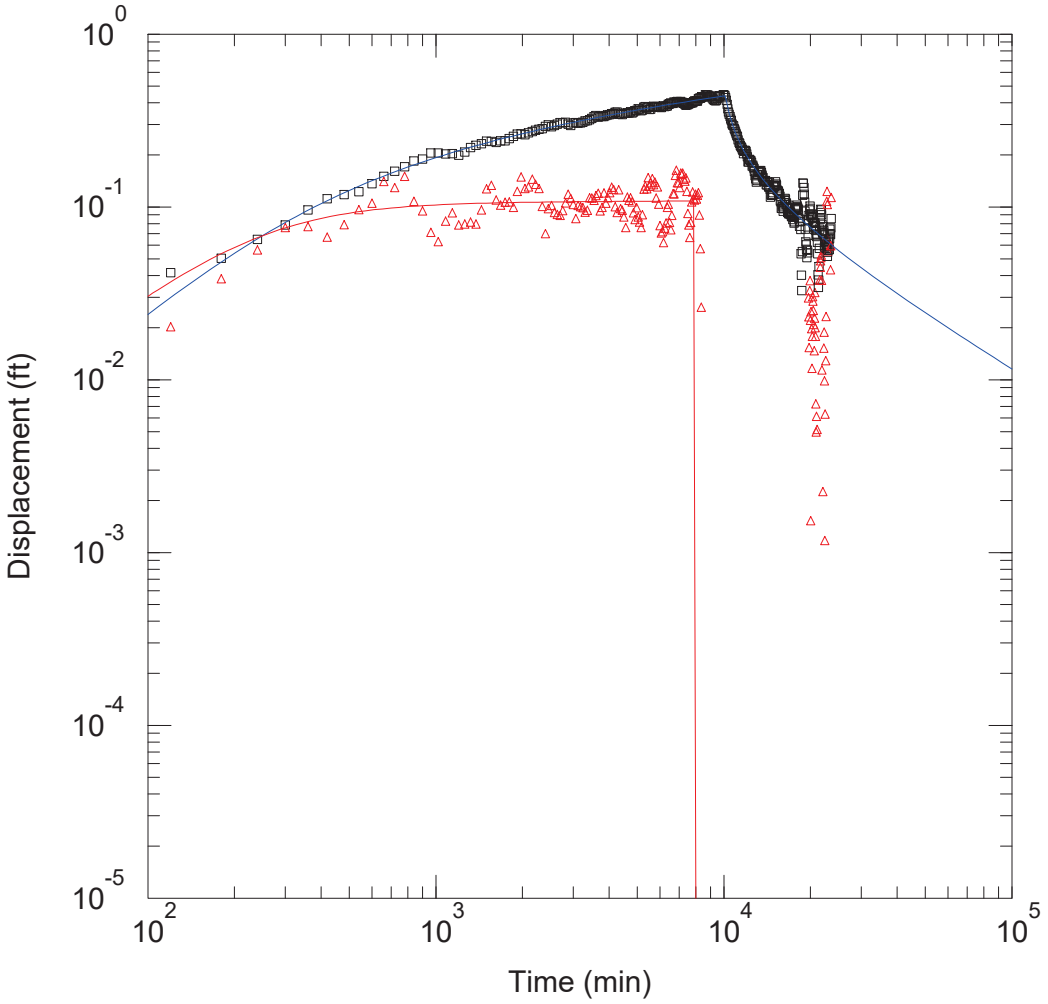

WELL TEST ANALYSIS

Data Set: D:\Projects\GRGID\modeling\aqtesolv\well9_test\well9_test_Sweetwater_dd_neumanwitherspoon.aqt
Date: 02/13/24 Time: 16:17:17

PROJECT INFORMATION

Company: DRI
Client: GRGID
Location: Garnderville Ranchos
Test Well: Well 5
Test Date: 3/29/22-4/4/22

AQUIFER DATA

Saturated Thickness: 315. ft
Aquitard Thickness (b'): 1. ft
Anisotropy Ratio (Kz/Kr): 1.
Aquitard Thickness (b"): 1. ft

WELL DATA

Pumping Wells

Well Name	X (ft)	Y (ft)
Well 9	855593.1842	14142654.9

Observation Wells

Well Name	X (ft)	Y (ft)
Sweetwater	857222.4684	14139938.87

SOLUTION

Aquifer Model: Leaky
Solution Method: Neuman-Witherspoon

T = 9569.6 ft^2/day
1/B = 0.002168 ft^{-1}
T2 = 9.965E+4 ft^2/day
S = 0.002126
ß/r = 0.0003508 ft^{-1}
S2 = 1.006E-10

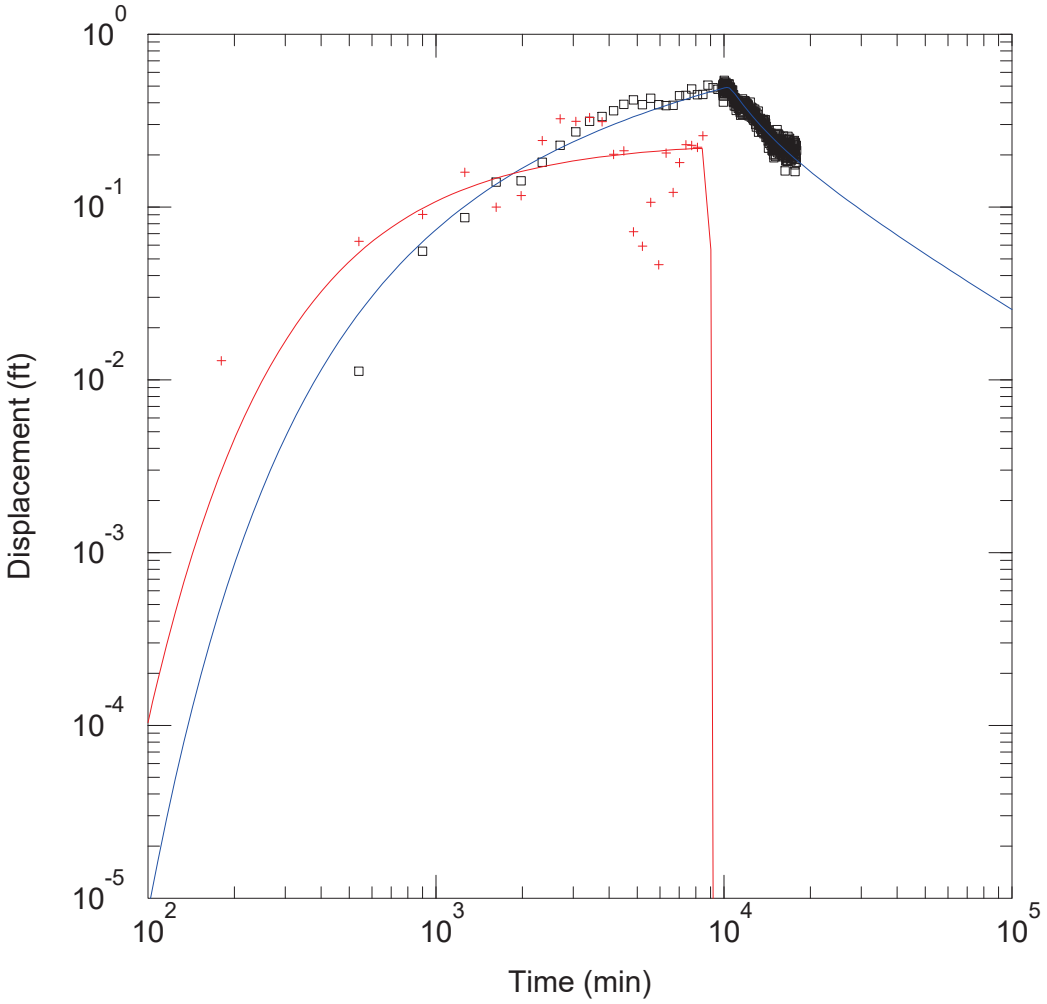

WELL TEST ANALYSIS

Data Set: D:\Projects\GRGID\modeling\aqtesolv\well9_test\well9_test_Well5.aqt
Date: 02/13/24 Time: 15:52:31

PROJECT INFORMATION

Company: DRI
Client: GRGID
Location: Garnderville Ranchos
Test Well: Well 5
Test Date: 3/29/22-4/4/22

WELL DATA

Pumping Wells

Well Name	X (ft)	Y (ft)
Well 9	855593.184	14142654.9

Observation Wells

Well Name	X (ft)	Y (ft)
Well 5	856665.845	14136595.44

SOLUTION

Aquifer Model: Confined
Solution Method: Theis

T = 4.91E+4 ft^2/day
S = 0.002916
Kz/Kr = 1.
b = 315. ft

STANDING DISTRIBUTION LIST

Greg Reed
District Manager
Gardnerville Ranchos General Improvement District
931 Mitch Drive
Gardnerville, NV 89460
agreed@grgid.com

Edwin James
General Manager
Carson Water Subconservancy District
777 E. William St., Suite 209
Carson City, NV 89703
edjames@cwsd.org

Nevada State Library and Archives
State Publications
100 North Stewart Street
Carson City, NV 89701-4285
NSLstatepubs@admin.nv.gov

Archives Getchell Library
University of Nevada, Reno
1664 N. Virginia St.
Reno, NV 89557
cklenke@unr.edu

Document Section, Library
University of Nevada, Las Vegas
4505 Maryland Parkway
Las Vegas, NV 89154
sue.wainscott@unlv.edu

†Library
Southern Nevada Science Center
Desert Research Institute
755 E. Flamingo Road
Las Vegas, NV 89119-7363

All on distribution list receive one PDF copy, unless otherwise noted.

---

† 2 copies; CD with pdf (from which to print)